

Novel Experimental and Analytical Concepts for the Characterization and Modeling of Soda-Lime Glass under Impact Conditions

Steffen Bauer

Vollständiger Abdruck der von der Fakultät für Bauingenieurwesen und Umweltwissenschaften der Universität der Bundeswehr München zur Erlangung des akademischen Grades

Doktor-Ingenieur (Dr.-Ing.)

genehmigten Dissertation.

Prüfungskommission:

Vorsitzender:	Univ.-Prof. Dr.-Ing. Geralt Siebert
Erstgutachter:	Prof. Dr.-Ing. habil. Stefan Hiermaier
Zweitgutachter:	Prof. Dr.-Ing. habil. Norbert Gebbeken
Externer Gutachter:	Prof. Nik Petrinic Dipl.-Ing. Ph.D. M.A.

Die Dissertation wurde am 10. Juni 2021 bei der Universität der Bundeswehr München eingereicht und durch die Fakultät für Bauingenieurwesen und Umweltwissenschaften am 2. November 2021 angenommen. Die mündliche Prüfung fand am 23. November 2021 statt.

Universität der Bundeswehr München
Fakultät für Bauingenieurwesen und Umweltwissenschaften

Thesis: Novel Experimental and Analytical Concepts for the Characterization and Modeling of Soda-Lime Glass under Impact Conditions

Author: Steffen Bauer

Board of examiners:

Chairman: Univ.-Prof. Dr.-Ing. Geralt Siebert

First examiner: Prof. Dr.-Ing. habil. Stefan Hiermaier

Second examiner: Prof. Dr.-Ing. habil. Norbert Gebbeken

External examiner: Prof. Nik Petrinic Dipl.-Ing. Ph.D. M.A.

Academic degree acquired by this dissertation: Doctor of engineering, Dr.-Ing.

Freiburg, December 06, 2021

Abstract

The objective of this thesis is to improve the predictive power of existing numerical simulation models of soda-lime glass (SLG), with the focus on highly dynamic impact scenarios. To achieve this goal, new characterization and analysis methods are developed. Furthermore, the new results are used to modify and improve an existing literature model.

Although the first academic works on the ballistic properties of glass date back over 90 years, certain issues are still unclear that are crucial to the material behavior of SLG in ballistic impact scenarios. One of the most important issues is the lack of experimental data characterizing the residual strength as a function of the degree of damage. Another important aspect is the determination of the equation of state (EOS) and the Hugoniot Elastic Limit (HEL). Both issues are addressed in this thesis by new experimental and evaluation methodologies.

Within the framework of this work, several novel methodologies for the characterization and modeling of SLG are developed and applied. Several experimental test series are designed and carried out covering quasi-static as well as highly dynamic loading rates. In addition, advanced analysis concepts are developed, which are supported by numerical simulations.

The first part of this work is focused on the characterization of the material properties under shock loading. An extensive planar plate impact (PPI) test series is carried out to determine the Shock Hugoniot, the HEL and the EOS of SLG. In addition, new insights into the failure front phenomena are obtained by means of a novel high-speed video observation setup. Several results of this test series have been pre-published by the author in [A1].

An incremental analysis concept is developed and applied to evaluate the PPI data. The validity of the concept is investigated by a simulation study. Furthermore, a novel error analysis approach is carried out for the determination of the Shock Hugoniot and the HEL. As a result, the Shock Hugoniot is determined for longitudinal compressive stresses of up to 20.8 GPa. Especially noteworthy are the derived Shock Hugoniot and the EOS, which clearly differ from reported literature data. In order to investigate the discrepancies, a selection of reported velocity profiles is digitized and analyzed using the derived analysis concept.

For the detailed investigation of the failure fronts, a novel methodology is developed, which includes a “streak analysis” of the high-speed videos. These results are combined with the laser interferometry results in a new way. Lagrange diagrams are created that allow for an in-depth investigation of the failure front properties.

The second part of this work is focused on the characterization of the shear strength of SLG. This includes both the strength of intact material at high pressures and the residual strength of pre-damaged SLG. A novel test methodology is developed to dynamically generate different degrees of pre-damage in small SLG cylinders. For this purpose, the cylinders are loaded by a plane stress wave, initiated by the impact of an aluminum plate at a defined velocity. This is done in a new way: the SLG is damaged dynamically by a shock wave while being completely confined by a demountable aluminum confinement. The confinement holds the SLG fragments in place, which are generated during the pre-damaging. This is essential, since the residual strength of the specimen strongly depends on the friction between the fragments. The residual strength is considerably higher if all fragments are kept in place and are “interlocking”, in contrast to a loose accumulation of fragments similar to e.g. rough gravel. In order to ensure that the fragments are kept in place in the subsequent characterization tests, a thin aluminum sleeve is retained around the SLG cylinder even after removing the demountable confinement.

This concept turns out to be a significant improvement in comparison to the characterization tests of previous studies, which used loosely poured glass quartz powder or granular silica sand.

A further significant improvement compared to previous studies is the contact-free investigation of the pre-damage prior to the measurement of the residual strength. An extensive CT test series is carried out in order to analyze and quantify the crack volume in the pre-damaged SLG cylinders. X-ray CT scans are conducted at two different facilities, at a micro-CT device of the Ernst-Mach-Institut and at the synchrotron of the Paul Scherrer Institut.

For the identification of the crack volume, a software tool developed by the Australian National University is used. Utilizing the advanced 3D image processing and segmentation techniques of the software, an analysis method for the SLG specimens is developed. As a result, the pre-damage of selected specimens is quantified and parameterized.

The residual strength of pre-damaged and categorized specimens is subsequently characterized in confined triaxial compression tests. These tests are an enhancement of experimental techniques reported in previous studies. One new aspect is that the steel confinement is replaced in most tests by a tungsten carbide confinement. This has the advantage that the occurring radial deformation of the SLG specimens is more limited. In addition, the loading of the tungsten carbide confinement can be regarded to be elastic since exceeding its elastic limit would result in brittle fracture. A second new aspect is that the experiments were supported by an elaborated simulation study. The results of the simulations allow accounting for the influence of friction and the effects of the detailed test setup. Additional tests on low-strength polyurethane specimens are conducted to verify the analysis methods.

As a result, new yield curves of SLG are obtained, which are functions of the hydrostatic pressure and the degree of initial pre-damage. The determined model parameters are especially suited for the simulation of ballistic impact scenarios, since the characterized pre-damaged SLG is representative for the damaged transparent armor in front of a bullet during impact.

In summary, the novel methodology developed within the second part of this work allows determining several yield curves that are dependent on the degree of initial damage. The results extend the available literature data in four ways. First, the pre-damage is created dynamically by means of defined PPI tests instead of a thermal shock. This allows a drastic increase of the degree of pre-damage, which represents the damage in front of a ballistic projectile more closely. Second, for the first time, the degree of pre-damage is directly measured and quantified using a novel X-ray CT analysis. Third, different yield curves for different degrees of pre-damage are determined. Finally, the resulting yield curve for entirely failed SLG is significantly different from curves that are used by other authors in constitutive models.

In the final part of this work, a new simulation concept is developed, which is based on the implementation of the novel results into a constitutive material model. A two-dimensional, axisymmetric model approach based on the Johnson-Holmquist-2 (JH2) model is chosen for this purpose. However, it is important to note that the concept is generally neither restricted to the JH2 model nor to the two-dimensional approach.

The new concept includes the implementation of the EOS found in the present work as well as the development of an improved strength model based on the new yield curves. In addition, a novel approach is developed that enables a coupling of the damage model to the experimentally observed damage. For this purpose, the improved model is utilized to reproduce the pre-damaging PPI tests.

This direct calibration of the damage model is a significant improvement, since in previous studies, these parameters had to be deduced simultaneously with several other parameters by matching the depth of penetration of experiments with long rods penetrating SLG laminates.

The performance of the improved SLG model is investigated in a representative ballistic impact scenario. It is demonstrated that the model represents an improvement for the investigated ballistic scenario.

Finally, it is noteworthy that the novel test and analysis methods are not restricted to the characterization of SLG only. In principle, most new concepts are suited to be applied to other materials, like ceramics, rocks or even high-strength steels. Especially for materials that do not exhibit a shock response with a clear two-wave structure, the incremental analysis represents an improvement to common analysis methods. Furthermore, the methodology of characterizing the residual strength of quantitatively pre-damaged specimens is also expected to be generally applicable to other brittle materials.

Kurzfassung

Das Ziel dieser Doktorarbeit ist es, die Prognosefähigkeit bestehender numerischer Simulationsmodelle von Kalknatronglas (SLG) zu verbessern, insbesondere im Hinblick auf hochdynamische Impaktszenarien. Um dieses Ziel zu erreichen, werden neue Charakterisierungs- und Analysemethoden entwickelt. Darüber hinaus werden die neuen Ergebnisse verwendet, um ein bestehendes Literaturmodell zu modifizieren und zu verbessern.

Obwohl die ersten wissenschaftlichen Arbeiten zu den ballistischen Eigenschaften von Glas über 90 Jahre zurückreichen, sind einige grundlegende Fragen immer noch ungeklärt, die für das Materialverhalten von SLG in ballistischen Impaktszenarien entscheidend sind. Einer der wichtigsten Punkte ist der Mangel an experimentellen Daten, die die Restfestigkeit in Abhängigkeit vom Schädigungsgrad charakterisieren. Ein weiterer wichtiger Aspekt ist die Bestimmung der Zustandsgleichung (EOS) und des Hugoniot Elastic Limit (HEL). Beide Fragestellungen werden in dieser Arbeit durch neue Experimente und Evaluationsmethoden adressiert.

Im Rahmen dieser Arbeit werden mehrere neuartige Methoden zur Charakterisierung und Modellierung von SLG entwickelt und angewendet. Es werden mehrere experimentelle Versuchsreihen konzipiert und durchgeführt, die sowohl quasistatische als auch hochdynamische Verzerrungsraten abdecken. Darüber hinaus werden verbesserte Analysekonzepte entwickelt, bei welchen numerische Simulationenmethoden miteinbezogen werden.

Der erste Teil dieser Arbeit beschäftigt sich mit der Charakterisierung der Materialeigenschaften unter Stoßbelastung. Zur Ermittlung der Shock Hugoniot, des HEL und der EOS von SLG wird eine umfangreiche Planar-Platten-Impakt-Versuchsreihe (PPI) durchgeführt. Darüber hinaus werden durch einen neuartigen Versuchsaufbau mit Hochgeschwindigkeits-Videokameras neue Erkenntnisse zum Phänomen der „Failure Front“ gewonnen. Mehrere Ergebnisse dieser Versuchsreihe wurden vom Autor bereits in [A1] veröffentlicht.

Zur Auswertung der PPI-Daten wird ein inkrementelles Analysekonzept entwickelt und angewendet. Die Validität des Konzepts wird durch eine Simulationsstudie untersucht. Darüber hinaus wird eine neuartige Fehlerbetrachtung zur Bestimmung der Shock Hugoniot und des HEL durchgeführt. Hierdurch wird die Shock Hugoniot für Drucklängsspannungen von bis zu 20,8 GPa bestimmt.

Besonders hervorzuheben sind die resultierende Shock Hugoniot und die EOS, die sich deutlich von veröffentlichten Literaturdaten unterscheiden. Um die Abweichungen zu untersuchen, wird eine Auswahl von Literatur-Geschwindigkeitsprofilen digitalisiert und mit dem entwickelten Analysekonzept ausgewertet.

Zur detaillierten Untersuchung der „Failure Fronts“ wird eine neuartige Methodik entwickelt, die eine „Streak-Analyse“ der Highspeed-Videos beinhaltet. Diese Ergebnisse werden auf neue Weise mit den Ergebnissen der Laserinterferometrie kombiniert. Es werden Lagrange-Diagramme erstellt, die eine detaillierte Untersuchung der „Failure Front“-Eigenschaften ermöglichen.

Der zweite Teil dieser Arbeit beschäftigt sich mit der Charakterisierung der Scherfestigkeit von SLG. Dies beinhaltet sowohl die Festigkeit von intaktem Material bei hohen Drücken, als auch die Restfestigkeit von vorgeschädigtem SLG. Es wird eine neuartige Versuchsmethodik entwickelt, um dynamisch unterschiedliche Vorschädigungsgrade in kleinen SLG-Zylindern zu erzeugen. Dazu werden die Zylinder durch eine ebene Spannungswelle belastet, die durch den

Aufprall einer Aluminiumplatte mit definierter Geschwindigkeit ausgelöst wird. Dies geschieht auf neue Weise: Das SLG wird durch eine Stoßwelle dynamisch geschädigt, während es vollständig von einem zerlegbaren Aluminiumgehäuse verdammt wird. Die Verdämmung verhindert ein Auseinanderbrechen der erzeugten SLG-Fragmente. Dies ist zwingend erforderlich, da die Restfestigkeit der Probe stark von der Reibung zwischen den Bruchstücken abhängt. Die Restfestigkeit ist wesentlich höher, wenn alle Bruchstücke an Ort und Stelle gehalten werden und „ineinandergreifen“, im Gegensatz zu einer lockeren Anhäufung von Fragmenten wie z.B. bei grobem Kies. Um ein Auseinanderbrechen der geschädigten SLG-Proben bei den nachfolgenden Charakterisierungsversuchen zu verhindern, bleiben die Proben nach dem Entfernen des zerlegbaren Aluminiumgehäuses von einer dünnen Aluminiumhülse umschlossen. Dieses Konzept erweist sich als deutliche Verbesserung im Vergleich zu den Charakterisierungsversuchen früherer Studien, bei denen beispielsweise lose geschüttetes Quarzpulver oder körniger Quarzsand verwendet wurden.

Eine weitere deutliche Verbesserung gegenüber früheren Studien ist die kontaktfreie Untersuchung der Vorschädigung vor der Messung der Restfestigkeit. Zur Analyse und Quantifizierung des Rissvolumens in den vorgeschädigten SLG-Zylindern wird eine umfangreiche CT-Versuchsreihe durchgeführt. Hierzu werden Röntgen-CT-Aufnahmen an zwei verschiedenen Anlagen und Einrichtungen erzeugt, an einem Mikro-CT-Gerät des Fraunhofer Ernst-Mach-Instituts und am Synchrotron des Paul Scherrer Instituts.

Zur Ermittlung des Rissvolumens wird ein von der Australian National University entwickeltes Softwaretool verwendet. Unter Verwendung der fortschrittlichen 3D-Bildverarbeitungs- und Segmentierungstechniken der Software wird eine Analysemethode für die SLG-Proben entwickelt. Als Ergebnis wird die Vorschädigung ausgewählter Proben quantifiziert und parametrisiert.

Die Restfestigkeit vorgeschädigter und kategorisierter Proben wird anschließend in verdämmten, triaxialen Druckversuchen charakterisiert. Diese Versuche stellen eine Verbesserung der experimentellen Techniken anderer wissenschaftlicher Studien dar. Neu ist, dass in den meisten Versuchen die Stahlverdämmung durch eine Wolframkarbiverdämmung ersetzt wird. Dies hat den Vorteil, dass die auftretende radiale Verformung der SLG-Proben stärker eingeschränkt wird. Außerdem kann die Belastung der Wolframkarbidverdämmung als elastisch angesehen werden, da eine Überschreitung der Elastizitätsgrenze zu einem Sprödbbruch führen würde. Ein zweiter neuer Aspekt ist, dass die Experimente durch eine umfangreiche Simulationsstudie unterstützt wurden. Die Ergebnisse der Simulationen erlauben es, den Einfluss der Reibung und die Auswirkungen des komplexen Versuchsaufbaus zu berücksichtigen. Zur Validierung der Analysemethoden werden zusätzliche Versuche an Polyurethan-Proben mit geringer Festigkeit durchgeführt.

Als Ergebnis werden neue Fließkurven von SLG ermittelt, die vom hydrostatischen Druck und dem Grad der anfänglichen Vorschädigung abhängig sind. Die ermittelten Modellparameter eignen sich besonders für die Simulation ballistischer Impaktszenarien, da das charakterisierte, vorgeschädigte SLG repräsentativ ist für die geschädigte transparente Panzerung, in die das Projektil eindringt.

Zusammenfassend ermöglicht die im zweiten Teil dieser Arbeit entwickelte, neuartige Methodik, die Ermittlung von mehreren schädigungsabhängigen Fließkurven. Die Ergebnisse erweitern die verfügbaren Literaturdaten in vierfacher Hinsicht. Erstens wird die Vorschädigung dynamisch durch definierte PPI-Tests anstelle eines thermischen Schocks erzeugt. Dies ermöglicht eine signifikante Erhöhung des Vorschädigungsgrades, sodass die Schädigung vor einem ballistischen Geschoss besser repräsentiert wird. Zweitens wird erstmals der Grad der Vorschädigung mit

einer neuartigen Röntgen-CT-Analyse direkt gemessen und quantifiziert. Drittens werden unterschiedliche Fließkurven für unterschiedliche Vorschädigungsgrade ermittelt. Viertens unterscheidet sich die resultierende Fließkurve von vollständig versagtem SLG deutlich von Kurven, die von anderen Autoren in konstitutiven Modellen verwendet werden.

Im letzten Teil dieser Arbeit wird ein neues Simulationskonzept entwickelt, welches eine Implementierung der neuen Ergebnisse in ein konstitutives Materialmodell ermöglicht. Dazu wird ein zweidimensionaler, axialsymmetrischer Modellansatz basierend auf dem Johnson-Holmquist-2-Modell (JH2) gewählt. Allerdings ist das Konzept im Allgemeinen weder auf das JH2-Modell noch auf den zweidimensionalen Ansatz beschränkt.

Das neue Konzept beinhaltet die Implementierung der neuen EOS sowie die Entwicklung eines verbesserten Festigkeitsmodells basierend auf den neuen Fließkurven. Darüber hinaus wird ein neuartiger Ansatz entwickelt, der eine Kopplung des Schädigungsmodells an den experimentell beobachteten Schädigungsgrad ermöglicht. Zu diesem Zweck werden mit dem verbesserten Modell die PPI-Tests reproduziert, mit welchen die Vorschädigung erzeugt wird.

Diese direkte Kalibrierung des Schädigungsmodells stellt eine signifikante Verbesserung dar, da in früheren Studien die Schädigungsparameter gleichzeitig mit mehreren anderen Parametern abgeleitet werden mussten. Die Kalibration erfolgte in den Literaturmodellen durch Abgleich der Eindringtiefen bei Experimenten mit langen Stabprojektilen, die in SLG-Laminaten eindrangen.

Die Prognosefähigkeit des verbesserten SLG-Modells wird in einem repräsentativen ballistischen Impaktszenario untersucht. Es wird gezeigt, dass sich die Simulationsergebnisse für das untersuchte ballistische Szenario mit dem neuen Modell signifikant verbessern.

Abschließend ist zu erwähnen, dass die neuartigen Test- und Analysemethoden nicht nur auf die Charakterisierung von SLG beschränkt sind. Grundsätzlich eignen sich die meisten neuen Konzepte auch für andere Werkstoffe wie Keramik, Gestein oder sogar hochfeste Stähle. Insbesondere bei Materialien, die kein Stoßverhalten mit deutlicher Zweiwellenstruktur aufweisen, stellt die inkrementelle Analyse eine Verbesserung gegenüber gängigen Analysemethoden dar. Darüber hinaus ist davon auszugehen, dass die Methodik zur Charakterisierung der Restfestigkeit von quantitativ vorgeschädigten Proben prinzipiell auch auf andere spröde Materialien angewendet werden kann.

Contents

1	Introduction	1
1.1	Motivation	1
1.2	Material characterization of soda-lime glass - current state of science	5
1.2.1	Chemical composition, elastic constants and the Hugoniot elastic limit	5
1.2.2	Failure and fracture propagation	7
1.2.3	Strength of intact and failed glass	11
1.2.4	Current issues and shortcomings	16
1.3	Objectives and layout of the thesis	20
2	Continuum mechanical basics	21
2.1	Stress and strain tensors	21
2.2	Elasticity, plasticity, failure and damage	26
2.2.1	Elasticity	26
2.2.2	Plasticity	27
2.2.3	Failure and damage	32
2.3	Wave theory	34
2.3.1	Classification of waves	35
2.3.2	Shock waves	36
2.4	Equation of state	43
3	Numerical modeling of soda-lime glass	49
3.1	Basics of hydrocodes	49
3.1.1	Discretization of the governing equations	49
3.1.2	The finite difference method	51
3.1.3	The finite element method	53
3.1.4	Differences and similarities between FEM and FDM	55
3.2	Numerical approaches for modeling soda-lime glass	55
3.2.1	Molecular dynamical models	55
3.2.2	Explicit crack propagation models	56
3.2.3	Continuum-mechanical models	56

4 Characterization of soda-lime glass under dynamic loading by means of novel PPI tests and an advanced analysis.....61

4.1	Derivation of an incremental analysis for planar plate impact tests.....	61
4.1.1	Concept of an “incremental analysis”	61
4.1.2	Derivation of the selective analysis as a special case of the incremental analysis ..	64
4.1.3	Numerical evaluation of the “incremental analysis” concept.....	66
4.1.4	Error estimation of the incremental analysis concept.....	70
4.2	Experimental setup.....	75
4.2.1	Conduction of planar plate impact tests.....	75
4.2.2	Velocity measurement systems	78
4.2.3	Setup for high-speed videos.....	80
4.3	Experimental results.....	81
4.3.1	New insights into the failure front phenomena	83
4.3.2	Incremental analysis of the loading paths.....	98
4.3.3	Derivation of an equation of state for soda-lime glass.....	103
4.4	Discussion of the planar plate impact results	110

5 Development of a novel methodology for generating, characterizing and pressure testing of defined damaged glass specimens.....115

5.1	Introduction.....	115
5.2	Generation of damaged glass specimens	115
5.2.1	Experimental setup.....	116
5.2.2	Experimental results	120
5.3	Characterization of damage by means of X-ray micro-CT and phase-contrast imaging 127	
5.3.1	Principles of the CT methods	127
5.3.2	Experimental facilities	128
5.3.3	Image processing and analysis of cracks.....	131
5.4	Pressure testing of intact and damaged soda-lime glass specimens.....	166
5.4.1	Experimental setup.....	166
5.4.2	General analysis considerations	169
5.4.3	Development of advanced analysis methods of confined compression tests using quasi-static numerical simulations	173
5.4.4	Experimental results	182
5.5	Discussion of the characterization results of defined damaged soda-lime glass.....	197

6	Development and application of an improved strength model for soda-lime glass.....	203
6.1	Formulation of an improved strength model.....	203
6.2	Coupling of the experimental and the simulative degree of damage.....	206
6.3	Performance of the improved model in an impact scenario	211
6.4	Comparison of new results with the original JH2 model and experimental data	219
7	Summary	225
8	Bibliography.....	231
9	Appendix.....	247
9.1	Transformation equation for the shock wave velocity.....	247
9.2	Material models used in Autodyn.....	248
9.3	Additional Lagrange diagrams	251
9.4	Loading path analysis diagrams for each PPI test.....	252
9.5	Incremental analysis of literature data	258
9.6	Influence of the CAC separation parameters	260
9.7	Compilation of all X-ray CT results of pre-damaged SLG cylinders.....	266
10	Notation and abbreviations	273
11	Acknowledgments	283

1 Introduction

1.1 Motivation

Silica-based glasses are a well-established material used as main component of windowpanes. The most prevalent type of glass is soda-lime glass (SLG), since it is relatively inexpensive and simple to manufacture. Despite its brittle nature, it can be well suited also as main component of a transparent armor. For example, bonding together several sheets of glass with transparent polymer layers significantly increases the resistance to ballistic threats. These “glass laminates”, used as vehicle windshields or windows in buildings, can withstand low-velocity impacts without shattering. A typical low-velocity impact is for example wind-borne debris impacting with a velocity in the order of 30 m/s to 50 m/s. Moreover, if the thickness of the glass laminate is thick enough, it can even withstand fragments or rifle bullets impacting with high velocities in the order of up to 1000 m/s.

The continuous enhancement of ballistic threats places increasing demands on the protective capabilities of the transparent armor systems. Especially for the use in military vehicles, the improvement of the armor is challenging due to strong restrictions on the available space and weight. In order to further enhance the transparent armor and support the development of new designs, it is essential to understand the response of SLG to dynamic impact. However, this objective cannot be achieved by means of a purely experimental approach since the material behavior is very complex. Instead, it is more efficient to use a combination of ballistic tests and numerical simulations. For the simulations, constitutive material models are needed describing the material behavior under various loading conditions. In order to set up and calibrate these models, basic characterization experiments with various, defined loading conditions are required.

The first academic works on the ballistic properties of glass date back over 90 years. For example, Preston published a study on the interaction of a bullet with a sheet of glass [1] already in 1927. Since then, much progress has been made in analyzing the material behavior of SLG. Major contributions were made by Schardin, who developed high-speed measurements techniques and investigated e.g. the propagation of stress waves and cracks in glass plates by means of Schlieren photography and shadowgraph imaging [2] [3].

Today, it is well established that the mechanical response of glass is significantly different under quasi-static and highly dynamic deformation rates (e.g. [4] [5] [6] [7]). On the one hand, SLG typically fails by the propagation of only a few discrete cracks, when loaded quasi-statically. On the other hand, a large number of micron- and sub-micron-size cracks is generated under dynamic loading. This results in a substantially larger degree of damage and comminution. In both cases, however, the cracks are presumably emerging from pre-existing flaws [8]. These flaws are typically small surface cracks ($\leq 20 \mu\text{m}$) introduced during the manufacturing or finishing process [9].

Developing models for brittle materials has been the focus of many studies since the work of Wilkins et al. [10], who investigated the ballistic penetration of ceramics. Important insights into the dynamic material behavior of SLG can also be inferred from the analysis of ceramics, since both types of materials exhibit similar brittle failure mechanics. Dandekar et al. [11] investigated the behavior of alumina ceramic under highly dynamic impact loading. They concluded that the impact process can be divided into four phases:

1. During the first few microseconds after impact, shock waves are induced in the projectile and the target generating large pressures. These shock waves are gradually attenuated as they propagate but can significantly alter the properties of the material ahead of the projectile.
2. In the second phase, the kinetic energy of the projectile is imparted to the target in a hydrodynamic manner. This means, that the densities and compressibilities of the materials as well as the velocity and the dimensions of the projectile govern the penetration process. Strength effects are negligible as long as the projectile velocity is high enough.
3. The third phase is initiated after the projectile is completely deformed and brought to rest. During this cavitation phase, shear deformation takes place parallel to the walls of the expanding penetration tunnel. At the same time, projectile and target fragments are ejected from the impact crater.
4. In the last phase, a contraction of the cavity/crater takes place. Here, brittle fracture of the crater surface may occur. In addition, materials beneath the crater surface can anneal and recrystallize.

For SLG, the development of the failure during an impact process was investigated in 1989 by Chaudhri et al. [12]. They reported that the failure process is complex, including radial cracking, ring cracking and the development of a fracture conoid. They further observed a comminuted region of SLG ahead of the projectile containing particulates and powder. Mescall et al. previously deduced the existence of such a highly stressed and finely comminuted volume from computations [13] [14]. This so-called Mescall zone was later also observed in impact tests and simulations with silicon carbide ceramic [15] [16]. Chocron et al. [17] concluded that although the material is failed, it is kept in place by inertia and by the confining intact material. Moreover, its elastic constants (Young's modulus, Poisson's ratio, etc.) are almost unchanged.

A penetrating projectile is therefore not in direct contact with intact material but instead with pre-damaged, failed material. This was investigated for several glasses and ceramics by different researchers (e.g. [15] [18] [19] [20]). As a result, the penetration resistance of a glass target is strongly influenced by the residual strength of the comminuted material, the friction between the comminuted particles and the confining strength of the undamaged, surrounding material. Here, the residual strength of the failed material is strongly dependent on the confining pressure [21] [22] [15] [23] [24].

Anderson et al. [25] [26] observed that as long as the impact velocity of the projectile is fast enough, the details of the transition from intact to failed glass are not important. However, if the impact velocity is too low to generate a minimum pressure, the assumption that the projectile is penetrating only failed material is incorrect. In case of a gold rod (inversely) penetrating borosilicate glass [20], a minimum pressure of 1.6 GPa was evaluated corresponding to an impact velocity of 768 m/s.

In conclusion, an adequate constitutive material model needs to describe the stress that SLG can support as a function of the hydrostatic pressure, strain, strain rate, temperature and state (intact, partially failed and failed). Further, it is important how the material undergoes the transition from the intact to the failed state.

The determination of these dependencies is challenging. In 2009, Shockey et al. reported that "the response of transparent armor to projectile attack cannot currently be computed with confidence [27] [28]. One reason is the lack of an adequate mathematical description of the failure processes occurring in the target material under high pressure and shear" [29].

Holmquist et al. [30] later developed a state-of-the-art constitutive model, the Holmquist-Johnson model. They stated that many different aspects of the complex material behavior of SLG have to be taken into account for adequate simulations of ballistic impact scenarios. A summary of the most important SLG properties is given in the following:

- SLG is very compressible and can exhibit permanent densification, presumably dependent on temperature and shear stress [31] [32] [33] [34] [35].
- The bulk modulus and probably also the shear modulus are not constant, but instead dependent on the pressure [36] [37] [38] [39]. As a result, the equation of state (EOS) and the compression curve (longitudinal stress vs. volumetric compression) exhibit a concave downwards shape in a certain pressure range. This leads to a complex shock response (no clear two-wave structure in the shock wave profiles) and thus to much ambiguity in the reported values of the Hugoniot elastic limit (HEL) (ref. Table 1.3).
- An increase of the occupied volume occurs upon fracture, referred to as bulking [40]. Bulking of up to at least 20 % was reported by Glenn et al. [41] [42].
- The internal tensile strength of intact SLG is very high (several authors were not able to produce spall at shock loadings between 3 to 8 GPa by means of planar plate impact (PPI) [43] [44] [45] or laser-driven shocks [46]).
In the failed state, however, the spall strength is reported to be 0.4 GPa [47] or almost negligible [48] [43] [44] [45] [48] (summary in Table 1.5).
- The transition from the intact to the failed state can be accompanied by a phenomenon referred to as failure wave or failure front. Reported values for the propagation velocities and initiation conditions are conflicting (see Table 1.4).
- Different authors reported that the failure process of SLG is also time-dependent [49] [50]. In contrast, e.g. Anderson et al. [51] reported that simulation results of impacted borosilicate glass yield better results if time-dependent failure is deactivated in the model.
- The strength of SLG increases with pressure. With increasing damage, the strength decreases. Nevertheless, even completely failed SLG exhibits a significant residual strength under confined compression [21] [22]. Bridgman et al. [52] [31] concluded that at high hydrostatic pressures, the growth of flaws is limited by the pressure.
- The strength is probably also dependent on the mode of deformation, more specifically on the intermediate principal stress (3^{rd} invariant effect). This means, that the strength is higher when the stress state is on the compressive meridian compared to the tensile meridian [53]. Similar conclusions were made by Gorfain et al. [54] who assumed that the failed strength could be significantly less under combined pressure-shear loading than under purely longitudinal compression.
- In addition, the strength is also dependent on the size and the surface finish. Smaller specimens are stronger than larger specimens are. This is probably due to the statistical occurrence of surface or internal flaws. The larger is the stressed volume, the higher is the chance of encountering a more severe flaw [55] [56].
In addition, specimens with a smooth surface are stronger than those with a rough surface [57] [58] [59].
- The strength of SLG is probably also strain-rate sensitive. Holmquist et al. [60] and Nie et al. [57] reported an increasing strength with increasing strain-rate. However, Chojnacki et al. [61] concluded that SLG is almost independent of strain rate effects under triaxial loading

conditions. In addition, it was demonstrated indirectly that there is no strengthening of failed borosilicate glass at high strain rates [62] [63].

- Holmquist et al. [30] mentioned that at high temperatures, approaching the glass transition temperature, glass is also temperature sensitive (increased ductility and decreased strength). However, Nie and Chen [64] reported that for temperatures up to 600° C, the dynamic strength of failed borosilicate glass (transition temperature in the range of 440 – 560° C [65]) is independent of the temperature.
- Under confinement, SLG can presumably flow plastically, i.e. undergo a brittle-ductile transition. For example, Peter [66] concluded that not all flow phenomena in glass can be explained as densification. Similar observations were made by Ernsberger [67] and for other brittle materials by Horii et al. [68] and Lankford et al. [69] [70].

Need for characterization experiments

Sophisticated material models for SLG account for all of the aforementioned characteristics. However, ballistic scenarios can only be adequately reproduced in the simulations, if all model parameters are set properly. The determination of these parameters is quite challenging since most parameters cannot be measured directly and independently. In addition, complex models can have a large number of material parameters. For example, the aforementioned Holmquist-Johnson model [30] requires the determination of 29 independent parameters.

If the parameters of such a sophisticated model are deduced solely from one specific ballistic scenario, it is not possible to predict the outcome of other arbitrary ballistic scenarios (e.g. [71] [72] [17]). It is therefore necessary to develop basic characterization experiments that allow for the determination of specific parameters. These experiments have two main advantages in contrast to the complex ballistic impact test:

- The loading state of the material can be kept simple (e.g. one-dimensional strain or stress state).
- More and/or better diagnostic devices can be employed (e.g. placement of stress-gauges, implementation of computed tomography (CT) scans due to the possibility of using small test specimens).

Basic characterization experiments for SLG developed within the last decades of extended research include e.g. planar-plate-impact, pressure-shear-plate-impact, split Hopkinson pressure bar tests, Taylor impact, tension tests and compression tests with unconfined or confined specimens. Measurement techniques comprise e.g. stress and strain gauges, laser interferometry, high-speed photography and X-ray CT.

As discussed in the next sections, much progress has been made in this field of research. Current material models, like e.g. the Holmquist-Johnson model, can already reproduce a variety of different ballistic scenarios.

However, the results of the models can still be improved, e.g. with respect to the description of failure. One way to achieve this objective is to develop new characterization techniques. The new results can then be used to improve model parameters for which reported values are conflicting or not available at all.

In addition, new techniques can also contribute to improve the understanding of other materials exhibiting similar characteristics, like e.g. ceramics or even high-strength steels.

1.2 Material characterization of soda-lime glass - current state of science

1.2.1 Chemical composition, elastic constants and the Hugoniot elastic limit

SLG consists mainly of silicon dioxide (SiO_2) and the modifiers sodium oxide (Na_2O) and calcium oxide (CaO). The detailed chemical composition can vary and is dependent on the manufacturer. However, no evidence was found in literature that those small variations have a significant influence on the crucial material properties. A representative chemical composition is presented in Table 1.1, as determined by Alexander et al. [39] and Chocron et al. [22] for the SLG Starphire[®]. For comparison, the composition of the borosilicate glass Borofloat[®]33 is also listed.

Table 1.1: Chemical composition of SLG and borosilicate glass determined by Alexander et al. [39] and Chocron et al. [22] by means of X-ray fluorescence analysis.

Component	SLG (Starphire [®])	Borofloat [®] 33
	Weight proportion [%]	Weight proportion [%]
SiO_2	73.20	80.50
Na_2O	14.70	3.50
CaO	10.28	0.02
Al_2O_3	1.44	2.50
SrO	0.20	-
MgO	0.08	-
ZrO_2	0.03	0.03
B_2O_3	-	12.70
K_2O	-	0.64
BaO	-	0.02

A summary of the elastic mechanical properties of SLG is provided in Table 1.2. The values listed in the table as well as parts of the literature research have already been pre-published by the author in [A1]. The given literature values for the shear modulus and the bulk modulus were calculated from the wave velocities determined by ultrasound measurements. The other elastic constants were calculated using the conversion formulae for homogeneous, isotropic, linear elastic materials (see e.g. [73](pp. 23, 81)).

The listed values are in good agreement with the wave speeds determined for the specimens used in this work: longitudinal wave speed $c_p = (5740 \pm 30)$ m/s and shear wave speed $c_s = (3610 \pm 60)$ m/s. The measurements were conducted using the ultrasonic detector USD 10 of the company Krautkrämer. Moreover, the listed Young's modulus is in excellent accordance with the results of this work obtained in unconfined compression tests.

Table 1.2: Literature data for the elastic properties of SLG [A1].

Property	Value	Source
Density ρ	2.53 g/cm ³	[60]
Shear modulus G	30.4 GPa	[60]
Bulk modulus K	42.8 GPa	[74]
Elastic modulus E	73.8 GPa	$= 2G \cdot (1 + \nu)$
Poisson's Ratio ν	0.21	$= (3K - 2G) / (6K + 2G)$
Longitudinal wave speed (c_p)	5740 m/s	$= \sqrt{(K + 4/3 G) / \rho}$
Shear wave speed (c_s)	3467 m/s	$= \sqrt{G / \rho}$

A crucial material property and focus of many studies is the so-called Hugoniot Elastic Limit (HEL), which is the principal compressive stress at the limit of the elastic response under one-dimensional strain conditions. Unfortunately, there is much ambiguity in the determined values of the HEL. This is because SLG exhibits no clear two-wave structure in its shock wave profiles, which makes the common analysis methods of ductile materials barely applicable. For example, Grady et al. [75] stated that some measured values were uncertain since a clear-cut method for the evaluation of stress levels is missing.

Bless et al. [76] shot copper disks on SLG with imbedded longitudinal and transversal stress gauges. They observed that below loadings of 10 GPa, the longitudinal stress signal ramped into a plateau of constant stress. At higher loadings, the stress immediately dropped after reaching the maximum. In addition, a reduction of shear strength was observed when shocked above 10 GPa. They concluded that both phenomena are related and possibly caused by densification. They evaluated a HEL of (6.0 ± 0.5) GPa.

Rosenberg et al. [77] inferred from double impact tests on ceramics that the HEL marks the point at which cracks coalesce into a network. Consequently, Rosenberg et al. [78] later concluded that the onset of failure in SLG at a stress of 4.0 GPa presents its HEL.

Subsequently, Alexander et al. [39] [79] [80] conducted an extensive study on the equation of state and the HEL for soda-lime and borosilicate glass, providing HEL values different from those of Bourne et al. [38]. By means of PPI tests with direct and reverse impact configurations, they induced shock loadings between 4.6 GPa and 40.9 GPa. As a result of an incremental analysis of the transmitted wave profiles and reverberation data, they determined shock velocity-particle velocity data ($U_s - u_p$) and a HEL of 3.5 GPa for SLG. In addition, they concluded that a complete loss of its strength at the HEL results in a pseudo-elastic behavior up to 7.5 GPa.

Table 1.3 provides a selection of HEL values evaluated by other authors.

Table 1.3: Selection of HEL values for soda-lime glass from other authors [A1].

Author	Year	HEL [GPa]
Kanel, Molodets, Dremin [81]	1977	7.5
Rosenberg, Yaziv, Bless [48]	1985	6.4
Bless, Brar, Rosenberg [76]	1988	6.0
Holmquist, Johnson, Grady, Lopatin, Hertel [60]	1995	5.95
Bourne, Rosenberg, Millet [82] [83]	1995	6.0
Grady, Chhabildas [75]	1996	4.5 – 6.0
Dandekar [84]	1998	3.1
Kanel, Bogatch, Razorenov, Chen [45]	2002	~ 8.0
Simha, Gupta [49]	2004	4.0
Alexander [80]	2007	4.3
Alexander, Chhabildas, Reinhart, Templeton [39]	2008	3.5 (7.5)*
Rosenberg, Ashuach, Dekel [78]	2008	4.0
Curran, Shockey, Simons [74]	2009	3.5 – 7.0

* pseudo-elastic behavior up to 7.5 GPa due to complete loss of strength

1.2.2 Failure and fracture propagation

Several studies have focused on visualizing the onset and propagation of the damage in transparent materials. Senf et al. [85] [86] developed edge-on-impact experiments, which enabled the observation of crack nucleation and propagation in single glass plates. This procedure has later been continued and improved by Strassburger et al. [87] [88] [7] [89] [90]. The more complex morphology of damage in multi-layer glass laminates was studied by Bless et al. [91] for high velocity impact (1118 m/s).

Strassburger et al. also developed an experimental technique, which facilitated the visualization of damage propagation in a complex laminate target during projectile penetration [92]. A combination of high-speed imaging, photonic Doppler velocimetry (PDV) and numerical simulations revealed a clear correlation between damage propagation, glass layer deformation and projectile position.

Various studies have also focused on the visualization of fracture propagation along glass bars (e.g. [93] [94] [95]). However, Walley concludes in a review paper [96] that even though some differences between the behaviors of soda-lime and borosilicate glass during symmetric rod impact have been reported, the origin of these differences is still not understood and has not been conclusively demonstrated.

For some brittle materials, the transition from the intact to the failed state is accompanied by a phenomenon, which is often referred to as failure wave or failure front. The assumption of its existence rationalized some of the conflicting results of previous studies. However, the nature of this phenomenon has not yet been conclusively understood.

First systematic investigations of the failure wave were conducted by Rasorenov, Kanel et al. [43] [97]. They used explosive charges and PPI tests to induce a plane shock wave in optical K19 glass (which is similar to SLG). At loads up to 4.2 GPa, they observed a “failure wave” which initially moved at 1500 m/s and was slowed down to less than 1000 m/s after travelling a distance of 3 mm. They also stated that the propagation of the failure wave is stopped, when interacting with the release wave from the back of the projectile. They further noticed that at high pressures, no failure wave arose which was attributed to plastic deformation preventing brittle fracture.

In contradiction, Brar et al. [98] [44] observed a failure wave at loadings above the HEL, moving with a velocity of 2200 m/s. A further discrepancy to Rasorenov et al. was that Raiser et al. [99] could not observe a reflection of the shock waves at the failure front.

Espinosa et al. [47] used plate and bar impact experiments to show that the failure wave is a propagating boundary of damaged material. They determined a threshold of a longitudinal stress of approximately 4 GPa for the onset of a failure wave in soda-lime and aluminosilicate glass. They further observed that the failure waves propagate at velocities between 1500 m/s and 2000 m/s. Their determined values for the spall strength were 2.6 GPa and 0.4 GPa in front of and behind the failure wave, respectively. However, they also pointed out that the lateral stress gauge concept bears the disadvantage of perturbation of the wave propagation due to the presence of a thin layer of material having a different impedance and mechanical response.

Simha and Gupta [49] provided a summary of all previously reported failure wave velocities lying between 1200 m/s and 2600 m/s. They found that the discrepancies are due to the fact that longitudinal and lateral gauge data indicate different features. They observed a strongly time-dependent material response and concluded that the lateral stress measurements of previous studies cannot be interpreted in terms of a moving wave or front. They also pointed out that deriving a wave velocity even from longitudinal gauge data is difficult.

Orphal et al. [100] later introduced the term failure front. They observed the phenomena during the impact of multiple co-axial spaced gold rods into borosilicate glass. Their conclusion was that the failure front stops shortly after the driving stress ceases, but is reinitiated by the impact of the next rod. Therefore, they assumed that the failure front cannot be a diffusion-like phenomenon but is rather a result of nucleation and growth of cracks and densification.

Table 1.4 summarizes the failure front velocities for reported peak loads in SLG determined in previous studies from other authors.

Some studies also have investigated the existence of failure fronts in other brittle materials, although it is still controversial if they exist in materials apart from silica glasses, as reported by Walley [96]. For example, Zubkov et al. [101] observed a failure front in polymethylmethacrylate (PMMA) by means of synchrotron radiation.

Table 1.4: Summary of failure front velocities in soda-lime glass from other authors [A1].

Author	Year	Stress [GPa]	v_{fail} [m/s]
Rasorenov, Kanel et al. [43] [97]	1991	4.2	1000-2000
Brar, Rosenberg, Bless [44]	1991	8.1	1700
Brar, Bless, Rosenberg [98]	1991	6.3	2200
Bourne, Rosenberg et al. [102]	1994	2.5	2000
		~5	5500
Dandekar, Beaulieu [103]	1995	4.5-5.3	1450-1620
Espinosa, Xu [47]	1997	7.0	1500-2000
Bourne, Millett, Rosenberg et al. [38] [104]	1998	4.5-7.2	1700-2500
		> 10	5500
Kanel [45]	2002	7.0	1550
Rosenberg [78]	2008	4-5	1270-1430

Bourne et al. [102] were the first to use high-speed photography for the visualization of the failure front propagation in SLG during PPI at loadings up to the HEL. They observed a ramping behavior of SLG through the whole elastic range that, to their knowledge, has been overlooked before. Grady et al. [75] later specified that the ramping is caused by dispersing precursor waves, which can be caused either by exceeding the HEL or by elastic softening under compression.

Bourne et al. [102] were also able to visualize an uneven failure front at an impact load of 2.5 GPa. The front was moving at 2000 m/s and was initialized by the release wave from the back of the projectile. At a higher impact load of almost 5 GPa, they observed a different behavior. In this case, the failure front was moving closely behind the shock front at 5500 m/s. This high velocity was in certain contradiction with earlier findings and the discrepancy could not be explained.

In additional test series [38] [104], they estimated a threshold stress of 4 GPa for the onset of a failure front, which lies below the value of the HEL. Furthermore, they examined the influence of an internal interface layer with polished or pre-damaged surfaces. By means of lateral strain gauges and high-speed imaging with 5 Mfps, they revealed that the polished interface resulted in a delay of the failure propagation and a change in the failure front velocity.

In consecutive studies [82] [83] [19], they also placed lateral stress gauges in front of and behind of the failure front, which enabled the determination of the shear strength of intact and damaged glass. They observed the same strength values for soda-lime, borosilicate and lead glass and concluded that the strength is mainly dependent on their common silicate network.

Grady et al. [75] used the timing of the stress relief to calculate the sonic release velocities at the stress amplitude of the Hugoniot state. They obtained values between 5300 m/s and 13300 m/s, which are noticeably higher than the elastic wave speed. Similar observations were made by Kanel et al. [45].

In contradiction, Bourne et al. [105] concluded that the earlier release is not caused by higher release velocities, but is rather an effect of the failure front reducing the shear strength. They based their conclusion on their observation that the distance between the failure front and the shock wave front reduces with rising loading stress.

As far as the author knows, the only other effort to visualize the compressive failure front in PPI tests, aside from Bourne et al. [106] [82] [102], was undertaken by Chocron et al. [107]. They conducted PPI tests with borosilicate glass in the elastic range at stress levels between 0.7 GPa and 2.0 GPa. While they could clearly observe a failure front at stress levels of 0.8 GPa, the simultaneously recorded velocity profiles did not show the expected recompression signal. They assumed that the recompression wave resulting from the reflection at the failure front was too small to be distinguished from the signal noise. From this, they wrapped up that previous studies could maybe mistakenly have concluded the non-existence of the failure front at low velocities. They also observed failure nucleation sites trailing the shock wave, which were getting closer to the shock front at higher impact velocities.

A promising alternative method of visualizing the internal fracture process are techniques based on X-ray CT. Several studies (e.g. [108], [109], [110]) have demonstrated that experiments observed by phase-contrast imaging (PCI) are well suited for the visualization of cracks in brittle materials even in highly dynamic events. For example, Chen et al. [108] conducted edge cutting on borosilicate glass while monitoring the time-dependent failure process with high-speed X-ray PCI capabilities.

1.2.3 Strength of intact and failed glass

Besides the HEL and the failure front phenomenon, much research effort has been dedicated to the determination of the material strength under dynamic and quasi-static loading. Figure 1.1 and Figure 1.2 provide a selection of strength values available in the open literature. The dynamic experimental techniques comprise planar plate impact tests (PPI), pressure-shear plate impact tests (PSPI) and split Hopkinson pressure bar tests (SHPB). In addition, spall tests (specific setup of PPI) allow for the determination of the dynamic tensile strength. Quasi-static techniques comprise confined pressure tests and uniaxial compression and tension tests.

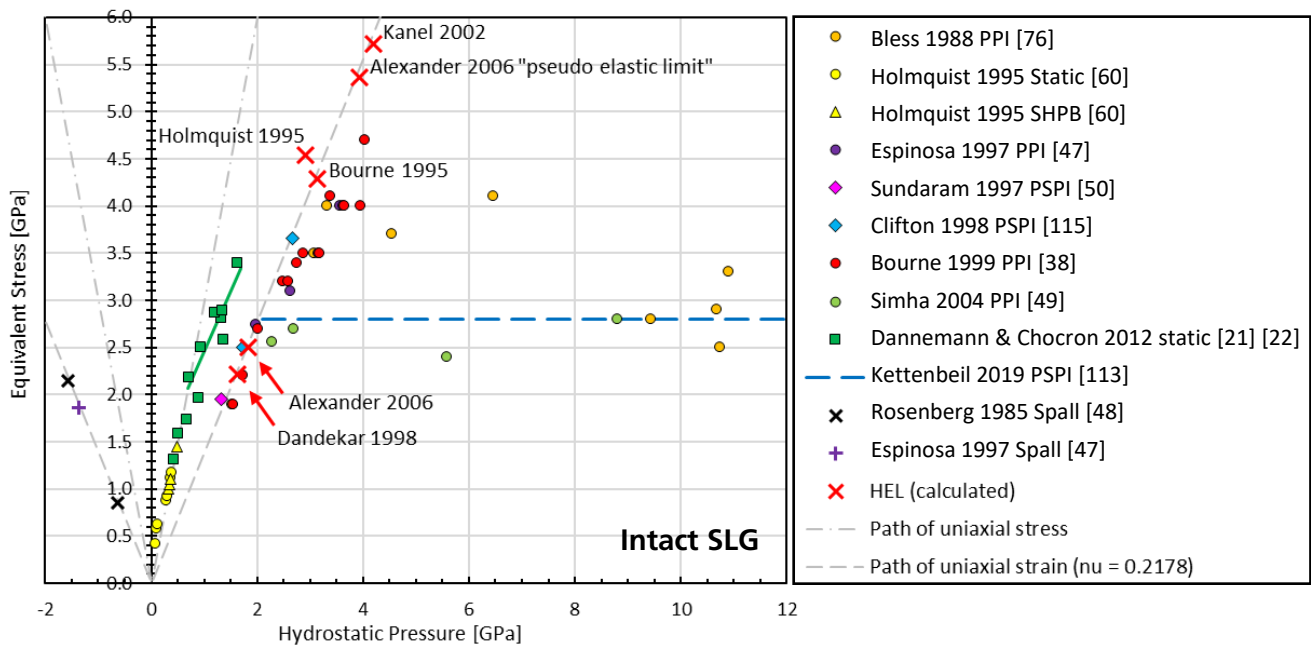


Figure 1.1: Strength of intact SLG: selection of values available in open literature.

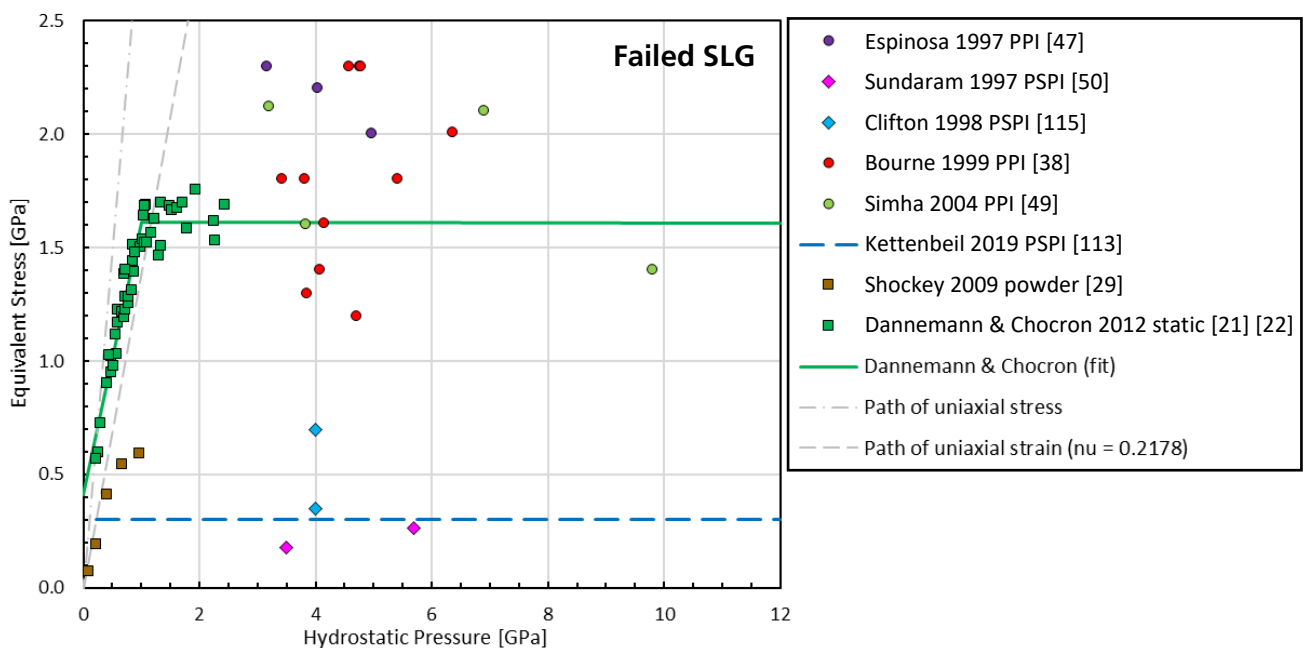


Figure 1.2: Strength of failed SLG: selection of values available in open literature.

The path of uniaxial strain (dashed gray line) is calculated assuming an elastic behavior. For a given longitudinal stress σ_x and a Poisson's ratio ν the hydrostatic pressure P and the equivalent stress σ_{eq} can be calculated as follows:

Combining $\sigma_y = \frac{\nu}{1-\nu} \sigma_x$ and $P = \frac{1}{3}(\sigma_x + 2\sigma_y)$ yields $P = \sigma_x \frac{1+\nu}{3(1-\nu)}$.

In addition, with $\sigma_{eq} = \frac{3}{2}(\sigma_x - P)$ follows $\sigma_{eq} = P \cdot 3 \frac{1-2\nu}{1+\nu}$. The indicated line is calculated with the Poisson's ratio $\nu = 0.22$ of Starphire reported by Chocron et al. [22].

The path of uniaxial stress (dash-dotted gray line) is given by $\sigma_{eq} = P \cdot 3$ (since $\sigma_y = \sigma_z = 0$).

The data of Dannemann & Chocron et al. (green squares) was derived from triaxial tests. Therefore, it falls between the path of uniaxial strain and the path of uniaxial stress (for a given Poisson's ratio).

The depicted HEL data (red crosses in Figure 1.1) is calculated using the equations above with $\sigma_x = \text{HEL}$. P and σ_{eq} at the HEL are calculated since these values are not directly provided by most authors listed in Table 1.3.

It has to be noted that the assumption that the elastic behavior is valid for stresses up to the HEL is not necessarily valid. For example, Holmquist et al. [60] assume a reduction of the elastic constants already at stresses below the HEL, due to densification. Their reported HEL is therefore not lying on the path of uniaxial stress calculated with $\nu = 0.22$, but on a path with a reduced ratio of $\nu = 0.191$. Nevertheless, the significant differences of the HEL positions (red crosses in Figure 1.1) cannot be explained solely by this densification effect.

In the following, some results of the reported studies are outlined in more detail. For an in-depth review of most of the literature data presented in Figure 1.1 and Figure 1.2, the reader is also referred to Gorfain et al. [54] and Walley [96].

1.2.3.1 Strength at high strain rates

In 1985, Rosenberg et al. [48] already used spall PPI experiments in combination with Manganin gauges to estimate the tensile spall strength of SLG. On the one hand, they were not able to produce spall at tensile stress levels up to 5.0 GPa. On the other hand, they observed that the spall strength is negligible above the HEL, for which they had assigned a value of 6.4 GPa. Espinosa et al. [47] later used the reported spall signals of Rosenberg to deduce a spall strength of 3.8 GPa for intact SLG.

In subsequent studies, Brar et al. [44] came to similar conclusions. Rasorenov et al. [43] also deduced that the spall strength exceeds 4.2 GPa. Analogical observations were made by Raiser et al. [99], who concluded from complex PPI tests that the spall strength of intact aluminosilicate glass has to be greater than 3.4 GPa, but that all spall strength is lost if the compressive stress is high enough. In addition, a phenomenological study was done by de Resseguier and Cottet [46], who discussed the complexities of glass fracture at the spall plane. Table 1.5 provides a selection of spall strength of intact and failed SLG evaluated by other authors.

Table 1.5: Selection of spall strength values for soda-lime glass from other authors.

Author	Year	Spall strength [GPa]	
		intact	failed
Rosenberg et al. [48]	1985	3.8	~ 0
Rasorenov et al. [43]	1991	> 4.2	~ 0
Brar et al. [44]	1991	> 3.0	~ 0
Rességuier et al. [46]	1995	> 8	
Espinosa et al. [47]	1997	2.6	0.4 at $\sigma_x = 7.5$ GPa
Kanel et al. [45]	2002	> 3	~ 0

Other studies focused on the determination of the shear strength under highly dynamic compression. Brar et al. [98] estimated a constant strength of approximately 2.2 GPa for damaged SLG at longitudinal stress levels between 4 GPa and 6 GPa. In subsequent studies, Bourne et al. [82] [83] concluded that the intact strength increases with the longitudinal stress up to the HEL, which they have defined at 6.0 GPa. Beyond the HEL, constants shear strengths of 4.0 GPa for intact and approximately 1.8 GPa for damaged SLG were inferred. Bourne et al. [19] later removed the cap on the intact strength due to one additional measurement at a longitudinal stress of 7.7 GPa yielding a shear strength of 4.7 GPa. Radford et al. [111] later also removed the cap on the failed strength. Based on PPI results with three dense glasses, they concluded that the failed strength increases linearly with the longitudinal stress for stress levels greater than 8 GPa.

Alexander et al. [39] [80] [112] inferred the strength of SLG from the release response observed in PPI tests. They assumed that SLG loses all strength at the HEL (for which they reported a value of 3.5 GPa). However, this is in contrast e.g. to experimental data obtained by Dannemann et al. [21] and Chocron et al. [22] by means of quasi-static confined compression tests.

Kettenbeil [113] used PSPI experiments to determine the strength of intact and failed SLG. He reported an intact strength of 2.8 GPa for all strain values below the onset of softening. For large plastic strains, a failed strength of 0.3 GPa was evaluated. The failed strength is based on additional measurements with granular silica sand conducted by Vogler et al. [114]. This value is significantly lower than the failed strength determined by other authors by means of PPI tests or confined pressure testes (ref. Figure 1.2). However, it is in good match with the results of other studies using PSPI [50] [115]. The observed discrepancies could be attributed to a strong dependence of the failed strength on the mode of deformation. Alternatively, the large shear strains attained in the PSPI tests could lead to the formation of more localized failure resulting in a lower strength.

Other notable experimental techniques are modified versions of the SHPB. Nie et al. [116] used cuboid borosilicate specimens oriented at different angles to the loading direction. They reported a decrease of the equivalent stress at failure when the shear component is increased. Furthermore, Nie et al. [117] used a ring-on-ring setup with the SHPB to measure the dynamic equibiaxial flexural strength of borosilicate glass.

Chen et al. [118] [119] developed a SHPB setup using a double pulse loading. After the specimen is crushed by the first pulse, the dynamic compressive response of the failed glass is determined by means of the second the pulse.

Chojnacki et al. [61] used a triaxial compression setup with a SHPB to pre-stress the glass specimen hydrostatically before it was loaded by a dynamical axial stress wave. As the results of

their dynamic triaxial compression experiments were similar to quasi-static results, they concluded that SLG and borosilicate glass are almost independent of strain rate effects under triaxial loading conditions.

It is worth mentioning that the geologic materials community has developed also highly notable characterization techniques for the comminution behavior of brittle materials. For example, Grady and Kipp [120] [121] [122] analyzed the grain size of oil shale fragments generated under dynamic expansion. They investigated the strength loss across shear bands developing in solid materials. Furthermore, they determined that the rate dependence of the failure under dynamic tensile loading is a consequence of a geometric inertia since the activation and growth times of the cracks are finite.

Another well-established technique for the characterization of geologic materials are confined compression tests (see e.g. Desai and Siriwardane [123]). Forquin et al. [124] proposed an original method for the analysis of these quasi-oedometric compression tests in order to characterize high-performance concretes. A similar characterization technique was developed by Dannemann et al. for the characterization of ceramics [125] and glasses [126] as presented in more detail in the next section.

1.2.3.2 Quasi-static compression strength

In Figure 1.1 and Figure 1.2, the majority of the data below hydrostatic pressures of 2 GPa has been determined by Dannemann and Chocron et al. [125] [126] [127] [17] [62] [63] [21] [22]. In the following, their experimental techniques and results are presented in more detail since they served as a basis and reference for the enhanced characterization tests developed as part of the current work.

Dannemann and Chocron et al. developed quasi-static ($\sim 10^{-3} \text{ s}^{-1}$), non-ballistic test setups for the characterization of intact and damaged brittle materials. More specifically, they used unconfined and confined compression experiments to determine the elastic properties as well as Drucker-Prager or Mohr-Coulomb constants [128] of SLG [21] [22], borosilicate glass [126] [127] [62] [63] and ceramics [125]. Here, pre-damage was created by means of a thermal shock or cyclic pressure loading. Following the compression tests, the degree of damage and the extent of comminution of selected samples were analyzed by means of sieving and microscopy investigations (optical and electron).

During the compression tests, a cylindrical specimen was positioned between two loading anvils and an axial load was applied by means of a mechanical testing servo-hydraulic (MTS) machine. Two different techniques were utilized to provide the lateral confinement of the specimens:

- Hydraulic pressure technique: The loading of the specimen took place inside a thick-walled steel pressure vessel filled with a hydraulic fluid. A steel piston connected the loading platens of the MTS machine with two tapered alumina (AD-995) loading anvils. Controlled by a pump, different constant fluid pressures were generated confining the specimen simultaneously in lateral direction. The achievable confinement pressures were limited to about 500 MPa restricted by the seals of the vessel [22].
- Confined sleeve technique: Ceramic plates and anvils (tungsten carbide or SiC-N) were used to apply the axial compressive stress. The lateral confinement was provided by an annular steel sleeve (Vascomax C350) instead of the hydraulic fluid. With this technique, higher confinement pressure could be achieved up to the yield limit of the steel sleeve [21].

During the loading tests, the acoustic emission was recorded in order to detect the onset of damage events. The axial stress in the specimen was measured by a load cell in the MTS machine. The axial strain was measured by an extensometer (clip gauge) placed between the two loading platens. In case of the confined sleeve tests, strain gauges were mounted on the outside surface of the sleeve in order to measure axial and hoop strains. The measured hoop strain was used to infer the radial stress on the inner surface of the sleeve, which equals the lateral confinement pressure of the specimen. For the calculation of this radial stress, the classical solution for a thick tube with an internal pressure [129] was used assuming an elastic behavior of the sleeve [22]. Concerning the axial stress measurement, the coefficient of friction between the steel sleeve and the specimen was predicted to be < 0.1 and it was reported that friction is not a major issue [127].

In the following, an overview of the most important results of the compression tests is given:

- Intact strength: Danneman et al. [21] [21] [22] observed considerable scatter in the strength of intact SLG (green squares in Figure 1.1) determined by means of unconfined and hydraulic confined compression tests. Until failure occurred, a linear increasing stress-strain curve was determined. After failure, no residual load carrying stress could be observed since the hydraulic confinement failed.
- Failed strength: With the pre-damaged (thermally shocked) specimens, a first drop in the load carrying capability was observed at an axial strain between 2 to 3 %. This initial failure resulted from the formation of a shear plane oriented at an angle of $50^\circ - 60^\circ$ for SLG, independent of the confinement pressure ($55^\circ - 70^\circ$ for borosilicate glass). Further compression lead to a sawtooth shaped stress-strain curve that was probably caused by the generation of additional shear planes or an unsteady slippage of the failure surfaces over each other. Although the additional shear planes were not as well defined as the initial shear plane, the induced secondary damage regions looked similar to the primary damage regions [21].
- Cap of the residual strength: The average of the sawtooth pattern of the stress-strain curve is referred to as residual strength. The corresponding equivalent stress increases linearly with increasing pressure until it reaches a plateau of (1.61 ± 0.08) GPa at a hydrostatic pressure of about 1 GPa. At higher pressures, the equivalent stress is independent of the pressure (green squares and lines in Figure 1.2). Both techniques (hydraulic pressure and confined sleeve) yield comparable results with the pre-damaged specimens [22]. The plateau value is also in rough agreement with the PPI data of Bourne et al. [38] and Simha et al. [49] (red and green circles in Figure 1.2). However, it is significantly higher than the reported strength values determined by means of PSPI tests (diamond-shaped data points and blue, dashed line in Figure 1.2) [50] [115] [113].
- Yield surface: The measured values for the intact and failed glass can be used to determine model constants describing the limits in the capability to support shear loading. This capability is referred to as "breaking strength and is significantly less than the theoretical strength" [21](p. 721). The limit of the material strength as a function of the hydrostatic pressure is represented by a surface. "For intact material, this might be thought of as a failure surface; for pre-damaged material, it might be a flow surface" [63](p. 3392).

Chocron and Dannemann et al. do not provide a description of the change of the residual strength as a function of the degree of damage [63]. However, they concluded that the residual strength is almost independent of the degree of damage for hydrostatic pressures between 1 and 7 GPa [22]. This was inferred from tests with multiple load-reload cycles and from the reasonable match with the PPI data of Bourne et al. [38].

- Strain rate dependence of failed glass: It was demonstrated indirectly that there is no strengthening of the damaged glass at high strain rates [62] [63].
- Post-test evaluations: Regions of compacted and sintered glass particles in borosilicate specimens could be observed by means of post-test microscopy evaluations. These regions did not occur in similar tests with SLG. In case of SLG, the pressure was relieved by the extension of pre-existing cracks and the formation of shear planes [21]. Post-test evaluations on initially intact borosilicate specimens revealed that the degree of damage generated during the compression varies widely. On the one hand, several specimens showed only external damage like chipping. On the other hand, some specimens exhibited extensive damage within the entire volume. It was inferred for intact borosilicate that the generated degree of damage does not correlate directly with the maximum load level or the amount of applied load-reload cycles. Instead, the variations were attributed to differences in the initial flaw populations (although pre-test stereomicroscopy did not reveal any striking differences) [127].
- Elastic constants: Chocron et al. [17] presented an analytical model of confined compression tests assuming an elastoplastic specimen and an elastic sleeve. It was shown that displacements, strains and stresses can be solved explicitly. They further showed that a highly comminuted specimen, which is well confined, exhibits almost the same elastic constants as those of an intact specimen. This means that the elastic modulus and the Poisson's ratio are not significantly affected by damage, which was an unexpected result.

Other quasi-static techniques worth mentioning were developed e.g. by Shockey et al. [29] and Wereszczak et al. [130]. Shockey et al. used a MTS axial-torsion machine to create pressure/shear load conditions in beds of glass fragments. They measured the shear resistance as a function of the normal load for quartz glass powder at sliding rates between $5 \cdot 10^{-2}$ to 1 mm/s. The observed shear resistance increased monotonically with increasing normal load until a constant maximum was reached (dictated by the friction between the steel anvil and the glass fragments) [29]. The achieved maximum equivalent stresses are plotted as brown squares in Figure 1.2. They are calculated from the reported maximum shear stresses τ and the corresponding normal stresses σ_x using $\sigma_{eq} = 2\tau$ and $P = \sigma_x - \frac{4}{3}\tau$.

Wereszczak et al. used a ring-on-ring technique to measure the quasi-static flexure strength of SLG and borosilicate glass. They also used the results of the generated flexure and indentation data to construct damage maps providing the critical load as a function of the thickness of the glass plates [130].

1.2.4 Current issues and shortcomings

The review of the current state of science outlined in the previous section illustrates that SLG has been the focus of extensive research since decades. Within the course of the studies, many insights into the constitutive characteristics of SLG could be gained. Nevertheless, the reported findings were sometimes conflicting and some issues are still open. For example, the overview of the HEL in Table 1.3 illustrates that the reported values vary considerably. Furthermore, the phenomenon of the failure front is not yet fully understood as indicated by the conflicting values of the reported propagation velocities (Table 1.4) and the observed initiation conditions. In addition, the reported values of the spall strength are partly contradicting (see Table 1.5).

For the understanding of a ballistic penetration process, the characterization of the shear strength of intact and damaged SLG is of special importance. Several studies have addressed this topic as summarized in Figure 1.1 and Figure 1.2. However, the plotted data exhibits significant scatter and is contradictory in some cases.

Looking at the intact strength (Figure 1.1), Alexander et al. [39] reported a pseudo-elastic behavior up to a HEL of 7.5 GPa, which is inconsistent e.g. with the data of Bourne et al. [38]. Therefore, Chocron et al. [22] assumed that the SLG of Bourne et al. could have been already pre-damaged during the placement of the stress gauges. The intact strength data of Chocron et al. [22] is also in conflict with the data of Alexander et al. [39] (who reported a complete loss of strength at a HEL of 3.5 GPa) and e.g. with the data of Kettenbeil [113]. Figure 1.1 also illustrates that the intact strengths reported by Espinosa et al. [47], Bourne et al. [38] and Clifton et al. [115] are significantly higher than the data of Simha et al. [49] and Kettenbeil [113], which is capped at 2.8 GPa.

Chocron et al. [63] further stated that their intact data should be used with care since small gaps inside the sleeve, misalignment or eccentricity have large influence on the results. Therefore, they did not conduct further analysis on intact borosilicate specimens with the confined sleeve technique [22].

Looking at the failed strength (Figure 1.2), the data of the quasi-static tests [29] [21] [22] and the PPI tests [47] [38] [49] are conflicting with the results of the PSPI tests [50] [115] [113]. The large spread in the data could be caused by the different modes of deformation or by the significantly larger shear strains attained in the PSPI tests, as assumed by Gorfain et al. [54]. This means that the failed strength could be significantly less under combined pressure-shear loading than under purely longitudinal compression.

For hydrostatic pressures up to 2.5 GPa, Dannemann and Chocron et al. [21] [22] conducted an extensive series of confined compression tests with pre-damaged glass specimens. Their determined failed strength is significantly larger than the values resulting from the tests of Shockey et al. [29]. The differences are probably attributed to the degree of pre-damage. On the one hand, Dannemann and Chocron et al. generated the pre-damage by means of a thermal shock. They exposed the glass specimens to two thermal cycles by heating up to 500° C and subsequently quenching in ice water [22] [21]. The resulting pre-damage consisted of an extensive network of interconnected cracks. The degree of pre-damage was however not quantified or checked pre-test to be uniform across all specimens. For example, the borosilicate specimens exhibited significantly coarser cracks due to their lower linear expansion coefficient [21].

On the other hand, Shockey et al. [29] used a fine quartz glass powder with 99 % of the particles being less than 13 μm in size. It is reasonable that the powder exhibits a lower failed strength than the thermally shocked glass cylinders that consist of significantly larger fragments "interlocked" with each other.

Therefore, the degree of damage has a significant influence on the residual strength at low hydrostatic pressures (< 1 GPa). However, Chocron and Dannemann et al. do not provide a description for this correlation [63]. Only for higher pressures between 1 and 7 GPa, they concluded that the residual strength is independent of the degree of damage [22].

In order to model a ballistic impact scenario against SLG, it is essential to describe the strength of the damaged glass correctly. In front of the projectile, the glass is highly comminuted (Mescall zone [131]). Therefore, characterization experiments with specimens exhibiting a similar degree of damage are necessary. On the one hand, the pre-damage generated in the tests by Dannemann and Chocron et al. is most probably too low [132]. On the other hand, the bed of

loosely poured powder used by Shockey et al. exhibits a too low residual strength since larger, interlocking particles are missing. In addition, Shockey et al. reported that the density, packing, temperatures, rates and pressures generated in their tests do not replicate those imposed by a penetrating projectile [29].

With the aim to investigate the pre-damage in front of the projectile, Shockey et al. [131] [133] developed an alternative test methodology. In ballistic tests, a steel rod partially penetrated large blocks of SLG or borosilicate glass encased by thick PMMA plates. After the rod was stopped, the extent of damage in the glass and the size distribution of the generated fragments were analyzed. However, Shockey et al. concluded that the observed damage was not representative of the dynamic processes occurring during a realistic impact scenario (no Mescall zone). This is probably due to the low impact velocities of the rod (300 to 600 m/s) and the gradual deceleration of the rod. Nevertheless, quantitative estimates of microcrack size and density in the Mescall zone were deduced from the sizes and shapes of fragments obtained from the penetration tunnel.

1.2.4.1 Issues of reported simulation results

The described shortcomings in the basic characterization experiments represent an additional challenge for the modeling efforts. In the following, a selection of reported simulation results is presented that explicitly list discrepancies to experimental results.

Chocron et al. [132] [63] used their characterization experiments for the simulation of experiments conducted by Behner et al. [20]. In these experiments, long gold rods (inversely) impacted borosilicate glass cylinders over a wide range of impact velocities (800 to 2800 m/s). In the simulations, the strength of the glass models (Drucker-Prager and Mohr-Coulomb) was significantly too high. Therefore, they concluded that the glass in front of the gold rod was more severely damaged than the specimens of the characterization tests. They further noticed that details of the transition of intact to damaged glass are important at early penetration times for the lower range of impact velocities.

That the transition from intact to damaged behavior of brittle materials under ballistic impact is not adequately addressed in existing models was also reported by Dannemann et al. [127]. They referred to the ceramic models of Johnson and Holmquist [134] [135] and others [136] [137] [138] who have made significant contributions in this field of research.

Anderson and Holmquist [51] used the state-of-the-art Holmquist-Johnson model [30] to simulate the experiments of Behner et al. [20] [139] as described above. The focus of the study was to investigate the ability of the model to replicate the rate and extend of the failure propagation and the penetration depths of the rod. Anderson et al. later reported that “the computations were illuminating, but model constants had to be modified to replicate the experimental results to a better degree of fidelity. This finding was not unexpected as [...] the independent laboratory experiments/results used to determine model constants are sparse and sometimes conflicting” [140](pp. 375+376).

In 2017, Holmquist et al. further improved the Holmquist-Johnson model by using an alternative formulation for the description of the interior and surface strength. The improved Holmquist-Johnson model was less dependent on the resolution of the discretization than the original Holmquist-Johnson model. They showed that the simulation results of specific impact scenarios on borosilicate glass were in good agreement with the experimental data [141].

Anderson et al. [25] also investigated the performance of a borosilicate glass model incorporating a Drucker-Prager constitutive model for the failed material. Several sets of model parameters were compared based on independent characterization experiments [63] [22]. They demonstrated that the EOS can have a significant effect on the computational results of the gold rod penetration. Furthermore, they reported that the experimental results of Behner et al. [20] could be replicated in the simulations, but only in scenarios where the penetration pressure was large enough and therefore details of the transition from intact to failed glass were not important. They concluded that for penetration pressures below 1.6 GPa (corresponding to an impact velocity of 768 m/s in case of the gold rod) “the assumption of penetrating failed material is clearly inappropriate” [25] (p. 1047).

Furthermore, Holmquist et al. [142] were able to infer the internal tensile strength of borosilicate glass by comparing the experimental results of laser shock tests with simulations using the Holmquist-Johnson model. However, the shape of the simulated failure was different from that observed in the experiments, which was attributed to a limitation of the model, constants, and/or numerical algorithms.

Later, Gorfain et al. [54] conducted an extensive literature research in order to develop a complete set of parameters for a Holmquist-Johnson model of SLG. The model was then used to simulate PPI tests and Taylor rod impact covering a wide range of impact velocities (370 m/s – 3220 m/s) and pressures (2.8 GPa – 41 GPa). Overall, the simulation results were found to be in good agreement with the experiments. However, the authors noted that “experimental data characterizing the strength of glass from the uniaxial stress compression load path through the hydrostatic tensile regime is clearly lacking, hence the current model description of this behavior should be considered preliminary. [...] Therefore, improvement upon the current results may be possible with some refinement of the soda-lime glass strength parameters better representing time-dependent loss of strength, modification to the assumed failed strength, and refinement of the failure strain in the damage model” [54](p. 303).

1.3 Objectives and layout of the thesis

The objective of this thesis is to improve the simulation capabilities of existing models of SLG, with the focus on highly dynamic impact scenarios. To achieve this goal, new characterization and analysis methods are developed. Furthermore, the new results are used to improve an existing model.

As summarized in the previous section (1.2.4), certain issues are still unclear that are crucial to the material behavior of SLG in ballistic impact scenarios. One of the most important issues is the lack of experimental data characterizing the residual strength as a function of the degree of damage. Another important aspect is the determination of the EOS and the HEL. Both issues are addressed by new experimental and evaluation methodologies.

The layout of this thesis is as follows. Chapter 2 provides the theoretical fundamentals required for the description of the constitutive material behavior in continuum mechanics.

Chapter 3 illustrates the numerical basics of hydrocodes. Different model approaches to describe the dynamic behavior of SLG are also presented.

Chapter 4 presents a new methodology to determine the dynamic behavior of SLG. The key innovations are experimental as well as analytical aspects. On the one hand, an extensive PPI test series is carried out over a wide range of shock loading stress levels instrumented by two high-speed cameras and laser interferometers (PDV and VISAR). On the other hand, a systematic analysis concept is developed and evaluated by numerical simulations. As a result, the EOS and the HEL for SLG are derived including an error estimation. Furthermore, new insights into the failure front phenomenon are gained by combining the results of the velocity profiles with the additional high-speed video observation.

Many results presented in this chapter have already been pre-published by the author in [A1] and are partly reproduced.

Chapter 5 presents a new methodology for the characterization of the residual strength as a function of the degree of damage. This includes a novel test setup to create different degrees of pre-damage in small SLG cylinders. A newly developed analysis method is subsequently used to determine the degree of damage contact-free by means of X-ray CT. Afterwards, the residual strength is measured in confined compression tests supported by numerical simulations. The obtained results are discussed and compared with reported literature data.

Chapter 6 illustrates how the new findings can be incorporated in an existing SLG model. A improved strength model is developed and implemented by means of a user subroutine in the Johnson-Holmquist-2 (JH2) model. Results of the original and the improved model are compared to the experimental results of a selected impact scenario.

In conclusion of the dissertation, all obtained results are summarized in Chapter 7.

2 Continuum mechanical basics

In this chapter, the theoretical principles of continuum mechanics are briefly introduced. The concept of strain and stress tensors are outlined, which are required for the analytical description and modeling of the material behavior. Furthermore, the concepts of elasticity and plasticity are introduced. In the course of this chapter, the most common criteria for the description of yield and failure are presented. More in-depth descriptions and further information and literature can be found e.g. in [143].

2.1 Stress and strain tensors

The continuum mechanical description of a body is realized by assigning to it a finite number of material points. Here, the real microstructure of the material is simplified into a smeared, homogenized microstructure. Each point is unambiguously defined at any point of time. Furthermore, it is assumed that two infinitely close material points remain infinitely close upon deformation of the body.

In the following, the so-called Lagrangian description is used, in which the focus is on material particles travelling through space. This approach is generally preferred in structural mechanics for the description of a solid state behavior.

An alternative approach is the so-called Eulerian description, in which the focus is on fixed positions in space that can be occupied by various particles over time. This spatial description is predominantly used in fluid mechanics. In section 4.1, the derivation of shock wave equations is done in the Eulerian description. The transformation from Eulerian to Lagrangian equations is provided in the appendix in section 9.1.

Figure 2.1 schematically illustrates the motion and deformation of a generic body in a Cartesian coordinate system.

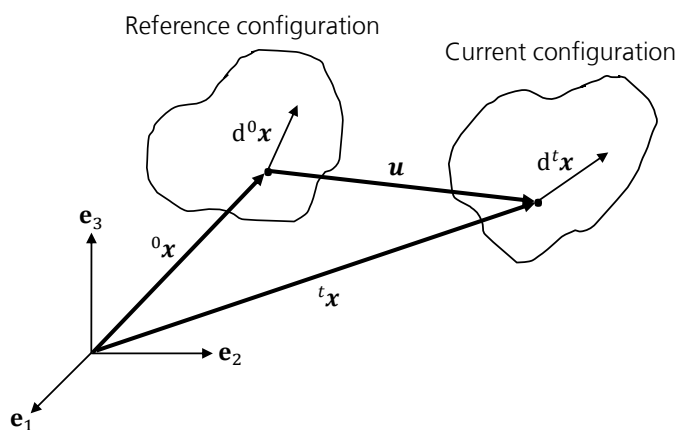


Figure 2.1: Schematic of body motion and deformation.

The displacement of material point M at time t is given by:

$$\mathbf{u} = {}^t\mathbf{x} - {}^0\mathbf{x} \quad 2.1$$

where ${}^0\mathbf{x}$ denotes the Cartesian coordinates in the reference configuration ($t = 0$) and ${}^t\mathbf{x}$ refers to the coordinates of the current configuration.

In order to describe the deformation of a body, a material deformation gradient \mathbf{F} is introduced. \mathbf{F} is a second-order tensor, which transforms an infinitesimal line element $d^0\mathbf{x}$ from the reference to the current configuration:

$$\mathbf{F} = \frac{d^t\mathbf{x}}{d^0\mathbf{x}} \quad \text{or, using indicial notation in a 3D space, } F_{ij} = \frac{d^t x_i}{d^0 x_j} \quad 2.2$$

For the description of finite strains, the second-order Green-Lagrange strain tensor \mathbf{E} is introduced, which is defined by the difference between the squared line elements of the current and those of the reference configuration:

$$d^t\mathbf{x} d^t\mathbf{x} - d^0\mathbf{x} d^0\mathbf{x} = 2 d^0\mathbf{x} \mathbf{E} d^0\mathbf{x} \quad 2.3$$

By using equation 2.2, the Green-Lagrange tensor can be written as:

$$\mathbf{E} = \frac{1}{2} (\mathbf{F}^T \mathbf{F} - \mathbf{I}) \quad 2.4$$

Combining equations 2.1 and 2.2 yields:

$$F_{ij} = \frac{\partial(^0x_i + u_i)}{\partial^0x_j} = \delta_{ij} + \frac{\partial u_i}{\partial^0x_j} \quad 2.5$$

where $\delta_{ij} = 1$ if $i = j$ and 0 otherwise. By using equation 2.5, \mathbf{E} can be written as:

$$E_{ij} = \frac{1}{2} \left(\frac{\partial u_i}{\partial^0x_j} + \frac{\partial u_j}{\partial^0x_i} \right) + \frac{1}{2} \frac{\partial u_k}{\partial^0x_i} \frac{\partial u_k}{\partial^0x_j} \quad 2.6$$

Here, \mathbf{E} is separated in a linear and a quadratic term. The quadratic term accounts for nonlinear strains, which allows for the description of finite strains and therefore large deformations. In case of infinitesimal small deformations, the material strain can be described by the linearized term only:

$$\varepsilon_{ij} = \frac{1}{2} \left(\frac{\partial u_i}{\partial^0x_j} + \frac{\partial u_j}{\partial^0x_i} \right) \quad 2.7$$

A common engineering approach for the measurement of strain is the so-called engineering strain, which is based on the displacement with regard to the reference configuration. In the one-dimensional case of uniaxial strain, equation 2.7 yields an engineering strain of

$$\varepsilon_{\text{engin}} = \frac{l - l_0}{l_0} = \frac{l}{l_0} - 1 \quad 2.8$$

where l_0 and l denote the length in the reference and the current configuration, respectively.

An alternative strain measure is the so-called true strain, which bases upon infinitesimal strain increments that relate the infinitesimal displacements to the current length [144]. The total true strain is derived by the integration over the length variation process:

$$\begin{aligned}\varepsilon_{\text{true}} &= \int_{l_0}^l \frac{dl}{l} \\ &= \ln\left(\frac{l}{l_0}\right) \\ &= \ln(\varepsilon_{\text{engin}} + 1)\end{aligned}\tag{2.9}$$

For a more generalized formulation of finite strain tensors, the reader is referred e.g. to [145], [146], [147] and [148].

In order to define a stress measure at any given point in the continuum, the second-order Cauchy stress tensor is introduced:

$$\sigma_{ij} = \begin{bmatrix} \sigma_{11} & \sigma_{12} & \sigma_{13} \\ \sigma_{21} & \sigma_{22} & \sigma_{23} \\ \sigma_{31} & \sigma_{32} & \sigma_{33} \end{bmatrix}\tag{2.10}$$

The Cauchy stress tensor describes the effect of a differential surface force acting on an infinitesimal surface area element in the current configuration. The corresponding stress vector \mathbf{t} is defined by the projection of the stress tensor on the surface normal vector \mathbf{n} :

$$\mathbf{t} = \boldsymbol{\sigma} \cdot \mathbf{n} \quad \text{or} \quad t_i = \sigma_{ij}n_j\tag{2.11}$$

Figure 2.2 illustrates the components of $\boldsymbol{\sigma}$ on the surfaces of an infinitesimal element in Euclidian space. The stress vector of each coordinate plane presents the surface traction, which can be decomposed into a normal and two shear components. Due to the conservation of angular momentum, the Cauchy stress tensor is symmetric:

$$\boldsymbol{\sigma} = \boldsymbol{\sigma}^T\tag{2.12}$$

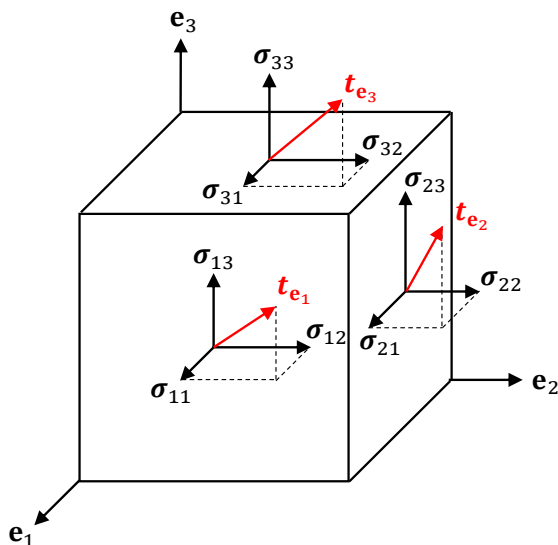


Figure 2.2: Schematic of stress components and surface tractions on an infinitesimal volume element.

The three eigenvalues $\sigma_I, \sigma_{II}, \sigma_{III}$ and the three eigenvectors of the Cauchy stress tensor are referred to as principal stresses and principal directions, respectively. If any arbitrary stress tensor is rotated in a way that the normal components are aligned with the principal directions, all shear components, i.e. all non-diagonal components, vanish.

By solving the characteristic equation

$$\sigma^3 - I_1\sigma^2 + I_2\sigma - I_3 = 0 \quad 2.13$$

the invariants I_1, I_2 and I_3 of the stress tensor are derived as follows:

$$I_1 = \text{tr}[\boldsymbol{\sigma}] = \sigma_{ii} = \sigma_{11} + \sigma_{22} + \sigma_{33} \quad 2.14$$

$$I_2 = \frac{1}{2}(\text{tr}^2[\boldsymbol{\sigma}] - \text{tr}[\boldsymbol{\sigma}^2]) = \sigma_{11}\sigma_{22} + \sigma_{22}\sigma_{33} + \sigma_{33}\sigma_{11} - \sigma_{12}^2 - \sigma_{23}^2 - \sigma_{31}^2 \quad 2.15$$

$$I_3 = \det[\boldsymbol{\sigma}] = \sigma_{11}\sigma_{22}\sigma_{33} + 2\sigma_{12}\sigma_{23}\sigma_{31} - \sigma_{12}^2\sigma_{33} - \sigma_{23}^2\sigma_{11} - \sigma_{31}^2\sigma_{22} \quad 2.16$$

which can be expressed in terms of the principal stresses as:

$$I_1 = \sigma_I + \sigma_{II} + \sigma_{III} \quad 2.17$$

$$I_2 = \sigma_I\sigma_{II} + \sigma_{II}\sigma_{III} + \sigma_{III}\sigma_I \quad 2.18$$

$$I_3 = \sigma_I\sigma_{II}\sigma_{III} \quad 2.19$$

For the formulation of plasticity and failure models, it is beneficial to decompose the stress tensor into a spherical tensor \mathbf{P} and a deviatoric tensor \mathbf{S} :

$$\boldsymbol{\sigma} = \mathbf{S} - \mathbf{P} \quad 2.20$$

The spherical tensor \mathbf{P} can be expressed through the first invariant of the Cauchy stress tensor:

$$\mathbf{P} = P\delta_{ij} = -\frac{1}{3}I_1\delta_{ij} \quad 2.21$$

where $P = -\frac{1}{3}I_1$ represents the hydrostatic pressure.

The invariants J_1, J_2 and J_3 of \mathbf{S} can be formulated accordingly to equations 2.14 to 2.16 as follows:

$$J_1 = \text{tr}[\mathbf{S}] = S_I + S_{II} + S_{III} = 0 \quad 2.22$$

$$J_2 = \frac{1}{2}S_{ij}S_{ij} = \frac{1}{6}[(\sigma_{11} - \sigma_{22})^2 + (\sigma_{22} - \sigma_{33})^2 + (\sigma_{33} - \sigma_{11})^2] + \sigma_{12}^2 + \sigma_{23}^2 + \sigma_{31}^2 \quad 2.23$$

$$J_3 = \frac{1}{3}S_{ij}S_{jk}S_{ki} = S_I S_{II} S_{III} \quad 2.24$$

A geometrical representation of the decomposition of the stress tensor is provided in the three-dimensional principal stress space, also referred to as Haigh-Westergaard space [149] [150]. In this space, all states of pure hydrostatic stresses ($S_I = S_{II} = S_{III} = 0$) are located on the spatial diagonal, also referred to as hydrostatic axis:

$$\sigma_I = \sigma_{II} = \sigma_{III} = \frac{1}{3}I_1 = -P \quad 2.25$$

Stress states of equal hydrostatic pressure are located on a plane that is normal to the hydrostatic axis. The family of normal planes are also called octahedral planes or deviatoric planes. The distance ξ between the deviatoric plane and the origin of the stress space represents the spherical component of the stress tensor and is given by:

$$\xi = -\sqrt{3} P \quad 2.26$$

The shortest stress vector pointing from the hydrostatic axis to the position of the stress state is called ρ and represents the deviatoric component. The length ρ of the vector is given by:

$$\rho = \sqrt{S_I^2 + S_{II}^2 + S_{III}^2} = \sqrt{2J_2} \quad 2.27$$

Furthermore, the so-called Lode angle θ between ρ and the first principal stress axis projected into the deviatoric plane is given by:

$$\cos(3\theta) = \frac{3\sqrt{3}}{2} \frac{J_3}{J_2\sqrt{J_2}} \quad 2.28$$

The variables ξ , ρ and θ are called the Haigh-Westergaard coordinates. They can be used to unambiguously define any stress state. For the experimental characterization of an isotropic material, it is sufficient to investigate only stress states in the section $0^\circ \leq \theta \leq 60^\circ$ due to material symmetry. Figure 2.3 illustrates an arbitrary stress state σ together with the corresponding Haigh-Westergaard coordinates in the principal stress space.

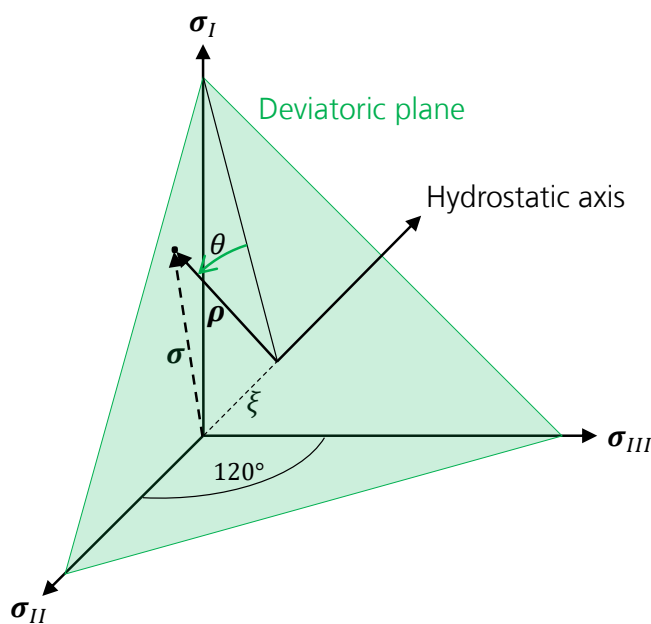


Figure 2.3: Illustration of the Haigh-Westergaard coordinates of an arbitrary stress state σ in the principal stress space.

Within the framework of this work, the calculation of strain and stress is generally realized by means of hydrocodes. In explicit solvers, the calculations of the current configuration are not referred to the reference configuration ($t = 0$). Instead, the current configuration is used to determine the current configuration of the next calculation cycle ($t + \Delta t$). In this case, the Cauchy stress tensor (eq. 2.10) and the linearized Green-Lagrange tensor (eq. 2.7) are well suited.

Alternative stress measures are required if a constitutive model is formulated with regard to the reference configuration. In this case, e.g. the first or second Piola-Kirchhoff stress tensors are suited (see e.g. [143]).

2.2 Elasticity, plasticity, failure and damage

This section gives a short overview of the basic concepts of elasticity, plasticity, failure and damage. For a more in-depth description, the reader is referred e.g. to [143].

2.2.1 Elasticity

Elasticity refers to a material behavior with a reversible and path-independent relation between stress and strain. More specifically, the material behavior is called Cauchy elastic, if the path-independence of the stress state is given by a constitutive equation. In case the path-independence of energy is guaranteed as well, the behavior is referred to as Green elasticity.

The stress-strain relation of a Cauchy elastic material is described by a three-dimensional form of Hooke's law, which is valid for infinitesimal strains:

$$\sigma_{ij} = E_{ijkl} \varepsilon_{kl} \quad 2.29$$

where E_{ijkl} denotes the fourth order elasticity tensor.

For a general description of elastic anisotropic material behavior and special cases like e.g. monoclinic elasticity or orthotropic elastic behavior, the reader is referred to [143]. In case of an elastic material response that is independent of the loading direction (isotropic), equation 2.29 can be simplified to:

$$\sigma_{ij} = 2\mu_L \varepsilon_{ij} + \lambda_L \varepsilon_{kk} \delta_{ij} \quad 2.30$$

or in matrix notation:

$$\begin{bmatrix} \sigma_{11} \\ \sigma_{22} \\ \sigma_{33} \\ \sigma_{23} \\ \sigma_{31} \\ \sigma_{12} \end{bmatrix} = \begin{bmatrix} \lambda_L + 2\mu_L & \lambda_L & \lambda_L & 0 & 0 & 0 \\ \lambda_L & \lambda_L + 2\mu_L & \lambda_L & 0 & 0 & 0 \\ \lambda_L & \lambda_L & \lambda_L + 2\mu_L & 0 & 0 & 0 \\ 0 & 0 & 0 & \mu_L & 0 & 0 \\ 0 & 0 & 0 & 0 & \mu_L & 0 \\ 0 & 0 & 0 & 0 & 0 & \mu_L \end{bmatrix} \begin{bmatrix} \varepsilon_{11} \\ \varepsilon_{22} \\ \varepsilon_{33} \\ 2\varepsilon_{23} \\ 2\varepsilon_{31} \\ 2\varepsilon_{12} \end{bmatrix} \quad 2.31$$

where λ_L and μ_L denote the Lamé constants.

The Lamé constants are defined through the elastic material parameters as follows:

$$\lambda_L = \frac{\nu E}{(1 + \nu)(1 - 2\nu)} \quad 2.32$$

$$\mu_L = \frac{E}{2(1 + \nu)} = G \quad 2.33$$

with the Young's modulus E , the Poisson's ratio ν and the shear modulus G .

Further important elastic material constants are the bulk modulus K and the longitudinal modulus M that are related to the Lamé constants as follows:

$$K = \lambda_L + \frac{2}{3}\mu_L \quad 2.34$$

$$M = \lambda_L + 2\mu_L \quad 2.35$$

2.2.2 Plasticity

For many engineering materials, the loading behavior is linear elastic only at small strains. Further loading generally results in permanent deformation caused by irreversible modifications of the initially unloaded material on a molecular scale. Typical modifications are e.g. dislocation movement, growth and coalescence of micro-defects or disentanglement of polymer chains.

The onset of these modifications is denoted in plasticity theory as the initiation of plastic yield. Specific stress and strain conditions are defined under which plastic yielding occurs. It has to be noted, however, that these so-called yield criteria are conventions since most materials do not exhibit a precise physical threshold separating purely elastic and plastic deformations.

A common yield criterion for uniaxial tension tests is the $R_{p0.2}$ -threshold. $R_{p0.2}$ defines the beginning of plastic flow at the stress-strain state that results in a permanent deformation of $\varepsilon = 0.2\%$ after total unloading. Figure 2.4 illustrates $R_{p0.2}$ in a stress-strain plot of an idealized elastic-plastic material. Up to the true yield stress Y , the behavior is linear elastic with slope E . From the yield point, further loading results in plastic flowing. The experimental determination of Y would lead to large measurement errors. However, $R_{p0.2}$ is straightforward to determine by intersecting the stress-strain curve with a line with slope E through the point ($\varepsilon = 0.2\%$, $\sigma = 0$).

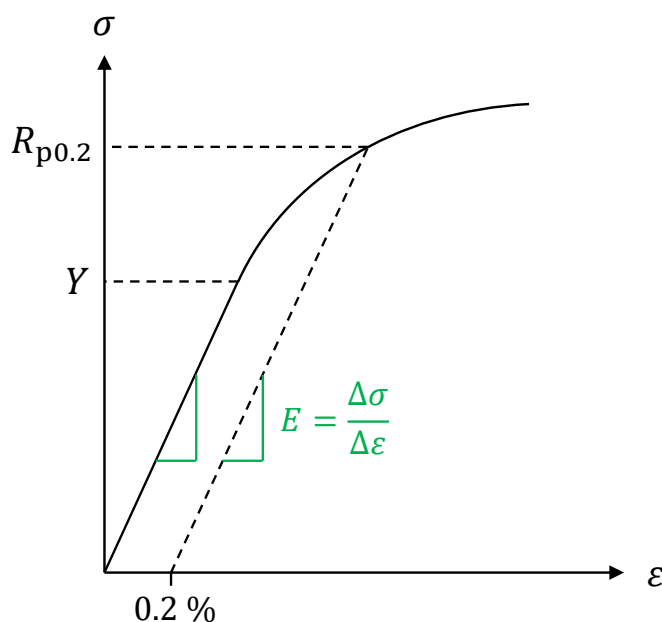


Figure 2.4: Stress-strain curve of an idealized elastic-plastic material under uniaxial tension.

In order to describe the beginning of plastic deformation for an arbitrary stress-strain condition, the concept of yield functions is introduced. In the six-dimensional stress space, all possible stress states at which plastic yield is initiated are located on a hypersurface. The yield function $F(\boldsymbol{\sigma})$ representing the yield criteria is defined to equal zero on this so-called yield surface:

$$F(\boldsymbol{\sigma}) = 0 \quad 2.36$$

Furthermore, $F(\boldsymbol{\sigma})$ is defined to be less than zero for all elastic states. Since stress states with $F(\boldsymbol{\sigma}) > 0$ are not allowed, the yield surface can be considered as a limiting envelope of all physically possible states.

Four of the most common yield surfaces for isotropic materials are illustrated in the principal stress space in Figure 2.5. In the following, an overview of the corresponding yield criteria is given. For additional yield criteria, like e.g. the anisotropic Hill criterion, the reader is referred to [143].

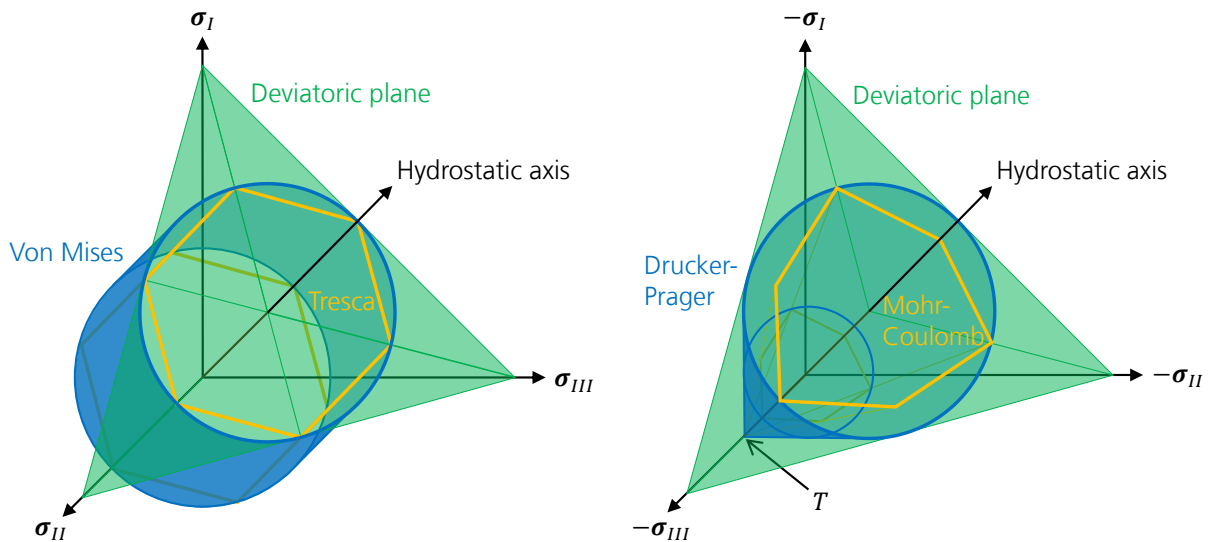


Figure 2.5: Illustration of most common yield surfaces: In the principal stress space, the von Mises yield surfaces is a cylinder with constant radius, independent on the hydrostatic pressure (blue surface in left image). The von Mises cylinder envelopes a hexagonal prism, which represents the Tresca yield surface (surface edges are depicted as yellow lines in left image). The right image illustrates the Drucker-Prager (blue) and the Mohr-Coulomb (yellow) yield surfaces. These two criteria are also dependent on the hydrostatic pressure and are intersecting the hydrostatic axis at the hydrostatic tensile limit T .

Von Mises criterion

A criterion that is well suited for ductile materials, like e.g. metals, is the von Mises criterion [151]. Based on experimental observations [52] the von Mises criterion postulates that the yield stress is independent on the hydrostatic pressure and the third invariant of the stress tensor.

In this case, equation 2.36 is reduced to:

$$F(\boldsymbol{\sigma}) = F(J_2) = J_2 - \kappa^2 = 0 \quad 2.37$$

where κ denotes the yield stress under pure shear loading.

Combining equations 2.27 and 2.37 yields:

$$\rho = \sqrt{2} \kappa \quad 2.38$$

Therefore, the von Mises yield surface is a cylinder with a constant radius in the principal stress space (ref. Figure 2.5). An important quantity is the corresponding yield stress under uniaxial tension, also referred to as the von Mises stress or the equivalent stress:

$$\sigma_{\text{eq}} = \sqrt{\frac{3}{2}} \rho = \sqrt{3J_2} = \frac{1}{\sqrt{2}} \sqrt{(\sigma_I - \sigma_{II})^2 + (\sigma_{II} - \sigma_{III})^2 + (\sigma_{III} - \sigma_I)^2} \quad 2.39$$

Tresca criterion

The Tresca yield criterion has been originally developed for the description of granular and soil material [152]. Similar to the von Mises criterion, the Tresca criterion postulates that the yield stress is independent on the hydrostatic pressure. However, the Tresca criterion adds a dependency on the third invariant of the stress tensor. The yield function is formulated in terms of the principal stresses as follows:

$$F(\boldsymbol{\sigma}) = F(\sigma_I, \sigma_{II}, \sigma_{III}) = \frac{1}{2} \max(|\sigma_I - \sigma_{II}|, |\sigma_{II} - \sigma_{III}|, |\sigma_{III} - \sigma_I|) - \kappa = 0 \quad 2.40$$

Therefore, plastic yielding starts when half of the highest principal stress difference equals the yield stress under pure shear. In the principal stress space, the Tresca yield surface is a hexagonal prism with infinite length, which is enveloped by the von Mises cylinder (ref. Figure 2.5). A disadvantage of the Tresca criterion in terms of model implementation is the non-continuous characteristic of the sharp edges of the hexagon.

Drucker-Prager criterion

For geological or porous materials, like e.g. rock or concrete, the yield criterion has to be also dependent on the hydrostatic pressure. This leads to the Drucker-Prager criterion, which is defined as follows:

$$F(\boldsymbol{\sigma}) = F(I_1, J_2) = \alpha I_1 + \sqrt{J_2} - \beta = 0 \quad 2.41$$

or expressed through the Haigh-Westergaard coordinates:

$$F(\boldsymbol{\sigma}) = F(\xi, \rho) = \sqrt{6} \alpha \xi + \rho - \sqrt{2} \beta = 0 \quad 2.42$$

where α and β are material constants.

Due to the independence on θ , the yield surface is invariant to rotation around the hydrostatic axis, similar to the von Mises yield surface. As illustrated in Figure 2.5, the pressure dependence results in a conical shape of the Drucker-Prager yield surface in the principal stress space. The origin of the cone is the so-called hydrostatic tensile limit T :

$$T = -\frac{\beta}{3\alpha} \quad 2.43$$

Mohr-Coulomb criterion

The Mohr-Coulomb criterion is a generalized formulation of the Tresca criterion. It is based on Coulomb's law of shear strength also postulating that yielding or failure is governed by the maximum shear stress. The resulting yield function is formulated using the lengths of the tangential component τ and the normal component σ_n of the stress vector \mathbf{t} (ref. equation 2.11):

$$F(\tau, \sigma_n) = \tau + \sigma_n \tan \phi - C = 0 \quad 2.44$$

where ϕ denotes the angle of internal friction and C represents the cohesion.

Using the Haigh-Westergaard invariants, equation 2.44 can be expressed as:

$$F(\xi, \rho, \phi) = \sqrt{2} \xi \sin \phi + \sqrt{3} \rho \sin \left(\theta + \frac{\pi}{3} \right) + \rho \cos \left(\theta + \frac{\pi}{3} \right) \sin \phi - \sqrt{6} C \cos \phi = 0 \quad 2.45$$

As illustrated in Figure 2.5, the Mohr-Coulomb yield surface has a hexagonal shape in the principal stress space. The shape of the hexagon is in correlation to the Drucker-Prager yield surface as follows: The outer apexes of the hexagon (compressive meridians) are located on a Drucker-Prager cone with parameters α_- and β_- . The inner apexes (tensile meridians) coincide with a Drucker-Prager cone given by the parameters α_+ and β_+ . These parameters are defined through ϕ and C as follows:

$$\alpha_{\pm} = \frac{2 \sin \phi}{\sqrt{3} (3 \pm \sin \phi)} \quad 2.46$$

$$\beta_{\pm} = \frac{6 C \cos \phi}{\sqrt{3} (3 \pm \sin \phi)} \quad 2.47$$

An alternative formulation of the Mohr-Coulomb yield criterion is obtained by rewriting equation 2.45 based on the invariants I_1 and J_2 :

$$F(I_1, J_2, \phi) = \frac{1}{3} I_1 \sin \phi + \sqrt{J_2} \sin \left(\theta + \frac{\pi}{3} \right) + \sqrt{\frac{J_2}{3}} \cos \left(\theta + \frac{\pi}{3} \right) \sin \phi - C \cos \phi = 0 \quad 2.48$$

Combining equation 2.48 with equations 2.25 and 2.36 yields:

$$F(P, \sigma_{\text{eq}}, \phi) = -P \tan \phi + \left[\frac{1}{\sqrt{3} \cos \phi} \sin \left(\theta + \frac{\pi}{3} \right) + \frac{1}{3} \tan \phi \cos \left(\theta + \frac{\pi}{3} \right) \right] \sigma_{\text{eq}} - C = 0 \quad 2.49$$

The term in squared brackets is called the Mohr-Coulomb deviatoric stress measure R_{mc} . For a given R_{mc} , equation 2.49 presents a straight-line equation. Therefore, the Mohr-Coulomb yield surface can be illustrated by a straight line in the $\sigma_{\text{eq}} R_{\text{mc}} - P$ -plane, defined by the internal friction C and the cohesion ϕ , as shown in Figure 2.6. The intersection of the straight line with the hydrostatic axis corresponds to the hydrostatic tensile limit $T = -\frac{C}{\tan \phi}$.

For the description of SLG, defining the yield surface in the equivalent stress-hydrostatic pressure plane is also a suitable approach. This is outlined in detail in section 3.2.3.1.

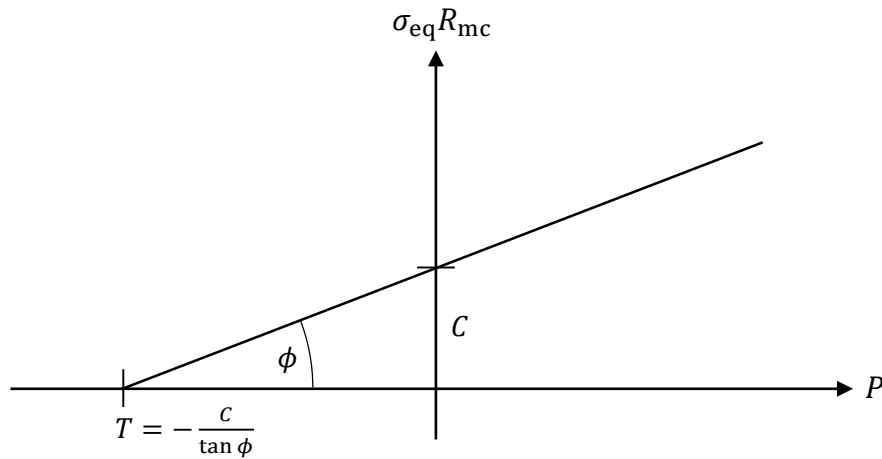


Figure 2.6: The Mohr-Coulomb yield surface is represented by a straight line with slope ϕ in the $\sigma_{\text{eq}}R_{\text{mc}}-P$ -plane.

As described above, the yield functions $F(\boldsymbol{\sigma})$ define the criteria for the initiation of plastic yield. Upon further loading of the material, plastic flow occurs accumulating irreversible deformations. The resulting plastic strain increments $d\boldsymbol{\varepsilon}^{\text{P}}$ are described by flow rules in classic plasticity theory. Based on Drucker's postulate, a stable material requires a convex yield surface and all plastic strain increments have to be normal to the yield surface. This so-called normality condition is formulated in case of associated flow as:

$$d\boldsymbol{\varepsilon}^{\text{P}} = d\lambda \frac{\partial F}{\partial \boldsymbol{\sigma}} \quad 2.50$$

where $d\lambda$ denotes a scalar factor. Due to the consistency condition, the occurrence of plastic flow ($d\lambda > 0$) requires the stress state to be located on the yield surface. In addition, in case of an elastic stress state ($F(\boldsymbol{\sigma}) < 0$), plastic flow cannot occur ($d\lambda = 0$).

Alternatively, a so-called non-associated flow rule can be defined. In this case, the increments in plastic strain are not described by the yield function, but instead by a plastic potential $G(\boldsymbol{\sigma})$:

$$d\boldsymbol{\varepsilon}^{\text{P}} = d\lambda \frac{\partial G}{\partial \boldsymbol{\sigma}} \quad 2.51$$

Typically, the yield stress increases with increasing plastic strain. This effect is referred to as hardening. In case of isotropic strain or work hardening, the initial yield function $F(\boldsymbol{\sigma})$ is expanded isotropically by subtracting a monotonically increasing function $K(g)$:

$$F(\boldsymbol{\sigma}) - K(g) = 0 \quad 2.52$$

where the hardening parameter g represents either the total plastic work or the effective plastic strain $\varepsilon_{\text{eff}}^{\text{P}} = \sqrt{\frac{2}{3} \boldsymbol{\varepsilon}_{ij}^{\text{P}} \boldsymbol{\varepsilon}_{ij}^{\text{P}}}$.

In case of kinematic hardening, the yield surface is translated in the stress space with increasing plastic strain. The shape and the size of the surface are not affected by this translation.

A so-called back stress tensor σ_B is defined, which describes the change from the initial yield surface:

$$F(\boldsymbol{\sigma} - \boldsymbol{\sigma}_B(\boldsymbol{\varepsilon}^p)) = 0 \quad 2.53$$

In addition to the outlined dependencies, the yield criteria of most materials are also dependent on the strain rate. Considering the rate dependence is especially important for dynamic processes, like e.g. impact of a projectile or deep drawing of metals. A variety of strain rate dependent formulations is used for the application in numerical models. A widely used phenomenological model is e.g. the Johnson-Cook yield model [153], which is not only strain and strain rate dependent, but also incorporates a dependency on the temperature. An overview of the most common models for strain rate dependent plasticity can be found e.g. in [143].

2.2.3 Failure and damage

The loss of the load carrying capacity of a structure or material unit is called material failure. The driving mechanisms of failure are the nucleation, coalescence and growth of voids and cracks. In case of SLG, the cracks are emerging from pre-existing flaws. These flaws are typically small surface cracks ($\leq 20 \mu\text{m}$) introduced during the manufacturing or finishing process.

Similar to the description of the yield criteria in plasticity theory, failure criteria are defined in failure theory to separate failed from intact states. Usually, two types of failure are distinguished, brittle failure and ductile failure. On the one hand, ductile materials, like metals or polymers, can accumulate several tens to hundreds of percents of plastic strain before failure occurs. During the ductile failure process, deformation energy can be dissipated. On the other hand, brittle materials, like glasses or ceramics, typically fail abruptly at strains of much less than one percent under tensile loading.

The failure criteria of many materials are also strain rate dependent. For example, the ductile behavior of metals at quasi-static loads can turn into brittle failure at high strain rates. As outlined in chapter 1, the mechanical response of SLG is significantly different under quasi-static and highly dynamic strain rates. On the one hand, SLG typically fails by the propagation of only few discrete cracks when loaded quasi-statically. On the other hand, a large number of micron- and sub-micron-size cracks is generated under dynamic loading. This results in a substantially larger degree of damage and comminution.

Depending on the investigated scale, different model approaches are used to describe failure. On a microscopic scale, elastic-plastic fracture mechanics is used to describe the initiation and local discontinuous propagation of individual cracks. Here, the crack propagation is described by failure criteria based on crack shapes and loading conditions. One approach to describe the unstable crack growth is Griffith's theory [55]. Based on energy considerations, a critical stress is determined, which is required for the extension of the crack tip.

For a detailed description of elastic and plastic fracture mechanics in solids the reader is referred e.g. to [55], [154], [155] and [156].

On a macroscopic scale, it is often more beneficial to use continuous formulations in contrast to the discretization of individual crack formations. In this case, the micro-mechanical processes need to be reflected in the constitutive macroscopic description. This is especially important if local failure effects make up a large part of the overall energy dissipation of a structure. Here, an adequate type of representation in the numerical discretization is required. In case of multiple fragmentation, mesh-free methods or advanced discretization methods like a cohesive zone approach [157] [158] could lead to results that are more accurate.

A common continuous formulation is a phenomenological approach that is called continuum damage mechanics. In the following, the basic concepts are briefly outlined. An in-depth discussion of the related theories can be found in [143], [159], [160] and [161].

The most common failure criteria are defined as failure surfaces in the stress or strain space, similar to the yield surfaces. Phenomenological failure criteria are e.g. a maximum stress or strain criterion and formulations similar to the von Mises, Tresca, Mohr-Coulomb, Drucker-Prager or Hill criterion. A common criterion that is based on a micro-mechanical theory is e.g. the Gurson criterion that is outlined in more detail in [143].

To describe the transition from microscopic to macroscopic failure in a continuum mechanical model, a scalar damage parameter D is introduced. The concept was originally proposed by Kachanov [162] and Rabatnov [163]. In a cross section of a representative volume element (RVE), D is defined to be the ratio between the damaged area S_D and the total area S , as illustrated in Figure 2.7.

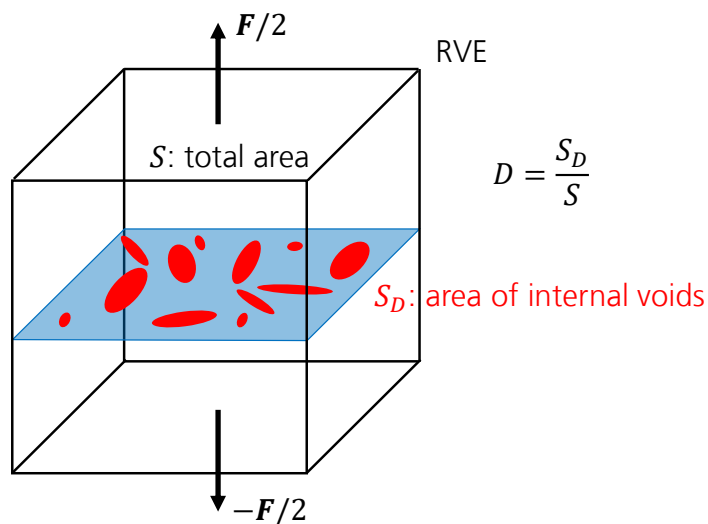


Figure 2.7: Definition of the damage parameter D in a cross sectional area S of a representative volume element loaded by a force F . D is defined to be the ratio between the total area S and the damaged sub-area S_D covered by internal voids.

The value of D varies between 0 for intact material and 1 for entirely failed material. The accumulation of damage is represented by the incremental increase of D . The actual value of D can be used to modify the stiffness, strength and other material parameters in the model.

A straightforward way to quantify D are non-destructive indirect measurements, as proposed by Lemaitre [164]. Alternatively, an elaborated modeling of the voids on the microscopic scale could be conducted. However, due to the complexity of the microanalysis, the experimental approach is in general more efficient. It is assumed that the components of the strain tensor in a homogeneously damaged material can be determined the same way as in the intact material. Then, e.g. the reduction of the Young's modulus as a function of D presents a possible measure of D :

$$D = 1 - \frac{E(D)}{E(D=0)} \quad 2.54$$

Therefore, D could be determined indirectly from the stress-strain curve of a cyclic uniaxial loading and unloading test, as illustrated in Figure 2.8.

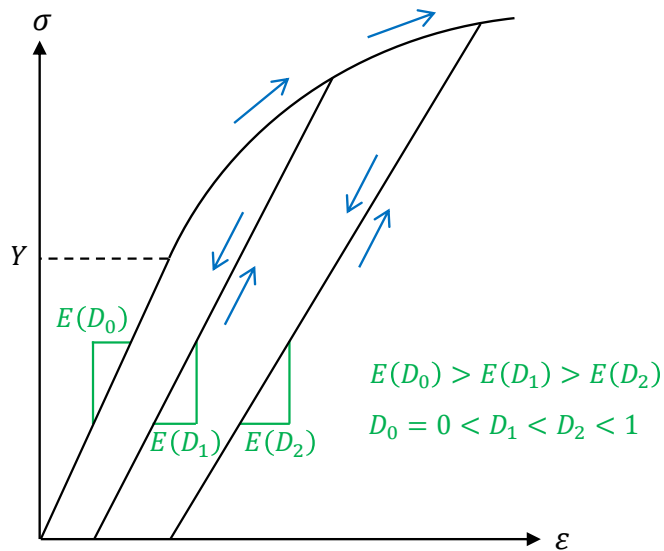


Figure 2.8: Indirect determination of D from a schematic stress-strain curve of a cyclic uniaxial loading and unloading test. The blue arrows indicate the loading path. The initial slope $E(D_0)$ corresponds to intact material. After exceeding the yield stress Y , damage starts to accumulate. Unloading and reloading of a partially damaged state results in lower slopes $E(D_1)$ and $E(D_2)$. D_1 and D_2 are calculated using equation 2.54.

In general, a criterion is defined that determines the accumulation of the damage parameter. A common criterion is the equivalent plastic strain to failure ϵ_p^f . The incremental increase of D is directly related to the incremental plastic strain $\Delta\epsilon_p$ normalized to ϵ_p^f :

$$D = \sum \frac{\Delta\epsilon_p}{\epsilon_p^f} \quad 2.55$$

This definition of D is also used in the Johnson-Holmquist models and is a suitable approach for the description of damage in SLG. A detailed description of the model is given in section 3.2.3.1.

2.3 Wave theory

In this section, the principles of wave propagation in solids are outlined briefly. An in-depth description on the topic can be found e.g. in [143] or [165]. For a detailed description of wave propagation and wave reflections, the reader is also referred to [2].

When a load is applied to a solid, the loading information propagates through the material in form of perturbation waves. At highly dynamic loading rates in the order of magnitude of the local speed of sound, so-called shock waves can be induced in the material. In order to describe the material response under such loading conditions, the wave propagation has to be resolved

in space and time. In the following, a short overview on the most common types of waves in solids is given. Afterwards, the concept of shock waves is presented in more detail. In addition, a common experimental approach for the characterization of shock behavior is outlined.

2.3.1 Classification of waves

Waves propagating in solids are typically classified based on specific boundary conditions and the direction of the perturbation propagation in relation to the motion of the particles. Here, the term particle refers to an infinitesimal discrete volume of the solid. The most common wave types are:

- Longitudinal waves, defined by a particle motion parallel to the direction of the wave propagation. Depending on whether the particle motion is pointing in the same or the opposite direction of the wave propagation, they are also referred to as compression or release waves, respectively. If an unbounded or laterally confined medium is considered, they turn out to be the fastest type of waves and their propagation velocity is usually denoted by c_p .
- Shear waves, defined by a particle motion perpendicular to the direction of the wave propagation. They have the second fastest propagation velocity, denoted by c_s .
- Rayleigh waves, propagating along the surface of the solid causing the particles to move elliptically.
- Flexural waves, describing the bending of one- or two-dimensional structures under dynamic loading.

The motion of a wave can be mathematically described using the sound speed of the material, the displacement and the spatial and time derivatives of the displacement. Based on equilibrium considerations, a one-dimensional wave is described by the equation:

$$\frac{\partial \sigma_x}{\partial x} = \rho \frac{d^2 u_x}{dt^2} \quad 2.56$$

where ρ denotes the material density and σ_x and u_x denote the one-dimensional stress and displacement, respectively. In a linear elastic solid, and considering a uniaxial stress state as could be achieved in an infinitely thin rod, equation 2.56 can be simplified using Hooke's law

$$\sigma_x = E \frac{\partial u_x}{\partial x}.$$

$$\frac{\partial^2 u_x}{\partial x^2} = \frac{\rho}{E} \frac{d^2 u_x}{dt^2} \quad 2.57$$

If now, an unbounded or laterally confined medium is considered, equation 2.57 turns into:

$$\frac{\partial^2 u_x}{\partial x^2} = \frac{1}{c_p^2} \frac{d^2 u_x}{dt^2} \quad 2.58$$

where the longitudinal sound speed c_p is related to the bulk modulus K and the shear modulus G as follows:

$$c_p = \sqrt{\frac{K + \frac{4}{3}G}{\rho}} \quad 2.59$$

Accordingly, the sound speed c_s of a shear wave and the bulk sound speed c_B can be identified as follows:

$$c_s = \sqrt{\frac{G}{\rho}} \quad 2.60$$

$$c_B = \sqrt{\frac{K}{\rho}} \quad 2.61$$

In case of a non-linear material behavior, the bulk modulus and the bulk sound speed are dependent on the specific material state. For an equation of state of the general form $P = P(\rho, e) = P(V, e)$, where e denotes the mass-specific internal energy and $V = 1/\rho$ denotes the mass-specific volume, the adiabatic bulk modulus is given by the partial derivatives of P with respect to ρ and e :

$$K = -V \left. \frac{\partial P}{\partial V} \right|_s = \rho \left. \frac{\partial P}{\partial \rho} \right|_s = \rho \left. \frac{\partial P}{\partial \rho} \right|_e + \frac{P}{\rho^2} \left. \frac{\partial P}{\partial e} \right|_\rho \quad 2.62$$

where S denotes the mass-specific entropy.

Therefore, the propagation velocity is pressure-dependent and related to the derivative of the state surface $P(V, e)$:

$$c_B = \sqrt{-V^2 \left. \frac{\partial P}{\partial V} \right|_s} = \sqrt{\left. \frac{\partial P}{\partial \rho} \right|_s} \quad 2.63$$

2.3.2 Shock waves

As a result of the pressure dependence of the wave propagation velocity (equation 2.63), a nonlinear pressure-density relation can lead to the formation of so-called shock waves. Shock waves in solids result from dispersion effects. If the propagation velocity increases with increasing pressure and the loading rate is rapid enough, a compressive wave gradually steepens as it propagates into the material. After a certain propagation distance, the rise time of the front becomes so short that it evolves into a discontinuous disturbance. It can be shown that the convexity of the pressure-volume curve is a mandatory requirement for the formation of shock waves [166]:

$$\left. \frac{\partial^2 P}{\partial V^2} \right|_s > 0 \quad 2.64$$

The thickness of a stable shock front results from two competing effects. While dissipative mechanisms such as viscosity or defect generation cause the wave front to spread out, the material non-linearity steepens the front. An in-depth description of stability criteria can be found in [166].

A common experimental technique for the characterization of the material behavior under shock compression are PPI tests. Here, a flat-ended projectile impacts a disk-shaped test specimen at a high velocity. As a result, the specimen undergoes a one-dimensional shock loading, which can

be observed experimentally by measuring the free surface velocity at the backside of the specimen.

Figure 2.9 illustrates a numerical simulation of a symmetrical PPI. Here, the term symmetrical relates to the fact that both the projectile and the target are made from the same material. The left image depicts the initial setup. The projectile plate impacts the target specimen from the left side at an impact velocity v_p . Before the impact, the target material is in the initial state $(P_0, \rho_0, e_0, u_{p,0})$, where P denotes the hydrostatic pressure, ρ denotes the density, e denotes the mass-specific internal energy and u_p denotes the particle velocity. The target is initially at rest and unstressed, therefore $P_0 = 0$ and $u_{p,0} = 0$. The image at the right side of Figure 2.9 illustrates the projectile and the target shortly after impact. As indicated by the contour plot of P , a sharp, plane shock front has formed, increasing the pressure from zero (light blue) to a high value (red). The shock wave is propagating at the shock velocity U_s lifting the material instantaneously from the initial state to the shocked state $(P_H, \rho_H, e_H, u_{p,H})$, also referred to as the Hugoniot state.

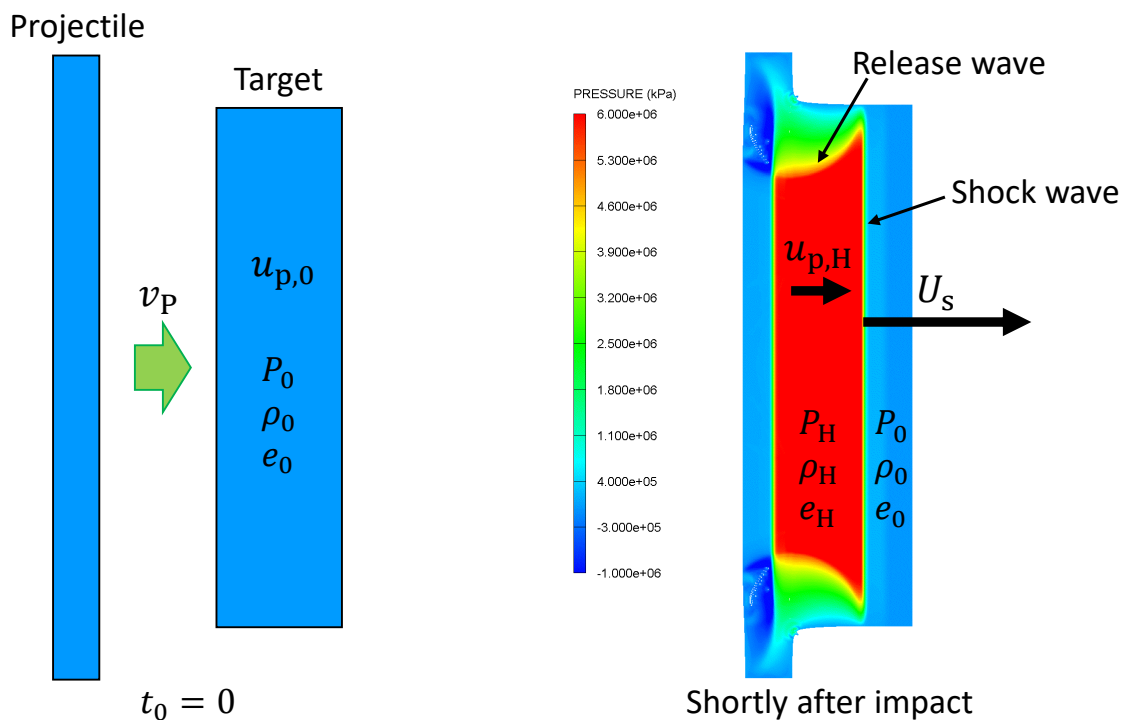


Figure 2.9: Simulated PPI: A projectile impacts a target plate at a velocity v_p . Shortly after impact, a plane shock front propagates at a shock velocity U_s lifting the material from the initial state $(P_0, \rho_0, e_0, u_{p,0})$ to the Hugoniot state $(P_H, \rho_H, e_H, u_{p,H})$.

The change of the state variables caused by the shock wave is described by a set of equations called Rankine Hugoniot relations. These equations are derived from the so-called shock tube problem or Riemann problem. The Riemann problem describes a plane shock wave propagating through a tube with a cross sectional area A . In principle, this is equivalent to the shock propagation during a PPI (ref. Figure 2.9), if the investigated cross section A is located in the central area of the target plate. In order to derive the Rankine Hugoniot relations, the conservation laws of mass, momentum and energy are applied to a certain volume that is

passed by the shock wave during a time increment dt . For a detailed derivation, the reader is referred to [143]. The resulting Rankine Hugoniot relations are:

Mass conservation:

$$\rho_0 A (U_s - u_{p,0}) dt = \rho_H A (U_s - u_{p,H}) dt \quad 2.65$$

or

$$\rho_0 (U_s - u_{p,0}) = \rho_H (U_s - u_{p,H})$$

Momentum balance:

$$\rho_H A (U_s - u_{p,H}) dt \cdot u_{p,H} - \rho_0 A (U_s - u_{p,0}) dt \cdot u_{p,0} = A (P_H - P_0) dt \quad 2.66$$

or

$$P_H - P_0 = \rho_0 (U_s - u_{p,0}) (u_{p,H} - u_{p,0})$$

Energy conservation:

$$P_H u_{p,H} - P_0 u_{p,0} = \rho_0 (U_s - u_{p,0}) (e_H - e_0) + \frac{1}{2} \rho_0 (U_s - u_{p,0}) (u_{p,H}^2 - u_{p,0}^2) \quad 2.67$$

or

$$e_H - e_0 = \frac{1}{2} (P_H + P_0) (V_0 - V_H)$$

where $V = 1/\rho$ denotes the mass-specific volume.

The Rankine Hugoniot relations can be rearranged to obtain the relation:

$$U_s = V_0 \sqrt{\frac{P_H - P_0}{V_0 - V_H}} \quad 2.68$$

Therefore U_s is proportional to the square root of the chord of the P - V curve. Consequently, the shocked state is assumed to be achieved along a straight line in the P - V plane, the so-called Rayleigh line. The Rayleigh line represents a non-equilibrium path. This is in contrast to an isentropic loading or release process for which the wave speed is given by a partial differentiation of the pressure function $P(V, e)$ as described in equation 2.62.

Equation 2.67 illustrates that the amount of energy dissipation of the instantaneous jump equals the triangular surface below the Rayleigh line. It can be shown that this amount of energy is larger than that of an isentropic release from the shocked state, which can be calculated incrementally using the following equation that can be derived from the first thermodynamic identity along an isentrope:

$$P(V, e) = - \frac{de}{dV} \quad 2.69$$

As a result, the energy difference between the shocked and released material is stored in the material resulting in an increase of the temperature.

Equation 2.67 defines a curve on the state surface of the material. This curve is called Shock Hugoniot, Hugoniot curve or Shock adiabatic. It represents the locus of all possible peak conditions (P_H, V_H, e_H) achieved when shock waves arise. The Shock Hugoniot can be

determined by combining the Rankine Hugoniot relations (equations 2.65, 2.66 and 2.67) with a relation between any two of the involved variables. A common approach is to postulate a polynomial dependence of U_s and $u_{p,H}$:

$$U_s = c_0 + \sum_{i=1}^n S_i u_{p,H}^i \quad 2.70$$

For gases or porous solids n is typically limited to three. For most other solids, however, already a linear correlation is sufficient. Assuming that the material is at rest in the initial state $u_{p,0} = 0$, a linear relation $U_s = c_0 + S u_{p,H}$ transforms the Rankine Hugoniot relations into the following set of equations:

$$\rho_H = \rho_0 \frac{c_0 + S u_{p,H}}{c_0 + u_{p,H}(S - 1)} \quad 2.71$$

$$P_H = P_0 + \rho_0 c_0^2 \frac{\eta}{(1 - S \eta)^2} \quad 2.72$$

$$e_H = e_0 + \frac{\eta}{\rho_0} P_H - \frac{\eta^2}{2} \frac{c_0^2}{(1 - S \eta)^2} \quad 2.73$$

where $\eta = 1 - \frac{\rho_0}{\rho_H}$.

Therefore, the shocked state (P_H, V_H, e_H) can be determined directly as a function of $u_{p,H}$ for a given set of material parameters (ρ_0, c_0, S). A graphical representation of the Shock Hugoniot in the P - V - e space is given in the next section in Figure 2.12.

A common approach for the experimental determination of the U_s - $u_{p,H}$ relation, is the conduction of multiple PPI tests at different peak loadings. In case of metals, where the U_s - $u_{p,H}$ relation is typically linear, two experiments are sufficient to determine c_0 and S . The same applies if only the material behavior at high pressures is of interest. However, if also the low-pressure range is of interest and if the material exhibits a more complex behavior, a larger number of experiments is required. This is illustrated schematically in Figure 2.10.

The diagrams on the left side of Figure 2.10 depict the P - V relation of a generic complex material. The material exhibits a relevant shear strength leading to a linear P - V relation in the low-pressure range. For pressures above the elastic limit, the linear curve turns into a concave upwards curve. At higher pressures, the curve exhibits a plateau-like discontinuity representing a polymorphic phase transformation. The diagrams on the right side illustrate the steady wave fronts resulting from the wave dispersion when shocked to a specific pressure. Here, the pressure amplitude is plotted against the propagated distance after a specific time. This time interval is chosen to be sufficiently long to allow for the formation of steady shock waves.

Each row represents a PPI test with a different peak pressure. As illustrated in the first row, a purely elastic loading results in a single elastic wave front. Above the elastic limit, dynamic yielding occurs creating an instability, as indicated by the two arrows in the second diagram on the left side. The wave propagation is proportional to the slope of the arrows (ref. equation 2.68). Consequently, the single wave splits into two waves, an elastic precursor and a plastic shock front. For the same reason, a peak pressure slightly above the phase transition results in a split into three distinctive wave fronts (diagrams in the third row). However, at even higher pressures, the information of the phase transition or even the elastic limit is lost, as illustrated in the fifth and last row, respectively. In the last case, a plastic shock wave is initiated that overtakes all other wave fronts. This is often referred to as the elastic limit is being overdriven.

The outlined example illustrates that the determination of an entire Shock Hugoniot can require multiple experiments. In addition, the peak pressures have to be chosen carefully, if the material exhibits a relevant shear strength or a complex compression curve due to e.g. phase transformations. A more in-depth description of the PPI analysis is given in the following section.

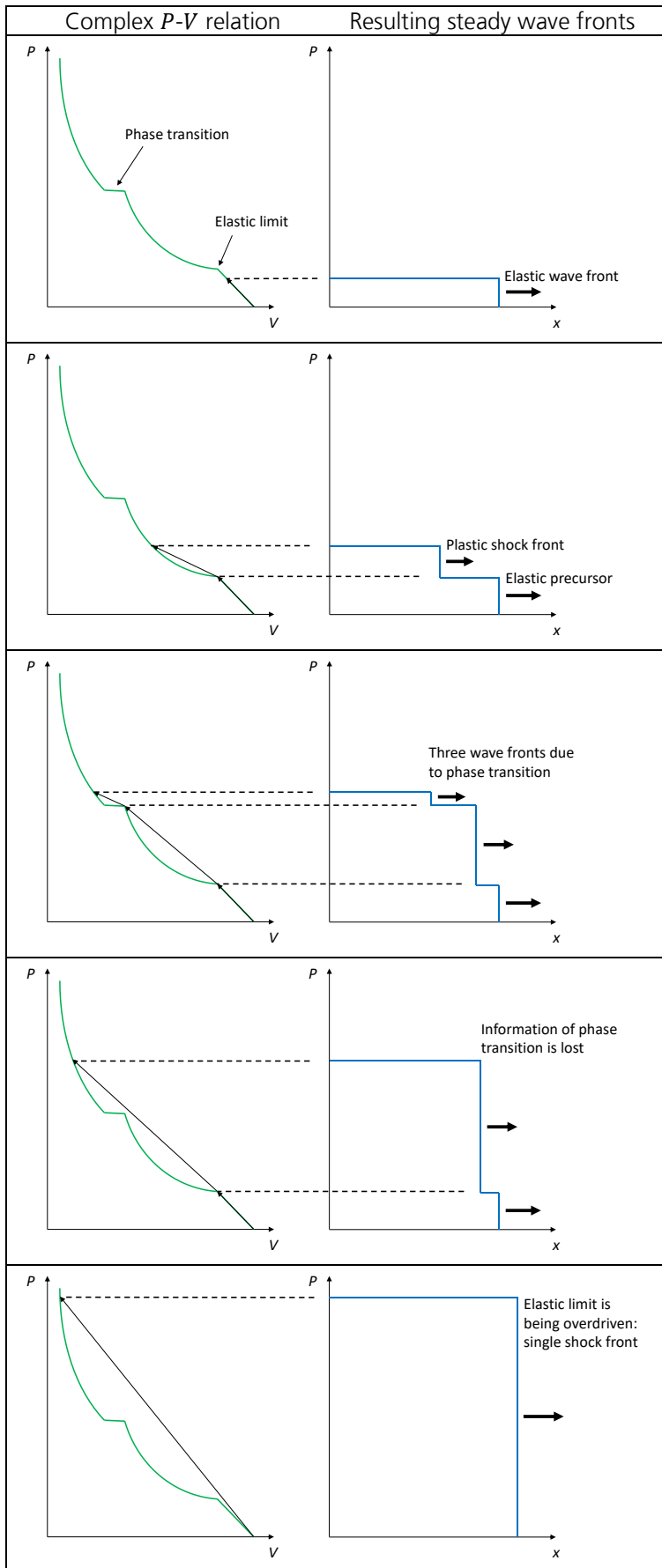


Figure 2.10: Schematic of resulting wave fronts at different peak pressures (right diagrams) in a material with a complex P - V relation (left diagrams).

2.3.2.1 Common analysis concept for PPI tests

As outlined in the previous section, PPI tests are a common experimental technique for the characterization of the material behavior under shock compression (see also [167] [168] [169] [170] [171] [172] [173] [174] [175]). In a PPI test, the material is shock loaded at high strain rates (order of $10^5/s$) in a well-defined state of one-dimensional strain (see Figure 2.9). Information on the Shock Hugoniot is derived from the free surface velocity as a function of time, which is measured at the backside of the target specimen. For the analysis of such a velocity profile, it is useful to investigate the propagation of the wave fronts in a so-called Lagrange diagram. In a Lagrange diagram, the position of each wave front is plotted against the time after impact. As indicated by the name, a Lagrangian description is used to define the positions. Figure 2.11 illustrates an exemplary Lagrange diagram in combination with the corresponding free surface velocity profile. In the Lagrange diagram, the spatial information is displayed in the horizontal direction while the temporal information is given in the vertical direction. Due to the Lagrangian description, the surfaces of the projectile and target have fixed positions and are therefore represented by vertical lines. The positions of the wave fronts are indicated by the black arrows. For illustration purposes, only a selection of the most important wave fronts is shown. The illustrated case corresponds to a PPI in which two steady wave fronts are initiated in the projectile and the target upon impact, an elastic precursor and a plastic shock wave (equivalent to the diagrams in the second row of Figure 2.10). In the diagram on the right side of Figure 2.11, the resulting free surface velocity at the backside of the target is shown as a function of time. Upon arrival of the wave fronts, the free surface velocity instantaneously increases. At a later point of time (indicated as "release"), the velocity starts to gradually decrease due to the arrival of a fan of release waves. These release waves result from the reflection of the initially compressive waves at the free surface of the rear side of the projectile. The depicted velocity profile further illustrates the influence of a so-called spallation. The superposition of the release waves from the projectile and target can result in a stress state of one-dimensional tension. In the illustrated case, this tension exceeds the tensile strength of the material leading to failure and the formation of a new free surface (indicated as "spall zone") inside the target.

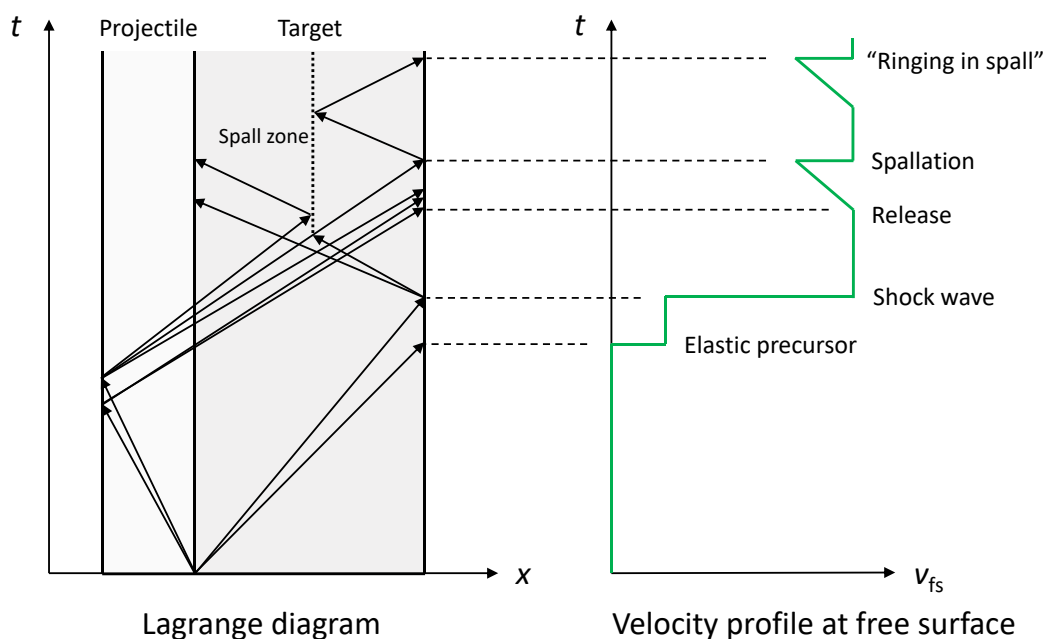


Figure 2.11: Lagrange diagram of a PPI (left) and corresponding free surface velocity profile (right).

The common analysis concept assumes a clear two-wave structure. The time difference $\Delta t_{\text{el-pl}}$ between the arrival of the elastic precursor and the plastic shock wave is measured together with the amplitudes of the free surface velocity. From these measured values, the stress σ_{final} and the strain $\varepsilon_{\text{final}}$ of the shocked state are derived as follows.

Using the free surface approximation [176] [177] [178] the particle velocity u_p is estimated from v_{fs} by the relation:

$$u_p \approx \frac{1}{2} v_{\text{fs}} \quad 2.74$$

The particle velocity behind the elastic precursor and the plastic shock wave are called $u_{p,\text{el}}$ and $u_{p,\text{final}}$, respectively.

The shock wave velocity U_s is calculated from $\Delta t_{\text{el-pl}}$ using the relation [174]:

$$U_s = \frac{c_p}{1 + \frac{c_p \Delta t_{\text{el-pl}}}{d_T}} \quad 2.75$$

where d_T denotes the thickness of the target and c_p denotes the longitudinal sound velocity.

The stress and the strain of the shocked state are subsequently determined using the following standard equations [174] (within the framework of this work, stresses and strains of shocked states are conventionally defined to be positive in compression):

$$\sigma_{\text{final}} = \rho_0 c_p u_{p,\text{el}} + U_s \rho_0 (u_{p,\text{final}} - u_{p,\text{el}}) \quad 2.76$$

$$\varepsilon_{\text{final}} = \frac{u_{p,\text{el}}}{c_p} + \frac{u_{p,\text{final}} - u_{p,\text{el}}}{U_s} \quad 2.77$$

This common analysis concept should only be applied if the examined material exhibits a clear two-wave structure under shock loading. If no steep velocity jumps arise, the determination of $\Delta t_{\text{el-pl}}$ is difficult and selective. Within the framework of this work, this analysis method is therefore referred to as "the selective analysis". Materials that exhibit a partially concave downward shaped P - V relation, like SLG, require a different analysis approach. This alternative approach is referred to as "incremental analysis" within this work. It is developed and outline in detail in section 4.1. There, the standard equations 2.76 and 2.77 are also derived in more detail as a special case of the incremental analysis.

2.4 Equation of state

Within the framework of this work, the term EOS refers to a formulation of the hydrostatic pressure P as a function of two independent thermodynamic state variables:

$$P = P(\rho, e) = P(V, T) = P(V, e) \quad 2.78$$

where ρ denotes the density, e denotes the mass-specific internal energy, V denotes the mass-specific volume and T denotes the temperature.

Equation 2.78 defines a surface in the P - V - e space on which all possible conditions of thermodynamic equilibrium of a specific material are located. For the applications within the framework of this work, this so-called incomplete EOS can be used since heat conduction effects can be neglected. For more information on complete EOS, the reader is referred to [179].

For many engineering applications, the EOS is derived from experimental observations as an empirical relation. In the following, a brief overview of three common formulations is given. For alternative formulations like the Tillotson EOS [180], which is able to describe phase changes, or Hermann's P -alpha EOS for porous materials [181] the reader is referred to the literature references.

Linear EOS:

The linear EOS assumes an isothermal process with a linear P - V or P - ρ relation. The EOS is derived from the adiabatic bulk modulus (ref. equation 2.62):

$$K = \rho \left. \frac{\partial P}{\partial \rho} \right|_S \quad 2.79$$

Since K is assumed constant, a separation of variables and a subsequent integration along an isentropic path joining two states (P_1, ρ_1) and (P_2, ρ_2) yields:

$$\int_{P_1}^{P_2} dP = K \int_{\rho_1}^{\rho_2} \frac{1}{\rho} d\rho \quad 2.80$$

$$P_2 - P_1 = K \ln \frac{\rho_2}{\rho_1} \quad 2.81$$

Using the Taylor approximation $\ln(1 + x) \approx x$ if $x \ll 1$ yields a simplified formulation:

$$P_2 - P_1 \approx K \left(\frac{\rho_2}{\rho_1} - 1 \right) \quad 2.82$$

Therefore, an arbitrary state $P(\rho)$ can be calculated for a given initial state $(\rho_0, P_0 = 0)$ as follows:

$$P(\rho) \approx K \left(\frac{\rho}{\rho_0} - 1 \right) = K \mu \quad 2.83$$

where μ denotes the volumetric compression:

$$\mu = \frac{\rho - \rho_0}{\rho_0} = \frac{\rho}{\rho_0} - 1 = \frac{V_0}{V} - 1 \quad 2.84$$

Mie-Grüneisen EOS

In case of shock loading, a common formulation is the so-called Mie-Grüneisen EOS. This formulation uses the Shock Hugoniot of the material as a baseline in combination with an assumption on the equilibrium conditions. More precisely, the one-dimensional Hugoniot curve is extrapolated to a two-dimensional EOS surface by estimating the pressure change off the Hugoniot-line along isochores.

The Grüneisen parameter $\Gamma(V)$ is introduced, which describes the relation between the volume change of a crystal lattice on its vibrational properties. Based on Grüneisen's theory [182] [183] [184], the crystal lattice can be described on the atomic level by a set of harmonic oscillators in order to derive macroscopic thermodynamic relations. It is shown that an isochoric process can be identified with the Grüneisen parameter as follows:

$$V \left. \frac{\partial P}{\partial e} \right|_V = \Gamma \quad 2.85$$

Using Γ , the Mie-Grüneisen EOS is formulated as

$$P(V, e) = P_H + \frac{\Gamma}{V} (e - e_H) \quad 2.86$$

where the Hugoniot state (P_H, e_H) is given by the Rankine Hugoniot relations (equations 2.65, 2.66 and 2.67) or, in case of a linear U_s - $u_{p,H}$ relation, by equations 2.72 and 2.73.

The Mie-Grüneisen EOS (equation 2.86) results from a first order approximation of the Shock Hugoniot with respect to the mass-specific energy variable by means of a Taylor series developed around the Hugoniot pressure:

$$P(V, e) = P_H + \left. \frac{\partial P}{\partial e} \right|_V (e - e_H) + \dots \approx P_H + \frac{\Gamma}{V} (e - e_H) \quad 2.87$$

As pointed out by Meyers [165], the Grüneisen parameter is related to the volumetric thermal expansion 3α , the isothermal bulk modulus K_T and the specific heat capacity at constant volume c_V as follows:

$$\Gamma = V \frac{3\alpha}{c_V K_T} \quad 2.88$$

Furthermore, for many materials gamma can be approximated by

$$\Gamma \approx \frac{V}{V_0} (2S - 1) \quad 2.89$$

where V_0 denotes the mass-specific volume at zero pressure and S denotes the constant of proportionality of a linear U_s - $u_{p,H}$ relation (ref. equation 2.70).

Figure 2.12 illustrates a three-dimensional representation of a Mie-Grüneisen EOS in the P - V - e space. All equilibrium states are located on the colored surface. The Shock Hugoniot of the initial state (P_0, V_0, e_0) is illustrated by a red solid line. In addition, a red dashed line indicates the Rayleigh line for a non-equilibrium path between the initial state and the shocked state (P_H, V_H, e_H) . The Rayleigh line is a chord of the Hugoniot curve and therefore not located on the surface. Furthermore, two isentropes (ref. equation 2.69) are illustrated as black curves that are located on the surface. One isentrope is intersecting the initial state while the other one is passing through the shocked state.

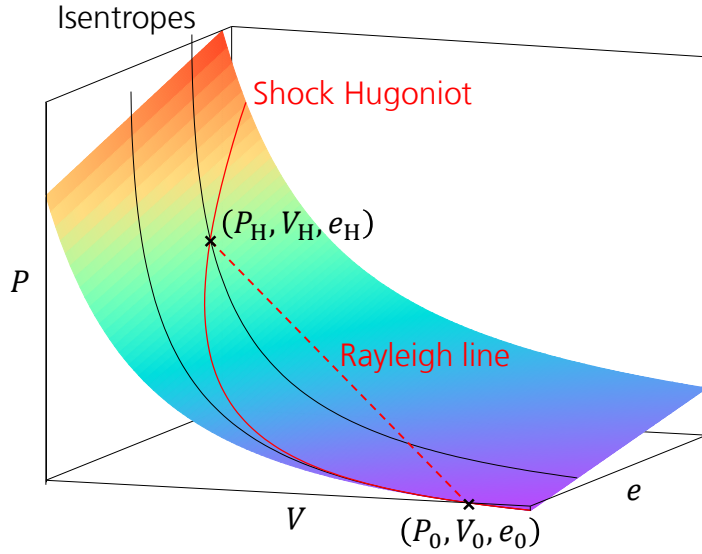


Figure 2.12: Illustration of the Mie-Grüneisen EOS as a colored surface in the P - V - e space. The red line depicts the Shock Hugoniot of the initial state (P_0, V_0, e_0) . The Rayleigh line (red dashed line) indicates the non-equilibrium path to the shocked state (P_H, V_H, e_H) . For both states, the corresponding isentrope is illustrated by a black curve.

Polynomial EOS

An often-used nonlinear EOS is a polynomial formulation based on the volumetric compression μ (ref. equation 2.84) of the form:

$$P(\mu, e) = K_1\mu + K_2\mu^2 + K_3\mu^3 + (B_0 + B_1\mu)\rho_0(e - e_H) \quad 2.90$$

Here, the parameters K_1 , K_2 and K_3 are adjusted to fit the Shock Hugoniot of the material. In case of the linear relation $U_s = c_0 + S u_{p,H}$, the Shock Hugoniot is defined by equations 2.71, 2.72 and 2.73, which yields:

$$K_1 = \rho_0 c_0^2 \quad 2.91$$

$$K_2 = \rho_0 c_0^2 [1 + 2(S - 1)] \quad 2.92$$

$$K_3 = \rho_0 c_0^2 [2(S - 1) + 3(S - 1)^2] \quad 2.93$$

Therefore, for small compressions ($\mu \ll 1$), the derivative of the P - μ -curve equals the compressive bulk modulus:

$$\left. \frac{\partial P}{\partial \mu} \right|_s = K_1 = K \quad 2.94$$

The parameters B_0 and B_1 are adjusted to reflect the pressure change off the Shock Hugoniot along isochores using the following relation:

$$\left. \frac{\partial P}{\partial e} \right|_V = \rho_0 (B_0 + B_1\mu) \quad 2.95$$

The polynomial EOS is often combined with an expansion EOS to allow for the description of the expansion regime of negative hydrostatic pressures:

$$P(\mu, e) = \tilde{K}_1 \mu + B_0 \rho_0 (e - e_H) \quad \text{if } P < 0 \quad 2.96$$

Since the Shock Hugoniot is related only to compressive states, there is in general no relation between \tilde{K}_1 and K_1 . However, a common approximation is to use the linear compressive bulk modulus also for the expansion EOS.

A polynomial EOS is also used in the Johnson-Holmquist models and is a suitable approach for the description of SLG. In contrast to the formulations 2.90 and 2.96, the energy dependent term is replaced by a pressure increment ΔP . This so-called bulking pressure represents the pressure increase due to energy dissipation during failure. A detailed description of the model is given in section 3.2.3.1.

3 Numerical modeling of soda-lime glass

The main objective of this thesis is to improve the simulation capabilities of existing models of SLG, with the focus on highly dynamic impact scenarios. Within the framework of this work, the term “simulation” refers to a numerical description of physical processes by means of hydrocodes. The term “material model” refers to a specific module of the hydrocode, which describes the material behavior, i.e. the response of the material to external loading conditions. More precisely, the material model consists of an EOS (ref. section 2.4), a constitutive equation describing the stress-strain relation (ref. section 2.2.2) and a failure model for the description of softening due to damage (ref. section 2.2.3).

Section 3.1 provides a brief introduction to the general concepts of hydrocodes. An overview of selected material models for the description of SLG is given in section 3.2.

3.1 Basics of hydrocodes

This section gives a brief overview on the most important aspects of hydrocodes. For an in-depth description, the reader is referred e.g. to [143] [185] [186] [187] [188].

3.1.1 Discretization of the governing equations

Hydrocodes are large computer programs that describe the dynamics of a continuous media by solving the following set of differential conservation equations:

Mass conservation:

$$\frac{d\rho}{dt} + \rho \frac{\partial v_i}{\partial x_i} = 0 \quad 3.1$$

Momentum balance:

$$\frac{dv_i}{dt} = f_i + \frac{1}{\rho} \frac{\partial \sigma_{ij}}{\partial x_j} \quad 3.2$$

Energy conservation:

$$\frac{de_{\text{tot}}}{dt} = f_i v_i + \frac{1}{\rho} \frac{\partial}{\partial x_j} (\sigma_{ij} v_i) \quad 3.3$$

where ρ is the density, t is the time, \mathbf{v} is the velocity, \mathbf{x} is the position, e_{tot} is the mass-specific total energy, $\boldsymbol{\sigma}$ is the stress tensor and \mathbf{f} are the external body forces per unit mass.

Together with an EOS, optional constitutive equations and optional failure models, equations 3.1, 3.2 and 3.3 represent a set of highly nonlinear equations that are solved simultaneously by the hydrocode.

In order to derive a solution, the governing equations are discretized in space and time. This means that a finite number of spatial locations and instants of time is defined at which the discretized equations are solved. A continuous solution is then approximated from the particular solutions at the discrete locations.

Depending on the specific application, a different discretization method might be preferred. The most common methods for a spatial discretization are the finite element method (FEM), the

finite difference method (FDM), the finite volume method (FVM) and mesh-free methods (MFM). For the time discretization, implicit or explicit schemes based on finite difference approximations are used. The decisive factors for the selection of a specific discretization method are in general consistency, accuracy, stability and efficiency, as outlined in detail in [185].

All simulations conducted within the framework of this work use FEM for the spatial discretization. This includes the highly dynamic simulations in chapters 4 and 6 as well as the quasi-static simulations in chapter 5. Concerning the time discretization, an explicit scheme is used in the highly dynamic simulations, while an implicit solver is utilized for the quasi-static simulations.

In the following, a brief overview of the basic concepts of FDM and FEM are given. An in-depth description of these methods and alternative methods can be found e.g. in [143] [185] [189] [190] [191].

3.1.1.1 Time discretization

Common approaches for the time discretization are explicit and implicit schemes based on finite difference approximations. The basic concept is outlined briefly in the following.

In order to replace the time derivative of the conservation equations (3.1, 3.2 and 3.3) by finite difference equations, the solution is advanced in time by using discrete time intervals, also referred to as time steps:

$$\Delta t = t^{n+1} - t^n \quad 3.4$$

where n denotes the index of the solution at time t^n . The time discretization is indicated by upper indices in order to differentiate from the lower indices of the spatial discretization.

A general formulation of the conservation equations is:

$$\frac{\partial U}{\partial t} = -\frac{\partial}{\partial x} F(U) \equiv G(U) \quad 3.5$$

As stated by the Mean Value Theorem [192], a mean value \bar{G} exists for the time interval $[t^n, t^{n+1}]$, which can be derived from the values of G at the times t^n and t^{n+1} :

$$\bar{G}(U) = \varepsilon G^{n+1} + (1 - \varepsilon) G^n \quad 3.6$$

where $\varepsilon \in [0,1]$.

Combining equations 3.5 and 3.6 and replacing the time derivatives by finite differences yields:

$$U^{n+1} = U^n + \Delta t(\varepsilon G^{n+1} + (1 - \varepsilon) G^n) \quad 3.7$$

On the one hand, for any $\varepsilon \neq 0$, the solution has to be determined iteratively since it depends upon both the current and the new values of the functions. This procedure is referred to as implicit scheme. On the other hand, if $\varepsilon = 0$, the solution at t^{n+1} can be determined directly from the known function values at t^n , which is referred to as explicit scheme.

Explicit formulations have a less computational cost, but their stability and precision are limited by the time step size. Implicit methods are capable of addressing large time steps at the same or higher accuracy and their precision can easily be controlled. However, for most dynamic processes, like e.g. impact scenarios, an explicit integration scheme is preferred since the

resolution of wave propagation effects demands extremely short time steps, thus eliminating the advantage of implicit methods.

3.1.1.2 Spatial discretization

The general concept of spatial discretization is to approximate the domain of interest by a lattice of grid points. In this context, two different formulation approaches are distinguished. On the one hand, in the Lagrangian or material description, the grid points are tied to material particles (ref. section 2.1). On the other hand, in the Eulerian or spatial description, all grid points are spatially fixed with time. The given formulations of the conservation equations (3.1, 3.2 and 3.3) refer to the Lagrangian description. Using the definition of the total time derivative

$$\frac{d}{dt} = \frac{\partial}{\partial t} + v_i \frac{\partial}{\partial x_i} \quad 3.8$$

the conservation equations can be transformed to the Eulerian description.

However, within the framework of this work, all simulations are conducted using the Lagrangian description. This is due to several reasons. First, the Lagrangian grid clearly defines material interfaces and boundaries. Second, the grid is only required at material locations, thus allowing for a higher spatial resolution for a given number of elements. Third, the history of a material particle can be easily tracked, which is essential for the accumulation of damage in the failure model. For a more in-depth discussion of the advantages and disadvantages of the two descriptions, the reader is referred e.g. to [185].

3.1.2 The finite difference method

In FDM, the spatial discretization is achieved by replacing the spatial derivatives of the differential equations by difference equations between adjacent grid points. The results is then taken as a pointwise approximation for a finite region of the grid. For a given functional F , common formulations to approximate the first derivative are:

$$\text{Forward differences: } \left. \frac{\partial F}{\partial x} \right|_{x_i} = \frac{F_{i+1} - F_i}{\Delta x} \quad 3.9$$

$$\text{Backward differences: } \left. \frac{\partial F}{\partial x} \right|_{x_i} = \frac{F_i - F_{i-1}}{\Delta x} \quad 3.10$$

$$\text{Central differences: } \left. \frac{\partial F}{\partial x} \right|_{x_i} = \frac{F_{i+1} - F_{i-1}}{2 \Delta x} \quad 3.11$$

where x_i is the position of the grid point with index i and Δx is the distance to the adjacent grid points.

It can be shown by Taylor series expansion [143] that the forward and backward methods ignore terms, which are negligible compared to Δx . They are therefore referred to as first-order accurate. In contrast, the central differences only ignore terms, which are negligible compared to Δx^2 . They have therefore a higher accuracy and are referred to as second-order accurate.

In order to solve the set of differential equations as a function of time and space, the spatial and temporal finite differences schemes have to be combined. A basic approach is, for example, the combination of forward differences for the time and backward differences for the space discretization. This first-order accurate explicit formulation is called Upwind or Forward Euler method.

An example for an explicit scheme with a higher, second-order accuracy is the Lax-Wendroff method, also referred to as the predictor-corrector scheme. This is a two-step method. In the first step, the values of U (equation 3.7) are calculated at half time steps and half space steps to identify the fluxes at these intermediate points. This so-called predictor is subsequently used in the second step to calculate U at the real grid point.

For any explicit scheme, Courant, Friedrich and Lewy [193] [194] have shown that it is only stable if the width of the time step Δt is limited by the ratio of the smallest Δx and the largest wave propagation speed c_{\max} . In case of a Lagrangian formulation, the resulting Courant-Friedrichs-Lewy (CFL) stability condition is therefore:

$$\Delta t \leq \frac{\Delta x}{c_{\max}} \quad 3.12$$

In contrast, the implicit schemes are unconditionally stable.

Equation 3.12 states essentially that no information can be allowed to propagate across the shortest dimension of the grid in a time Δt . This can be illustrated geometrically in a Lagrange diagram. Figure 3.1 shows the Lagrange diagram of a one-dimensional space discretization that takes only neighboring grid points into account. For a maximum wave speed c_1 , the CFL criterion defines a maximum time step width Δt_1 . The corresponding solution at grid point x_i is indicated as $F_i^{\Delta t_1}$. All information that can have an influence on $F_i^{\Delta t_1}$ is located in the triangular area defined by the wave front positions (solid black diagonal lines). If the maximum wave speed is increased from c_1 to c_2 , the area of influence also increases (upper red diagonal lines). In this case, spatial positions outside of the interval $[x_{i-1}, x_{i+1}]$ influence the solution $F_i^{\Delta t_1}$. Therefore, the area of influence is underestimated using Δt_1 . Since these influences are not covered by the numerical scheme, the solution turns unstable. According to the CFL criterion, a shorter time step Δt_2 is required to account for the higher propagation velocity c_2 .

On the contrary, if the shorter time step Δt_2 is used in a case where the maximum velocity is only c_1 , the zone of interest is overestimated (black dotted lines). In this case, the scheme remains stable, but systematic errors are induced that can reduce the accuracy of the solution. In summary, for a given c_{\max} the smallest grid interval defines the time step width Δt . In addition, large variations in the grid resolution may reduce the accuracy of the solution drastically.

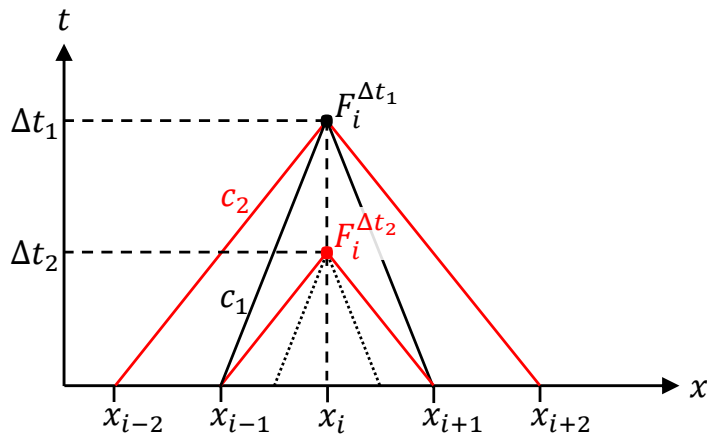


Figure 3.1: Graphical interpretation of the CFL condition in a Lagrange diagram.

3.1.3 The finite element method

One of the most commonly known numerical discretization techniques is the FEM. In contrast to the pointwise discretization of the FDM, the FEM is based on a piecewise discretization of the differential equations (3.1, 3.2 and 3.3). The discretization is achieved by decomposing the solution region into many small elements. Grid points, also referred to as nodes, are assigned to each element. The deformation distribution over an element is approximated by interpolating functions, the so-called shape functions. The shape functions are defined to be continuous functions on the domain of the element. For each node i of the element, a shape function exists that yields a value of 1 at the position of node i and a value of 0 at the positions of all other nodes. Furthermore, at any position in the element, the sum of all shape functions equals 1. A common approach is to use polynomial shape functions. The degree of the polynomials is related to the structure of an element, i.e. the number of nodes and the degrees of freedom of the nodes. Using higher order polynomials increases the accuracy of the solution, similar to the usage of higher order difference schemes in the FDM.

In the FEM, the displacements of the nodes can be regarded as the basic unknowns. At each time step, the displacement of all nodes is derived by solving simultaneously the set of conservation equations 3.1, 3.2 and 3.3 in combination with the material model and external conditions. The resulting displacements and history variables are then provided as initial conditions for the next time step. Figure 3.2 schematically shows the corresponding computational cycle, as implemented in the commercial FEM hydrocode Autodyn® [195]. The computational cycle can basically be divided into the following nine calculation steps:

1. Starting from the initial conditions at time t_0 , the maximum time step width is calculated using the CFL criterion (equation 3.12) for each element. The time step width of the current computation cycle is then set to the value of the minimum element time step.
2. From the displacements of the nodes, the strain state and strain rate state within each element are calculated.
3. With regard to the mass conservation (equation 3.1), the density of each element is determined.
4. Using the energy conservation (equation 3.3), the specific internal energy of each element is calculated.

5. The hydrostatic pressure within each element is calculated. For this step and the following step, it is assumed that the stress tensor can be separated into a hydrostatic and a deviatoric component (ref. equation 2.20). The pressure is determined from the volume and specific internal energy using the EOS of the material model (ref. section 2.4).
6. The deviatoric stresses are calculated using the stress-strain relation provided by the constitutive equations of the material model. Depending on the material model, the yield surface of the constitutive relation can be modified by a failure model. For example, the degree of damage of each element could be tracked by a damage parameter D (ref. equation 2.55). Upon total failure ($D = 1$), the yield surface could be set to $F(\boldsymbol{\sigma}) \equiv 0, \forall \boldsymbol{\sigma}$ so that the element is treated purely hydrodynamically, unable to carry shear stresses anymore (ref. section 2.2.2). Usually, a cutoff criterion on negative pressures is also activated upon total failure in order to prevent failed elements from carrying tensile pressures.
 The final stress state is determined in a two-step method. In the first step, the stress state is regarded as purely elastic. Consequently, the stress state may be located beyond the yield surface $F(\boldsymbol{\sigma}) > 0$. In the second step, if $F(\boldsymbol{\sigma}) > 0$, the stress deviator is relaxed back perpendicular to the yield surface. This technique ensures that only the deviatoric components are affected.
7. Using the momentum balance (equation 3.2) the forces on the nodes are calculated considering also external loads and contact forces.
8. The acceleration of each node is calculated from its mass and the acting force using Newton's second law of motion. Integration of the acceleration over the current time step width yields the velocity.
9. Integration of the velocities yields the nodal displacements. These are provided as initial conditions for the next time step / calculation cycle.

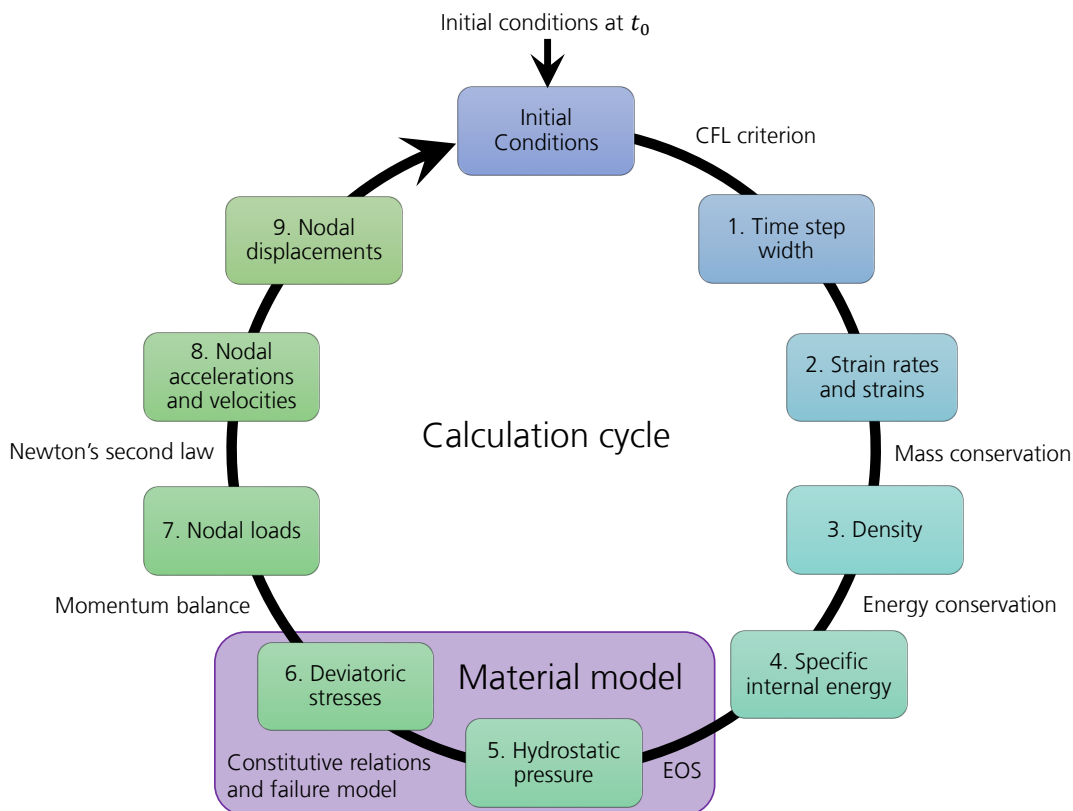


Figure 3.2: Schematic of a computation cycle in the FEM hydrocode Autodyn®.

3.1.4 Differences and similarities between FEM and FDM

In FEM, the equations of motion are solved locally for each element based on its nodal forces. These equations are therefore independent of the shape of the neighboring elements. This is in contrast to FDM, in which the equations of motion are formulated directly in terms of stress gradients of the neighboring grid points [185].

However, Anderson summarizes that nowadays, there is no large difference between FEM and FDM since in principle both “techniques provide different algorithms for obtaining solutions to the same differential equations” [185]. Therefore, the difference between both methods is not the mathematical description but rather the implementation technique.

In both FEM and in FDM, the time step width is restricted by the CFL criterion (equation 3.12). For the investigation of processes including shock waves, both techniques require the implementation of an artificial viscosity if the grid resolution does not have a similar size as the thickness of the shock front (for more details on artificial viscosity, the reader is referred to [143]). Furthermore, using a Lagrangian description, both techniques require an erosion criterion if processes with large deformations are investigated. For isotropic materials, a strain-based erosion criterion is commonly used. Upon exceeding a specific equivalent strain, an element is either discarded from the calculation or transformed into a free mass point that is no longer connected to the original grid. In case of the transformation, the free mass point may further interact with other elements [195].

The erosion criterion is necessary for two reasons. First, in case of large deformations, a highly distorted element can lead to a drastic decrease of the time step width due to the CFL criterion. Second, a penetration process, such as a projectile penetrating a glass laminate, cannot be modeled without erosion in the Lagrangian scheme.

3.2 Numerical approaches for modeling soda-lime glass

The current state of science with respect to the characterization and modeling of SLG was outlined in detail in chapter 1. In particular, the current issues and shortcomings of reported simulation results were presented in section 1.2.4.1. In the following, a brief overview of common modeling approaches for SLG is presented. The selected material models are categorized into molecular dynamical models, explicit crack propagation models and continuum-mechanical models.

A particular emphasis is placed on the continuum mechanical material model JH2 [60], which is described in more detail in section 3.2.3.1. Within the framework of this work, the JH2 model is taken as a representative reference model to illustrate how the novel results can be used to improve the simulation capabilities. For a detailed discussion of the reasons and results, see chapter 6.

3.2.1 Molecular dynamical models

Molecular dynamical models are used to investigate the material behavior on an atomic scale (order of 10^{-10} m). In general, movements of atoms and molecules are determined based on interatomic potentials or molecular mechanical force fields. The focus of many studies on different kinds of glasses was the investigation of permanent densification at hydrostatic

pressures of up to 10 GPa. For example, Grujicic et al. have shown on a molecular scale that SLG exhibits irreversible densification upon exceeding pressures of 4 GPa. They reported that “this process is associated with an increase in the average coordination number of the silicon atoms, and the creation of two to fourfold (smaller, high packing-density) Si–O rings” [196] [197]. Another application example of molecular modeling is the examination of the fracture of silica glass during hypervelocity impact. Holmström et al. investigated the initiation and propagation of cracks in a 24 nanometer thick glass layer [198]. Furthermore, Hu et al. reported that multiscale models, in which molecular dynamics models are coupled with FEM models, enable the modeling of macroscale structures. In this case, it is important to describe the entire structure since the propagation and reflection of stress waves have significant influence on the evolution of damage [199]. Further results of molecular dynamics models can be found e.g. in [200] [201] [202] [203] [204].

3.2.2 Explicit crack propagation models

Explicit crack propagation models describe the fracture process on a microscopic scale. Usually, the glass is treated as a linear elastic material in which the initiation and propagation of local discrete cracks is described by means of fracture mechanics ([55] [154] [155] [156]). Fracture results from the nucleation, propagation and coalescence of the discrete cracks. In FEM, the propagation can be realized by node splitting at the tip of the crack. Here, cohesive zone models can be used to account for the cohesive forces during the node splitting. A high grid resolution or an adaptive re-meshing is required to allow for enough possible propagation directions around the crack tip.

A major disadvantage of this approach is the required large computational effort. Especially when the number of cracks increases, the simulation of macroscopic realistic armor configurations becomes impracticable.

Examples of explicit crack modeling of glass are provided e.g. in [205], [206] or [207]. Discrete crack models are also a common approach to investigate the behavior of other brittle materials. For example, already in the late 1960s, discrete crack models were used to simulate the fracture of concrete [208] [209].

3.2.3 Continuum-mechanical models

Continuum-mechanical models are well suited for the simulation of ballistic impact scenarios on a macroscopic scale. The general assumption is that glass can be treated as a continuum material in which cracks are not explicitly modeled. Instead, softening is described phenomenologically as the result of the accumulation of micron and submicron sized cracks that are smeared over a discrete area, such as e.g. the volume of a single element in a FEM model. A common approach is to define a damage parameter D describing the failure history of the area. D is usually increased incrementally based on specific stress or strain criteria. The stiffness or the strength of the material is then locally reduced with respect to D (see also section 2.2.3).

Common continuum-mechanical models for glass are e.g. [4] [5] [8] [30] [141] [210] [211] [212] [213] [214]. One of the earliest attempts to model glass under impact loads was made already in 1976 by Glenn. He conducted finite-difference calculations to investigate the brittle fracture of glass blocks during projectile impact [42].

Some continuum models account for the interaction between cracks by introducing so-called shielding zones. Furthermore, some models also distinguish between fine-scale fragmentation due to micro-cracking and coarse fragmentation due to macro-cracking. For example, Grujicic et al. developed a stochastic brittle model for SLG. The model assumes different Weibull-type distributions of preexisting flaws for the surface and interior regions. The separation of the coarse and fine fragmentation mode is controlled by a critical deformation rate [4] [210] [215].

Another example for a continuum model is the ARL glass model [216]. This model was developed especially for the simulation of silicate glasses subjected to shock wave propagation, porous compaction and spallation. A modified version of the ARL glass model also incorporates a stochastic parameterization [217]. It was reported that this model is severely dependent on the mesh resolution for two reasons. First, less energy is dissipated by the localized, failing material if smaller elements are used. Second, the mesh size directly influences the thickness of surface regions exhibiting different constitutive properties than the interior material.

The ARL model shares several similarities with models developed by Johnson and Holmquist that are described in more detail in the following.

3.2.3.1 The Johnson & Holmquist brittle material models

Johnson and Holmquist developed several continuum-mechanical models that are commonly used for the simulation of ballistic impact scenarios on brittle materials. The first version of the model is called Johnson-Holmquist-1 (JH1) model [218]. It was developed especially for the simulation of ballistic impact scenarios on ceramics. However, it is also well suited for the description of other brittle materials, like e.g. glass, concrete or rocks, subjected to large pressures and shear strain at high strain rates. The model was later improved by incorporating gradual softening due to incrementally growing damage. In addition, the piecewise linear formulation of the yield surfaces was replaced by smoothly varying functions in order to avoid non-continuous characteristics. This improved version of the JH1 model, the so-called JH2 model [213] [60] is outlined in more detail in the following.

The JH2 model includes a polynomial EOS, a constitutive relation based on two yield surfaces and a failure model. Figure 3.3 illustrates the EOS in the left diagram and the yield surfaces in the right diagram for the original parameter set of SLG [60].

The hydrostatic pressure is given similar to equation 2.90 as a function of the volumetric compression μ (ref. equation 2.84). For compressive states, the pressure is given by three material parameters K_1 , K_2 and K_3 where K_1 represents the bulk modulus:

$$P(\mu, \Delta P) = K_1\mu + K_2\mu^2 + K_3\mu^3 + \Delta P \quad \text{if } \mu \geq 0 \quad 3.13$$

For the description of expansion processes, a linear expansion EOS is adopted (ref. equation 2.96) using the bulk modulus K_1 :

$$P(\mu, \Delta P) = K_1\mu + \Delta P \quad \text{if } \mu < 0 \quad 3.14$$

The EOS does therefore not include the energy dependent terms of the Mie-Grüneisen EOS. This assumption is based on the observation that energy effects are not significant at the pressures occurring in ballistics problems. Instead, a pressure increment ΔP is added. This so-called bulking pressure is based on energy considerations and is incrementally increased when damage occurs.

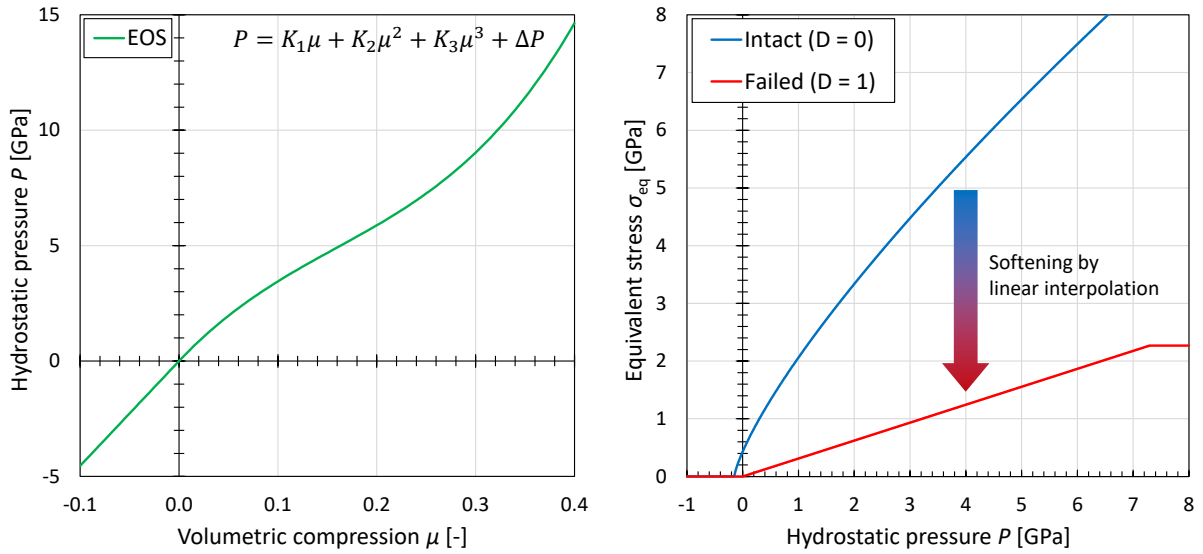


Figure 3.3: The JH2 model includes a polynomial EOS (left diagram) in combination with a constitutive relation based on two yield surfaces for intact and failed material (right diagram).

It is assumed that the bulking pressure results from a volumetric dilatation due to shear deformation. The decrease of internal elastic energy during the accumulation of damage is converted to potential, hydrostatic internal energy. The elastic internal distortional energy is related to the equivalent stress and the shear modulus as follows [219](p.62):

$$U = \frac{\sigma_{eq}^2}{6G} \quad 3.15$$

If damage is accumulated at time step n , the increase of the potential internal energy is approximately [213]:

$$\Delta U \cdot \beta = \frac{1}{2} \frac{(\Delta P^{n+1})^2 - (\Delta P^n)^2}{K_1} + (\Delta P^{n+1} - \Delta P^n) \mu_f^{n+1} \quad 3.16$$

where ΔP^n is the bulking pressure at time step n and μ_f^n denotes the corresponding volumetric compression. $\beta \in [0,1]$ is a parameter representing the fraction of internal energy loss converted to potential hydrostatic energy.

Solving equation 3.16 yields:

$$\Delta P^{n+1} = -K_1 \mu_f^{n+1} + \sqrt{(K_1 \mu_f^{n+1} + \Delta P^n)^2 + 2\beta K_1 \Delta U} \quad 3.17$$

ΔP is only accumulated for failure under compression as the potential energy under extension can be neglected.

The constitutive relation uses two yield surfaces that are defined based on the von Mises yield criterion by two curves in the equivalent stress - hydrostatic pressure plane. This is illustrated in

the right diagram of Figure 3.3. The upper curve is used for intact material ($D = 0$) and the lower curve corresponds to completely failed material ($D = 1$). The damage parameter D (ref. equation 2.55) is used to identify the degree of fracture. If plastic strain occurs during a computational cycle, D is incrementally increased as follows:

$$\Delta D = \frac{\Delta \varepsilon_p}{\varepsilon_p^f} \quad 3.18$$

where $\Delta \varepsilon_p$ is the incremental plastic strain during the calculation cycle and ε_p^f is the pressure dependent plastic strain to fracture. ε_p^f is calculated from P as follows:

$$\varepsilon_p^f(P) = D_1 \left(\frac{P - T}{P_{\text{HEL}}} \right)^{D_2} \quad 3.19$$

where D_1 , D_2 , T and P_{HEL} are material parameters. T is the hydrostatic tensile limit, which is conventionally defined to be negative in tension within the framework of this work. P_{HEL} is the hydrostatic pressure at the Hugoniot elastic limit. If the pressure is less than the hydrostatic tensile limit ($P < T$), the material instantaneously fails ($D = 1$).

In order to determine P_{HEL} , the volumetric compression μ_{HEL} at the Hugoniot elastic limit is calculated by solving the following equation [213]:

$$HEL = K_1 \mu_{\text{HEL}} + K_2 \mu_{\text{HEL}}^2 + K_3 \mu_{\text{HEL}}^3 + \frac{4}{3} G \left(\frac{\mu_{\text{HEL}}}{1 + \mu_{\text{HEL}}} \right) \quad 3.20$$

Inserting μ_{HEL} into the EOS (equation 3.13) yields:

$$P_{\text{HEL}} = K_1 \mu_{\text{HEL}} + K_2 \mu_{\text{HEL}}^2 + K_3 \mu_{\text{HEL}}^3 \quad 3.21$$

Furthermore, the equivalent stress at the Hugoniot elastic limit can be determined by:

$$\sigma_{\text{HEL}} = \frac{3}{2} (HEL - P_{\text{HEL}}) \quad 3.22$$

It has to be noted that the calculation of P_{HEL} and σ_{HEL} in the commercial hydrocode Autodyn® (version 19.1) is assumed to be different. This assumption is based on discrepancies observed by the author in single-element studies that were conducted within the framework of this work.

P_{HEL} and σ_{HEL} are used together with a set of material parameters (C , A , N , B , M , σ_{max}) to define the equivalent stress of the intact $\sigma_{D=0}(\dot{\varepsilon}^*, P)$ and failed $\sigma_{D=1}(\dot{\varepsilon}^*, P)$ yield curves as follows:

$$\sigma_{D=0}(\dot{\varepsilon}^*, P) = \sigma_{\text{HEL}} \cdot (1 + C \cdot \ln(\dot{\varepsilon}^*)) \cdot A \cdot \left(\frac{P - T}{P_{\text{HEL}}} \right)^N \quad 3.23$$

$$\sigma_{D=1}(\dot{\varepsilon}^*, P) = \begin{cases} \sigma_{\text{HEL}} \cdot (1 + C \cdot \ln(\dot{\varepsilon}^*)) \cdot B \cdot \left(\frac{P}{P_{\text{HEL}}} \right)^M, & \text{if } \sigma_{D=1} < \sigma_{\text{max}} \\ \sigma_{\text{max}}, & \text{else} \end{cases} \quad 3.24$$

where σ_{max} optionally defines a cap of the failed curve and C provides a measure of the strain rate effect.

For $C \neq 0$, the yield curves are dependent on the normalized equivalent strain rate $\dot{\epsilon}^*$, which is calculated from the strain rate tensor as follows [220]:

$$\dot{\epsilon}^* = \frac{1}{\dot{\epsilon}_0} \frac{\sqrt{2}}{3} \sqrt{(\dot{\epsilon}_{11} - \dot{\epsilon}_{22})^2 + (\dot{\epsilon}_{22} - \dot{\epsilon}_{33})^2 + (\dot{\epsilon}_{33} - \dot{\epsilon}_{11})^2 + 6(\dot{\epsilon}_{12}^2 + \dot{\epsilon}_{23}^2 + \dot{\epsilon}_{31}^2)} \quad 3.25$$

where $\dot{\epsilon}_0 = 1.0 \text{ s}^{-1}$ is the reference strain rate.

The yield curve of a partially failed element ($0 < D < 1$) is determined by a linear interpolation between the intact and failed yield curve with respect to D . Therefore, the final yield stress is given by:

$$\sigma_{\text{yield}}(\dot{\epsilon}^*, P, D) = \sigma_{D=0} - D(\sigma_{D=0} - \sigma_{D=1}) \quad 3.26$$

In 2011, Holmquist et al. developed an improved version of the JH2 model, the so-called Holmquist-Johnson model [30]. The key feature of the new model is a formulation of the material strength that is also dependent on the location of the material. More specifically, three different yield curves are defined for intact material in addition to the failed yield curve: one for intact material in the interior, one for intact material on the surface and one for intact material that is adjacent to entirely failed material. Further improvements allow for the description of thermal softening, time-dependent softening and a dependence of the yield curves on the Lode angle. In addition, the EOS is modified to allow for permanent densification and a variable shear modulus.

Due to the formulations of the interior and surface strength, the first version of the Holmquist-Johnson model was severely dependent on the mesh resolution. This issue was addressed later in the improved Holmquist-Johnson model, published in 2017 [141]. In the improved Holmquist-Johnson model, a single yield curve is used for the intact strength that is independent of the material location. However, minimum values are introduced for the interior and surface strength resulting in a higher strength at low or negative pressures in comparison to material that is adjacent to failed material. These minimum values are not dependent on the pressure or the strain rate. A further improvement is the decoupling of the damage model from the strength model. This is achieved by replacing T in equation 3.19 by a new material parameter that represents the pressure at which plastic strain begins to accumulate. This leads to more flexibility in defining the accumulation of damage.

4 Characterization of soda-lime glass under dynamic loading by means of novel PPI tests and an advanced analysis

In this chapter, a new methodology is presented to determine the dynamic behavior of SLG. The key innovations are experimental as well as analytical aspects. On the one hand, an extensive PPI test series is carried out over a wide range of shock loading stress levels instrumented by two high-speed cameras and laser interferometers (PDV and VISAR). On the other hand, a systematic analysis concept is developed and evaluated by numerical simulations. As a result, the EOS and the HEL for SLG are derived including an error estimation. Furthermore, new insights into the failure front phenomenon are gained by combining the results of the velocity profiles with the additional high-speed video observation.

As outlined in section 1.3, several results presented in this chapter have already been pre-published by the author in [A1].

4.1 Derivation of an incremental analysis for planar plate impact tests

In this section, the derivation and evaluation of an “incremental analysis” concept for the PPI tests is outlined. Such an incremental analysis of the differential form of the Rankine-Hugoniot equations is not completely new, as similar approaches have been used before e.g. by Alexander et al. [39] or Reinhart et al. [221]. Information about the derivation of the concept and the corresponding formulas, however, is sparse in the literature. Furthermore, there has to be taken great caution when considering different frames of reference (Lagrangian vs. Eulerian) to avoid calculation errors on the wave speeds.

In addition to the derivation of the concept, this work presents a novel methodology for an evaluation. The validity of the concept is investigated by means of numerical simulations. Furthermore, an error estimation is conducted to evaluate the influence of measurement errors.

4.1.1 Concept of an “incremental analysis”

The concept of the “selective analysis”, described in the theoretical principles section (2.3.2.1), works well as long as the examined material shows a clear two-wave structure under shock loading. Materials, which exhibit a concave downward shaped P - V relation in the loading range of interest, however, do not show this behavior. The reason for this is that an increase of the stress within this loading range results in a decrease of the wave speeds, which in turn prevents the formation of a sharp wave front (see e.g. Figure 4.3). Therefore, the application of the “selective analysis” on this kind of material, like it is done e.g. in [75], requires a different approach for the determination of precursor and shock front arrival times and particle velocities for equations 2.75, 2.76 and 2.77, which may increase the measurement uncertainties. For this reason, a different concept, the so-called “incremental analysis” is developed and used within this work, as outlined in this section.

The starting point is the passing of a shock wave increment with a constant shock velocity \tilde{U}_s , which lifts the material almost instantaneously from one stress and compression level to a higher level. This causes a discontinuous jump of stress and velocity as a function of time. Thereby, the

material states on both sides of the shock front are related through mass, momentum and energy conservation laws, as outlined in section 2.3.2.

For the incremental concept, equations 2.65 and 2.66 are reformulated as:

Mass conservation:

$$\rho_i(\tilde{U}_{s,i+1} - u_{p,i})dt = \rho_{i+1}(\tilde{U}_{s,i+1} - u_{p,i+1})dt \quad 4.1$$

Momentum balance:

$$\rho_{i+1}(\tilde{U}_{s,i+1} - u_{p,i+1})dt \cdot u_{p,i+1} - \rho_i(\tilde{U}_{s,i+1} - u_{p,i})dt \cdot u_{p,i} = (\sigma_{i+1} - \sigma_i)dt \quad 4.2$$

where, the states in front of the shock wave with wave velocity $\tilde{U}_{s,i+1}$ are denoted by the index i and behind the shock wave by the index $(i + 1)$. Furthermore, the material density, the particle velocity and the longitudinal stress are denoted by ρ , u_p and σ . Within the framework of this analysis, stress and strain are conventionally defined to be positive in compression.

Combining equations 4.1 and 4.2 yields the longitudinal stress state behind the shock front:

$$\sigma_{i+1} = \sigma_i + \rho_i(\tilde{U}_{s,i+1} - u_{p,i})(u_{p,i+1} - u_{p,i}) \quad 4.3$$

For the concept of the "incremental analysis", it is postulated that the complete loading path of the material can be divided in a series of infinitesimal small step loadings (for a numerical evaluation see section 4.1.3). Each loading step i is induced by the corresponding shock wave with wave velocity $\tilde{U}_{s,i+1}$.

Thus, the final stress state σ_{final} of a complete loading path of N small step loadings is given by the Riemann sum:

$$\sigma_{\text{final}} := \sigma_N = \sigma_0 + \sum_{i=0}^{N-1} (\sigma_{i+1} - \sigma_i) \quad 4.4$$

$$\sigma_{\text{final}} = \sigma_0 + \sum_{i=0}^{N-1} (\rho_i(\tilde{U}_{s,i+1} - u_{p,i})(u_{p,i+1} - u_{p,i})) \quad 4.5$$

Analogously, rearranging equation 4.1 leads to the density and strain:

$$\rho_{i+1} = \rho_i \frac{\tilde{U}_{s,i+1} - u_{p,i}}{\tilde{U}_{s,i+1} - u_{p,i+1}} \quad 4.6$$

$$\varepsilon_{i+1} := 1 - \rho_0 / \rho_{i+1} \quad 4.7$$

$$\varepsilon_{\text{max}} := \varepsilon_N = \varepsilon_0 + \sum_{i=0}^{N-1} (\varepsilon_{i+1} - \varepsilon_i) \quad 4.8$$

The conservation equations 4.1 and 4.2 are formulated in the space-fixed laboratory system, i.e. the Eulerian frame of reference. Therefore, the shock wave velocity $\tilde{U}_{s,i+1}$ is referenced to the Eulerian frame of reference as well, which is denoted by the tilde. Since $\tilde{U}_{s,i+1}$ has to be calculated from time and distance measurements it is, however, more convenient to transform the velocity into the Lagrangian frame of reference.

This is achieved by rearranging equation 9.5 to:

$$U_{s,i+1} = \frac{\rho_i}{\rho_0} (\tilde{U}_{s,i+1} - u_{p,i}) \quad 4.9$$

Substituting equation 4.9 in equations 4.3, 4.6 and 4.7 yields the final set of equations for the “incremental analysis”:

$$\sigma_{i+1} = \sigma_i + \rho_0 U_{s,i+1} (u_{p,i+1} - u_{p,i}) \quad 4.10$$

$$\rho_{i+1} = \rho_i \frac{U_{s,i+1}}{U_{s,i+1} + \frac{\rho_i}{\rho_0} (u_{p,i} - u_{p,i+1})} \quad 4.11$$

$$\varepsilon_{i+1} = \varepsilon_i + \frac{u_{p,i+1} - u_{p,i}}{U_{s,i+1}} \quad 4.12$$

Since the shock wave velocity $U_{s,i+1}$ is referenced to Lagrangian coordinates, it can be calculated directly from the experimentally measured quantities d_T and Δt_{i+1} . Here, d_T refers to the test sample thickness while $\Delta t_{i+1} = (t_{i+1} - t_0)$ is the time difference between the arrival of the shock wave and the arrival of the elastic precursor.

Figure 4.1 shows a schematic of the corresponding Lagrange diagram.

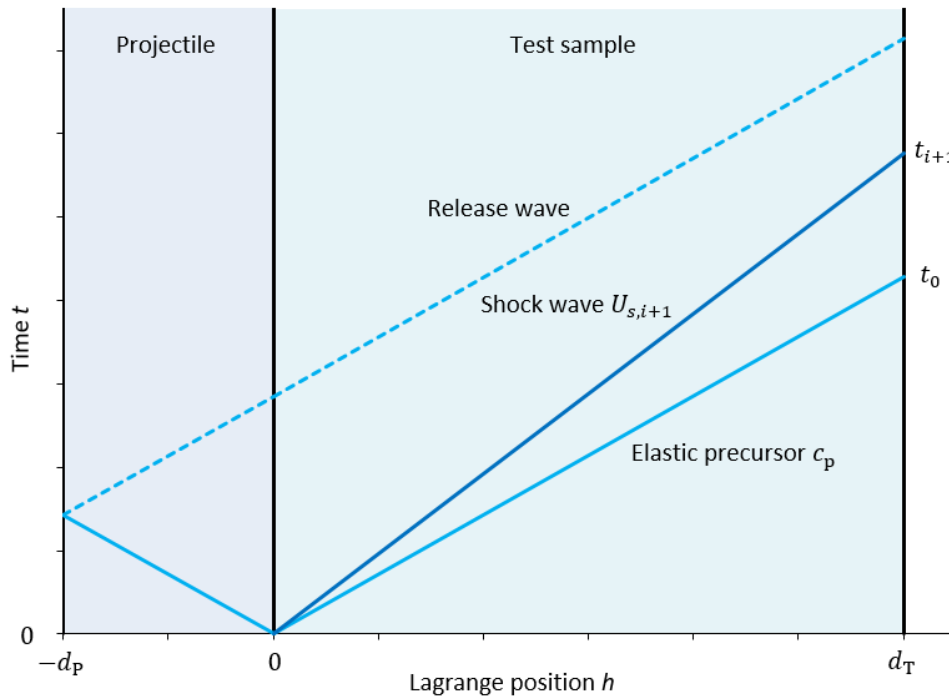


Figure 4.1: Lagrange diagram illustrating the relation between shock wave velocity and time measurement [A1].

The elastic precursor arrives at the time

$$t_0 = \frac{d_T}{c_p} \quad 4.13$$

Here, the longitudinal wave velocity c_p is derived from the elastic material properties (see Table 1.2). Since the elastic wave travels through unstressed material, its Lagrangian and Eulerian wave speeds are identical. Furthermore, the point of the time measurement, that is the free surface of the test specimen, stays at a constant Lagrangian position $h = d_T = \text{const}$ for all times.

The shock wave arrives at the time

$$t_{i+1} = \frac{d_T}{U_{s,i+1}} \quad 4.14$$

Combining equation 4.13 with 4.14 and rearranging yields the Lagrangian shock velocity as a function of the experimentally observed time difference Δt_{i+1} :

$$U_{s,i+1}(\Delta t_{i+1}) = \frac{c_p}{1 + \frac{c_p(t_{i+1} - t_0)}{d_T}} = \frac{d_T}{\frac{d_T}{c_p} + \Delta t_{i+1}} \quad 4.15$$

4.1.2 Derivation of the selective analysis as a special case of the incremental analysis

This section provides a short illustration how the equations of the selective analysis can be derived from the incremental equations. It is also demonstrated that the selective method can be inaccurate and not well reproducible when the velocity profile does not exhibit a clear two-wave structure.

In the common selective analysis, only four discrete values are deduced from the free surface velocity profile. These are the arrival times t_{e1} and t_{p1} of the elastic and plastic wave as well as the corresponding particle velocities u_{e1} and $u_{final} = u_{e1} + u_{p1}$. Inserting these values in equations 2.75, 2.76 and 2.77 leads to the stress σ_{final} and strain ε_{final} of the final state.

The equations of the selective analysis can be derived from the incremental analysis equations 4.10 and 4.12 by setting the number of incremental jumps to two, that is $N = 2$. This leads to:

$$\begin{aligned} \sigma_{final} &= \sigma_2 \\ &= \sigma_1 + \rho_0 U_{s,2} (u_{p,2} - u_{p,1}) \\ &= \sigma_0 + \rho_0 U_{s,1} (u_{p,1} - u_{p,0}) + \rho_0 U_{s,2} (u_{p,2} - u_{p,1}) \end{aligned}$$

$$\begin{aligned} \varepsilon_{final} &= \varepsilon_2 \\ &= \varepsilon_1 + \frac{u_{p,2} - u_{p,1}}{U_{s,2}} \\ &= \varepsilon_0 + \frac{u_{p,1} - u_{p,0}}{U_{s,1}} + \frac{u_{p,2} - u_{p,1}}{U_{s,2}} \end{aligned}$$

Together with the following substitutions

$$\sigma_0 = 0, U_{s,1} = c_p, U_{s,2} = U_s, u_{p,0} = 0, u_{p,1} = u_{p,HEL}, u_{p,2} = u_{p,final}$$

the selective equations 2.76 and 2.77 are derived.

Figure 4.2 and Figure 4.3 illustrate two representative particle velocity profiles created by finite element simulations. In the first figure, the result of a symmetric PPI of steel impacting steel at

500 m/s is depicted as a blue line. The profile exhibits a clear two-wave structure and the discrete values for the arrival times and particle velocity plateaus (dashed and dotted lines) can be assigned with acceptable measurement errors.

By contrast, the particle velocity profile of a simulated PPI test, in which steel impacts SLG at 1000 m/s, does not show this clear two-wave structure (Figure 4.3). In this case, the values for t_{el} and u_{final} are chosen to be the correct values, while u_{el} and t_{pl} are solely estimated on the curve progression of the velocity profile (dashed and dotted lines). The displayed values yield final compression and stress values, which are 1 % too low. Shifting the value of t_{pl} by only 200 ns, which is still a reasonable estimation, already increases this error to more than 5 %. This shows that the results of the selective analysis are highly dependent on the estimations of the evaluator and are not well reproducible. On the contrary, the incremental analysis provides reproducible results, which differ less than 0.4 % from the simulated values (see Table 4.1 in the next section).

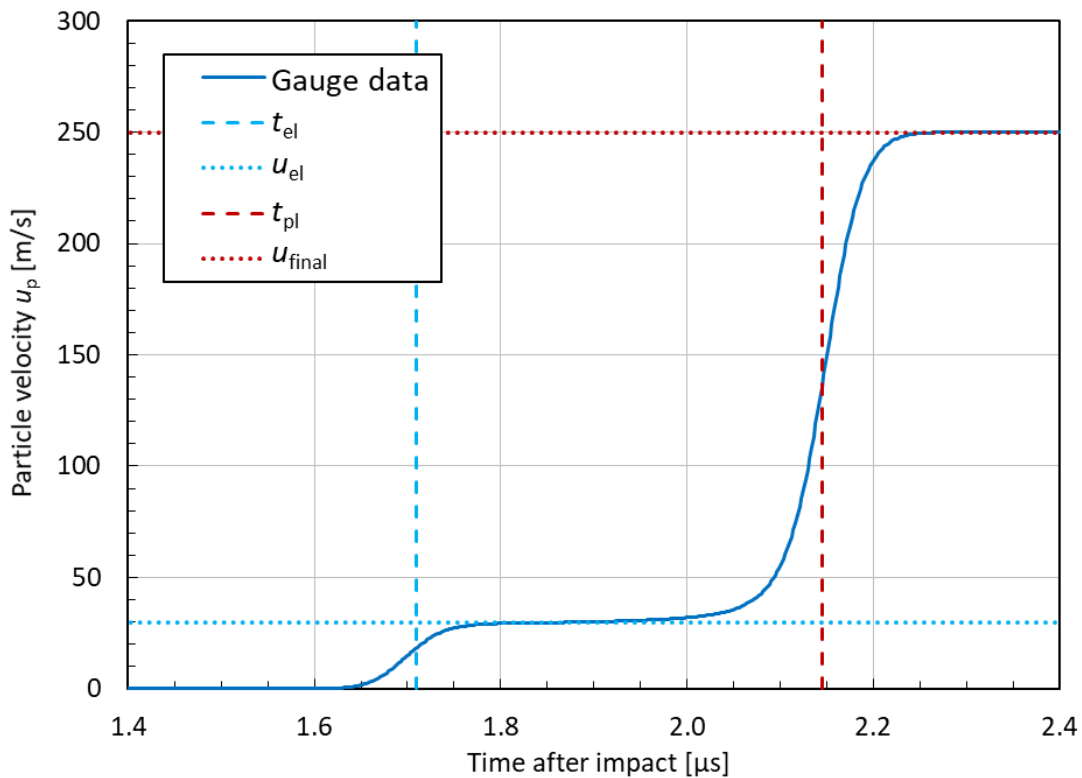


Figure 4.2: Particle velocity profile of a simulated symmetric PPI test; steel impacting steel at 500 m/s.

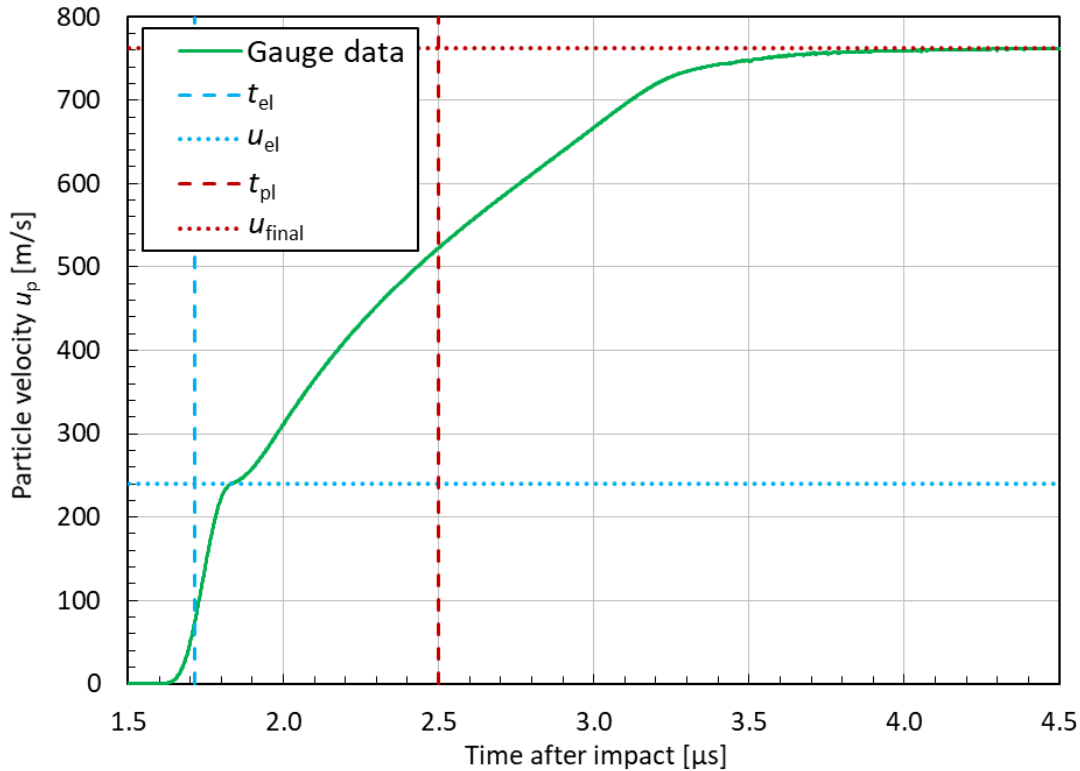


Figure 4.3: Particle velocity profile of a simulated PPI test; steel impacting SLG at 1000 m/s.

4.1.3 Numerical evaluation of the “incremental analysis” concept

In section 4.1.1, a set of equations (4.10, 4.11, 4.12 and 4.15) for the “incremental analysis” was derived. Given a measured free surface velocity profile of a shock loaded test sample, the formulas provide a way to calculate the stress-strain-states of the material as a function of time. In this section, numerical simulation results are analyzed in order to evaluate the postulated concept that the loading path can be divided in a series of infinitesimal small step loadings.

The simulations were conducted with the commercial hydrocode Autodyn® (version 19.1). Here, finite element models of three different PPI test scenarios were investigated. PPI tests are designed in a way to ensure that there is a state of one-dimensional strain in the region of the measurement axis for the whole measurement time. Therefore, it is sufficient to simulate the PPI plates as one-dimensional chains of elements. In Autodyn®, this was realized by a discretization of the material volume into two-dimensional Lagrange elements in combination with a boundary condition. The boundary condition was applied to all nodes constraining the movement perpendicular to the impact axis. The length of all Lagrange elements was set to 0.02 mm in order to enable a satisfactory resolution of the sharp shock wave fronts.

The setup for all three PPI simulations is depicted in Figure 4.4. In the first scenario (top of the picture), a 10 mm thick steel plate impacted a 20 mm thick plate of the same material. In the middle of the impacted plate a measurement gauge was placed, which provided the simulated measurement values. The impact velocity was set to 500 m/s.

In the second and third scenario, a 10 mm steel plate impacted a 20 mm plate of SLG at two different impact velocities (1000 m/s and 2000 m/s).

The constitutive material models were taken from the literature (steel 4340 by Johnson et al. [222] and SLG by Holmquist et al. [60]). The model parameters are listed in Table 9.2 and Table 9.3 in the appendix.

In order to evaluate the differential analysis concept, the simulated particle velocity of the gauge point was analyzed analogously to the experimental measured particle velocities. In case of the experimental evaluation, the true values for the stress and the compression are not known and therefore the accurateness of the analysis concept is unknown. The advantage of the simulated values is, however, that the results of the incremental analysis can be checked directly against the true values provided by the gauge point.

Figure 4.5 shows the simulated particle velocity as a function of time for all three impact scenarios. The starting time $t_0 = 0 \mu\text{s}$ corresponds to the arrival time of the elastic wave, calculated using equation 4.13. The symmetric impact of steel vs. steel (blue line) shows a clear two-wave structure. First, the elastic wave accelerated the particles to a velocity of about 50 m/s. The plastic shock wave arrived almost $0.5 \mu\text{s}$ later, further accelerating the material to the final particle velocity of about 250 m/s.

The scenarios with the glass targets show a different behavior. After the elastic ramp, no plateau of constant particle velocity developed. Instead, the particles were accelerated continuously. This ramping behavior is caused by the concave downwards shape of the P - V relation of SLG in the intermediate pressure range. Since there is no clear two-wave structure, the common "selective analysis" is not suitable. This especially applies for intermediate loading range like e.g. at an impact velocity of 1000 m/s (green line).

In addition to the particle velocities, the gauge points also provide the calculated time-dependent values for the longitudinal stress and the true compression. These are illustrated in Figure 4.6 and Figure 4.7 as colored lines. The black dashed lines are the results of the incremental analysis applied to the corresponding particle velocity profiles (Figure 4.5). Evidently, the agreement between the results of the incremental analysis and the true simulated values is excellent for all times.

For a quantitative comparison, the final values at $t = 2.5 \mu\text{s}$ of the stress and compression are listed in Table 4.1. The last column provides the percentage difference between the incremental analysis results and the true values. The low deviations of less than 0.4 % strongly support the postulated concept, that the loading path can be divided into a series of infinitesimal small step loadings. Therefore, the incremental analysis method is reasonable.

Characterization of soda-lime glass under dynamic loading by means of novel PPI tests and an advanced analysis

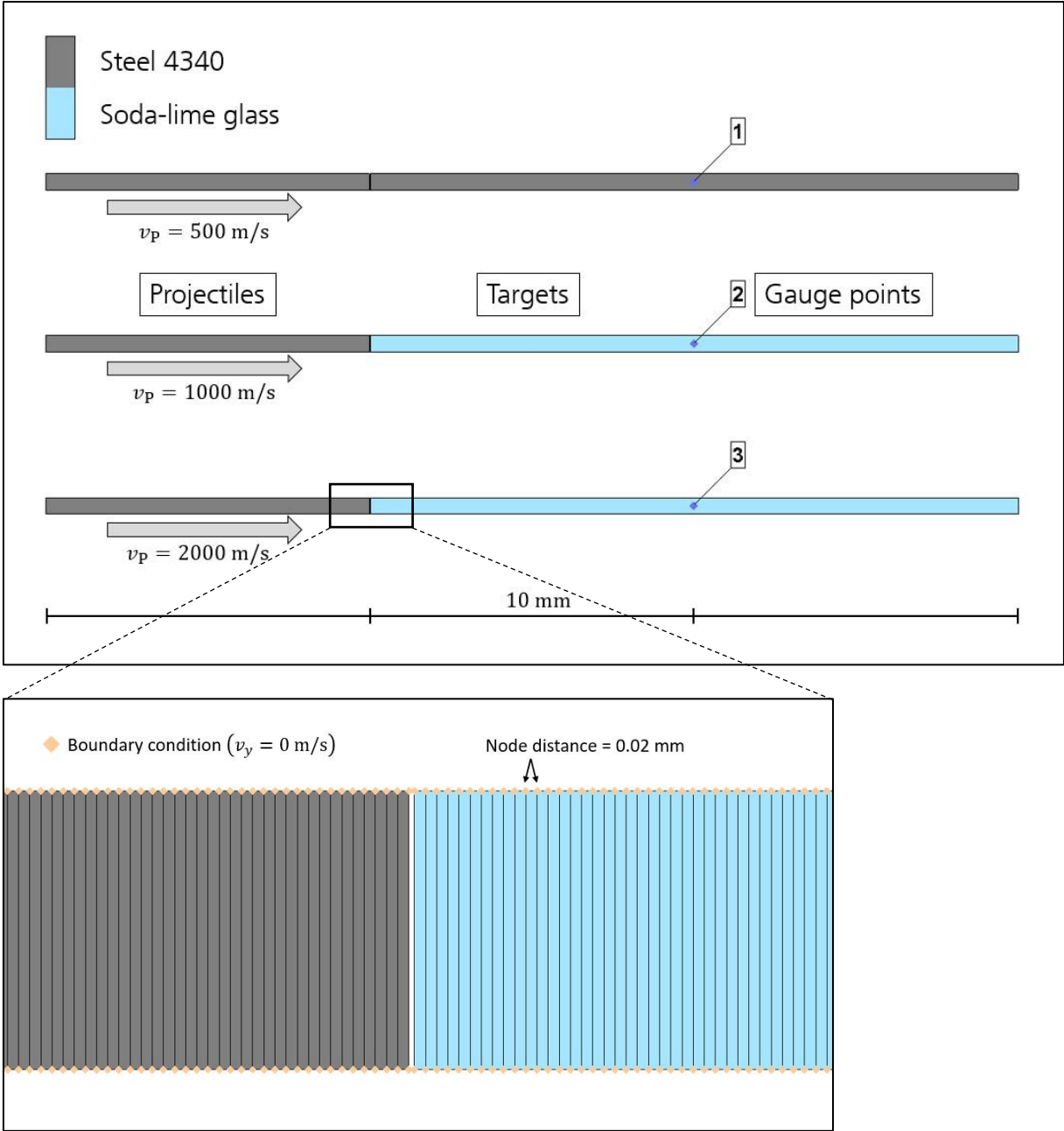


Figure 4.4: Setup of the simulations for testing the incremental analysis. Three different scenarios were simulated: steel vs. steel with an impact velocity $v_p = 500 \text{ m/s}$ (top), steel vs. glass with $v_p = 1000 \text{ m/s}$ (middle) and steel vs. glass with $v_p = 2000 \text{ m/s}$ (bottom). At the lower edge, an enlarged picture detail is featured illustrating the element size and boundary condition.

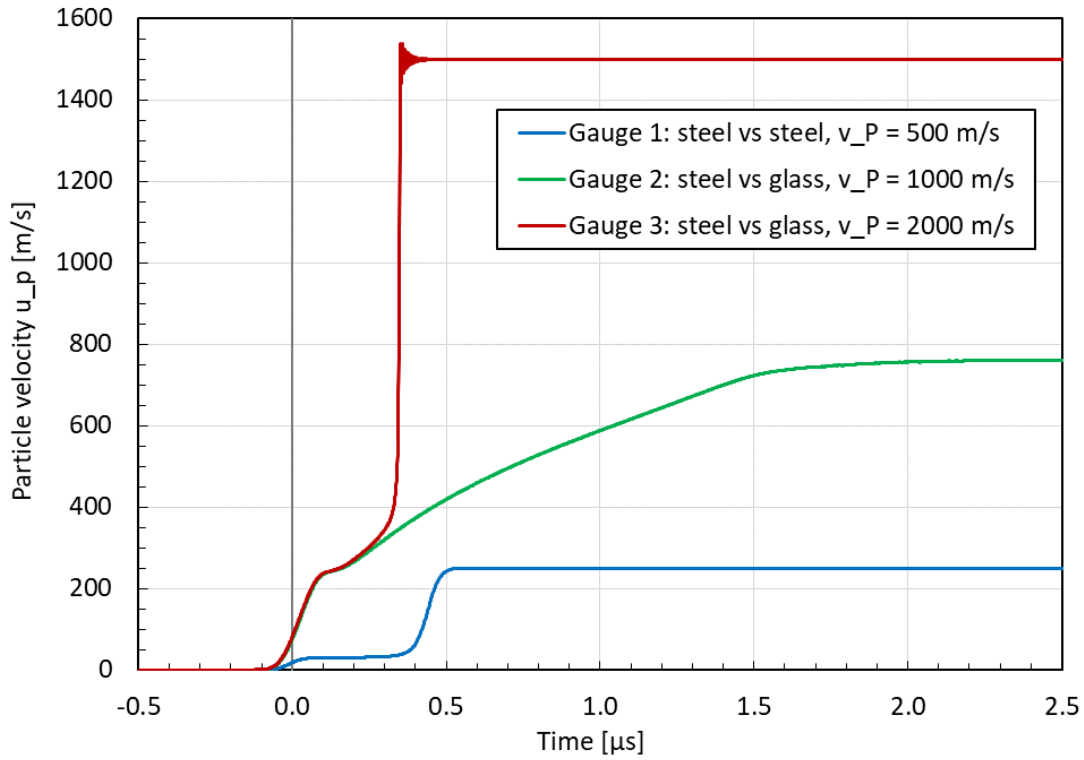


Figure 4.5: Results of the PPI simulations: Particle velocities vs. time provided by a gauge point located at a distance of 10 mm to the impact surface.

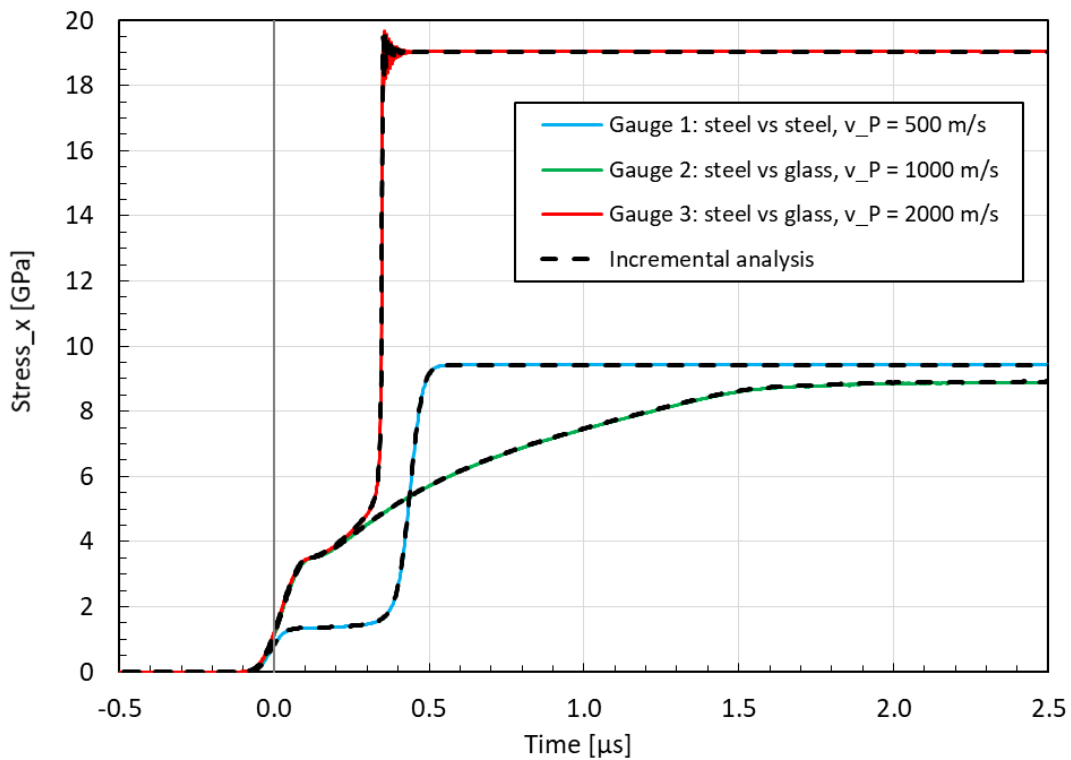


Figure 4.6: Results of the PPI simulations: Longitudinal stress vs. time. The colored lines are the true values provided by the gauge point. The black dashed lines are the results of the incremental analysis applied to the corresponding particle velocity profiles (Figure 4.5).

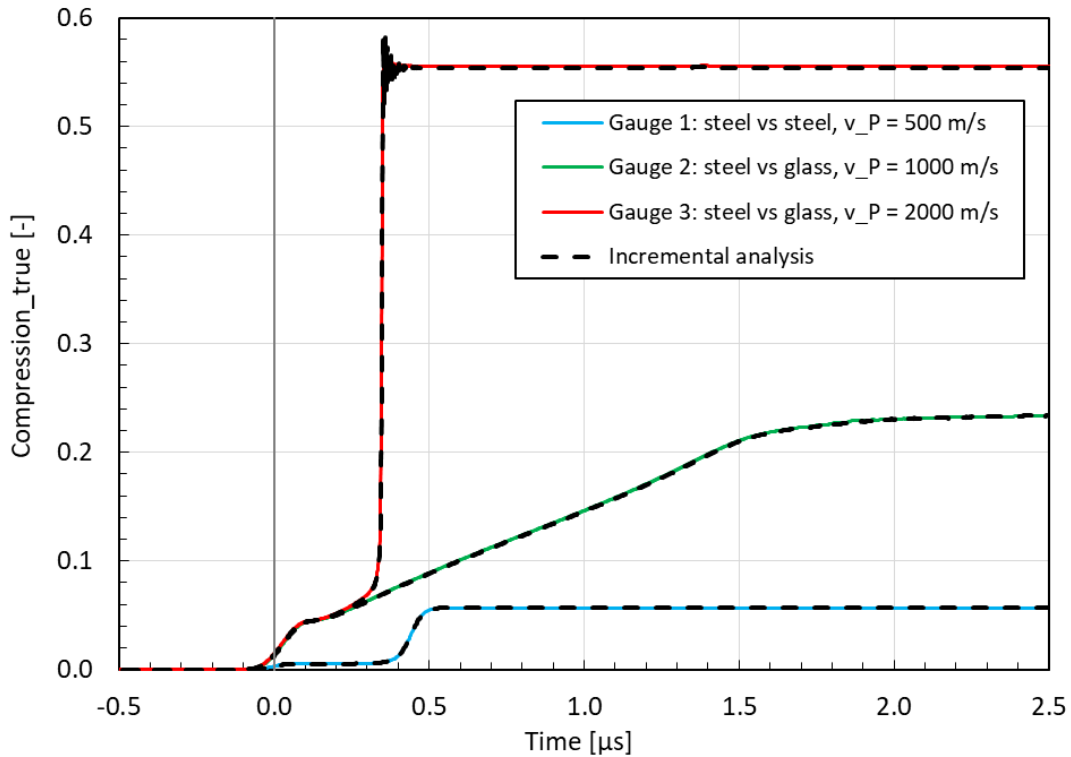


Figure 4.7: Results of the PPI simulations: Compression vs. time. The colored lines are the true values provided by the gauge point. The black dashed lines are the results of the incremental analysis applied to the corresponding particle velocity profiles (Figure 4.5).

Table 4.1: Comparison of final stress and compression values. Column “gauge data” contains the values, which are directly provided by the gauge point of the simulation. Column “incremental analysis” shows the corresponding values, calculated with the incremental analysis. The last column gives the percentage difference.

Projectile	Target	v_p [m/s]	Gauge data		Incremental analysis		Difference	
			σ_{final} [GPa]	$\mu_{true,final}$ [-]	σ_{final} [GPa]	$\mu_{true,final}$ [-]	$\Delta\sigma_{final}$ [%]	$\Delta\mu_{true,final}$ [%]
Steel	Steel	500	9.42	0.057	9.40	0.057	0.2	-0.3
Steel	Glass	1000	8.87	0.234	8.90	0.235	-0.3	-0.3
Steel	Glass	2000	19.04	0.556	19.02	0.555	0.1	0.2

4.1.4 Error estimation of the incremental analysis concept

As shown in the previous section, the incremental analysis provides stress and compression values, which almost exactly correspond to their true simulated results. However, this is only strictly true, if the time of impact or the arrival time t_0 of the elastic wave together with its velocity c_p are known.

In this section, an error estimation is carried out based on the assumption that the utilized t_0 or c_p are flawed. This is realized by applying the incremental analysis with a shift on t_0 .

Characterization of soda-lime glass under dynamic loading by means of novel PPI tests and an advanced analysis

For the investigated impact scenarios, a shift of ± 50 ns on t_0 is chosen. On the one hand, this value can represent a relative error of 3 % on the estimation of the arrival time. On the other hand, it can represent a relative error of 3 % on the measured value of c_p . These values are summarized in Table 4.2 for the different impact scenarios. In a realistic experimental analysis scenario t_0 and c_p can be assumed to have relative errors of less than 3 %, but non-negligible. Therefore it is feasible to take the shift of ± 50 ns as a combined error for the measurement errors on t_0 or c_p .

Table 4.2: Percentage error on t_0 and c_p if a shift of ± 50 ns is applied.

Projectile	Target	v_p [m/s]	Correct values		$t_0 + 50$ ns equals		$t_0 - 50$ ns equals	
			c_p [m/s]	t_0 [μ s]	Δt_0 [%]	or Δc_p [%]	Δt_0 [%]	or Δc_p [%]
Steel	Steel	500	5851	1.709	2.9	3.0	-2.9	-2.8
Steel	Glass	1000	5828	1.716	2.9	3.0	-2.9	-2.8
Steel	Glass	2000	5828	1.716	2.9	3.0	-2.9	-2.8

Figure 4.8 and Figure 4.9 illustrate the influence of the t_0 shift for the impact scenarios steel on steel with $v_p = 500$ m/s and steel on glass with $v_p = 1000$ m/s, respectively. The left column shows the particle velocity as a function of time, whereas the right column provides the corresponding longitudinal stress.

The true arrival time of the elastic wave is illustrated as a vertical dashed gray line. In addition, the value of t_0 , which is used for the analysis, is depicted as a vertical solid gray line. The diagrams of the top row depict the reference analysis, without a shift on t_0 . Hence in this case, both gray lines lie on top of each other. The values provided by the gauge point are outlined as blue curves (steel on steel) and green curves (steel on glass). These are the true values, with which the results of the incremental analysis should match. The input and output values of the analysis are indicated as black dashed lines.

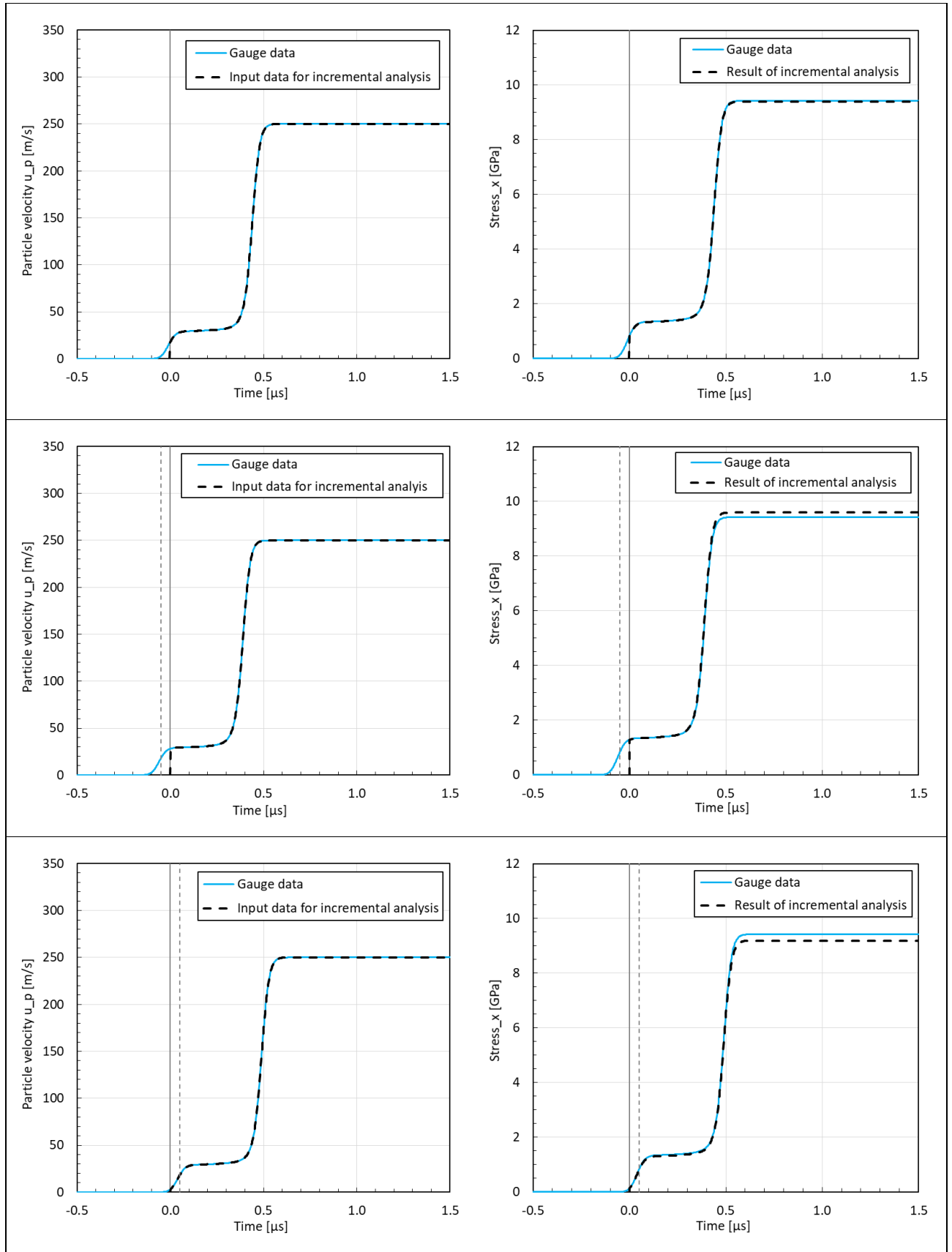


Figure 4.8: Influence of the t_0 shift, steel vs steel, $v_p = 500$ m/s: The left column shows the particle velocity, which is used as input for the incremental analysis, as a black dashed line. The right column shows the result of the incremental analysis (black dashed line) and the true values of the simulation gauge (blue line). In the first row, no shift on t_0 is applied. In the second and third row, shifts of +50 ns and -50 ns are applied, respectively.

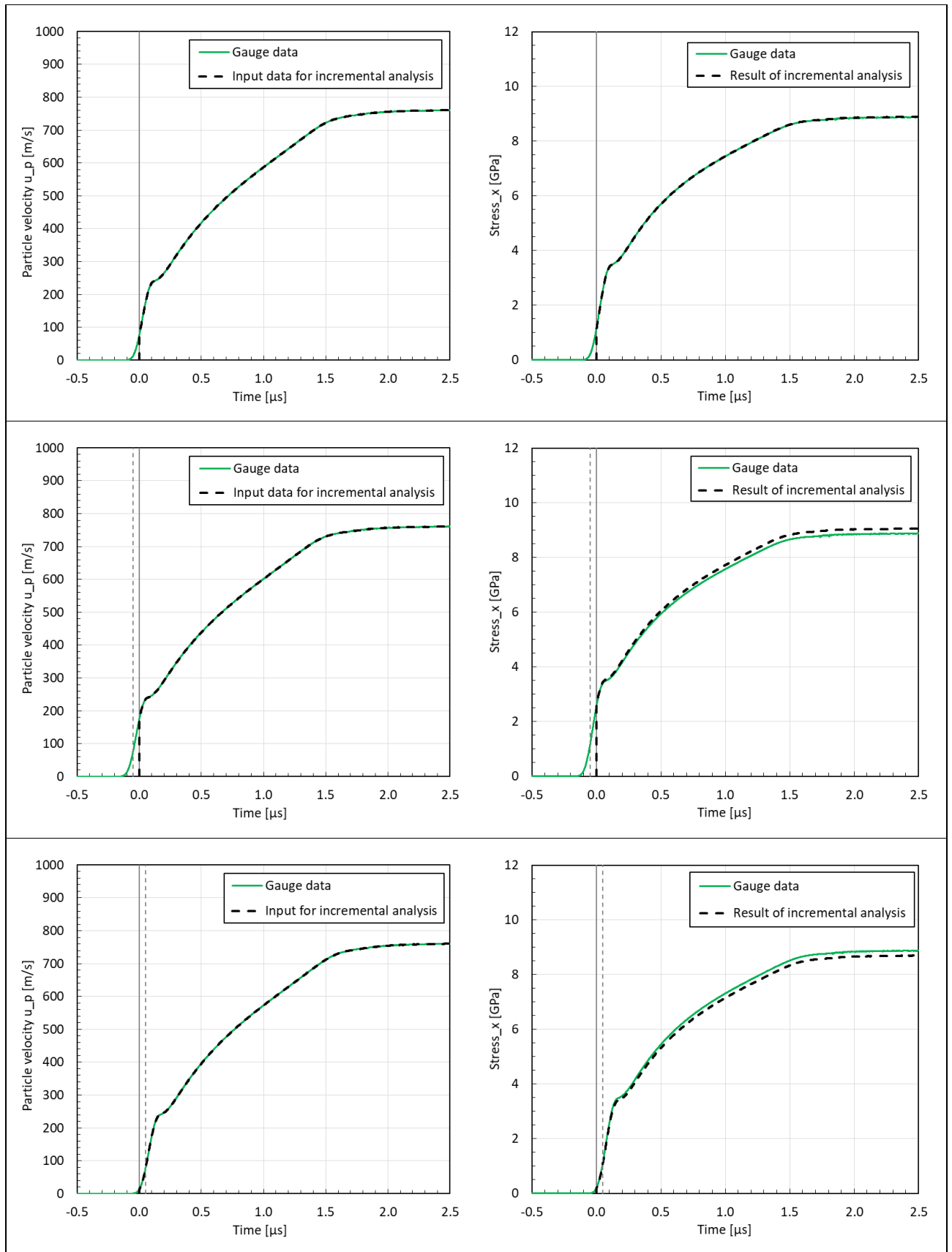


Figure 4.9: Influence of the t_0 shift, steel vs glass, $v_p = 1000$ m/s: The left column shows the particle velocity, which is used as input for the incremental analysis, as a black dashed line. The right column shows the result of the incremental analysis (black dashed line) and the true values of the simulation gauge (green line). In the first row, no shift on t_0 is applied. In the second and third row, shifts of +50 ns and -50 ns are applied, respectively.

Without a shift on t_0 , the results of the incremental analysis reproduce the true gauge values. However, if a shift of +50 ns is applied, the calculated results differ from the true values. This is illustrated in the diagrams of the middle row in Figure 4.8 and Figure 4.9. In this case, the final stress value of the incremental analysis is approximately 2 % too high. Conversely, a shift of -50 ns on t_0 , leads to an underevaluation of the final stresses (diagrams of the bottom row).

Table 4.3 and Table 4.4 contain a summary of the resulting errors for the scenarios where t_0 is shifted by +50 ns or -50 ns towards the true value. In addition to the longitudinal stress of the final state and its relative error, the volumetric compression and its error is also listed.

Table 4.3: Resulting errors on the incremental analysis results, if t_0 is shifted by +50 ns.

Projectile	Target	v_p [m/s]	Incremental analysis with $t_0 + 50$ ns			
			σ_{final} [GPa]	$\mu_{\text{true,final}}$ [-]	$\Delta\sigma_{\text{final}}$ [%]	$\Delta\mu_{\text{true,final}}$ [%]
Steel	Steel	500	9.60	0.055	1.9	-2.1
Steel	Glass	1000	9.06	0.229	2.1	-2.5
Steel	Glass	2000	19.44	0.532	2.1	-4.3

Table 4.4: Resulting errors on the incremental analysis results, if t_0 is shifted by -50 ns.

Projectile	Target	v_p [m/s]	Incremental analysis with $t_0 - 50$ ns			
			σ_{final} [GPa]	$\mu_{\text{true,final}}$ [-]	$\Delta\sigma_{\text{final}}$ [%]	$\Delta\mu_{\text{true,final}}$ [%]
Steel	Steel	500	9.19	0.058	-2.5	2.8
Steel	Glass	1000	8.70	0.240	-1.9	2.6
Steel	Glass	2000	18.57	0.581	-2.5	4.5

In summary, if there is a relative error of approximately 3 % on t_0 or c_p , or a corresponding combined error, the results of the incremental analysis are flawed on a similar scale. Of the cases examined, the analysis results for the impact of steel on glass at 2000 m/s yield the biggest deviation from the true values. In this scenario, the calculated stress of the final state is 2.5 % too low and its volumetric compression is 4.5 % too high.

4.2 Experimental setup

The specimens that are investigated by means of PPI tests, were manufactured from commercial grade SLG sheets of 3 different thicknesses: (2.86 ± 0.05) mm, (4.85 ± 0.05) mm and (7.85 ± 0.05) mm.

For the tests with high-speed video observation, 50 mm x 50 mm square shaped specimens with polished side faces were cut. For all other tests, round discs with a diameter of 33 mm or 40 mm were prepared by means of water jet cutting.

Table 1.2 provides a summary of the typical material parameters. Values were taken from literature data or calculated by means of the conversion formulae of the elastic properties.

4.2.1 Conduction of planar plate impact tests

PPI experiments were conducted with 3 different acceleration facilities with diverse gun barrel diameters at Fraunhofer EMI (two single-stage facilities located in Freiburg and a two-stage facility at the EMI location in Kandern). The general setup of the impact experiments is depicted in Figure 4.10.

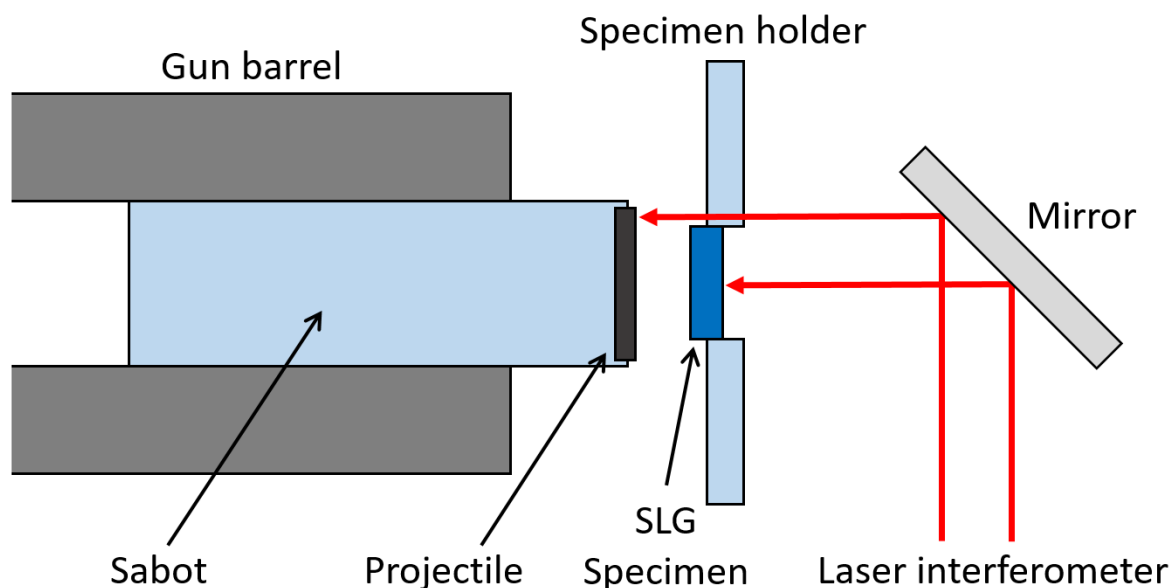


Figure 4.10: Scheme of the experimental setup of the PPI tests (not to scale); the detailed arrangement depends on the specific facility used for the tests.

The specimen geometry is flat such that a uniaxial state of strain is obtained in the specimen during the time of interest. In all tests, a massive polycarbonate sabot (PC) was used to accelerate the impactor plate in a gun barrel. The sabots were produced to fit smoothly in the specific gun barrels. Impactor plates were made from commercial C45 steel or Aluminum 6061 T6511 (denoted as Al in the following). All tests were conducted as direct impacts, in which the specimen plate is observed directly by the laser interferometer (no window applied). In order to establish a reflection of the laser light only from the surface of the specimen, a thin layer of gold was vapor-deposited on each specimen.

Characterization of soda-lime glass under dynamic loading by means of novel PPI tests and an advanced analysis

In case of the two-stage accelerator, the specimen was placed inside an adjustable target holder, which was mounted directly on the gun muzzle. Figure 4.11 shows pictures of a long polycarbonate sabot with an aluminum projectile (left side) and the target holder with the gold covered SLG specimen.



Figure 4.11: Picture of a long polycarbonate sabot with an aluminum projectile (left) and the target holder with the gold covered SLG specimen (right).

Table 4.5 provides a summary of all analyzed PPI tests conducted at the two-stage light gas gun (see Figure 4.12). Additional information, like the mass of the used gunpowder and the measured impact velocities of the projectiles, is listed in Table 4.6. In order to illustrate the high loading of the accelerator, one column lists the maximum pressure that was measured in the conical pressure coupling.

For tests with numbers 0112, 0113 and 0114, a shortened sabot was used (70 mm length instead of 150 mm), which reduced the total weight of the projectile-sabot-combination by more than 50 %.

The two-stage accelerator was driven by propellant for the first acceleration stage and helium gas (filling pressures between 10 bar and 15 bar) for the second acceleration stage. The bore diameter of the second acceleration stage was 45 mm. The sabots had lengths of 150 mm and 70 mm with masses of 270 g and 122 g, respectively.

The chamber of the two-stage facility was evacuated to the level of typically 7 mbar or below.

In addition, a summary of all evaluated PPI tests conducted at the single-stage guns (powder or gas) is shown in Table 4.7. For most of these tests, a 70 mm gun barrel was used and the sabots had a total length of 50 mm and a mass without impactor plate of about 190 g. For three tests (0855, 0856 and 0857), another single-stage accelerator operated with propellant was used. In those tests, a gun barrel with an 18.35 mm bore was utilized. The total length of the sabots was 32 mm, the mass of the sabots themselves was 8.7 g and impact velocities were calculated using a well-known impact velocity-amount of propellant-relationship (accuracy better than ± 2 %). These measurements were conducted in order to bridge the impact velocity range to the capabilities of a two-stage accelerator applied for this kind of investigation. The chambers of the single-stage facilities were evacuated to the level of typically 2 mbar or below.

In all tests, the specimens fragmented completely to fine dust, so that no fragments could be recovered.

Characterization of soda-lime glass under dynamic loading by means of novel PPI tests and an advanced analysis

Table 4.5: Summary of all analyzed PPI tests conducted at the two-stage light gas gun (v_p = impact velocity); (Table was pre-published by the author [A1]).

Test No.	Projectile				Target			Planned v_p [m/s]
	Material	Thickness [mm]	Diameter [mm]	Mass (+ sabot) [g]	Material	Thickness [mm]	Diameter [mm]	
0099	Al	2	40	275.9	SLG	4.85	33	1700
0100	Al	2	40	275.5	SLG	4.85	33	1900
0102	Al	2	40	276.2	SLG	4.85	33	3000
0110	C45	2	33	282.0	SLG	4.85	33	1700
0111	C45	2	33	282.6	SLG	4.85	33	1700
0112	C45	2	33	134.4	SLG	4.85	33	2400
0113	C45	2	33	134.7	SLG	4.85	33	2400
0114	Al	2	40	134.7	SLG	4.85	33	2400

Table 4.6: Additional information of the two-stage light gas gun tests; the last two columns show the measured impact velocities.

Test No.	Filling pressure of compression chamber [bar]	Mass of gun-powder [g]	Load in conical pressure coupling [bar]	v_p measured by PDV [m/s]	v_p measured by trigger pins [m/s]
0099	10.3	500	1345	1703	1667
0100	13.1	600	2030	-	1875
0102	12.8	1200	7255	3029	2947
0110	10.0	500	1565	1686	1685
0111	10.0	500	1945	1685	1685
0112	13.0	620	900	2456	2419
0113	13.0	620	825	2440	2419
0114	13.0	620	975	2447	2419

Table 4.7: Summary of all evaluated PPI tests conducted at single-stage guns (v_p = impact velocity); (Table was pre-published by the author [A1]).

Test No.	Projectile				Target			Planned v_p [m/s]
	Material	Thickness [mm]	Diameter [mm]	Mass (+ sabot) [g]	Material	Thickness [mm]	Diameter / width [mm]	
3783	Al	2	40	190	SLG	4.85	33	1100
3786	Al	2	40	190	SLG	4.85	33	900
3787	Al	2	40	190	SLG	4.85	33	600
0855	C45	1.5	14	10.55	SLG	2.86	33	1700
0856	C45	1.5	14	10.57	SLG	2.86	33	1200
0857	C45	1.5	14	10.61	SLG	2.86	33	1300
3909	C45	2	58	259	SLG	4.85	33	1000
4042	Al	2	58	248	SLG	4.85	50 quad	500
4143	Al	3	58	228	SLG	7.85	50 quad	900
4144	Al	2	58	220	SLG	7.85	50 quad	500
4145	Al	2	58	220	SLG	7.85	50 quad	1100
4146	Al	2	58	220	SLG	7.85	50 quad	500



Figure 4.12: Two-stage light gas gun at the testing ground of Fraunhofer EMI at Kandern.

4.2.2 Velocity measurement systems

In case of the single-stage accelerators, a VISAR [223] [224] [225] [226] interferometric system was utilized for measuring the free surface velocity in the center of the rear face of the specimen. The focus point of the VISAR had a diameter of approximately 0.5 mm. The accuracy of the velocity measurement with the VISAR was $\pm 2\%$, since typically 1.0 to 1.5 fringes were captured [226] during the experiments. The time resolution of the system is better than 2 ns. The impact velocity was determined by a shortcut trigger arrangement of three pins in the muzzle region of the gun with a typical accuracy of $\pm 3\%$.

In combination with the two-stage accelerator, a two-beam PDV [227] [228] [229] was used. With one (collimated) beam, the complete acceleration path of the sabot was measured, giving the impact velocity with an accuracy of at least $\pm 1\%$. This beam was positioned slightly above the SLG target measuring the projectile velocity either directly at the front of the projectile plate (if the projectile diameter was larger than the target) or at the front face of the sabot. The other beam was used, as in case of the VISAR measurements mentioned above, to determine the free surface velocity of the specimens in their rear face center region. This beam of the PDV was focused and had a diameter of approximately 1 mm.

Figure 4.13 shows pictures of the experimental PDV setup. The left picture was taken outside of the red blast tank, in which the PPI took place. It illustrates the optical bench with a built up lens system for the focusing and alignment of the PDV laser beams. The interior of the blast tank is displayed in the right picture. The infrared beams enter the tank through a transparent window and are reflected by means of an adjustable mirror, as indicated by the red dashed lines.

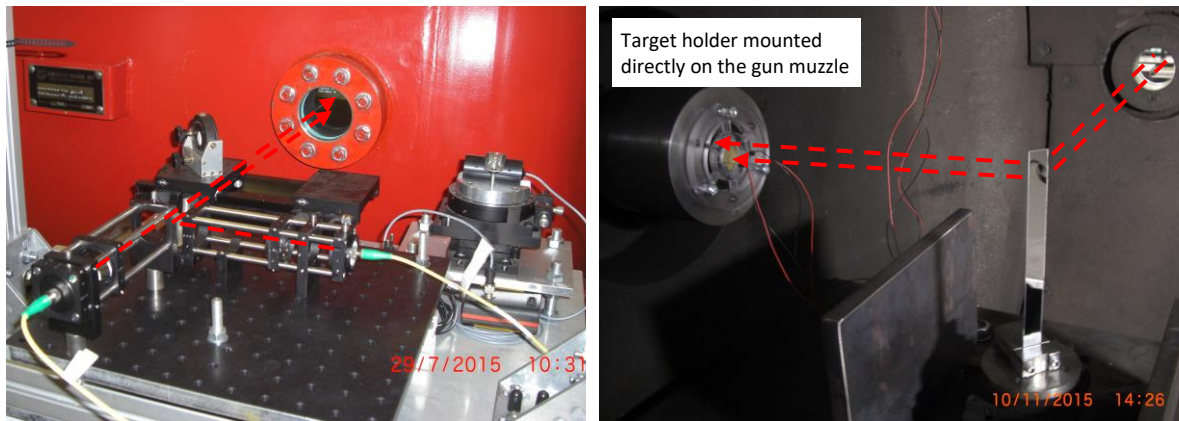


Figure 4.13: Left: optical bench of the PDV system positioned at the side of the blast tank; right: interior view of the blast tank; the PDV laser beams enter the blast tank through a transparent window and are reflected by means of an adjustable mirror onto the back face of the SLG specimen and the projectile, as indicated by the red dashed lines.

In case of the PDV, the time resolution σ_t and the accuracy of the velocity measurement σ_v are connected to the wavelength λ_0 of the laser by the relation $2\sigma_v \cdot 2\sigma_t = \frac{\lambda_0}{2\pi}$ and depend strongly on the parameters of the applied fast Fourier transform (FFT) analysis [230]. This is demonstrated in Figure 4.14, which illustrates the analysis results of test no. 0113 for two different parameter sets. Both diagrams show a spectrogram of the measured free surface velocity as a function of time, whereby the z-axis displays the intensity of the reflected laser light for each velocity. In the top spectrogram, the resolution of the time is prioritized, whereas in the bottom spectrogram the velocity resolution is higher. For the top diagram, a FFT window length of 4096 sample points with an overlap of 95 % was chosen, resulting in a time step of 4.1 ns and a minimum velocity step of 9.5 m/s. Increasing the FFT length to 16384 sample points yields a larger time step of 16.4 ns but a smaller minimum velocity step of 2.38 m/s, as illustrated in the bottom diagram.

For all analyzed PPI tests instrumented with PDV, a minimal time resolution between 3 ns to 8 ns could be achieved.

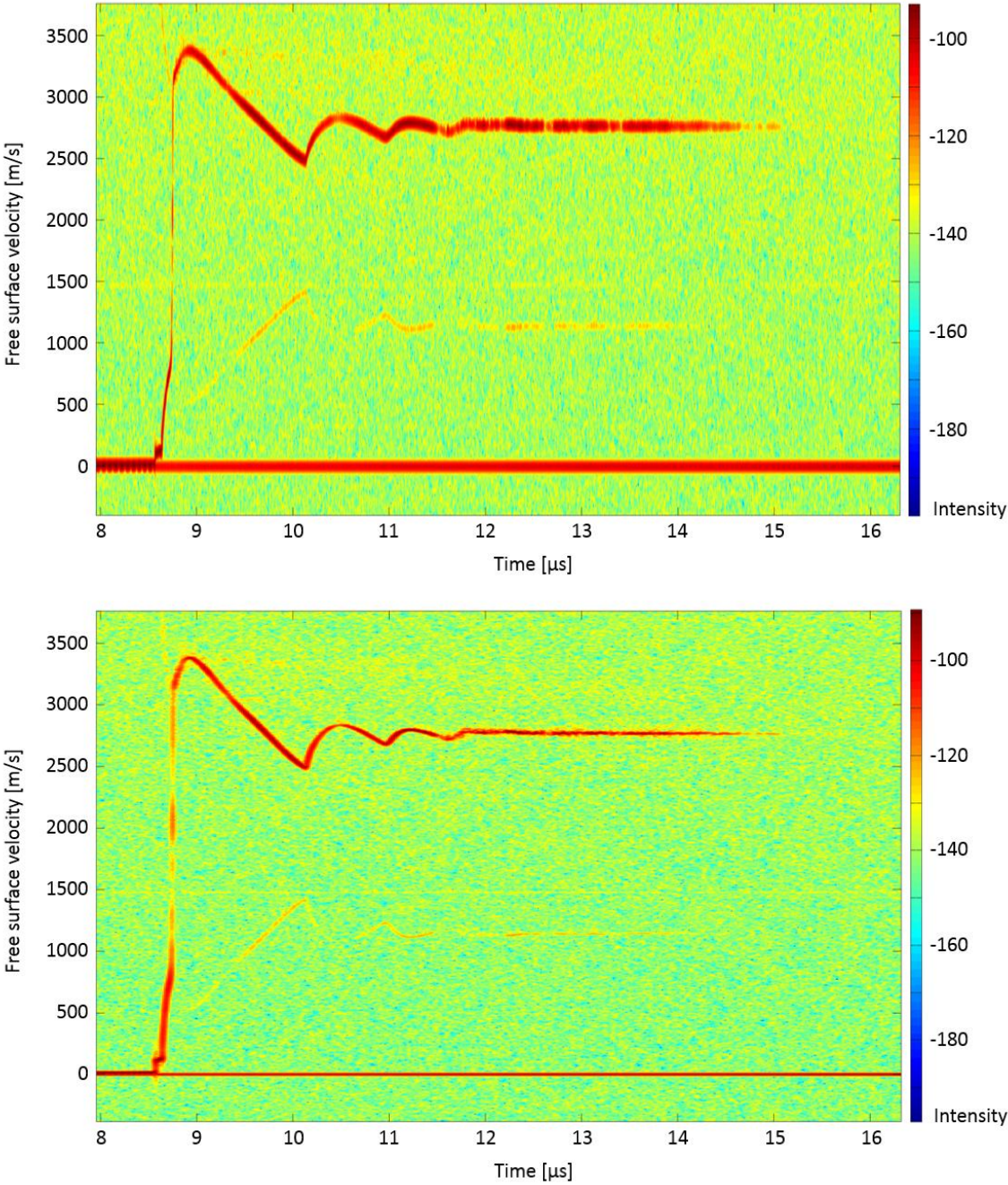


Figure 4.14: Free surface velocity spectrograms of test no. 0113 for different parameter sets of the fast Fourier transform: In the top diagram, the resolution of the time is prioritized, whereas in the bottom spectrogram the velocity resolution is higher.

4.2.3 Setup for high-speed videos

Some measurements conducted with the 70 mm single-stage facility were accompanied by high-speed video camera observation (tests 4042 and 4143 to 4146, see Table 4.7). In order to give the camera a free view onto the specimen, the specimen holder system indicated in Figure 4.10 was replaced by a simplified specimen holder technique. The specimen were glued with a two-component epoxy onto a glass bar. The glass bar was fixed in a two angle-y-alignment unit

so that the specimen could be oriented perpendicularly to the shot axis as in all other experiments.

High-speed videos were recorded with two sub-microsecond cameras. One camera observed the specimen directly from the side (side view, in order to make wave propagation processes visible and determine wave propagation speeds). A second camera observed the rear side of the specimen by the help of a mirror. As the cameras were exactly synchronized, it was possible to clearly distinguish waves at the specimen lateral surface (edge) from waves in the specimen center by comparing pictures from the different views at certain times. This rear side perspective is also used for receiving a qualitative impression of the effects of the waves and the resulting damage in the glass. The angle of observation as well as the portion of the specimen visible in the rear side view videos differ slightly from experiment to experiment since the mirror is individually positioned in each experiment and destroyed in the test.

The time step between adjacent video images was set to $0.2 \mu\text{s}$. A maximum of 128 images (400×250 pixels) could be recorded in each test by each camera. Results of the high-speed videos are discussed in section 4.3.1.

4.3 Experimental results

The measured free surface velocity v_{fs} as a function of time is presented in Figure 4.15 for all tests with an aluminum projectile and in Figure 4.16 for the configurations with the steel projectiles. All velocity curves were shifted in such a way that they reach a value of $v_{fs} = 300 \text{ m/s}$ at t_0 . This point of time is set to be the arrival time of the elastic wave. The 300 m/s are selected in order to ensure that the amplitude of the air shock lies below this value while the rise of the velocity signal is still steep (approximately the midpoint of the elastic precursor). This is quite similar to Grady's method of selecting an amplitude of 400 m/s [75].

The tests with very high impact velocities exhibit a small velocity plateau at negative times, which lies in the range between 30 m/s and 120 m/s . For test 0102, the plateau lies even higher at a velocity of 280 m/s . This rise of velocity is not induced by the impact of the projectile, but rather caused by the arrival of a preceding front of compressed residual gas. This so-called "air shock" probably emerges due to two factors. On the one hand, a faster acceleration of the projectile results in a higher compression of the residual gas in the last part of the gun barrel and the target chamber. On the other hand, the high pressures of the accelerator gas enhance the amount of gas bypassing the sabot. For test 0102, a large quantity of gunpowder was used (1.2 kg), which resulted in a very high pressure of 7255 bar in the conical pressure coupling, a high acceleration of the projectile of $3.3 \cdot 10^6 \text{ m/s}^2$ and therefore in the largest air shock. However, since the amplitude of the air shock is in all cases small in comparison to the shock loading induced by the impact of the projectile, the air shock is neglected in the analysis. This means that v_{fs} was set to 0 m/s for all times before the arrival of the elastic wave ($t < t_0$).

The four tests with the lowest impact velocities ($v_p \leq 601 \text{ m/s}$) indicate an elastic behavior. After a steep rise, v_{fs} reaches a plateau of constant velocity, which equals roughly the impact velocity (since the acoustic impedances of SLG and aluminum are almost equal). $0.63 \mu\text{s}$ later, the release wave from the projectile back surface arrives at the free surface, dropping v_{fs} to a lower level of about 200 m/s .

In all other tests, the velocity curve exhibits a concave downwards shape during the loading process. Therefore, SLG shows no clear two-wave structure when loaded above its elastic limit.

Characterization of soda-lime glass under dynamic loading by means of novel PPI tests and an advanced analysis

This makes a classical “selective” analysis approach inappropriate (a detailed comparison of the analysis methods is outlined in section 4.1).

As observed in the elastic regime, unloading takes place when the release wave from the projectile back surface arrives at the free surface. At high loads ($v_p > 1300$ m/s), this happens even before a plateau of constant velocity can form. This can be explained with the assumption that the velocity of the unloading wave increases once a certain stress level is exceeded.

Looking only at the free surface measurements, it is not possible to determine if spallation is taking place. However, combining them with Lagrange diagrams from the high-speed videos enables a better understanding of the underlying processes. As outlined in the following (see section 4.3.1), no spallation is taking place. Instead, the reverberation signal is induced by the interaction of the release waves from the glass free surface with a failure front.

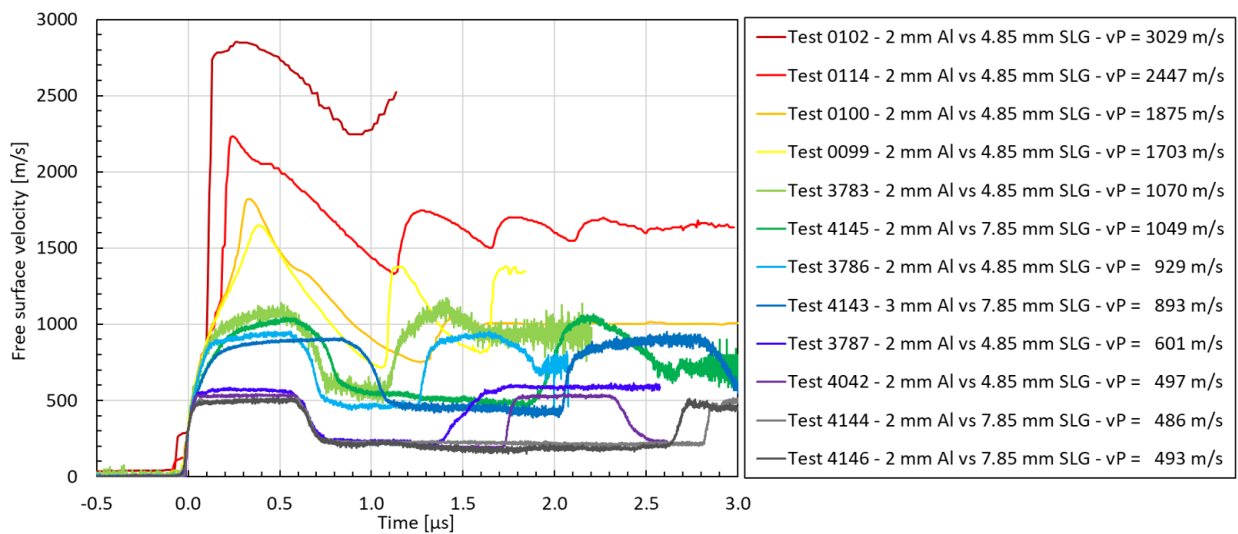


Figure 4.15: Velocity profiles of tests with an aluminum (Al) projectile (Figure was pre-published by the author in [A1]).

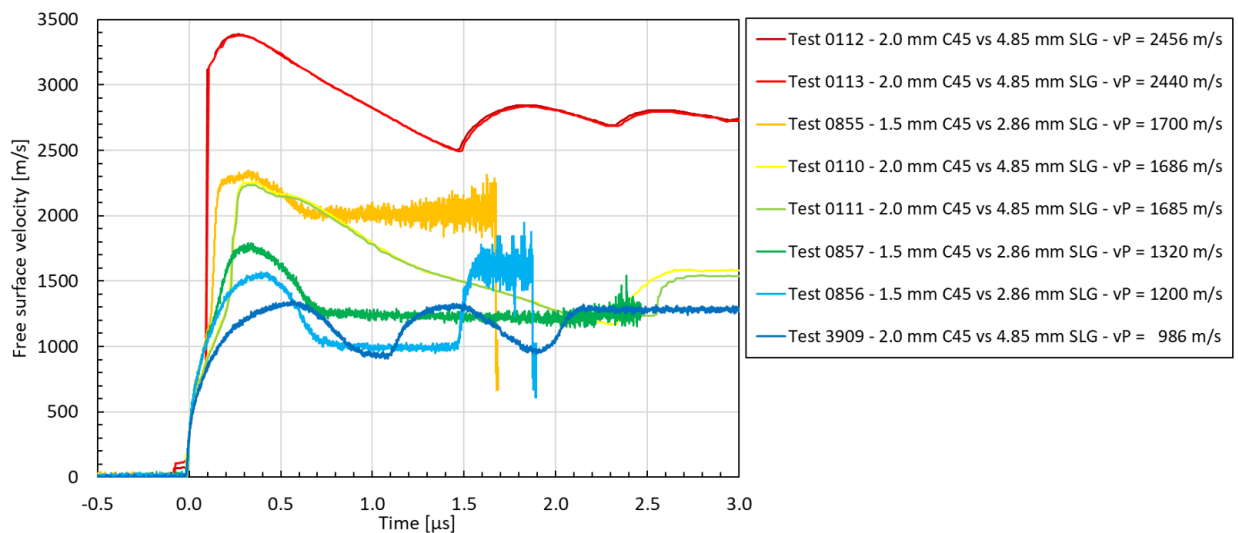


Figure 4.16: Velocity profiles of tests with a steel (C45) projectile (Figure was pre-published by the author in [A1]).

4.3.1 New insights into the failure front phenomena

The high-speed videos provide valuable information on the occurrence and velocities of damage and shock waves during the impact process of tests no. 4042 and 4143 to 4146. In particular, the simultaneous observation of the glass target from the lateral and rear side enables a more detailed localization of the damage sites. As the cameras are synchronized, it is possible to distinguish well between interior phenomena and phenomena on the lateral surface. No spallation plane can be witnessed in these tests.

In combination with the incremental analysis of the loading paths, it is possible to identify a minimum load limit for the onset of a failure front within the glass samples. For this purpose, Lagrange diagrams need to be carefully drawn and compared with the observations. The process is explained in detail in this section.

Figure 4.17 depicts a selection of nine pairs of high-speed images from test no. 4143. In this experiment, a 2 mm thick aluminum projectile impacted a 7.85 mm SLG target plate at a velocity of 893 m/s. The upper half of each image shows the side view and the lower half displays the back view observed by means of a mirror. The indicated times refer to the time of the impact.

The impact caused the formation of an elastic wave, which can be identified in the side view as a gray area moving from left to right through the white glass. This is because the high compression of the SLG changes its optical properties resulting in a significant different light transmission. The elastic wave is immediately followed by a darker failure front, which consists of a network of cracks at the lateral free surface. In the side view of the second picture ($t = 0.4 \mu\text{s}$), the position of the wave front and the surface failure front is indicated by a small arrow. The corresponding rear view shows the bright glow of an impact flash. This flash can be clearly identified by analyzing the videos; it clearly appears before failure in the glass starts. The thin layer of gold, which was vapor-deposited on each specimen, appears as a black square. In the center of the square is a white spot, which emerges from the VISAR laser.

The surface failure front following the shock wave is initially located only near the edges of the SLG specimen and therefore denoted as such. From there, it propagates inwards to the center of the target in the shape of a circular front. After $2 \mu\text{s}$, it enters the field of view of the rear camera (image at the left bottom of Figure 4.17).

In both of the last images' side views ($t = 4 \mu\text{s}$ and $t = 6 \mu\text{s}$), an additional failure front can be seen. This second failure front moves planar inside the whole target, as opposed to the surface failure front. It directly influences the measured free surface velocities in the center of the target. This gets evident when examining the corresponding Lagrange diagrams.

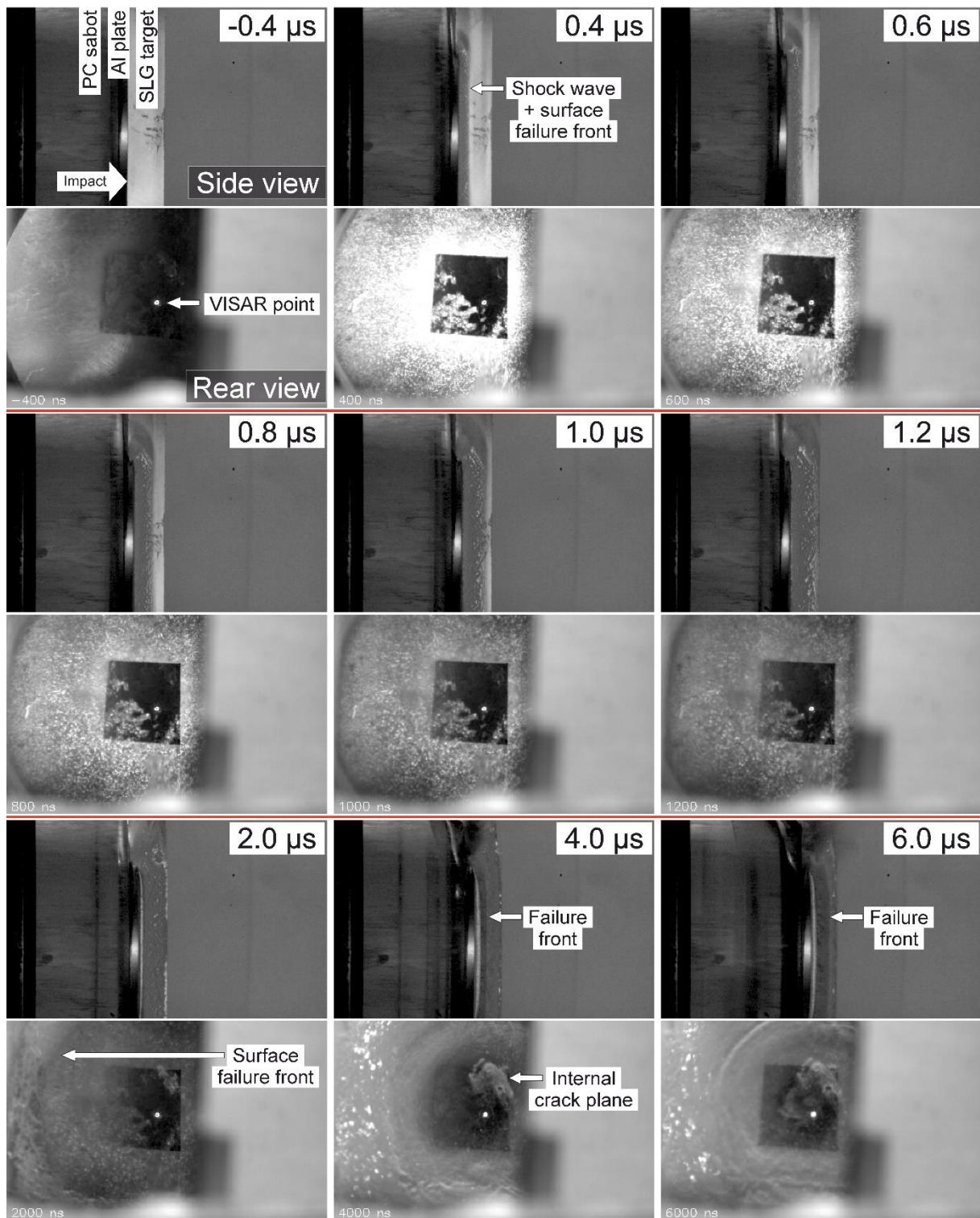


Figure 4.17: Selection of nine pairs of high-speed images from test no. 4143 (2 mm Al vs. 7.85 SLG, $v_p = 893$ m/s). The upper half of each image shows the side view of the SLG target plate. The lower half displays the back view observed by means of a mirror (Figure was pre-published by the author in [A1]).

In order to correlate the high-speed images with the free surface velocity measurements, Lagrange diagrams are particularly suitable. The input values for these diagrams are the positions of the different wave fronts as a function of time. To extract the values from the videos, the concept of a “streak analysis” is introduced.

The principle of the streak analysis is illustrated in Figure 4.18. The intention is to discard redundant information in the pictures by focusing on the central part only. For each time step, a narrow strip is cut out of the corresponding camera image. The strips are then stacked to form a new image. This new image provides the wave positions in an Eulerian frame of reference. The temporal propagation of the waves and the development of the failure is displayed in the vertical direction, while the horizontal direction contains the spatial information.

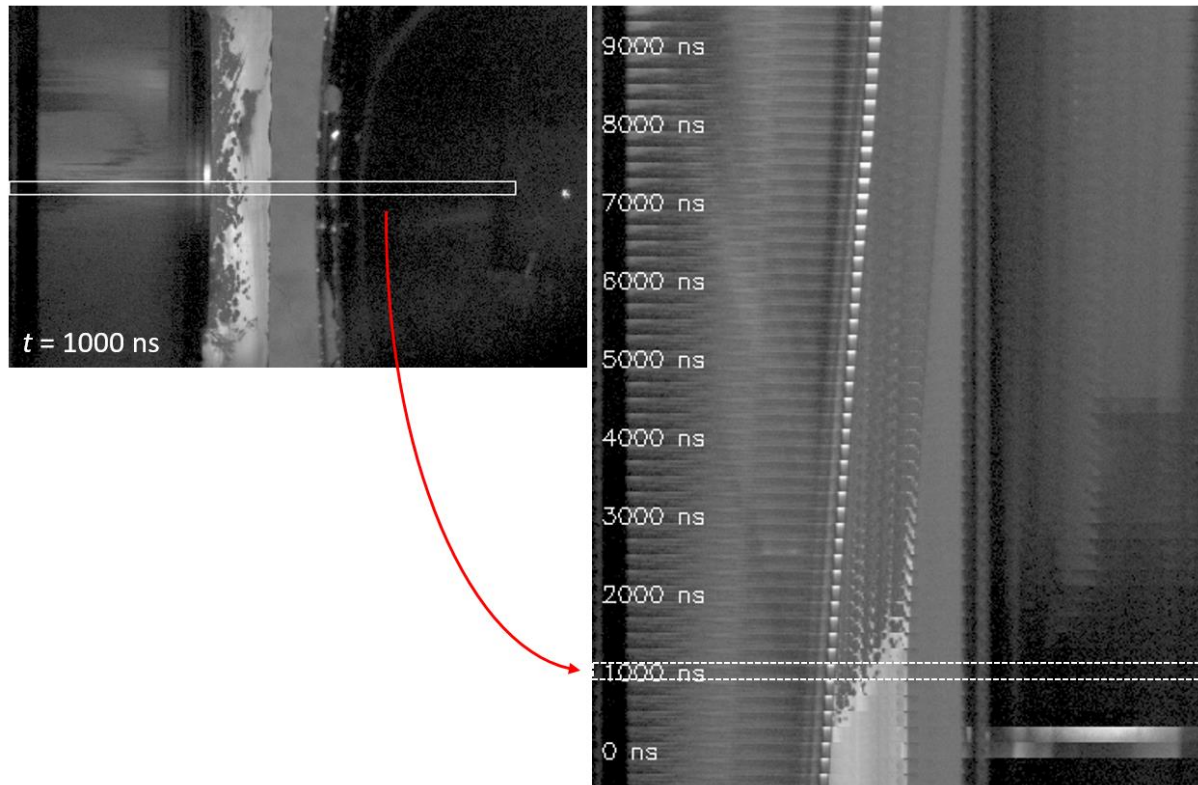


Figure 4.18: Principle of the streak analysis: For each time step, a narrow strip is cut out of the corresponding camera image. The strips are then stacked to form a new image. This new image provides the wave positions in an Eulerian frame of reference. The temporal propagation of the waves and the development of the failure is illustrated in the vertical direction, while the horizontal direction contains the spatial information. The white rectangle in the left pictures shows the cut out position of the strips for test no. 4144. The resulting final, piled up image is shown on the right side [A1].

The next step is to extract the information from the Eulerian frame of reference and transfer it to the Lagrangian. In the Lagrangian diagram, the positions of the front and rear sides of the SLG target are fixed and the wave positions are provided relative to the material frame of reference. Therefore, only the corresponding starting and arrival times have to be determined from the Eulerian diagrams.

This is achieved by applying a linear best-fit line to every wave front. Figure 4.19 illustrates the result for test no. 4144 (2 mm aluminum impacting 7.85 mm SLG at 486 m/s). The left side shows the original stacked image. The impact time is labeled with 0 ns and the time interval between two stripes is 200 ns. In the right picture, three fit lines are indicated for the positions of the shock wave, the surface failure front and the interface between the aluminum projectile and impact face of the SLG. The intersection of the interface line and the shock wave line determines the time of the impact. Furthermore, the starting point of the failure front can be

obtained at the intersection point of the interface line and failure front line.

The end points of the fit lines at the rear side of the SLG target analogously determine the arrival times. The resulting start and end times are then used to draw the corresponding lines in the Lagrangian diagram.

In Figure 4.20, the initial shock wave arrives at the free surface about 1.4 μs after impact, indicating a wave velocity of 5760 m/s. Since the wave is moving through unloaded material, this velocity is the same for the Lagrangian and the Eulerian frame of reference. It is in good agreement with the literature sound velocity of 5740 m/s (ref. Table 1.2). The failure front starts with a delay of 0.2 μs , but moves slightly faster with an Eulerian velocity of 5790 m/s or a Lagrangian velocity of 6000 m/s respectively.

In addition, the impact also initiates a shock wave inside the aluminum projectile. This wave propagates leftwards in the Lagrange diagram, arriving at the back face of the projectile after 0.3 μs . Since it cannot be observed directly in the high-speed images, its position is inferred from the longitudinal sound velocity of aluminum (6300 m/s). When it arrives at the projectile's back face, it partially transmits into the polycarbonate sabot. The majority of its amplitude however is reflected back into the aluminum as a release wave. Up to a loading stress of 6.7 GPa, all release waves are assumed to propagate with the sound velocity of the respective material. This assumption is validated by comparing the Lagrange diagram with measurements of the free surface velocity. The simplified Lagrange diagrams (with constant wave velocities and no wave interactions) are obviously sufficient to explain the crucial features of the velocity profiles. A more in-depth analysis by means of numerical simulations is presented in section 4.3.1.1.

The Lagrange diagram in Figure 4.20 includes on the right side the free surface velocity of the central target area. The first rising edge of the velocity signal corresponds to the arrival of the elastic precursor. In order to synchronize the time axis of the velocity measurement and the Lagrange diagram, the velocity signal is shifted in time, so that the arrival times match. Upon the arrival of the shock wave, the free surface velocity rises to about 500 m/s. This value is in good agreement with the theoretical free surface velocity that can be calculated using the measured impact velocity together with the acoustic impedances of aluminum and SLG,

$$\left(\rho_{\text{SLG}} \cdot c_{\text{p,SLG}} \cdot \frac{v_{\text{fs}}}{2} = \rho_{\text{Al}} \cdot c_{\text{p,Al}} \cdot \left(v_{\text{P}} - \frac{v_{\text{fs}}}{2} \right) \right).$$

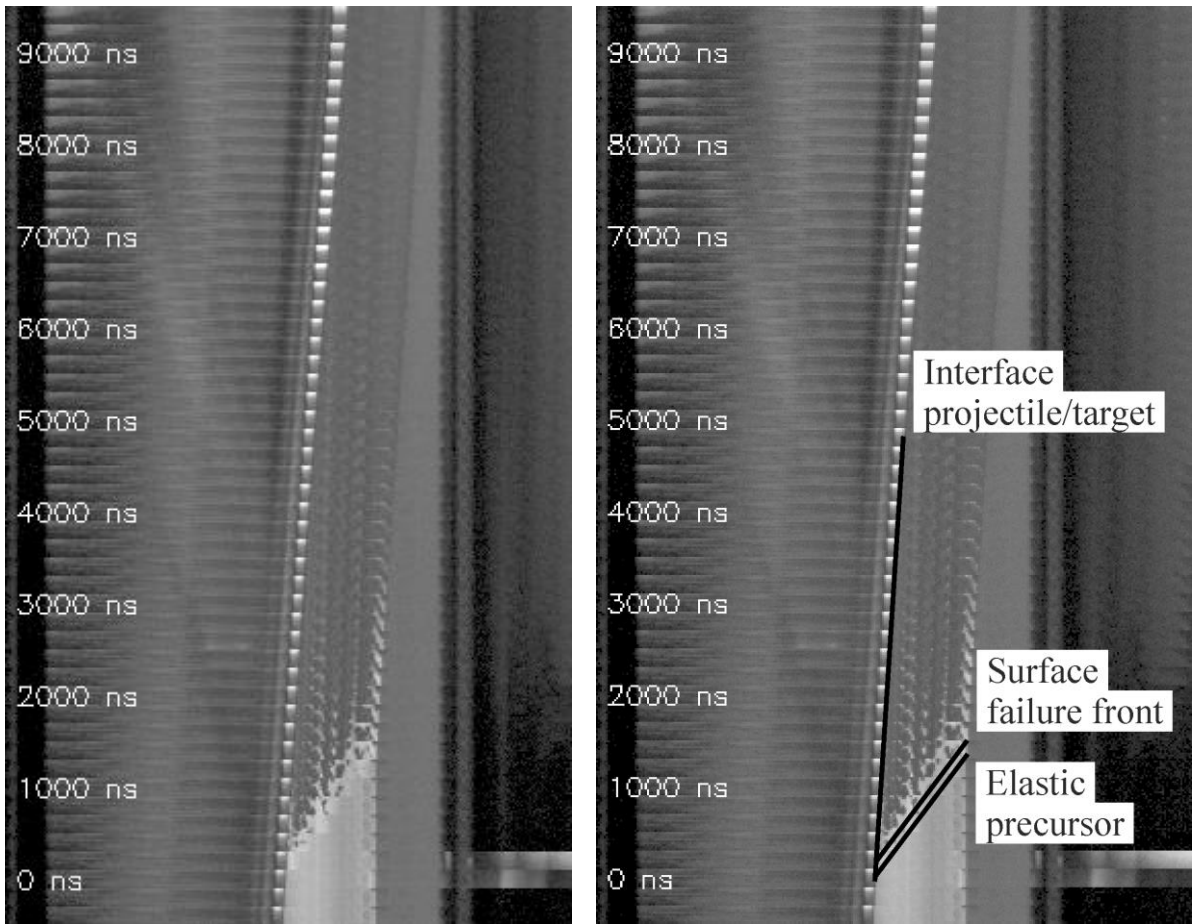


Figure 4.19: Streak analysis for test no. 4144: 2 mm Al vs. 7.85 mm SLG, $v_p = 486$ m/s [A1].

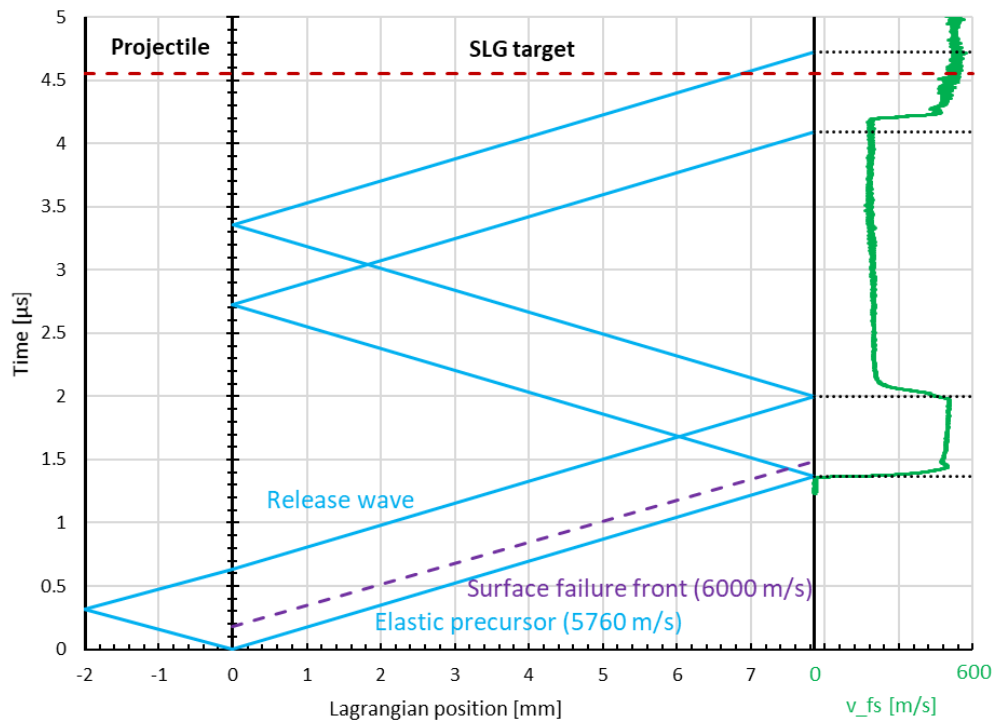


Figure 4.20: Lagrangian diagram for test no. 4144: 2 mm Al vs. 7.85 mm SLG, $v_p = 486$ m/s [A1].

2 μs after impact, the velocity drops to about 230 m/s. The Lagrange diagram reveals that this drop is caused by the arrival of the release wave from the back of the projectile. The velocity does not drop all the way down to 0 m/s since the release wave is partially reflected at the aluminum/polycarbonate interface. This supports the observation that the fast failure front starts from the edge zone of the SLG target. If the damage were also in the central region, the release wave would be influenced by the failure front before it reaches the velocity measurement point. Furthermore, the initial shock wave in the SLG is reflected at the free surface and undisturbedly passes all the way back to the projectile/target interface as a release wave. There, it is subsequently reflected and moves through the SLG once more as a compression wave. After 4.1 μs , it arrives at the free surface again, which is in good agreement with the experimentally observed velocity rise at 4.2 μs .

The expected velocity drop after 4.7 μs does not occur. This can be attributed to the fact that the lateral release waves from the target edges arrive at the velocity measurement point after 4.55 μs , removing the one-dimensional strain condition (red dashed line in Figure 4.20). In addition, it can be deduced that spallation does not take place, since the velocity signal shows no signs of “ringing in spall”. Consequently, the spall strength of the SLG has to be greater than: $\sigma_{\text{spall}} = \frac{1}{2} \rho_0 U_p \Delta v_{\text{fs}} = \frac{1}{2} \cdot 2.5 \frac{\text{g}}{\text{cm}^3} \cdot 5760 \frac{\text{m}}{\text{s}} \cdot 270 \frac{\text{m}}{\text{s}} = 1.9 \text{ GPa}$ [231].

Figure 4.21 and Figure 4.22 illustrate the results for test no. 4042. In this experiment, the original thickness of the SLG target was only 4.85 mm, which is considerable smaller than the target of the aforementioned test no. 4144. The impact velocity, however, was almost the same (497 m/s).

The observations of both tests are in good accordance. First, an impact-induced elastic wave travels through the SLG target at a constant velocity of 5743 m/s. Its arrival at the target rear leads to a sharp rise of the measured free surface velocity to about 530 m/s. After 1.5 μs , the release wave from the backside of the projectile arrives, dropping the free surface velocity to roughly 220 m/s.

Both waves are reflected at the free surface and move undisturbedly back and forth inside the SLG. They arrive at the free surface after 2.53 μs and 3.17 μs respectively, which is in very good agreement with the measured times of the velocity jumps (2.57 μs and 3.17 μs).

With the 7.85 mm thick target, the second arrival of the release wave cannot be observed since the release waves from the target edges arrive ahead in time. The 4.85 mm target solves this problem, as the shock wave travelling times are much shorter, whereas the lateral dimensions are identical.

One difference of test no. 4042 in comparison to no. 4144 is the starting time and the velocity of the failure front. It initiates 0.5 μs after impact and moves slightly slower. The observed velocities are 5285 m/s in the Eulerian frame of reference and 5581 m/s in the Lagrangian. Nevertheless, the failure front is again limited only to the fringe area of the SLG target.

Test no. 4146 used the same setup as test no. 4144, producing the same results. For the sake of completeness, the corresponding diagrams can be found in the appendix (Figure 9.1 and Figure 9.2).

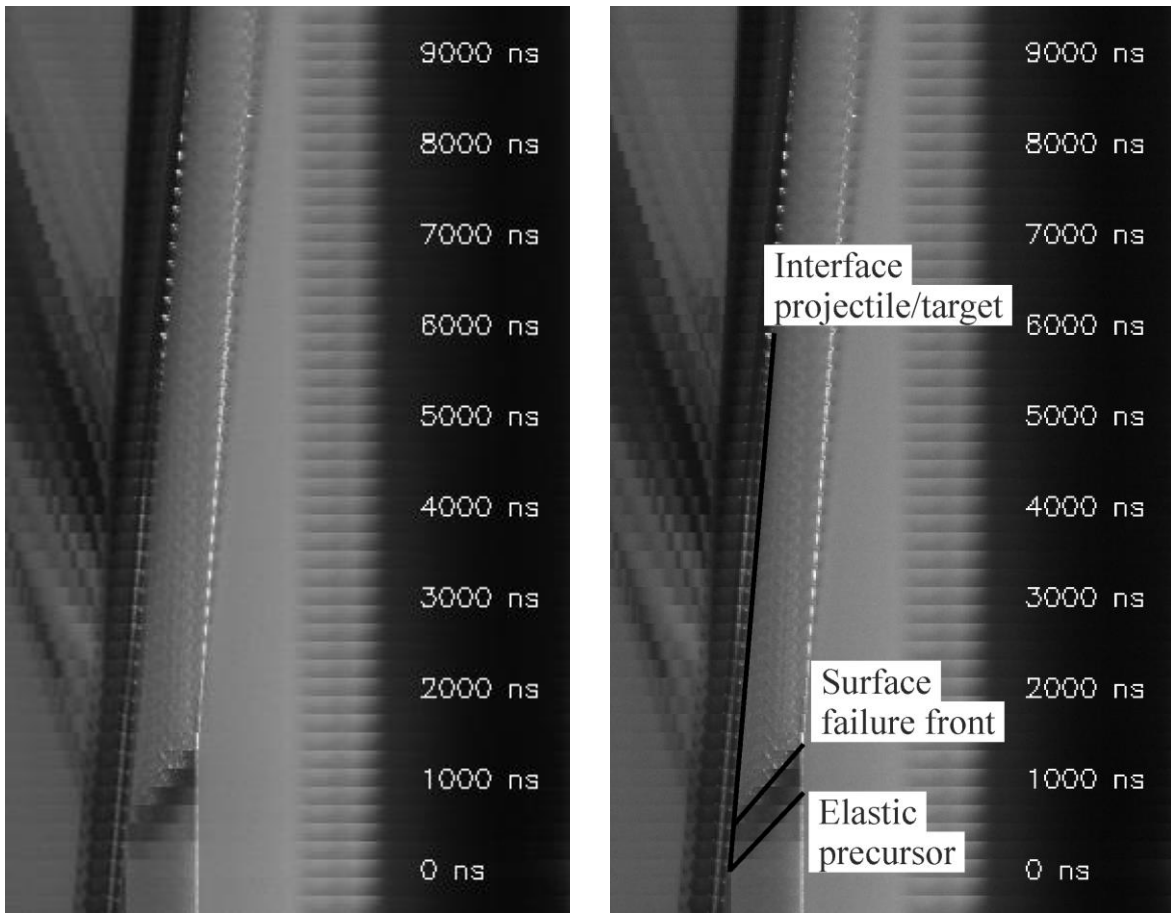


Figure 4.21: Streak analysis for test no. 4042: 2 mm Al vs. 4.85 mm SLG, $v_p = 497$ m/s [A1].

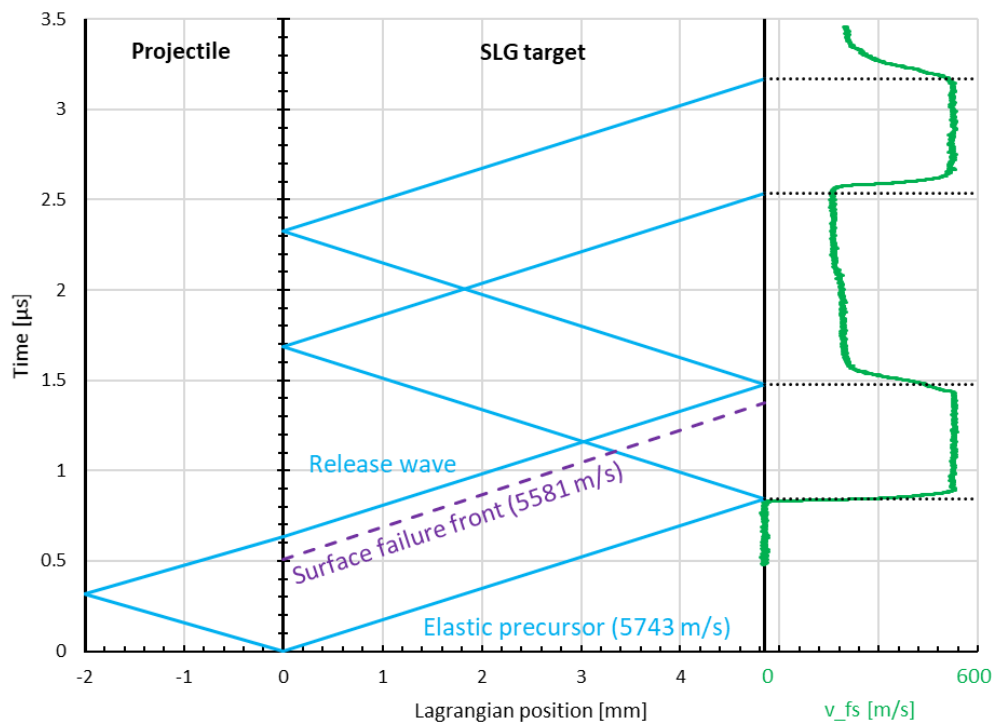


Figure 4.22: Lagrangian diagram for test no. 4042: 2 mm Al vs. 4.85 mm SLG, $v_p = 497$ m/s [A1].

The three tests with impact velocities of about 500 m/s do not exhibit a planar failure front inside the whole SLG target, instead the observed damage is located only near the edge zones of the target plate. This changes fundamentally in the tests with higher impact velocities (test no. 4143 and 4146), which are analyzed in the following.

Figure 4.23 and Figure 4.24 show the results for test no. 4143 (3 mm aluminum impacting 7.85 mm SLG at 893 m/s). The initial shock wave propagates at 5710 m/s, which is in good agreement with the longitudinal sound velocity. The surface failure front directly follows the shock wave, making both fronts indistinguishable. A clear difference to the tests with lower impact velocities is the occurrence of a second failure front after 0.86 μ s. It is most likely initiated by the release wave coming from the backside of the aluminum projectile. The analysis of the stacked high-speed image shows that this failure front moves significantly slower with an Eulerian velocity of 1660 m/s or a Lagrangian velocity of 1040 m/s respectively.

The free surface velocity exhibits a second rise 3.4 μ s after impact, followed by a drop at 4.2 μ s. This can be explained by a second reflection of the initial shock wave at the failure front after it has been reflected at the sample free surface as a release wave. This is reasonable since the glass exhibits a lower acoustic impedance after failure (see e.g. [78]). If the waves were passing undisturbedly through the whole SLG target after their reflection at the free surface, they would arrive more than 0.7 μ s too late. Figure 4.24 illustrates that the interaction of the reflected initial shock wave with the failure front at 2.4 μ s results in an arrival time at the target backside after 3.5 μ s. This is in good agreement with the free surface velocity rise after 3.4 μ s. Likewise, the second arrival of the release wave from the projectile precisely matches the velocity drop at 4.2 μ s.

The reflection at the failure front at 2.4 μ s is also evident in the high-speed images. During the process, the formation of an internal fracture plane is initiated. Its growth can be observed in the rear view of the high-speed images, since the additional surface reflects the light of the flash. In Figure 4.17 it is tagged with an arrow at 4.0 μ s.

After 4.6 μ s, the velocity signal collapses, which is in good agreement with the theoretically expected arrival time of the release waves from the target edges (red dashed line in Figure 4.24).

The fundamental effects observed in test no. 4143 are reproduced in test no. 4145 (see Figure 4.25 and Figure 4.26). In this test, a 2 mm aluminum projectile impacts a 7.85 mm SLG target at 1049 m/s. The second front is again initiated at the arrival of the release wave from the back of the projectile, which is about 0.3 μ s earlier than in test no. 4143 due to the thinner projectile. The release waves from the target edges arrive 4.6 μ s after impact, ending the velocity measurement at the free surface.

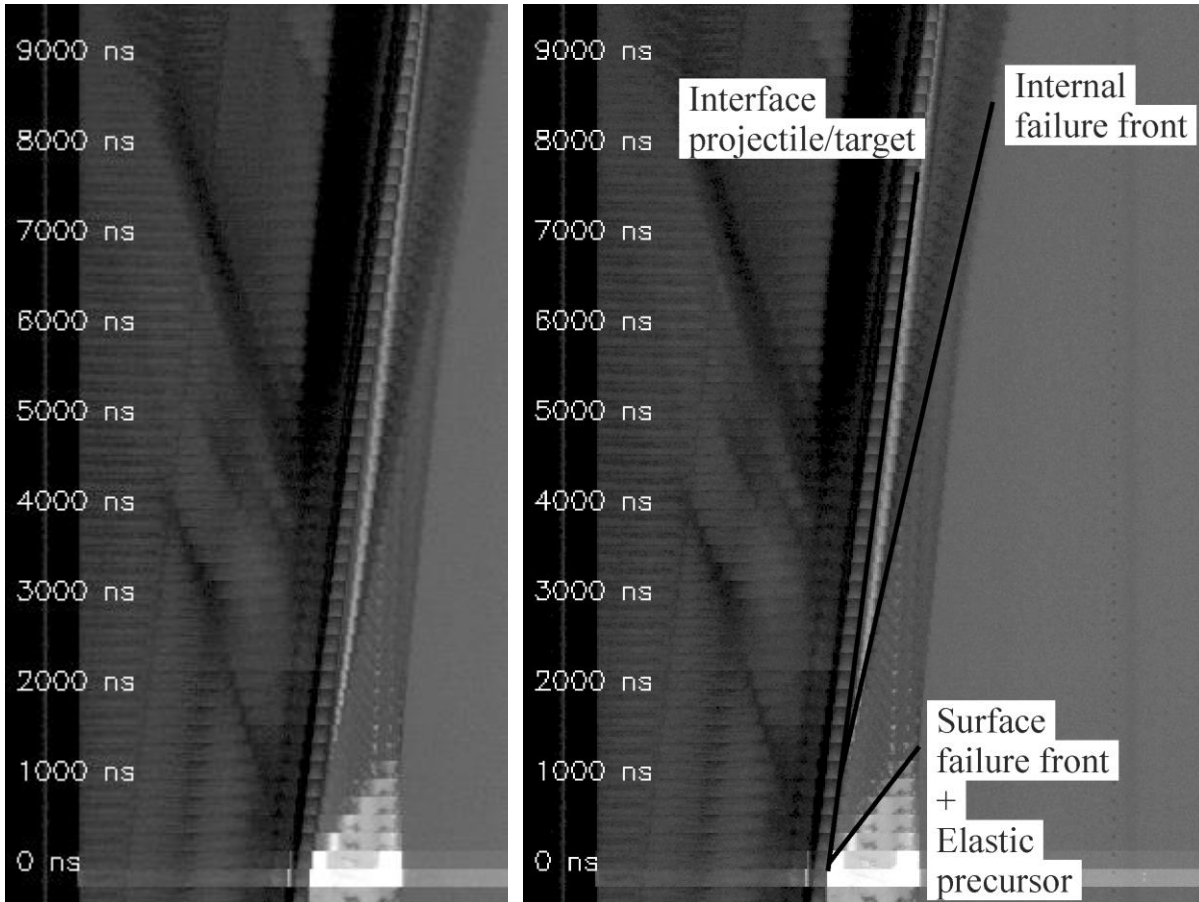


Figure 4.23: Streak analysis for test no. 4143: 3 mm al vs. 7.85 SLG mm, $v_p = 893$ m/s [A1].

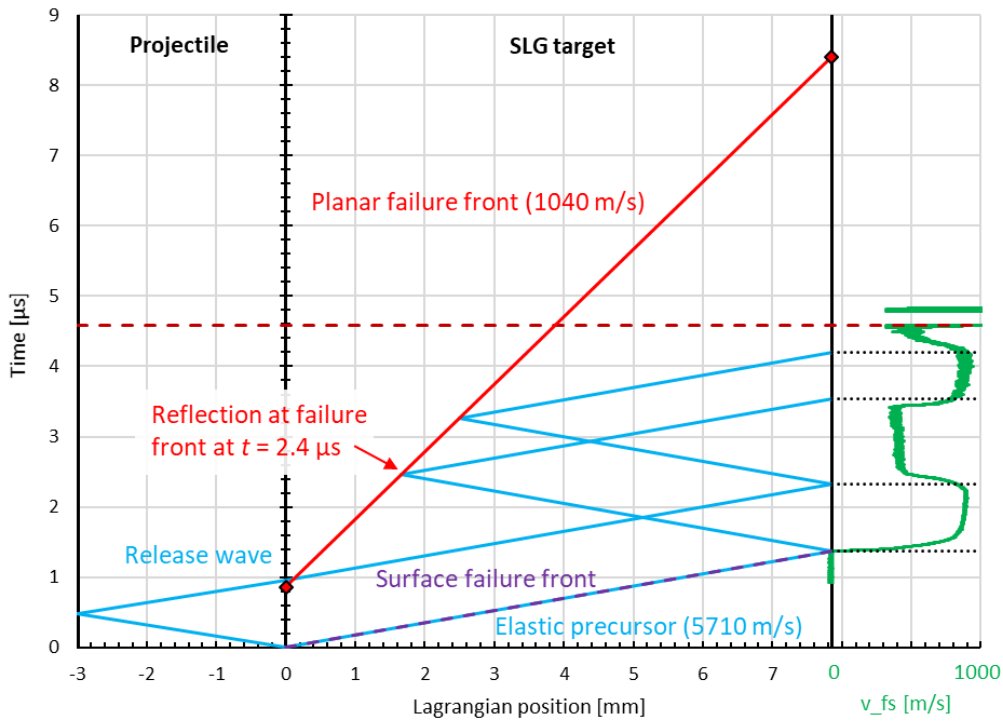


Figure 4.24: Lagrangian diagram for test no. 4143: 3 mm Al vs. 7.85 mm SLG, $v_p = 893$ m/s [A1].

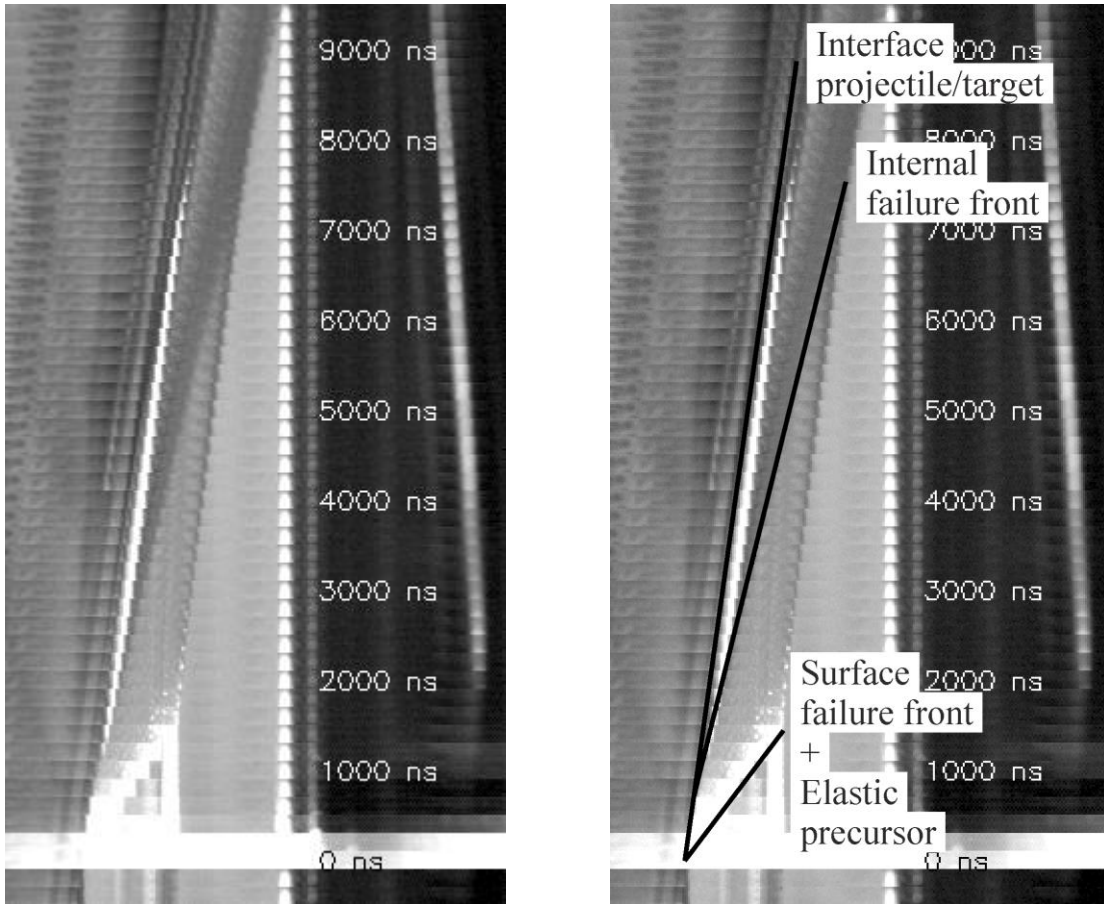


Figure 4.25: Streak analysis for test no. 4145: 2 mm Al vs. 7.85 mm SLG, $v_p = 1049$ m/s [A1].

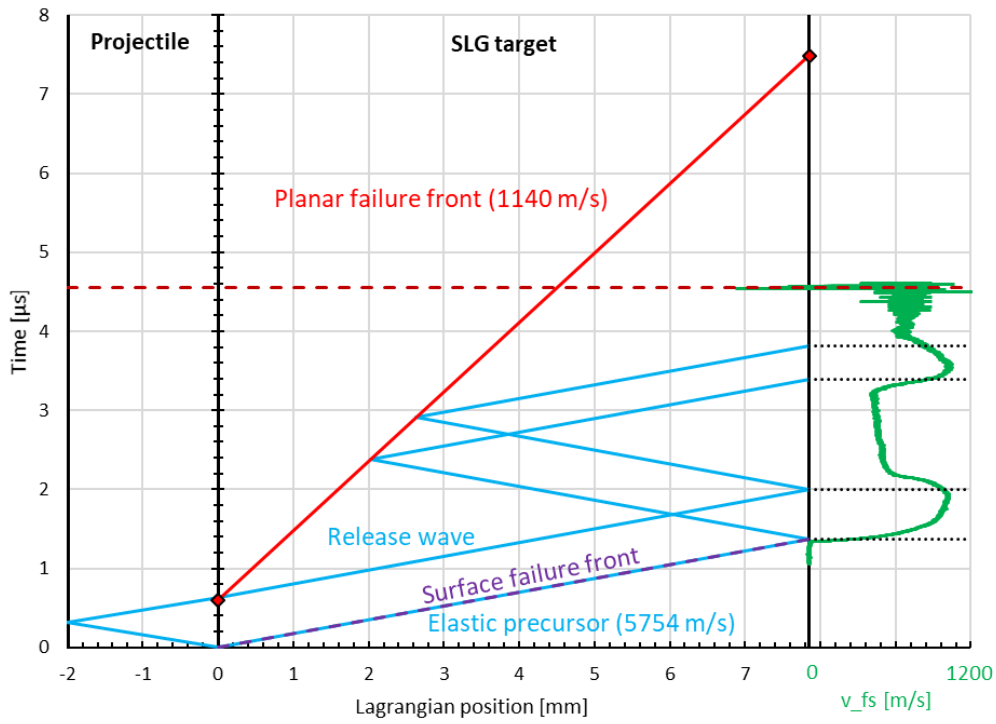


Figure 4.26: Lagrangian diagram for test no. 4145: 2 mm Al vs. 7.85 mm SLG, $v_p = 1049$ m/s [A1].

In the previous section, only the results of the five planar plate tests, which were accompanied by high-speed video cameras, are discussed. The analysis reveals that a minimum load is required for the onset of a planar failure front within the whole glass target. This limit can be determined more accurately by analyzing the velocity signals of additional planar plate tests (without camera observation).

Figure 4.27 shows the measured free surface velocity (green curve) for test no. 3787 (2 mm aluminum impacting 4.85 mm SLG at 601 m/s) in combination with the corresponding Lagrange diagram (blue and red lines). Note that the positions of the waves and failure front are not based on optical measurements, since this test was not accompanied by video cameras. Instead, they are reconstructed based on the findings of the previous tests. The velocity of the shock and release waves is set to 5740 m/s, resulting in a good match between the arrival of the release wave at the free surface at $1.48 \mu\text{s}$ and the first drop in the velocity curve.

If no failure front were generated within the central area of the target, the second rise of the free surface velocity would be expected at $2.53 \mu\text{s}$ similar to test no. 4042. However, the velocity rise is observed significantly earlier at about $2.23 \mu\text{s}$. This can be explained with the presence of an internal failure front, reflecting the waves similar to test no. 4143 and 4145. Accordingly, the timing for the onset of the failure front is set to the arrival of the first release wave at the projectile/target interface at $0.635 \mu\text{s}$. The velocity of the failure front is subsequently adjusted to match the second arrival of the shock wave with the velocity rise at $2.53 \mu\text{s}$. This gives a failure front velocity of 800 m/s, which is considerably slower than the failure fronts of test no. 4143 (1040 m/s) and 4145 (1140 m/s). It can therefore be suggested, that not only the presence of the failure front but also its velocity is dependent on the impact load (increasing with increasing impact velocity).

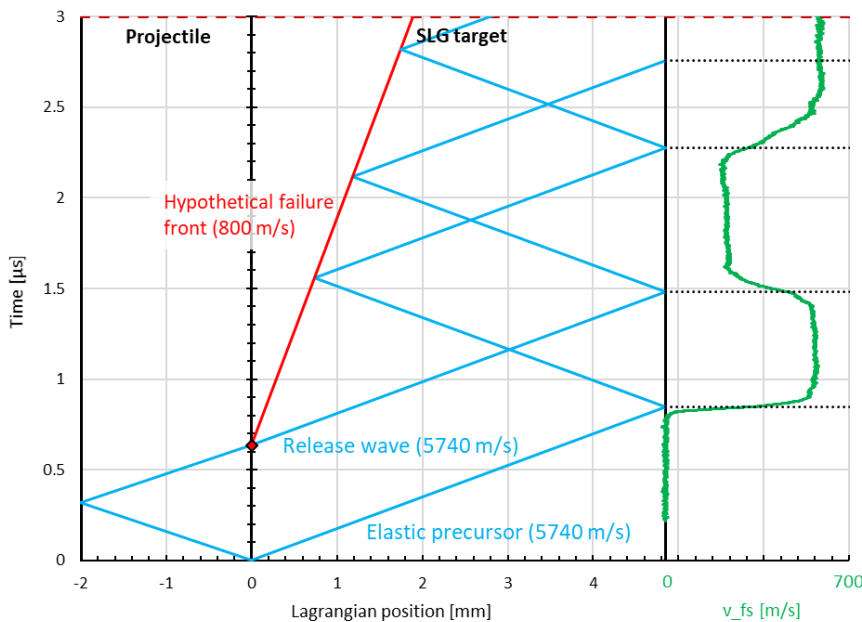


Figure 4.27: Lagrangian diagram for test no. 3787: 2 mm Al vs. 4.85 mm SLG, $v_p = 601 \text{ m/s}$ [A1].

Analogously to test no. 3787, two high velocity tests (no. 0099 and 0114) are analyzed in order to estimate the failure front velocities.

Figure 4.28 displays the result for test no. 0099, in which an aluminum projectile impacted the SLG target at 1703 m/s, inducing a longitudinal stress of 10.6 GPa. To match the rising and falling edges of the free surface velocity, a failure front velocity of 2100 m/s has to be assumed.

This is almost twice the value of the failure front velocity at a stress level of 6.7 GPa (test no. 4145).

In addition, the speed of the release wave has to be increased, in order to explain the drop of the free surface velocity at $t \approx 1.25 \mu\text{s}$. An estimated wave speed of 7500 m/s yields a good correlation. These assumptions also provide an explanation for the declining velocity maximum of the second peak. The second arrival of the compression wave at $1.95 \mu\text{s}$ is immediately followed by the overtaking release wave. As a result, the free surface velocity starts decreasing before reaching the maximum level of the initial shock.

Moreover, it can be inferred that no spallation takes place. Therefore, the spall strength, when shocked to a longitudinal stress of 10.6 GPa, has to be greater than

$$\sigma_{\text{spall}} = \frac{1}{2} \rho_0 U_p \Delta v_{\text{fs}} = \frac{1}{2} \cdot 2.5 \frac{\text{g}}{\text{cm}^3} \cdot 5760 \frac{\text{m}}{\text{s}} \cdot 936 \frac{\text{m}}{\text{s}} = 6.7 \text{ GPa} [231].$$

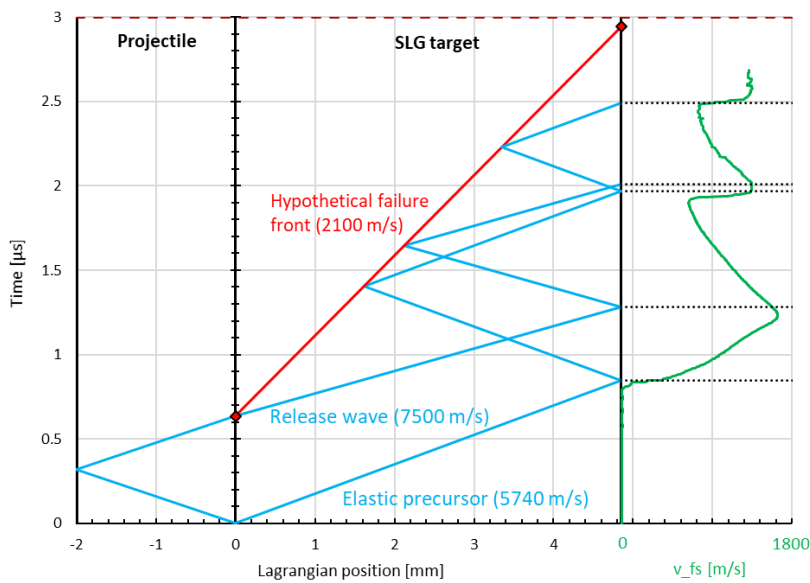


Figure 4.28: Lagrangian diagram for test no. 0099: 2 mm Al vs. 4.85 mm SLG, $v_p = 1703 \text{ m/s}$ [A1].

At even higher impact velocities, the aforementioned observations are basically the same. Figure 4.29 shows the resulting Lagrange diagram for test no. 0114. In this case, a 2 mm aluminum projectile impacted the SLG with a velocity of 2447 m/s. A good match between the arrival times of the waves and the measured free surface velocity can be achieved by assuming a failure front velocity of 2100 m/s and a release wave speed of 9500 m/s.

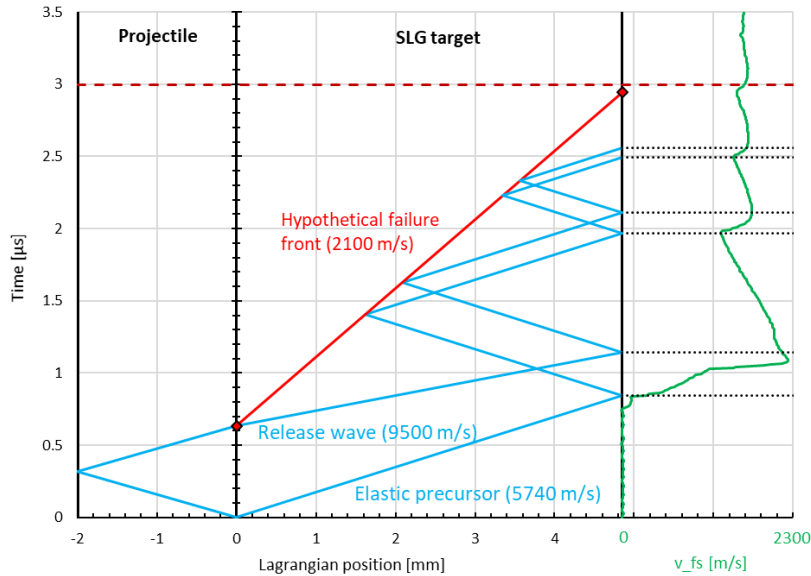


Figure 4.29: Lagrangian diagram for test no. 0114: 2 mm Al vs. 4.85 mm SLG, $v_p = 2447$ m/s [A1].

Table 4.8 contains a summary of all resulting failure front velocities and initial release wave speeds. They are dependent on the applied load, which is linked to the impact velocity and the material of the projectile. All listed tests used an aluminum projectile with impact velocities between 486 m/s and 2447 m/s as specified in the first column. The corresponding induced longitudinal stress results from the incremental analysis of the loading paths (section 4.3.2) and is given in column two.

In summary, two important conclusions can be derived from Table 4.8:

- First, the properties of the failure front are highly dependent on the impact load. When shocked to a longitudinal stress of 3.8 GPa or less, no failure front emerges inside the SLG. The damage, which can be observed in the high-speed videos, is limited solely on the lateral fringe area of the target. At a longitudinal stress of 3.9 GPa, a plane failure front arises inside the whole SLG plate, propagating at a velocity of 800 m/s. This front is induced by the arrival of the release wave from the back of the projectile. When the impact velocity, and therefore the longitudinal stress, is further increased, faster moving failure fronts are generated. The highest failure front velocity of 2100 m/s is inferred from tests with longitudinal stresses of 10.6 GPa and 14.2 GPa. Since there is no further rise of the velocity, 2100 m/s could be an upper limit.
- Second, the velocity of the initial release wave is also dependent on the impact load. For all tests with a longitudinal stress of up to 6.7 GPa, a constant velocity of 5740 m/s is inferred. Therefore, the velocity of the release wave equals the velocity of the preceding compression wave, within this loading range. A sharp increase is observed in the two tests with higher stresses. At a longitudinal stress of 10.6 GPa, the release wave moves 30 % faster, with a velocity of 7500 m/s. A further increase to a stress of 14.2 GPa results in an even higher release velocity of 9500 m/s. It can therefore be concluded that the release wave velocity has an upper limit higher than 9500 m/s, which is much higher than the failure front velocity.

The comparison with literature data of Grady [75] yields a good coherence. He determined a constant release velocity of about 5700 m/s up to a longitudinal stress of 7.0 GPa. He further observed velocities of 7740 m/s at 11.46 GPa, 8900 m/s at 14.25 GPa and 13,280 m/s at 23.91 GPa.

Table 4.8: Summary of resulting velocities of initial release wave (c_{release}) and planar failure front (c_{fail}) [A1].

Impact velocity [m/s]	Long. stress [GPa]	c_{release} [m/s]	c_{fail} Lagrangian [m/s]	c_{fail} Eulerian [m/s]
≤ 500	≤ 3.8	5740	-	
601	3.9	5740	800	
893	5.8	5740	1040	1660
1049	6.7	5740	1140	1850
1703	10.6	7500	2100	
2447	14.2	9500	2100	

4.3.1.1 Supporting simulations for the investigation of the internal failure front

The reasonableness for the presence of an internal failure front is also supported by numerical simulation results. In the simulations, the time-dependent free surface velocity for eight different tests is evaluated. The utilized setup is comparable to the simulations for the validation of the incremental analysis concept (ref. Figure 4.4). More specifically, the projectile and the target are represented as one-dimensional chains of elements. Here, the movement of these elements perpendicular to the impact axis is constrained by a boundary condition. The free surface velocity is provided by a gauge point placed within the outermost element of the SLG target. Two different approaches for the material model of SLG are investigated. On the one hand, a simplified perfectly elastic material model without failure is used. On the other hand, the elastic model is combined with an artificial failure front. This failure front is realized by a user-defined erosion criterion. All elements, which lie behind the position of the experimentally determined failure front, are eroded. The position is time-dependent and taken from the Lagrange diagrams of the corresponding experiments. By eroding the elements, a free surface is created at which all waves are reflected.

Figure 4.30 shows the resulting free surface velocity of four tests with a 4.85 mm thick SLG target. The top diagram illustrates the differences between the free surface velocities of the experiments (light curves) and simulations (dark curves). Four different impact velocities, ranging from 497 m/s (green curves) to 1070 m/s (blue curves) are investigated. In case of the lowest impact velocity, the loading remains purely elastic and the simulation is in good agreement with the experiment. In particular, the arrival of the release wave at $0.6 \mu\text{s}$ and the second arrival of the compression wave at $1.7 \mu\text{s}$ are matching. In case of the simulation results at higher impact velocities, the unloading at $0.6 \mu\text{s}$ is also reproduced. However, the reloading at $1.7 \mu\text{s}$ clearly differs from the experimental data. If the artificial failure front is added, these differences vanish, as illustrated in the bottom diagram of Figure 4.30. The additional free surface reflects all compression and release waves resulting in earlier arrival times of the reloading. With the failure front, the simulated reloading takes place at $1.1 \mu\text{s}$ ($1.25 \mu\text{s}$, $1.4 \mu\text{s}$) for an impact velocity of 1070 m/s (929 m/s, 601 m/s). This is in very good agreement with the timing of the experimentally observed velocity rise.

Similar results are observed with a 7.85 mm thick SLG target (Figure 4.31). It can therefore be concluded that, despite the simplification, these models clearly show that the proposed internal failure fronts are very reasonable.

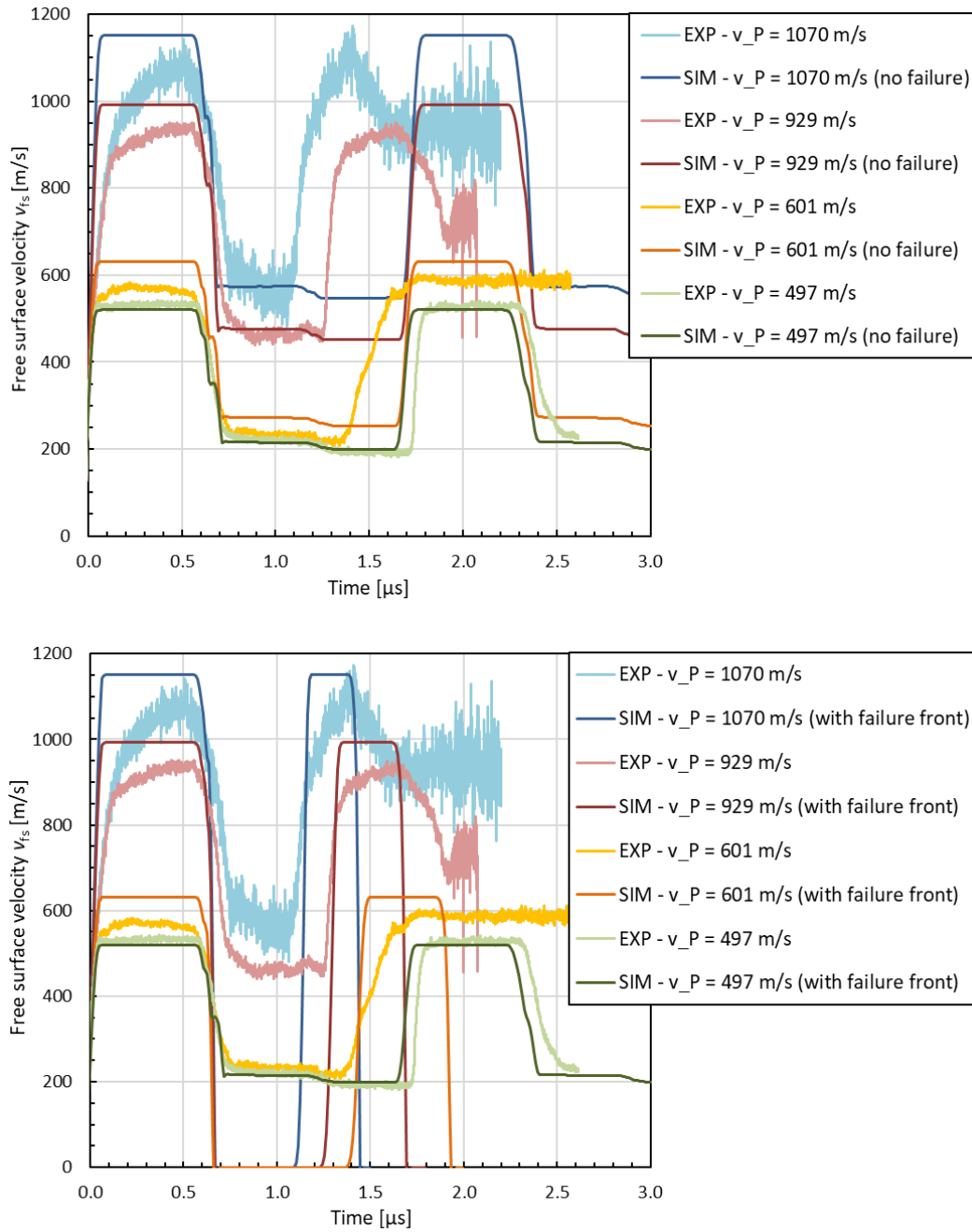


Figure 4.30: Simulation and experimental results of four PPI tests with a 4.85 mm thick SLG target: a perfectly elastic model without failure front does not reproduce the timing of the reflected signal (top diagram); the addition of an artificial failure front results in correct arrival times of the reflected signal (bottom diagram).

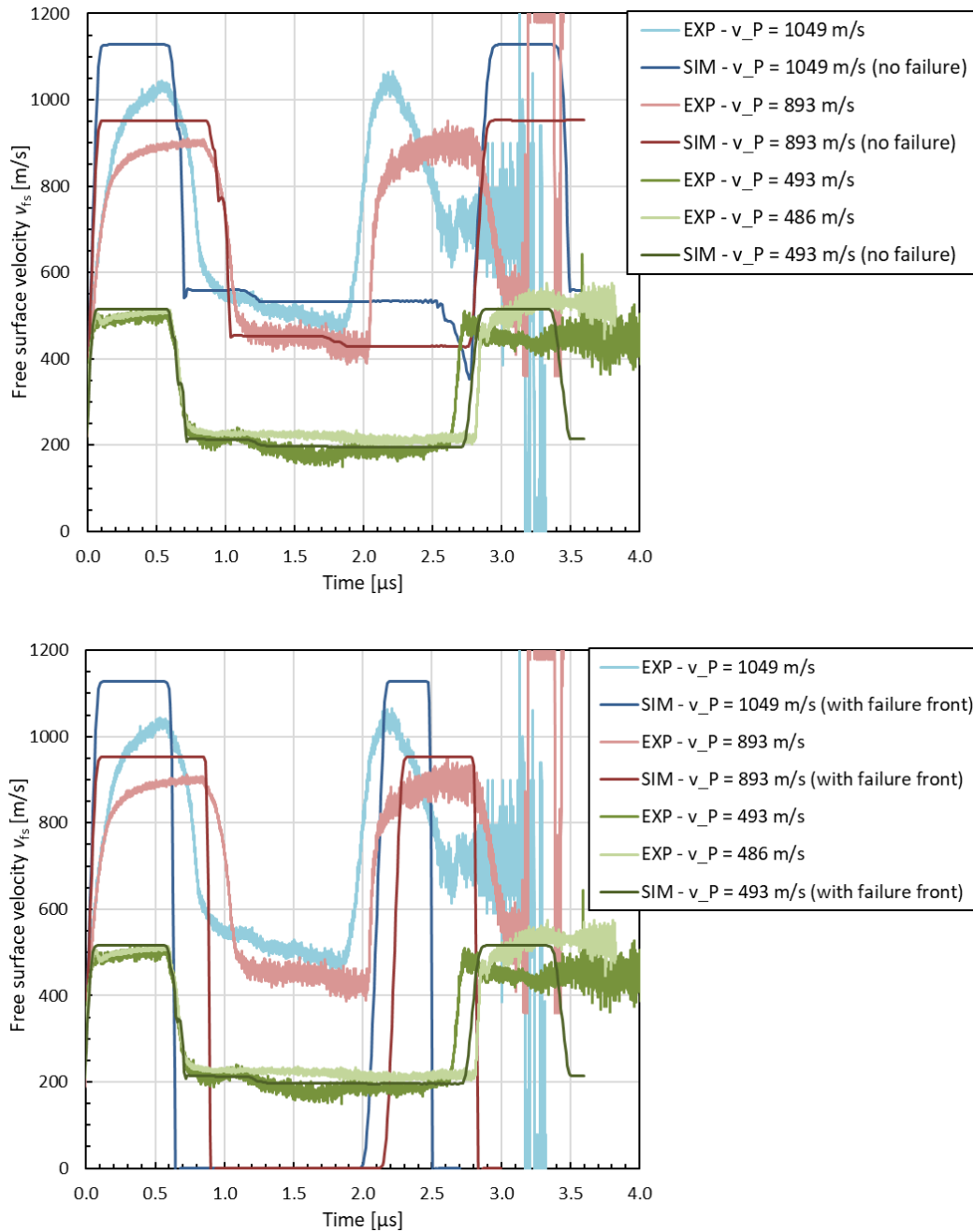


Figure 4.31: Simulation and experimental results of four PPI tests with a 7.85 mm thick SLG target: a perfectly elastic model without failure front does not reproduce the timing of the reflected signal (top diagram); the addition of an artificial failure front improves the arrival times of the reflected signal (bottom diagram).

4.3.2 Incremental analysis of the loading paths

In this section, the Shock Hugoniot of SLG is determined. This is achieved through an incremental analysis of the free surface velocity measurements [165].

Figure 4.32 shows the free surface velocity of test no. 3787 in which a 2 mm aluminum projectile impacted a 4.85 mm thick SLG target with a velocity of 601 m/s. The blue line is the

unsmoothed velocity signal derived from the interferometry measurement at the back face of the SLG. The smoothed red line results from a moving average over 35 data points.

The ending point of the loading path, i.e. the final state, is obtained by analyzing the derivative of the velocity signal. Figure 4.33 illustrates the original velocity signal from test 3787 during the first 0.3 μs as a dark blue line. The light blue line depicts the derivative, i.e. the acceleration of the free surface. Since the absolute values of the acceleration are not of interest, a normalized representation is chosen. After a sharp increase, the acceleration rapidly decreases, reaching a value of almost zero at 0.06 μs . This inflection of the curve is marked by a red dashed line in the diagram and is set to be the ending point of the loading path.

The final state variables of the shocked SLG, like the longitudinal stress and the volumetric compression, are then calculated using formulas 4.10, 4.11, 4.12 and 4.15. Here, an elastic wave speed of $c_p = 5740 \text{ m/s}$ is chosen (ref. Table 1.2).

As described in section 4.1.4, an error estimation is needed in order to quantify the uncertainty associated with possible errors of the arrival time t_0 of the elastic wave and the velocity c_p . This is realized by conducting two additional incremental analysis with shifts of $\pm 50 \text{ ns}$ on t_0 . Figure 4.34 illustrates the resulting input curves of test no. 3787. The green curve marks the velocity signal used for the standard analysis. By applying a shift of -50 ns (red graph) and $+50 \text{ ns}$ (yellow graph) two additional velocity curves are created.

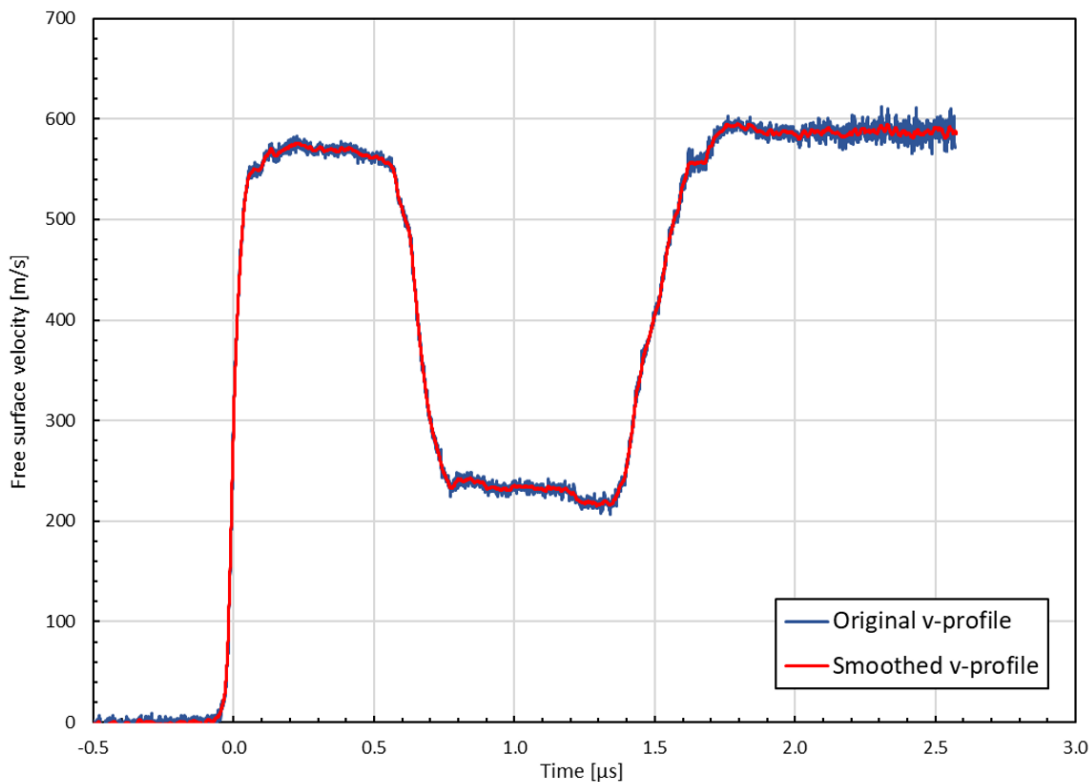


Figure 4.32: Original and smoothed velocity profile for test 3787 (Figure was pre-published by the author in [A1]).

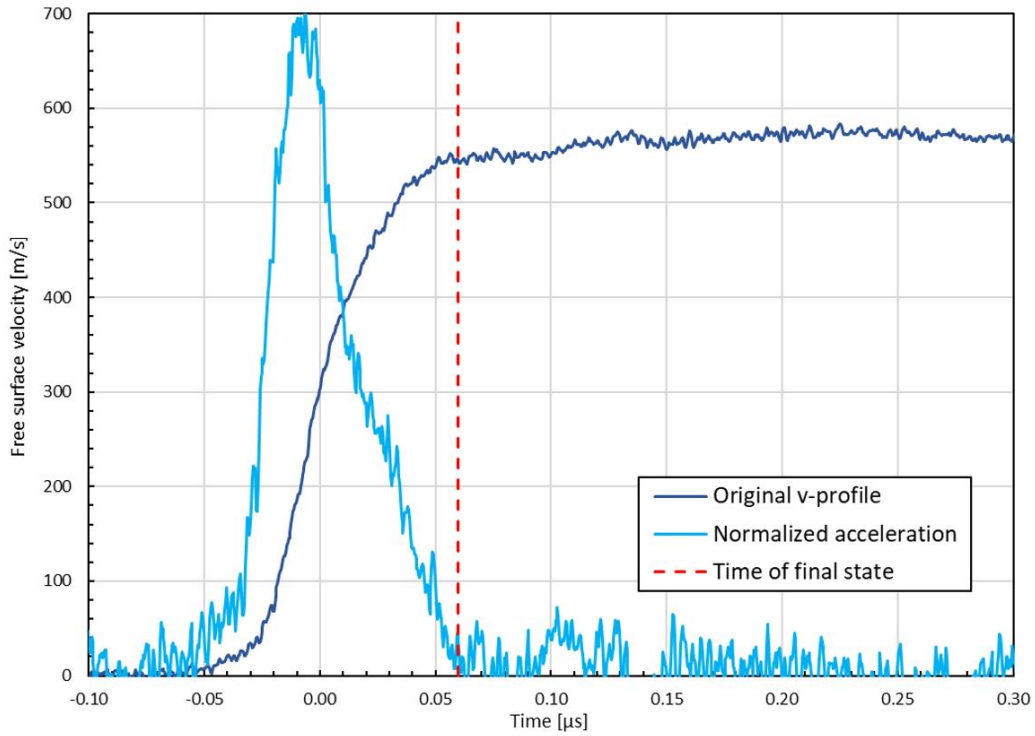


Figure 4.33: Determination of the time of the final state using the normalized acceleration for test 3787 [A1].

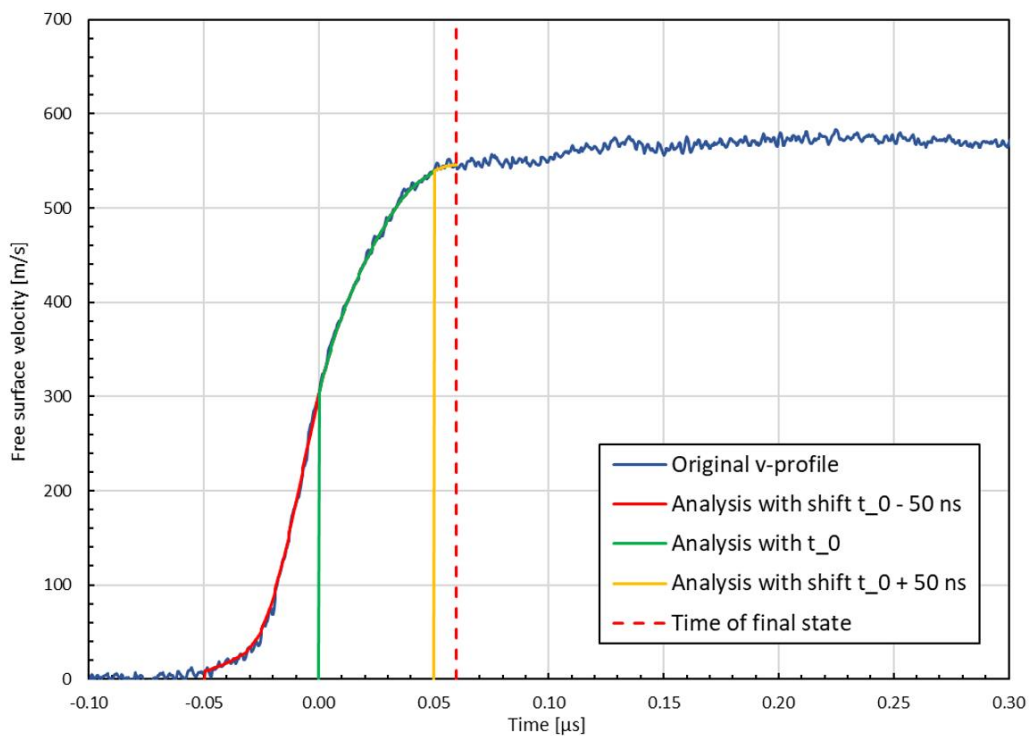


Figure 4.34: Input data for the incremental analysis of test 3787; different t_0 offsets are indicated by different colors: original t_0 = green, $t_0 - 50$ ns = red, $t_0 + 50$ ns = yellow [A1].

The outlined analysis and error estimation concept is applied to all PPI tests. The result is depicted in the diagram in Figure 4.35, where the longitudinal stress is plotted versus the

volumetric compression. Each green point represents the final state of one PPI test, resulting from the standard incremental analysis. In addition, the results from the shifted analysis are marked as red and yellow circles. The diagram illustrates that a shift of -50 ns yields a lower longitudinal stress but a higher volumetric compression than the corresponding standard value. For a shift of +50 ns, the opposite applies. The size of the errors bars (black markers) of the standard analysis is chosen to be the difference between the green and yellow data points. With this assumption, all shifted results lie within a range of one to two error bars.

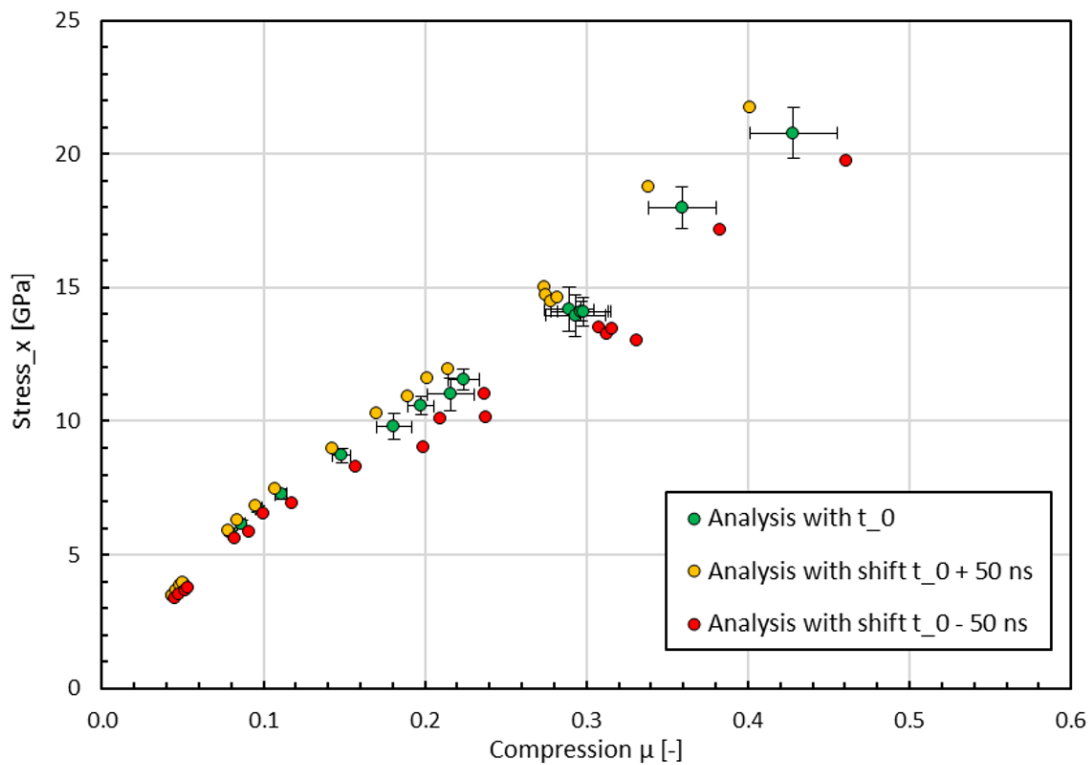


Figure 4.35: Resulting final states: the results of the standard analysis are illustrated by the green circles. The yellow and red circles represent the results for the analysis in which t_0 was shifted by ± 50 ns [A1].

All values illustrated in Figure 4.35 are listed in Table 4.9 together with some additional results. The first three columns provide information on the experimental setup and impact conditions. There, the thicknesses of the projectile and target are given together with the used material and the measured impact velocity v_p . Columns 4 and 5 show the resulting particle velocity u_p and shock wave velocity U_s of the final state. The next two columns contain the corresponding density and volumetric compression. In the last column, the induced longitudinal stress σ_x is given.

The rows are sorted by ascending stress values. Together with the findings of the previous section (4.3.1) these stress values can be used to determine the minimum stress needed to induce an internal failure front. Only in case of the three tests with the lowest longitudinal stress, no internal failure front was present. This leads to the conclusion, that the minimum stress needed to create a failure front lies within the range of 3.8 GPa to 3.9 GPa.

Table 4.9: Summary of all calculated values in the final states (incremental analysis without shift on t_0) (Table was pre-published by the author in [A1]).

Test No.	Configuration	v_p [m/s]	u_p [m/s]	U_s [m/s]	ρ [g/cm ³]	μ [-]	σ_x [GPa]
4146	2.0 mm Al → 7.85 mm SLG	493	240	5506	2.641	0.044	3.5
4144	2.0 mm Al → 7.85 mm SLG	486	251	5491	2.646	0.046	3.6
4042	2.0 mm Al → 4.85 mm SLG	497	267	5416	2.655	0.049	3.8
3787	2.0 mm Al → 4.85 mm SLG	601	273	5359	2.658	0.051	3.9
4143	3.0 mm Al → 7.85 mm SLG	893	411	5040	2.731	0.080	5.8
3786	2.0 mm Al → 4.85 mm SLG	929	439	4924	2.748	0.086	6.1
4145	2.0 mm Al → 7.85 mm SLG	1049	484	4707	2.775	0.097	6.7
3783	2.0 mm Al → 4.85 mm SLG	1070	534	3896	2.811	0.111	7.3
3909	2.0 mm St → 4.85 mm SLG	986	663	3477	2.906	0.149	8.7
0856	1.5 mm St → 2.86 mm SLG	1200	763	3499	2.988	0.181	9.8
0099	2.0 mm Al → 4.85 mm SLG	1703	824	3959	3.030	0.198	10.6
0857	1.5 mm St → 2.86 mm SLG	1320	870	3698	3.076	0.216	11.0
0100	2.0 mm Al → 4.85 mm SLG	1875	908	4161	3.096	0.224	11.6
0111	2.0 mm St → 4.85 mm SLG	1685	1112	4247	3.271	0.293	14.0
0110	2.0 mm St → 4.85 mm SLG	1686	1124	4255	3.281	0.297	14.1
0855	1.5 mm St → 2.86 mm SLG	1700	1125	4215	3.283	0.298	14.1
0114	2.0 mm Al → 4.85 mm SLG	2447	1117	4473	3.262	0.289	14.2
0102	2.0 mm Al → 4.85 mm SLG	3029	1368	4964	3.438	0.359	18.0
0113	2.0 mm St → 4.85 mm SLG	2440	1568	5090	3.613	0.428	20.8

Figure 4.36 shows a graph of the U_s - u_p -relation of the final states. The results of the present work are illustrated by the green circles. For longitudinal stresses of 8.7 GPa and higher, an almost linear correlation ($U_s = 1.88 u_p + 2230$ m/s) is observed, as indicated by the dashed line. For comparison, the literature data of Alexander et al. [39] is shown as gray triangles.

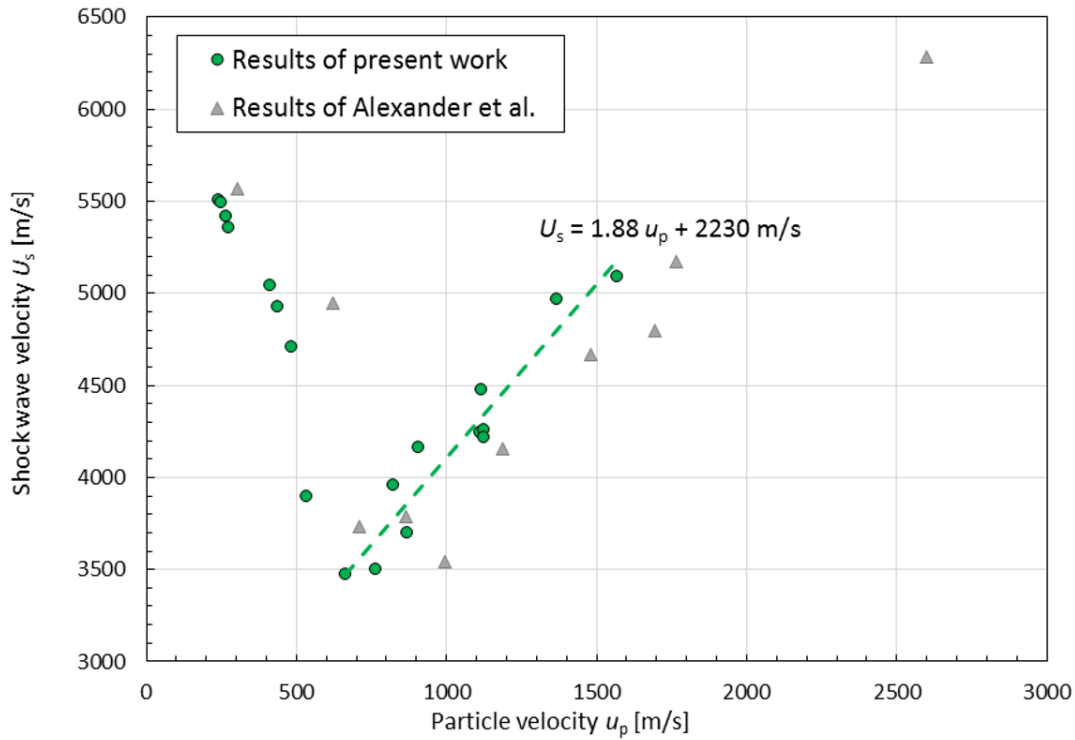


Figure 4.36: U_s - u_p -relation for the final states: the results of the present work are illustrated by the green circles together with a dashed line indicating a linear correlation at higher stresses. The results of Alexander et al. [39] are indicated by the gray triangles (Figure was pre-published by the author in [A1]).

4.3.3 Derivation of an equation of state for soda-lime glass

In this section, it is outlined how an EOS for SLG can be derived from the Shock Hugoniot deduced in the previous section (Figure 4.35). The EOS of the JH2 material model for glass [60] is taken as a representative example.

In this EOS, a polynomial formulation of the relation between the hydrostatic pressure and the volumetric compression is used. In order to determine the parameters, the hydrostatic pressure has to be derived from the longitudinal stress of the Shock Hugoniot. The approach chosen here is to identify the HEL and the yield strength by means of the von-Mises yield criterion, in order to subtract the shear-resisting term from the Shock Hugoniot.

The hydrostatic pressure P can be expressed through the first invariant of the total stress tensor, which is one third of the sum of the principal stresses $\sigma_{x,y,z}$ (ref. equation 2.21). In the following, stresses are taken to be positive in compression:

$$P = \frac{1}{3}(\sigma_x + \sigma_y + \sigma_z) \quad 4.16$$

During the loading by a planar shock wave, the material is in a uniaxial strain state. Therefore, the stresses σ_y and σ_z which are perpendicular to the shock direction are:

$$\sigma_y = \sigma_z \quad 4.17$$

Combining equations 4.16 and 4.17 yields:

$$P = \frac{1}{3}(\sigma_x + 2\sigma_y) \quad 4.18$$

With the von-Mises yield criterion, the yield strength Y can be written as:

$$Y = \frac{1}{\sqrt{2}} \sqrt{(\sigma_x - \sigma_y)^2 + (\sigma_y - \sigma_z)^2 + (\sigma_z - \sigma_x)^2} \quad 4.19$$

$$\stackrel{eq.4.17}{=} |\sigma_x - \sigma_y|$$

which is identical to the Tresca yield condition in this case.

Combining equations 4.18 and 4.19 yields:

$$P = \sigma_x - \frac{2}{3}Y \quad 4.20$$

For uniaxial strain conditions, the HEL marks the longitudinal stress at which plastic deformations arise. In the elastic regime, below the HEL, Hooke's law is applied:

$$\sigma_y = \frac{\nu}{1-\nu} \sigma_x \quad 4.21$$

where ν denotes the Poisson's ratio.

Since the transition from elastic to plastic behavior has to be continuous, equations 4.19 and 4.21 have to be equal when $\sigma_x = \text{HEL}$ which yields:

$$Y = \text{HEL} \frac{1-2\nu}{1-\nu} \quad 4.22$$

A possible approach to estimate P from σ_x is therefore to calculate P with equation 4.20 within the plastic regime ($\sigma_x \geq \text{HEL}$). The elastic curve is then determined by a linear interpolation between $\sigma_x = 0$ and $\sigma_x = \text{HEL}$.

The required value for Y can be determined using equation 4.22. Alternatively, Y can be taken from experimental shear strength data in the literature, which varies typically between 0.3 GPa and 4.1 GPa (ref. Figure 1.1 and Figure 1.2). For example, Bourne [82] [19] [83] and Radford [111] used internal stress gauges to determine the strength for various σ_x .

The literature values for the HEL vary quite considerably between 3.1 GPa and 8.0 GPa as outlined in section 1.2 in Table 1.3. In order to identify the HEL of the present data, a new approach has been developed, which is applied as described in the following.

Figure 4.37 displays the experimentally determined data points of the Shock Hugoniot. The four data points at the lowest longitudinal stresses are in line with a linear fit through the origin. They are therefore identified as purely elastic states and represented as purple circles as opposed to the green circles of the plastic states. A polynomial fit of third degree through the plastic states results in the orange curve. Here, each data point is weighted with its corresponding measurement errors (black markers). The red lines represent the resulting confidence intervals of the fit. This means that with a probability of 68 % the true Shock Hugoniot is lying within

the 1 standard deviation (SD) interval (area between the bright red lines) and with a probability of 95 % within the 2 SD interval (area between the dark red lines).

The HEL is subsequently defined to be the intersection point between the polynomial fit of the plastic regime and the linear fit of the elastic regime. This is illustrated in Figure 4.38, where the linear fit is represented as a purple line. The intersection point yields a value for the HEL of (5.0 ± 0.2) GPa. Here, the standard deviation of the HEL is estimated from the intersections of the linear fit line with the 1 SD confidence interval of the polynomial fit. The corresponding volumetric compression at the HEL is $\mu_{\text{HEL}} = 0.063$.

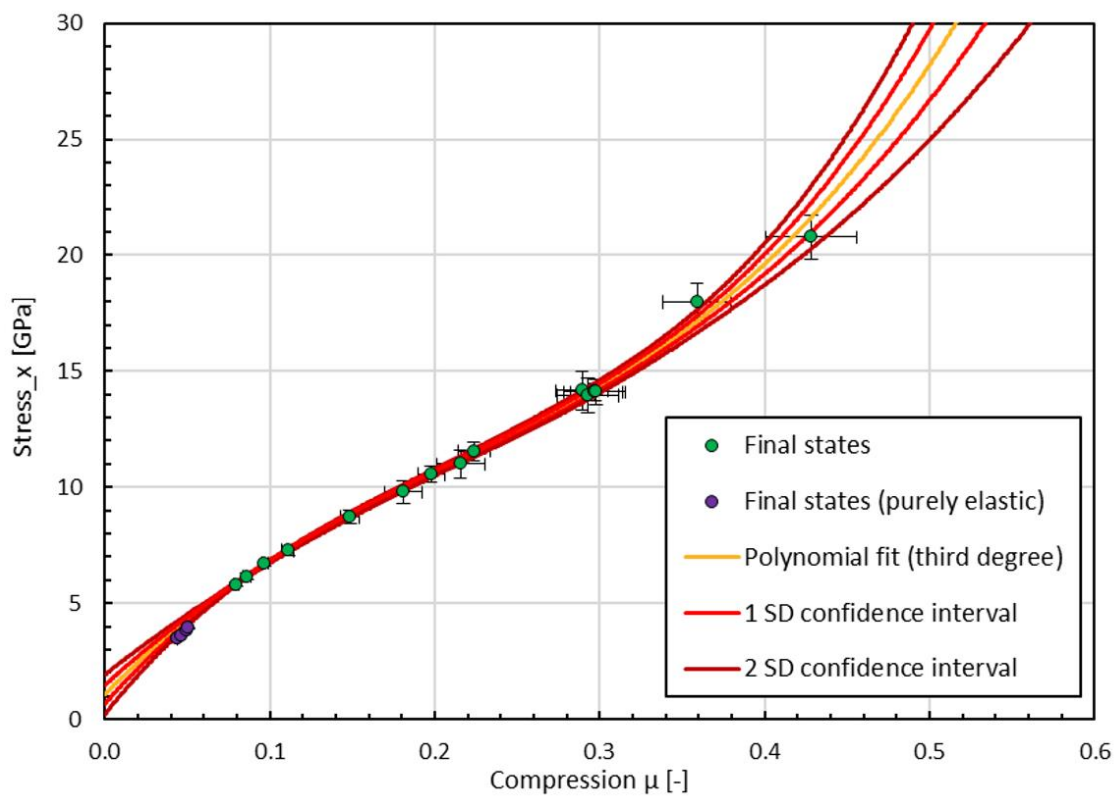


Figure 4.37: Final states resulting from the PPI tests. The purple points represent final states in the purely elastic range. The orange curve represents a polynomial fit of third degree through all other final states (green points). Here, the red lines indicate the corresponding 68 % and 95 % confidence intervals (1 and 2 standard deviations). (Figure was pre-published by the author in [A1]).

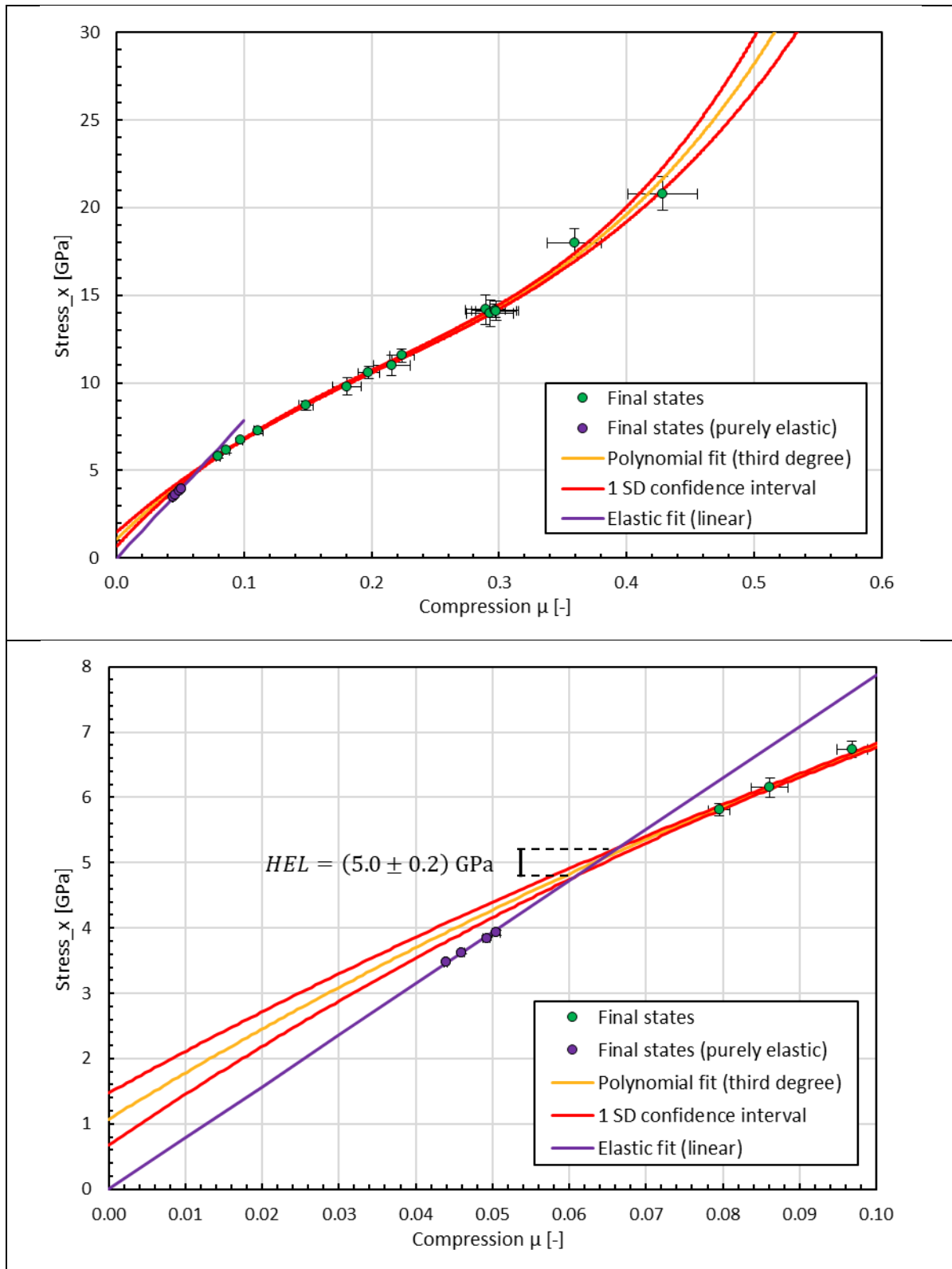


Figure 4.38: Determination of the HEL: The purple line represents a linear fit through the purely elastic final states. The orange curve represents a polynomial fit of third degree through all other final states. Here, the red lines indicate the corresponding 68 % confidence interval (1 standard deviation). The intersection of both fits corresponds to the HEL. This can be seen in more detail in the bottom diagram, which shows an enlarged section in the low compression range. The standard deviation of the HEL is estimated from the intersections of the linear fit line with the 1 SD confidence interval of the polynomial fit. (Figure was pre-published by the author in [A1]).

The HEL can be used to get an estimation for Y . Together with a Poisson's ratio of $\nu = 0.21$ (see Table 1.2), equation 4.22 gives a yield strength of $Y = (3.65 \pm 0.15)$ GPa.

As mentioned above, an alternative value for Y can be inferred from the reported experimental shear strength data shown in Figure 1.1. Here, the strength curve of intact material is used since the failure front moves significantly slower than the shock waves (see section 4.3.1). The data of Bless et al. [76], Espinosa et al. [47] and Bourne et al. [38] indicate a cap of the intact strength in the range of $3.7 < Y < 4.7$ GPa.

Considering these results, a constant yield strength of $Y = 4$ GPa has been selected for the calculation of P with equation 4.20. On the one hand, this is in good agreement with Bourne's estimated cap of $Y = 4$ GPa, reported in [82] and [83]. On the other hand, this value is reasonably close to the estimation based on Hooke's law and the von-Mises yield criterion of $Y = (3.65 \pm 0.15)$ GPa. It is also in rough agreement with the measured static yield strength of 4.3 GPa [232].

On top of that, this approach results in an EOS with a very plausible bulk modulus of $K_1 = 42.5$ GPa at low hydrostatic pressures (Figure 4.40).

The resulting hydrostatic pressures are presented as blue squares in Figure 4.39. Here, the illustrated error markers are adopted from the corresponding errors of the Shock Hugoniot values (green circles). This is done since the errors on Y are considered negligible compared to the errors of the Shock Hugoniot states.

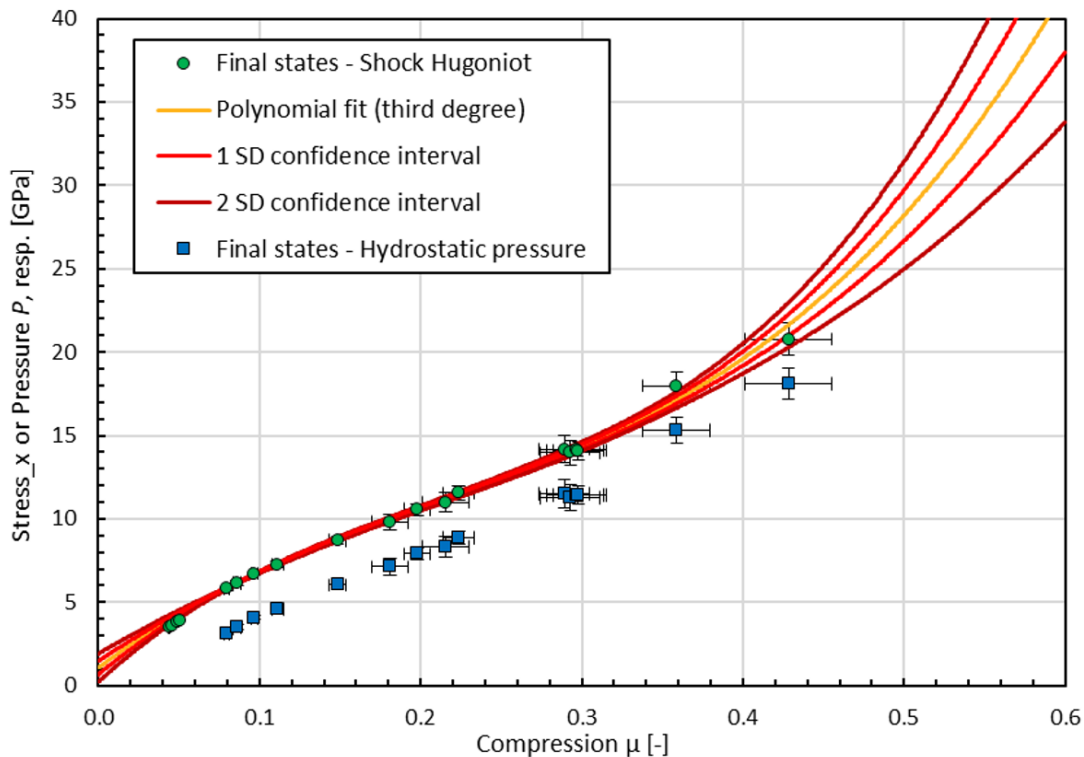


Figure 4.39: Final states resulting from the PPI tests. The green points are the longitudinal stress values lying on the Shock-Hugoniot, represented by the orange polynomial fit curve. The blue points are the hydrostatic pressure states, calculated by subtracting two thirds of the yield stress (Figure was pre-published by the author in [A1]).

Applying a polynomial fit of third degree through the hydrostatic pressure points finally yields the EOS of the form

$$P = K_1 \cdot \mu + K_2 \cdot \mu^2 + K_3 \cdot \mu^3 \quad 4.23$$

with $K_1 = (42.5 \pm 1.5)$ GPa, $K_2 = (-24.6 \pm 16.9)$ GPa and $K_3 = (51.8 \pm 40.5)$ GPa.

The result is plotted in the top diagram of Figure 4.40 as a light blue line. The darker blue lines represent the corresponding 1 SD and 2 SD confidence intervals of the fit. For pressures and compressions greater than the highest measurement point at $\mu = 0.43$ and $P = 18.1$ GPa, the confidence intervals widen significantly. Therefore, an extrapolation to higher values has to be used with care. However, in case of a typical impact scenario on a glass laminate target, this uncertainty has no relevance since the highest occurring pressures are expected to be well below 10 GPa.

In the low-pressure range, the derivative of the EOS corresponds to the elastic bulk modulus. The bottom diagram of Figure 4.40 depicts an enlarged section of this regime. The red dashed line represents the gradient at zero pressure, which equals K_1 . The comparison of $K_1 = (42.5 \pm 1.5)$ GPa with the literature value of $K = 42.8$ GPa (Table 1.2) yields a very good agreement. This is an important observation, as they could be different if the inelastic deformation was due to brittle failure and not due to plastic flow.

With equation 4.23 and the volumetric compression at the HEL of $\mu_{\text{HEL}} = 0.063$, the hydrostatic pressure at the HEL is $P_{\text{HEL}} = 2.595$ GPa. The corresponding equivalent stress is $\sigma_{\text{HEL}} = 3.608$ GPa. These values can be used as normalization values in the JH2 model.

In summary, a novel concept for the determination of the EOS was developed and applied. The resulting EOS is compared to literature data in the discussion in the next section (4.4). Furthermore, the new results are implemented in an improved SLG model in chapter 6.

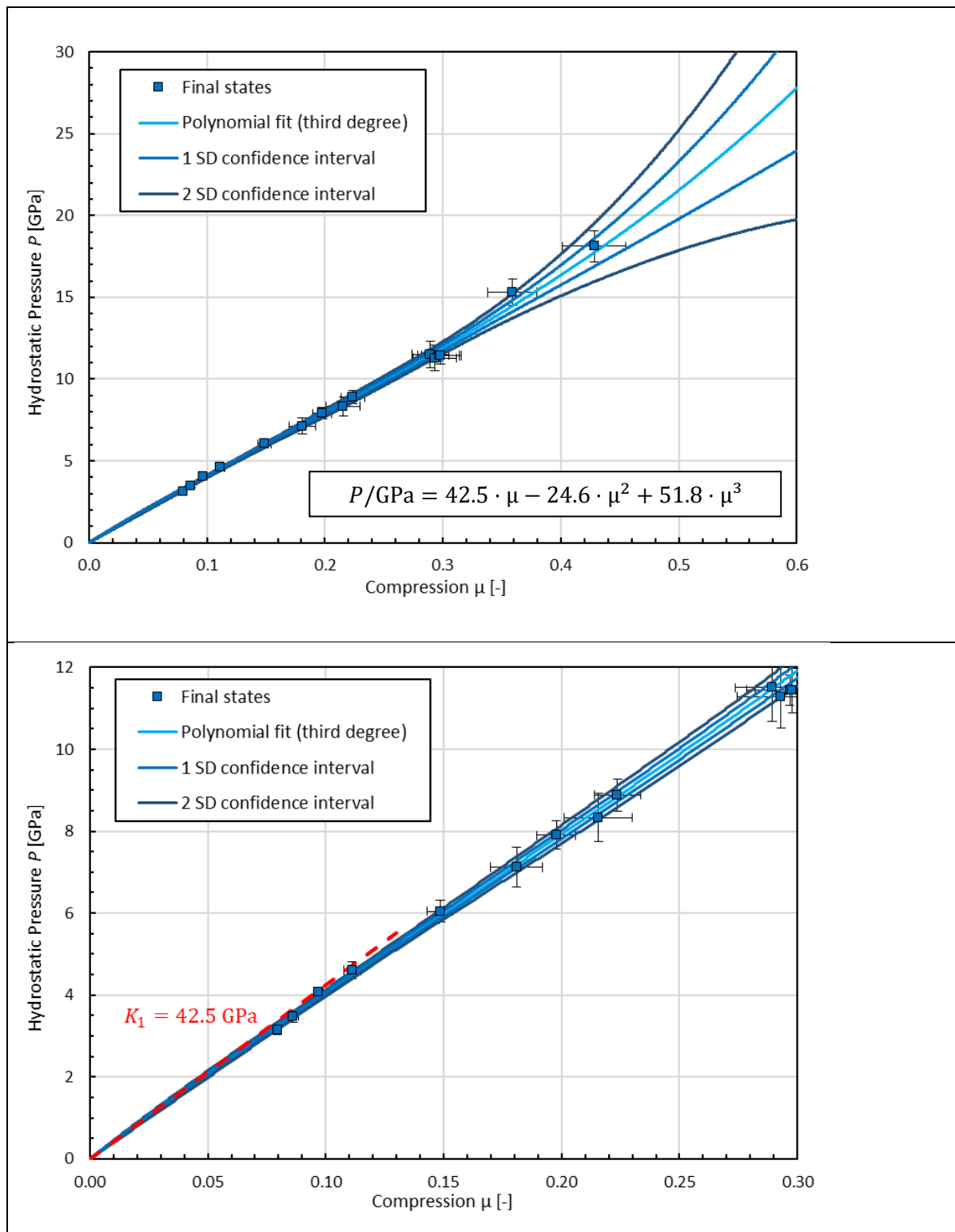


Figure 4.40: Determined equation of state for SLG:

Each blue square corresponds to the final state of one PPI test. The light blue curve is the related EOS resulting from a polynomial fit of third degree. The 68 % and 95 % confidence intervals (1 and 2 standard deviations) are shown as dark blue lines.

The bottom diagram shows an enlarged section in the low compression range. Here, the red dashed line corresponds to the resulting bulk modulus at zero pressure (Figure was pre-published by the author in [A1]).

4.4 Discussion of the planar plate impact results

Parts of the findings on the PPI experiments have already been published by the author in [A1] and are reproduced in this section.

Important results of the extensive PPI test series are the new insights into the failure front phenomena, which were outlined in section 4.3.1. They deliver arguments that support some and refute other assumptions of previous studies, which sometimes contradicted. The results are discussed in the following.

The determined onset of the failure front between 3.8 GPa and 3.9 GPa is in good agreement with the literature value of 4.0 GPa from Simha et al. [49] and Rosenberg et al. [78]. On the contrary, the observation of Dandekar and Beaulieu [103], that the failure front is initiated at stress levels between 4.7 GPa and 5.2 GPa, is not supported. These stress levels correspond to the HEL, which was determined as (5.0 ± 0.2) GPa in this study.

Therefore, it can be concluded that the HEL does not represent the threshold for the initiation of damage.

In all conducted experiments, the internal failure front was initialized by the release wave from the back of the projectile. This is concluded from the comparison of the high-speed observation (high-speed videos and velocimetry data) with the corresponding Lagrange diagrams. In particular, the variation of the projectile thickness showed a clear correlation with the initiation time of the failure front (e.g. Figure 4.24 and Figure 4.26).

This is in agreement with the observations of Bourne et al. [102]. Furthermore, the assumption of Kanel et al. [43] [97], Brar et al. [44] and Espinosa et al. [47] that the failure front originates at the sample surface at the start of compression, is not supported.

Horie [233] summarized that it is not established whether failure fronts occur above the HEL. The results of the present work however strongly support the hypothesis of their occurrence. At 6.7 GPa, a failure front with a velocity of 1140 m/s was evidenced by means of high-speed videos as well as laser interferometry. For stress levels of 10.6 GPa and higher, the presence of a failure front with a velocity of 2100 m/s could be inferred from the interferometry data. Since the latter velocity surpasses the ultimate speed of growth of cracks of 1500 m/s in glasses [45], the failure front describes a different phenomenon and instead presumably consists of a propagating front of crack nucleation sites.

From the results of the present work, it is concluded that this propagating front is caused by the combination of a compression and a subsequent release of the material stress. The unidirectional compression induces a shear loading, which is assumed to lead to the formation of micro cracks that are not visible in the high-speed videos. Despite the micro cracks, the material response remains elastic, if the loading stress is lower than the HEL. Upon release, the micro cracks turn into nucleation sites of macroscopic cracks forming the failure front, which is observed in the high-speed videos.

By means of high-speed imaging, Chocron et al. [107] could observe a failure front in borosilicate glass at very low stress levels of 0.8 GPa. Since they could not detect the recompression wave in the velocity profile, which originates from the reflection of the unloading wave from the surface at the failure front, they assumed that previous studies could maybe mistakenly have concluded the non-existence of the failure front at low velocities.

The results of the present work do not support this conclusion for SLG. At stress levels below 3.9 GPa, solely a surface failure front could be observed that originates at the specimen's lateral

free surface. This front exhibited failure nucleation sites trailing the shock wave, which were closer to the shock wave at higher impact velocities, similar to Chocron's observations and the observations of Bourne et al. [102].

Only at higher stress levels, an internal failure front could be identified. The correlation with the corresponding velocity profiles revealed that this second front was located inside the whole glass specimen.

The differences to Chocron's observation could be attributed to several reasons. First, it could be due to a different behavior of soda-lime and borosilicate glass. Second, it might have been difficult to separate the internal from the surface failure front. However, Chocron et al. used the intensity of the laser interferometer as an indication for the damage to be in the interior of the specimen.

Further important results of the PPI test series are the determined EOS as well as the HEL for SLG. The evaluated HEL of (5.0 ± 0.2) GPa lies well within the range of the reported literature values between 3.1 GPa and 8.0 GPa (see Table 1.3). The discrepancies in the literature are mainly due to the fact that SLG exhibits no clear two-wave structure in its shock wave profiles making the common analysis methods of ductile materials hardly applicable. A major source of error was the lack of a clear-cut method for the evaluation of stress levels as pointed out by Grady et al. [75].

The elaborated incremental analysis approach of this work however provides a solution, which is less prone to errors. An incremental analysis of the differential form of the Rankine-Hugoniot equations is not completely new, as it was already used e.g. by Alexander et al. [39] or Reinhart et al. [221]. Information about the derivation of the concept and the corresponding formulas as well as an error estimation, however, is sparse in the literature and not given in [39] and [221]. Furthermore, there has to be taken great caution when considering different frames of reference (Lagrangian vs. Eulerian) to avoid calculation errors on the wave speeds.

The determined Shock Hugoniot and EOS significantly differ from the reported results of Grady et al. [75], Alexander et al. [39] and Holmquist et al. [60] as illustrated in Figure 4.41 and Figure 4.42. While there is a good agreement in the elastic range up to a volumetric compression of roughly $\mu = 0.1$, the curves clearly diverge in the plastic regime. For equal levels of compression, the Shock Hugoniot of the literature lies at stress values that are 3 to 5 GPa lower than that of the present work. Most notably, the Shock Hugoniot of the present work does not exhibit the plateau of constant stress at $\sigma_x \approx 7$ GPa.

The differences may most likely be attributed to the applied analysis methods. This finding is based on a reevaluation of some selected velocity profiles from the aforementioned publications. The selected profiles (for details see Figure 9.9 and Figure 9.10 in the appendix) were digitized and the stress and compression of the final states were recalculated by means of the analysis method outlined in this work. The result is illustrated in Figure 4.41 by blue squares. The final states move to lower compressions as indicated by the blue arrows. The fact that the recalculated values are in good agreement with the Shock Hugoniot of the present work suggests that the differences are due to the analysis methods and not due to the material properties.

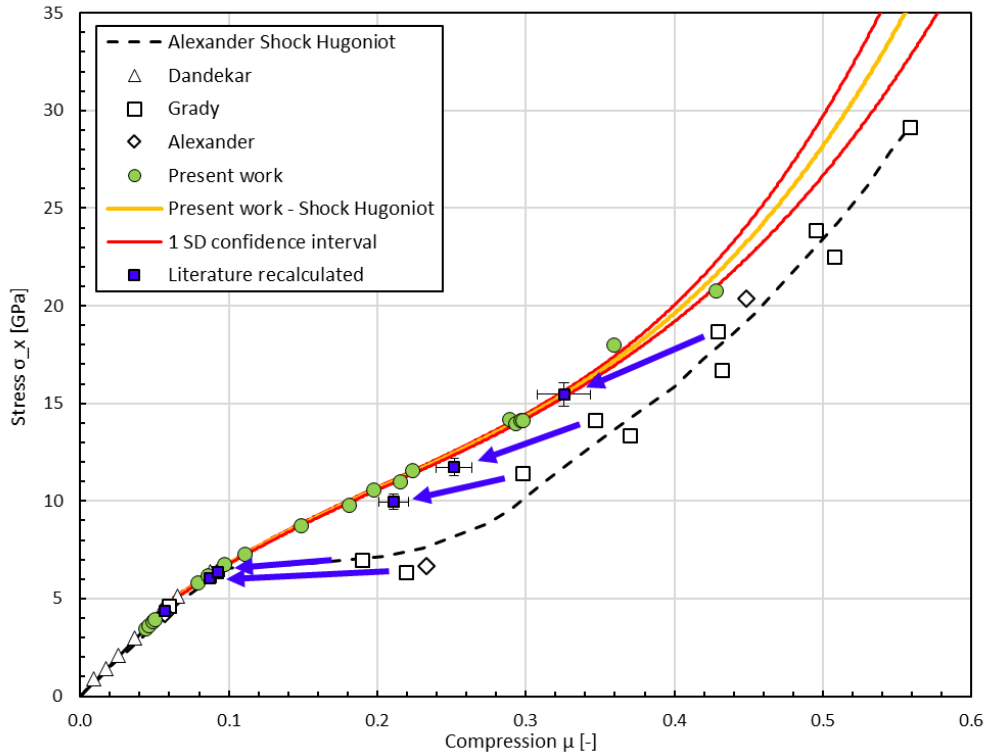


Figure 4.41: Comparison of the present results (green circles and colored lines) with literature data (white symbols and dashed line). The present data matches the literature data for SLG within the low-pressure range (elastic behavior). For stresses higher than 7 GPa, the literature data is shifted towards higher compressions. Recalculation of some selected literature velocity curves from [75] and [39] yields a shift to lower compressions (blue symbols) [A1].

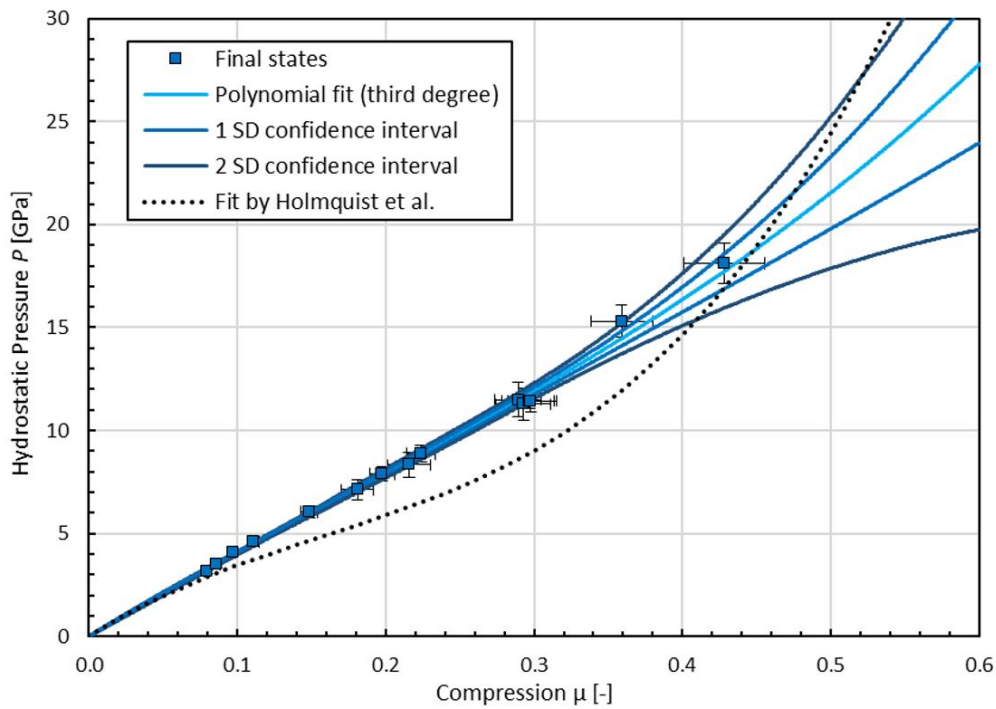


Figure 4.42: Equation of state for SLG: Each blue square corresponds to the final state of one PPI test. The light blue curve is the related EOS resulting from a polynomial fit of third degree. The 95 % and 68 % confidence intervals (2 or 1 standard deviation) are shown as dark blue lines. The black spotted line is the EOS derived by Holmquist et al. [60] [A1].

In case of Grady's data, the difference is most likely due to the lack of a clear-cut method as outlined above. In case of Alexander's data, the analysis was also conducted by means of an incremental approach. Nevertheless, differences could arise from different estimations of the wave velocities and impact times or even the use of a different set of differential equations.

Further important results of the PPI tests can be deduced from the observed release response:

- The spall strength of SLG has to be greater than 6.7 GPa, when shocked to a longitudinal stress of 10.6 GPa. This is inferred from test no. 0099, in which the SLG target was impacted with an aluminum plate at 1703 m/s and no spallation signal could be observed (Figure 4.28). The result is in contrast to Rosenberg et al. [48] and Espinosa et al. [47], who determined a spall strength of 3.8 GPa and 2.6 GPa, respectively. It supports, however, the observations of the other authors listed in Table 1.5.
- Determined release wave velocities of 5740 m/s and 9500 m/s are in good agreement with the data of Grady et al. [234], which lies in the range of 5300 m/s to 13300 m/s. In contradiction, Bourne et al. [105] concluded that the earlier release is not caused by higher release velocities, but is rather an effect of the failure front reducing the shear strength. They base their conclusion on their observation that the distance between the failure front and the shock wave front reduces with rising loading stress. The present work, however, implies that the failure front velocity does not rise with increasing stresses above 10.6 GPa. The presented results therefore support the argument of high release wave velocities as supposed by Grady et al. [234] and Kanel et al. [45].

5 Development of a novel methodology for generating, characterizing and pressure testing of defined damaged glass specimens

5.1 Introduction

One of the main objectives of this work is the experimental determination of the material properties of SLG that are constitutive for its ballistic resistance during a ballistic impact. In a typical ballistic impact scenario, with a bullet impacting a transparent armor, the resistance of the armor is strongly governed by the strength of the material in front of the bullet. In case of SLG, the material in front of the bullet is already pre-damaged when interacting with the bullet. This is due to impact-induced shock waves, which precede in front of the bullet and subject the SLG to high loads. Since the fragments of the damaged material are kept in place by the surrounding intact material, the residual strength is still significantly high despite the pre-damage.

In this chapter, a novel methodology is presented, which facilitates the direct experimental determination of the crucial material properties for the strength model of SLG in dynamic impact scenarios. On the one hand, this approach comprises an innovatively way to dynamically generate and quantify a defined degree of damage in small SLG cylinders. On the other hand, the residual strength of the pre-damaged specimens is determined by an advanced confined pressure test.

As a result, the yield curves of SLG as a function of the hydrostatic pressure and the degree of pre-damage are obtained. The determined model parameters are especially suited for the simulation of ballistic impact scenarios, since the characterized pre-damaged SLG is representative for the damaged transparent armor in front of a bullet during impact.

5.2 Generation of damaged glass specimens

First, the SLG is pre-damaged by means of a defined, highly dynamic shock loading. For this purpose, a novel test setup is developed, in which a small SLG cylinder is impacted planar by an aluminum projectile with a defined impact velocity. Here, the SLG specimen is completely confined by a demountable aluminum confinement holding the resulting SLG fragments in place. This is essential, since the residual strength of the specimen strongly depends on the friction between the fragments. This means, that the residual strength is considerably higher if all fragments are kept in place and are "interlocking" in contrast to a loose accumulation of fragments similar to e.g. rough gravel.

In order to ensure that the fragments are still kept in place in the subsequent characterization tests, a thin aluminum sleeve is retained around the SLG cylinder even after removing the demountable confinement.

5.2.1 Experimental setup

The specimen cylinders are cut from a 1.5 m long commercial grade SLG bar with a diameter of 6 mm, which was purchased from the German wholesale glass company "GLS Spezial- & Farbglasshandel GmbH". The demountable confinements and the projectile plates are made of aluminum EN AW 2007 T4 (Al F34-F37). The setup procedure is illustrated in Figure 5.1 and described in the following:

1. First, the SLG cylinder is placed in an aluminum sleeve with a wall thickness of 0.5 mm. The initial heights of the sleeve and the cylinder are a few millimeters larger than 6 mm to allow for a surface adjustment in step 3 by means of grinding and polishing.
2. The SLG cylinder with the aluminum sleeve is clamped inside the center hole of a large aluminum disk, which provides the lateral confinement. The disk has a diameter of 60 mm with a central hole of 7 mm diameter. The clamping of the specimen can be slightly adjusted. For this purpose, a thin slit is cut in one side of the disk. The slit width is then adjusted by a fixing screw after the specimen is in place.
3. The disk is placed in a depression inside a large aluminum confinement. The confinement consists of a 100 mm x 100 mm x 25 mm block and an 8 mm thick cover plate. The disk has two screw holes, which allow for the mounting inside the block. Before the cover plate is mounted on top by four additional screws, all other components of the confinement together with the SLG cylinder are grinded and polished to ensure a flat surface. The final height of the SLG cylinder is 6 mm. Figure 5.2 shows a picture of 12 polished confinements without their cover plates.
4. To induce the shock wave and generate the pre-damage inside the SLG, an aluminum projectile impacts the cover plate of the confinement. The projectile consists of a 3 mm thick aluminum disk with a diameter of 30 mm, which is placed in front of a hollow 60 mm long polycarbonate sabot.

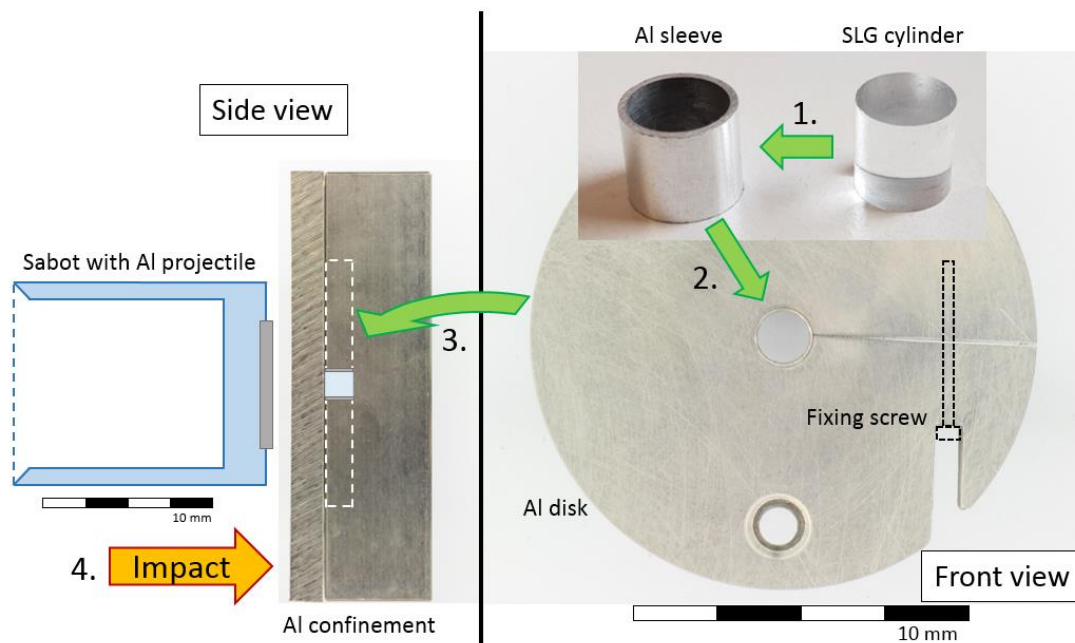


Figure 5.1: Illustration of setup procedure for the pre-damaging: 1. The SLG cylinder is placed inside an aluminum sleeve; 2. The cylinder with the sleeve is clamped by means of a fixing screw inside an aluminum disk; 3. The disk with the specimen is mounted inside a large aluminum block and confined by a cover plate; 4. A shock wave is induced by the impact of an aluminum projectile.



Figure 5.2: Twelve polished confinements with intact SLG cylinders. Before the impact tests are conducted, cover plates are mounted on each confinement by four fixing screws through the holes.

The projectile was accelerated by means of a single-stage gas gun with a bore diameter of 48 mm, which was driven by compressed air or helium as propellant gas.

A total of 20 tests were conducted out of which 12 were selected for the further characterization procedures. Table 5.1 gives a summary of all tests. The first columns list the test number and the length of the used gun barrel. Columns 3, 4 and 5 give the information on the used propellant gas, the filling pressure and the measured impact velocity. In the last three columns, the characterization technique that was subsequently applied is indicated by an "X".

Two test series with two different gun barrels were conducted. In the first series (test no. 20979 to 20987), only a 2 m long gun barrel was available. This limited the maximum achievable impact velocity to 250 m/s. In the second test series (test no. 21192 to 21202), the gun barrel was replaced by a 6 m long barrel enabling impact velocities of up to about 400 m/s. Figure 5.3 shows an image of the test facility with the 6 m gun barrel.

In the majority of the tests, a ring-shaped depression was cut into the polycarbonate sabot to form a predetermined breaking point during the impact. This resulted in a more defined destruction of the sabot preventing the sabot to hit the confinement multiple times due to a re-acceleration by the residual gas.

Development of a novel methodology for generating, characterizing and pressure testing of defined damaged glass specimens

Table 5.1: Test matrix for the generation and characterization of pre-damaged SLG specimens.

Test No.	Gun barrel length [m]	Propellant gas	Filling pressure [bar]	v_p [m/s]	Micro-CT	Phase-contrast imaging	Confined compression testing
20979	2	Air	1.0	69	X + X*	X*	X + X**
20980	2	Helium	16.0	257	X		X
20981	2	Air	1.0	70	X		X
20982	2	Air	1.0	73	X		X
20983	2	Air	6.5	186	X		X
20984	2	Air	4.0	146	X		X
20985	2	Air	4.0	149	X		X
20986	2	Helium	16.0	235	X		X
20987	2	Helium	16.0	203			
21192	6	Air	1.1	62			
21193	6	Air	1.3	85			
21194	6	Air	2.6	144	X	X	X
21195	6	Air	2.7	150			
21196	6	Air	9.6	258			
21197	6	Air	9.6	253			
21198	6	Helium	20.8	391			
21199	6	Helium	21.7	397			
21200	6	Helium	21.8	407	X	X	X
21201	6	Air	9.6	266	X	X	X
21202	6	Air	1.1	72	X	X	X

X* = additional micro-CT and phase-contrast imaging after the confined compression test

X** = additional second confined compression test after the phase-contrast imaging

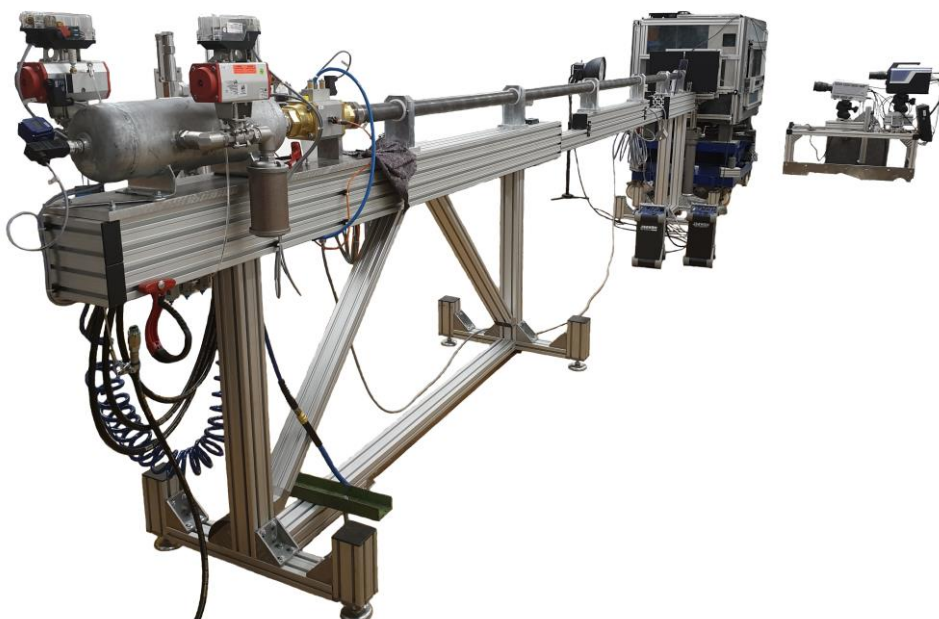


Figure 5.3: Single-stage gas gun with 6 m long barrel.

Development of a novel methodology for generating, characterizing and pressure testing of defined damaged glass specimens

To ensure that a plane shock wave is induced in the confinement and the SLG specimen, the confinement block was aligned parallel to the muzzle of the gun barrel. This was achieved by means of a movable "barrel extender" as illustrated in Figure 5.4. This is a massive steel cylinder, which fits smoothly around the gun barrel. After the confinement block is placed on the target holder, the barrel extender is slid until it is in contact with the surface of the confinement. The exact position of the confinement can then be adjusted. This procedure must be finished within several seconds since a layer of hot adhesive is put onto the target holder. After the adhesive has cooled off, the position of the confinement can no longer be adjusted. The fixation using the glue is necessary to avoid an acceleration of the confinement prior to the projectile impact, which can be induced by the preceding front of compressed air.

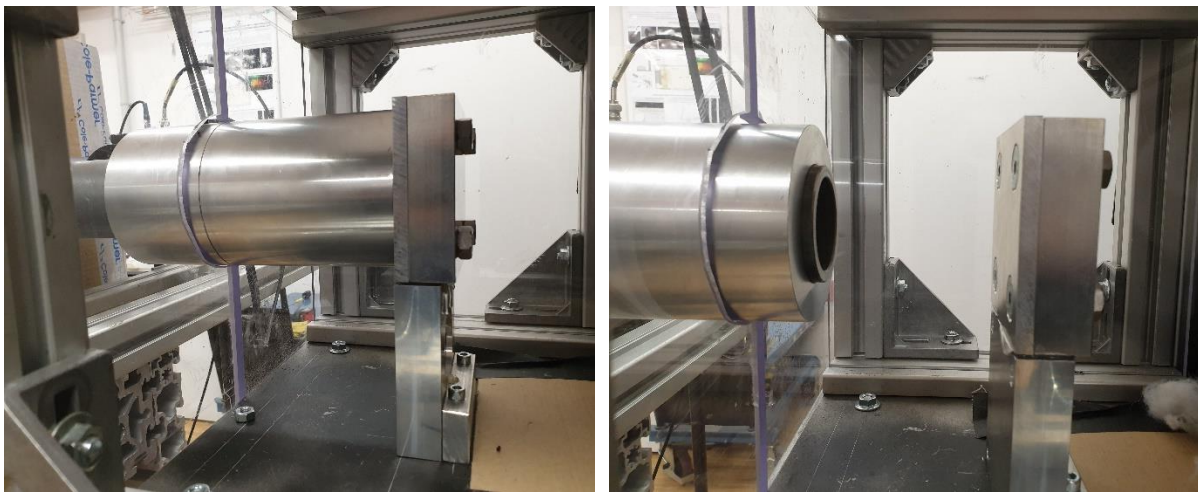


Figure 5.4: Alignment of the confinement by means of a movable "barrel extender": a massive steel cylinder is brought into contact with the surface of the confinement block (left); after the confinement is aligned, the barrel extender is pushed back onto the gun barrel (right). The confinement block is mounted onto the target holder by a layer of hot glue.

In all tests, the impact velocity of the projectile was measured by means of two light barriers, which were positioned near the muzzle of the gun barrel, where four small holes were drilled into the barrel. In addition, all tests were accompanied by high-speed video camera observation. On the one hand, the videos allow for a further measurement of the impact velocity. On the other hand, the videos provide essential information on the planarity of the impact and the movement of the projectile and the confinement after the impact. Figure 5.5 illustrates the setup of the high-speed cameras and the light barriers. The laser barriers are the four black cylinders next to the gun barrel. The two high-speed cameras are positioned one above the other at the side of the confinement. The impact is taking place inside a target box with polycarbonate windows in order to protect the cameras from possible flying fragments during the impact.

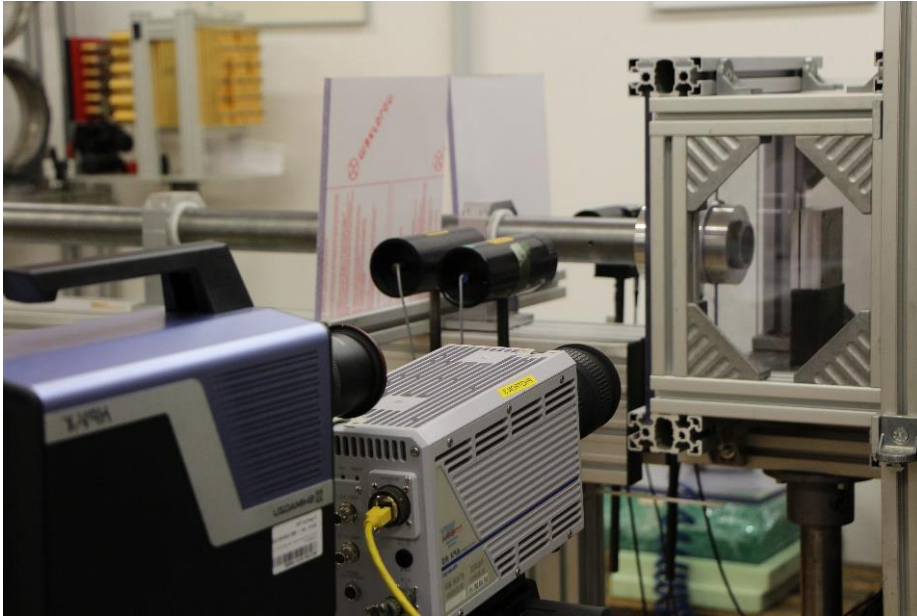


Figure 5.5: Setup of high-speed cameras and light barriers.

The two cameras allowed for recording images at two different orders of magnitude of frame rates. The top camera was a Shimadzu HPV-X with a maximum frame rate of 200,000 frames per second. The used settings enabled the recording of up to 128 images resulting in a total observation time of 640 μ s.

The bottom camera was a Photron high-speed camera with a lower frame rate of 15,000 frames per second. Depending on the settings, between 150 and 450 images were recorded in each test resulting in a total observation time of up to 30 ms.

After the impact, the confinement box was softly caught and stopped in a pile of rags to prevent additional damaging of the SLG during the deceleration.

5.2.2 Experimental results

In order to investigate if the impact of the projectile was sufficiently planar, the high-speed images of the Shimadzu HPV-X (200,000 fps), recorded around the time of the impact, are closely examined. Figure 5.6 illustrates a selection of six images recorded during the impact of test no. 21202. The high-speed photograph in the middle of the first row shows the projectile and the confinement 10 μ s before impact. The width of the gap between the surface of the projectile and the confinement is constant across the whole impact surface. Therefore, within the measurement uncertainty of the camera setup (0.36 mm pixel size), no discrepancies from a perfectly planar impact are observed. The symmetric deformation of the polycarbonate sabot in the subsequent images and the homogeneous illumination of the sabot caused by the impact flash (see photograph at 10 μ s after impact, Figure 5.6) also indicate that the impact was planar.

The videos also imply that the mounting of the confinement onto the target holder by means of the hot glue was strong enough to withstand the pressure of the preceding front of compressed air.

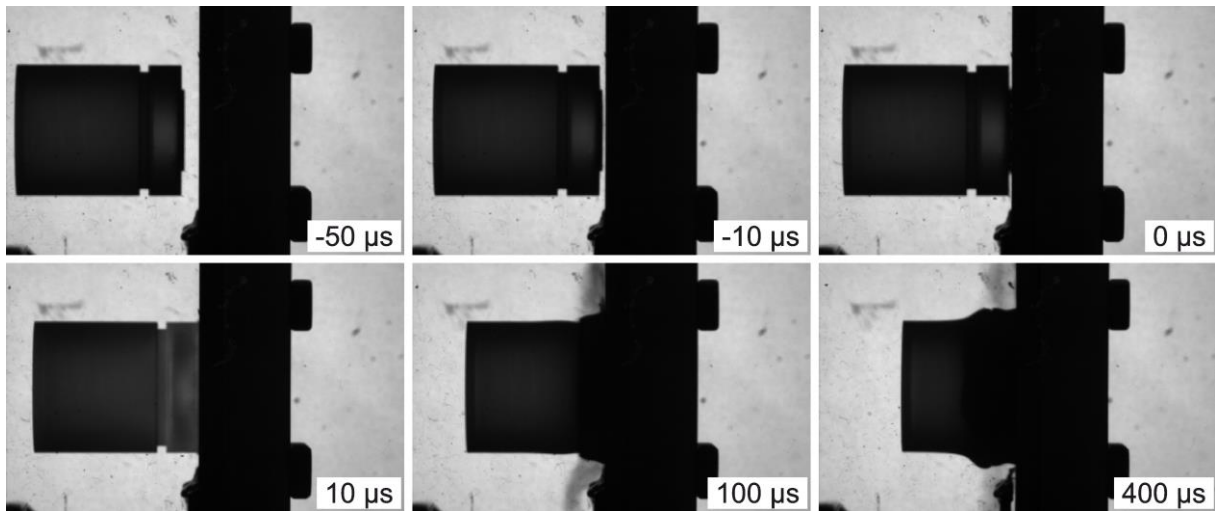


Figure 5.6: Selection of six Shimadzu HPV-X images from test #21202 ($v_p = 72$ m/s).

In all tests, which were selected for the further characterization procedures (cf. Table 5.1), no deviation from a planar impact is observed in the HPV-X images. This is illustrated in Figure 5.7 in which an image captured shortly before the impact is shown for each test. In three tests (21202, 20986 and 20980), the time of impact was not captured in the high-speed videos because of a misaligned trigger signal. In these cases, the image that was closest to the time of impact is depicted.

While the videos with the high capture rate provide crucial information on the planarity of the impact, they do not show the movement of the projectile and the confinement several milliseconds after the impact. The post-impact behavior is therefore analyzed in the high-speed videos of the Photron camera, which had a total observation time of up to 30 ms.

Figure 5.8 shows a selection of six Photron images from test no. 21202. In this test, the impact velocity was 72 m/s. Since the absolute point of time of the images is of no further importance, the denoted times are arbitrarily set to be 0 ms at the last image before impact. In the illustrated test, the polycarbonate sabot did not have a predetermined breaking point by means of a ring-shaped depression, as mentioned above. This resulted in an undefined breakage of the sabot directly after the impact (cf. image at $t = 1$ ms). The cleaved remains of the sabot were then accelerated backwards until they were pushed again into the direction of the confinement by the residual gas after 7 ms. The aluminum plate transferred its kinetic energy completely into the confinement during the impact and stood almost stationary afterwards (cf. images between $t = 1$ ms and $t = 10$ ms).

The confinement block was quickly detached from the layer of glue within the first few milliseconds after the impact and accelerated to the right. Outside of the field of view of the camera, the confinement was later softly caught and stopped in a pile of rags to prevent additional damaging of the SLG during the deceleration.

As intended, both the sabot and the aluminum plate only impacted the confinement block once. Multiple impacts due to a re-acceleration by the residual gas could therefore be prevented.

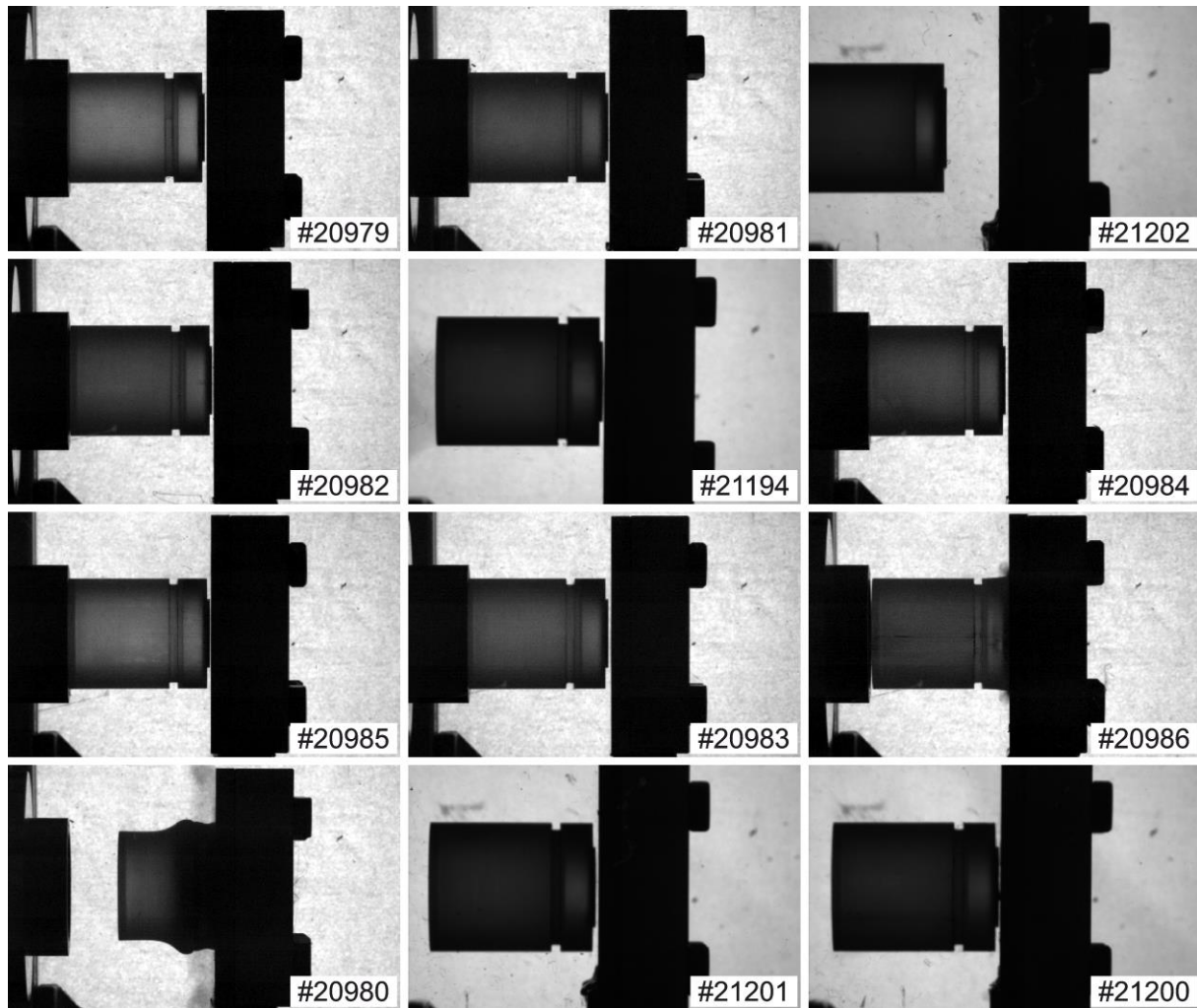


Figure 5.7: Compilation of HPV-X images from all tests with further characterization procedures. The images illustrate the planarity of the projectile impact. If available, an image captured shortly before the impact is shown. In test no. 21202, 20986 and 20980 the time of impact was not captured in the high-speed videos because of a misaligned trigger signal. The tests are arranged by rising impact velocities from left to right and top to bottom.

For comparison, a selection of six Photron images from a test with a higher impact velocity of 266 m/s is illustrated in Figure 5.9. In this case, the polycarbonate sabot broke into two defined parts during the impact due to the predetermined breaking point. Afterwards, the larger part was accelerated backwards, while the front part kept flying closely to the confinement. The aluminum plate remained in contact with the confinement after the impact. This led to further contacts between the front part of the sabot and the aluminum plate with the confinement (e.g. at $t = 9$ ms). However, since these parts were flying with almost the same velocity, these contacts are marginal and are not expected to increase the damage of SLG specimen any further.

The confinement was accelerated significantly faster as it was the case at the lower impact velocity (Figure 5.8) leaving the field of view already after 9 ms.

Development of a novel methodology for generating, characterizing and pressure testing of defined damaged glass specimens

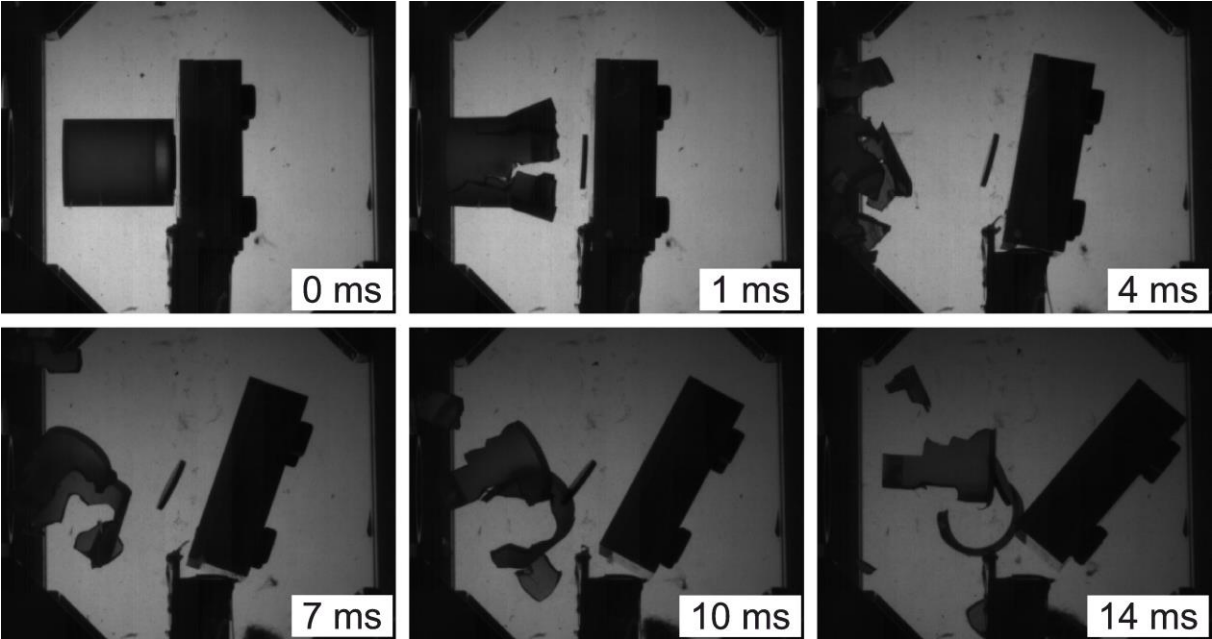


Figure 5.8: Selection of six Photron images from test #21202 ($v_p = 72$ m/s).

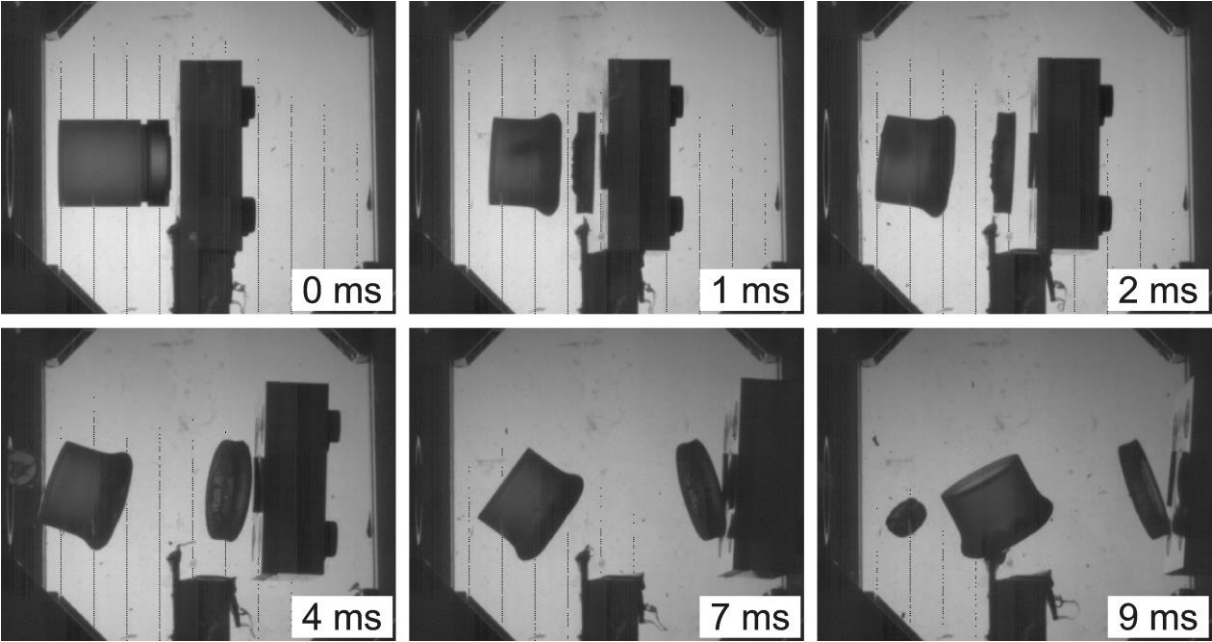


Figure 5.9: Selection of six Photron images from test #21201 ($v_p = 266$ m/s).

After the impact test, the confinement was recovered from the pile of rags and carefully disassembled. Figure 5.10 shows a picture of the recovered sabot and the aluminum plate on the left side. On the right side, a picture of the recovered confinement after the removal of the cover plate is displayed. The pre-damaged SLG cylinder is visible in the center of the confinement appearing dark since the internal crack surfaces diffuse the light.

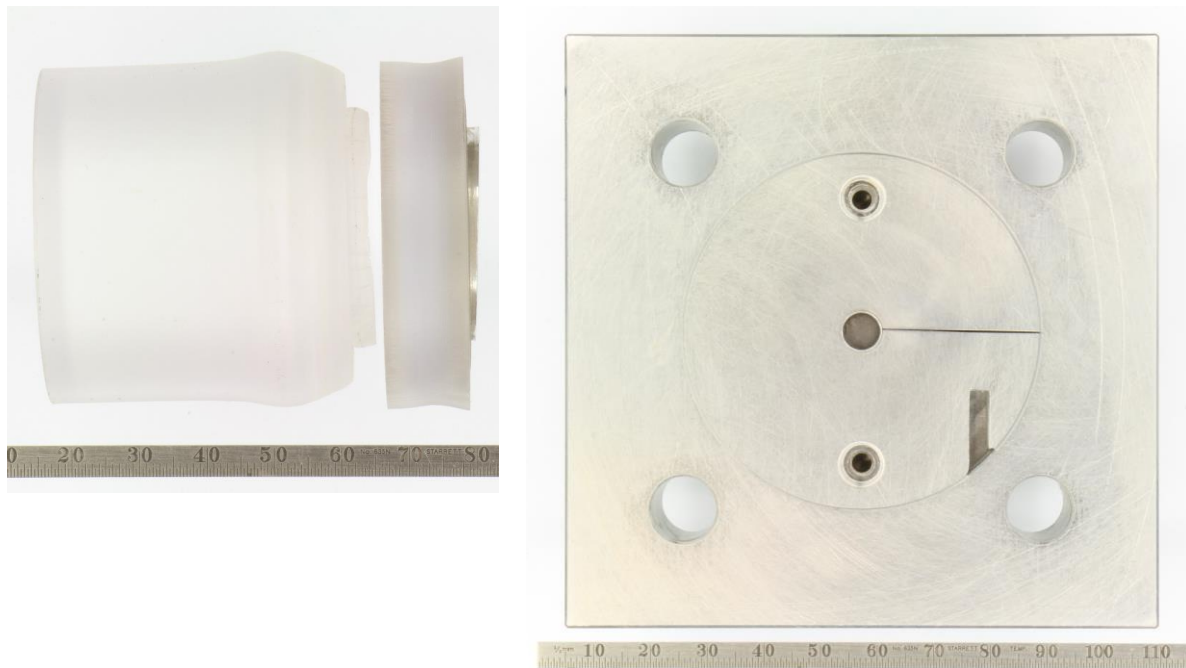


Figure 5.10: Recovered polycarbonate sabot and aluminum plate (left picture) and recovered confinement after the removal of the cover plate (right picture) from test #20987 ($v_p = 203$ m/s).

In order to get a first estimate of the generated damage, the recovered SLG specimens were placed on top of a bright light source and transmitted light images were taken. Figure 5.11 shows the images of the twelve specimens, which have been selected for the further characterization procedures. The crack planes inside the SLG specimens diffract the transmitted light leading to a darker appearance of regions with a higher crack density. The images are arranged by rising impact velocities from left to right and top to bottom. At the lowest impact velocities of about 70 m/s, only a few crack planes are visible. Large areas appear bright indicating that the impact generated only a coarse fragmentation. At higher impact velocities, the amount of visible crack planes significantly increases. At the highest velocities, above 250 m/s (pictures in the bottom row), the SLG specimens are strongly fragmented and a dense network of crack planes is visible.

Although these transmitted light images clearly show the dependence of the impact velocity on the generated degree of damage, they are not suitable for a systematic quantification. The amount of the transmitted light is strongly dependent on the position and orientation of the crack planes as well as the position of the light source and the camera settings. Furthermore, in some cases, a thin layer of aluminum residues attached at the SLG surface obstructed the light transmission.

Development of a novel methodology for generating, characterizing and pressure testing of defined damaged glass specimens

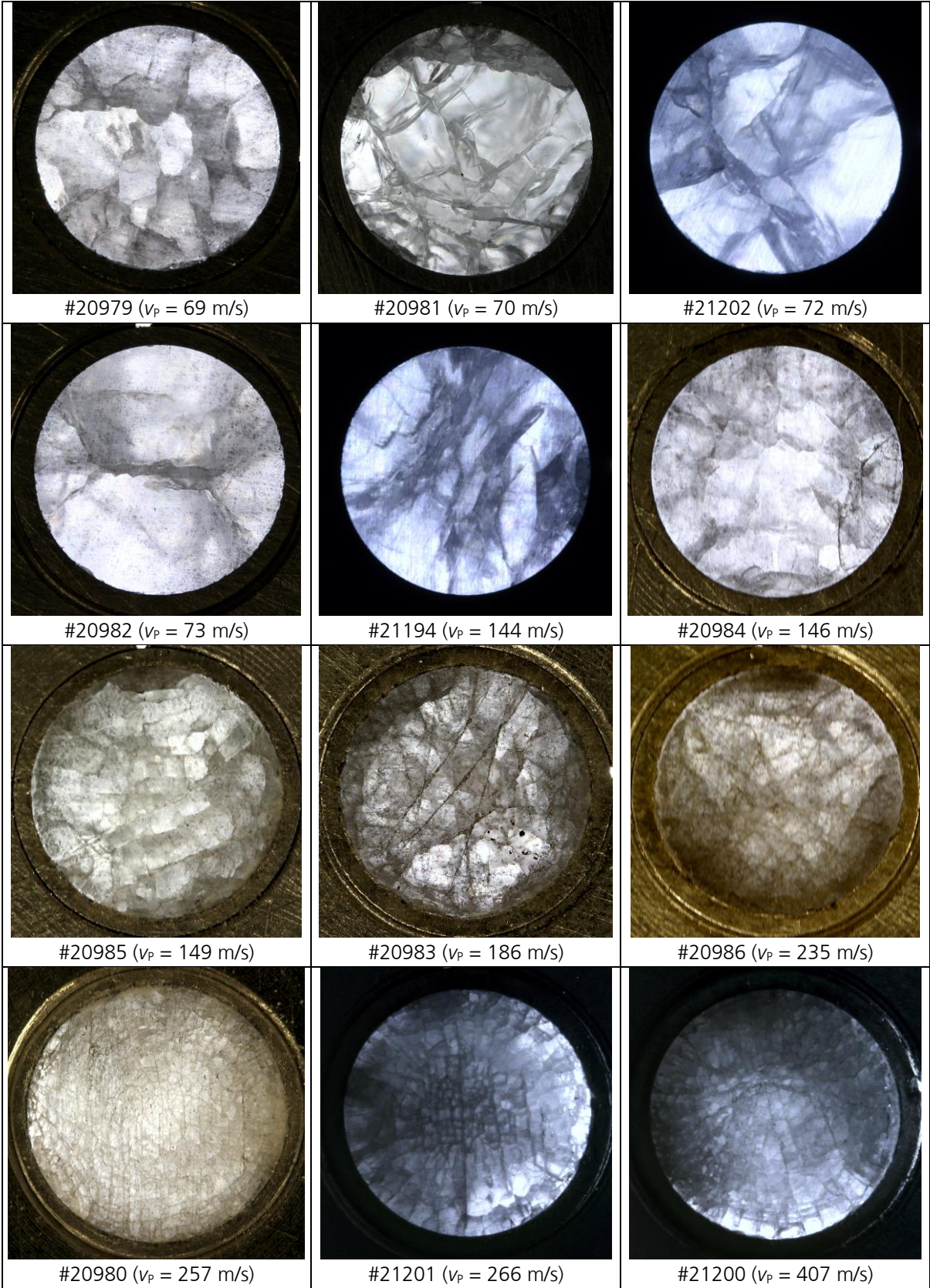


Figure 5.11: Transmitted light images of all test specimens with further characterization procedures. At higher impact velocities (v_p), the amount of visible crack planes significantly increases.

In order to gain a direct insight into the damaged SLG and visualize the positions and orientations of the crack planes, a microsection of one specimen was made. This was done for the specimen of test no. 20987, which has been impacted at $v_p = 203$ m/s. The damaged SLG cylinder was taken off the aluminum sleeve and covered with transparent adhesive. After the adhesive had infiltrated the cavities and had been cured, one half of the specimen was polished down. The result of a transmitted light image of this microsection is illustrated in the left image of Figure 5.12. The fracture planes appear dark spreading over the whole specimen. Although fewer cracks are visible on the left side of the central region. The surface, which was facing into the direction of the impact, is located at the upper margin of the picture. At the opposite side of the specimen, at the bottom of the picture, a heavily fractured layer of glass with a thickness of about 0.2 mm is missing. This part was lost during the extraction from the aluminum sleeve due to the severe fragmentation in this region and the related loss of integrity. The black circles below the specimen are cavities of air trapped inside the adhesive.

The presented method of taking a microsection enables a better visualization of the pre-damage, however, the specimen is destroyed in the process making a characterization of the residual strength in a subsequent pressure test impossible. Furthermore, for a defined quantification of the whole volume, other methods are required.

A more advantageous method is therefore a contactless and non-destructive determination of the total crack volume by means of X-ray CT and PCI. These characterization techniques are presented in the next sections.

For comparison, an exemplary result of the PCI is illustrated in the right image of Figure 5.12. The image shows the central y-slice of the PCI from test specimen #20201 that was pre-damaged at $v_p = 266$ m/s. Both illustrated specimens have a similar degree of pre-damage. In the PCI, the cracks appear as dark, fine lines, while the intact glass appears as brighter areas. In both pictures, the density of horizontal crack planes is high at a distance of about 1 mm to the top surface. In the central part, larger regions with only few crack planes are present. Near the bottom surface, the crack density is significantly higher than in the central and upper regions and a large number of horizontal crack planes are apparent.

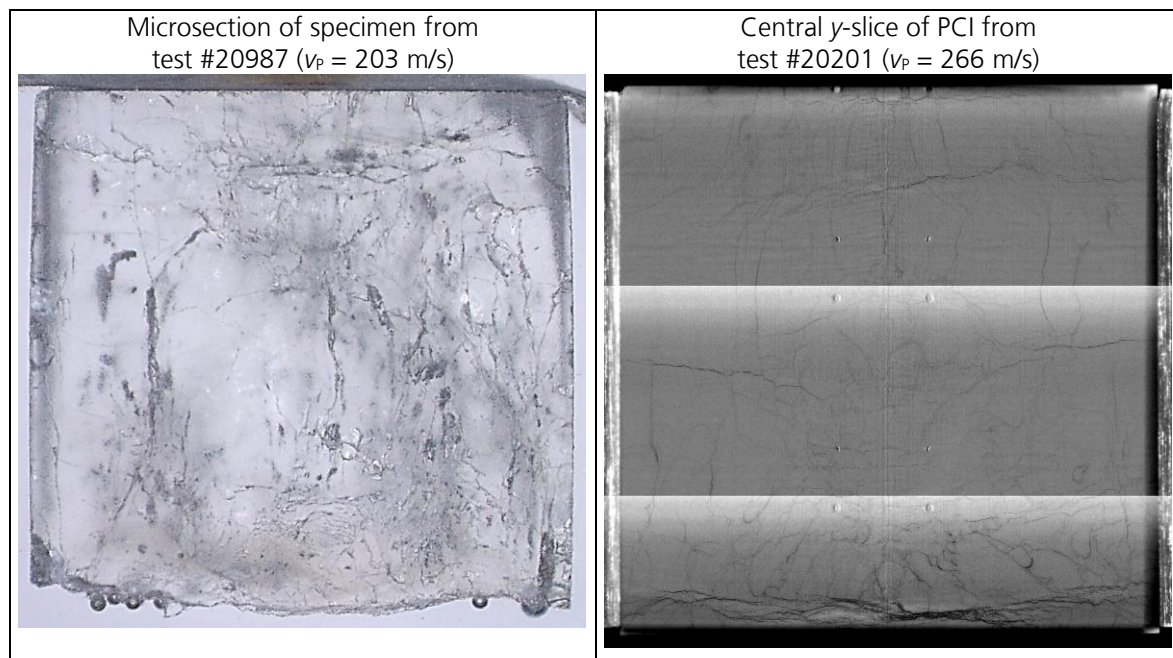


Figure 5.12: Comparison of a microsection and a phase-contrast image for two specimens with similar degree of pre-damage: The left picture shows a microsection through the center of test specimen #20987 ($v_p = 203$ m/s); the right picture shows the central y-slice of the PCI from test specimen #20201 ($v_p = 266$ m/s).

5.3 Characterization of damage by means of X-ray micro-CT and phase-contrast imaging

In the previous section, the new method for the generation of a defined pre-damage inside small SLG cylinders is outlined. The subsequent procedure of quantifying the degree of damage is described in this section. The key innovation is a contactless, non-destructive damage characterization by means of X-ray CT prior to the pressure testing. As far as the author knows, this is the first time that this characterization technique has been used to quantify the degree of damage of glass specimens.

5.3.1 Principles of the CT methods

X-ray CT is a method of generating image data by means of X-ray transmission. The objective of the CT is to create a three-dimensional image of a specimen. One method used in this work is conventional absorption-based X-ray imaging in the form of a micro-CT system. Here, an X-ray tube generates bremsstrahlung covering a broad continuum of energies (polychromatic beams). The cone of X-ray beams penetrates the specimen and is spatially detected by detector panels behind the specimen. Each beam is attenuated based on the absorption properties of the passed material resulting in a specific intensity in the detector. This creates a two-dimensional projection of the specimen referred to as "projection image". If multiple projections (typically between 800 and 1200) are generated from different perspectives, a three-dimensional image can be reconstructed. The different projections are created by an incremental rotation of the specimen. For the reconstruction, the specimen is virtually divided into a matrix of voxels. Using the information of the different projections, the level of attenuation in each voxel is calculated and represented by a gray scale value in the resulting 3D-representation. To allow for a visualization of the three-dimensional information, the results are presented as two-dimensional slices in this work.

Several aspects can lower the quality of the resulting reconstructed slice images. One aspect is the so-called probabilistic noise leading to a graininess in the resulting images. This noise is caused by the probabilistic nature of the physical effects during the scans. For example, the generation of the X-ray photons and the interaction of the photons with the specimen and the detector follow Poisson or binomial distributions. In order to reduce the noise, each projection is measured several times and then an averaged image is calculated.

Another aspect is the so-called beam-hardening. The attenuation of the X-ray beams is not only dependent on the absorption properties of the passed material, but also on the energy of the X-rays. The lower the energy of a photon is, the more it gets attenuated when passing through the same material. As a result, the effective energy of a polychromatic X-ray beam gradually increases during the penetration process (beam-hardening) [235]. In the reconstructed image, this causes the material deeper inside the specimen to appear darker as the surrounding material with the same absorption properties. The generated artificial gray scale gradients are referred to as beam-hardening artifacts.

Noise and beam-hardening are not the only artifacts that can be present in the reconstructed images. Common other artifacts are for example line artifacts and ring artifacts [236] [237]. In the presented work, especially the ring artifacts are particularly evident. These artifacts are induced by errors or drifts in single elements of the detector array. A single element of the array detects all beams passing through the specimen at a specific distance from the rotation axis. In the reconstructed image, the crossing points of these beams are located on a ring around the

rotation axis. Therefore, a drift of one detector element creates a ring-shaped structure with shifted gray scale values.

An in-depth description of the principles is provided for example by Buzug [238] or Goldman [239] [240].

The second illustration method for the damage characterization used in this work is the PCI. This method is superior to the conventional absorption-based imaging for the visualization of edges or cracks in the specimens. The PCI enhances the contrast of interfaces between the features inside the specimen (edge enhancement). The method takes advantage of the circumstances that the X-ray phases change as they pass through the specimen. The different wave fronts interfere and overlap with each other influencing the measured intensity at the detector. As the absorption and the diffraction of the beams are energy-dependent, an essential requirement for the PCI method is a monochromatic X-ray source.

For a more in-depth description of the PCI method, the reader is referred e.g. to [241] [242] [108].

5.3.2 Experimental facilities

The tomographic experiments were conducted at two different facilities. On the one hand, high-resolution absorption-based X-ray CTs were carried out at the Fraunhofer EMI by means of a micro-CT system. On the other hand, PCI measurements were conducted at a synchrotron beamline of the Paul Scherrer Institut (PSI).

Conventional absorption radiography with a micro-CT system:

The used micro-CT system is an in-house system of the EMI, which has been developed and manufactured by the Fraunhofer EZRT in cooperation with the company MacroScience Technology GmbH. The system generates polychromatic X-rays with a bremsstrahlung spectrum specific to the material of the X-ray tube. For the examined glass specimens, the micro-focus-source was operated at 80 keV source voltage with an operating current of 75 μA . The illumination time for a single image was set to 4 s. For each specimen a total of 1200 projections were recorded each averaged over 8 images. This yields a total illumination time of more than 10 hours per specimen. With these settings, a voxel resolution in the range between 3.6 μm and 3.8 μm was achieved. Figure 5.14 shows a picture of the experimental setup within the micro-CT system. For each specimen, a stack of nearly 1800 TIF files was reconstructed. Each file represents a horizontal slice of the scanned specimen, containing roughly 1800 x 1800 voxels with 16 bit gray scale values. The resulting data size for a complete scan of one specimen is about 8 GB. This comparatively low data size enables short analysis times.

However, with the resulting images of the conventional absorption radiography, a quantitative evaluation of the degree of damage is very difficult. The analyzed specimens contain fine crack structures that exhibit relatively low density differences. In addition, the aluminum sleeve surrounding the glass cylinder lowers the achievable contrast. Furthermore, distinct beam-hardening and ring artifacts are present obscuring the crack structures.

Phase-contrast-imaging at a synchrotron beamline:

In order to take advantage of the edge enhancing properties of the PCI, additional experiments at a beam line of the PSI were conducted as a supplementary method. The measurements were performed at the TOMCAT [243] (Tomographic Microscopy and Coherent rAdiology experimenTs) X02DA-beamline of the SLS synchrotron (Swiss Light Source). The SLS features a 2.4 GeV electron storage ring of 288 m circumference providing continuous high flux, high coherency, monochromatic X-rays [244]. Figure 5.13 shows a picture of the PSI with the SLS in front.

The X02DA-beamline offers absorption-based imaging as well as PCI with achievable isotropic voxel sizes between 0.16 to 11 μm in an energy range between 8 to 45 keV. The generation of the phase-contrast images is achieved by means of simple edge enhancement techniques based on propagation [245] [246] or by grating interferometry [247]. The reconstruction of the 3D tomographic datasets from the recorded 2D projections is performed by a software based on Fourier methods [248] [249].

For the present work, a 360°-eccentric rotation was used in order to get a horizontal field of view of about 8 mm. The vertical field of view is energy dependent and was about 2.4 mm with a set energy between 30 and 40 keV. With these settings, a voxel resolution of 1.65 μm was achieved. Each specimen was scanned at three different vertical positions in order to cover the total height of 6 mm. Figure 5.15 shows a picture of the experimental setup within the beamline. The specimens were placed on a movable and rotatable specimen holder as shown enlarged on the right side of the figure.

Each scan had a measurement time of about 20 min resulting in a stack of 1462 reconstructed horizontal slices. The images were provided as 32 bit gray scale images containing 4201 x 4201 voxels. The resulting data size for a complete CT reconstruction of one specimen is about 288 GB as opposed to the 8 GB of the micro-CT at EMI.

The PCI data is 36 times larger than the micro-CT leading to a much more time-consuming analysis. However, the higher resolution in combination with the edge enhancing reconstruction allowed for a significantly more detailed evaluation of the degree of pre-damage.

Development of a novel methodology for generating, characterizing and pressure testing of defined damaged glass specimens

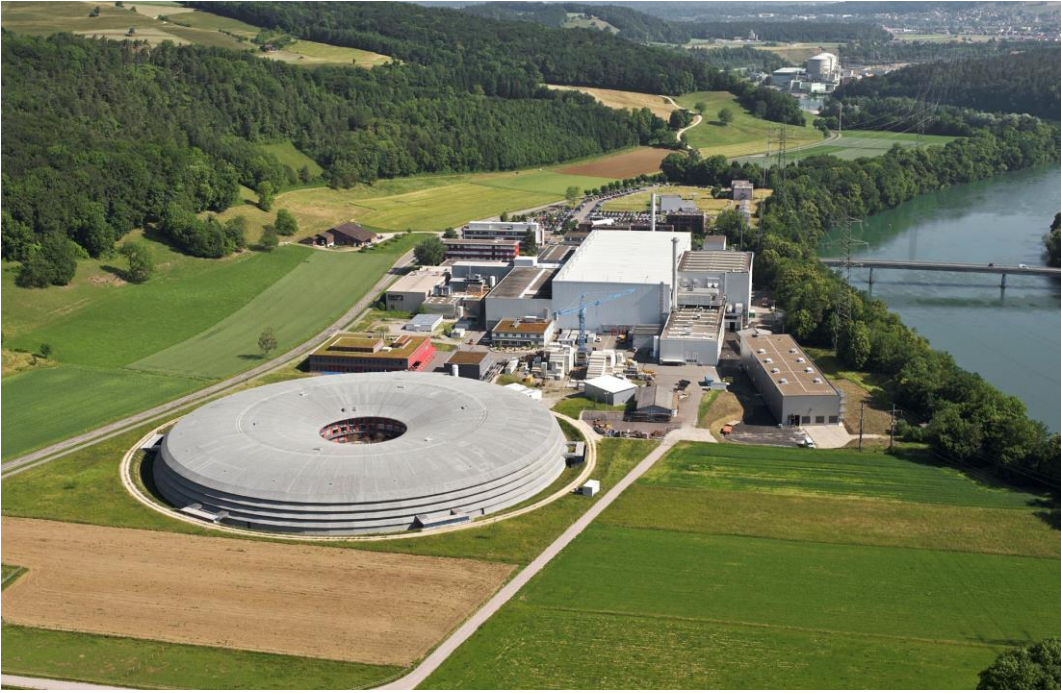


Figure 5.13: Aerial view of the Paul Scherrer Institut with the SLS in front (external source [250]).

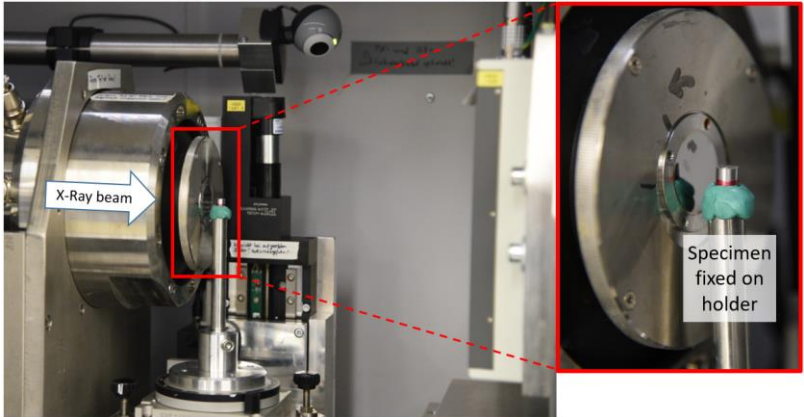


Figure 5.14: Photograph of the experimental setup in the micro-CT at the EMI.

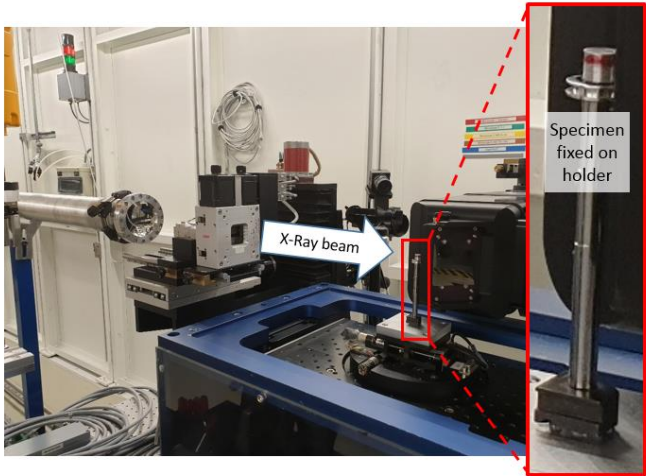


Figure 5.15: Photograph of the experimental setup at the tomography beamline TOMCAT at the PSI.

5.3.3 Image processing and analysis of cracks

In the previous section, it is outlined how the tomographic data was obtained. In the next step of the characterization, the data is processed and analyzed in order to quantify the degree of damage. This is done in detail only for the phase-contrast images. The quality of the micro-CTs is insufficient to quantify the degree of damage by means of the segmentation algorithms. However, the results of the micro-CT are compared to the phase-contrast images for a visual comparison in section 5.3.3.6.

The cracks inside the pre-damaged glass specimens appear as a network of dark voxels in the reconstructed tomograms. However, a crack plane, which was originally smooth and continuous, can be disconnected and disturbed by bright voxels caused due to reconstruction artifacts in the tomogram. In addition, the intensity of the cracks in the tomogram can vary strongly depending only on their position. These observations are due to several reasons. The noise of the X-ray detectors can be a large issue, if the ratio of the real measurement signal and the noise signal is too low. Furthermore, artifacts resulting from the reconstruction process can obscure the real crack structures or can mistakenly be identified as cracks. In addition, some reconstruction artifacts, like e.g. beam hardening, can generate significant intensity gradients within the final tomogram. Besides that, the size of some cracks can partially or completely exceed the resolution capacity of the X-ray detectors.

An exemplarily tomogram reconstructed from the synchrotron CT is illustrated in Figure 5.16. The figure displays a virtual vertical cut through the center of the pre-damaged SLG specimen from test no. 21202. At each position, the gray scale value of the voxel is connected to the X-ray absorbing properties of the related material. The damage inside the SLG manifests as air-filled cracks, which appear noticeably darker as the surrounding material. The aluminum sleeve appears as bright voxels on the left and right side of the image. In addition to the dark cracks, some other dark structures are visible near the horizontal rotation axis in the center of the cylinder. These are mainly tomographic artifacts, which are generated during the reconstruction process.

Since the vertical field of view of the synchrotron detector is not large enough to fit in the whole specimen, the final image is merged from three individual CT scans. Each scan can cover a height of up to 2.4 mm, which allows for a small overlap between adjacent scans. These overlaps ensure that the scans comprise the whole specimen and they are manually removed during the subsequent merging process.

The gray scale value distribution can differ significantly between the different scans. In addition, there is a significant gray scale gradient within each scan, causing the voxels in the upper region of the tomogram to be much brighter than the other voxels. These circumstances impose a major challenge for an automated quantification of the degree of damage. However, a systematic analysis process has been developed as part of this work, which allows for a semi-automated quantification.

The plausibility of the results of the semi-automated quantification is checked for each specimen by a visual comparison of the original tomogram and the separated crack patterns. This additional quality check is carried out since the human eye is specialized in finding patterns and is therefore able to identify the crack patterns more successfully than the automated algorithms.

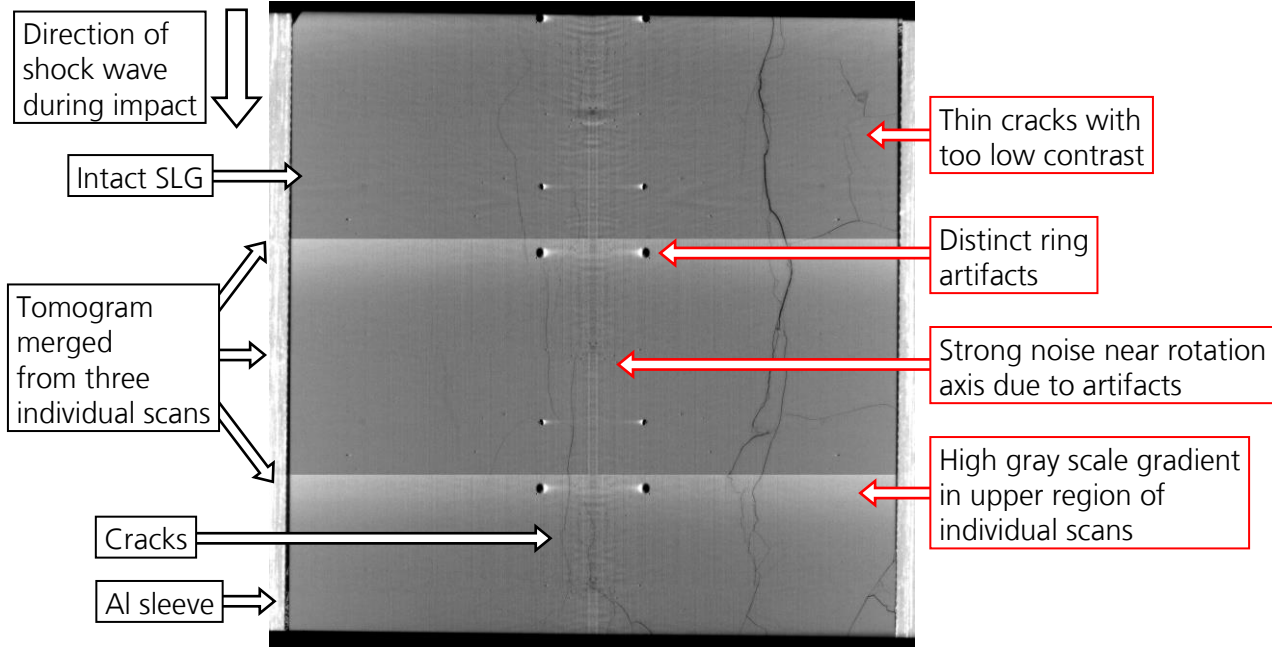


Figure 5.16: Exemplary tomogram reconstructed from synchrotron CT by means of PCI (specimen no. 21202); for the characterization of the degree of damage, the dark crack patterns have to be identified and separated; the separation process is challenging due to reconstruction artifacts, gray scale gradients and limited spatial resolution.

5.3.3.1 Analysis Software

In order to characterize the degree of damage of the pre-damaged SLG specimens, the cracks have to be identified and separated in the tomograms. This process is challenging due to the aforementioned issues, like reconstruction artifacts, gray scale gradients and noise. Therefore, an analysis software is required, which allows for 3D image processing as well as advanced segmentation techniques.

These requirements are perfectly fulfilled by the software tool “Mango” (Medial axis and network generation), which has been developed by the Australian National University (ANU) in collaboration with the German Friedrich-Alexander-Universität. Mango allows for a high parallelization of tasks, which is crucial for the processing of the 288 GB large synchrotron data sets. Mango is specially designed to handle tomographic data from X-ray tomography [251] [252]. The software is running on the Fujitsu Primergy cluster “Raijin”, which is located at the campus of the ANU and managed by the high performance computing center NCI (National Computational Infrastructure). Raijin was officially launched in 2013 being one of the most powerful computer facilities in the world at that time. It features a main memory of 160 TB and a disk storage of 10,000 TB. With more than 57,000 processor cores, it can provide a peak performance of $1.2 \cdot 10^{15}$ floating point operations per second [253].

Mango can be accessed through the browser based interface software “WebMango” allowing one to set up and start runs remotely on Raijin. The data files used by Mango are mainly NetCDF files (Network Common Data Format) consisting of three-dimensional image data. However, the software also supports the upload and conversion of other formats, like TIFF or PNG.

Within the scope of this work, the access to Mango was granted as a collaborative arrangement with the department of applied mathematics of the ANU.

5.3.3.2 Image processing

Before the cracks can be identified by means of a segmentation technique, the original CT images have to be preprocessed. For this purpose, the image processing tools of Mango are used to prepare the images by removing reconstruction artifacts and unnecessary information. Figure 5.17 illustrates an entire process chain of the image processing exemplarily for the specimen of test no. 21202.

In step 1, the stack of TIFF files is imported into Mango and converted into NetCDF files. The original TIFF files are 32 bit float grayscale images and have to be converted into 16 bit unsigned integer grayscale images. Therefore, the $\sim 3.4 \cdot 10^{38}$ gray values have to be scaled down to $(2^{16} - 1) = 65,535$ values. This is achieved by manually applying a shift and a multiplication factor. In order to use the down scaled value range most efficiently, unimportant information has to be removed in this process. For all histograms, a gray scale range of $\min_{\text{float}} = -1.0 \cdot 10^{-6}$ to $\max_{\text{float}} = 3.0 \cdot 10^{-6}$ is evaluated. All other values do not appear inside the specimens and can be removed. Therefore, the data has to be shifted by \min_{float} first and then scaled by a factor of $65,535 / (\max_{\text{float}} - \min_{\text{float}}) = 1.638375 \cdot 10^{10}$. In the resulting images a gray scale value of 0 is represented by a black voxel and 65535 corresponds to a white voxel.

Development of a novel methodology for generating, characterizing and pressure testing of defined damaged glass specimens

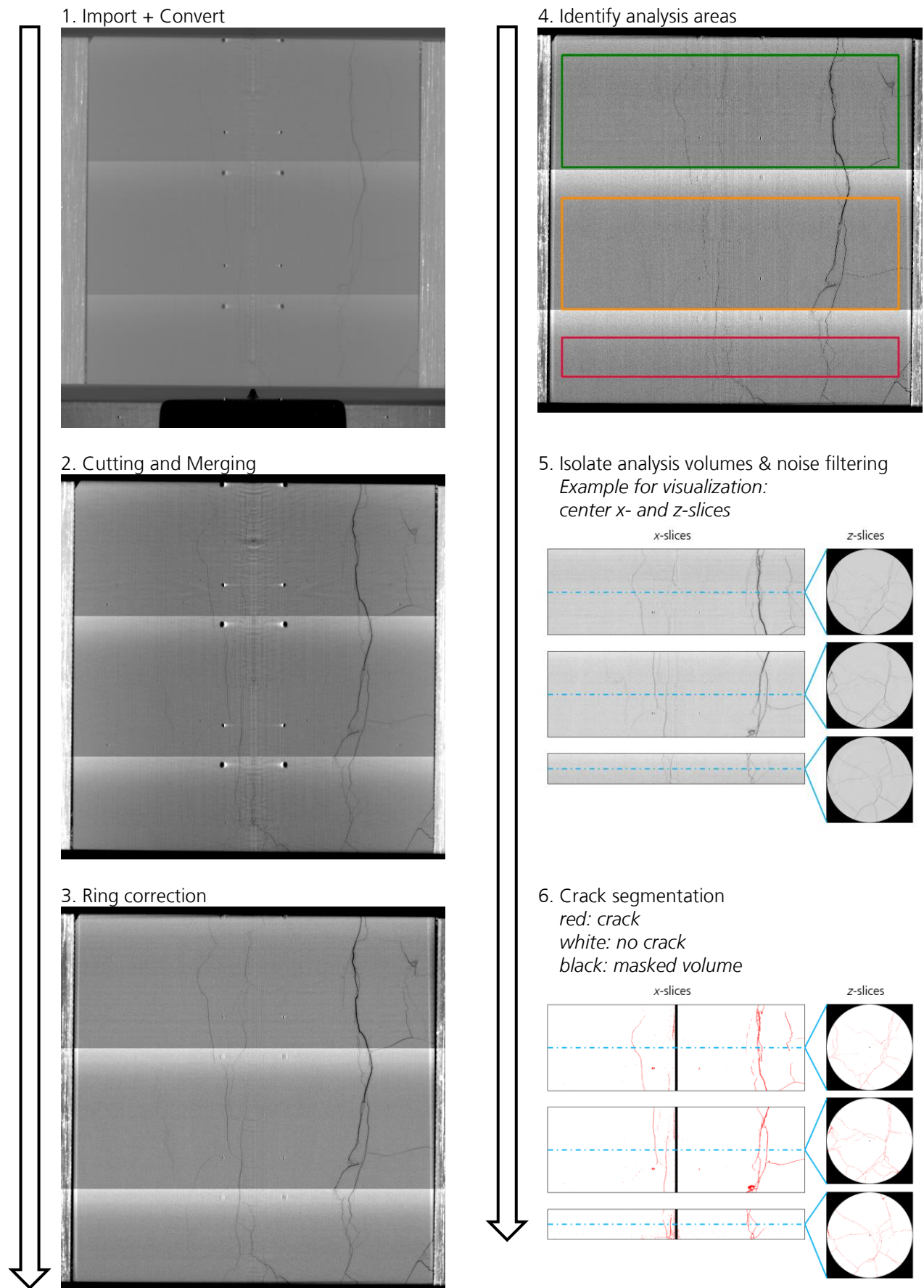


Figure 5.17: CT imaging process of test no. 21202 (steps 1 to 4 display the center x-slice).

In step 2, overlapping areas are removed and the resulting images get merged. This is necessary since the imported tomogram consists of three overlapping stacks of images each belonging to a different scanning process.

In step 3, a ring correction is applied to remove the majority of the tomographic artifacts. For this purpose, a correction algorithm of Mango is used. The algorithm calculates the mean gray scale value of each ring and normalizes this value to the mean gray scale value of the whole sample. Here, a ring is defined as the set of all voxels in one z-slice, which have an equal distance to the rotation axis. The input parameters for the correction algorithm are the rotation axis, a maximum radius and optional gray scale thresholds.

The rotation axis of the ring artifacts corresponds to the rotation axis of the specimen holder during the X-ray scan. This axis is not identical with the symmetry axis of the cylindrical glass specimen or the aluminum sleeve and has therefore to be determined manually for each test individually. The maximum radius is set to 2000 voxels (= 3.3 mm) to ensure that the whole specimen is captured. The optional gray scale thresholds can be used to exclude voxels with too high or too low gray values from the calculation of the mean values. However, the best result is achieved without setting any threshold.

This is exemplarily illustrated in Figure 5.18. The top row shows a z-slice of the tomogram from test no. 21201 and the bottom row shows an x-slice zoomed in on a cross section of a large ring artifact. The left column depicts the original tomogram containing many dark ring artifacts in the central region of the z-slice. The middle column shows the same slices after applying the ring correction with a maximum threshold of 36,000. In this case, only voxels that have a gray value below 36,000 are used for the calculation of the normalization values. Most of the artifacts get removed, but the bright region of the artifact in the x-slice remains.

The right column shows the same slices after the ring correction without a threshold. In this case, the bright voxels are included during the correction. This yields a better result since the bright artifacts also vanish and more cracks can be observed. However, a small disadvantage is that a dark halo can emerge in the fringe areas of the specimen, as it can be seen in the z-slice of the right column. The halo is a result of the offset between the rotation axis of the rings and the specimen. Because of that, rings in the fringe area contain not only voxels from the glass specimen, but also voxels from the aluminum sleeve. Since the aluminum voxels are much brighter, the mean gray scale value of these rings is too high resulting in much darker voxels after the correction. However, since the halo region can be easily excluded from the analysis area, the method of setting no thresholds is preferred in the following.

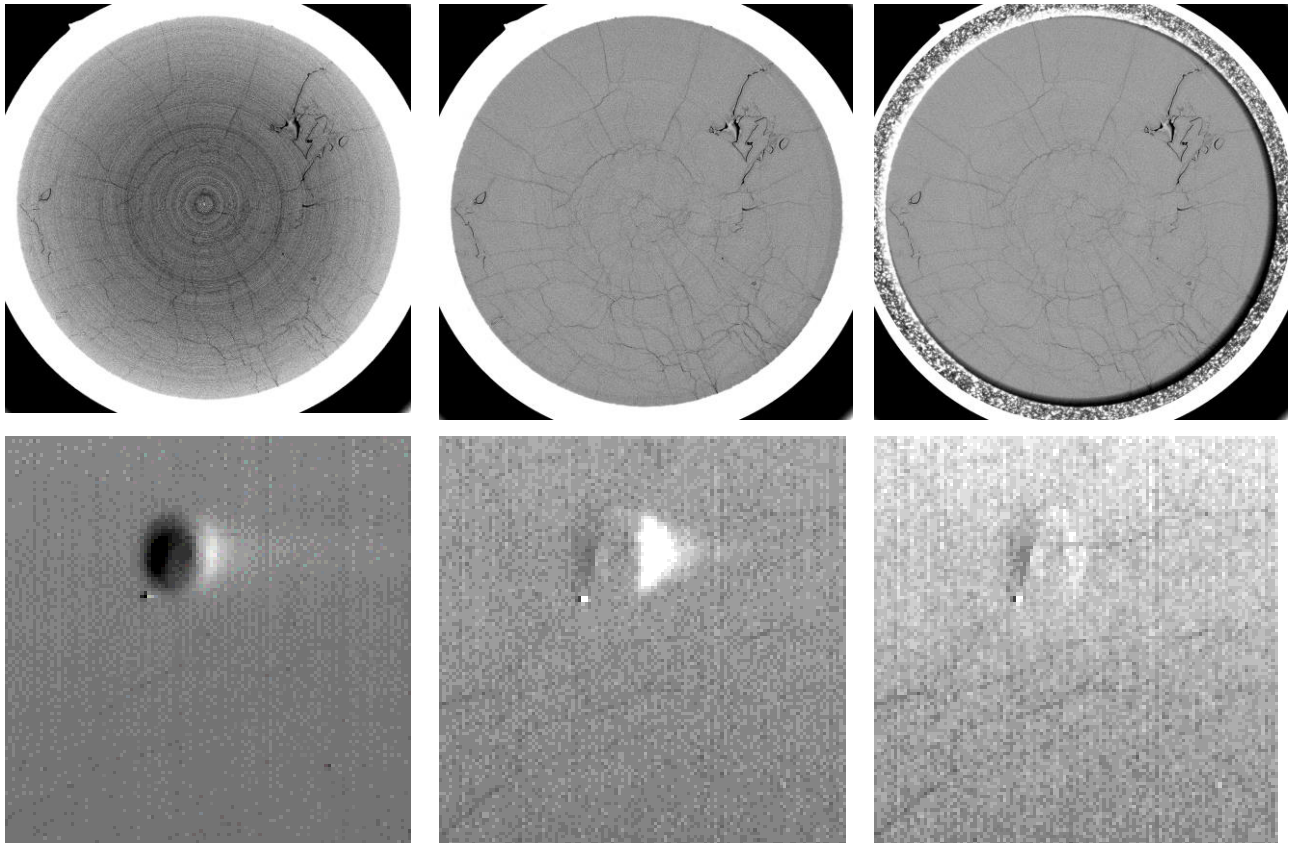


Figure 5.18: Influence of a threshold in the ring correction algorithm: The top row shows a z-slice of the tomogram from test no. 21201 and the bottom row shows an x-slice zoomed on a cross section of a large ring artifact. The left column depicts the original tomogram; the middle column shows the same slices after applying the ring correction with a threshold of 36,000; the right column shows the same slices after the ring correction without a threshold.

In step 4 of the analysis process, the analysis volumes are identified (colored rectangles in the top right image of Figure 5.17). Only the damage inside these volumes is analyzed and quantified later. The rest of the specimen volume is being neglected. The degree of damage of the total specimen is then extrapolated from the analysis volumes. Therefore, the volumes have to be determined in such a way that they are representative of the whole specimen. This means that they have to be sufficiently large to cover a majority of the total specimen volume. In addition, the crack density inside the analysis volumes must not differ significantly from the residual specimen volume.

There are two reasons for the necessity of the analysis volumes as opposed to the analysis of the total specimen volume. On the one hand, there is a significant gray scale gradient in vertical direction within the individual scans of each specimen, as illustrated in Figure 5.16. On the other hand, most images exhibit a dark artifact halo in the fringe areas after the ring correction, as described above (top right picture in Figure 5.18).

To ensure comparability between the analyses of the different specimens, the size and relative positions of the analysis volumes are chosen to be identical. This is realized by determining the largest mainly artifact-free volumes in each specimen first. Afterwards, the analysis volumes are defined to be the partial volumes, which all specimens have in common. Table 5.2 provides a summary of the evaluated analysis volumes. All volumes have a diameter of 5.57 mm. The top volume has a height of 1.86 mm and is 0.32 mm away from the top surface of the specimen, which is facing into the direction of the impact.

Development of a novel methodology for generating, characterizing and pressure testing of defined damaged glass specimens

positioned 2.69 mm away from the top surface. Finally, the bottom volume is only 0.65 mm high, positioned 0.46 mm away from the bottom surface.

Table 5.2: Definition of analysis volumes.

Volume	Height [mm]	Definition of area position		Position of z-slice for overview
		Distance [mm]	from	Distance from top surface [mm]
Top	1.86	0.32	top surface	1.25
Middle	1.85	2.69	top surface	3.62
Bottom	0.65	0.46	bottom surface	5.3 +/- 0.1

The combination of all three analysis volumes covers 63 % of the initial SLG volume (cylinder with 6 mm height and 6 mm diameter). Neither in the fringe areas, near the aluminum sleeve, nor in the areas between the different analysis blocks, significant differences of the crack patterns are apparent. This can be seen, for example, in the compilation of the central vertical cross sections depicted in Figure 5.19 and Figure 5.20. Therefore, it is concluded that the chosen analysis volumes are sufficiently representative for the estimation of the degree of damage. In addition, the extent and position of the analysis volumes are identical for all specimens, as mentioned above. The analysis results are therefore well suited to be compared with one another, which is one of the main objectives of the scans.

Figure 5.19 and Figure 5.20 also show that the different impact velocities have generated significantly different degrees of pre-damage. At the lowest impact velocities, only few isolated cracks are apparent. At 72 m/s (images in the first row of Figure 5.20), these crack planes are mainly oriented in the vertical direction. At 144 m/s (images in the second line), additional horizontal cracks are present. At the high impact velocities of 266 and 407 m/s (images in the first and second row of Figure 5.20), the crack density is significantly higher within the entire SLG. In addition, the amount of horizontal cracks at the bottom of the specimens is considerably larger.

The highest crack density is visible in the specimen that was scanned after the confined pressure testing (images in bottom row of Figure 5.20).

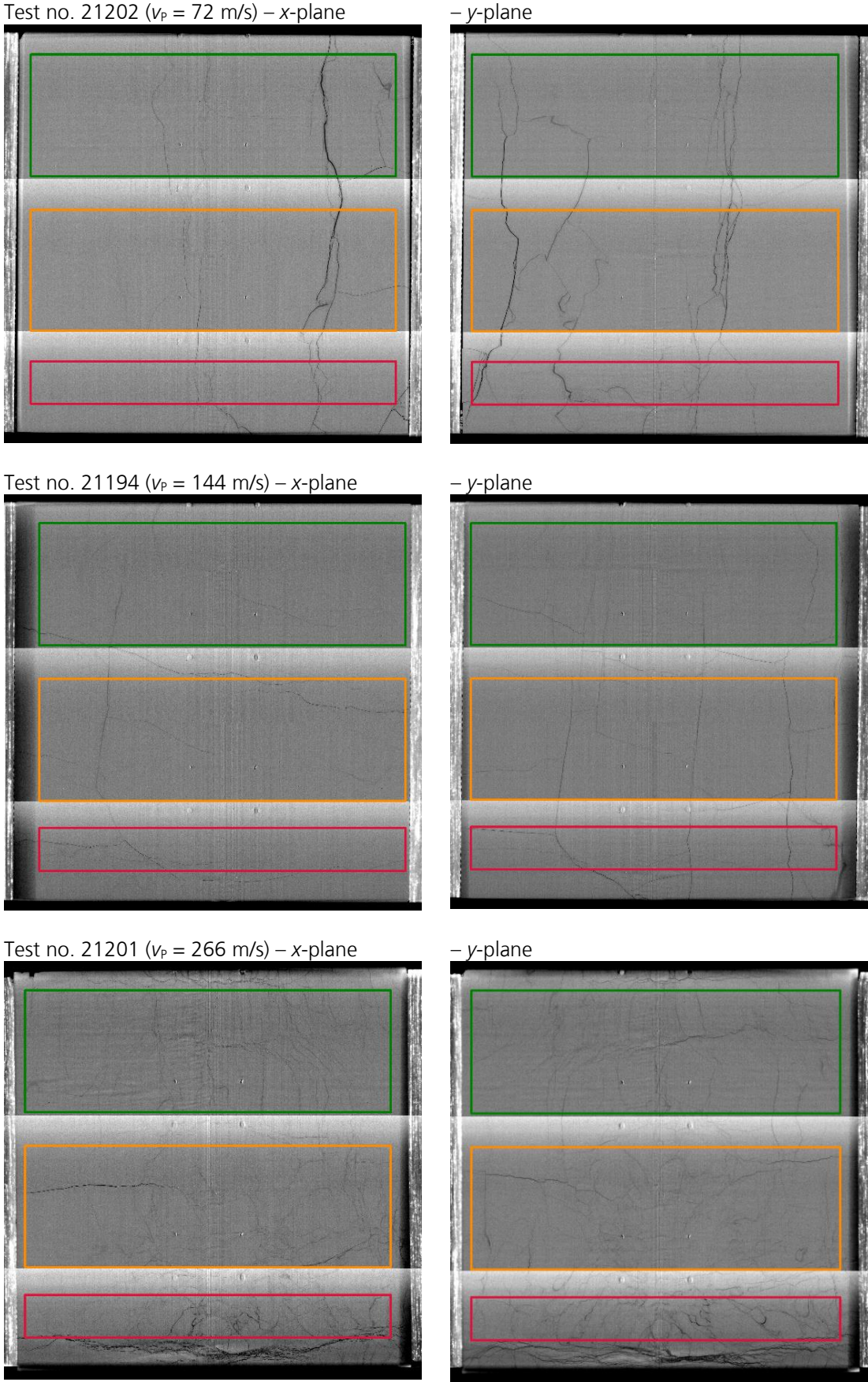


Figure 5.19: Final CT images of tests 21202, 21194 and 21201; the left column represents the central x-slice (vertical cut through the middle of the specimen), the right column represents the central y-slice (perpendicular to the x-slice). The colored squares indicate the analysis areas.

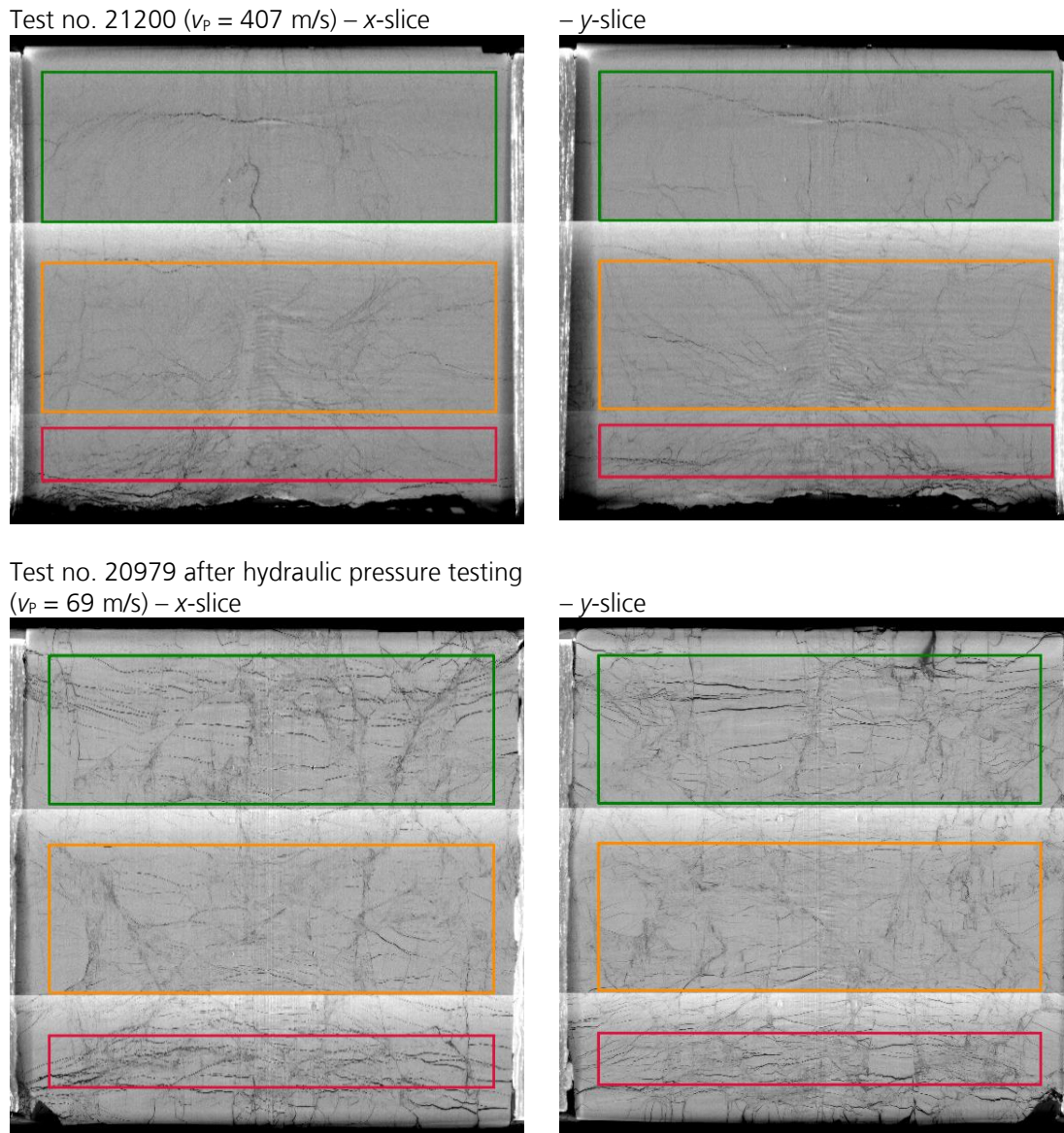


Figure 5.20: Final CT images of test 21200 and test 20979 after pressure testing; the left column represents the central x-slice (vertical cut through the middle of the specimen), the right column represents the central y-slice (perpendicular to the x-slice). The colored squares indicate the analysis areas.

In step 5, all voxels apart from the analysis volumes are either removed directly or covered by a geometrical mask (black areas in the middle and bottom right image of Figure 5.17) excluding these voxels from the subsequent analysis. Afterwards, a complex image enhancing filter is applied, which smooths the image by reducing the noise in the gray scale values. The filter of choice is an iterated bilateral de-noise filter provided by Mango. The main parameters of the filter are a set of range sigma factors and the maximum number of iterations. While the range sigma factors are kept at the default values, the maximum number of iterations is reduced from eight to three, since the filter is very time-consuming.

For the visual comparison, five cross sectional views are generated for each specimen. Figure 5.21 schematically illustrates their positions in the SLG specimen. A horizontal slice is positioned at the middle of each of the three analysis volumes. In addition, two vertical slices are generated, which are perpendicular to each other. In the following, the horizontal slices are referred to as z-slices and the vertical slices as x- and y-slice. The position of the x- and y-slice is

randomly determined by the positioning of the specimen on the holder in the X-ray CT and therefore not linked to the specimen orientation during the impact test. The middle right image of Figure 5.17 shows exemplarily the resulting x-slice and the three z-slices of test specimen no. 21202.

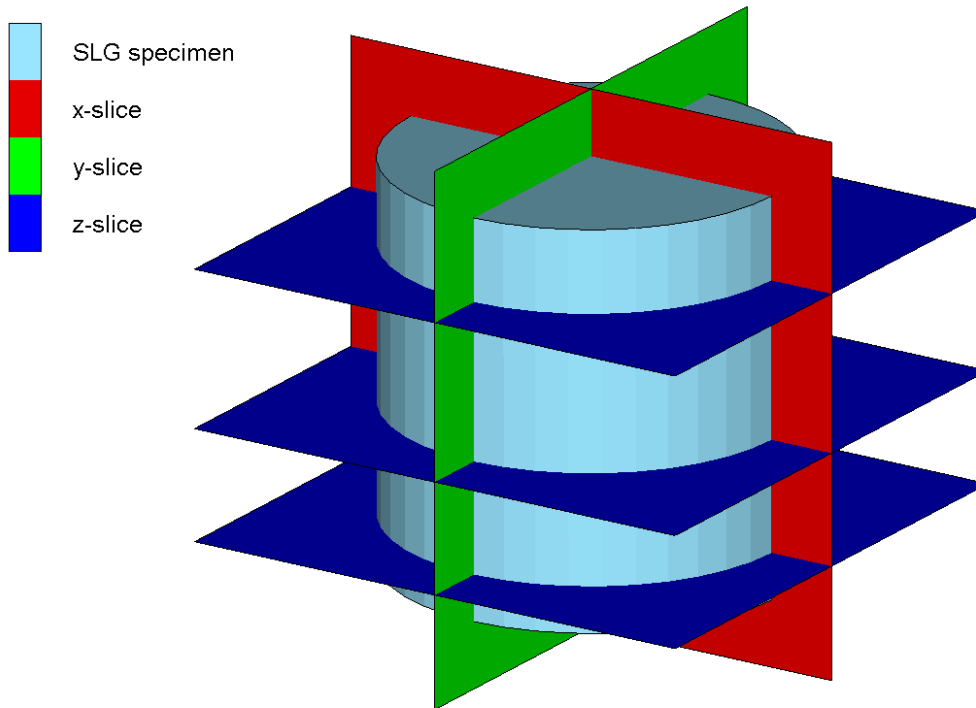


Figure 5.21: Schematic of tomographic slice positions. The shock wave generating the pre-damage enters the specimen through the top surface.

In step 6, the segmentation process is carried out. This process separates the image from 65,535 different gray scale values down to only two values, representing the intact glass and the cracks. The method of choice is a region-growing algorithm called "Converging Active Contours" (CAC). The CAC process is in principle an enhanced version of a simple thresholding segmentation. In a thresholding segmentation, the classification of the voxels is based simply on their gray scale value. If the value is greater than or equal to a critical threshold, it is identified as glass, otherwise it is identified as crack. Therefore, only one input parameter is required, namely the critical threshold. Unfortunately, this simple thresholding segmentation does not produce usable results when applied to the CT data of the pre-damaged SLG specimens. The CAC segmentation, however, is noise tolerant producing rather smooth interfaces. It is therefore well suited for the identification of the crack planes in phase-contrast images. The bottom right image of Figure 5.17 shows an exemplary segmentation result; voxels identified as glass are shown in white and cracks are shown in red.

The CAC process is quite complex and requires a variety of input parameters. The operating principle and the method of obtaining the parameters are described in more detail in the next sections.

5.3.3.3 The “Converging Active Contours” separation process

Mango provides a variety of segmentation techniques. The aim of a segmentation process is to identify and separate different phases of a dataset. In case of the present work, the segmentation is used to convert the gray scale images of the pre-damaged SLG into two-phase images. This means, that the large number of gray scale values are split into two values only. One phase is the intact SLG while the other phase is the air inside the cracks, in the following referred to as phase “glass” and phase “crack”, respectively.

In the first step of the CAC process, each voxel is classified as “glass”, “crack” or “undefined”. This is achieved by choosing two threshold values for the gray scale intensity. Figure 5.22 illustrates the procedure for the y-slice of the middle analysis volume of specimen no. 21202. Row “A” shows the input gray scale tomogram together with its intensity histogram. In the intensity histogram, the number of voxels is plotted against the different gray scale values. Row “B” depicts the same tomogram after setting an upper intensity threshold. All voxels above this threshold are identified as “glass” and colored blue in the image for visualization purpose. Row “C” shows the same tomogram after setting an additional lower intensity threshold. All voxels below this second threshold are identified as “crack” and colored red. The remaining voxels with a gray scale value between both thresholds are marked as “undefined”. They are typically located between the other two phases, in the surrounding areas of the cracks. Only in the last step of the CAC process, these “undefined” voxels are reassigned as “glass” or “crack”.

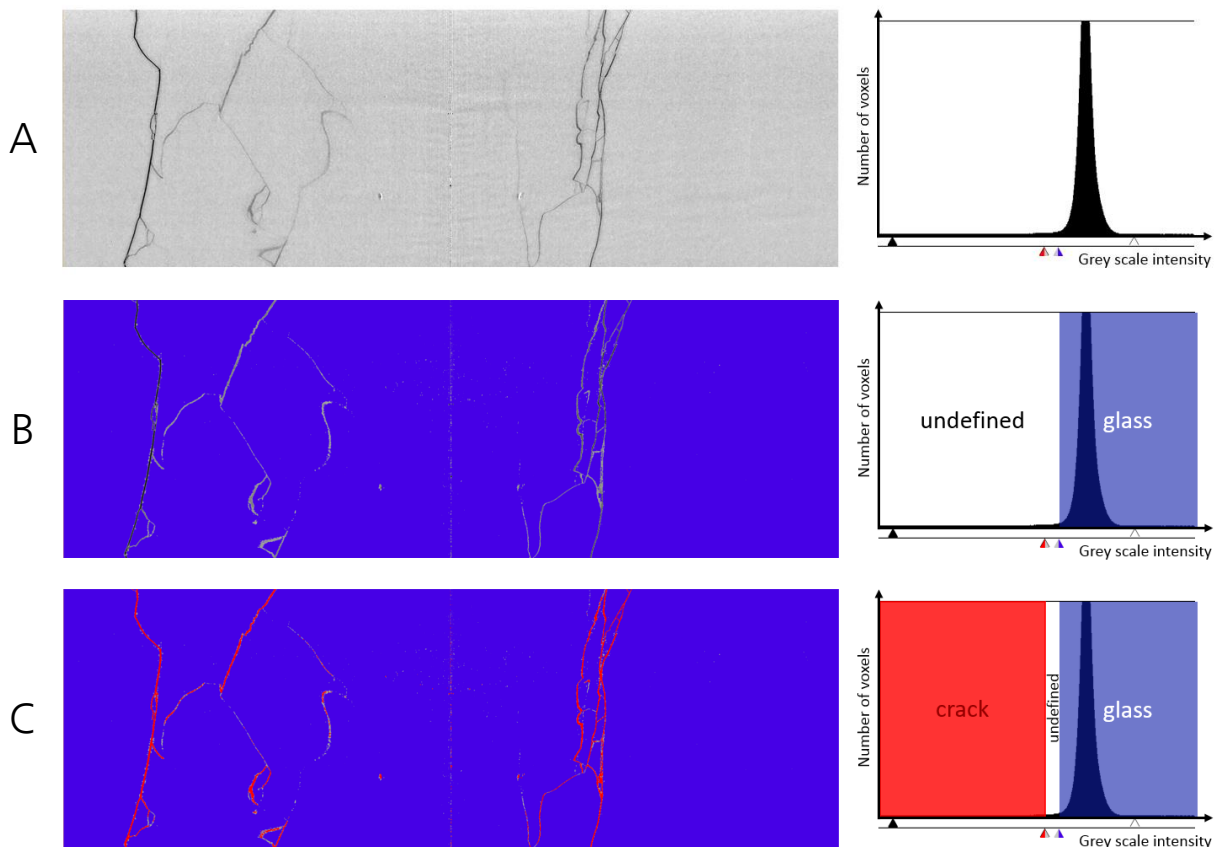


Figure 5.22: In the first segmentation step of the CAC process, two gray scale intensity thresholds are set (visualization example: test no. 21202, y-slice of middle analysis volume);
A: Gray scale intensity tomogram with intensity histogram.
B: All voxels above a critical intensity threshold are identified as “glass” and colored blue.
C: All voxels below a second intensity threshold are identified as “crack” and colored red; voxels with a gray scale value between both thresholds are marked as “undefined”.

In the second step of the CAC segmentation, some of the voxels, which had been mistakenly identified as "glass" or "crack" in the first step, may be reassigned as "undefined". The objective of this process step is to reduce the number of initially mislabeled voxels. These mislabeled voxels can be present in particular next to the boundaries of cracks and reconstruction artifacts, where the gray scale intensity varies significantly.

In order to identify these specific voxels, two additional gray scale gradient thresholds are defined. The gradient of a voxel gives the rate of change, how the gray scale intensity differs compared to its surrounding voxels. In the used standard setting, only voxels sharing at least one edge are considered adjacent. That means that each enclosed voxel has six neighbors.

Figure 5.23 illustrates the setting of the gradient thresholds for the *y*-slice of the middle analysis volume of specimen no. 21202. Row "A" shows the gray scale gradient tomogram together with its gradient histogram. Voxels with a small gradient are displayed dark, while those with high gradients appear bright. The majority of the voxels is located inside the rather uniform areas of intact glass therefore having only small gradients. Only near the boundaries of the cracks and reconstruction artifacts, the gradient is large.

Row "B" depicts the same tomogram after setting a "not glass" gradient threshold. All voxels having a gradient above this threshold are colored green and all other voxels are colored black in the gray scale gradient tomogram, for visualization purpose. All voxels, which had been identified as "glass" in the first step and are above the "not glass" threshold in the second step, are reassigned to "undefined".

Row "C" depicts the gradient tomogram after setting a "not crack" gradient threshold. Again, all voxels having a gradient above this threshold are colored green in the gray scale gradient tomogram. All voxels, which had been identified as "crack" in the first step and are above the "not crack" threshold in the second step are reassigned to "undefined".

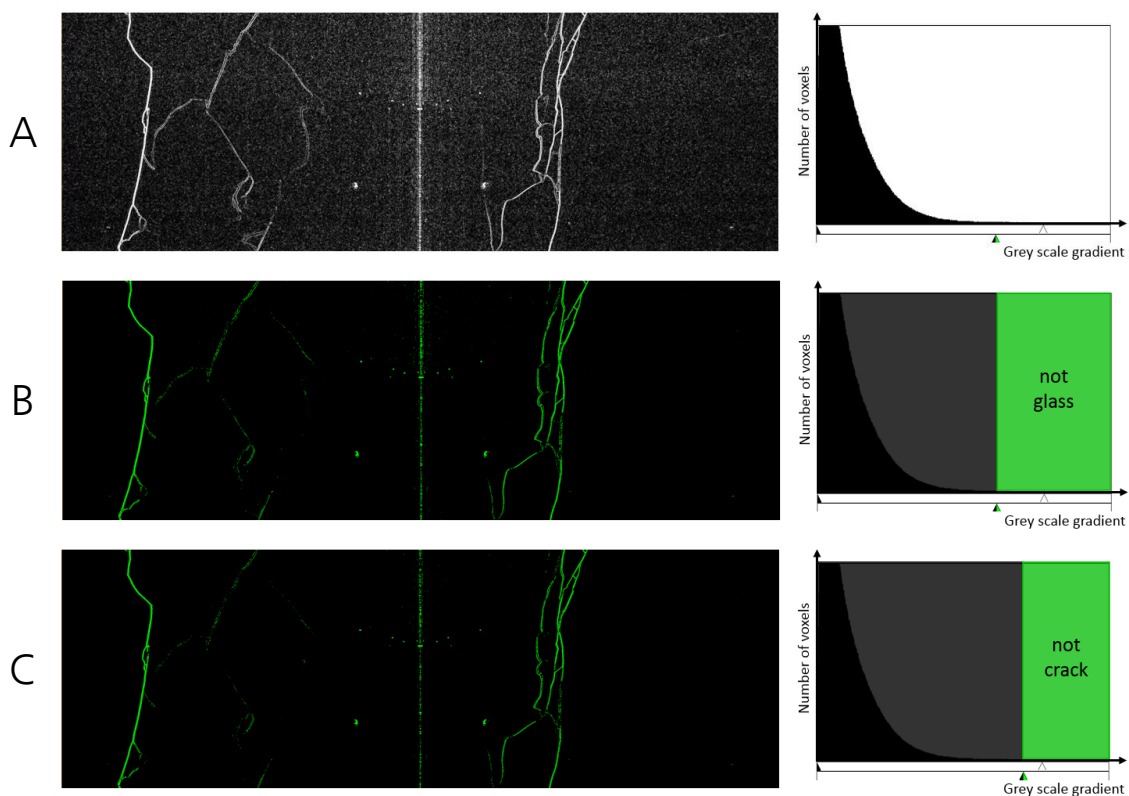


Figure 5.23: In the second segmentation step of the CAC process, two additional gray scale gradient thresholds are set (visualization example: test no. 21202, *y*-slice of middle analysis area); A: Gray scale gradient tomogram with gradient histogram; B: All voxels above a critical gradient threshold are regarded as not belonging to "glass" and colored green; C: All voxels above a second gradient threshold are regarded as not belonging to "crack" and colored green.

This process is schematically illustrated in Figure 5.24. After step 1 of the CAC process (left diagram), every voxel is identified based on its gray scale intensity as either “crack”, “glass” or “undefined”. The corresponding parameter areas are represented by the red, white and blue areas. In step 2, critical voxels are reassigned to “undefined” based on their gray scale gradient. As a result, the parameter area of the “undefined” voxels increases.

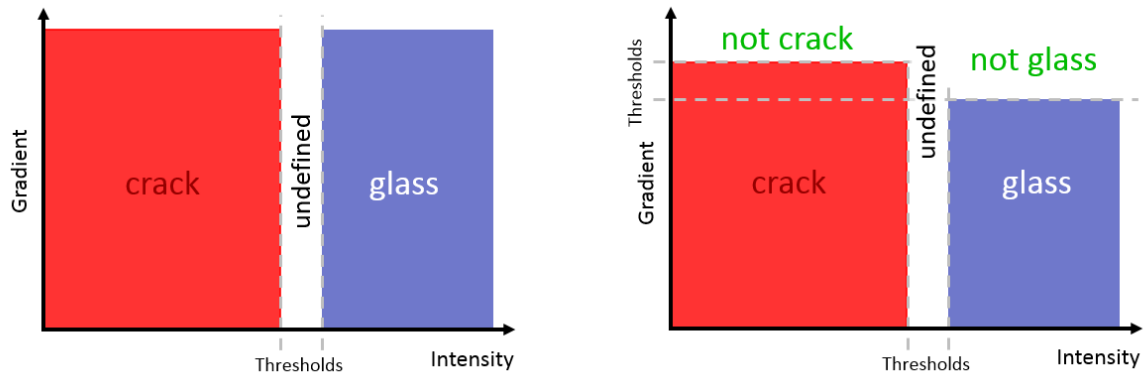


Figure 5.24: Schematic of the combination of intensity and gradient thresholds;
Step 1 (left diagram): Intensity thresholds separate the voxels into three identification classes;
Step 2 (right diagram): Additional gradient thresholds further tighten the criteria for a voxel being identified as “crack” or “glass”.

Before the final step of the CAC process is conducted, the amount of “undefined” voxels is reduced in an additional processing step. This is necessary since the final step is very time consuming and strongly depending on the amount of “undefined” voxels. In order to reduce the amount of “undefined” voxels, four additional tight thresholds are used. The tight thresholds separate some of the “undefined” voxels into “maybe glass” or “maybe crack”. Subsequently, a connected region of “maybe glass”, which is adjacent to “glass”, is relabeled into “glass”. After this, all voxels of “maybe glass” that are disconnected from the “glass” region are set to “undecided” again. The same procedure applies for the “maybe crack” and “crack” regions.

In the final step of the CAC process, the regions “glass” and “crack” simultaneously grow towards another resolving the “undefined” region. The growth is controlled by a speed function depending on the local gray scale gradients. The higher the gradient is, the slower is the growth. Since phase boundaries exhibit a high gradient, the growth of an arriving region is slowed down, enabling the other region to arrive at the boundary as well.

The result of the CAC process is a 3D tomogram, in which each voxel belongs either to the phase “glass” or to the phase “crack”. The positions and the amount of the “crack” voxels are subsequently evaluated to determine the degree of damage.

5.3.3.4 Determination of the CAC thresholds

Finding the optimal set of eight threshold parameters for the CAC segmentation process is quite challenging and time-consuming. In an ideal scenario, all analyzed CTs have similar gray value distributions, without significant noise and artifacts. In this case, one set of segmentation

Development of a novel methodology for generating, characterizing and pressure testing of defined damaged glass specimens

parameters could be used to analyze all specimens providing consistent and comparable results with less effort.

The CTs of the pre-damaged SLG specimens, however, have strongly varying gray scale values as well as detector noise and reconstruction artifacts, as described in the previous sections. Therefore, it is not possible to use the same set of parameters for the CAC segmentation of the different specimens or even for different analysis volumes within one specimen. Nevertheless, an approach described in the following is used in order to create a sufficient degree of consistency.

The parameters are determined individually for each analysis volume of every specimen. Table 5.3 and Table 5.4 summarize the final threshold parameters for the CAC segmentation of the five specimens, for which a PCI was conducted.

Table 5.3: Final threshold parameters for the CAC segmentation of specimens no. 21202, 21194 and 21201; ITH = Intensity threshold, GTH = Gradient threshold, TITH = Tight intensity threshold, TGTH = Tight gradient threshold.

CAC separation parameters	21202			21194			21201		
	Top	Mid	Bot	Top	Mid	Bot	Top	Mid	Bot
"crack" ITH	32400	32600	32800	33000	33000	33000	33200	33200	32900
"glass" ITH	32800	33000	33100	33200	33400	33200	33350	33500	33100
"not crack" GTH	1100	1100	1300	1000	1100	900	900	1000	800
"not glass" GTH	950	950	1000	800	850	800	800	850	700
"maybe crack" TITH	32600	32800	32950	33100	33200	33100	33300	33350	33000
"maybe glass" TITH	32800	33000	33100	33200	33400	33200	33350	33500	33100
"maybe not crack" TGTH	1100	1100	1300	1000	1100	900	900	1000	800
"maybe not glass" TGTH	1100	1100	1300	1000	1100	800	900	1000	800

Table 5.4: Final threshold parameters for the CAC segmentation of specimens no. 21200 and 20979+P; ITH = Intensity threshold, GTH = Gradient threshold, TITH = Tight intensity threshold, TGTH = Tight gradient threshold.

CAC separation parameters	21200			20979+P		
	Top	Mid	Bot	Top	Mid	Bot
"crack" ITH	33000	33200	32200	30600	31500	30600
"glass" ITH	33400	33400	32700	31200	32200	31200
"not crack" GTH	800	900	1050	1800	1700	1800
"not glass" GTH	650	800	800	1500	1400	1500
"maybe crack" TITH	33200	33300	32400	30900	31800	30900
"maybe glass" TITH	33400	33400	32700	31200	32200	31200
"maybe not crack" TGTH	800	900	1050	1800	1700	1800
"maybe not glass" TGTH	800	900	1050	1800	1700	1800

In order to determine the threshold of a specific volume, its central x-, y- and z-slice are loaded into an image editing software. Each threshold is then determined individually by varying its value and visually comparing the resulting threshold segmentation with the visible cracks of the original tomogram. Thereby, some of the remaining reconstructions artifacts are usually mistakenly identified as cracks. However, since their total volume is small compared to the total crack volume, their influence on the result is negligible. The determination process for each threshold is listed in the following:

- For the determination of the "crack" intensity threshold, the positions of all voxels below the threshold are examined while the threshold is varied. The threshold is then set to the highest value at which none of these voxels appears outside of the visible cracks. This means that none of the visual "glass" voxels is incorrectly identified as "crack", but some of the visual "crack" voxels are above the threshold. For the analyzed specimens, the evaluated threshold intensities lie in the range of 30600 to 33200.
- For the determination of the "glass" intensity threshold, again all voxels below the threshold are examined. The threshold is then set to a value at which more of the visual "crack" voxels are below the threshold, but some of the visual "glass" voxels are also below the threshold. This means that some of the visual "glass" voxels are not identified as "glass". In addition, some of the visual "crack" voxels are incorrectly identified as "glass". The determined thresholds are 150 to 700 gray values higher than the "crack" intensity threshold.
- For the determination of the "not glass" gradient threshold, the positions of all voxels above the threshold are examined while the threshold is varied. The threshold is then set to the lowest value at which only few of these voxels appears outside of the visible crack boundaries. This means that all of these voxels are reassigned to "undefined" if they have been identified as "glass" previously. The resulting gradients lie in the range of 650 to 1500.
- For the determination of the "not crack" gradient threshold, the process is similar to the determination of the "not glass" gradient threshold. However, the "not crack" gradient threshold is set to the lowest value at which no voxel appears outside of the visible crack boundaries. This leads to smaller amount of voxels on the crack boundaries as well. The resulting gradient threshold is 100 to 300 higher. This means that fewer "crack" voxels are reassigned to "undefined" allowing more of the thin cracks to be preserved. This can be seen exemplarily in Figure 5.23, where fewer voxels appear on the left side of the gradient tomogram in column C in comparison to column B.
- The "maybe crack" tight intensity threshold is set to approximately the mean value of the intensity thresholds "crack" and "glass".
- The "maybe glass" tight intensity threshold is set to the same value as the "glass" intensity threshold.
- The tight gradient thresholds "maybe not crack" and "maybe not glass" are both set to the value of the "not crack" gradient threshold.

After the CAC segmentation is carried out with the determined thresholds, the final separation results are checked for plausibility by a visual comparison of the segmented and the original tomograms with all five center slices (ref. Figure 5.21). This procedure is described in the next section.

In addition to the parameter sets of Table 5.3 and Table 5.4, some threshold variations are analyzed in section 9.6, in the appendix. These are used to evaluate the influence on the resulting total crack volume allowing for an estimation of the analysis errors.

5.3.3.5 Separation results of phase-contrast images

In this section, the results of the PCI are presented. As summarized in Table 5.1, five SLG specimens were analyzed by PCI, each pre-damaged at a different impact velocity. The chosen specimens cover the whole range of available impact velocities. Specimen no. 21202 is representative for the lowest impact velocities of about 70 m/s. The intermediate velocities are represented by specimen no. 21194 ($v_p = 144$ m/s) and no. 21201 ($v_p = 266$ m/s). Representative for the highest impact velocities of about 400 m/s is specimen no. 21200. In addition, specimen no. 20979 was not analyzed by PCI directly after the impact ($v_p = 69$ m/s), but after the subsequent pressure test.

The resulting gray scale tomograms as well as the segmented tomograms contain a lot of information. An ambitious approach would be to describe the morphology of the crack patterns by means of Minkowski functionals. This method emerged from the field of statistical physics, aiming to quantify the geometry of an object by intrinsic values like the volume, the surface area, the average mean curvature, the Euler number or similar quantities [254] [255].

Mango provides tools to perform a Minkowski analysis with segmented data, however, in case of the presented results, such an analysis is not appropriate. This is due to the fact, that the separated crack planes are incomplete. Figure 5.25 shows a 3D model of the separated cracks in the middle analysis volume of specimen no. 21202. The model was created from a stack of segmented DICOM-images (Digital Imaging and COMMunications in medicine) using the software Scan-IP. It consists of 172 million finite elements requiring a large memory size of 12 GB. The incompleteness of the crack planes is visible, for example, in the lower right region. As the crack planes are not closed surfaces, the calculation of a surface, a surface to volume ratio or a degree of branching are unsuitable.

However, the total crack volume is rather slightly affected by the missing crack voxels. For the further analysis, the degree of damage is therefore simplified to only one value, namely the total volume fraction of the cracks $V_{f,c}$. This can be done since similar damage features are present in all specimens and the crack density does not vary significantly within each specimen. This approach is especially suited for the intended implementation into a numerical model, in which a description of the degree of damage by only one parameter is preferred.

Figure 5.26 exemplarily shows the resulting $V_{f,c}$ of test specimen no. 21202. On the left side, the center x-slice is shown to indicate the positions of the analysis volumes. On the right side, $V_{f,c}$ is plotted as a function of the z position. The diagram on the right side thus comprises the crack densities of the entire three-dimensional analysis volumes, whereas the tomogram on the left side only shows a two-dimensional selection.

The z position is defined relative to the top surface of the specimen, which was facing towards the incoming shock wave during the impact. $V_{f,c}(z)$ is calculated by dividing the amount of "crack" voxels at position z ($N_{crack}(z)$) by the total amount of voxels within the analysis volume at the same z position ($N_{crack}(z) + N_{glass}(z)$):

$$V_{f,c}(z) = N_{crack}(z) / (N_{crack}(z) + N_{glass}(z)) \quad 5.1$$

The mean total volume fraction of the cracks $\bar{V}_{f,c}$ is calculated by taking the arithmetic mean over all z positions within the analysis volumes of the specimen:

$$\bar{V}_{f,c} = \int_z V_{f,c}(z) dz / \int_z dz \quad 5.2$$

$V_{f,c}(z)$ is only determined at discrete z values each belonging to one horizontal slice of the PCI. Therefore, $V_{f,c}$ can also be regarded as a function of the horizontal slice index i . With N being the total number of slices lying within the analysis volumes of the specimen, equation 5.2 can be simplified by the sum:

$$\bar{V}_{f,c} = \left(\sum_{i=1}^N V_{f,c}(i) \right) / N \quad 5.3$$

The corresponding standard deviation of the mean is calculated by:

$$s(\bar{V}_{f,c}) = \sqrt{\frac{1}{N(N-1)} \sum_{i=1}^N (V_{f,c}(i) - \bar{V}_{f,c})^2} \quad 5.4$$

As illustrated exemplarily in Figure 5.26, $V_{f,c}$ is only calculated at z positions lying within the analysis volumes. This leads to gaps in the diagram at z positions around -2.5 mm and -5 mm. The degree of damage of the total specimen is estimated by $\bar{V}_{f,c}$ (equations 5.3 and 5.4). In the illustrated example, $V_{f,c}$ varies between 0.3 % and 1.5 % resulting in a mean value of $\bar{V}_{f,c} = (0.853 \pm 0.004) \%$.

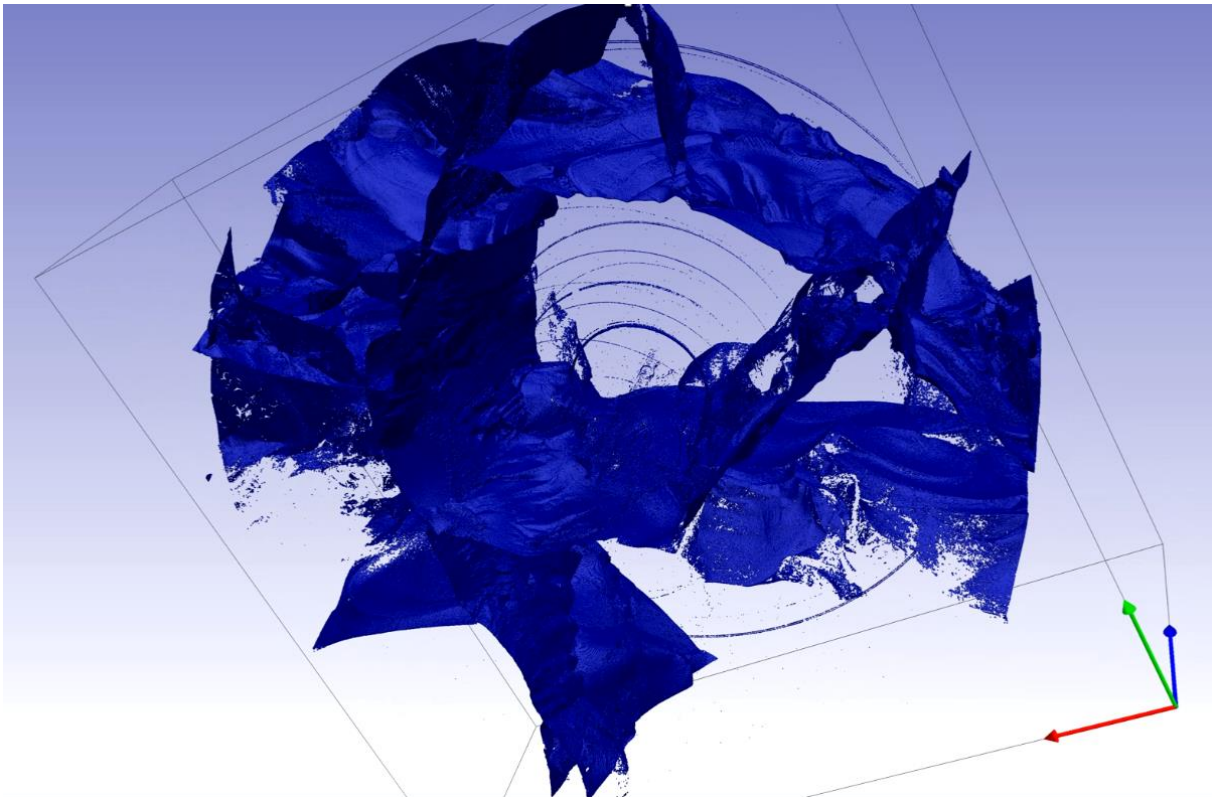


Figure 5.25: 3D visualization of identified crack voxels of test no. 21202 (middle analysis volume): FE-model with 172 million elements generated with the software Scan-IP from a stack of segmented DICOM-images (requires a large memory size of 12 GB).

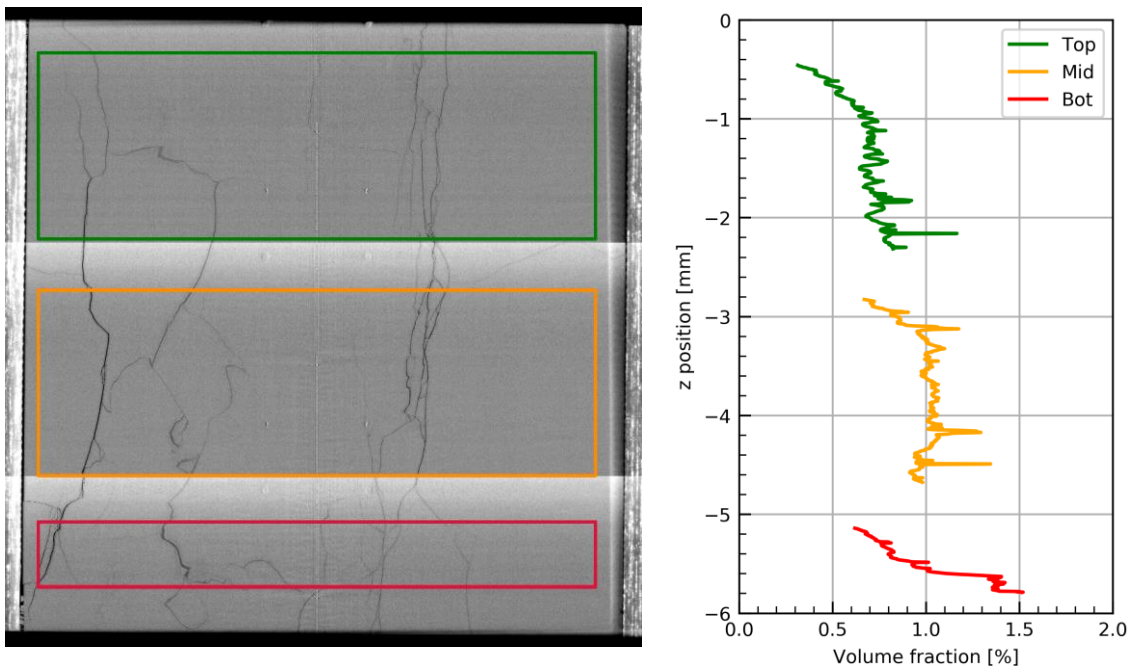


Figure 5.26: Exemplary illustration of a damage quantification result (test 21202, $v_p = 72$ m/s): left: center x -slice of the tomogram with highlighted analysis volumes; right: total volume fraction of cracks in the SLG specimen as a function of the distance to the impact surface.

The final separation results are arranged in Figure 5.27, Figure 5.28, Figure 5.29, Figure 5.30 and Figure 5.31. The figures show the final PCI tomograms of the analysis volumes together with the corresponding separation images. In the separated images, all voxels identified as “crack” are displayed in red. The “glass” voxels are shown in white and the masked areas, which are excluded from the analysis, are colored black.

The illustrated slices are taken from the positions as indicated schematically in Figure 5.21. The images in the first row of each figure show the x -slices. The y - and z -slices are illustrated in the second and third row, respectively. On the bottom right side, $V_{f,c}$ is presented in a diagram as a function of the z position.

Separation result of specimen no. 21202 ($v_p = 72$ m/s)

Figure 5.27 shows the results of the specimen pre-damaged with the lowest impact velocity of 72 m/s (test no. 21202). The PCI tomograms have a good contrast resulting in good separation results. This is evaluated by a visual comparison of the black cracks in the tomograms with the red cracks in the separated images. Most of the visible black cracks could be identified successfully. In addition, no significant reconstruction artifacts are apparent.

Only very thin cracks with a low contrast are mistakenly identified as intact glass. This can be seen, for example, in the left central region of the x -slice of the middle analysis volume. In this area, a vertical crack is visible in the tomogram, which is entirely missing in the separated image. Apart from the missing cracks, some of the thin cracks are only partially separated. This is apparent, for example, in the z -slices, where the continuous cracks of the tomogram, in some instances, result in disconnected lines in the separated images.

The crack planes visible in the x - and y -slices are primarily oriented in the vertical direction. The z -slices show that the crack patterns form a coarse mesh within the horizontal slices. Comparing the z -slices of the different positions (top, mid, bot) reveals that the patterns are relatively similar throughout the entire length of the specimen.

In the region of the rotation axis, a small amount of voxels got removed from the analysis volumes. These masked voxels are colored black in the separated images. They are excluded from the analysis since a large amount of reconstruction artifacts remain in the region of the rotation axis, even after applying the ring correction algorithm. These central artifacts are primarily excluded since they are easy to identify, however, their removal has only a minor influence on the resulting $V_{f,c}$ (the masked volume is much smaller than the total volume).

As mentioned above, the incompleteness of the separated crack planes makes the determination of a surface or degree of branching unsuitable. However, since the missing volume is small in comparison to the total crack volume, $V_{f,c}$ is only slightly affected by this measurement error. Especially for the comparison of the degree of damage between the different specimens, the missing crack volume does not significantly influence the results since the thin cracks are missing equally in all tomograms.

Furthermore, several parameter studies are presented in the appendix in section 9.6 that allow for a quantitative estimation of the influence of the CAC parameters on $V_{f,c}$.

The resulting $V_{f,c}$ of specimen 21202 (72 m/s) is illustrated in the diagram at the bottom right of Figure 5.27. The values vary only slightly between 0.3 % and 1.5 %, indicating that the crack density is relatively homogenous within the entire specimen. This supports the observation that the crack patterns are relatively similar throughout the entire length of the specimen as described above. With equations 5.3 and 5.4 and a total number of $N = 2642$ slices lying within the analysis volumes, the resulting $\bar{V}_{f,c}$ is (0.853 ± 0.004) %.

Separation result of specimen no. 21194 ($v_p = 144$ m/s)

Figure 5.28 shows the results of the specimen pre-damaged with a higher impact velocity of 144 m/s (test no. 21194). The crack planes in the x - and y -slices are primarily oriented in vertical direction, similar to the ones observed in specimen 21202. However, additional horizontal cracks connecting the vertical patterns are visible. The crack patterns visible in the z -slices differ from the ones of specimen 21202. They are not building a coarse mesh, but rather a set of planes running parallel to each other.

A visual comparison of the black cracks in the tomograms with the red cracks in the separated images reveals that a greater proportion of cracks could not be identified successfully by the separation algorithm. This is particularly apparent in the slices of the top analysis volume. The reasons for the inferior segmentation are a lower contrast of the PCI and more residual reconstruction artifacts. Especially in the central region of the top y -slice, asymmetrical horizontal artifact stripes are visible exhibiting high gray scale gradients. Similar artifacts are also apparent in specimens 21201 and 21200, but the reason for the manifestation of these artifacts is not examined in detail in this work.

The CAC separation parameters were chosen in such a way that the stripe artifacts are not identified as "crack". However, as the artifacts have similar gray scale characteristics as the real cracks, the real cracks in this region are also not identified as "crack". Nevertheless, this method is preferred over a parameter set that identifies more cracks correctly but also identifies a large part of the artifacts as "crack". The missing crack volume influences $V_{f,c}$ to a lesser degree as the incorrect "crack" identification of a large number of artifacts would do.

The resulting $V_{f,c}$ of specimen 21194 (144 m/s) is illustrated in the bottom right diagram of Figure 5.28. In the top region of the specimen ($z > -1.6$ mm), the crack density is significantly lower than in the residual analysis volumes. The lower value is due to the missing crack volume, which is caused by the presence of the residual stripe artifacts, as described above. The resulting mean value for the entire sample $\bar{V}_{f,c}$ is (0.45 ± 0.01) %.

At some z positions, $V_{f,c}$ is noticeably larger reaching values of about 1.3 % at $z = -3.2$ mm and almost 1.9 % at $z = -5.6$ mm. These high values are, however, restricted only to a small number of horizontal slices, in which a higher amount of horizontal crack planes is apparent in the tomograms.

The statistical error of $\bar{V}_{f,c}$ is very small since the number of analyzed z positions is large and $V_{f,c}$ does not vary considerably. However, regarding the large amount of cracks that are not correctly identified in the separation process, the systematical error is assumed to be significantly greater.

Separation result of specimen no. 21201 ($v_p = 266$ m/s)

Figure 5.29 shows the results of the specimen pre-damaged with a high impact velocity of 266 m/s (test no. 21201). The crack patterns look significantly different from those of the two specimens with lower impact velocities (Figure 5.27 and Figure 5.28). The amount of cracks is higher forming a fine mesh rather than a coarse mesh. This higher degree of fragmentation was also observed in the previously conducted transmitted light images (ref. Figure 5.11).

While at lower degrees of pre-damage primarily vertical crack planes are observed, a larger number of horizontal cracks is apparent in the x - and y -slices of Figure 5.29. Especially noticeable are the distinct horizontal crack planes in the top and middle analysis volumes. These horizontal crack planes are localized at z positions of about -1 mm and -3.4 mm. In the diagram at the bottom right of Figure 5.29, local maximums of $V_{f,c}$ of about 6 % and 3.5 %, respectively, are visible at the z positions of the distinct horizontal crack planes. At almost all other z positions, $V_{f,c}$ is lower yielding a mean value of $\bar{V}_{f,c} = (1.95 \pm 0.03)$ % for the entire specimen. Only near the bottom of the specimen, a significantly higher value of $V_{f,c} = 15$ % is observed.

The localized, high crack density near the bottom of the specimen as well as the distinct horizontal crack plane at $z = -1$ mm are also apparent in a microsection of a specimen with similar degree of damage (specimen 20987 shown in Figure 5.12).

The CAC segmentation works sufficiently for the majority of the analysis volumes of specimen 21201, however, some cracks visible in the tomograms are notably missing in the separated images. This can be clearly seen, for example, in the left half of the top x -slice or the bottom x - and y -slices. The missing cracks in the top volume are primarily due to the presence of stripe artifacts similar to those observed in the PCI of specimen 21194. These artifacts impede the separation of the cracks and are particularly evident in the upper left region of the top z -slice and in the left half of the top x - and y -slice.

The missing cracks in the bottom volume are caused by the presence of a gray scale gradient. The upper region of the bottom volume is significantly brighter than the bottom region.

Therefore, it is not possible to separate the bright cracks while simultaneously avoid identifying the dark glass voxels mistakenly as "crack".

Separation result of specimen no. 21200 ($v_p = 407$ m/s)

Figure 5.30 shows the results of the specimen pre-damaged with the highest impact velocity of 407 m/s (test no. 21200). The observed crack patterns are quite similar to those of specimen 21201. The cracks form a fine mesh spreading over large parts of the specimen. At a z position 1 mm away from the top surface, a distinct horizontal crack plane is evident. At the bottom of the specimen, the crack density is significantly higher. The cracks in the bottom x - and y -slice form a conical crack pattern that emerges from the center of the specimen spreading towards the lower surface. $V_{f,c}$ varies considerably between the different analysis volumes. This is evident in the diagram at the bottom right of Figure 5.30. In the top region of the specimen ($z > -2.4$ mm), mostly values between 1 % and 3 % are observed. Only at the position of the distinct horizontal crack plane, at $z = -1$ mm, a large $V_{f,c}$ of about 11 % is apparent. In the middle analysis volume, at -2.8 mm $> z > -4.6$ mm, $V_{f,c}$ is almost linearly increasing from about 1.5 % to 8 % with increasing distance to the upper surface. In the bottom analysis volume, $V_{f,c}$ further increases reaching a maximum of almost 16 % at $z = -5.5$ mm, which is quite similar to the pattern of specimen no. 21201. However, the mean value of $\bar{V}_{f,c} = (3.81 \pm 0.05)$ % is almost twice as large as the mean value of specimen 21201.

The quality of the segmentation is better than those of specimen 21201 since fewer stripe artifacts are present. Most of the cracks visible in the tomograms are identified correctly.

Separation result of specimen no. 20979+P ($v_p = 69$ m/s + pressure testing)

Figure 5.31 shows the results of the specimen (test no. 20979+P), which was pre-damaged with an impact velocity of 69 m/s and afterwards subjected to a high quasi-static load in a confined pressure test with a maximum axial force of 115 kN. The damage generated by the pressure test differs from the pre-damage of the dynamic impact tests. Especially in the top analysis volume, more horizontal crack planes are apparent connecting the vertical crack planes. In addition, some cracks are significantly thicker. The higher amount of horizontal cracks leads to a rather homogenous crack density with a mean value of $\bar{V}_{f,c} = (5.85 \pm 0.04)$ %. This is the highest mean value of all five PCI specimens surpassing even the 3.81 % of specimen no. 21200 (pre-damaged at the highest impact speed of 407 m/s).

The quality of the segmentation is sufficient. Only in the lower region of the top analysis volume, some thin cracks are missing resulting in an underestimation of $V_{f,c}$ at positions of about -1.2 mm $> z > -2.4$ mm. Near the bottom of the specimen ($z < -5.8$ mm), large values of $V_{f,c} > 9$ % are observed, similar to specimens no. 21200 and 21201.

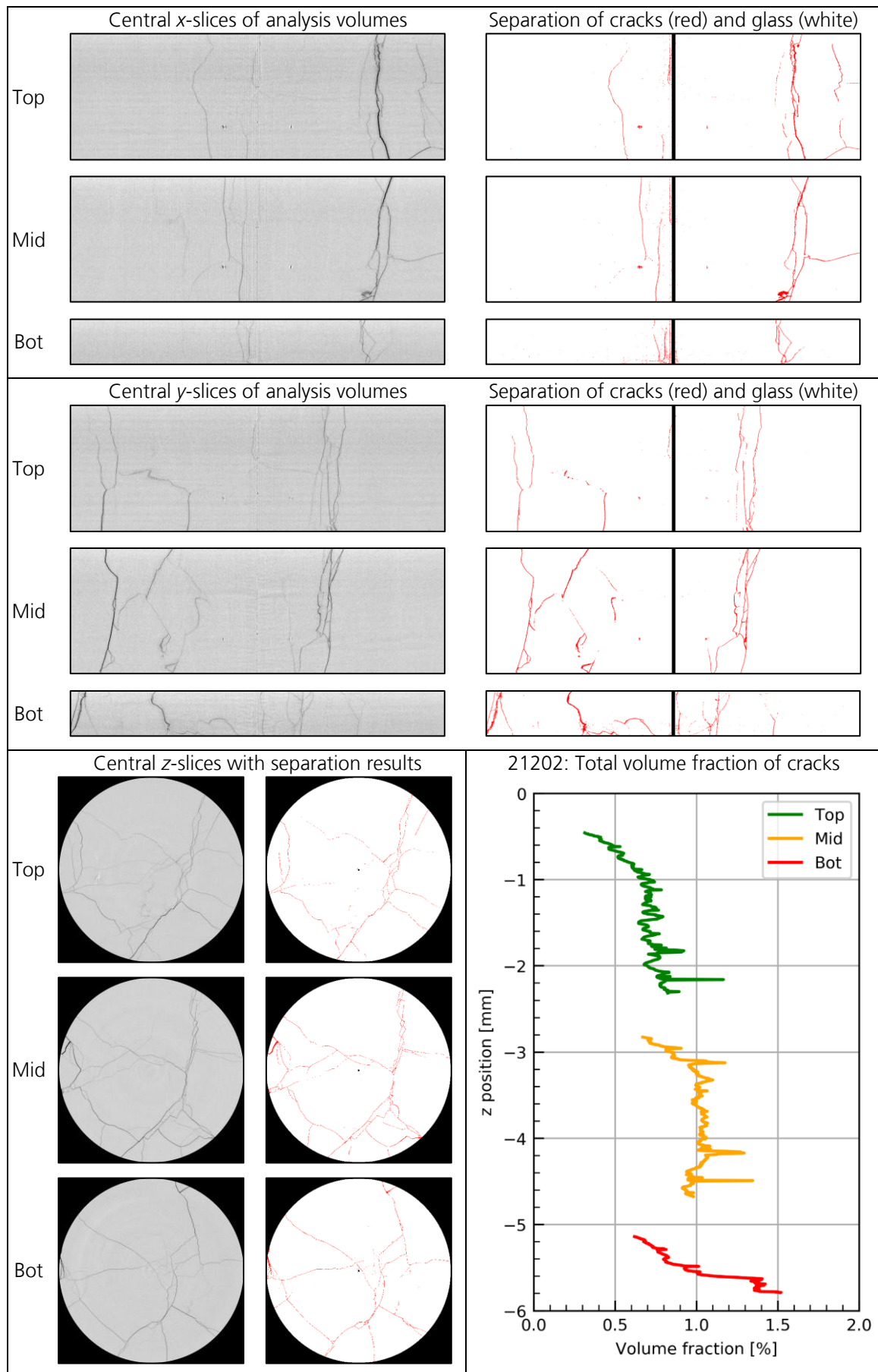


Figure 5.27: Separation results of test no. 21202 (72 m/s): Center slices of final analysis volumes (gray scale images) and corresponding separation of cracks (red) and glass (white).

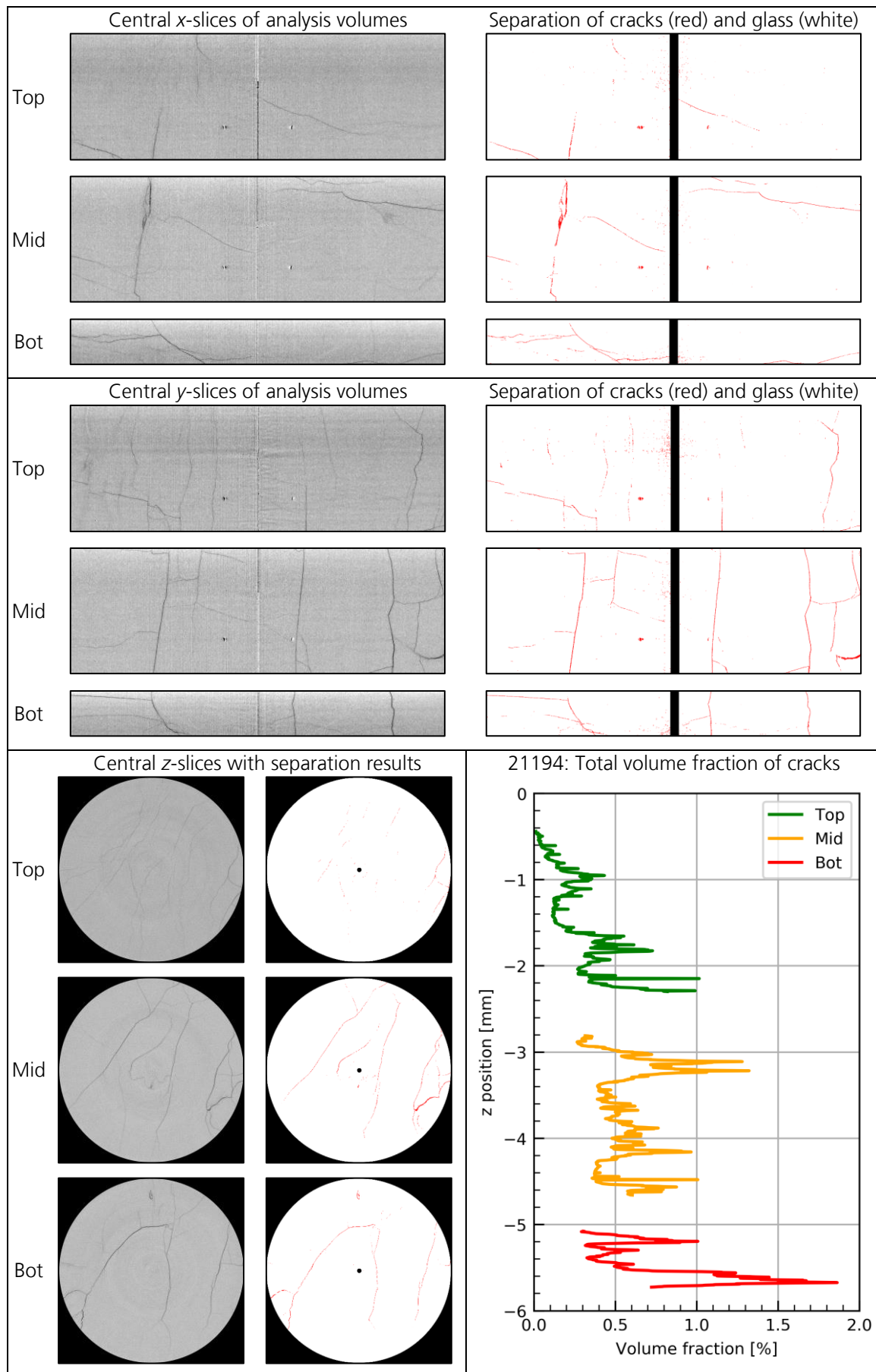


Figure 5.28: Separation results of test no. 21194 (144 m/s): Center slices of final analysis volumes (gray scale images) and corresponding separation of cracks (red) and glass (white).

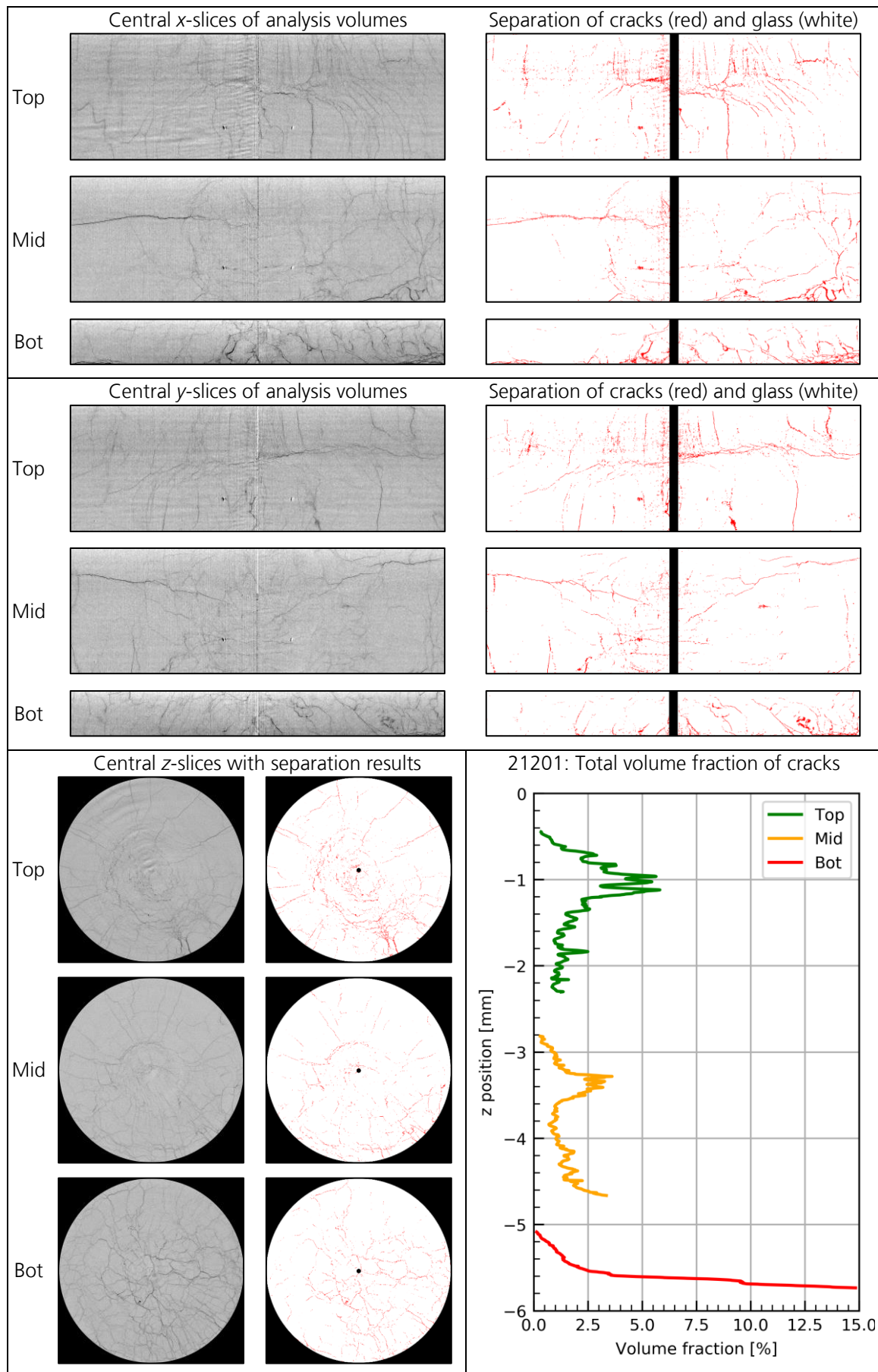


Figure 5.29: Separation results of test no. 21201 (266 m/s): Center slices of final analysis volumes (gray scale images) and corresponding separation of cracks (red) and glass (white).

Development of a novel methodology for generating, characterizing and pressure testing of defined damaged glass specimens

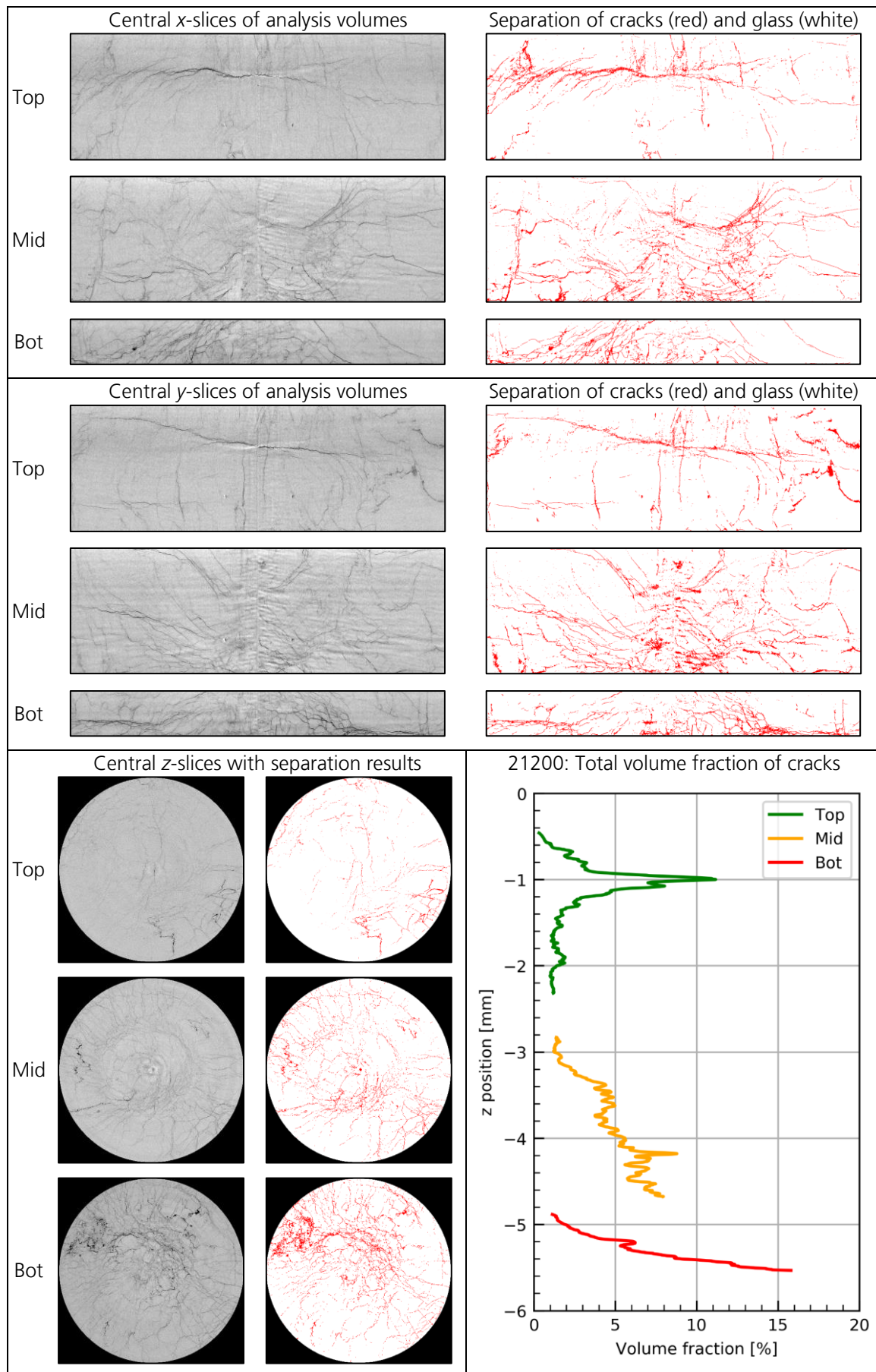


Figure 5.30: Separation results of test no. 21200 (407 m/s): Center slices of final analysis volumes (gray scale images) and corresponding separation of cracks (red) and glass (white).

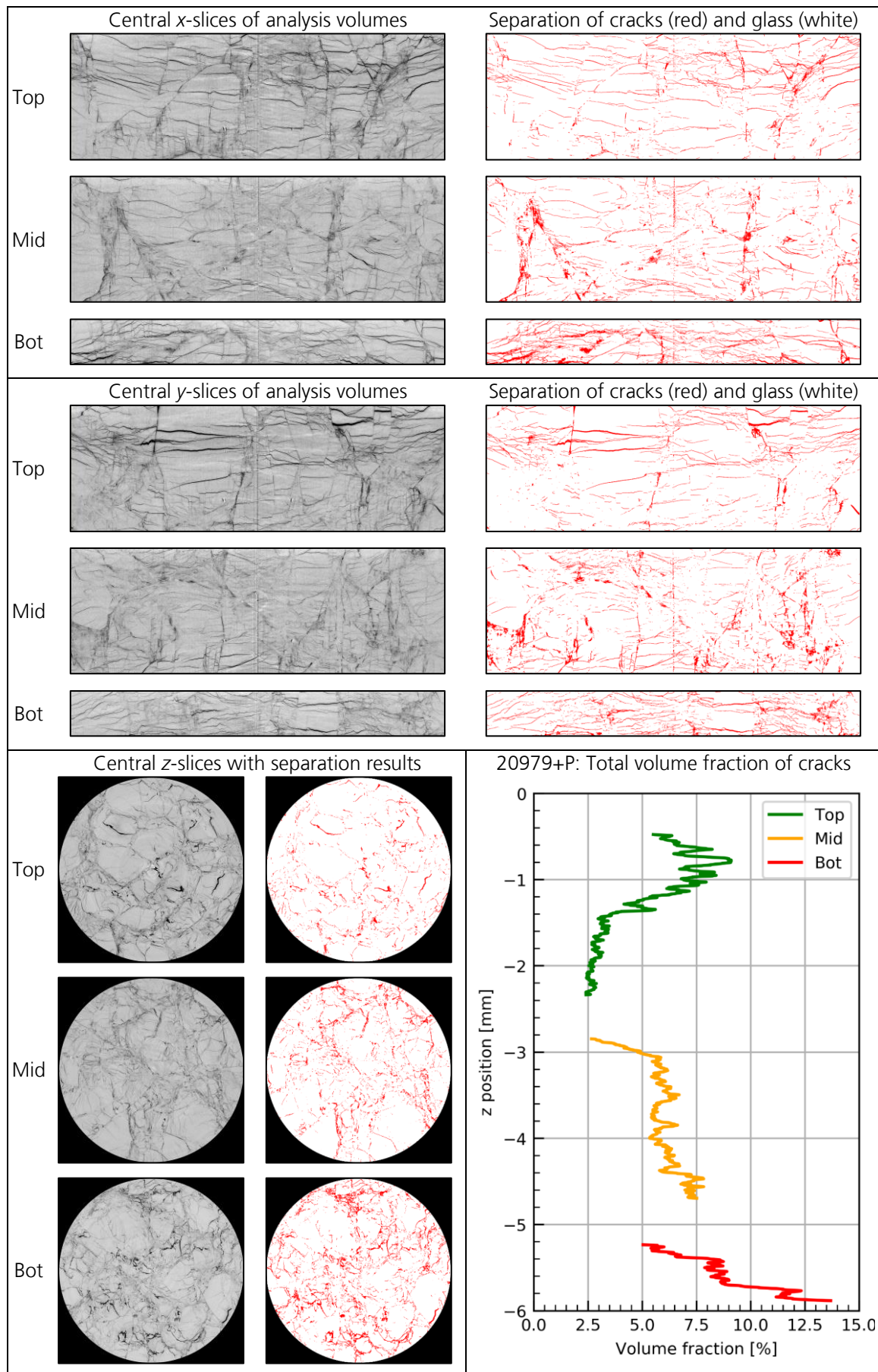


Figure 5.31: Separation results of test no. 20979+P (69 m/s + P): Center slices of final analysis volumes (gray scale images) and corresponding separation of cracks (red) and glass (white).

A compilation of the evaluated $V_{f,c}(z)$ of all five PCI scans is shown in Figure 5.32. Specimen no. 21202 was pre-damaged at the lowest impact speed of 72 m/s. The observed crack planes are primarily oriented in vertical direction. The corresponding $V_{f,c}(z)$ is illustrated as a dark blue line and varies only slightly. The dashed line of the same color indicates the resulting mean value of $\bar{V}_{f,c} = (0.9 \pm 0.2) \%$. This result is also summarized in Table 5.5. The given error refers to the systematical measurement error $s^*(\bar{V}_{f,c})$ estimated by a CAC parameter variation (appendix, section 9.6). For completeness, the statistical error $s(\bar{V}_{f,c})$ is also listed in Table 5.5.

The resulting $V_{f,c}(z)$ and $\bar{V}_{f,c}$ of specimen 21194 are shown as light blue lines in Figure 5.32. This specimen was pre-damaged at 144 m/s. Similar to specimen no. 21202, the observed crack planes are mainly oriented in vertical direction. In addition, some horizontal cracks are apparent. However, a large amount of cracks could not be identified correctly in the separation process leading to a low mean value with a comparatively large systematical measurement error of $\bar{V}_{f,c} = (0.5 \pm 0.4) \%$.

The specimens pre-damaged at higher impact velocities exhibit significantly different crack patterns. The amount of observed cracks is higher and the cracks form a fine mesh rather than a coarse mesh. $V_{f,c}(z)$ and $\bar{V}_{f,c}$ of specimens 21201 ($v_p = 266$ m/s) and 21200 ($v_p = 407$ m/s) are shown in Figure 5.32 as green and yellow lines, respectively. In the top analysis volume ($z < -2.2$ mm), the lines of both specimens are almost identical exhibiting a local maximum at $z \approx -1$ mm. The reason for this maximum is a distinct horizontal crack plane.

In the middle and bottom analysis volumes, specimen 21200 has a significantly higher degree of damage. Consequently, specimen 21200 has a higher mean value of $\bar{V}_{f,c} = (3.8 \pm 0.6) \%$ in comparison to specimen 21201 that has a mean value of $\bar{V}_{f,c} = (2.0 \pm 0.6) \%$. Near the bottom surface of both specimens, a sharp increase of the crack density is evident.

The highest amount of cracks is observed in specimen 20979+P. This specimen was pre-damaged with an impact velocity of 69 m/s and subjected to a high quasi-static load in a confined pressure test, prior to the PCI analysis. More horizontal crack planes are observed connecting numerous vertical crack planes. In addition, some cracks are significantly thicker than the cracks observed in the other specimens. The resulting $V_{f,c}(z)$ and $\bar{V}_{f,c}$ are illustrated by the red lines in Figure 5.32. In the lower region of the top analysis volume, some thin cracks could not be identified by the separation process resulting in an underestimation of $V_{f,c}$ at positions of about -1.2 mm $> z > -2.4$ mm. In the residual volume, $V_{f,c}$ varies comparatively little. The resulting mean value of $\bar{V}_{f,c} = (5.9 \pm 0.6) \%$ is 2.1 % larger than the mean value of the specimen that was impacted at the highest velocity.

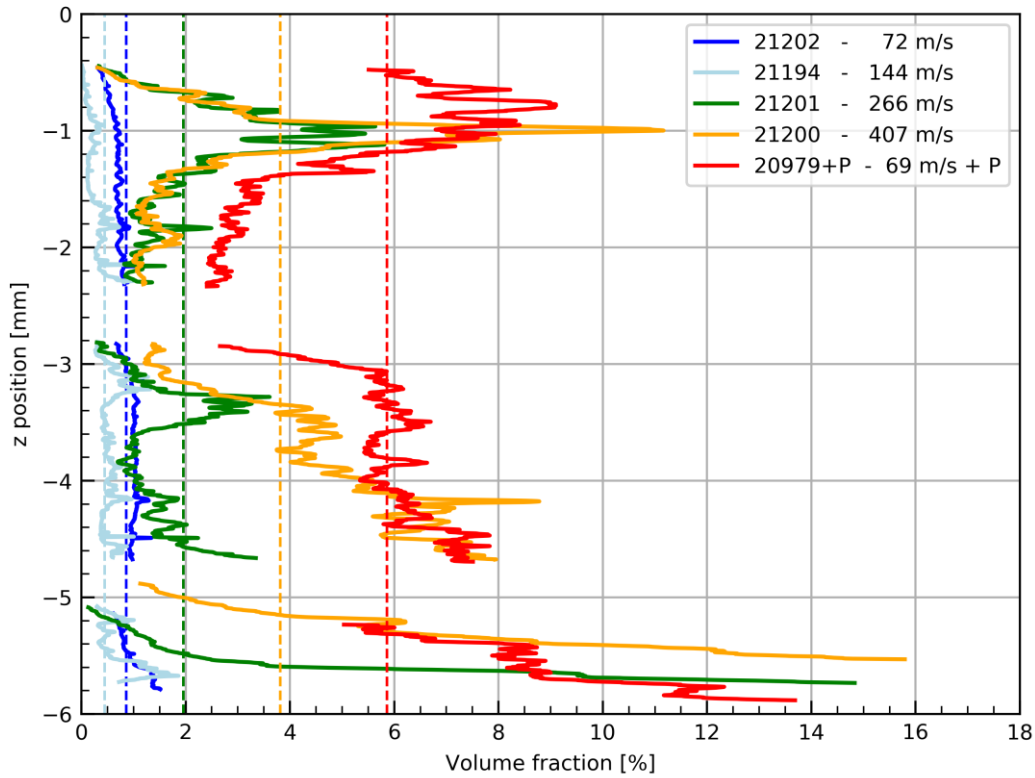


Figure 5.32: Final result of the PCI: total volume fraction of cracks $\bar{V}_{f,c}$ in the SLG specimens as a function of the distance to the impact surface z ; the quantified crack volume correlates with the impact velocity of the pre-damaging process (mean values $\bar{V}_{f,c}$ are indicated by dashed lines).

Table 5.5: Summary of PCI results: mean total volume fraction of cracks $\bar{V}_{f,c}$ and corresponding measurement errors. The statistical error $s(\bar{V}_{f,c})$ is calculated by equation 5.4 and the systematical error $s^*(\bar{V}_{f,c})$ is estimated by a CAC parameter variation (appendix, section 9.6).

Specimen no.	v_p for pre-damage [m/s]	$\bar{V}_{f,c}$ [%]	$s(\bar{V}_{f,c})$ [%]	$s^*(\bar{V}_{f,c})$ [%]
21202	72	0.853	0.004	0.2
21194	144	0.45	0.01	0.4
21201	266	1.95	0.03	0.6
21200	407	3.81	0.05	0.6
20979 + P	69 + P	5.85	0.04	0.6

5.3.3.6 Results of the micro-CT and comparison with PCI results

The results of the PCI analysis are presented in the previous sections. However, the PCI analysis comprises only five out of the twelve specimens that are subsequently characterized in a confined pressure test (section 5.4). In this section, the results of the micro-CT are presented. Within the scope of this thesis, the measurement time (and therefore the amount of examined specimens) of the PCI analysis was limited. In contrast, all twelve specimens could be analyzed by means of the micro-CT as these measurements were conducted at an in-house system (overview in Table 5.1).

Unfortunately, the quality of the micro-CT is insufficient to quantify the degree of damage of the specimens by means of the segmentation algorithms. The main reasons are a too low contrast, higher noise and residual reconstruction artifacts that introduce large gray scale gradients. However, the results of the micro-CT are sufficient for a visual comparison of selected tomogram slices. The slices being compared are the center x -, y - and z -slices, as illustrated in Figure 5.21. Therefore, the slices can also be used for a direct comparison of the micro-CT data and the PCI data.

A compilation of all CT results can be found in the appendix in section 9.7 (Figure 9.15, Figure 9.16, Figure 9.17, Figure 9.18, Figure 9.19 and Figure 9.20).

Specimens pre-damaged at low velocities (~70 m/s)

Figure 5.33 shows the results of the specimens pre-damaged at the lowest impact velocities of about 70 m/s. In the first row, the slices of the PCI of specimen 21202 are depicted. These are discussed in detail in the previous section. In the z -slice of the PCI, a black mask covers the aluminum sleeve.

In the second row, the corresponding slices of the micro-CT are shown. The crack patterns of the micro-CT and the PCI in the x - and y -slices cannot be compared directly with each other since the specimen did not have an identical orientation in both scans. However, the z -slice of the micro-CT is rotated by the offset angle to allow for a direct comparison. In the micro-CT, the contrast is significantly lower than in the PCI. The thicker cracks can be identified visually, but the noise and reconstruction artifacts cover the thinner cracks. Particularly problematic for an automated segmentation process are the residual artifacts. These are ring artefacts visible in the z -slice and diagonal line artifacts near the top and bottom of the specimen visible in the x - and y -slices.

The crack patterns of specimens 20981 ($v_P = 70$ m/s) and 20979 ($v_P = 69$ m/s) are shown in the third and fourth row of Figure 5.33. The x - and y -slices look very similar, exhibiting mainly vertical cracks. The cracks visible in the z -slices form a coarse mesh, similar to specimen 21202 ($v_P = 72$ m/s). The slices of specimen 20982 ($v_P = 73$ m/s) are depicted in the last row looking only slightly different.

In summary, the generated pre-damage at about 70 m/s is sufficiently reproducible. All four specimens exhibit primarily vertical crack planes forming a coarse mesh in the vertical slice.

Specimens pre-damaged at intermediate velocities (140 to 190 m/s)

Figure 5.34 shows the results of the specimens pre-damaged at intermediate impact velocities between 140 to 190 m/s. The first two rows contain the PCI and micro-CT slices of specimen 21194 ($v_P = 144$ m/s). As discussed in the previous section, the cracks of this specimen are difficult to identify in the PCI. In the micro-CT slices, even a visual identification is almost impossible. In comparison to the other specimens of this velocity range, significantly fewer cracks are visible. Possible explanations for this observation are that the impact has generated

actually less damage or that the generated cracks are much thinner. However, it is unlikely that less damage has been generated, as the high-speed video of the impact does not differ from those of the other specimens (ref. 21194 in Figure 5.7).

The crack patterns of specimens 20984 ($v_p = 146$ m/s) and 20983 ($v_p = 186$ m/s) are shown in the third and fourth row of Figure 5.34. Although specimen 20983 was pre-damaged at a 27 % higher impact velocity, the visible crack patterns are quite similar. The cracks apparent in the z-slices form a finer mesh than those of the low velocity specimens (ref. Figure 5.33).

The slices of specimen 20985 ($v_p = 149$ m/s) are depicted in the last row showing a significantly different crack pattern. The specimen is highly fragmented in a region next to the aluminum sleeve. This is evident on the right side of the y- and z-slices. The cause of the strongly asymmetrical fracture is not clear as the high-speed video of the pre-damaging test indicates a plane impact (ref. 20985 in Figure 5.7).

In summary, the four specimens pre-damaged at 140 to 190 m/s exhibit significantly different crack patterns. Therefore, it is inferred that the generation of a reproducible degree of damage is more difficult in this velocity range. Specimen 20985 is strongly asymmetrically fractured.

Probably too few cracks are identifiable in specimen 21194 ($v_p = 144$ m/s). Specimens 20984 ($v_p = 146$ m/s) and 20983 ($v_p = 186$ m/s) exhibit comparable crack patterns. These patterns are similar to those of the low velocity range, but with a higher crack density (finer mesh in z-slices). Therefore, it is proposed to take these specimens as representative for the intermediate velocity range.

Specimens pre-damaged at high velocities (230 to 270 m/s)

Figure 5.35 shows the results of the specimens pre-damaged at high impact velocities between 230 to 270 m/s. In the first row, the slices of the PCI of specimen 21201 ($v_p = 266$ m/s) are illustrated. As discussed in the previous section, the cracks of this specimen look significantly different from those of the specimens damaged at lower impact velocities. The amount of cracks is higher forming a fine mesh rather than a coarse mesh. Especially noticeable are distinct horizontal crack planes in the top and middle analysis volumes.

The results of the micro-CT of the same specimen are shown in the second row. Unfortunately, the contrast of the cracks is too low for a sufficient identification. Only a distinct horizontal crack is apparent in the center right region of the x- and y-slices. In the z-slice, many residual ring artifacts are evident. The correction algorithm has not been able to remove these artifacts as they exhibit significantly varying gray scale values along the circumference (one half of a single ring is bright, while the other half is dark). The residual artifacts additionally prevent an identification of the cracks.

Similar observations apply to the slices of specimens 20986 ($v_p = 235$ m/s) and 20980 ($v_p = 257$ m/s) shown in the third and fourth row of Figure 5.35. Only some distinct horizontal crack planes are apparent in the x- and y-slices. In addition, many residual ring artifacts are visible in the z-slices. In contrast to specimen 21201, some distinct vertical cracks are evident in the z-slices, especially in the upper area of specimen 20986.

As most cracks are not visible in the micro-CT slices, it is not possible to estimate the level of reproducibility of the generated pre-damage in this velocity range. Therefore, the PCI results of specimen 21201 ($v_p = 266$ m/s) are regarded as representative.

Specimens with the largest crack volume (no. 21200 and 20979+P)

Figure 5.36 shows the results of the specimens with the largest crack volume. In the first row, the slices of the PCI of specimen 21200 damaged at the highest impact velocity ($v_P = 407$ m/s) are illustrated. As discussed in the previous section, the cracks form a fine mesh spreading over large parts of the specimen. The segmentation algorithm identifies most of the cracks visible in the tomograms correctly.

In contrast, far less cracks are visible in the micro-CT slices of the same specimen, shown in the second row of Figure 5.36. This observation is similar to those of the micro-CT slices of the high velocity range ($230 \text{ m/s} < v_P < 270 \text{ m/s}$), in which many cracks can neither be identified.

Therefore, the micro-CT data is not suited for the evaluation of the pre-damage at this velocity range, which is similar to the results of the micro-CT data at 230 – 270 m/s.

The slices of specimen 20979+P are shown in the last two rows of Figure 5.36. This specimen was pre-damaged at 69 m/s and afterwards subjected to a high quasi-static load in a confined pressure test. The slices of the PCI are depicted in the third row. As described in the previous section, the damage generated by the pressure test differs from the pre-damage of the dynamic impact tests. More horizontal crack planes are apparent that are thicker than the cracks observed in the other specimens. As the cracks are thicker overall, they can be identified visually in the micro-CT slices (fourth line), as well. Here, the identifiability of the cracks is comparable to those of the cracks generated at ~ 70 m/s (Figure 5.33). Nevertheless, residual ring artifacts, gray scale gradients and a lower contrast impede an automated segmentation.

The micro-CT slices of specimen 20979 in the fourth row of Figure 5.33 illustrate the same specimen before it has been loaded in the confined pressure test.

In summary, the micro-CT data is not suited for a quantitative analysis of the crack volume in the analyzed specimens. Most of the cracks generated at high velocities (230 – 400 m/s) cannot be identified by a segmentation process (or even just visually).

However, the micro-CT data is well suited to supplement the PCI data of the specimens pre-damaged at lower velocities (70 – 190 m/s). In these specimens, most of the cracks visible in the PCI slices are also apparent in the micro-CT slices. Therefore, the crack patterns can be described qualitatively. Similar observations apply to the cracks generated by the loading in a confined pressure test.

The benefit of the micro-CT is that the amount of analyzed specimens was not limited, within the scope of this thesis, as opposed to the PCI. Therefore, the micro-CT data increases the sample size allowing the identification of specimens with representative crack patterns.

In particular, the comparison of the specimens pre-damaged at 140-190 m/s indicates that specimen no. 21194 is not representative for this velocity range.

Development of a novel methodology for generating, characterizing and pressure testing of defined damaged glass specimens

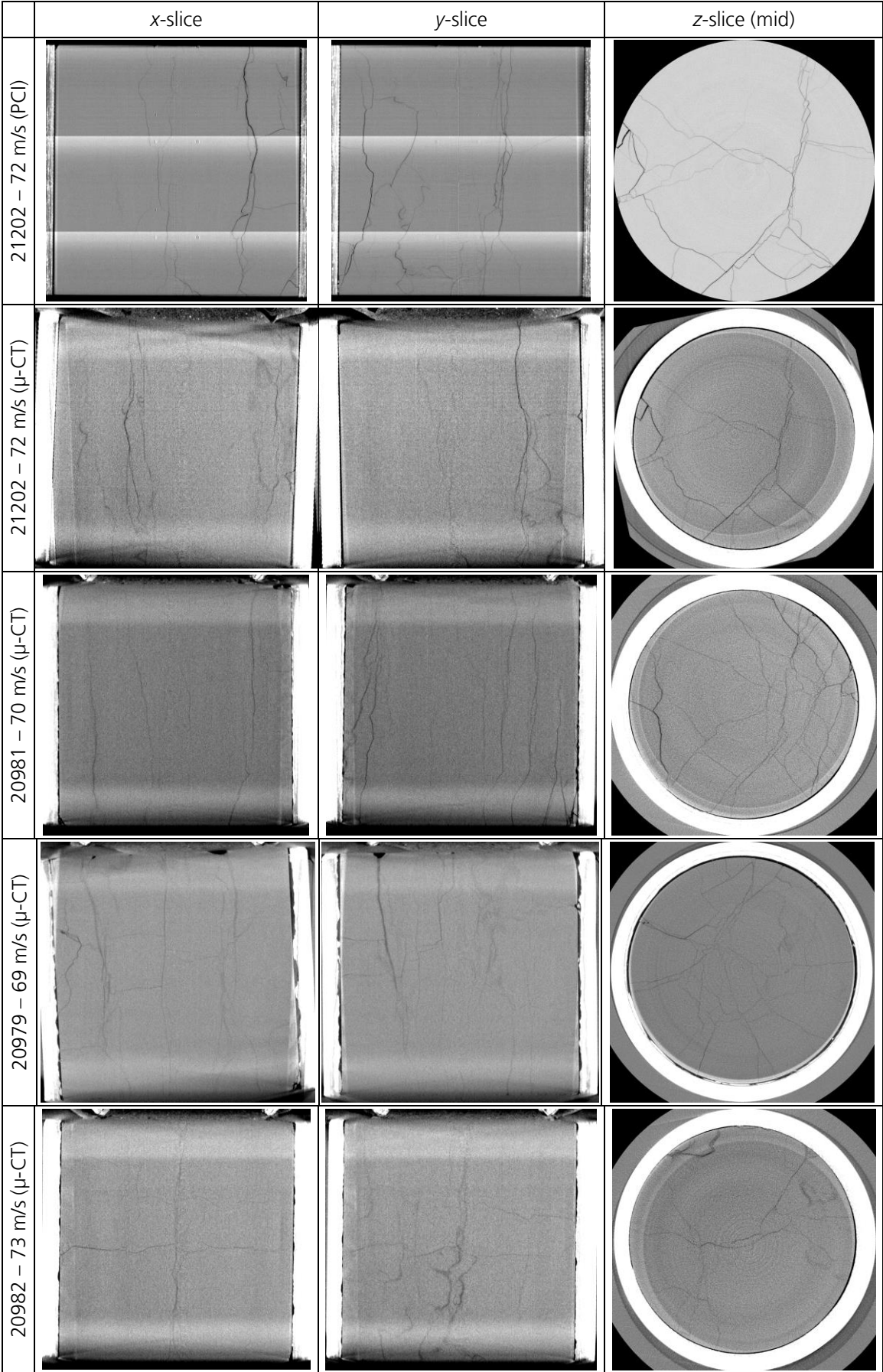


Figure 5.33: Comparison of tomograms from SLG specimens pre-damaged at ~70 m/s.

Development of a novel methodology for generating, characterizing and pressure testing of defined damaged glass specimens

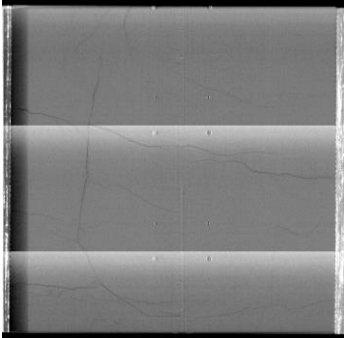
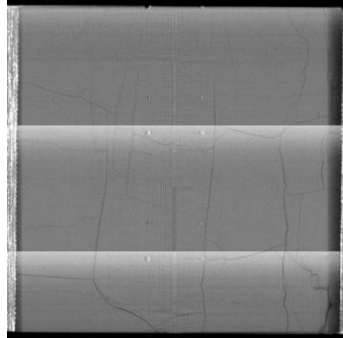
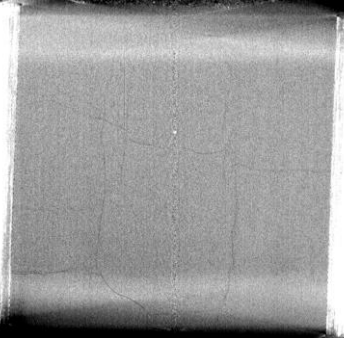
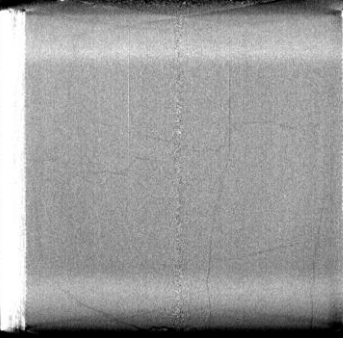
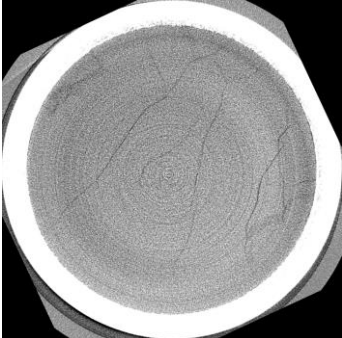
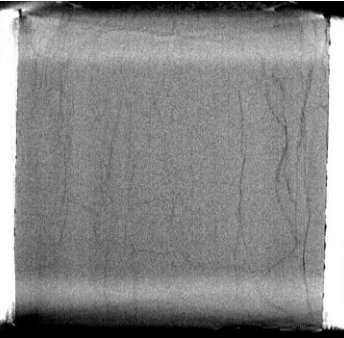
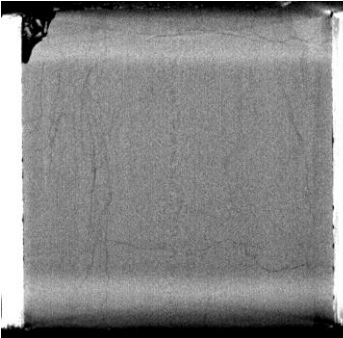
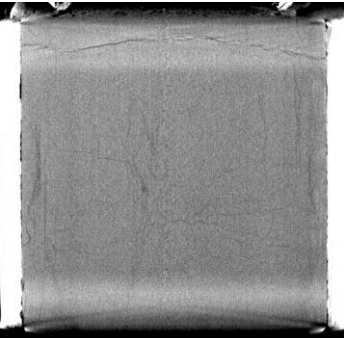
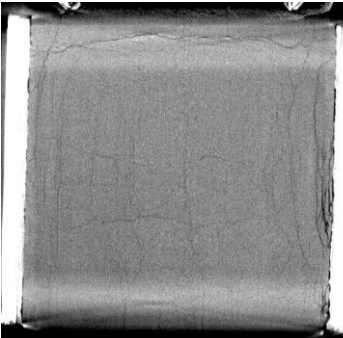
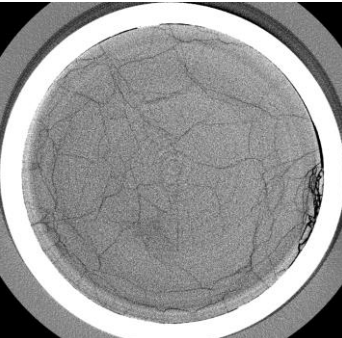
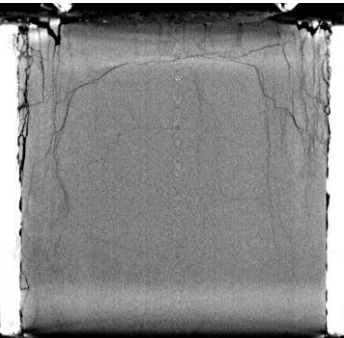
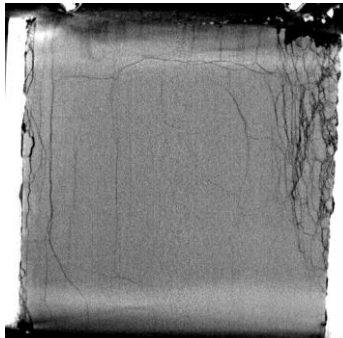
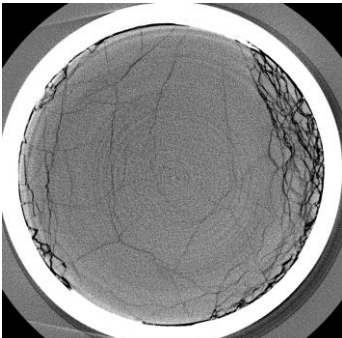
	x-slice	y-slice	z-slice (mid)
21194 – 144 m/s (PCI)			
21194 – 144 m/s (μ-CT)			
20984 – 146 m/s (μ-CT)			
20983 – 186 m/s (μ-CT)			
20985 – 149 m/s (μ-CT)			

Figure 5.34: Comparison of tomograms from SLG specimens pre-damaged at 140-190 m/s.

Development of a novel methodology for generating, characterizing and pressure testing of defined damaged glass specimens

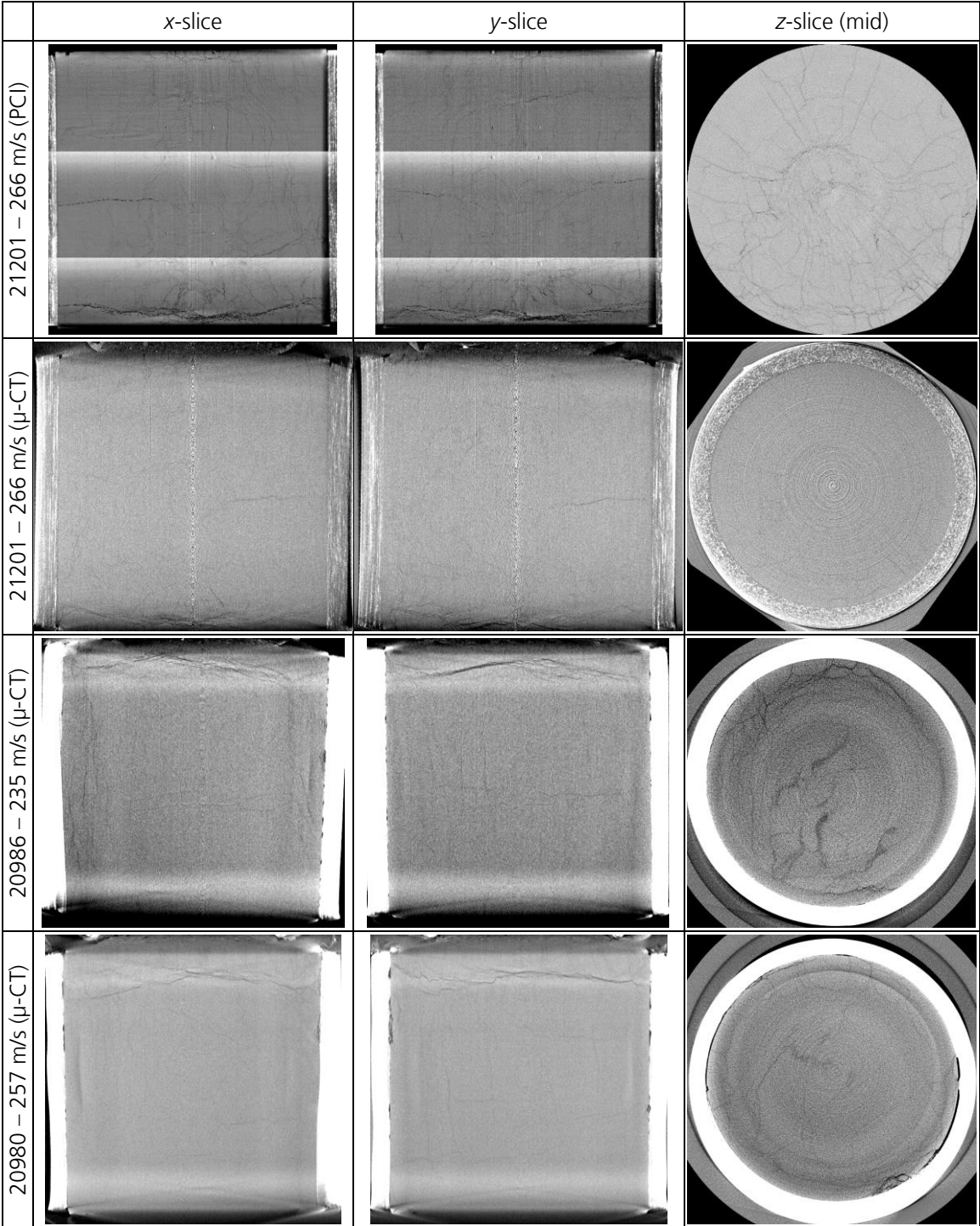


Figure 5.35: Comparison of tomograms from SLG specimens pre-damaged at 230-270 m/s.

Development of a novel methodology for generating, characterizing and pressure testing of defined damaged glass specimens

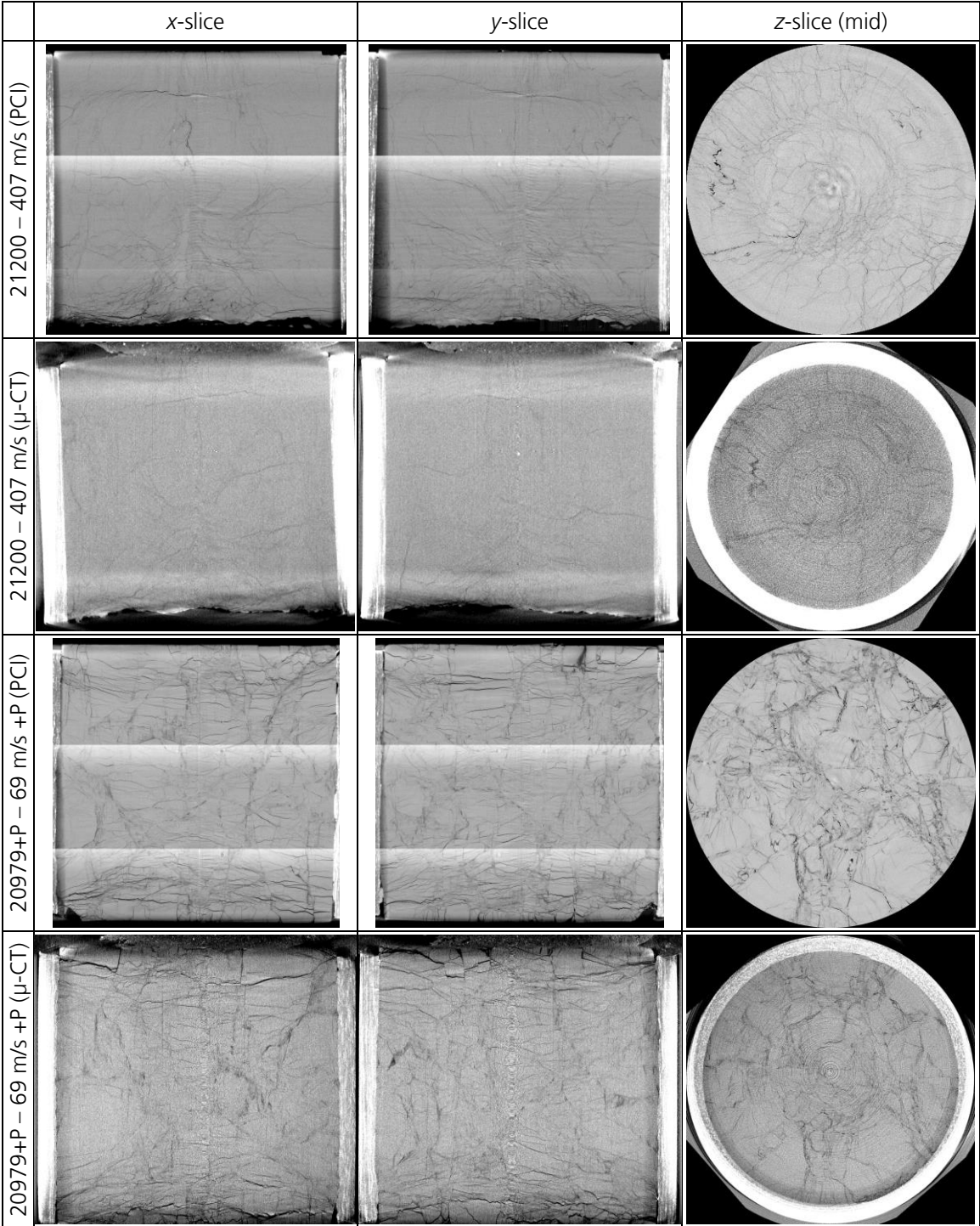


Figure 5.36: Comparison of tomograms from SLG specimens 21200 (pre-damaged at 407 m/s) and 20979+P (pre-damaged at 69 m/s and loaded in confined pressure test).

5.4 Pressure testing of intact and damaged soda-lime glass specimens

In this section, it is outlined how the strength of SLG is determined as a function of the hydrostatic pressure and the degree of pre-damage. Intact specimens as well as pre-damaged specimens were loaded quasi-statically under compression by means of a MTS machine. Intact specimens were tested with and without confinement in order to determine Young's modulus and the strength of intact SLG under uniaxial stress and triaxial stress conditions. Confined compression tests on specimens with different degrees of pre-damage (quantified by means of X-ray CT, ref. section 5.3) were conducted in order to measure the residual strength of failed SLG.

Based on experimental techniques reported in the literature ([125] [126] [127] [17] [62] [63] [21] [22] [124]), enhanced testing and analysis methods were developed. One new aspect is that the steel confinement was replaced in most tests by a tungsten carbide confinement. This has the advantage that the occurring radial displacement of the SLG specimens is more limited. In addition, the loading of the tungsten carbide confinement can be regarded to be elastic since exceeding its elastic limit would result in brittle fracture. A second new aspect is that the experiments were supported by an elaborated simulative study. The results of the simulations allowed accounting for the influence of friction and the more complex test setup (SLG specimens were within aluminum sleeves, which is a novelty). Additional tests on low-strength polyurethane specimens were conducted to verify the analysis methods.

5.4.1 Experimental setup

All compression tests were conducted on a MTS machine from the company Zwick-Roell. The specimens were placed between two cylindrical tungsten carbide cylinders. The axial compressive stress was applied on the cylinders by means of two tungsten carbide plates placed between the mounting surfaces of the MTS. All specimens were loaded quasi-statically by moving the actuator with a displacement velocity of 1 mm / min.

For the triaxial tests, a lateral confinement was provided by means of a tungsten carbide or hardened steel sleeve. Figure 5.37 shows a schematic of the triaxial test setup.

The steel sleeves were made of 30CrNiMo8 (#1.6580) heat treated under inert gas by the company VTN Fritz Düsseldorf GmbH to increase the yield strength from about 900 MPa to almost 1400 MPa. The tungsten carbide sleeves, plates and cylinders were manufactured by the company SMT Sondermetalltechnik. The tungsten carbide had a submicron grain size and 10 % cobalt binder exhibiting a nominal compressive strength of 6.6 GPa and flexural strength of 4 GPa (manufacturer's designation "CTS20"). Both types of confinement had a length of 24 mm, which is considerably longer than the length of the SLG specimens (6 mm). The confinements could therefore be used as lateral guidance for the tungsten carbide cylinders. The outer radii were 11.5 mm for the steel confinement and 10 mm for the tungsten carbide confinement. For both materials, the inner radii were in the range of 3.505 to 3.520 mm (manufacturing tolerance). The tungsten carbide cylinders had a length of 12 mm and a radius of 3.5 mm matching the radius of the test specimens (SLG + aluminum sleeve). The tungsten carbide plates had a size of 50 mm x 50 mm x 8 mm.

The SLG test specimens were intact and pre-damaged cylinders of radius 3 mm and length 6 mm surrounded by a 0.5 mm thick aluminum sleeve. Two types of polyurethane specimens were prepared from Sikaflex®-252: cylinders with the same size as the SLG specimens,

surrounded by the aluminum sleeve, and larger cylinders of radius 3.5 mm and length 6 mm without a sleeve. Polyurethane was chosen as it is easy to cast into shape and has a negligible shear strength.

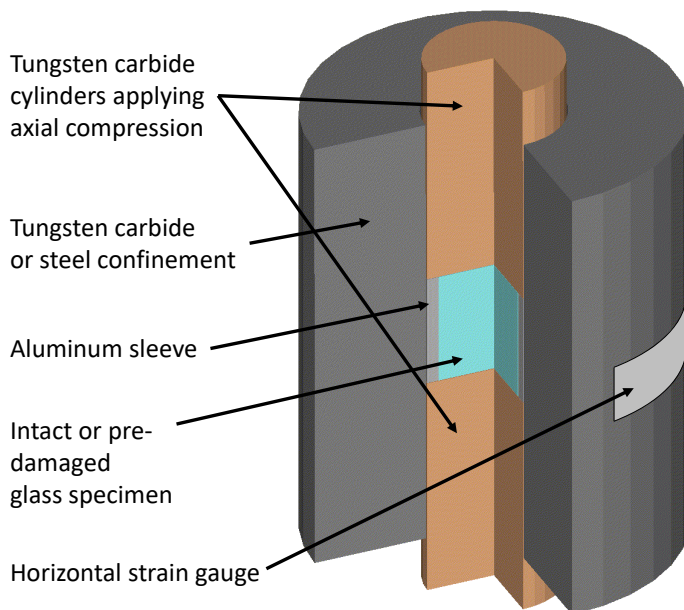


Figure 5.37: Schematic of triaxial test setup. The setup is placed in the MTS machine between two tungsten carbide plates applying the axial load.

In all tests, the axial force F_{axi} was measured by a load cell in the MTS machine. Two horizontal strain gauges mounted on opposite sides of the external surface of the confining sleeve were used to measure the hoop strain ϵ_{hoop} . In addition, the displacement Δl_{stamp} of the tungsten carbide cylinders was measured by means of continuous edge tracking using two high-resolution cameras.

Figure 5.38 shows a picture of the MTS machine. The detailed setup between the mounting surfaces of the machine is illustrated in Figure 5.39. The picture on the left side shows a setup without test specimen and confinement. This setup is used as reference to determine the displacement caused solely by the elastic deformation of the tungsten carbide cylinders. This displacement needs to be subtracted in the subsequent characterization tests in order to determine the axial strain in the specimens. The picture on the right side of Figure 5.39 shows the setup of a triaxial characterization test. The confinement was placed on an elastomeric O-ring to adjust its initial vertical position. One quarter of the O-ring has been removed previously in order to provide visibility on the bottom cylinder for the edge tracking.

The confined tests were stopped at a maximum axial force of 115 kN to limit the stress exerted on the confinement.

After each triaxial compression test, the test specimen was extracted from the confinement. For this purpose, an extraction unit was developed (see Figure 5.40). The unit consists of two hollow, cylindrical steel parts that can be clamped onto the confinement. The hole in the bottom part provides a lateral guidance for a long brass rod. By means of the MTS, the brass rod is used to push the test specimen and the tungsten carbide cylinders upwards into the cavity of the top part of the extraction unit.

Development of a novel methodology for generating, characterizing and pressure testing of defined damaged glass specimens



Figure 5.38: MTS machine of company Zwick-Roell used for the compression tests.

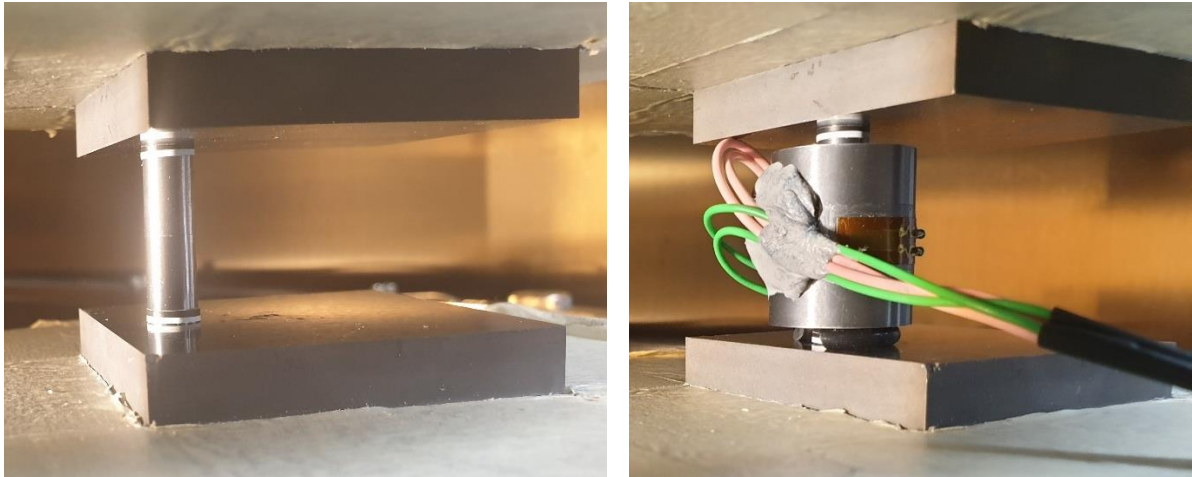


Figure 5.39: Experimental setup within the testing machine:
Left picture: reference test setup with two tungsten carbide stamps between two tungsten carbide plates. The affixed black-and-white stripes are used for the edge tracking.
Right picture: characterization setup with test specimen placed between the cylinders, surrounded by a tungsten carbide confinement.

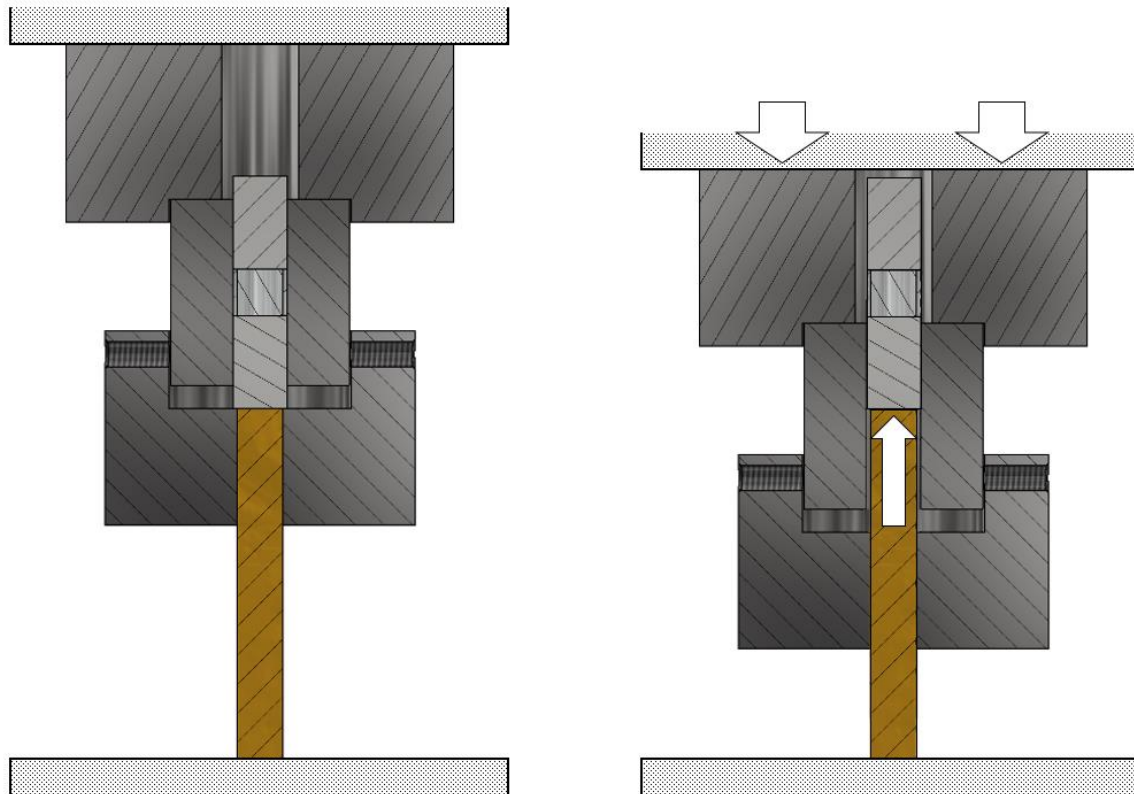


Figure 5.40: Schematic of the extraction unit: After each compression test, the unit is used to extract the specimen from the confinement. The specimen and the tungsten carbide cylinders are pushed upwards into a cavity by means of a long brass rod.

5.4.2 General analysis considerations

In this section, it is outlined how the elastic constants as well as the strength of the specimens are derived from the measured quantities.

The experimentally measured quantities are the axial force F_{axi} in the load cell of the MTS machine, the displacement Δl_{test} between the black-and-white striped markers affixed to the tungsten carbide cylinders and the bridge output voltage U_d of the strain gauges used to determine the hoop strain $\varepsilon_{\text{hoop}}$ at the outer surface of the confinement.

5.4.2.1 Analysis of unconfined compression tests

The unconfined compression tests are used to determine the Young's modulus and the maximum axial stress at failure. For the determination of Young's modulus, the derivative of the stress-strain-curve under uniaxial stress conditions has to be determined. In the unconfined tests, the (engineering) stress σ_{axi} and strain ε_{axi} in the specimen are measured in axial direction and the radial stress is always zero $\sigma_{\text{rad}} = 0$. For small strains ($\varepsilon_{\text{axi}} \ll 0.1$), Young's modulus is given by:

$$E = \frac{d\sigma_{\text{axi}}}{d\varepsilon_{\text{axi}}} \quad 5.5$$

If the radii of the cylindrical specimen and the stamps are equal $r_{0,\text{spec}} = r_{\text{stamp}}$, σ_{axi} is deduced from the measured axial force F_{axi} as follows:

$$\sigma_{\text{axi}} = \frac{F_{\text{axi}}}{A_{\text{stamp}}} = \frac{F_{\text{axi}}}{\pi \cdot r_{\text{stamp}}^2} \quad 5.6$$

The axial strain is the change of the specimen length Δl_{spec} divided by its initial length $l_{0,\text{spec}}$:

$$\varepsilon_{\text{axi}} = \frac{\Delta l_{\text{spec}}}{l_{0,\text{spec}}} \quad 5.7$$

Δl_{spec} is inferred from the measured displacement $\Delta l_{\text{test}}(F_{\text{axi}})$ of the markers on the stamps. Here, two important aspects have to be taken into account. On the one hand, the displacement caused by the elastic deformation of the stamps has to be determined and subtracted. On the other hand, gaps or misalignments at the beginning of the experimental tests can lead to an initial displacement, which also has to be determined and subtracted.

In order to determine the elastic deformation of the stamps, experiments with a reference setup are conducted in addition to the test setup with the specimen. In the reference setup, the specimen is removed, so that the stamps press directly against each other. Figure 5.41 illustrates schematically the reference setup (illustrations a), b) and c)) and the test setup with specimen d). The measured displacement of the reference setup a) is subtracted from the measured displacement of the test setup d) in order to receive the displacement of the specimen. However, the initial displacement caused by gaps or misalignments has to be removed prior to the subtraction. For the reference setup, this displacement is visualized in Figure 5.41 a) by the red crosses ($\Delta l_{\text{align,ref}}$). The reference length of the aligned stamps is the difference of the initial distance $l_{0,\text{ref}}$ between the markers and $\Delta l_{\text{align,ref}}$ (ref. Figure 5.41 b)). The force per displacement, required to close the gaps, is significantly lower than the force per elastic displacement of the stamps (due to the large Young's modulus). Therefore, $\Delta l_{\text{align,ref}}$ can be deduced from the force-displacement-curve by a linear extrapolation. The same considerations apply to the initial distance $l_{0,\text{test}}$ between the markers in the test setup and the corresponding initial displacement $\Delta l_{\text{align,test}}$ (ref. Figure 5.41 d)). This is exemplarily shown in Figure 5.42 for the measured curves of test #21202. The diagram on the left displays the axial force versus the axial displacement in the reference setup, $\Delta l_{\text{ref}}(F_{\text{axi}})$ (blue line), and in the test setup with specimen, $\Delta l_{\text{test}}(F_{\text{axi}})$ (green line). Two force thresholds ($F_{\text{TH,low}}$ and $F_{\text{TH,high}}$) are specified, as indicated by the horizontal dashed lines. Between the thresholds, linear best-fit lines are determined. The extrapolation of the fit lines to $F_{\text{axi}} = 0$ yields $\Delta l_{\text{align,ref}}$ and $\Delta l_{\text{align,test}}$, respectively. Subtracting $\Delta l_{\text{align,ref}}$ and $\Delta l_{\text{align,test}}$ from the corresponding measurement curves yields $\Delta l_{\text{ref}}^*(F_{\text{axi}})$ and $\Delta l_{\text{test}}^*(F_{\text{axi}})$:

$$\Delta l_{\text{ref}}^*(F_{\text{axi}}) = \Delta l_{\text{ref}}(F_{\text{axi}}) - \Delta l_{\text{align,ref}} \quad 5.8$$

$$\Delta l_{\text{test}}^*(F_{\text{axi}}) = \Delta l_{\text{test}}(F_{\text{axi}}) - \Delta l_{\text{align,test}} \quad 5.9$$

Δl_{ref}^* is also visualized in Figure 5.41 c). $\Delta l_{\text{ref}}^*(F_{\text{axi}})$ and $\Delta l_{\text{test}}^*(F_{\text{axi}})$ are plotted in the right diagram of Figure 5.42. For a given axial force F_{axi} , the difference between both curves yields the displacement in the specimen $\Delta l_{\text{spec}}(F_{\text{axi}})$:

$$\Delta l_{\text{spec}}(F_{\text{axi}}) = \Delta l_{\text{test}}^*(F_{\text{axi}}) - \Delta l_{\text{ref}}^*(F_{\text{axi}}) \quad 5.10$$

Development of a novel methodology for generating, characterizing and pressure testing of defined damaged glass specimens

The initial length of the specimen $l_{0,spec}$ is the difference of the marker distances in both setups after closing the gaps:

$$l_{0,spec} = (l_{0,test} - \Delta l_{align,test}) - (l_{0,ref} - \Delta l_{align,ref}) \quad 5.11$$

Together with equations 5.6 and 5.7, the stress-strain-curve is plotted and E (equation 5.5) is determined by means of a linear best-fit line.

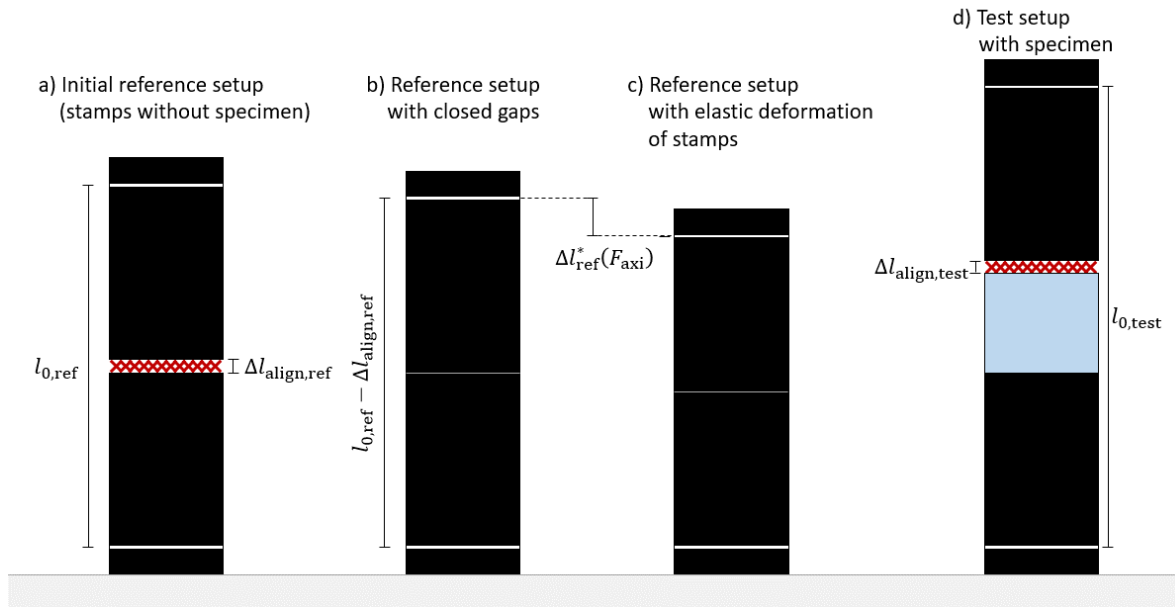


Figure 5.41: Schematic of reference setup and test setup with specimen:

- The initial distance $l_{0,ref}$ between the markers includes a displacement $\Delta l_{align,ref}$ (red crosses) caused by gaps or misalignment.
- The reference length of the stamps is obtained by subtracting $\Delta l_{align,ref}$.
- $\Delta l_{ref}^*(F_{axi})$ is the displacement caused by the elastic deformation of the stamps.
- The initial distance $l_{0,test}$ between the markers in the test setup also includes a displacement $\Delta l_{align,test}$ caused by gaps or misalignment.

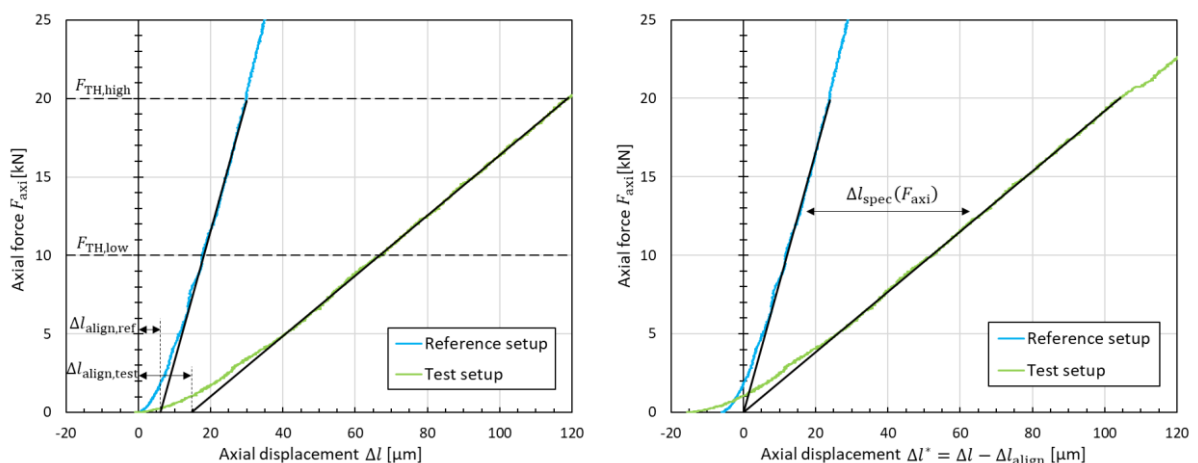


Figure 5.42: Axial force versus axial displacement for the reference setup (blue line) and the test setup (green line) measured with specimen #21202.

Left diagram: With the measured data linear best-fit lines are determined between two force thresholds (horizontal dashed lines). $\Delta l_{align,ref}$ and $\Delta l_{align,test}$ are obtained by extrapolating the fit lines to $F_{axi} = 0$. Right diagram: Subtracting $\Delta l_{align,ref}$ and $\Delta l_{align,test}$ from the measured data yields $\Delta l_{ref}^*(F_{axi})$ and $\Delta l_{test}^*(F_{axi})$. The difference between both curves is the displacement $\Delta l_{spec}(F_{axi})$ of the specimen.

5.4.2.2 Analysis of confined compression tests

The purpose of the confined compression tests is to determine the strength of the specimens as a function of the hydrostatic pressure. Here, strength refers to the capability of supporting shear loading. The limit of this strength is represented by a surface in the principal stress space. Chocron et al. suggested that "For intact material, this might be thought of as a failure surface; for pre-damaged material, it might be a flow surface" [63](p.3392). When plotting the equivalent stress versus the hydrostatic pressure P , the limit is represented by a line.

In the confined compression tests, the loading state is axisymmetric. In consequence, σ_{eq} and P can be calculated from the axial stress σ_{axi} and radial stress σ_{rad} as follows (see e.g. [21] or [124]):

$$\sigma_{eq} = |\sigma_{axi} - \sigma_{rad}| \quad 5.12$$

$$P = -\frac{1}{3}(\sigma_{axi} + 2 \cdot \sigma_{rad}) \quad 5.13$$

Therefore, it is sufficient to determine the axial and radial stress exerted on the specimen. In principle, σ_{axi} is calculated from the axial force applied by means of the MTS machine. Simultaneously, σ_{rad} is inferred from the elastic properties of the confinement and the hoop strain ε_{hoop} at the external surface of the confinement.

Here, ε_{hoop} is measured by means of two strain gauges used in a half bridge configuration. The hoop strain is calculated from the measured bridge output voltage U_d as follows [256]:

$$\varepsilon_{hoop}(U_d) = \frac{2}{k} \cdot \frac{U_d}{U_s} \cdot \frac{1}{f_{amp}} \quad 5.14$$

with: gauge factor $k = 2.05 \pm 0.02$, amplification factor $f_{amp} = 1000$ and bridge power supply $U_s = 5 \text{ V}$.

The in-depth methods for the determination of σ_{axi} and σ_{rad} are strongly dependent on the setup of the confined compression tests. Especially in case of the pre-damaged SLG specimens, which are surrounded by thin aluminum sleeves, numerical simulations are required for the analysis. The developed methods are presented in the next section (5.4.3).

The confined compression tests can also be used to determine the bulk modulus K of the specimens, which is the derivative of the pressure-compression-curve:

$$K = \frac{dP}{d\mu} \quad 5.15$$

The hydrostatic pressure P is determined using equation 5.13. In order to determine the volumetric compression (ref. equation 2.84), the initial volume $V_{0,spec}$ and the actual volume V_{spec} of the specimen are required:

$$\mu = \frac{V_{0,spec}}{V_{spec}} - 1 = \left(\frac{l_{0,spec} \cdot r_{0,spec}^2}{(l_{0,spec} - \Delta l_{spec}) \cdot (r_{0,spec} + \Delta r_{spec})^2} \right) - 1 \quad 5.16$$

Where the radial displacement Δr_{spec} of the specimen is deduced from numerical simulations as outlined in the following section.

5.4.3 Development of advanced analysis methods of confined compression tests using quasi-static numerical simulations

As outlined in the previous section, the axial and radial stress exerted on the specimen have to be determined in order to determine the specimen strength. The exact procedure is however dependent on the specific confined test setup. In the following three different setups are investigated that are illustrated in Figure 5.43.

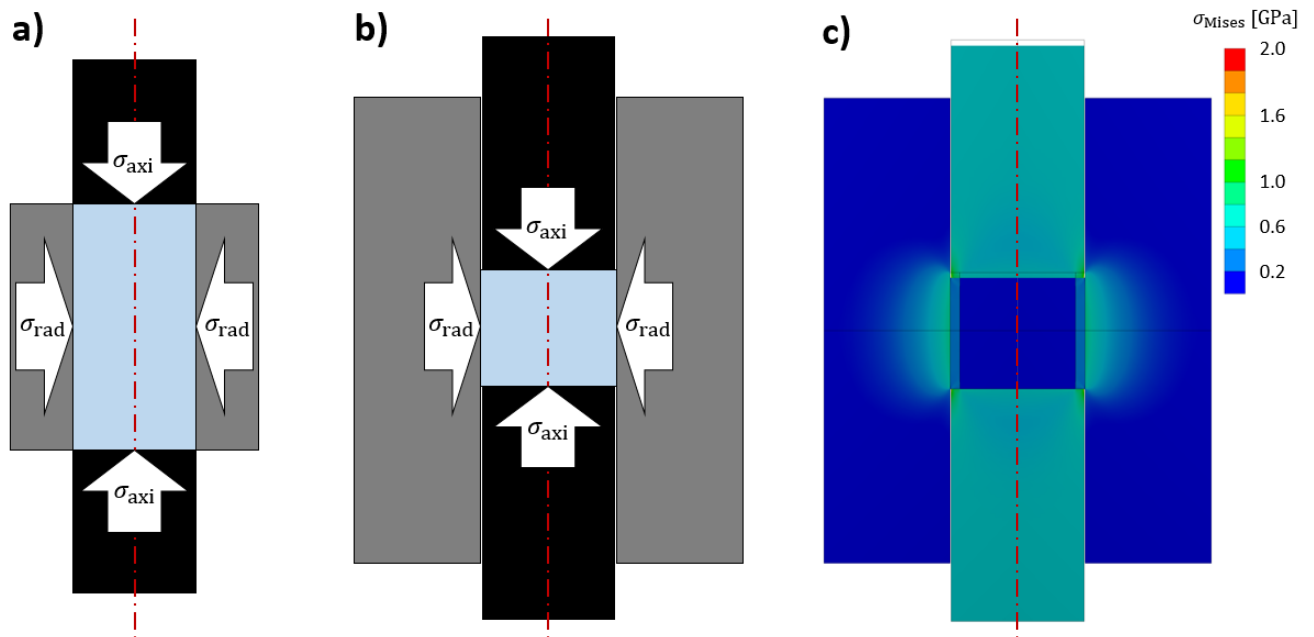


Figure 5.43: Schematic of stresses in triaxial compression tests (the axis of rotation is illustrated as dash-dotted red line). Three different setups are investigated:
a) the specimen (blue) is confined by a sleeve of equal length (gray). If the black cylinders apply an axial stress, the specimen exerts a radial stress on the entire inner surface of the confinement, which is also the confinement pressure of the specimen.
b) The length of the confinement is bigger than that of the specimen. In this case, the radial stress is only exerted on the contact surface between specimen and confinement. This leads to bulging of the confinement.
c) The axial stress is applied to a specimen surrounded by a thin aluminum sleeve. In this case, the calculation of the stress state in the specimen is more complex. The illustration shows a contour plot of the equivalent stress for a polyurethane cylinder within a thin aluminum sleeve under an axial load of 600 MPa.

5.4.3.1 a) Confined compression test with equal lengths of specimen and confinement

The simplest setup is illustrated in Figure 5.43 a). In this case, the length of the specimen (blue) and the confinement (gray) are equal. In addition, the radii of the cylindrical stamps (black) and

the specimen are also equal. The specimen exerts a radial stress on the entire inner surface of the confinement, which is also the confinement pressure of the specimen.

This setup was used e.g. by Dannemann and Chocron et al. [21] [22]. The axial stress is obtained directly by dividing the axial force F_{axi} , measured by the load cell of the MTS, by the circular area of the stamps (see equation 5.6).

The radial stress is calculated analytically assuming a perfectly elastic deformation of the confinement. In this case, the relation between σ_{rad} and the hoop strain $\varepsilon_{\text{hoop}}$ at the outer surface of the confinement is given by Lamé's equations for a thick walled cylinder (ref. e.g. [257]):

$$\sigma_{\text{rad}}(\varepsilon_{\text{hoop}}) = \varepsilon_{\text{hoop}} \cdot \frac{1}{m} \tag{5.17}$$

$$\text{with: } m = \frac{2 \cdot r_{\text{inner}}^2}{E_{\text{conf}} \cdot (r_{\text{outer}}^2 - r_{\text{inner}}^2)}$$

where r_{outer} and r_{inner} denote the outer and inner radius of the confinement and E_{conf} denotes its Young's modulus.

However, this method is only applicable if the lengths of the specimen and the confinement are equal. When the axial load is applied, the specimen gets compacted and its length decreases. As a result, the radial stress is not exerted on the entire inner surface of the confinement, but only on the contact surface between specimen and confinement. The larger the difference between the length of the specimen and the confinement is, the larger is the discrepancy between the real σ_{rad} and the analytical solution (eq. 5.17).

A more suitable approach is therefore to deduce the relation between σ_{rad} and $\varepsilon_{\text{hoop}}$ by means of quasi-static numerical simulations, as outlined in the next section (5.4.3.2). A similar approach was used e.g. by Forquin et al. [124] for the characterization of concrete specimens.

5.4.3.2 b) Confined compression test with long confinement and shorter specimen

Figure 5.43 b) illustrates a test setup with a confinement that is significantly longer than the specimen. This configuration has the advantage, that the longer confinement can be used as lateral guidance for the cylindrical stamps. The calculation of the axial stress on the specimen is the same as with setup a) (eq. 5.6). On the contrary, the analytical solution (eq. 5.17) for the determination of σ_{rad} cannot be used since only the central region of the confinement is exposed to the loading. However, σ_{rad} as a function of $\varepsilon_{\text{hoop}}$ and the specimen length L can be deduced from a numerical parameter study.

In the following, the simulation results for a tungsten carbide confinement with $r_{\text{inner}} = 3.5 \text{ mm}$, $r_{\text{outer}} = 10 \text{ mm}$ and a length of 24 mm are presented. The resulting $\sigma_{\text{rad}}(\varepsilon_{\text{hoop}}, L)$ is used in section 5.4.4.2 for the analysis of a low-strength polyurethane specimen.

The simulation is conducted using the implicit solver of the Ansys workbench module "Mechanical". In the left image of Figure 5.44 the initial setup is depicted. Due to the symmetry of the problem, a two-dimensional model can be used. The rotation axis is indicated by a red dash-dotted line and the mirror plane is represented by a blue dotted line. The radial stress is applied on the inner surface by means of a boundary condition. In the illustrated case, a stress of 1 GPa is applied to a length of 3 mm as indicated by the red thick line and the arrow. This

configuration corresponds to a specimen length of $L = 6 \text{ mm}$. The resulting hoop strain is illustrated in the contour plot on the right side of Figure 5.44. A gauge point positioned at the center of the outer surface (red cross) provides the hoop strain corresponding to the measurement value of the strain gauges in the experiments. For the purpose of illustrating the bulging of the confinement, it is shown in an exaggerated way (times 50).

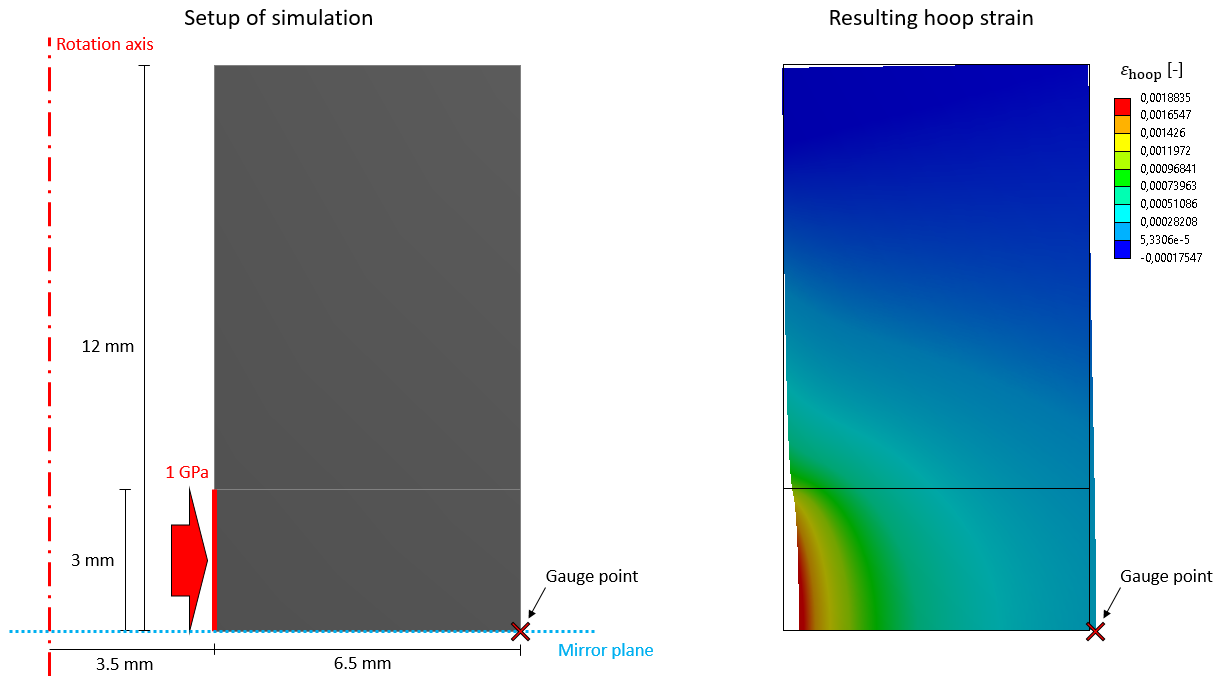


Figure 5.44: Schematic of a numerical simulation: The illustration on the left shows the initial setup for a confinement of a specimen with 6 mm length. Due to the symmetry, a two-dimensional model can be used (rotation axis = red dash-dotted line; mirror plane = blue dotted line). A radial stress of 1 GPa is applied on the inner surface by means of a boundary condition (red arrow and line). The right side shows a contour plot of the resulting hoop strain. The deformation is shown exaggerated (times 50) to illustrate the bulging of the confinement.

In order to determine the relation between σ_{rad} and $\varepsilon_{\text{hoop}}$, a parameter study was conducted. On the one hand, $\varepsilon_{\text{hoop}}$ in the gauge point is evaluated for different values of σ_{rad} , while keeping the length of the specimen constant ($L = 6 \text{ mm}$). On the other hand, $\varepsilon_{\text{hoop}}$ is determined for different values of L , while keeping the radial stress constant ($\sigma_{\text{rad}} = 1 \text{ GPa}$).

The left diagram of Figure 5.45 shows the resulting $\varepsilon_{\text{hoop}}(\sigma_{\text{rad}})|_{L=6 \text{ mm}}$ for an elastic tungsten carbide confinement with a Poisson's ratio of $\nu = 0.21$ and Young's modulus $E_{\text{conf}} = 625.7 \text{ GPa}$. The green circles denote the resulting $\varepsilon_{\text{hoop}}$ for different σ_{rad} in the range of 0 and 2 GPa. The green line illustrates that the radial stress increases linearly with increasing hoop strain with a proportionality factor of

$$m(L = 6 \text{ mm}) = \frac{\varepsilon_{\text{hoop}}(\sigma_{\text{rad}})|_{L=6 \text{ mm}}}{\sigma_{\text{rad}}} = 2.788 \cdot 10^{-4} \frac{1}{\text{GPa}} \quad 5.18$$

This factor is depending on L . The dependency is deduced from the diagram shown on the right side of Figure 5.45. In this diagram, the green circles denote the resulting $\varepsilon_{\text{hoop}}(L)|_{\sigma_{\text{rad}}=1 \text{ GPa}}$ for different values of L at a constant radial stress of $\sigma_{\text{rad}} = 1 \text{ GPa}$. The dependency of $\varepsilon_{\text{hoop}}$ on L can be approximated by a cubic polynomial (green line).

Dividing the polynomial by the constant radial stress yields the proportionality factor as a function of L and consequently the conversion formula:

$$\sigma_{\text{rad}}(\varepsilon_{\text{hoop}}, L) = \varepsilon_{\text{hoop}} \cdot \left(-1.9888 \cdot 10^{-6} \frac{L^2}{\text{mm}^2} + 6.0775 \cdot 10^{-5} \frac{L}{\text{mm}} - 1.4253 \cdot 10^{-5} \right)^{-1} \text{ GPa} \quad 5.19$$

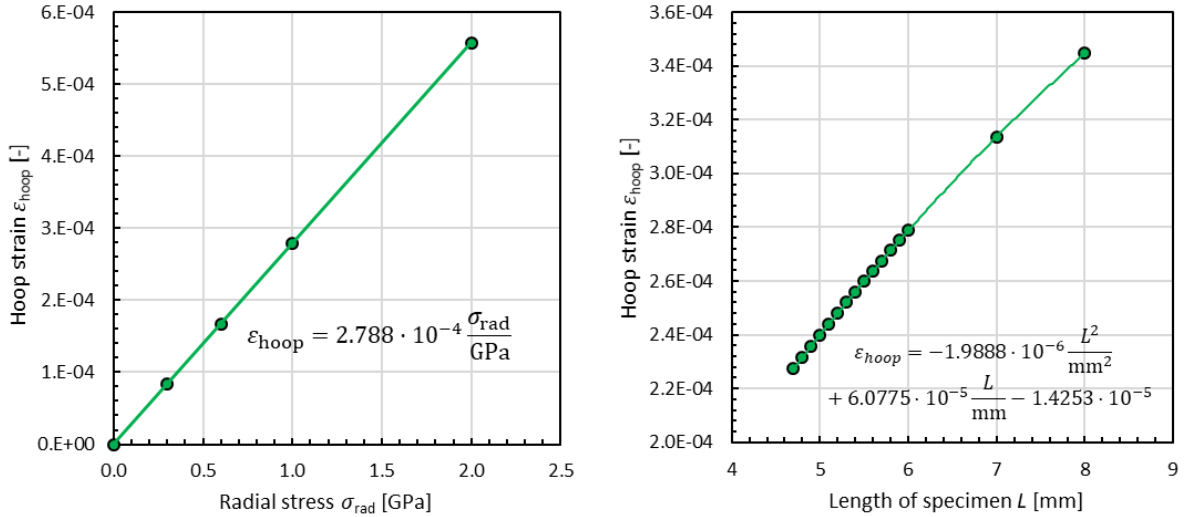


Figure 5.45: Simulation results for an elastic tungsten carbide confinement.
 Left diagram: simulated radial stress as a function of the hoop strain for a constant specimen length of $L = 6 \text{ mm}$.
 Right diagram: simulated hoop strain as a function of the specimen length for a constant radial stress of $\sigma_{\text{rad}} = 1 \text{ GPa}$.

It should be noted that the polynomial dependency shown in Figure 5.45 (right diagram) is not valid for significantly larger specimen lengths. Reaching the maximum value of $L = 24 \text{ mm}$ has to result in the proportionality factor of equation 5.17 that is

$$m = \frac{2r_{\text{inner}}^2}{E_{\text{conf}}(r_{\text{outer}}^2 - r_{\text{inner}}^2)} = 4.462 \cdot 10^{-4} \frac{1}{\text{GPa}}$$

In addition to the determination of σ_{rad} , the model is also used to determine the radial displacement at the central inner surface of the confinement. This equals the radial displacement Δr_{spec} of the specimen that is required to calculate its volumetric compression (ref. equation 5.16). Similar to the derivation of equation 5.19, Δr_{spec} is determined as a function of σ_{rad} and L yielding the dependency:

$$\Delta r_{\text{spec}}(\sigma_{\text{rad}}, L) = \sigma_{\text{rad}} \cdot \left(-0.0379 \frac{L^2}{\text{mm}^2} + 0.8944 \frac{L}{\text{mm}} + 2.5947 \right)^{-1} \mu\text{m} \quad 5.20$$

5.4.3.3 c) Confined compression test with a specimen surrounded by a thin aluminum sleeve within the confinement

Figure 5.43 c) illustrates the most complex test setup. This setup was used in all confined compression tests with glass specimens and in a validation test with a polyurethane specimen. In these setups, the specimen is surrounded by an additional 0.5 mm thick aluminum sleeve within the confinement. The radius of the cylindrical stamps equals the outer radius of the aluminum sleeve, so that axial stress is applied not only to the specimen but also to the sleeve. In this case, both σ_{axi} and σ_{rad} have to be inferred from numerical simulations.

The setup of the simulation is illustrated in Figure 5.46. In contrast to setup b) (ref. Figure 5.44) not only the confinement (gray) but also the specimen (blue), the aluminum sleeve (purple) and the cylindrical stamps (black) have to be taken into account in the model. The axial load is applied by means of a boundary condition on the upper surface of the top cylinder (red arrow and line). The bottom surface of the lower cylinder is fixed in axial direction by means of a frictionless support boundary condition.

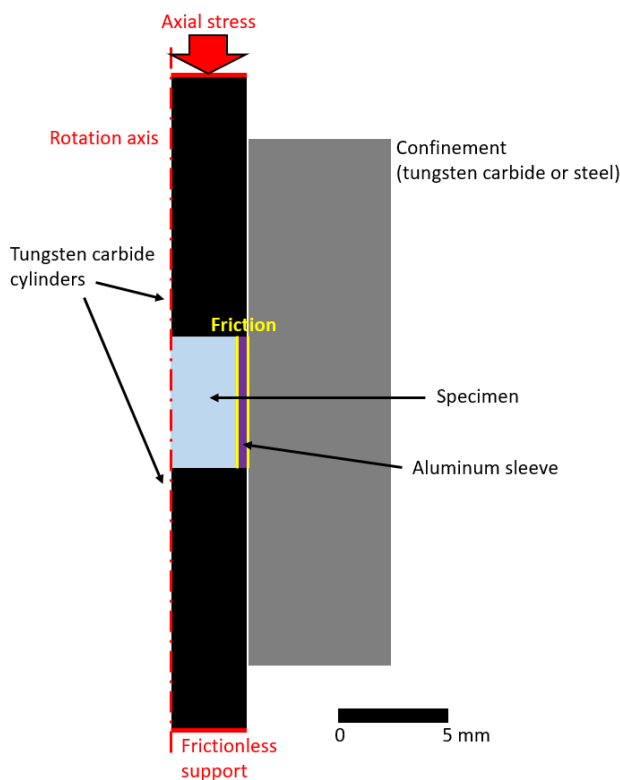


Figure 5.46: Schematic of a complete simulation model including the confinement (gray), the specimen (blue), the aluminum sleeve (purple) and the cylindrical stamps (black). The axial stress is applied to the upper cylinder (red arrow) while the bottom of the lower cylinder is fixed in axial direction by a boundary condition. The model also accounts for the influence of friction between specimen, aluminum sleeve and confinement (yellow lines).

This complete model enables the determination of σ_{axi} at the center of the specimen as a function of the axial stress σ_{stamp} applied to the tungsten carbide cylinder. In addition, the dependency of σ_{rad} on ϵ_{hoop} can be deduced while taking the aluminum sleeve into account. An additional advantage of this model is that it also accounts for the influence of friction between specimen, aluminum sleeve and confinement (yellow lines in Figure 5.46). This is

important since friction could lead to an overestimation of the axial stress in the specimen, if the confinement is loaded by friction supporting some of the axial load.

Since the stamp applies the axial load not only to the specimen, but also to the aluminum sleeve, equation 5.6 is not valid for this configuration. Instead, σ_{axi} is a function of σ_{stamp} depending on the materials of the specimen, sleeve and confinement. In particular, the compressibility and strength of the specimen has a significant influence on this dependency. In case of the low-strength polyurethane specimen, the aluminum sleeve is expected to accommodate more axial stress than the specimen. Therefore, $\frac{\sigma_{axi}}{\sigma_{stamp}}$ is anticipated to be smaller than 1. In contrary, $\frac{\sigma_{axi}}{\sigma_{stamp}}$ is expected to be greater than 1 in case of the SLG specimens.

The material models used for the simulations are listed in Table 5.6. Perfectly elastic constitutive models were chosen for polyurethane, tungsten carbide and steel. Values for the steel model were taken from literature [222]. For polyurethane, the density and Poisson's ratio were taken from the ANSYS Autodyn® database [258] and the bulk modulus was experimentally measured (ref. section 5.4.4.2). For tungsten carbide, the Poisson's ratio was taken from the database of ANSYS Workbench (Granta Design sample materials [259]) and the Young's modulus was experimentally measured.

For SLG and aluminum, plastic behavior was added by means of a bilinear isotropic hardening (yield strength + tangent modulus). The values for the aluminum model were taken from the database of ANSYS Workbench. The values for SLG were taken from Table 1.2. The model of SLG is very simple reflecting only a simplified elastic-plastic material behavior. However, this approach is sufficient for the estimation of $\sigma_{axi}(\sigma_{stamp})$.

In order to evaluate the influence of the used model, a second parameter set for SLG was also investigated. In this second model, referred to as "SLG -10%", all elastic constants as well as the yield strength have been reduced by 10 % compared to the first SLG model.

Table 5.6: Material models used for the quasi-static numerical simulations of confined compression tests.

	Specimens			Confinements		Sleeve
	Poly-urethane	SLG (Table 1.2)	SLG -10%	Tungsten carbide	Steel [222]	Aluminum [259]
Density ρ [g/cm ³]	1.35 [258]	2.53	2.53	14.45	7.83	2.68
Elastic modulus E [GPa]	0.02	73.8	66.4	625.7	209.5	73.0
Bulk modulus K [GPa]	2.73	42.8	38.5	359.6	159.0	71.6
Shear modulus G [GPa]	0.007	30.4	27.4	258.6	81.8	27.4
Poisson's ratio ν [-]	0.49875 [258]	0.21	0.21	0.21 [259]	0.28	0.33
Yield strength [GPa]	-	2.00	1.80	-	-	0.25
Tangent modulus [GPa]	-	0	0	-	-	1.54

A total of eight simulations were conducted in order to determine $\sigma_{axi}(\sigma_{stamp})$ and $\sigma_{rad}(\epsilon_{hoop})$ for different material combinations and different coefficients of friction. Table 5.7 provides a detailed overview of the investigated combinations.

In all cases, $\sigma_{\text{rad}}(\epsilon_{\text{hoop}})$ is well approximated by a linear fit:

$$\sigma_{\text{rad}}(\epsilon_{\text{hoop}}) = a_1 \cdot \epsilon_{\text{hoop}} + a_0 \quad 5.21$$

In the SLG and SLG -10% simulations, $\sigma_{\text{axi}}(\sigma_{\text{stamp}})$ is well approximated by a polynomial fit of second degree of the form:

$$\sigma_{\text{axi}}(\sigma_{\text{stamp}}) = a_2 \cdot \sigma_{\text{stamp}}^2 + a_1 \cdot \sigma_{\text{stamp}} \quad 5.22$$

In the polyurethane simulations, σ_{axi} equals zero until a minimum axial stress in the stamp is reached. This is due to the aluminum sleeve accommodating the entire load at low stresses. After exceeding a certain stress level, σ_{axi} increases linearly with increasing σ_{stamp} . Therefore, $\sigma_{\text{axi}}(\sigma_{\text{stamp}})$ is well approximated by a bilinear relation in case of the polyurethane specimen.

Table 5.7: Overview of conducted simulations for the confined compression tests including the aluminum sleeve (PU: polyurethane, Al: aluminum, TC: tungsten carbide). The resulting coefficients for equations 5.21 and 5.22 are listed in the last four columns.

Sim #	Simulation setup				Results			
	Specimen	Sleeve	Confinement	Coeff. of friction	$\sigma_{\text{axi}}(\sigma_{\text{stamp}})$		$\sigma_{\text{rad}}(\epsilon_{\text{hoop}})$	
					a_2 [MPa ⁻¹]	a_1 [-]	a_1 [MPa]	a_0 [MPa]
1	SLG	Al	TC	0.05	2.391e-5	1.074	3.505e6	-5.125
2	SLG	Al	TC	0.1	2.649e-5	1.063	3.466e6	-5.543
3	SLG -10%	Al	TC	0.05	1.570e-5	1.082	3.504e6	-6.094
4	SLG	Al	Steel	0.05	1.464e-5	1.113	1.794e6	-6.274
5	SLG	Al	Steel	0.1	1.954e-5	1.100	1.771e6	-6.599
6	SLG -10%	Al	Steel	0.05	4.190e-6	1.123	1.794e6	-7.139
7	PU	Al	TC	0.0	bilinear*		3.367e6	-17.45
8	PU	Al	TC	0.3	bilinear**		3.129e6	-18.18

* $\sigma_{\text{axi}} = 0.8256 \cdot \sigma_{\text{stamp}} - 66.6$ MPa if $\sigma_{\text{stamp}} > 81$ MPa; else: $\sigma_{\text{axi}} = 0$

** $\sigma_{\text{axi}} = 0.7009 \cdot \sigma_{\text{stamp}} - 61.4$ MPa if $\sigma_{\text{stamp}} > 88$ MPa; else: $\sigma_{\text{axi}} = 0$

The corresponding diagrams are shown in Figure 5.47, Figure 5.48 and Figure 5.49. In the simulations with the polyurethane specimen (Figure 5.47), the axial stress in the specimen σ_{axi} is always lower than the axial stress in the stamp σ_{stamp} , as expected. Two different coefficients of friction were investigated. Increasing the coefficient from 0.0 (green circles and lines) to 0.3 (red rectangles and lines) results in significant lower slopes of the linear fits. Both cases are investigated during the analysis of the experimental tests in section 5.4.4.4 in order to assess the real friction occurring in the tests.

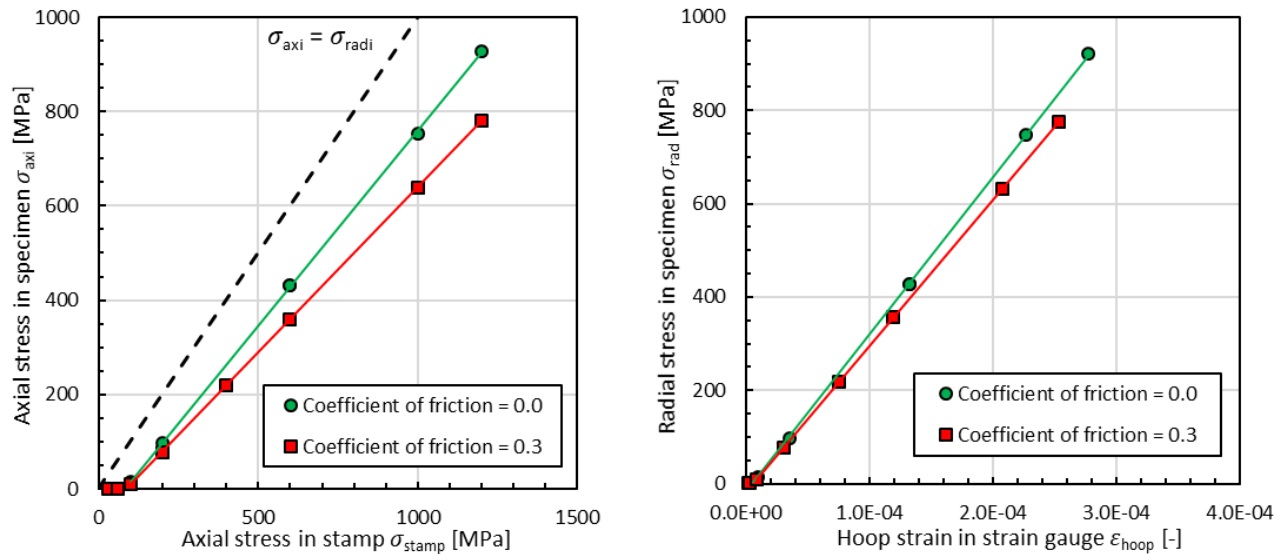


Figure 5.47: Simulation results for the confined compression test on a **polyurethane specimen** surrounded by an aluminum sleeve and **confined by tungsten carbide**. The diagrams illustrate $\sigma_{axi}(\sigma_{stamp})$ (left diagram) and $\sigma_{rad}(\epsilon_{hoop})$ (right diagram) for two different coefficients of friction between specimen, sleeve and confinement (ref. rows 7 and 8 of Table 5.7).

The results for the SLG specimen are presented in Figure 5.48 for the tungsten carbide confinement and in Figure 5.49 for the steel confinement. The results of the SLG model in combination with a coefficient of friction of 0.05 are represented by green circles and lines. Increasing the friction to a value of 0.10 results in the red data points and lines. The blue data illustrates the result for the SLG -10 % model and a coefficient of friction of 0.05. The differences between the three investigated cases are only marginal and therefore the lines are almost indistinguishable. Of particular importance is that the doubling of the coefficient of friction has no significant influence, in contrast to the simulations with the polyurethane specimen (ref Figure 5.47). In addition, the reduction of the elastic constants and the yield stress in the SLG -10% model also does not influence the resulting fit lines.

The axial stress in the specimen σ_{axi} is always higher than the axial stress in the stamp σ_{stamp} (left diagrams of Figure 5.48 and Figure 5.49). The radial stress as a function of the hoop strain $\sigma_{rad}(\epsilon_{hoop})$ is however significantly different for the different confinements. With the tungsten carbide confinement (right diagram in Figure 5.48), the slope of the linear fit line is about twice the slope of the fit line with the steel confinement (right diagram in Figure 5.49). The dependency of the slope on the Young's modulus of the confinement is however not as strong as with configuration a) (ref. Figure 5.43), for which a factor of about three ($= E_{TC} / E_{Steel}$) is derived with equation 5.17.

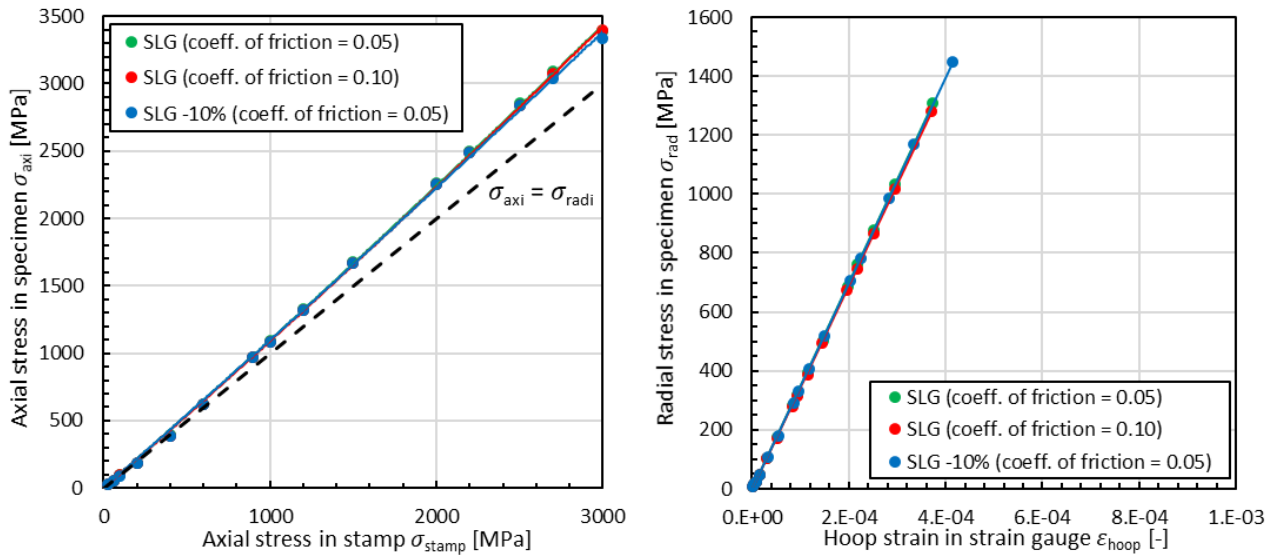


Figure 5.48: Simulation results for the confined compression test on a **SLG specimen** surrounded by an aluminum sleeve and **confined by tungsten carbide**.

The diagrams illustrate $\sigma_{axi}(\sigma_{stamp})$ (left diagram) and $\sigma_{rad}(\epsilon_{hoop})$ (right diagram) for two different coefficients of friction between specimen, sleeve and confinement (green and red points and lines). In addition, the result of the modified model SLG -10% is shown in blue. The differences between the three results are only marginal (ref. rows 1, 2 and 3 of Table 5.7).

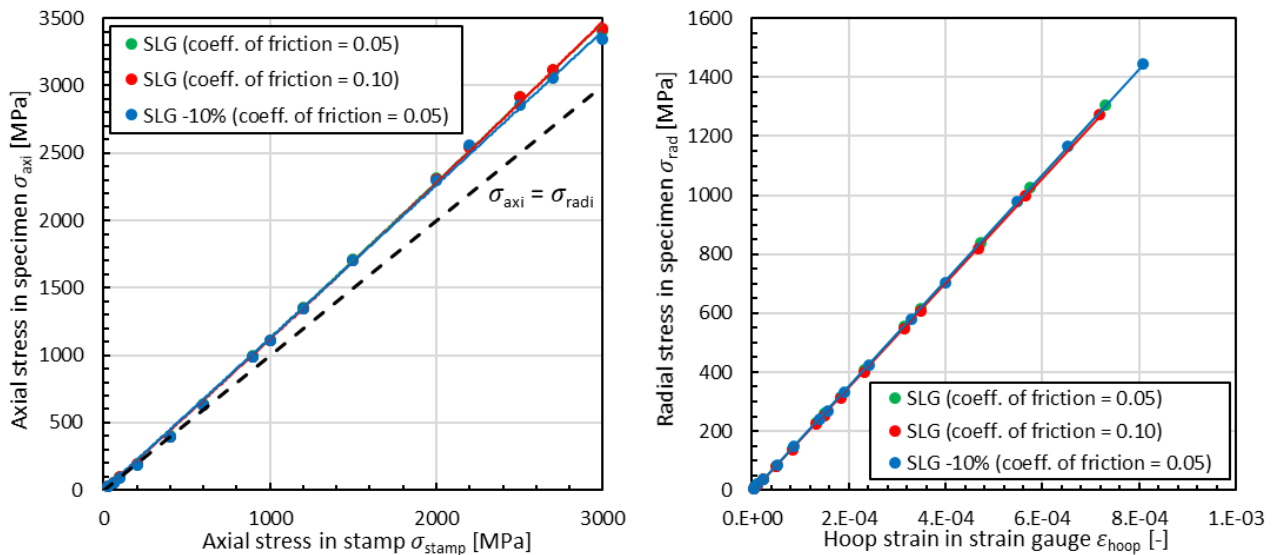


Figure 5.49: Simulation results for the confined compression test on a **SLG specimen** surrounded by an aluminum sleeve and **confined by steel**.

The diagrams illustrate $\sigma_{axi}(\sigma_{stamp})$ (left diagram) and $\sigma_{rad}(\epsilon_{hoop})$ (right diagram) for two different coefficients of friction between specimen, sleeve and confinement (green and red points and lines). In addition, the result of the modified model SLG -10% is shown in blue. The differences between the three results are only marginal (ref. rows 4, 5 and 6 of Table 5.7).

5.4.4 Experimental results

In the following, the experimental results of the compression tests are presented. In the first section (5.4.4.1), it is outlined how the materials of the confinement (tungsten carbide and steel) are characterized. In section 5.4.4.2, the results of validation tests on polyurethane specimens are presented. In section 5.4.4.3, the results of the unconfined compression tests on intact SLG specimens are described. The results of the confined compression tests on intact and pre-damaged SLG specimens are presented in section 5.4.4.4.

5.4.4.1 Characterization of the tungsten carbide and steel confinements

Before conducting the confined compression tests, the Young's moduli of the tungsten carbide and steel confinements were determined. Figure 5.50 shows photographs of the setup within the MTS machine. The axial load was applied directly on the confinement by means of the tungsten carbide plates, i.e. no cylindrical stamps were used. The black and white striped markers for the edge tracking were applied at the top and bottom areas of the outer surface of the confinement.

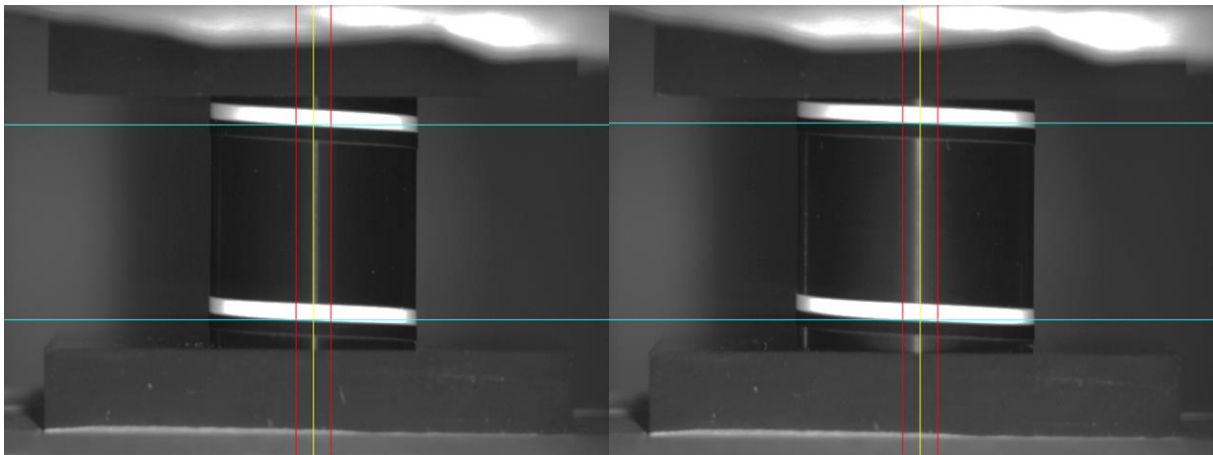


Figure 5.50: Setup of the confinement characterization tests. The tungsten carbide confinement is shown in the left photograph. The steel confinement is depicted in the right photograph. The axial load is applied directly to the confinement by means of two tungsten carbide plates. Black and white striped markers applied to the confinement allow for a direct measurement of the axial displacement.

The Young's modulus is determined by a linear best-fit line applied to the axial stress-strain curve (equation 5.5). The resulting curves are shown in Figure 5.51. The diagram on the left illustrates the axial stress versus the axial strain in the tungsten carbide confinement. The linear fit yields a Young's modulus of $E_{\text{conf}} = 625.7 \text{ GPa}$. This value is used for the tungsten carbide model in the implicit simulations (ref. Table 5.6). The right diagram of Figure 5.51 illustrates the result for the steel confinement. The evaluated Young's modulus is $E_{\text{conf}} = 211.5 \text{ GPa}$, which is in good accordance to the literature value of $E_{\text{conf}} = 209.5 \text{ GPa}$ [222]. However, at low stresses, the gradient of the stress-strain curve is significantly lower. This is due to a non-parallelism of the ending surfaces of the steel confinement (that is not relevant for the confined compression tests on specimens). Therefore, the literature value is more accurate and taken for the simulation model.

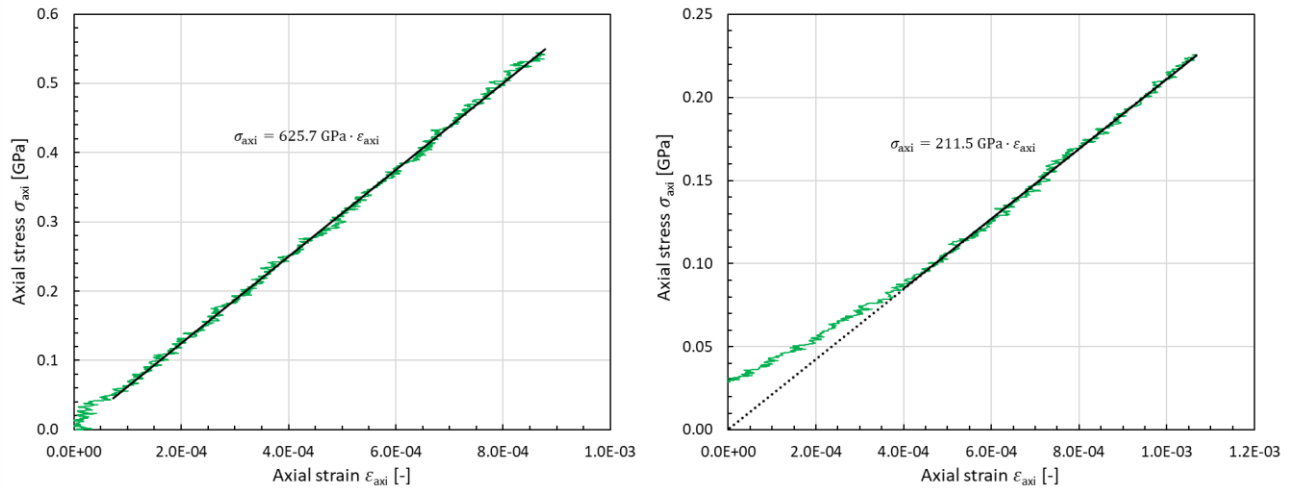


Figure 5.51: Axial stress-strain curves of the tungsten carbide (left diagram) and steel (right diagram) confinements. The Young's moduli are determined by linear best-fit lines (black lines). The determined Young's modulus of tungsten carbide (625.7 GPa) is used in the quasi-static simulations (ref. Table 5.6).

5.4.4.2 Validation tests on polyurethane specimens

Validation tests on low-strength polyurethane specimens were conducted in two different compression setups with the tungsten carbide confinement. In the first setup, the cylindrical specimen had a diameter of 7 mm, which equals the radius of the cylindrical stamps (configuration b) in Figure 5.43). In the second setup, the specimen had a diameter of 6 mm and was surrounded by a 0.5 mm thick aluminum sleeve inside the confinement (configuration c) in Figure 5.43).

First, the bulk modulus of the polyurethane specimen is determined with configuration b). Without the aluminum sleeve, the axial stress is calculated using equation 5.6. It is therefore independent of any model assumptions. The radial stress results from equation 5.19, which is only dependent on the material model of the tungsten carbide confinement. With both stresses, the hydrostatic pressure is calculated (equation 5.13). Furthermore, the volumetric compression is determined by combining equations 5.16 and 5.20. The resulting pressure-compression curve is plotted in Figure 5.52 as blue line. The left diagram depicts the complete loading path. At low compressions, the pressure increases linearly with increasing compression. However, for larger compressions $\mu \gtrsim 0.025$ the curve significantly differs from the linear course. This is probably caused by the polyurethane starting to squeeze into the gap between the stamps and the confinement. The bulk modulus of the polyurethane can therefore only be deduced from the data at low compressions. The right diagram of Figure 5.52 shows an enlarged section of the low-compression range. A linear best-fit line (black line) is applied yielding a bulk modulus of $K = 2.73 \text{ GPa}$ (ref. equation 5.15). This value is used for the material model of polyurethane, required for the analysis of validation test with configuration c).

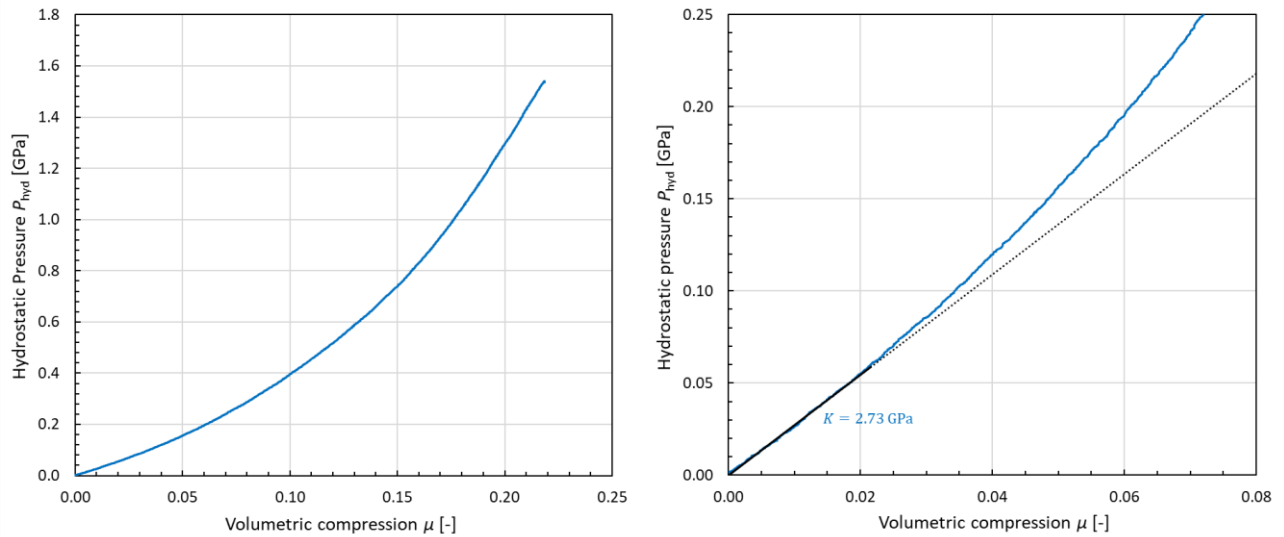


Figure 5.52: Hydrostatic pressure versus volumetric compression for the polyurethane specimen measured without aluminum sleeve in the tungsten carbide confinement (ref. configuration b) in Figure 5.43). The diagram on the right side shows an enlarged section of the low-compression range. The determined bulk modulus (2.73 GPa) is used in the quasi-static simulations (ref. Table 5.6).

In configuration c), the axial stress of the stamps is partially applied to the aluminum sleeve surrounding the polyurethane specimen. The calculation of the axial and radial stress is therefore more complex and requires material models not only for the tungsten carbide confinement, but also for the aluminum sleeve and the polyurethane specimen. Furthermore, the result is dependent on the coefficient of friction between specimen, sleeve and confinement. The axial and radial stresses were calculated for two different coefficients of friction in order to investigate the influence of friction. The radial and axial stress are calculated with equations 5.21 and 5.22. Here, the parameter sets for coefficients of friction of 0.0 and 0.3 were used (ref. lines 7 and 8 in Table 5.7). The resulting pressure-compression curves are plotted in the diagrams in Figure 5.53. The diagram on the left side shows the complete loading paths, while the diagram on the right depicts an enlarged section of the low-compression range. The green line results with a coefficient of friction of 0.0 and the red line corresponds to a coefficient of friction of 0.3. For comparison, the result of configuration b) (ref. Figure 5.52) is plotted again as blue line.

Despite the different coefficients of friction, the green and red line are almost equal. It is therefore concluded, that friction has a negligible influence on the determination of the bulk modulus. In contrast to configuration b) (blue line), the curves of configuration c) exhibit a linear course even at larger compressions. This is expected, since the aluminum sleeve surrounding the specimen prevents the polyurethane from squeezing into the gap between the stamps and the confinement. The resulting bulk moduli of $K = 2.96$ GPa (coefficient of friction = 0.0) and $K = 2.88$ GPa (coefficient of friction = 0.3) are in good match with bulk modulus determined with setup b), as illustrated in the right diagram of Figure 5.53.

From this, it is concluded that the simulation models are sufficiently accurate to be used for the analysis of the tests.

For a further validation of the analysis methodology, the resulting radial stress in the polyurethane specimen is directly compared to its axial stress. Since the specimen exhibits only negligible shear strength, the axial stress is expected to equal the radial stress $\sigma_{rad} \approx \sigma_{axi}$ in

Development of a novel methodology for generating, characterizing and pressure testing of defined damaged glass specimens

both compression setups. This loading path is represented in Figure 5.54 by a black dashed line. The results of the tests are illustrated by the colored lines. The blue line (configuration b)) and the green line (configuration c) without friction) are in good agreement with the expected black dashed line. This further validates the accuracy of the analysis. However, the red line (configuration c) with coefficient of friction = 0.3) diverges with increasing stress. It is therefore concluded, that the model yields better results without friction. This means, that the real friction occurring in the experimental tests was significantly lower than 0.3.

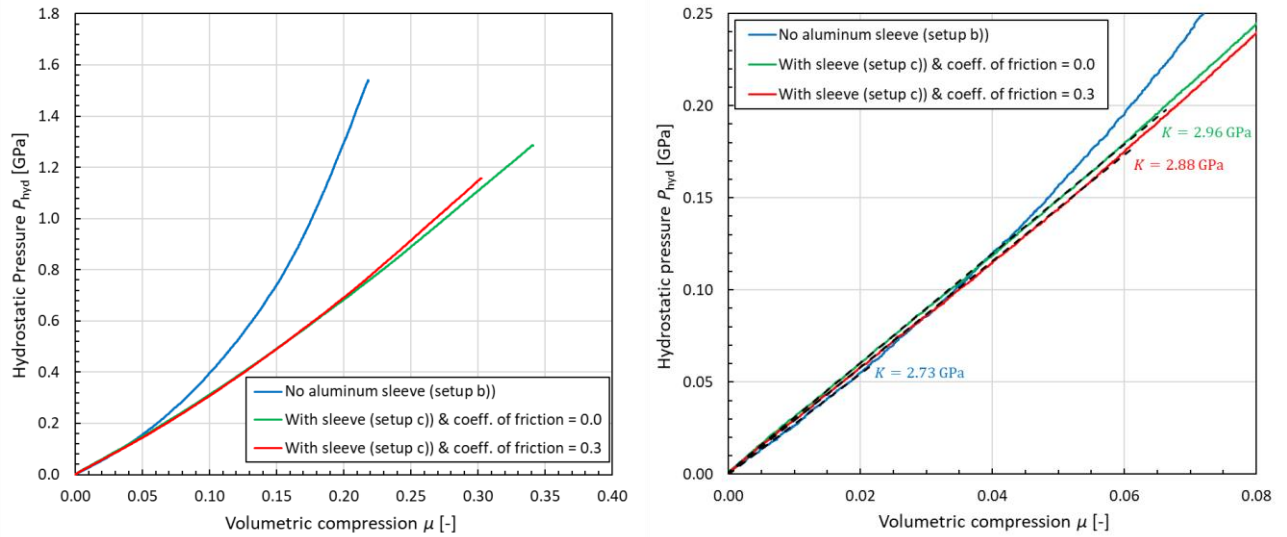


Figure 5.53: Hydrostatic pressure versus volumetric compression for the polyurethane specimens measured with the tungsten carbide confinement in different configurations (blue line: without aluminum sleeve; green line: with aluminum sleeve, no friction in analysis; red line: with aluminum sleeve, coefficient of friction = 0.3 in analysis). The black dashed lines illustrate the linear fits for the determination of the bulk modulus.

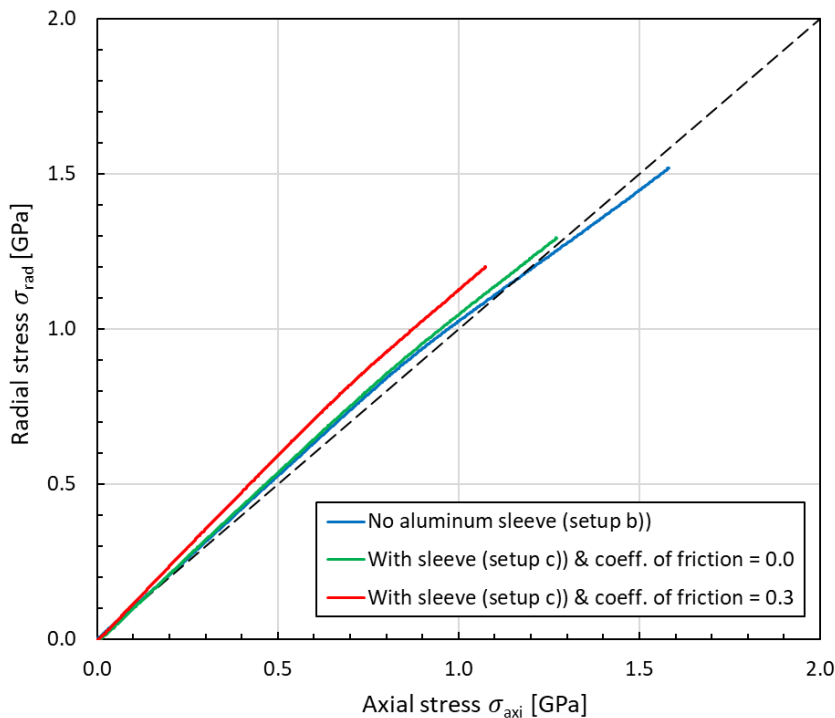


Figure 5.54: Radial versus axial stress in the polyurethane specimens. The colored lines refer to the same configurations as described in Figure 5.53. The black dashed line illustrates the expected response of a material without shear strength.

5.4.4.3 Unconfined characterization tests on intact SLG specimens

Two unconfined compression tests were conducted on intact SLG specimens in order to determine the Young's modulus and the failure stress under uniaxial stress conditions. Figure 5.55 shows an image of the setup of these tests. The cylindrical SLG specimen is placed between the two tungsten carbide stamps applying the axial load. The axial strain of the specimen is inferred from the axial displacement of the stamps measured at the black and white markers by means of edge tracking. The analysis is conducted as outlined in section 5.4.2.1.

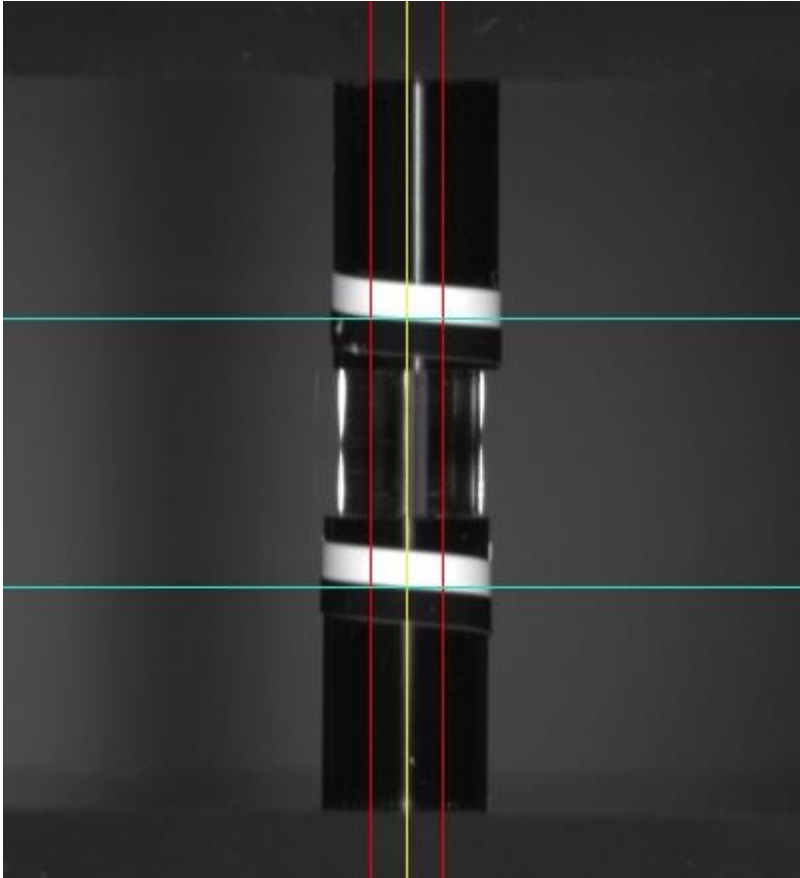


Figure 5.55: Image of the setup of an unconfined compression test with an intact SLG specimen. The cylindrical specimen is placed between the two tungsten carbide stamps. The axial strain of the specimen is inferred from the axial displacement of the stamps measured at the black and white markers by means of edge tracking.

Figure 5.56 shows the resulting axial stress-strain curves. For both specimens, a linear increase of the axial stress with increasing axial strain was observed. The linear best-fits (black dashed line) yield Young's moduli of $E = 73.8$ GPa for specimen 1 (purple curve) and $E = 74.2$ GPa (orange curve). These values are in excellent agreement with the literature value of $E = 73.8$ GPa (ref. Table 1.2). Specimen 1 failed at a maximum axial strain of $\epsilon_{\text{axi,max}} = 1.85 \cdot 10^{-2}$ reaching a maximum axial stress of $\sigma_{\text{axi,max}} = 1.35$ GPa. Specimen 2 failed at $\epsilon_{\text{axi,max}} = 1.86 \cdot 10^{-2}$ and $\sigma_{\text{axi,max}} = 1.37$ GPa, which is in good accordance with specimen 1. These values also match well with the results of the confined compression tests on intact SLG specimens, as discussed in the next section.

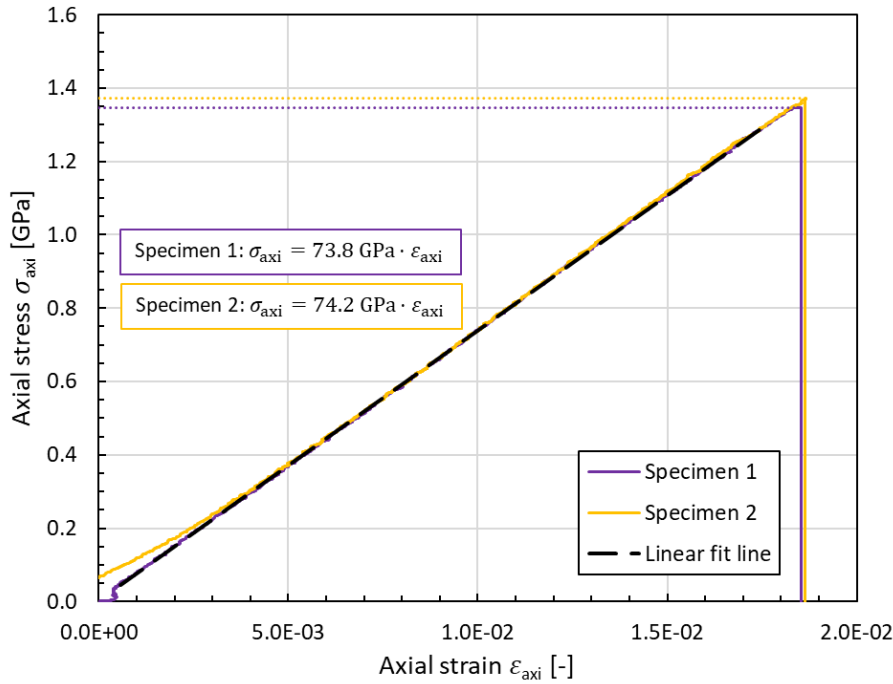


Figure 5.56: Results of the unconfined compression tests on intact SLG specimens.

5.4.4.4 Confined characterization tests on intact and pre-damaged SLG specimens

Seventeen confined compression tests were conducted on intact and pre-damaged SLG specimens. These tests comprise four tests on intact specimens and twelve tests on specimens that have been dynamically pre-damaged and characterized (ref. Table 5.1). In addition, a second characterization cycle (CT-analysis and confined compression test) was conducted with specimen 20979 after the first compression testing. Table 5.8 provides an overview of all tests. The second column lists the material of the used confinement (steel or tungsten carbide (TC)). The third column contains the impact velocity of the projectile used to generate the pre-damage. The fourth column gives the corresponding classification of the impact velocities as defined in section 5.3.3.6. The fifth column provides the mean total crack volume of the pre-damage (if available), determined by means of PCI (ref. Table 5.5). The last column lists a rough classification of the residual strength resulting from the confined compression tests. The strength is classified into five groups (highest, high, intermediate, low, lowest) based on the resulting yield curves. This is outlined in more detail in the following.

Development of a novel methodology for generating, characterizing and pressure testing of defined damaged glass specimens

Table 5.8: Summary of confined compression tests on intact and pre-damaged SLG specimens.

Test No.	Confinement	v_p of pre-damaging [m/s]	Classification of v_p	Crack volume of pre-damage [%]	Classification of residual strength
Intact 1	Steel	-	-	-	Highest
Intact 2	Steel	-	-	-	Highest
Intact 3	TC	-	-	-	Highest
Intact 4	TC	-	-	-	Highest
20979	TC	69	Low		Intermediate
20981	TC	70	Low		High
21202	TC	72	Low	0.9 ± 0.2	Intermediate
20982	Steel	73	Low		High
21194	TC	144	Intermediate	0.5 ± 0.4	Low
20984	TC	146	Intermediate		Intermediate
20985	TC	149	Intermediate		Low
20983	TC	186	Intermediate		Intermediate
20986	TC	235	High		Low
20980	TC	257	High		Intermediate
21201	TC	266	High	2.0 ± 0.6	Intermediate
21200	TC	407	Highest	3.8 ± 0.6	Lowest
20979+P*	TC	$69 + P^*$	Low + high pressure	5.9 ± 0.6	Lowest

* specimen of test no. 20979 after first confined compression test

As outlined in section 5.4.2.2, the purpose of the confined compression tests is to determine the strength of the specimens as a function of the hydrostatic pressure. The limits are represented by curves in the σ_{eq} - P -diagram. σ_{eq} and P are determined from the measured values F_{axi} and ε_{hoop} by combining equations 5.12, 5.13, 5.21 and 5.22. The resulting curves are shown in Figure 5.57. The curves are colored according to the classification by the impact velocity. The results of the intact specimens are represented by blue lines. The green lines represent the low impact velocity range (~70 m/s). The intermediate range (140 – 190 m/s) is colored orange. Results of the high velocity range (230 – 270 m/s) are colored red. The curve of the specimen pre-damaged at the highest velocity (~400 m/s) is colored purple. The dark purple line represents the result of the second compression test on specimen 20979.

From the diagram, it can be deduced that there is a certain correlation between the curve progression and the impact velocity. The purple curves are significantly lower than all other curves. The red curves (high pre-damage velocities) are lying between the purple and the green curves (low velocities). The orange curves exhibit some scatter, with two of them lying slightly below the red ones while the other two are positioned slightly above them. There is also a little scatter between the green curves. Two of them are lying closely to the highest red and orange

curves, while the other two are lying clearly higher. The blue curves (intact specimens) reach significantly higher equivalent stresses up to their first drop. This drop is caused by the initial failure of the SLG specimen resulting in a significant softening. After the failure, the curves further progress similar to some of the pre-damaged curves.

The diagram also shows a notable difference between the results of intact specimens confined by tungsten carbide (dark blue curves) and steel (light blue curves). With the steel confinement, the intact SLG specimens initially failed at considerable lower hydrostatic pressures of 0.54 and 0.63 GPa in comparison to the failure pressures of 0.91 and 1.01 GPa with the tungsten carbide confinement. This could be attributed to the lower Young's modulus of the steel confinement leading to larger radial strains in the specimen.

The tests with the steel confinement were stopped at lower pressures in order to ensure that the confinement did not undergo plastic deformation.

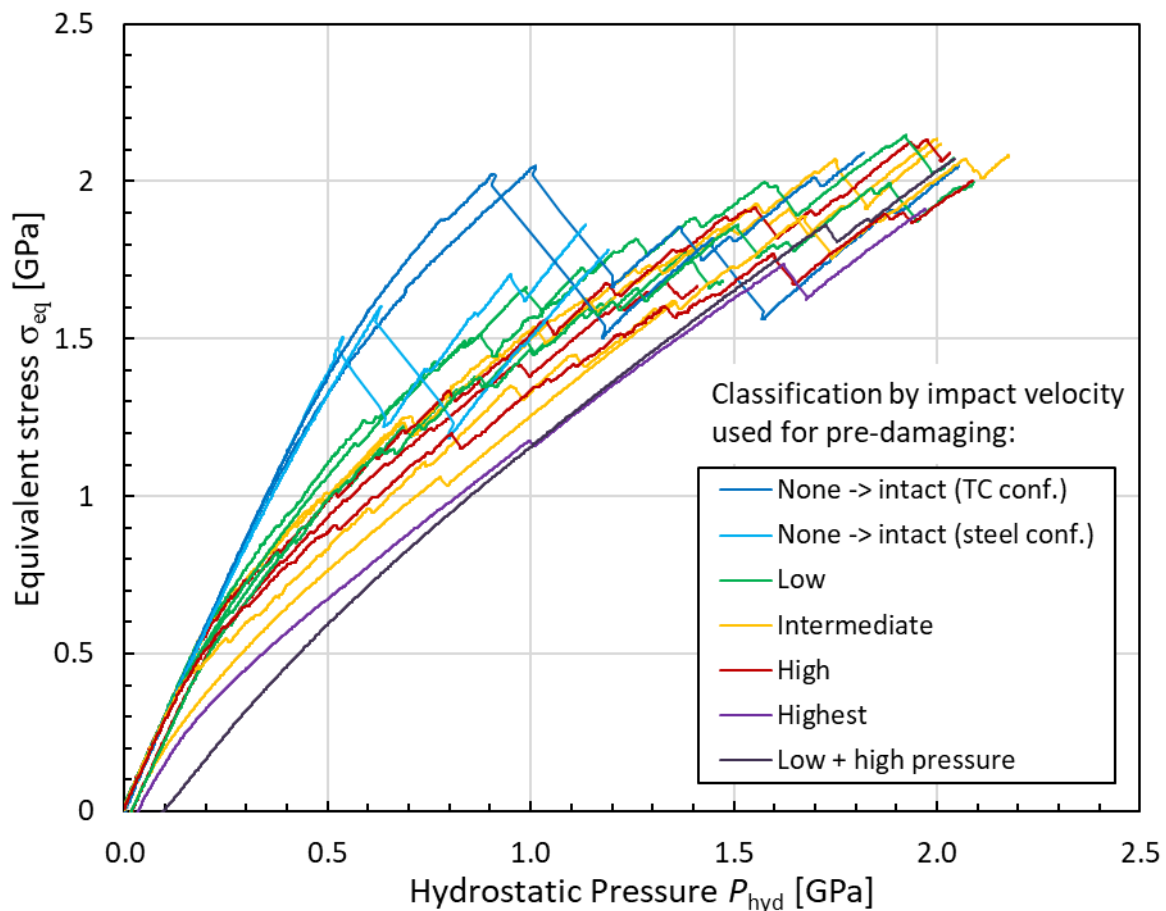


Figure 5.57: Result of confined compression tests on intact and pre-damaged SLG specimens.

The curves shown in Figure 5.57 result from the analysis based on the reference SLG model and a coefficient of friction of 0.05 (rows 1 and 4 in Table 5.7). In order to evaluate the influence of friction and the analysis model, two additional analyses were conducted. Figure 5.58 shows the resulting σ_{eq} - P -curves for an increased coefficient of friction (center diagram) and a softened SLG model (right diagram) in comparison to the reference analysis (left diagram). The differences between the different analysis are only marginal. At lower pressures, the curve progressions and positions of the local maximums are equal for all three analyses. At high pressures, small differences are observed between the reference analysis and the analysis with the reduced SLG

model. With the reduced model (right diagram), the equivalent stresses reached at high pressures are slightly lower than those of the reference analysis (left diagram). The horizontal dashed lines help to illustrate the differences in the equivalent stresses of the highest local maximums (corresponding to the green curve of specimen #20985). In the reference analysis, a value of 2.07 GPa is reached, whereas the reduced model results in a value of 2.02 GPa. The difference is only 50 MPa, which is significantly less than the differences between the models (in the reduced SLG model, the yield stress is reduced from 2000 MPa to 1800 MPa, ref. Table 5.6). It is therefore concluded that the reference analysis yields reasonable results within the uncertainty introduced by the simplification of the model. Furthermore, doubling the friction coefficient from 0.05 to 0.10 does not result in any noticeable difference. Therefore, the uncertainty of the real friction has no influence on the results. Higher coefficients of friction were not investigated since Dannemann et al. [127] reported an upper limit of 0.10 for the friction in their compression tests. In addition, the validation tests on the polyurethane specimens revealed that the friction has to be significantly less than 0.3 (ref. section 5.4.4.2).

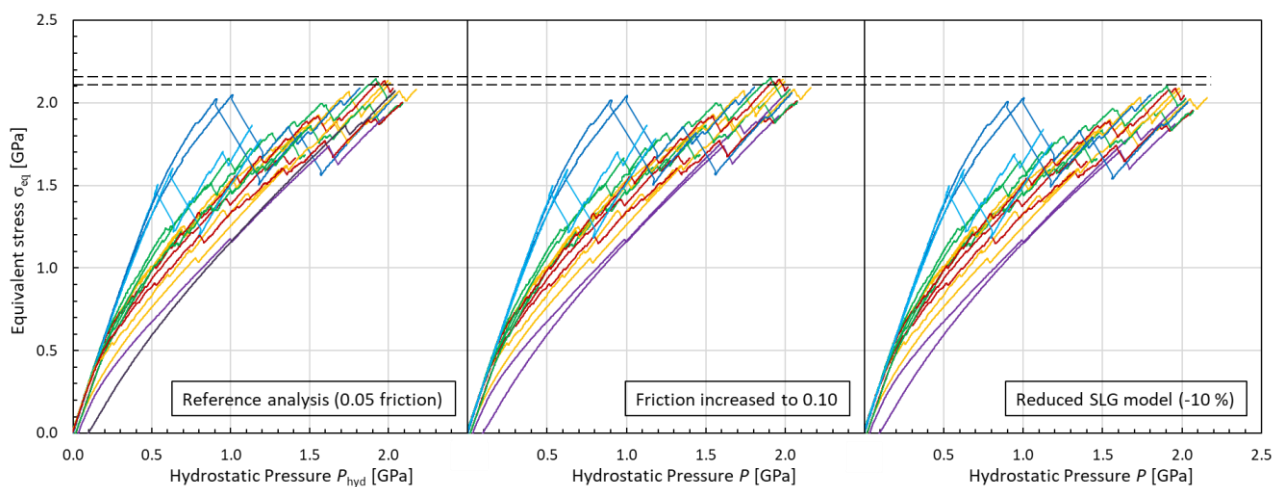


Figure 5.58: Comparison of final experimental curves resulting from different analysis sets (ref. Table 5.7). Left diagram: analysis based on parameter set of reference model; center diagram: analysis with increased coefficient of friction (0.10 instead of 0.05); right diagram: analysis with reduced SLG model (-10 % elastic constants and yield strength).

In the following, yield curves are deduced and parameterized based on the σ_{eq} - P -curves of the reference analysis (Figure 5.57). Every curve exhibits small drops of the equivalent stress, caused by internal fractures and slippage during the loading process. This results in a number of local maximums spread along the loading path. It is assumed that for each curve all local maximums are lying on a corresponding yield curve. Therefore, the yield curve envelopes the σ_{eq} - P -curve.

For each confined compression tests, all local maximums along the σ_{eq} - P -curve are identified. The yield curve is determined by applying a best-fit function to these maximums. Here, the maximums of different tests are combined if they share a similar curve progression. Combining similar tests bears the advantage that the statistical error is reduced. This means that for all tests with similar σ_{eq} - P -curves, a mean yield curve is determined that is less influenced by the statistical scatter of the individual tests.

The goal of the analysis is to determine several mean yield curves, each representing the residual strength for a different degree of pre-damage. Figure 5.59 shows the σ_{eq} - P -curves of Figure 5.57 reclassified by the curve progression instead of the impact velocities. Tests with similar

curves and therefore similar yield curves are colored uniformly. The colors are representing five different groups: highest (blue), high (green), intermediate (orange), low (red) and lowest (purple) yield curve.

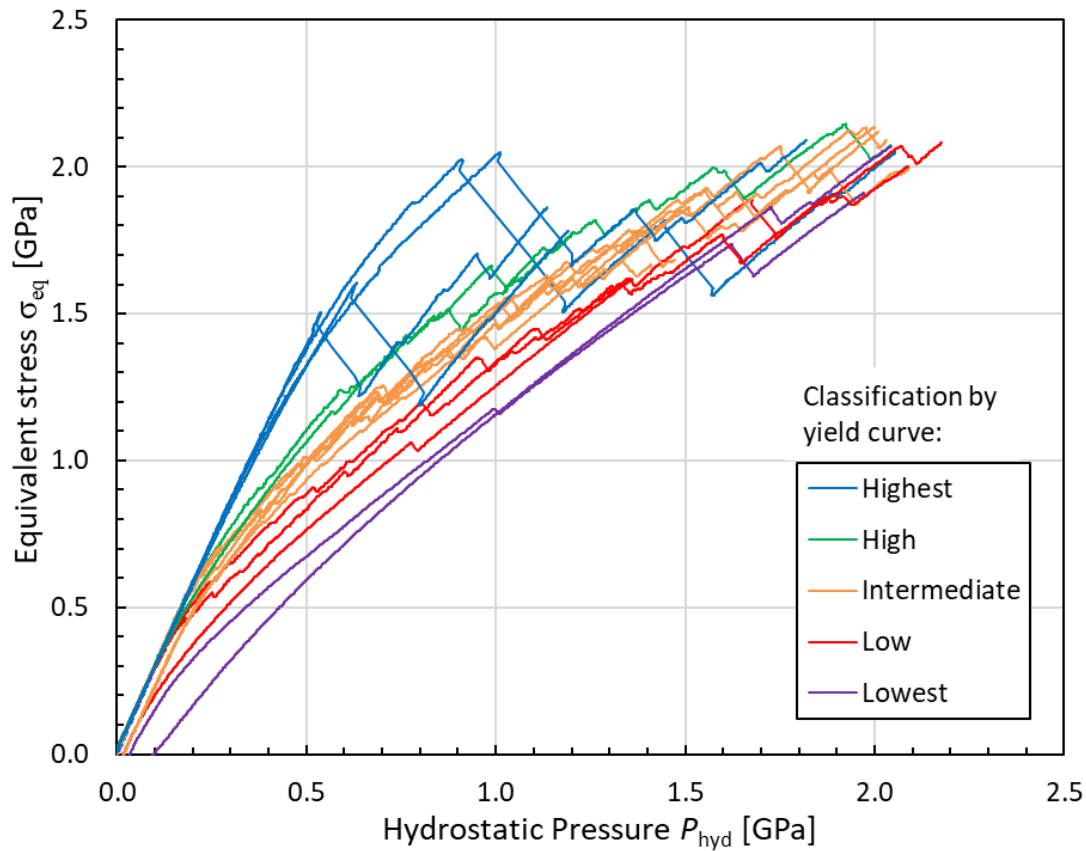


Figure 5.59: Result of confined compression tests on intact and pre-damaged SLG specimens.

For each category, all local maximums are identified and the corresponding yield curve is determined by means of a best-fit function. The used fit functions were taken from the JH2 model since they provide a good fit to the data. A detailed overview of the JH2 model is given in section 3.2.3.1. The fit function used for the initial maximums of the intact data (blue curves) is:

$$\sigma_{eq} = \sigma_{HEL} \cdot (1 + C \cdot \ln(\dot{\epsilon}^*)) \cdot A \cdot \left(\frac{P - T}{P_{HEL}}\right)^N \quad 5.23$$

where A and N denote the fit parameters. The dimensionless strain rate is $\dot{\epsilon}^* = \dot{\epsilon}/\dot{\epsilon}_0$, where $\dot{\epsilon} = 6 \cdot 10^{-4} \frac{1}{s}$ is the actual strain rate of the compression tests and $\dot{\epsilon}_0 = 1 \frac{1}{s}$ is the reference strain rate. A strain rate factor of $C = 0.003$ is adopted from Holmquist et al. [60]. The normalization constants $\sigma_{HEL} = 3.608$ GPa and $P_{HEL} = 2.595$ GPa are taken from the results of the PPI characterization (chapter 4). The hydrostatic tensile limit is adopted from Richards et al. $T = -35$ MPa [260].

The fit function used for all pre-damaged data is:

$$\sigma_{\text{eq}} = \sigma_{\text{HEL}} \cdot (1 + C \cdot \ln(\dot{\epsilon}^*)) \cdot B \cdot \left(\frac{P}{P_{\text{HEL}}}\right)^M, \quad \sigma_{\text{eq}} \leq \sigma_{\text{max}} \quad 5.24$$

where B and M denote the fit parameters. The parameter σ_{max} presents a cap to the equivalent strength. In the literature, this cap is observed for entirely failed SLG. For the presented analysis, a cap of $\sigma_{\text{max}} = 2.1$ GPa is chosen for the “intermediate”, “low” and “lowest” yield curves, while the “highest” and “high” yield curves are not limited. The limit is chosen based on the current results and reported values of 2.2 GPa by Brar et al. [98] and 1.8 GPa by Bourne et al. [82] [83] as well as further data presented in Figure 1.2.

In the following, the σ_{eq} - P -curves are presented together with the identified local maximums and the resulting fit line.

Figure 5.60 illustrates the determination of the “highest” yield curve (intact SLG). On the left side, the results of the compression tests with the four intact SLG specimens are shown. The right side indicates the positions of the identified local maximums by circles. The yield curve resulting from the fit is illustrated as black line in the right diagram. Only the first maximum of each curve is taken since the intention is to determine the yield curve of intact SLG. The first drop is caused by fracture of the specimen increasing the degree of damage strongly. The subsequent maximums are therefore lying on yield curves of significant higher degrees of damage. They are not used in further analyses since the corresponding degree of damage is not quantified.

Figure 5.61 illustrates the determination of the yield curve classified as “high”. The left side shows the corresponding compression curves of specimens 20981 and 20982. Both specimens were pre-damaged at a low impact velocity of ~ 70 m/s. The curves are very similar although specimen 20981 was tested with the tungsten carbide confinement, while specimen 20982 was tested with the steel confinement. This observation is in contrast to the results of the intact compression tests (Figure 5.60). In these tests, the intact SLG specimens with steel confinement failed at significant lower pressures. The failure at lower pressures is attributed to the lower Young’s modulus of the confinement leading to larger radial displacements in the specimen. It is therefore concluded that the failure of intact specimens is very sensitive to the radial strain. Gaps or misalignments between specimen, aluminum sleeve and confinement can also be a contributing factor. In contrast, the already pre-damaged specimens do not show a large drop of the strength upon further failure. They are not as sensitive to the used confinement or initial misalignments as the intact specimens are.

Figure 5.62 illustrates the determination of the “intermediate” yield curve. The corresponding compression curves of test specimens 20979, 20980, 20983, 20984, 21202 and 21201 are shown on the left side. The identified local maximums are depicted on the right side. Although the maximums exhibit more scatter than those of Figure 5.61, the fit function (black line) provides a sufficient approximation.

The determination of the yield curve classified as “low” is illustrated in Figure 5.63. The corresponding compression curves are those of test specimens 20985, 20986 and 21194.

Figure 5.64 illustrates the determination of the “lowest” yield curve, deduced from specimens 21200 and 20797+P. Specimen 21200 was dynamically pre-damaged at a high impact velocity of ~ 400 m/s. 20797+P denotes the specimen 20797 after the first compression cycle (ref. Figure 5.62). It was dynamically pre-damaged at a much lower impact velocity of ~ 70 m/s, but the additional compression cycle significantly increased the degree of damage. Although the degree

of pre-damage of 21200 and 20797+P was noticeable different, the maximums of both tests can be approximated by the same yield curve (black line in the right diagram).

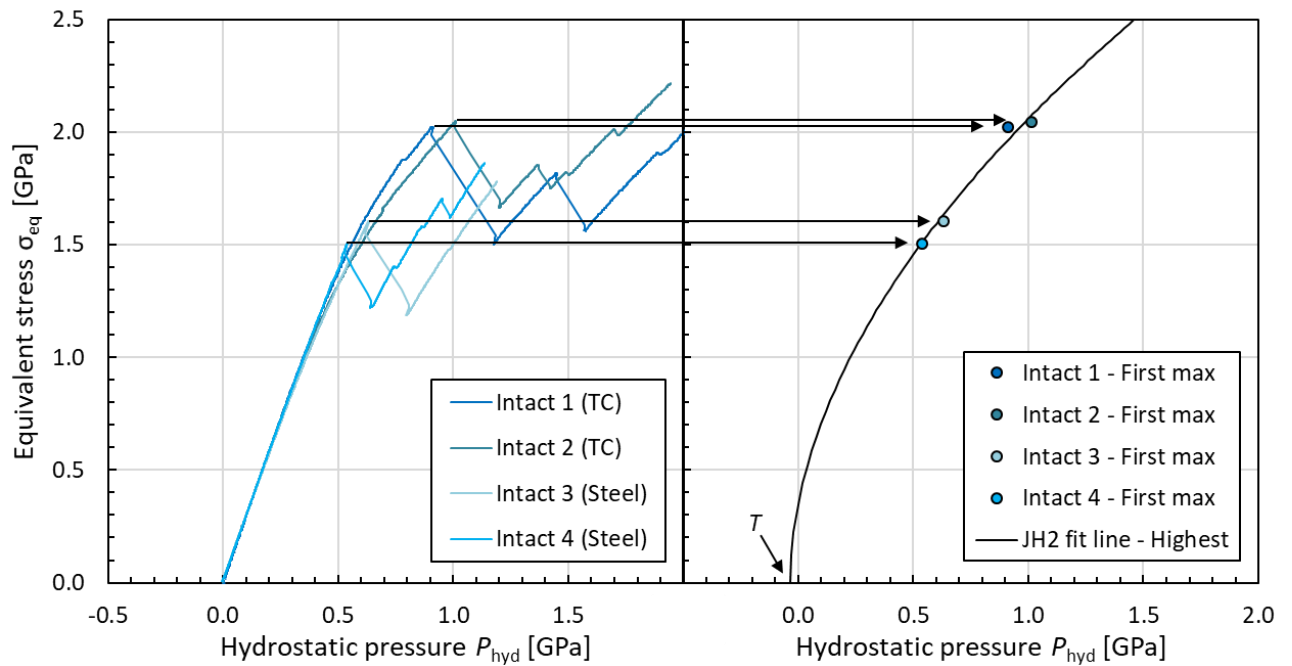


Figure 5.60: Highest yield curve (black line) deduced from first maximums (arrows) of the compression curves of intact specimens; T denotes the hydrostatic tensile limit of -35 MPa.

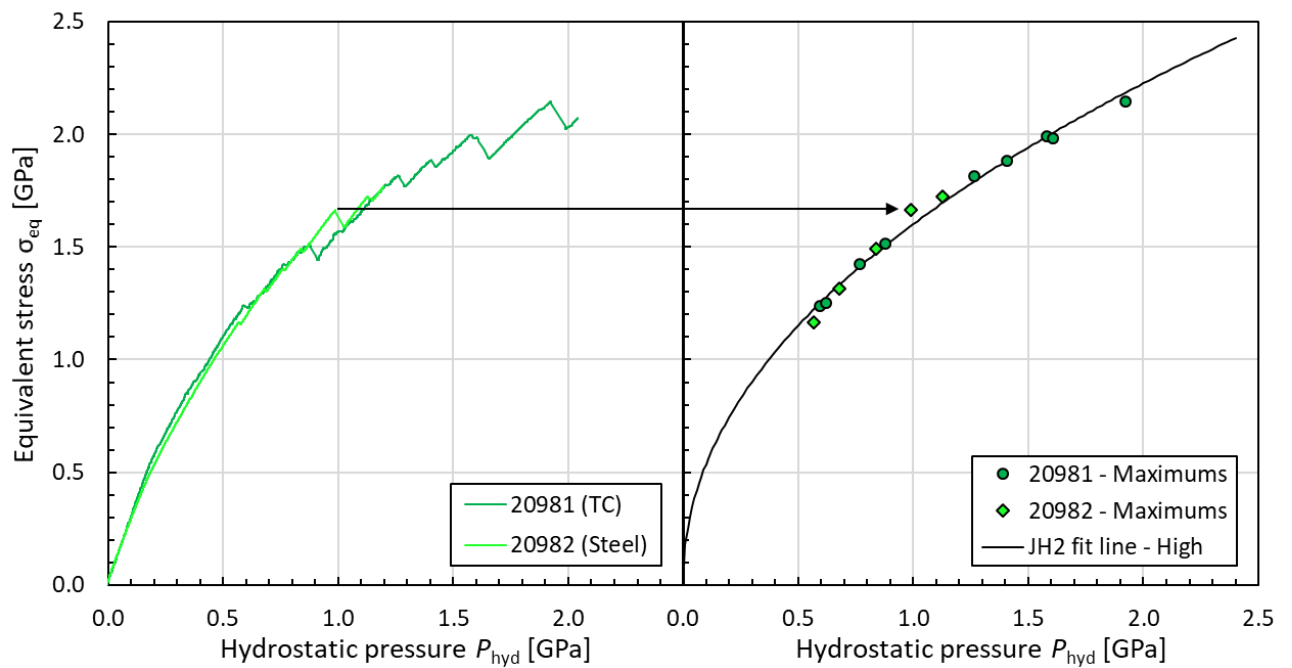


Figure 5.61: High yield curve (black line) deduced from specimens 20981 ($v_p = 70$ m/s) and 20982 ($v_p = 73$ m/s).

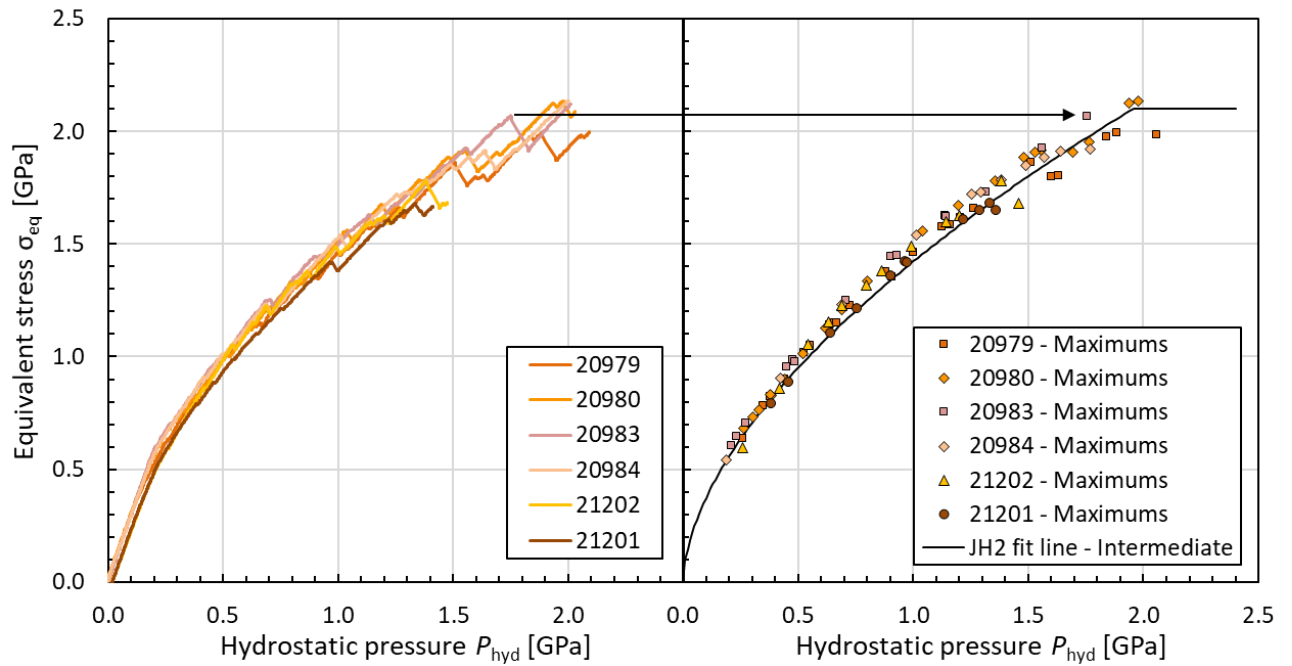


Figure 5.62: Intermediate yield curve (black line) deduced from specimens 20979 ($v_p = 69$ m/s), 20980 ($v_p = 257$ m/s), 20983 ($v_p = 186$ m/s), 20984 ($v_p = 146$ m/s), 21202 ($v_p = 72$ m/s) and 21201 ($v_p = 266$ m/s).

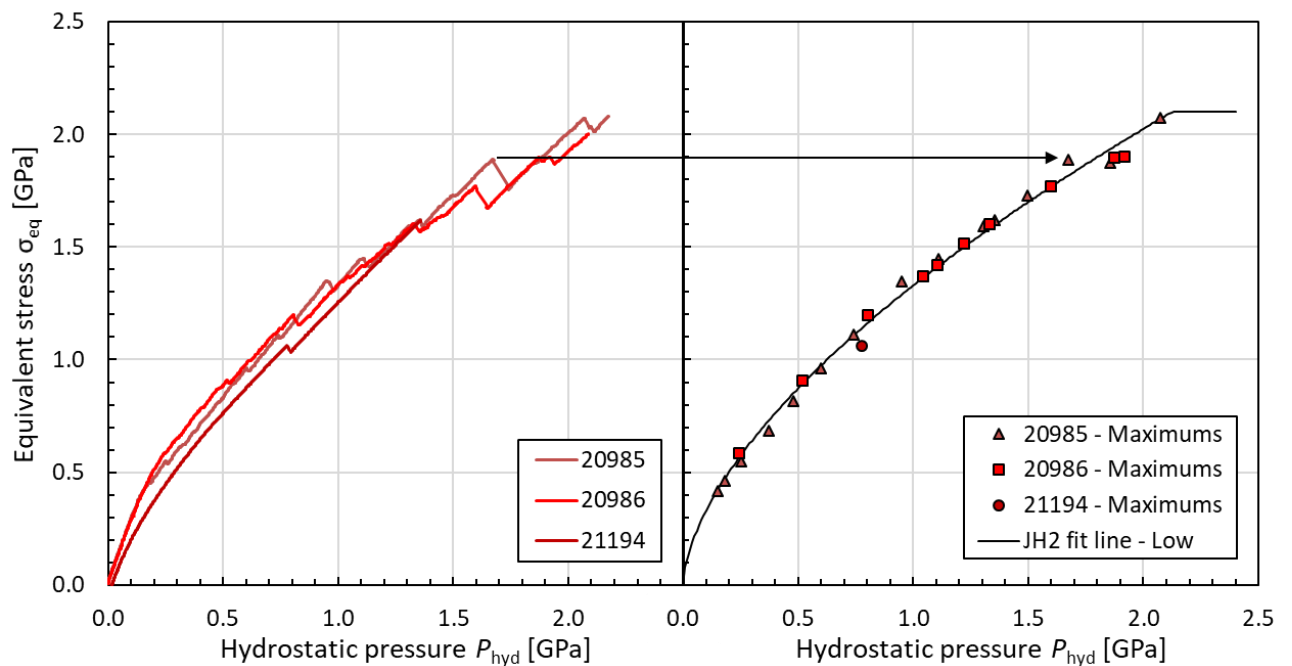


Figure 5.63: Low yield curve (black line) deduced from specimens 20985 ($v_p = 149$ m/s), 20986 ($v_p = 235$ m/s) and 21194 ($v_p = 144$ m/s).

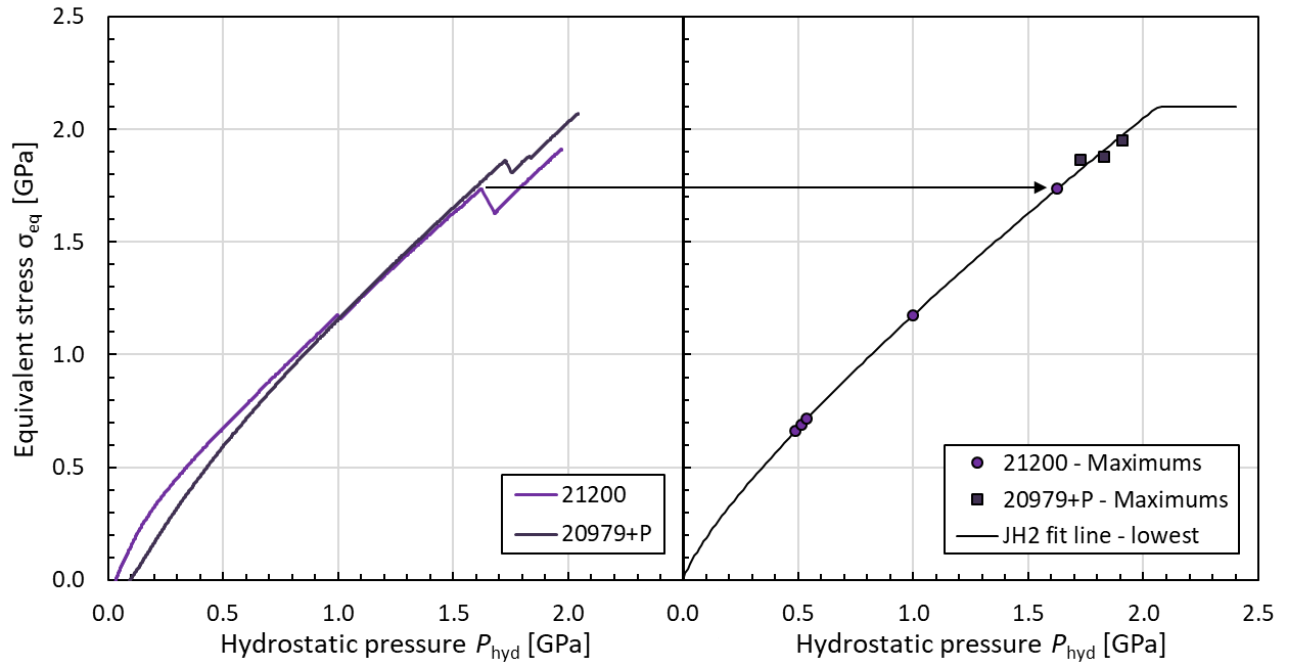


Figure 5.64: Lowest yield curve (black line) deduced from specimens 21200 ($v_p = 407$ m/s) and 20979+P ($v_p = 69$ m/s + compression cycle).

A compilation of all resulting yield curves is shown in Figure 5.65. The solid lines represent the yield curves at a quasi-static strain rate of $\dot{\epsilon} = 6 \cdot 10^{-4} \frac{1}{s}$. For the highest yield curve (that is the failure surface of intact SLG), the dynamic curve is indicated by a blue dashed line. This line results from equation 5.23 with a strain rate of $\dot{\epsilon} = 5 \cdot 10^5 \frac{1}{s}$. For comparison, other results of tests conducted within this work are also shown in the diagram. The failure stresses of the unconfined compression tests (ref. section 5.4.4.3) are indicated by the red "+". The values of 1.35 GPa and 1.37 GPa are in good agreement with the blue fit line resulting from the confined compression tests. A red "X" indicates the elastic limit of the PPI tests (ref. chapter 4). The strain rate of this HEL is about $\dot{\epsilon} = 5 \cdot 10^5 \frac{1}{s}$, deduced from PPI test #3787 ($\epsilon_{final} \approx 0.05$ and $\Delta t \approx 0.1 \mu s$). The HEL is therefore also in excellent agreement with the dynamic yield curve deduced by the confined compression tests (blue dashed line).

Table 5.9 summarizes the parameters of the determined yield curves. In addition, the initial crack volume for each yield curve is given in the second row. These values are deduced from the PCI analysis conducted prior to the compression tests (ref. section 5.3.3.5). For the category "lowest", both tested specimens have been also analyzed by PCI. The resulting crack volumes are significantly different (3.8 % for specimen 21200 and 5.9 % for specimen 20979+P). However, both specimens share the same yield curve. It is therefore concluded that this yield curve is representative for completely failed SLG. A further increase of the initial crack volume (and the initial degree of damage) does not result in further softening.

For the "low" yield curve, no crack volume is listed in Table 5.9. The only specimen of this category that has been analyzed by means of PCI is considered as being not representative (specimen 21194 with an initial crack volume of (0.45 ± 0.40) %).

The initial crack volume of (2.0 ± 0.6) % of specimen 21201 is chosen to be representative for the "intermediate" yield curve. This category includes a second specimen that has also been analyzed by PCI. This specimen was pre-damaged at low impact velocity and had a lower initial

crack volume (specimen 21202 with $(0.9 \pm 0.2) \%$). This crack volume is however chosen to be representative for the “high” yield curve, since the micro-CT analysis of the corresponding specimens (20981 and 20982) revealed no striking differences to specimen 21202. Although specimens 20981 and 20982 have not been analyzed by PCI, it is therefore concluded that they exhibited also an initial crack volume of about 0.9 %. A possible explanation for the intermediate yield curve of specimen 21202 could be a larger increase of the degree of damage at the beginning of the confined compression tests. This could have been caused for example by a larger misalignment of specimen, sleeve and confinement.

For a comparison of the initial crack patterns, a compilation of the CT results is presented in the appendix in section 9.7 (Figure 9.15, Figure 9.16, Figure 9.17, Figure 9.18, Figure 9.19 and Figure 9.20). The CT images of the specimens are sorted by the category of the corresponding yield curve (“high”, “intermediate”, “low” and “lowest”) in order to visualize the correlation between the initial degree of damage and the residual strength.

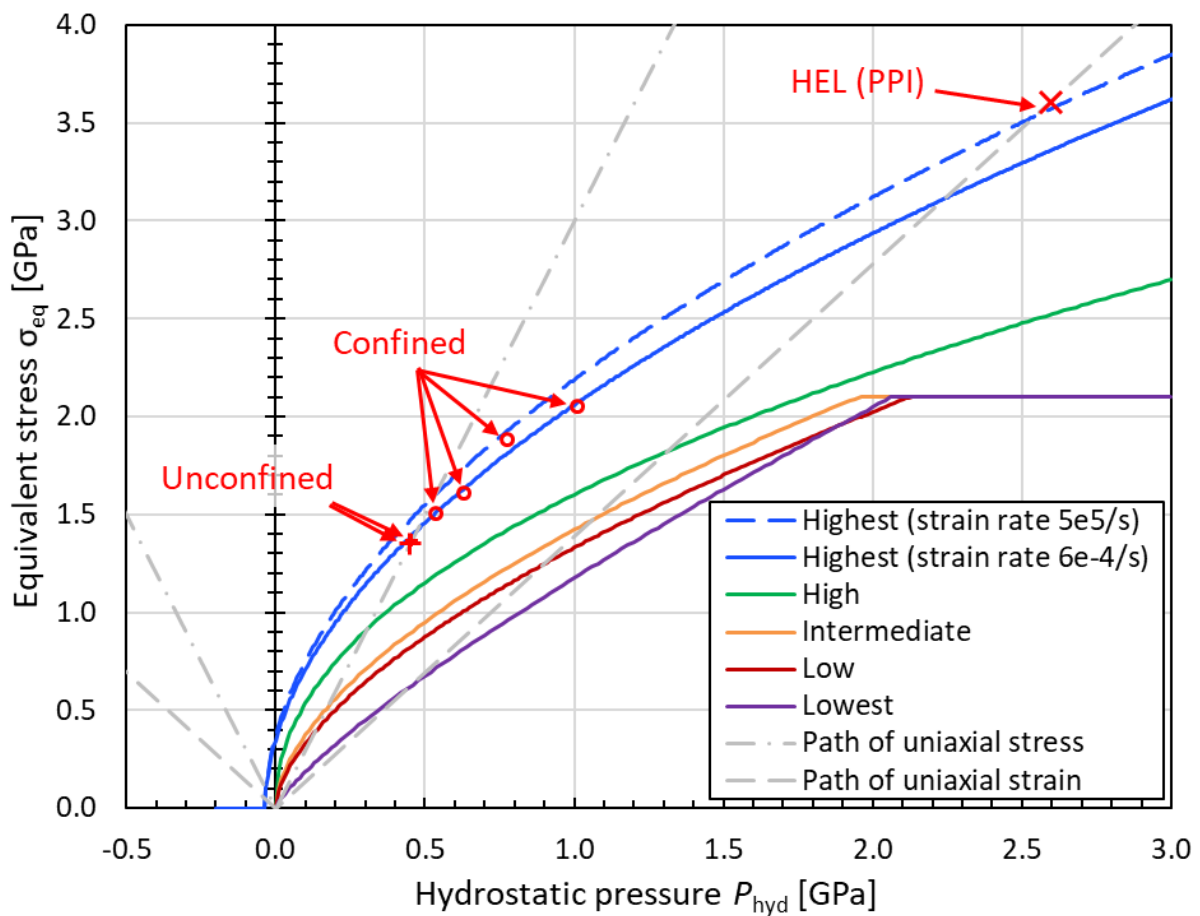


Figure 5.65: Compilation of yield curves resulting from the confined compression tests. For comparison, the results of the unconfined compression tests (red “+”) and the highly dynamic PPI tests (red “X”) are also shown.

Table 5.9: Final JH2 parameters of yield curves. The quasi-static curves are plotted for a strain rate of $\dot{\epsilon} = 6 \cdot 10^{-4} \frac{1}{s}$. The strain rate factor is $C = 0.003$. For the highest curve (intact strength), an hydrostatic tensile limit of $T = -35 \text{ MPa}$ is chosen. Normalization values are taken from the PPI results: $P_{HEL} = 2.595 \text{ GPa}$ and $\sigma_{HEL} = 3.608 \text{ GPa}$.

Classification of yield curve	Highest (intact)	High	Intermediate	Low	Lowest (failed)
Initial crack volume [%]	0	0.9 ± 0.2	2.0 ± 0.6	Not available	3.8 ± 0.6 5.9 ± 0.6
<i>A</i>	0.94525	-	-	-	-
<i>N</i>	0.52471	-	-	-	-
<i>B</i>	-	0.71438	0.70185	0.67186	0.71543
<i>M</i>	-	0.47539	0.58138	0.60594	0.80122
$\sigma_{\max}/\sigma_{HEL}$	-	-	0.582	0.582	0.582

5.5 Discussion of the characterization results of defined damaged soda-lime glass

Within the framework of this work, important new insights into strength of intact and damaged SLG were gained. A novel methodology for the characterization of the residual strength as a function of the degree of damage has been developed, as described in the previous sections. This includes a novel test setup to create different degrees of pre-damage in small SLG cylinders. A newly developed analysis method was subsequently used to determine the degree of damage contact-free by means of X-ray CT. Afterwards, the residual strength was measured in confined compression tests and evaluated using numerical simulations. The main result of these characterization tests are yield curves for different degrees of pre-damage. In this section, the determined yield curves are discussed and compared to the data available in the literature.

Intact strength

Figure 5.66 presents the equivalent stress as a function of the hydrostatic pressure for intact SLG. The blue lines indicate the determined yield curves of the present work at a quasi-static strain rate (solid blue line) and for a highly dynamic strain rate of $\dot{\epsilon} = 5 \cdot 10^5 \frac{1}{s}$ (dashed blue line). At low hydrostatic pressures, the solid line is in good accordance to the data of Holmquist et al. [60] (yellow symbols) and to some data points of Dannemann et al. [21] [22] (green squares). However, Dannemann et al. also reported values in the range of about $0.7 \text{ GPa} < P < 1.6 \text{ GPa}$ that are shifted towards higher equivalent stresses. They deduced a linear dependency within this pressure range, which is indicated in Figure 5.66 by a solid green line. These results are clearly conflicting with reported results of PPI and PSPI tests at pressures of up to 2 GPa. The PSPI data (rhombuses) of Sundaram et al. [50] and Clifton et al. [115] as well as the PPI data of Bourne et al. [38] (red circles) and Espinosa [47] (purple circles) are in better agreement with the results of the present work (blue lines). For larger pressures of $2 \text{ GPa} < P < 4 \text{ GPa}$, the dynamic

yield curve of the present work (blue dashed line) is also in good agreement with the data of Clifton et al., Bourne et al., Espinosa et al. and one data point of Bless et al. [76] (orange circles). However, at pressures above 4 GPa, the available literature data of Bless et al., Simha et al. [49] (green circles) and Kettenbeil [113] (horizontal gray dashed line) tends towards a constant equivalent stress of $\sigma_{\text{eq}} = 2.8$ GPa. It is possible that in these tests the stress state was not measured in intact material, but in material that had already undergone some damaging or failure due to inelastic deformation.

It has to be noted, that yield curves of the present work (blue lines) are deduced from four quasi-static data points acquired in the pressure range of $0.5 \text{ GPa} < P < 1 \text{ GPa}$. The extrapolation to higher pressures and higher strain rates is based on the formulation of the yield surface adopted from the JH2 model. The uncertainty of the yield curves therefore increases with increasing pressure. However, the excellent agreement with the measured HEL value at $P = 2.595 \text{ GPa}$ and $\sigma_{\text{eq}} = 3.608 \text{ GPa}$ supports the validity of the extrapolation to pressures of up to 2.6 GPa.

Figure 5.66 also illustrates yield curves of intact SLG used by other authors in constitutive models. The black dotted line presents the intact strength deduced by Richards et al. [260] for the JH2 model. The curve is noticeable steeper reaching a value of $\sigma_{\text{eq}} = 6.2$ GPa at $P = 5$ GPa ($\sigma_{\text{eq}} = 10.6$ GPa at $P = 10$ GPa). Richards et al. used ballistic penetration tests on glass laminates as reference to modify the original JH2 parameters of Holmquist et al. Although the resulting curve is not based on basic characterization experiments and clearly differs from the literature data, the model is capable of reasonably predicting the residual projectile velocities in specific ballistic scenarios.

In contrast, Gorfain et al. [54] deduced an intact reference strength for the Holmquist-Johnson model based primarily on basic characterization experiments. The resulting curve is illustrated in Figure 5.66 as black solid line. In this model approach, the intact strength is capped at a maximum equivalent stress of $\sigma_{\text{max}} = 4.3$ GPa (at the reference strain rate $\dot{\epsilon}_0 = 1 \frac{1}{s}$). Due to the cap, the yield curve is significantly lower at larger pressures than the curves of Richards et al. and the present work. At smaller pressures of $P < 4$ GPa, however, the equivalent stress is significantly higher (up to 1 GPa). The reason for this is that Gorfain et al. wanted the curve to match the upper quasi-static data points of Dannemann et al. (green squares with green line) and the dynamic HEL reported by Holmquist et al. and Bourne et al. (gray X's in Figure 5.66, see also Figure 1.1 for labels). Gorfain et al. used the model to simulate PPI and Taylor rod impact tests with generally good agreement between simulated and experimental results. However, they did not validate the model for ballistic penetration scenarios.

In summary, it is not possible to define a yield curve for intact SLG that matches all reported data shown in Figure 5.66. The curve deduced within this work is in good agreement with the presented results of quasi-static compression tests and highly dynamic PPI tests. It is however in clear contrast to the yield curves used by other authors in constitutive models of SLG. Richards et al. used a yield curve that is considerably higher at larger pressures to simulate ballistic penetration scenarios. Gorfain et al. used a yield curve that is higher at low pressures, but lower at large pressures to simulate PPI and Taylor rod impact tests.

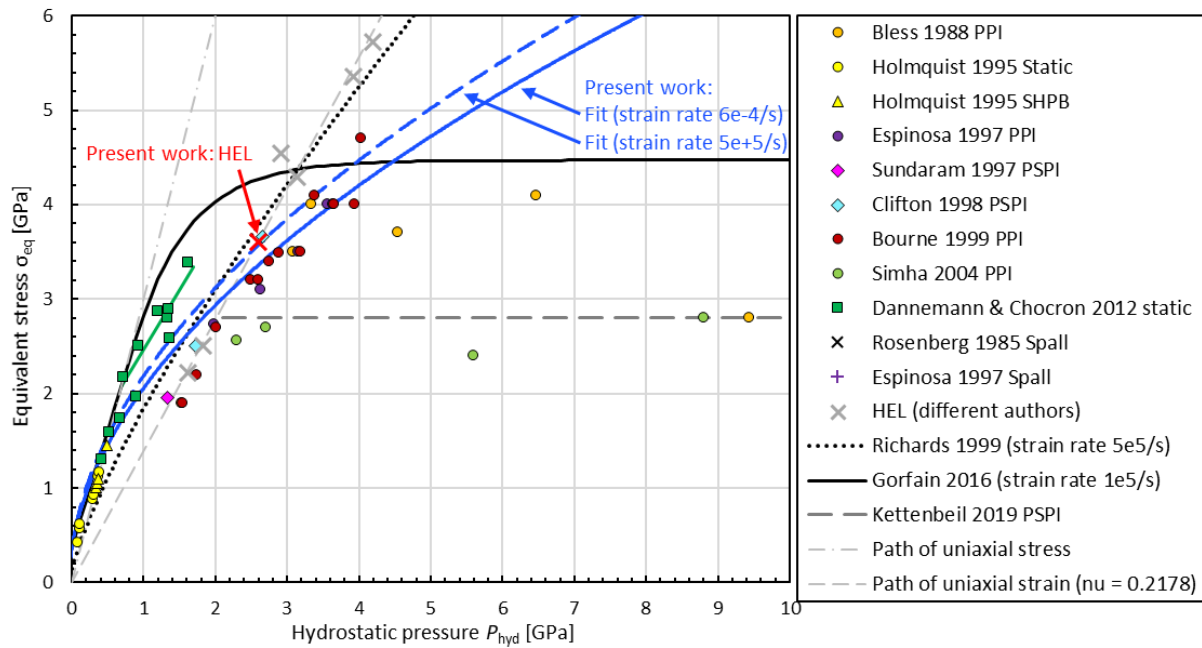


Figure 5.66: Intact SLG: equivalent stress as a function of hydrostatic pressure; comparison of new results (blue lines) with literature data.

Failed strength

Figure 5.67 presents the equivalent stress as a function of the hydrostatic pressure for damaged SLG. The upper diagram gives an overview for large pressures up to 7 GPa. The lower diagram depicts an enlarged section of the low-pressure range. The colored solid lines indicate the yield curves of the present work. The green line presents the “high” strength corresponding to an initial crack volume of 0.9 %. The “intermediate” (2.0 % crack volume) and “lowest” (> 3.8 % crack volume) strength curves are illustrated by the orange and purple line, respectively. The “lowest” strength curve represents completely failed SLG and is capped at a maximum equivalent stress of 2.1 GPa (top diagram in Figure 5.67). This cap is based on failed strength values reported by Espinosa et al. [47], Bourne et al. [38] and Simha et al. [49]. The “intermediate” strength curve shares the same cap, since it is assumed that it also represents completely failed material for pressures above ~2 GPa. This is deduced from the fact that the “intermediate” strength curve converges towards the lowest curve, intersecting at around 2 GPa. The deduced maximum equivalent stress of completely failed SLG of 2.1 GPa is therefore consistent with the curve progression (orange and purple lines) and with the reported PPI data (purple, blue and red circles). However, it is significantly higher than the reported results of PSPI tests. Clifton et al. [115] (blue rhombs), Sundaram et al. [50] (pink rhombs) and Kettenbeil [113] (horizontal gray dashed line, based on additional measurements with granular silica sand conducted by Vogler et al. [114]) deduced failed strength values in the range of 0.2 to 0.7 GPa. The differences could be attributed to the different modes of deformation or to the significantly larger shear strains attained in the PSPI tests, as assumed by Gorfain et al. [54]. It has to be noted that the confined compression tests conducted within the present work did not allow acquiring data above hydrostatic pressures of 2.1 GPa.

The results for pressures of up to 2 GPa are illustrated in the enlarged bottom diagram of Figure 5.67. The “high” strength curve (green line) is in good agreement with the highest data points of Dannemann and Chocron et al. [21] [22] (red symbols) in the pressure range of

0.4 GPa < P < 1.1 GPa. Dannemann et al. conducted confined compression tests using two different techniques, the hydraulic pressure technique and the confined sleeve technique (ref. section 1.2.3.2). Especially the data obtained by means of the hydraulic pressure technique (red rhombs) are matching the “high” strength curve within this pressure range. The other data points of Dannemann et al. are mainly positioned between the “high” and the “intermediate” strength curve. It is therefore concluded that the pre-damage of these tests was comparable to a total crack volume in the range of 0.9 to 2.0 %. There are two main differences between the data of Dannemann et al. and the yield curves of the present work. First, the results of Dannemann et al. obtained by means of the confined sleeve technique (red squares) are reaching a maximum equivalent stress of about 1.6 GPa for pressures larger than 1 GPa (horizontal red dashed line). In contrast, the present results do not exhibit a cap for pressures of up to about 2 GPa, reaching higher equivalent stresses of up to 2.1 GPa. Second, Dannemann et al. did not report any data points lying below the “lowest” strength curve for pressures of up to about 1.3 GPa. Most probably, the degree of pre-damage created by Dannemann et al. by means of a thermal shock was considerably lower than the pre-damage generated in the present work by means of highly dynamic PPI. However, it is unclear why the specimens of Dannemann et al. that were tested in cyclic loading did not result in a significant softening. The difference of the observed cap of the maximum equivalent stress could be attributed to the different materials of the confinement sleeves. The tungsten carbide confinement used in the present work did limit the radial displacement of the SLG more strongly than the steel confinement used by Dannemann et al. This prevented the formation of shear bands in the glass, which caused the failure in the specimens of Dannemann et al. Consequently, no distinct shear planes were observed in the present work after the confined pressure testing (ref. Figure 5.31).

Figure 5.67 also shows the shear resistance of quartz glass powder reported by Shockey et al. [29] (yellow squares). The data points are lying below the “lowest” strength curve of the present work, which represents completely failed SLG. It is therefore concluded that there is a significant difference between the residual strength of loosely poured powder and thermally or dynamically shocked glass cylinders consisting of significantly larger fragments “interlocked” with each other.

For comparison, Figure 5.67 also illustrates the yield curves of entirely failed SLG used by other authors in constitutive models. These models are the JH2 model modified by Richards et al. [260] and the Holmquist-Johnson model calibrated by Gorfain et al. [54], as previously described. The failed strength curve of Richards et al. (black dotted line) is significantly different from the failed strength curve of the present work (purple line). For pressures in the range of about 0.7 GPa < P < 6.3 GPa, it is lying below the purple line. For higher pressures, it surpasses the curve of the present work since Richards et al. decided to adopt the maximum failed strength of 2.27 GPa, as reported by Holmquist et al. As a result, the curve of Richards et al. is matching neither the present results nor any of the data reported by Dannemann et al. It is therefore expected that the new yield curves deliver different results in ballistic impact simulations, as demonstrated in section 6.4.

The model curve of Gorfain et al. (black solid line in Figure 5.67) is close to the “intermediate” yield curve of the present work for pressures of up to about 0.7 GPa. For higher pressures, the curve of Gorfain et al. is significantly lower since they decided to take an average of all available data, including the PSPI test, resulting in a maximum equivalent stress of 1.35 GPa. However, it would be probably more beneficial to account for the PSPI results by adding for example a dependency on the 3rd invariant effect.

Development of a novel methodology for generating, characterizing and pressure testing of defined damaged glass specimens

In summary, the novel methodology developed within the framework of this work allowed determining several yield curves that are dependent on the degree of initial damage. The results are largely consistent with the data of Dannemann and Chocron et al. and reported PPI data in the pressure range up to 1.5 GPa for small and intermediate damage. The present results extend the available literature data in four ways. First, the pre-damage was created highly dynamically by means of defined PPI tests instead of a thermal shock. This allowed a drastic increase of the degree of pre-damage, which represents the damage in the Mescall-zone more closely. Second, for the first time, the degree of pre-damage was directly measured and quantified using a novel X-ray CT analysis. Third, different yield curves for different degrees of pre-damage were determined.

Finally, the resulting yield curve for entirely failed SLG is significantly different from curves that are used by other authors in constitutive models.

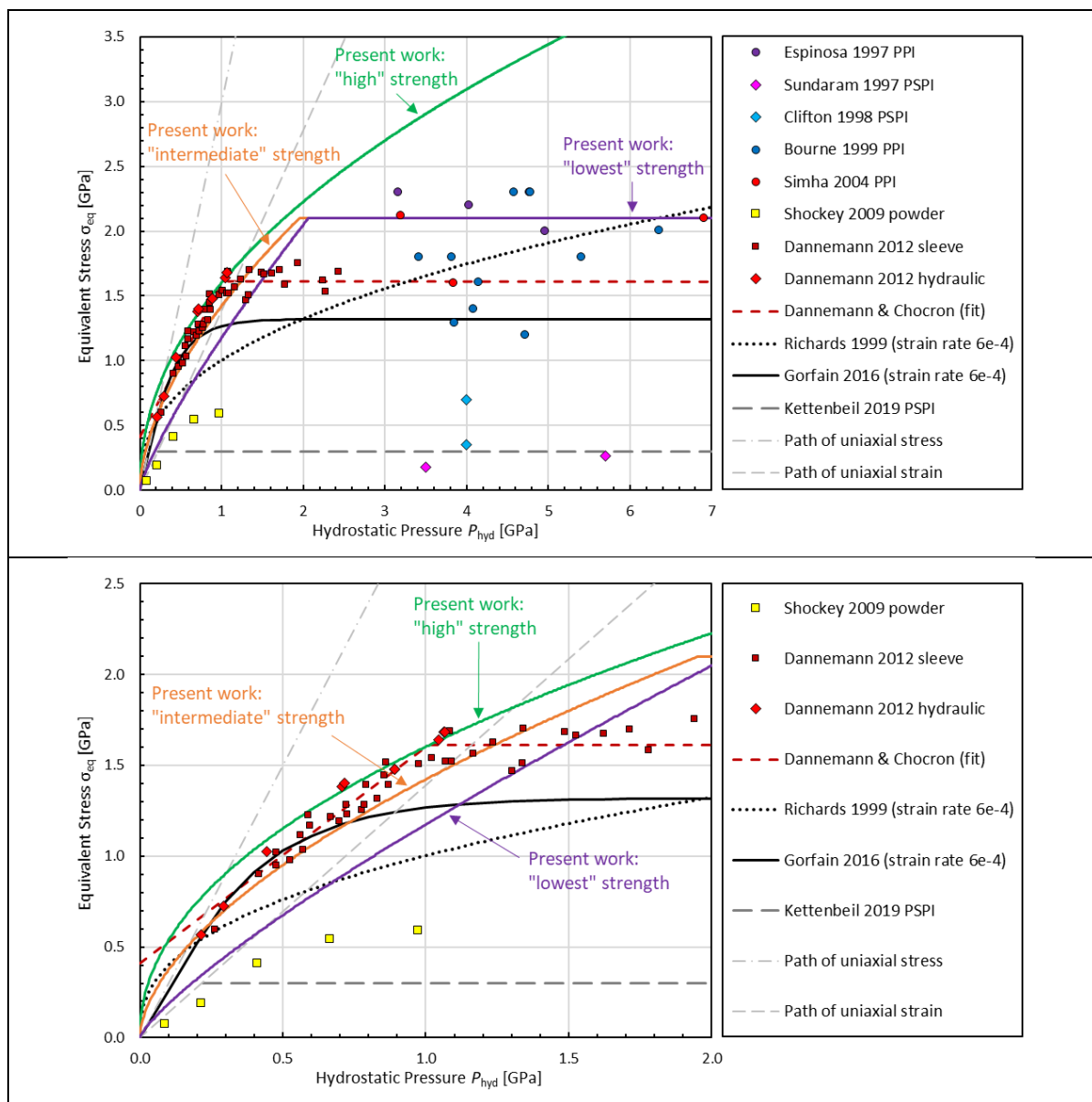


Figure 5.67: Failed SLG: equivalent stress as a function of hydrostatic pressure: comparison of new results (colored solid lines) with literature data; the bottom diagram shows an enlarged version of the low-pressure range.

6 Development and application of an improved strength model for soda-lime glass

This chapter presents an improved strength model for SLG that is based on the new experimental results. The strength model, which comprises the new experimentally derived yield curves, is implemented as a new user subroutine into an existing constitutive model for SLG.

The model of choice is the JH2 described in section 3.2.3.1. JH2 is used as reference model since it comprises the crucial phenomena listed in section 1 and is available in the commercial hydrocode Autodyn[®]. While not being as complex as other models like the Holmquist-Johnson model, the JH2 model uses the same approach for the calculation of the degree of damage and the description of the failed strength. In addition, the JH2 model turned out to be even superior to the Holmquist-Johnson model in some scenarios (e.g. penetration of a steel bar into borosilicate simulated by Talladay et al. [261] or Anderson et al. [51]). It has to be noted that the JH2 model does not incorporate thermal softening, the 3rd invariant effect and an EOS with permanent densification. However, for example Gorfain et al. [54] have deactivated the first two of these features in the Holmquist-Johnson model anyway, since no specific experimental data was available.

The JH2 model is modified in two ways: First, the new results of the PPI tests (chapter 4) are used to modify the EOS. Second, the insights into the strength of intact and failed SLG (chapter 5) are used to develop and implement an improved strength model. The model modifications are implemented in Autodyn[®] by means of a new user subroutine.

A two-dimensional model approach is chosen to minimize computation times. This allows the final model to be used in real impact scenarios, e.g. with large laminates. Although the two-dimensional approach leads to rotationally symmetric damage, various studies have demonstrated that ballistic scenarios can be reproduced adequately [92] [260]. However, the methodology is not restricted to the two-dimensional case.

The performance of the resulting improved model is evaluated for a selected ballistic impact scenario. Here, the results of the improved model are compared to the original model and to experimental results.

6.1 Formulation of an improved strength model

In the original JH2 model, two yield curves are defined; one is representing the strength of intact SLG while the other one describes the residual strength of entirely failed material (ref section 3.2.3.1). The degree of damage is parameterized by the damage parameter D . D increases incrementally from 0 (intact) to 1 (entirely failed) if the material undergoes plastic deformation. The strength of partially failed material ($0 < D < 1$) is determined by a linear interpolation between the intact and failed yield curves.

Holmquist et al. [60] determined a set of constitutive parameters for the JH2 model of SLG. This was done by iterating various hydrostat constants, damage model constants and failed strength constants until the simulation results were in sufficient accordance with selected ballistic scenarios. The resulting model is capable of reproducing the velocity profiles of the selected PPI tests and the depth of penetration of long tungsten-alloy rods penetrating thick SLG laminates.

Richards et al. [260] later had to modify the strength curves iteratively in order to reproduce the ballistic limits of 7.62 mm NATO ball rounds impacting thinner glass laminates.

A major disadvantage of these iterative calibration techniques is that the adaption to specific ballistic scenarios does not necessarily lead to a model that is able to predict the outcome of other arbitrary ballistic scenarios (e.g. [71] [72] [17]). Therefore, Gorfain et al. [54] developed a complete set of parameters for the Holmquist-Johnson model, based primarily on the results of basic characterization tests available in the literature. Overall, the simulation results were found to be in good agreement with the experiments. However, the authors noted that “Experimental data characterizing the strength of glass from the uniaxial stress compression load path through the hydrostatic tensile regime is clearly lacking, hence the current model description of this behavior should be considered preliminary. [...] Therefore, improvement upon the current results may be possible with some refinement of the SLG strength parameters better representing time-dependent loss of strength, modification to the assumed failed strength, and refinement of the failure strain in the damage model.” [54](p.303).

The first part of the novel approach of the present work is the implementation of the new experimental yield curves into the JH2 model. In contrast to the original model, not only the intact and entirely failed strength curves are implemented but also two curves of partially failed material. This improves the strength description of the model since the additional curves serve as interpolation points for partially failed states. Note this approach also allows for a stepwise linear interpolation of the dependence of strength on damage, in contrast to the purely linear interpolation in the original approach.

Figure 6.1 shows the new yield curves of the improved strength model. The curves are adopted directly from the “highest”, “high”, “intermediate” and “lowest” strength curve resulting from the confined compression tests (ref. Figure 5.65 and Table 5.9). Here, the parameterization of the damage is based on the mean total volume fraction of cracks $\bar{V}_{f,c}$. The “highest” yield curve (blue line) corresponds to intact SLG and therefore a damage parameter of $D = 0$ is assigned. The “lowest” yield curve (purple line) is representative for two specimens with initial crack volumes of about 4 % and 6 %. Since increasing the crack volume from 4 % to 6 % did not result in further softening, the lowest yield curve is representative for the highest degree of damage, and therefore $D = 1$. The damage parameters of the “high” (green line) and “intermediate” (orange line) curves are assigned by assuming a linear proportionality between the total crack volume and D . This leads to $D \approx 0.25$ for the “high” curve (crack volume of about 1%) and $D \approx 0.5$ for the “intermediate” curve (crack volume of about 2 %). Table 6.1 provides the exact values together with the corresponding measurement errors. The errors of D were calculated from the errors of $\bar{V}_{f,c}$ using the same linear proportionality. In addition, the last column lists representative impact velocities for the generation of the damage (deduced from specimens 21202, 21201 and 21200).

Table 6.1: Mean total volume fraction of cracks $\bar{V}_{f,c}$ and corresponding damage parameters D . The last column lists representative impact velocities for the generation of the damage.

$\bar{V}_{f,c}$ [%]	D [-]	v_P [m/s]
0.9 ± 0.2	0.24 ± 0.05	70
2.0 ± 0.6	0.53 ± 0.16	270
3.8 ± 0.6	1.00 ± 0.16	400

The yield strength $\sigma_{\text{yield}}(P, D)$ for a given hydrostatic pressure and damage parameter D is implemented in the new user subroutine of the model through the equation:

$$\sigma_{\text{yield}}(P, D) = \begin{cases} \sigma_{\text{eq,high}} + (\sigma_{\text{eq,highest}} - \sigma_{\text{eq,high}}) \cdot \frac{D-0.25}{0.00-0.25}, & \text{for } D < 0.25 \\ \sigma_{\text{eq,interm}} + (\sigma_{\text{eq,high}} - \sigma_{\text{eq,interm}}) \cdot \frac{D-0.50}{0.25-0.50}, & \text{for } 0.25 \leq D < 0.50 \\ \sigma_{\text{eq,lowest}} + (\sigma_{\text{eq,interm}} - \sigma_{\text{eq,lowest}}) \cdot \frac{D-1.00}{0.50-1.00}, & \text{for } D \geq 0.50 \end{cases} \quad 6.1$$

where $\sigma_{\text{eq,highest}}$ ($\sigma_{\text{eq,high}}$, $\sigma_{\text{eq,interm}}$, $\sigma_{\text{eq,lowest}}$) denotes the equivalent stress of the “highest” (“high”, “intermediate”, “lowest”) yield curve at the given pressure.

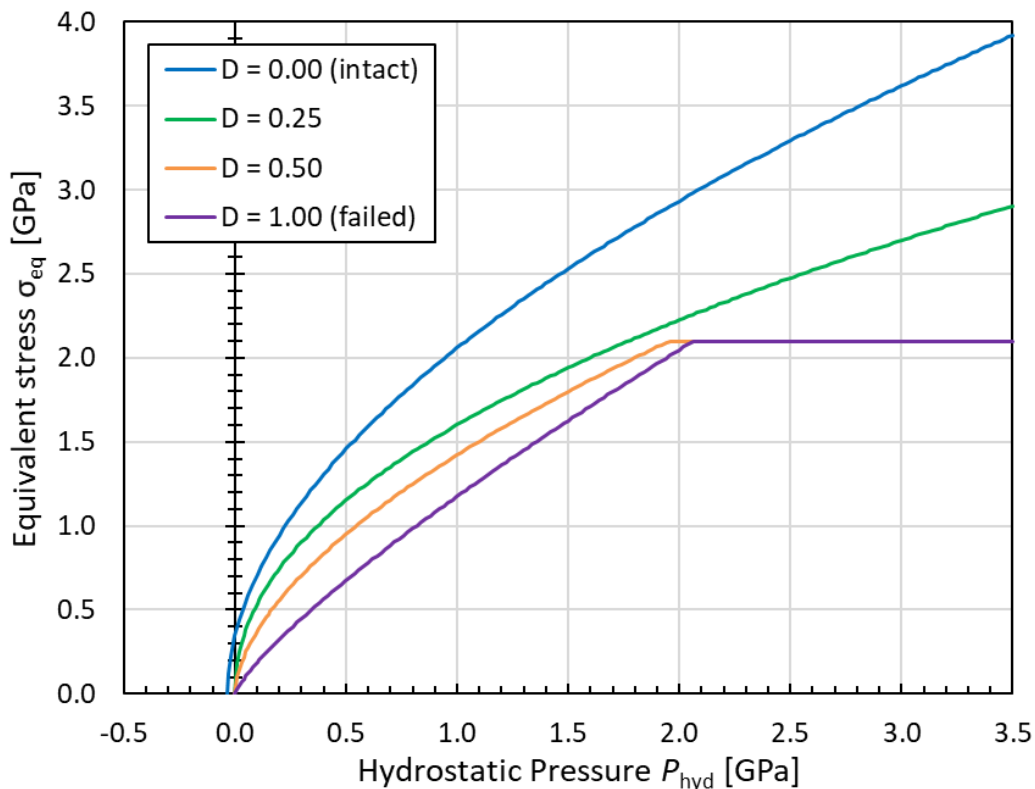


Figure 6.1: Yield curves of the improved strength model; the equivalent stress is defined as a function of the hydrostatic pressure and the degree of damage described by the damage parameter D .

It has to be noted that this implementation assigns a constant value of D for each yield curve. This value is inferred from the initial pre-damage. However, every local maximum observed in the experimental loading curves indicates the occurrence of additional failure (ref. Figure 5.60 to Figure 5.64). Therefore, the degree of damage is expected to increase incrementally during the compression loading. This increase could be determined experimentally by interrupting the compression tests at different pressures and conducting additional PCI analyses to investigate the increase of the crack volume. However, such an extensive test series is beyond the scope of this work. Moreover, the incremental increase of the damage during the compression loading can be assumed to be small. This assumption is inferred from the curve progressions. The curves of $D = 0.25$ and $D = 0.5$ do not touch or intersect the curve of $D = 1$ within the pressure range of the experiments ($P \lesssim 2$ GPa). Further, it is concluded that the major increase of the total crack volume and of the degree of damage occurs during the unloading. This is inferred from

specimen #20979, which had undergone two pressure cycles. Initially, a value of $D = 0.25$ had been observed and the corresponding stress-pressure-curve of the first cycle was consistently higher than the $D = 1.0$ curve. After the first unloading, an increased initial value of $D = 1.0$ was derived with an accordingly lower stress-pressure-curve during the second loading cycle. Consequently, the simplification of assuming that each of the yield curves can be assigned a constant D value is made in the new model. The improved simulation results of a specific ballistic impact scenario (ref. section 6.4) further indicate that the outlined assumption is reasonable.

6.2 Coupling of the experimental and the simulative degree of damage

The previous section describes the implementation of the new yield curves for the improved strength model. The resulting yield strength depends on the degree of damage, which is parameterized by the damage parameter D . Here, D is inferred from the total crack volume observed after the generation of pre-damage by means of a PPI on the confined SLG specimen.

In this section, a new methodology is outlined that allows for a coupling of the experimental and the simulative degree of damage. This means that the calculation of D in the model is iteratively calibrated until the resulting D reproduces the pre-damage generated in the PPI tests.

Figure 6.2 illustrates the geometry of the PPI model. In the model, the experimental confinement (see Figure 5.1) is approximated by a cylinder with 30 mm radius. The 8 mm thick cover plate is not joined to the confinement since the SLG specimen is kept in place by inertia during the time of interest. The projectile is a 3 mm thick disk of radius 15 mm impacting the cover plate from the left side. The SLG specimen is a cylinder of 6 mm height and 3 mm radius. It is surrounded by a 0.5 mm thick aluminum sleeve and positioned in the central cavity of the confinement. The material model of the aluminum is taken from the literature database of Autodyn®. It comprises a shock EOS and a Steinberg Guinan formulation of the strength. For the material model of the SLG specimen, the modified JH2 model is used. Equation 4.23 provides the EOS with the parameters derived from the present PPI study. The strength model is modified as described in the previous section. The calculation of D in the JH2 model is controlled by two parameters, D_1 and D_2 (ref. equations 3.18 and 3.19). These parameters are iteratively modified until the mean damage in the specimen is in agreement to the experimental results. It has to be noted that failure under hydrostatic tension is deactivated for these simulations, as this mode of failure would lead to complete failure in all investigated scenarios.

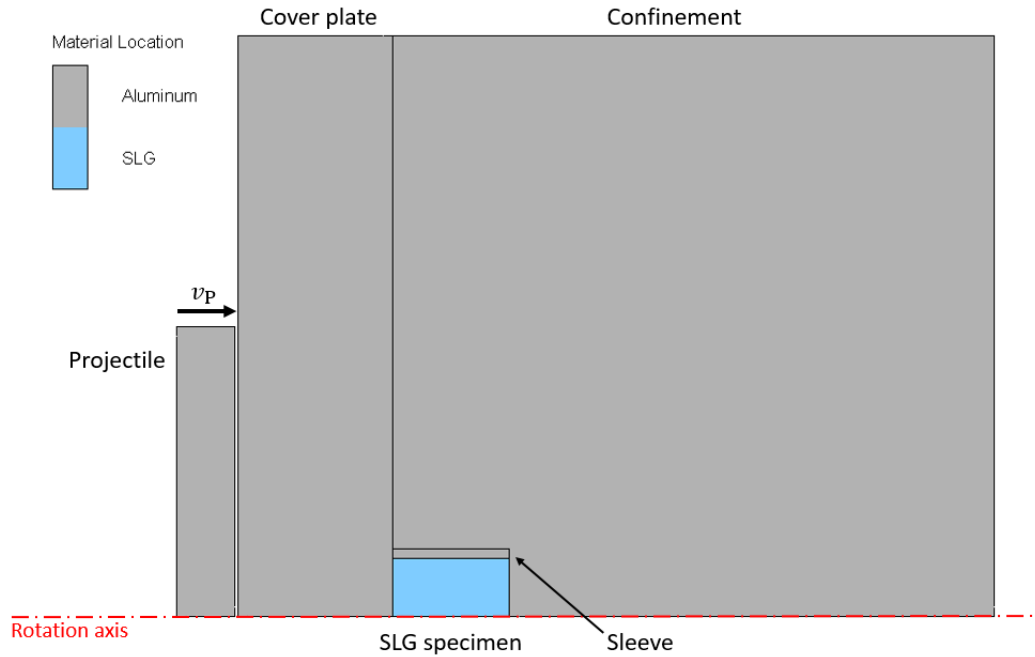


Figure 6.2: Setup of the PPI model for the simulation of the generation of the pre-damage in the SLG specimens. A two-dimensional model approach is used (the axis of rotation is indicated by the red dash-dotted line).

Three different impact velocities are investigated: a low impact velocity of 70 m/s corresponding to test 21202, a velocity of 270 m/s representing test 21201 and a high velocity of 400 m/s corresponding to test 21200. The experimentally observed total crack volumes of these tests are listed in Table 5.5. The parameterization described in the previous section is used to transform the total crack volumes into the corresponding values of D (ref. Table 6.1). This yields a target value of $D = 0.24 \pm 0.05$ for an impact velocity of 70 m/s, $D = 0.53 \pm 0.16$ for 270 m/s and $D = 1.00 \pm 0.16$ for 400 m/s. For each velocity, the resulting mean damage in the SLG specimen is calculated. The parameters D_1 and D_2 are iteratively modified until the mean damage is in sufficient accordance to the target value. The overall best match is achieved with values of $D_1 = 0.4$ and $D_2 = 0.4$. As illustrated in Figure 6.3, these values result in significantly different ξ_p^f than the values used by Richards et al. [260] ($D_1 = 0.053$ and $D_2 = 0.85$) or Gorfain et al. [54] ($D_1 = 0.0736$ and $D_2 = 0.085$).

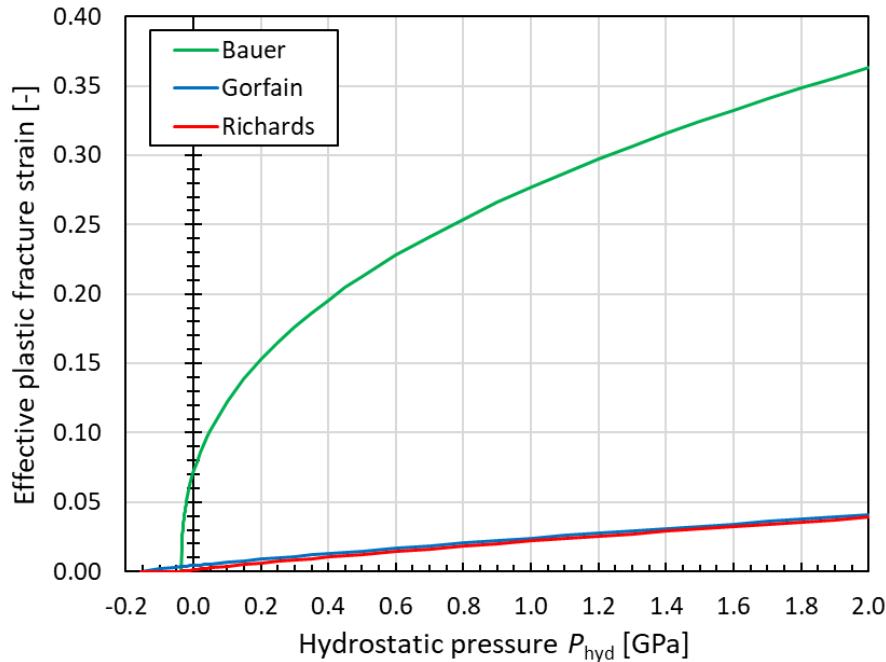


Figure 6.3: Effective plastic fracture strain as a function of the hydrostatic pressure; comparison of new parameters ($D_1 = 0.4$ & $D_2 = 0.4$) with parameters of existing models (Holmquist-Johnson parameters by Gorfain et al. [54] and JH2 parameters by Richards et al. [260]).

Figure 6.4 shows a selection of the simulation results with $D_1 = 0.4$ and $D_2 = 0.4$. The first column illustrates a cross-section of the impact process for an impact velocity of 70 m/s. The results for higher impact velocities of 270 m/s and 400 m/s are shown in the second and third column, respectively. The development over time is illustrated from top to bottom with the time after impact given on the left side. The growth of the damage parameter in the SLG specimen is illustrated as contour plot. Intact elements ($D = 0$) are colored blue and failed elements ($D = 1$) are colored red (ref. legend on the right side). At 70 m/s (first column), no damage is observed in the specimen after 5 μ s. At later points of time, damage starts to accumulate in the center of the specimen. At 270 m/s (second column), the damage increases significantly faster. After 5 μ s, several elements are already entirely failed (red elements). At the highest impact velocity (third column), the damage in the specimen is initiated at the left surface and is moving to the right side, similar to a failure front. In this case, nearly all elements are entirely failed after 50 μ s.

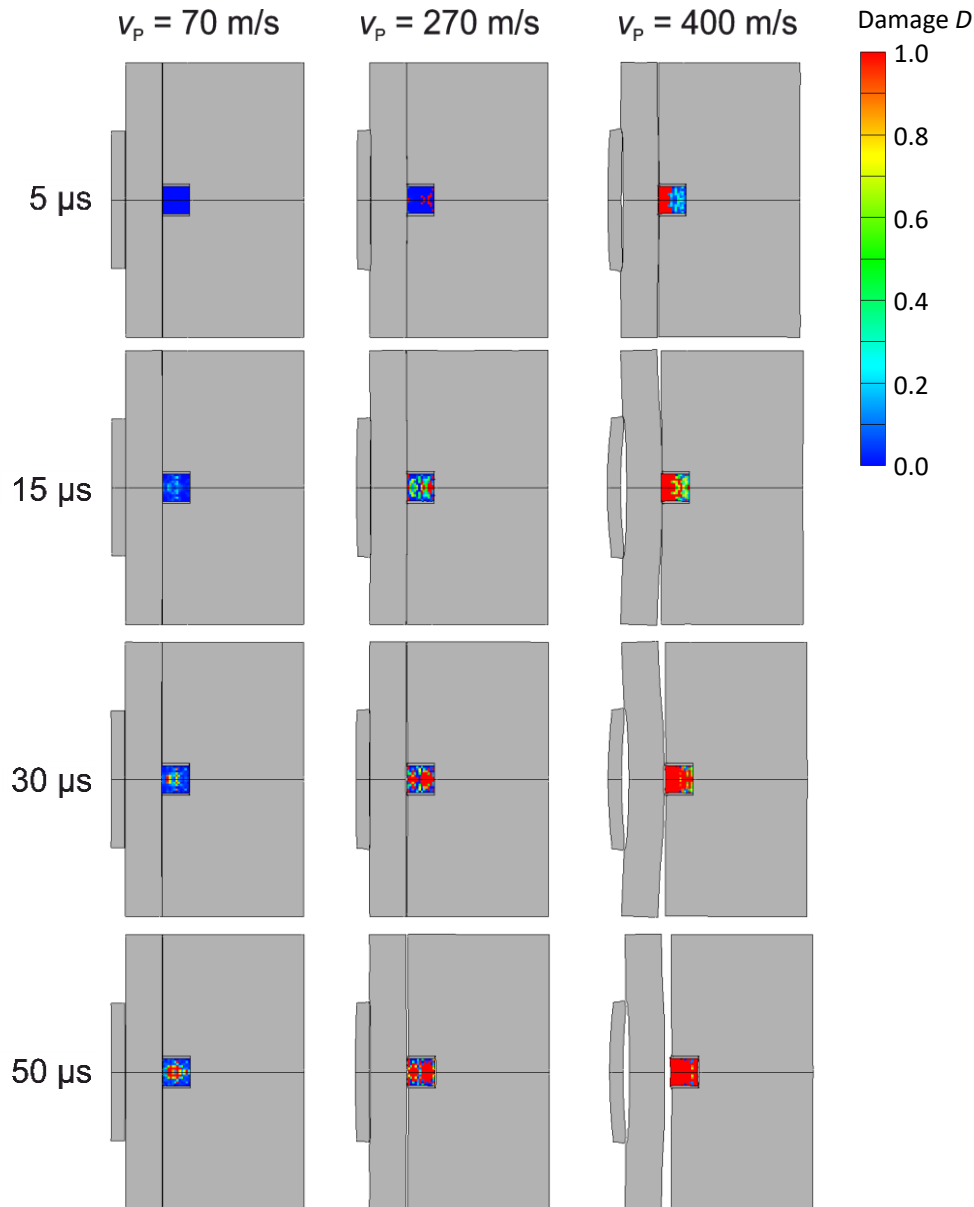


Figure 6.4: Selection of the simulation results with the improved SLG model (with $D_1 = 0.4$ and $D_2 = 0.4$). The columns illustrate a cross-section of the confined impact for different impact velocities of 70 m/s (left column), 270 m/s (middle column) and 400 m/s (right column). The development over time is illustrated from top to bottom with the time after impact given on the left side. The damage in the SLG specimen is illustrated by a contour plot of D (legend on the right side).

The simulated damage patterns in the specimens are not directly compared to the crack patterns observed in the experimental CT analysis. Instead, the mean damage \bar{D} of the simulated specimen is compared to the D value inferred from the mean total crack volume $\bar{V}_{f,c}$ of the experiments. The simulated mean damage is calculated as follows. The specimen is discretized by N Lagrange elements. Each element represents a ring-shaped volume due to the two-dimensional modeling approach. \bar{D} is calculated by a weighted sum over all elements:

$$\bar{D} = \frac{\sum_{i=1}^N D_i \cdot V_i}{\sum_{i=1}^N V_i} \quad 6.2$$

where D_i and V_i denote the damage parameter and the ring-shaped volume of element i .

The resulting mean damage as a function of the time after impact is illustrated in the diagram of Figure 6.5. The curves represent the simulation results for the different impact velocities of 70 m/s (green), 270 m/s (orange) and 400 m/s (purple). The horizontal lines of the same color indicate the corresponding target values as summarized in Table 6.1. These values were inferred from the mean total crack volume $\bar{V}_{f,c}$ of the PCI analysis, as described in the previous section. The colored areas indicate the corresponding error bands. 100 μ s after impact, no further significant accumulation of damages occurs. The contour plots on the right side of Figure 6.5 illustrate the damage of the specimens after 100 μ s. The black dash-dotted lines indicate the rotation axis of the cylinders. Each specimen consists of 6 x 12 Lagrange elements of 0.5 mm x 0.5 mm size. The color of each element indicates its damage parameter according to the legend on the right side. The resulting values of \bar{D} are 0.26, 0.61 and 0.92 for the impact velocities of 70 m/s, 270 m/s and 400 m/s, respectively. In all three cases, the final \bar{D} of the simulation is in good agreement to the experimental target value within the measurement errors. It is therefore concluded that the developed methodology is well suited to determine the parameters D_1 and D_2 for the improved JH2 model. This is a significant innovation since in previous studies (e.g. [60]), these parameters had to be deduced simultaneously with several other parameters by matching the depth of penetration in experiments with long rods penetrating SLG laminates.

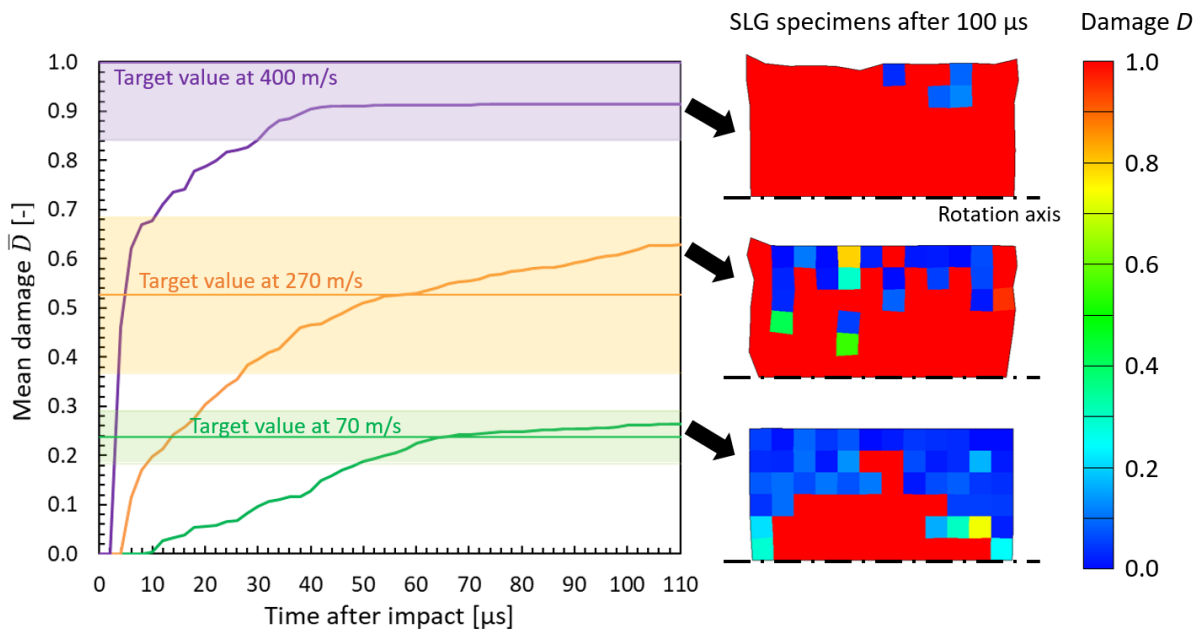


Figure 6.5: Damage development in confined specimens during PPI simulations (with $D_1 = 0.4$ & $D_2 = 0.4$); the diagram on the left side illustrates the mean damage as a function of time for three different impact velocities.

It has to be noted that in the JH2 model, the accumulation of damage is very sensitive to the resolution of the Lagrange mesh. The damage parameter D is generally increasing more slowly if the element size is increased. This is due to the practically smeared crack model assuming a constant stress across each element. Depending on the element size, strong stress gradients cannot be resolved, which can lead to a reduction of the stress peaks. As a result, the energy to failure depends on the element size.

For the outlined calibration simulations, an element size of 0.5 mm was used. As a result, the determined parameter set of $D_1 = 0.4$ and $D_2 = 0.4$ has to be used with a similar element size for the simulation of ballistic impact scenarios.

6.3 Performance of the improved model in an impact scenario

In the previous sections, the improved JH2 model is outlined. In this section, the performance of the new model is investigated in a specific ballistic impact scenario. In particular, the calculated stress and pressure of SLG elements in front of the projectile are investigated in detail. Stress-pressure-plots of the first microseconds after impact are created to evaluate the significance of the novel yield curves. In order to compare the simulation with experimental results (ref. section 6.4), the ballistic limit velocity and the final damage pattern of the laminate are also determined.

In the investigated scenario, a 7.62 mm armor-piercing projectile with tungsten carbide core (AP8 projectile) impacts a representative transparent armor laminate. The impact velocities are in the range of $600 \text{ m/s} < v_p < 1100 \text{ m/s}$. The laminate consists of four layers of SLG in front of a 3 mm thick polycarbonate layer. The total thickness of the SLG layers is $10 \text{ mm} + 3 \times 12 \text{ mm} = 46 \text{ mm}$. Between all adjacent layers, 0.8 mm thick bonding layers of polyurethane are placed.

The setup is adopted from an experimental test series conducted by Strassburger et al. [92]. In these experiments, the laminate was rectangular with lateral dimensions of 500 mm x 500 mm. For the simulations, a two-dimensional approach is chosen. Here, the laminate is modelled as a cylindrical plate with a radius of 150 mm. For the SLG, the modified JH2 material model is used. A modified EOS is utilized which is based on the new results of the PPI tests (chapter 4). In addition, the improved strength model (sections 6.1 and 6.2) is employed. The tungsten carbide core of the projectile is modelled as rigid body since neither deformation nor fragmentation was observed in the experiments. The constitutive models of all used materials are listed in the appendix in section 9.2.

Figure 6.6 illustrates the geometrical setup of the model. On the right side of the figure, an enlarged section of the impact area is shown. In this illustration, black grid lines indicate the discretization of the model. The SLG layers are discretized by rectangular Lagrange elements of size 0.5 mm x 0.5 mm. This way, the mesh resolution is in accordance with the simulations that are described in the previous section (6.2). The polycarbonate layers and the projectile have a smaller average element size of about 0.25 mm in order to enable a suitable meshing of thin layers. The enlarged illustration in Figure 6.6 also depicts the positions of three gauge points. Each gauge point is tied to one Lagrange element providing time-dependent local stress, strain and damage data. This information is used to create stress-pressure-plots for a comparison of the occurring stresses with the novel yield curves. Gauge 1 is positioned close to the impact surface at $x = y = 0.75 \text{ mm}$, where x denotes the horizontal distance to the impact surface and y denotes the vertical distance to the rotation axis. Gauges 2 and 3 are positioned at a larger depth of $x = 2.25 \text{ mm}$. While gauge 2 is placed directly next to the rotation axis ($y = 0.25 \text{ mm}$), gauge 3 is placed at a vertical distance of $y = 2.75 \text{ mm}$, which is similar to the radius of the projectile core.

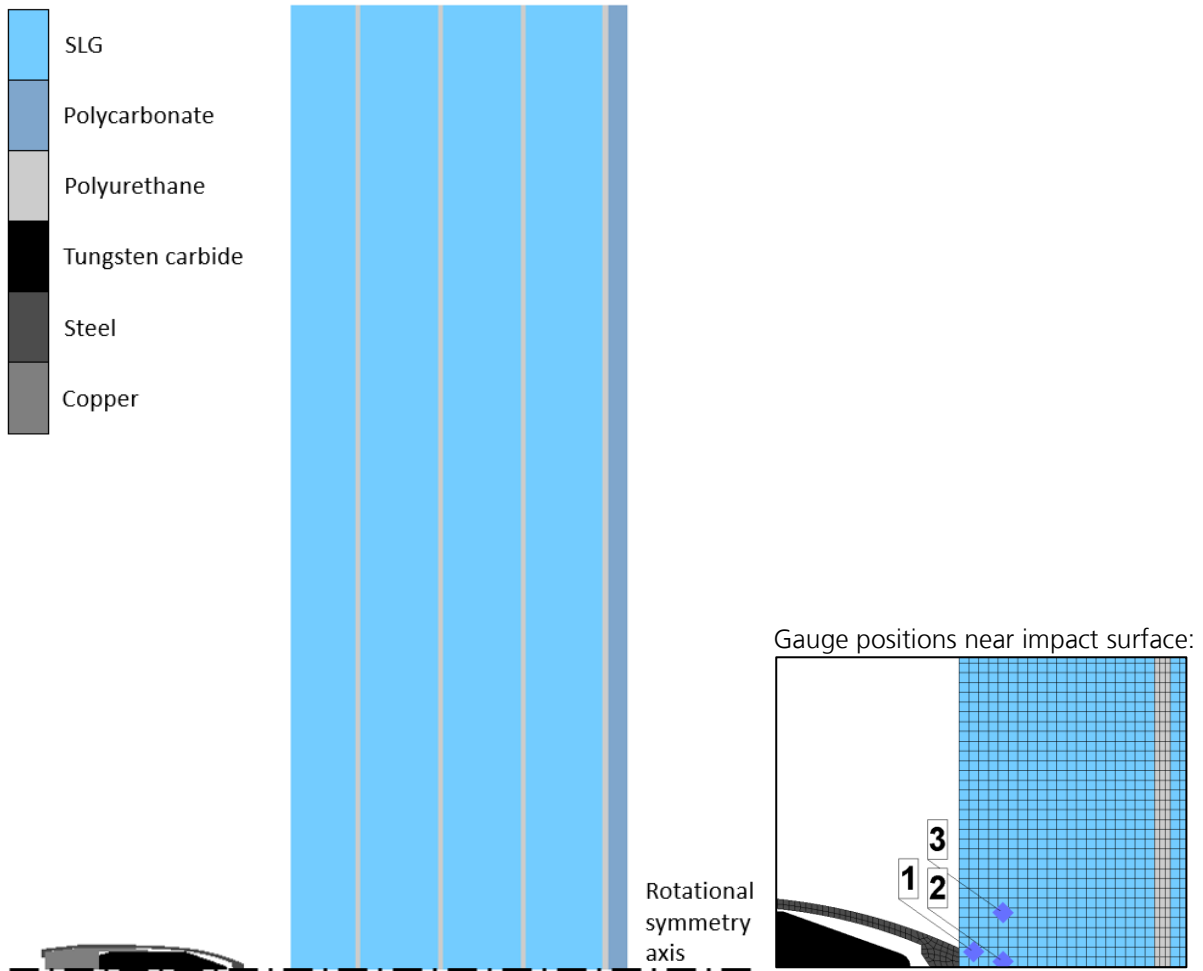


Figure 6.6: Simulation model of a 7.62 mm armor-piercing projectile with tungsten carbide core (AP8 projectile) impacting a SLG laminate from the left side. The setup of the model is two-dimensional axisymmetric. The black dash-dotted line indicates the rotational symmetry axis. The SLG layers have a total thickness of $10 \text{ mm} + 3 \times 12 \text{ mm} = 46 \text{ mm}$, with a radius of 150 mm. The illustration on the right side shows an enlarged section near the impact surface. Three gauge points are tied to Lagrange elements in the first SLG layer for a subsequent analysis of the occurring stress, strain and damage.

Figure 6.7 shows the simulation results during the first $7 \mu\text{s}$ of an impact at $v_p = 900 \text{ m/s}$. For a better visualization, only an enlarged section of the first SLG layer and the projectile is shown. The damage in the SLG is visualized by a contour plot. Blue elements represent intact material ($D = 0$) while red elements indicate completely failed material ($D = 1$). After $1 \mu\text{s}$, several SLG elements close to the point of impact are already significantly damaged (their green coloring indicates $0.4 \lesssim D \lesssim 0.6$). At this time, the projectile jacket penetrated the laminate only slightly to a depth of 0.5 mm. The damaged area is created by compression and shear loads that are induced in the SLG upon impact. Since the waves are preceding the projectile, the projectile is primarily interacting with damaged SLG during the entire penetration process. At the same time, the damaged material is surrounded by intact material providing a significant confinement pressure. As a result, even entirely failed SLG can support a significant shear stress counteracting the penetration of the projectile.

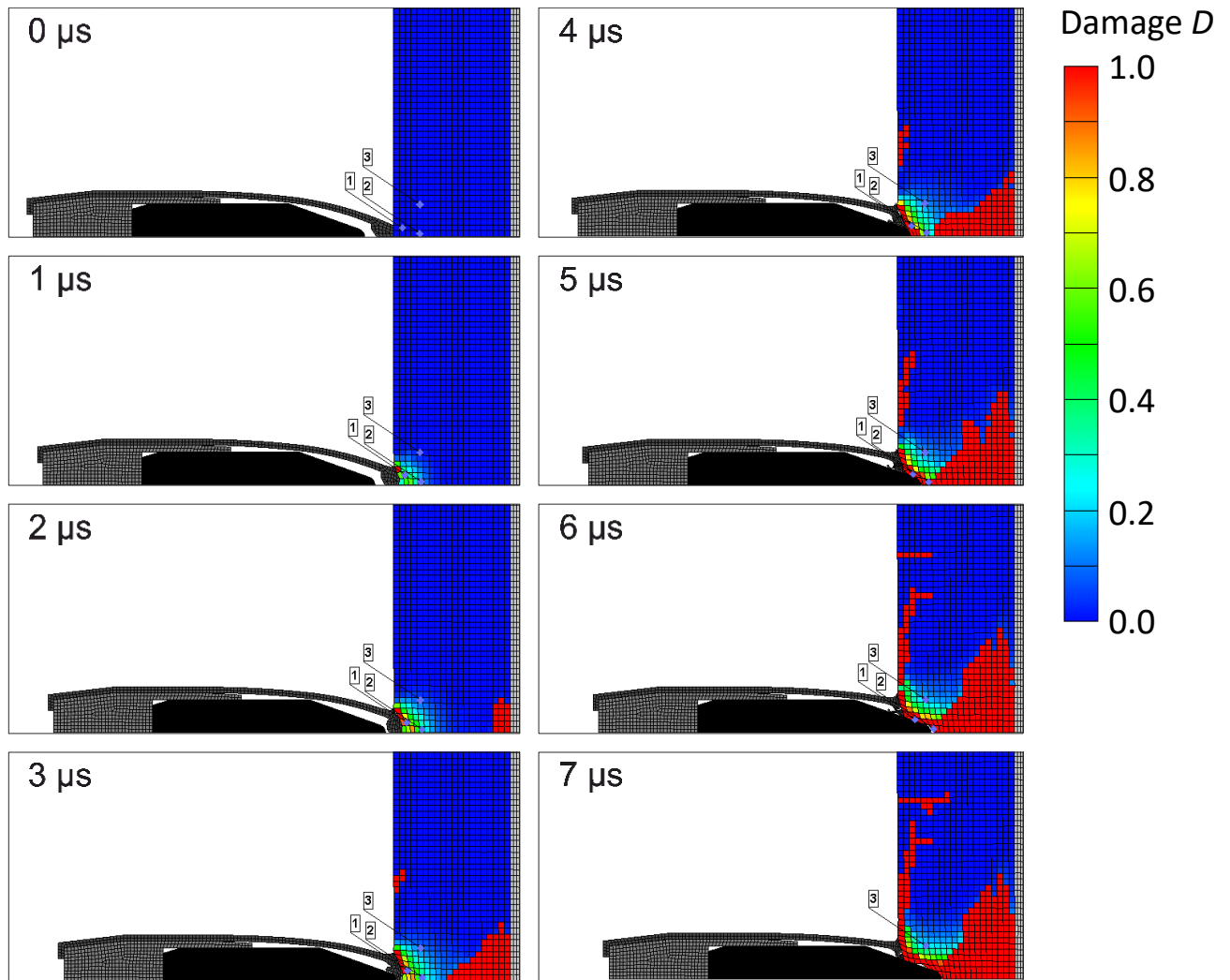


Figure 6.7: Simulated penetration process during the first 7 μs ($v_p = 900$ m/s); For a better visualization, only an enlarged section of the first SLG layer and the projectile is shown. The damage in the SLG is indicated by a contour plot (legend on the right side).

The exact values at the positions of the three gauge points are provided in the diagrams of Figure 6.8. The upper diagrams show the hydrostatic pressure and the equivalent stress as a function of time. The bottom diagrams illustrate the damage parameter D and the strain rate as a function of time. After 1 μs , both the hydrostatic pressure and the equivalent stress in gauge point 1 (blue lines) are about 2 GPa. The accumulated damage is $D \approx 0.6$, as previously deduced from the green color of the damage area in Figure 6.7 at 1 μs . At this time, gauge points 2 and 3, which are positioned at a larger distance to the impact surface, are exposed to smaller pressure. As a result, damage accumulates significantly slower at these positions (red and green line in the bottom left diagram of Figure 6.8). After 4 μs , the material at gauge 1 is entirely failed, while at gauge 2 and 3 significantly lower values of $D \approx 0.4$ and $D \approx 0.14$ are observed. At 4.6 μs , the material at gauge 2 instantaneously fails. This failure is not due to the incremental accumulation of damage but caused by tensile failure. The pressure falls below the hydrostatic tensile limit of $T = -35$ MPa resulting in immediate failure.

The tensile failure is also evident in Figure 6.7. At 2 μs , several elements at the backside of the first glass layer are entirely damaged. In the following microseconds, the failed area spreads enclosing the position of gauge 2 after 5 μs . Figure 6.7 also shows that at 7 μs , gauges 1 and 2

are missing. This is due to the erosion of the corresponding Lagrange elements caused by the penetration of the projectile core. The erosion of the elements is also evident in the diagrams of Figure 6.8, where the blue and red lines end after 6.2 μs and 6.5 μs , respectively.

The diagrams of Figure 6.8 also provide important insights into the magnitudes of the occurring stress and strain levels. The hydrostatic pressures observed at all three positions are primarily below 5 GPa. Only at the position of gauge 2 (placed next to the shot axis), a temporarily higher pressure of almost 7 GPa arises. This pressure range is sufficiently covered by the PPI tests that have been used for the determination of the new EOS (ref. Figure 4.40 and Table 4.9).

In addition, the strain rates observed during the ballistic scenario are similar to those generated in the PPI tests ($\approx 5 \cdot 10^5 \frac{1}{\text{s}}$). The bottom right diagram of Figure 6.8 shows that in the impact scenario, the strain rates are primarily in the order of $10^4 \frac{1}{\text{s}}$ to $10^6 \frac{1}{\text{s}}$.

An important conclusion is therefore that the new EOS is suitable for the description of the representative ballistic scenario.

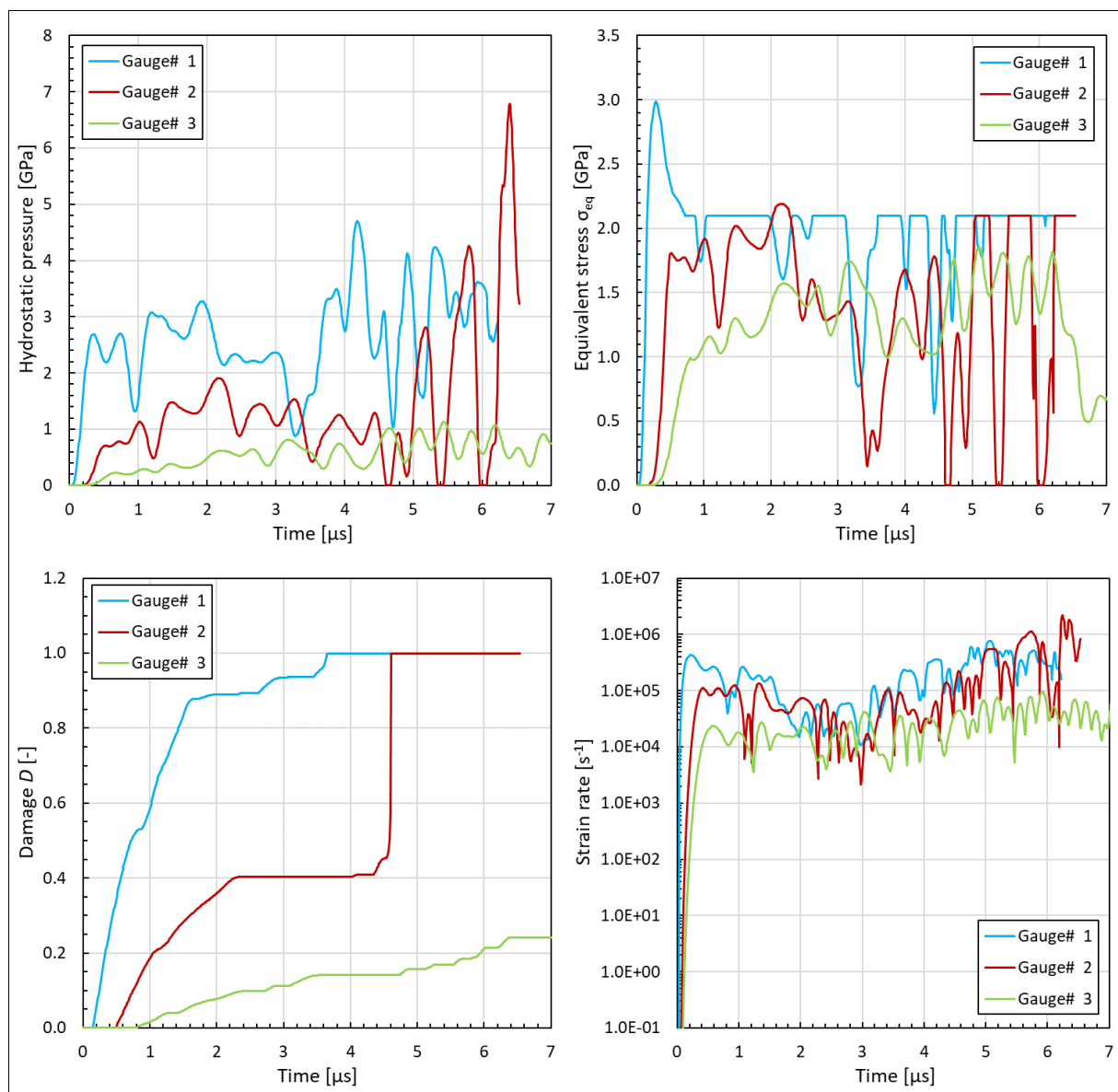


Figure 6.8: Simulation results for a ballistic impact at 900 m/s. The diagrams illustrate the hydrostatic pressure, the equivalent stress, the damage and the strain rate as a function of the time after impact. The three gauge points provide values at three different locations in the first SLG layer (see Figure 6.6 and Figure 6.7).

For a direct comparison of the occurring stresses with the new yield curves of the improved strength model, stress-pressure-plots are created from the data presented in Figure 6.8. The yield curves for a quasi-static strain rate are indicated in Figure 6.9 by the thick solid gray lines (for a detailed description see Figure 6.1). In addition, the gray dashed line represents the intact yield curve for a dynamic strain rate of $5 \cdot 10^5 \frac{1}{s}$. The stress-pressure-states observed at the gauge points are shown by colored circles. Each circle represents the result of one calculation cycle (= one time step). To guide the eye, the circles of consecutive cycles are connected by straight black lines. The color of each circle provides the corresponding damage parameter in accordance to the legend on the right side.

The top diagram illustrates the loading curve at a position close to the impact point (gauge 1, $x = y = 0.75$ mm). In the beginning, the equivalent stress increases almost linearly with increasing pressure. At a pressure of about 0.8 GPa, the equivalent stress reaches the dynamic yield curve of intact material (gray dashed line). In the subsequent cycles, the pressure increases further while the increase of the equivalent stress is limited by the yield curve. While moving along the yield surface, damage accumulates, which is indicated by the change of color from dark blue to cyan. With increasing damage, the guiding yield curve shifts incrementally from the intact yield curve to the lower yield curves. The yield curve of $D = 0.25$ is significant for the description of the material behavior during these cycles. After reaching a damage of $D = 0.5$, the loading path is quite complex and difficult to identify in the diagram. However, from the progression in the pressure range between 1 GPa and 2 GPa, it is concluded that the yield curves of $D = 0.5$ and $D = 1.0$ have a significant influence on the material behavior, at least at this position in the laminate.

The center diagram of Figure 6.9 illustrates the loading curve at the position of gauge 2 ($x = 2.25$ mm and $y = 0.25$ mm). At this position, the damage accumulates more slowly (see also red line in the bottom left diagram of Figure 6.8). The loading path is complex, but it can be concluded that for pressures below 2 GPa all yield curves have a significant influence. At the position of this gauge point, large pressures of up to almost 7 GPa are observed for a short time. These pressures are created by a shock wave directly in front of the penetrating projectile core. All loading states above pressures of 3.5 GPa are lying directly on the lowest yield curve. Therefore, the lowest yield curve (and especially its cap) has a significant influence on the penetration process.

The bottom diagram of Figure 6.9 illustrates the loading curve at a position further away from the shot axis (gauge 3, $x = 2.25$ mm and $y = 2.75$ mm). In contrast to the other two gauge points, the damage does not increase above a value of $D \approx 0.24$. In this case, the material strength is limited by the yield curves of $D = 0$ and $D = 0.25$.

It has to be noted that only the loading states of the first 7 μ s after impact are illustrated. At later times, the lower yield curves are also important as the damage further increases.

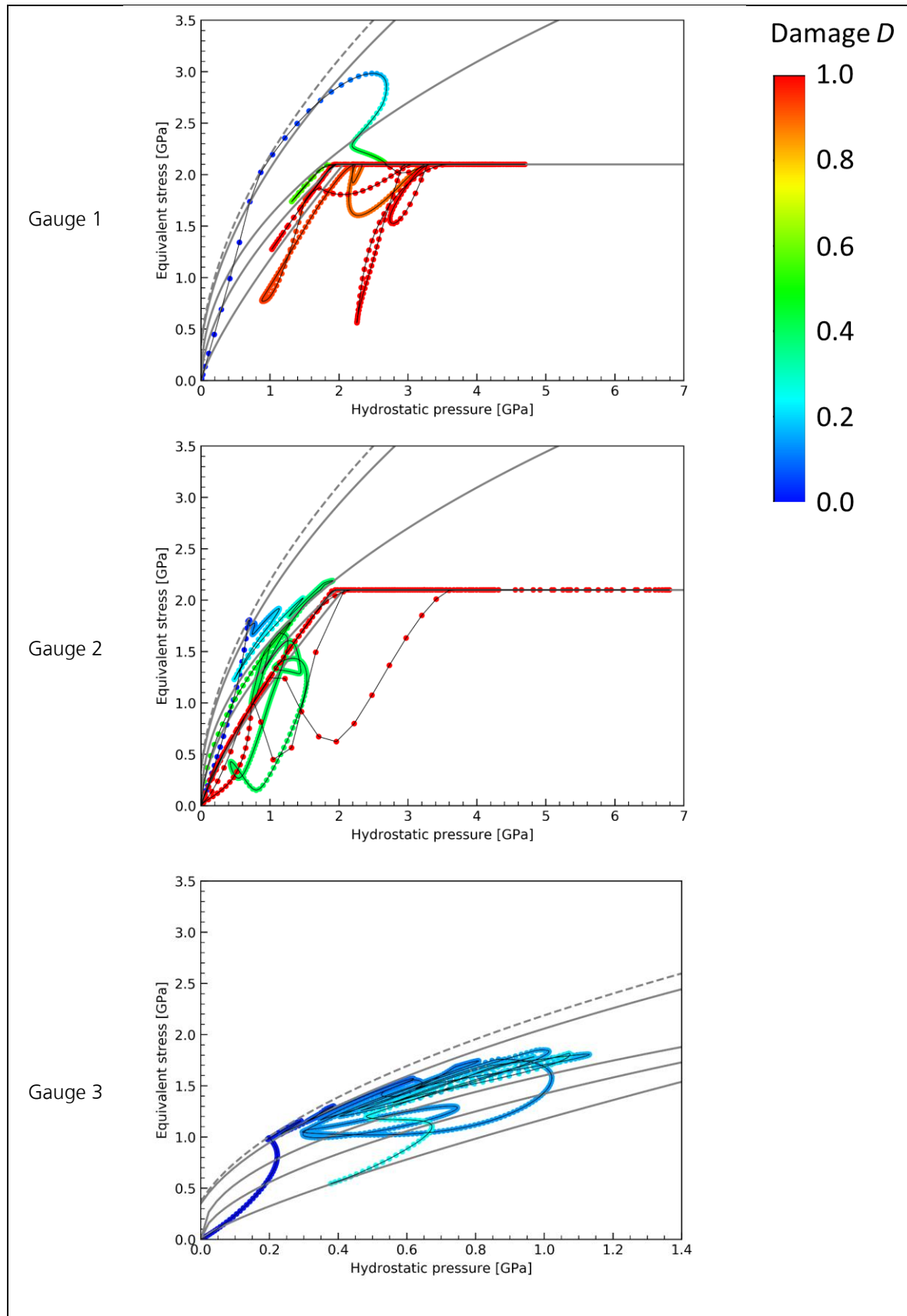


Figure 6.9: Loading path in a ballistic impact scenario, in which an AP8 projectile impacts a glass laminate at 900 m/s. The diagrams illustrate the equivalent stress-hydrostatic pressure-paths at three selected locations (gauge points 1-3, ref. Figure 6.7) during the first 7 μ s after impact. Each circle indicates the loading state after one time step in the simulation. The color represents the damage parameter D (see legend on the right side).

The previous observations are based on the first 7 μs of the impact process. During this time period, the projectile core is slightly decelerated from a mean velocity of 900 m/s to 880 m/s. The entire deceleration process of the projectile core takes about 200 μs . Figure 6.10 shows the complete process at six selected points of time. Similar to the previous illustrations, the damage in the SLG layers is visualized by a contour plot. In the last picture ($t = 207 \mu\text{s}$), the projectile core is stopped and all SLG layers are extensively damaged. Here, two different modes of failure can be identified. A fine network of cracks is spread over large parts of all SLG layers. These cracks consist of chains of Lagrange elements that are completely failed ($D = 1$). In this case, the failure was initiated instantaneously by exceeding the hydrostatic tensile limit. The second mode shows areas of gradual failure (cyan, green or yellow color shades) that are visible in a region close to the shot axis. These areas are conically shaped within the individual SLG layers. They were initiated by compression and shear loads that are localised more closely to the projectile core. The conical shape spreads over a radial distance of several projectile core radii and is particularly visible in the second and third layer at $t = 57 \mu\text{s}$ (Figure 6.10).

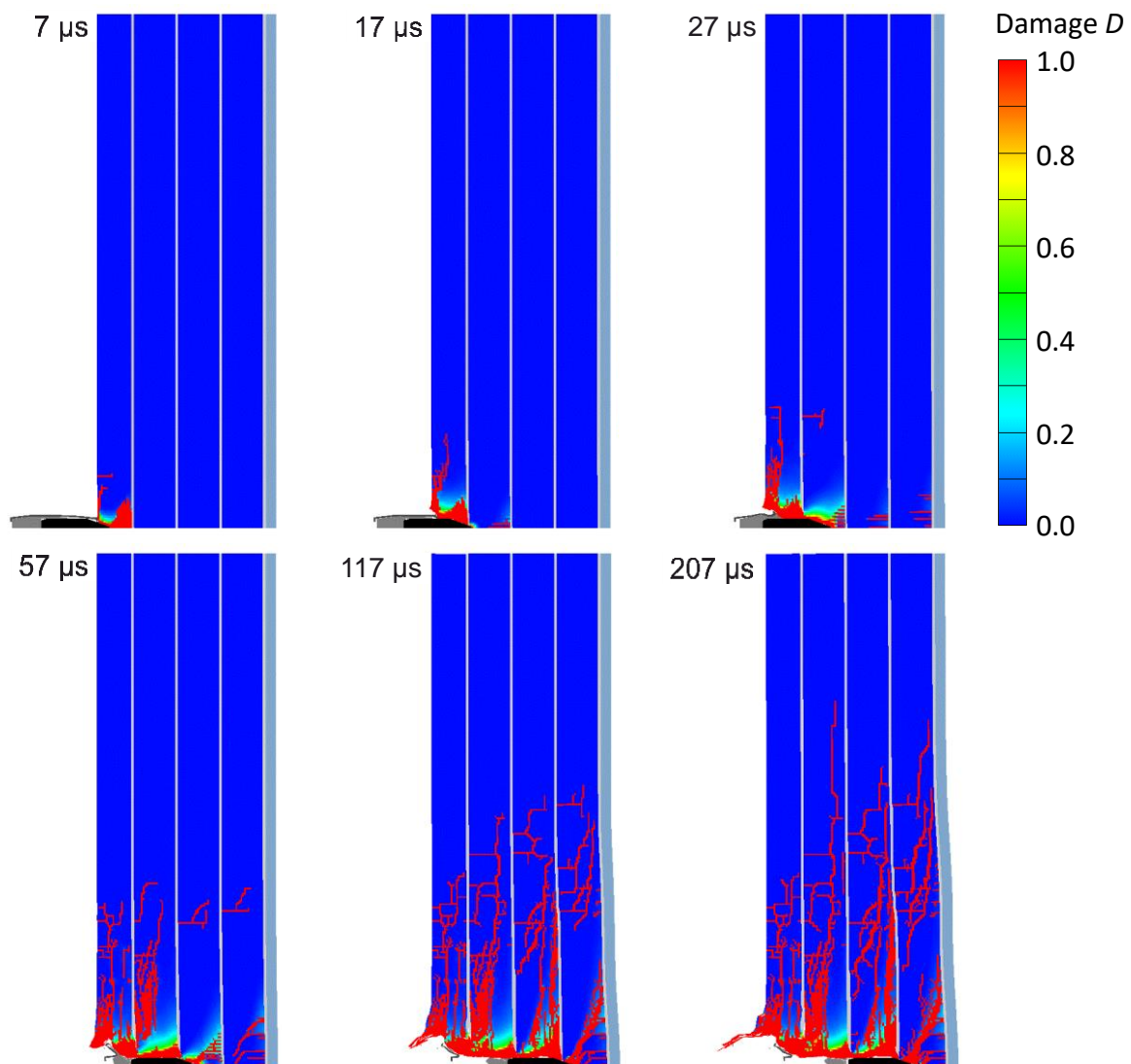


Figure 6.10: Entire penetration process ($v_p = 900 \text{ m/s}$) at six selected points of time. The damage in the SLG layers is visualized by a contour plot (intact SLG = blue, entirely failed SLG = red).

The previous observations refer to an impact velocity of $v_p = 900$ m/s. In this case, the projectile is completely stopped inside the laminate. However, at higher impact velocities, the projectile can fully penetrate all layers, emerging from the laminate at a residual velocity v_R . For a comparison with experimental data, the so-called ballistic limit velocity v_{BL} is of special importance. v_{BL} is defined as the lowest impact velocity at which the laminate is fully penetrated ($v_R > 0$).

In order to determine the v_{BL} of the laminate model, a series of simulations with different v_p is conducted. For each v_p the mean residual velocity v_R of the projectile core is calculated. v_{BL} is then determined from $v_R(v_p)$ by means of a best-fit method. Here, a modified Jonas-Lambert fit function is adopted from [92]. The fit function is based on energy conservation considerations (for more details see [262]) and is defined as follows:

$$v_R(v_p) = \begin{cases} \alpha \cdot \sqrt{v_p^2 - v_{BL}^2}, & \text{if } v_p > v_{BL} \\ 0, & \text{if } v_p \leq v_{BL} \end{cases} \quad 6.3$$

where α and v_{BL} are the independent fit parameters that are determined by a least squares fit.

Figure 6.11 shows the resulting $v_R(v_p)$ of the conducted simulation series as green rhombs. The green curve indicates the corresponding Jonas-Lambert fit (eq. 6.3) for resulting values of $\alpha = 0.71$ and $v_{BL} = 932$ m/s. Therefore, the projectile is expected to fully penetrate the investigated glass laminate for impact velocities of $v_p \geq 932$ m/s. This value is used in the next section for a comparison with the experimental data.

It has to be noted that the results of individual simulations may vary from the expected Jonas-Lambert fit. This statistical variance is caused primarily by the description of the material strength in the JH2 model. Especially upon tensile failure, the material strength can change discontinuously from intact to completely failed. Due to the discontinuity, small changes of the initial conditions (like a different v_p) can result in larger differences of the resulting damage patterns and residual velocities.

Similar observations apply in general to experimental ballistic tests involving brittle materials. In this case, the statistical nature of the crack development can lead to a variance of the results. This effect is particularly pronounced for impact velocities that are close to the ballistic limit velocity (see also e.g. [262]).

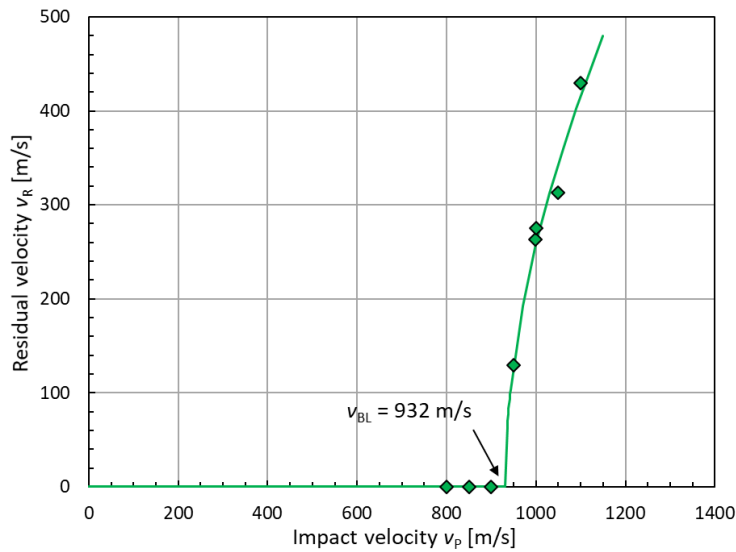


Figure 6.11: Simulation results with the improved JH2 model: residual velocity of the projectile core as a function of the impact velocity (armor-piercing projectile impacting a laminate with a total thickness of the SLG layers of 46 mm); a modified Jonas-Lambert fit yields a ballistic limit velocity of $v_{BL} = 932$ m/s.

6.4 Comparison of new results with the original JH2 model and experimental data

In this section, the results of the improved SLG model are compared to experimental data and to results of a literature JH2 model. The investigated ballistic scenario and the corresponding results of the improved model are outlined in detail in the previous section (6.3).

The experimental data is taken from a test series conducted by Strassburger et al. [92]. In these tests, an armor-piercing projectile impacts SLG laminates with a total thickness of the glass layers of 46 mm. In the following, for the determination of the ballistic limit velocity, all reported $v_R(v_P)$ are used. These include tests on glass laminates bonded with polyurethane as well as polyvinylbutyral.

The results of a literature JH2 model are determined by conducting an additional series of simulations. Here, the same model setup is used as with the improved model (ref. Figure 6.6). For the SLG layers, the original JH2 model is used with a parameter set reported by Richards et al. [260].

Figure 6.12 shows the resulting residual velocity as a function of the impact velocity. The green rhombs are the results of the improved model, as outlined in the previous section. The experimental data is illustrated by purple circles. The blue data presents the simulation results with the literature JH2 model. The corresponding Jonas-Lambert fits (eq. 6.3) are indicated by the colored lines. The fits yield ballistic limit velocities of 932 m/s for the improved model, 837 m/s for the experimental data and 720 m/s for the literature JH2 model. Therefore, the ballistic limit velocity of the improved model is 95 m/s higher than the experimentally determined v_{BL} . In contrast, the v_{BL} of the original JH2 model is 117 m/s lower than the experimental value. With a percentage difference of +11 %, the improved model is therefore slightly closer to the experimental data than the original model (-14 %). However, both models are in reasonable agreement with the experimental data.

The key difference is that the strength parameters from Richards et al. [260] have no direct physical justification, but were iteratively tuned such that the results of ballistic experiments were reproduced. In contrast, the new model was directly parametrized from material characterization experiments, no additional tuning was performed.

As a result, the strength curves of the improved model are in accordance to the data of the characterization experiments while the strength curves of Richards et al. clearly differ from the literature data of basic characterization experiments (see Figure 5.66 and Figure 5.67).

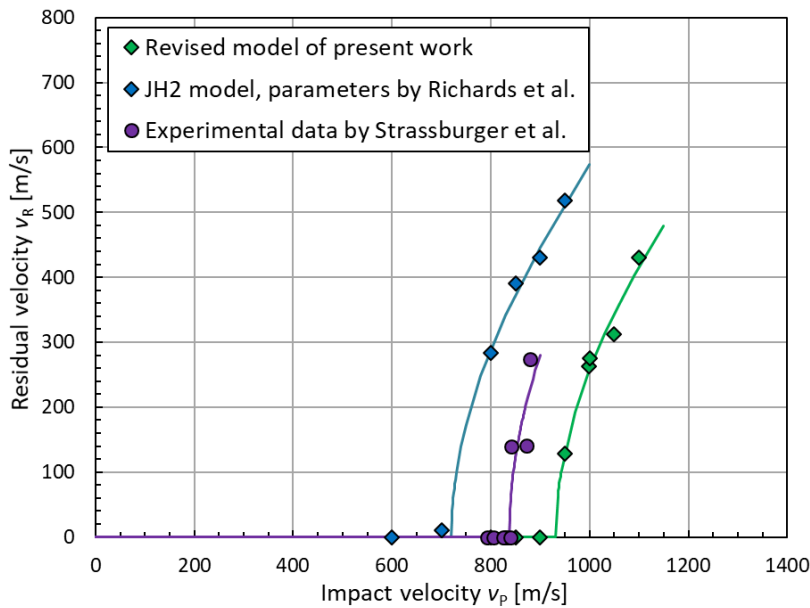


Figure 6.12: Residual velocity of the projectile core as a function of the impact velocity (AP8 projectile impacting a laminate with a total thickness of the SLG layers of 46 mm); comparison of the improved SLG model (green data) with the original JH2 model (blue data; parameters by Richards et al. [260]) and with experimental data (purple data) by Strassburger et al. [92]. The colored lines indicate the modified Jonas-Lambert fits for the determination of the ballistic limit velocities.

An important conclusion is that the ballistic resistance of the improved model is higher than that of the original JH2 model (with the parameters of Richards et al.). This is due to the higher strength of failed material and due to the slower accumulation of damage in the improved model.

For a comparison of the damage development, experimental and simulative results for an impact velocity of $v_P = 800$ m/s are investigated in more detail in the following.

Figure 6.13 illustrates the penetration process at three selected points of time. The images do not show the entire laminate, but an enlarged section near the shot axis (field of view of about 70 mm). The first row shows the results of the improved model. Similar to previous illustrations, the damage in the SLG layers is illustrated by a contour plot (blue = intact, red = entirely failed). The middle and bottom rows show the results of the original JH2 model and the experimental results, respectively. The experimental images are extracted from the work of Strassburger et al. [92]. These images were taken by means of a backlit technique. A light source was placed behind the laminate and the transmitted light was observed by a high-speed video camera. As cracks in the glass layers diffract the light, damaged material appears black in the images. In contrast, intact material appears significantly brighter. A more in-depth description of the technique and the experimental results is given in the publication of Strassburger et al. [92].

The development of the damage in the improved model (first row in Figure 6.13) is similar to the observations outlined in the previous section (ref. Figure 6.10 and Figure 6.7). Therefore, lowering the impact velocity from 900 m/s to 800 m/s does not have a significant influence on the observed damage.

However, with the original JH2 model (second row in Figure 6.13), the development of the damage is significantly different. The conical damage within each glass layers spreads more extensively. After 30 μ s, almost the entire visible areas of the first and second layers are completely failed. In addition, large failure cones are visible at the backsides of the third and fourth layers. In comparison, significant less damage is apparent in the improved model at 30 μ s. At 50 μ s, all four layers are extensively damaged in case of the JH2 model. The damaged elements form closed surfaces rather than the single tensile cracks observed in the improved model.

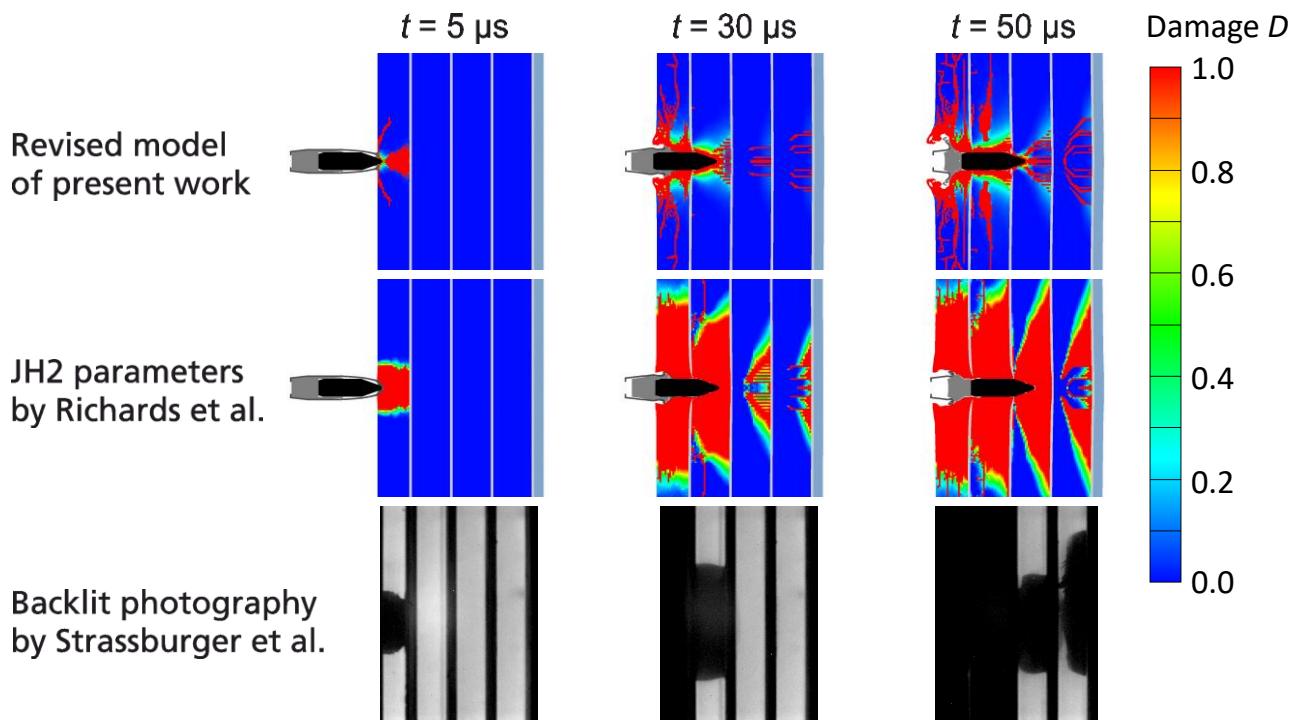


Figure 6.13: Development of the damage in an SLG laminate during the impact of an armor-piercing projectile at 800 m/s. For three selected points of time (columns), the results of the improved model (top row), the original JH2 model (second row; parameters by Richards et al. [260]) and the experimental results of Strassburger et al. [92] (bottom row) are shown. In the experimental images, failed material inside the layers appears black. In the simulations, failure is illustrated by a contour plot (legend on the right side).

In the experimental images (third row in Figure 6.13), only a small area is damaged in the center of the first layer (black round area) after 5 μ s. This observation is in agreement with both simulation models. After 30 μ s, the first layer is entirely failed and about one half of the visible area of the second layer is also damaged. The third and fourth layer are completely intact at this point of time. This observation is in contrast to the original JH2 model, where large failure cones are apparent in all four layers. With the improved model, the observed damage is in better agreement to the experiment, although some isolated cracks have already formed in the last two layers. At 50 μ s, the first two layers are failed to a degree that no light is transmitted over the entire field of view in the experiment. In the third and fourth layer, damaged areas are visible. In the third layer, this area covers about one third of the field of view. In the last layer,

the damaged area covers a larger part and is not connected to the front side of the layer. The damage in this layer was therefore clearly initiated at the backside. These observations are in good accordance to the improved model. In the improved model, cracks are spreading over the entire visible area of the first two layers. In the third layer, a damaged area is visible covering about one third of the visible height. In the last layer, the damage covers a larger area and is not connected to the front side of the layer.

In contrast, all four layers are almost entirely failed in the original JH2 model (last image in second row of Figure 6.13).

In conclusion, the calculated damage with the improved model is more realistic than the damage of the original JH2, for the investigated ballistic scenario. This conclusion is further confirmed by an additional comparison, which is outlined in the following.

For an investigation of the final state of the laminate, an additional impact test has been conducted. In this test, a similar armor-piercing projectile impacted the glass laminate at 807 m/s. After the projectile core had been stopped inside the laminate, a low viscosity resin was introduced in the penetration tunnel in order to fix the positions of the glass fragments. After the resin had hardened, the laminate was cut into two halves. The cutting plane was positioned in the direction of the shot axis, so that all layers and the arrested projectile were cut in half. One half of the laminate was subsequently polished at the cutting plane and investigated by microscopy. The resulting micro section is shown in Figure 6.14 on the left side. The image depicts the last three SLG layers with the polycarbonate layer on the backside. The first SLG layer is not visible, as it was too heavily fragmented. The projectile core appears white due to the good reflective properties of the polished tungsten carbide. Cracks inside the SLG layers appear significantly darker than intact material since they are diffracting the light.

The comparison of the experimental micro section with the final state of the improved model (second image in Figure 6.14) yields a good agreement. In the first two visible layers, a conically shaped area around the arrested projectile core is heavily fragmented. From this area, individual cracks are spreading in radial direction. In the last SLG layer, a failure cone is visible with larger parts of intact material inside. In addition, the final position of the core, that is the penetration depth, is in good agreement as the nose of the core slightly penetrates the front face of the last SLG layer.

In contrast, the results of the original JH2 model (third image in Figure 6.14) are not in good agreement with the experiment. The damage spreads too extensively, with the majority of the visible area being entirely failed. In addition, the depth of penetration of the projectile core is not reproduced. In the illustrated image, the core is still moving at a velocity of 370 m/s. In the final state, the laminate is completely penetrated and the core has left the laminate at a residual velocity of about 280 m/s.

In summary, the experimentally observed final state of the laminate is well reproduced in the simulation with the improved strength model. The projectile is stopped, the depth of penetration of the core as well as the overall damage pattern are in good agreement. In contrast, with the original JH2 model, too extensive damage is obtained. In addition, the projectile is not stopped at an impact velocity of 800 m/s, which is in contrast to the experiment. The main advantage of the improved model is that it is exclusively derived from characterization experiments and no additional tuning of parameters is required to match ballistic tests.

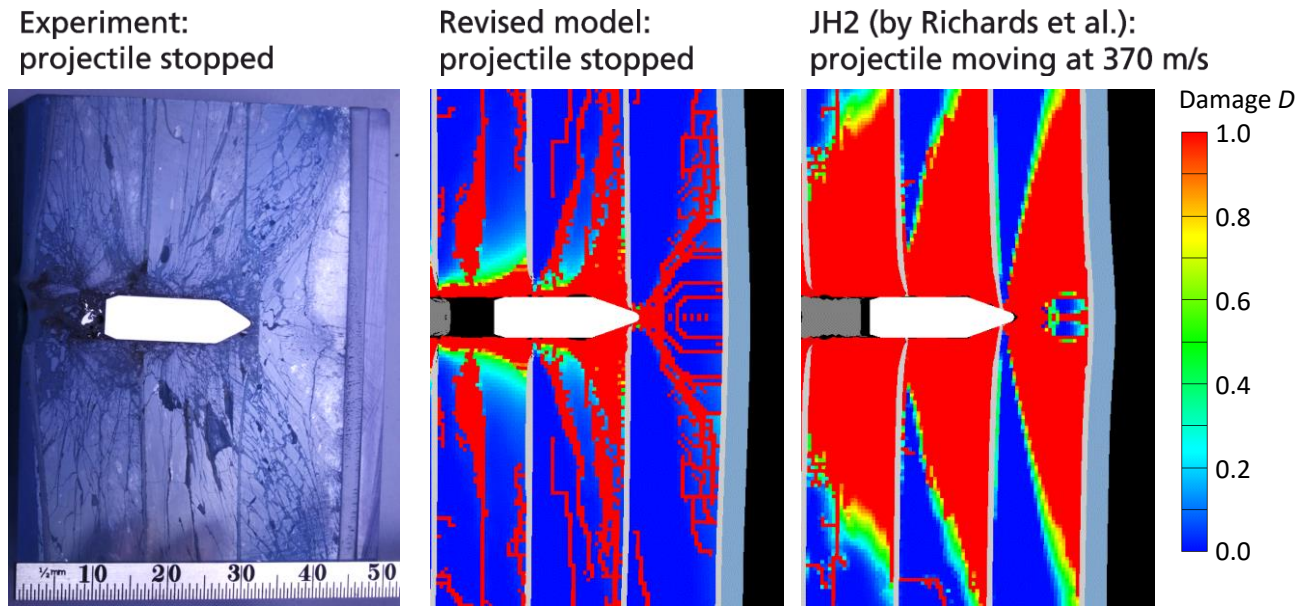


Figure 6.14: Comparison of the damage in a SLG laminate impacted by an armor-piercing projectile at 800 m/s. The left image shows the experimental result of the final state. The laminate and the projectile were cut in half and a micro section of the polished cutting plane was taken. The result of the improved SLG model (middle image) is in good agreement with the experiment. With the original JH2 model (right image), the damage spreads too extensively.

7 Summary

Within the framework of this work, several novel methodologies for the characterization and modeling of SLG have been developed and applied. Several experimental test series have been designed and carried out covering quasi-static as well as highly dynamic loading rates. In addition, advanced analysis concepts have been developed, which are supported by numerical simulations.

The first part of this work is focused on the characterization of the material properties under shock loading. An extensive PPI test series was carried out to determine the Shock Hugoniot, the HEL and the EOS of SLG. In addition, new insights into the failure front phenomena were obtained by means of a novel high-speed video observation setup. Several results of this test series have been pre-published by the author in [A1].

Altogether, twenty PPI tests with impact velocities between 500 m/s to 3000 m/s were conducted on three different test facilities. All tests were instrumented by high-resolution velocity measurements by means of laser interferometers (PDV and VISAR). In addition, five tests were instrumented by two synchronized high-speed video cameras with capture rates of 5 Mfps. With the cameras, shock waves and failure fronts were observed from the side and rear view simultaneously.

An incremental analysis concept has been developed and applied to evaluate the PPI data. The validity of the concept was investigated by a simulation study. Furthermore, a novel error analysis approach has been carried out for the determination of the Shock Hugoniot and the HEL. As a result, the Shock Hugoniot was determined for longitudinal compressive stresses of up to 20.8 GPa. A HEL value of (5.0 ± 0.2) GPa was determined.

Especially noteworthy are the derived Shock Hugoniot and the EOS, which clearly differ from reported literature data. The new Shock Hugoniot does not exhibit a distinctive plateau of constant stress for volumetric compressions in the range from 0.1 to 0.2. This is in contrast e.g. to the Shock Hugoniot data reported by Grady et al. [75] and Alexander et al. [39]. In order to investigate the discrepancies, a selection of reported velocity profiles has been digitized and analyzed by the derived analysis concept. The resulting Hugoniot states are in good agreement with the results of the present work. It is therefore concluded that the discrepancies are attributed to the analysis method and not to differences in the measurement data. The validity of the derived method has been confirmed by means of a numerical study.

The test series also revealed new results on the failure front phenomena. This has been achieved using a new diagnostic setup, which allowed for the first time a simultaneous observation of shock loaded SLG at stresses of up to 6.7 GPa by means of two synchronized high-speed cameras and a laser interferometer. For the detailed investigation of the failure fronts, a novel methodology has been developed, which includes a "streak analysis" of the high-speed videos. These results were combined with the laser interferometry results in a new way. Lagrange diagrams have been created that allow for an in-depth investigation of the failure front properties.

As a key result, at loading stresses of 3.9 GPa and higher, a planar failure front in the SLG could be clearly identified. The failure front is initialized by the arrival of the release wave coming from the back of the projectile. This result is in contrast to the assumption of several other authors who reported that the failure front originates directly at the start of compression.

It is therefore concluded that this propagating front is caused by successive compression and release of the material stress. The unidirectional compression induces a shear loading, which is

assumed to lead to the formation of micro cracks that are initially not visible in the high-speed videos. Despite the micro cracks, the material response remains elastic, if the loading stress is lower than the HEL (5 GPa). Upon release, the micro cracks turn into nucleation sites of macroscopic cracks forming the failure front, which is observed in the high-speed videos. The minimum loading stress required for the onset of this internal failure front was determined to a value of 3.8 to 3.9 GPa. At this stress, the failure front is propagating at a velocity of 800 m/s. With increasing stress, the failure front velocity is also increasing. At stresses of 10.6 GPa and higher, a maximum velocity of 2100 m/s was determined (ref. Table 4.8).

In addition to the internal planar failure front, a surface failure front was observed in all high-speed videos. This second failure front was initiated at the lateral free surface of the SLG directly upon impact. From the outer rear zones, it propagated radially inwards towards the center of the SLG specimen. The differentiation between the two failure fronts was accomplished by combining the information of the high-speed videos from the rear and side view together with the velocity data obtained by the VISAR.

Further notable results of the PPI tests were obtained from the Lagrange diagrams. It is concluded that no spallation has taken place in all PPI tests. Therefore, the spall strength is determined to be higher than 6.7 GPa. The propagation velocity of the release wave in the SLG is depending on the loading stress and could be quantified. For a longitudinal stress of up to 6.7 GPa, a constant release velocity of 5740 m/s was determined. This value is equal to the elastic longitudinal sound velocity (ref. Table 1.2). At higher stresses of 10.6 GPa and 14.2 GPa, larger release velocities of 7500 m/s and 9500 m/s were determined. This observation is in contrast to conclusions of Bourne et al. [105]. However, it is in good agreement with reported results by Grady et al. [234] and Kanel et al. [45].

The second part of this work is focused on the characterization of the shear strength of SLG. This includes both the strength of intact material at high pressures and the residual strength of pre-damaged SLG. A novel test methodology has been developed to dynamically generate different degrees of pre-damage in small SLG cylinders. For this purpose, the cylinders were loaded by a plane stress wave, initiated by the impact of an aluminum plate at a defined velocity. This was done in a new way: the SLG was damaged dynamically by a shock wave while being completely confined by a demountable aluminum confinement. The confinement holds the SLG fragments in place, which were generated during the pre-damaging. This is essential, since the residual strength of the specimen strongly depends on the friction between the fragments. The residual strength is considerably higher if all fragments are kept in place and are "interlocking", in contrast to a loose accumulation of fragments similar to e.g. rough gravel. In order to ensure that the fragments were kept in place in the subsequent characterization tests, a thin aluminum sleeve was retained around the SLG cylinder even after removing the demountable confinement. This concept turned out to be a significant improvement in comparison to the characterization tests of previous studies, which used loosely poured glass quartz powder [29] or granular silica sand [114].

A further significant improvement compared to previous studies is the contact-free investigation of the pre-damage prior to the measurement of the residual strength. An extensive CT test series has been carried out in order to analyze and quantify the crack volume in the pre-damaged SLG cylinders. X-ray CT scans were conducted at two different facilities, at a micro-CT device at EMI and at the synchrotron at PSI. In terms of contrast and resolution, the resulting three-dimensional CT images, which were obtained by means of phase-contrast imaging, turned out to be superior in comparison to the common absorption-based imaging of the micro-CT.

For the identification of the crack volume, the software tool “Mango” was used. This tool has been developed by the Australian National University in collaboration with the German Friedrich-Alexander-Universität. The author was granted access to Mango and the Fujitsu Primergy cluster “Raijin” as a collaborative arrangement with the department of applied mathematics of the ANU. The advanced 3D image processing and segmentation techniques of Mango were used to develop an analysis method for the SLG specimens. As a result, the pre-damage of selected specimens was quantified and parameterized. At the lower impact velocities of 72 and 144 m/s, a coarse mesh of cracks was identified consisting primarily of vertical crack planes. In contrast, higher velocities of 266 and 407 m/s resulted in a fine mesh of cracks and a higher degree of fragmentation. Total volume fractions of the cracks of $(0.9 \pm 0.2) \%$, $(2.0 \pm 0.6) \%$ and $(3.8 \pm 0.6) \%$ were found to be representative for impact velocities of 72 m/s, 266 m/s and 407 m/s (ref. Table 5.5). A further increase of the volume fraction to a value of $(5.9 \pm 0.6) \%$ was observed in a specimen, which had been pre-damaged at 69 m/s and had undergone a pressure cycle in the MTS machine.

The residual strength of pre-damaged and categorized specimens was subsequently characterized in confined compression tests. These tests are an enhancement of experimental techniques reported in previous studies (e.g. [21] [22]). One new aspect is that the steel confinement was replaced in most tests by a tungsten carbide confinement. This has the advantage that the occurring radial displacement of the SLG specimens is more limited. In addition, the loading of the tungsten carbide confinement can be regarded to be elastic since exceeding its elastic limit would result in brittle fracture. A second new aspect is that the experiments were supported by an elaborated simulative study. The results of the simulations allowed accounting for the influence of friction and the effects of the complex test setup, as the SLG specimens were contained in aluminum sleeves inside the tungsten carbide confinements). Additional tests on low-strength polyurethane specimens were conducted to verify the analysis methods.

As a result, new yield curves of SLG were obtained, which are functions of the hydrostatic pressure and the degree of initial pre-damage. The determined model parameters are especially suited for the simulation of ballistic impact scenarios, since the characterized pre-damaged SLG is representative for the damaged transparent armor in front of a bullet during impact.

Several mean yield curves have been determined, each representing the residual strength for a different degree of pre-damage or intact SLG, respectively.

The resulting yield curve of intact SLG is in good agreement with other results obtained within the framework of this work. On the one hand, the quasi-static curve matches the point of failure of the unconfined compression tests (uniaxial stress). On the other hand, the high-strain rate curve is in good agreement with the HEL, which had been determined in the first part of this work by means of PPI (ref. Figure 5.65). For the determination of the strain-rate dependency, the correlation factor reported by Holmquist et al. [60] has been adopted.

The lowest determined yield curve is assumed to be representative for completely failed SLG. This conclusion is based on the observation that an increase of the initial crack volume from 3.8 % to 5.9 % did not result in further softening.

In summary, the novel methodology developed within the second part of this work allowed determining several yield curves that are dependent on the degree of initial damage. The results are largely consistent with the data of Dannemann and Chocron et al. and reported PPI data in the pressure range up to 1.5 GPa for small and intermediate damage (ref. Figure 5.66 and Figure 5.67).

The present results extend the available literature data in four ways. First, the pre-damage was created highly dynamically by means of defined PPI tests instead of a thermal shock. This allowed a drastic increase of the degree of pre-damage, which represents the damage in the Mescall-zone more closely. Second, for the first time, the degree of pre-damage was directly measured and quantified using a novel X-ray CT analysis. Third, different yield curves for different degrees of pre-damage were determined.

Finally, the resulting yield curves show significant differences to the yield curves used by other authors in constitutive models (e.g. [54] [260]).

In the final part of this work, a new simulation concept has been developed, which is based on the implementation of the novel results into a constitutive material model. A two-dimensional, axisymmetric model approach based on the JH2 model [60] has been chosen for this purpose. This approach enables short computation times and allowed the final model to be used more efficiently in real impact scenarios with large laminates. Moreover, the model accounts for the constitutive material properties that are crucial for the description of a ballistic impact scenario, as listed in section 1.1. In addition, the original JH2 model is available in the commercial hydrocode Autodyn® and could be used in combination with the new strength model, which was implemented as a new user subroutine.

However, it is important to note that the concept is generally neither restricted to the JH2 model nor to the two-dimensional approach. In future work, the application to other continuum models and three-dimensional approaches is planned.

The new concept includes the implementation of the EOS found in the present work as well as the development of a improved strength model based on the new yield curves. In addition, a novel approach has been developed that enables a coupling of the damage model to the experimentally observed damage. For this purpose, the improved model was utilized to reproduce the pre-damaging PPI tests. Here, the model parameters D_1 and D_2 have been iteratively modified until the calculated degree of damage was matching the results of the CT analysis.

This direct calibration of the damage model is a significant improvement since, in previous studies, these parameters had to be deduced simultaneously with several other parameters by matching the depth of penetration of experiments with long rods penetrating SLG laminates. [60] Therefore, the present work directly addresses the recommendations of Gorfain et al. who reported that a "modification to the assumed failed strength, and refinement of the failure strain in the damage model" [54](p.303) are required to improve the model.

The performance of the improved SLG model was investigated in a representative ballistic impact scenario. The scenario was adopted from an experimental test series conducted by Straßburger et al. [92], in which a 7.62 mm armor-piercing projectile with tungsten carbide core impacted a transparent armor laminate. The results of the improved model were compared to experimental results and to results of the original JH2 model. The experimentally observed final state of the laminate was well reproduced in the simulation with the improved strength model. The depth of penetration of the core as well as the overall damage pattern were in good agreement. In contrast, the original JH2 model resulted in too extensive damage development and too high penetration velocities. Therefore, it has been demonstrated that the improved model represents an improvement for the investigated representative ballistic scenario.

Finally, it is noteworthy that the novel test and analysis methods are not restricted to the characterization of SLG only. In principle, most new concepts are suited to be applied to other materials, like ceramics, rocks or even high-strength steels. Especially for materials that do not

exhibit a shock response with a clear two-wave structure, the incremental analysis represents an improvement to common analysis methods. Hereby, the Shock Hugoniot, the HEL and the EOS are expected to be determined with higher accuracy and reproducibility. In addition, the outlined error analysis allows for a detailed evaluation of the principal uncertainties of the results.

Furthermore, the methodology of characterizing the residual strength of quantitatively pre-damaged specimens is also expected to be generally applicable to other brittle materials.

8 Bibliography

Pre-publication of partial results:

- [A1] S. Bauer, F. Bagusat, E. Strassburger, M. Sauer, S. Hiermaier, "New insights into the failure front phenomenon and the equation of state of soda-lime glass under planar plate impact", *J. dynamic behavior mater.*, 7, pp. 81-106, 2021, <https://doi.org/10.1007/s40870-020-00268-2>
- [1] F. W. Preston, „On shooting through glass with a rifle,“ *J. Soc. Glass Technol.* 11, pp. 283-286, 1927.
- [2] H. Schardin, „Ergebnisse der kinematographischen Untersuchung des Glasbruchvorganges,“ *Glastechnische Berichte*, 23, pp. 1-10, 67-79, 325-336, 1950.
- [3] H. Schardin, „Velocity effects in fracture,“ in *Fracture*, New York, Averbach, Felbeck, Hahn, Thomas (editors), John Wiley & Sons, 1959, pp. 297-329.
- [4] M. Grujicic, B. Pandurangan, N. Coutris, B. A. Cheeseman, C. Fountzoulas, P. Patel and E. Strassburger, „A Ballistic Material Model for Starphire, a Soda-Lime Transparent-Armor Glass,“ *Mater. Sci. Eng. A*, 491(1-2), pp. 397-411, 2008.
- [5] F. Hild, C. Denoual, P. Forquin and X. Brajer, „On the probabilistic and deterministic transition involved in a fragmentation process of brittle materials,“ *Comput. Struct.*, 81, pp. 1241-1253, 2003.
- [6] E. Strassburger, P. Patel, J. W. McCauley, C. Kovalchick, K. T. Ramesh and D. W. Templeton, „High-Speed transmission Shadowgraphic and Dynamic Photoelasticity Study of Stress Wave and Impact Damage Propagation in Transparent Materials and Laminates Using the Edgeon Impact Method,“ *Proceedings of the 23rd Int. Symp. on Ballistics*, April 2007.
- [7] E. Strassburger, P. Patel, J. W. McCauley and D. W. Templeton, „Visualization of Wave Propagation and Impact Damage in a Polycrystalline Transparent Ceramic – ALON,“ *Proc. 22nd Int. Symp. Ballistics*, 2, pp. 769-776, 2005.
- [8] M. Grujicic, B. Pandurangan, N. Coutris, B. A. Cheeseman, C. Fountzoulas and P. Patel, „A Simple Ballistic Material Model for Soda-Lime Glass,“ *Int. Journal of Impact Engng*, 36, pp. 386-401, 2009.
- [9] S. Freiman, „The Fracture of Glass: Past, Present, and Future,“ *Int. Journal of Applied Glass Science*, 3(2), pp. 89-106, 2012.
- [10] M. Wilkins, C. Honodel and D. Sawle, „Approach to the Study of Light Armor,“ *Tech. Rep. UCRL-50284, Lawrence Radiation Laboratory*, June 1967.
- [11] D. P. Dandekar and P. Bartkowski, „Strength of AD995 Alumina under Impact Loading,“ *Presentation at the Army Science Conference, Orlando, FL*, 21-24 June 1994.
- [12] M. Chaudhri and C. Liangyi, „The Orientation of the Hertzian Cone Crack in Soda-Lime Glass Formed By Oblique Dynamic and Quasi-Static Loading With a Hard Sphere,“ *J. Mater. Sci.*, vol. 24, pp. 3441-3448, 1989.
- [13] J. Mescall and C. Tracy, „Improved Modeling of Fracture in Ceramic Armor,“ *Proceedings of the 1986 Army Science Conference, U.S. Military Academy, West Point*, 17-20 June 1986.

- [14] J. Mescall and V. Weiss, „Materials Behavior Under High Stress and Ultra-High Loading Rates - Part II,“ *Proceedings of the 29th Sagamore Army Conference, Army Materials and Mechanics Research Center, Watertown, MA*, 1984.
- [15] D. A. Shockey, A. H. Marchand, S. R. Skaggs, G. E. Cort, M. W. Burkett and R. Parker, „Failure Phenomenology of Confined Ceramic Targets and Impacting Rods,“ *Int. J. Impact Eng.*, 9(3), pp. 263-275, 1990.
- [16] R. W. Klopp and D. A. Shockey, „The Strength Behavior of Granulated Silicon Carbide at High Strain Rates and Confining Pressure,“ *J. Appl. Phys.*, 70, pp. 7318-7326, 1991.
- [17] S. Chocron, J. D. Walker, A. E. Nicholls, K. A. Dannemann and C. E. J. Anderson, „Analytical Model of the Confined Compression Test Used to Characterize Brittle Materials,“ *J. Appl. Mech.*, 75, p. 7pp, 2008.
- [18] Y. Partom, „Modeling Failure Waves in Glass,“ *Int. J. Impact Eng.*, 21(9), pp. 791-799, October 1998.
- [19] N. K. Bourne, J. C. F. Millett and J. E. Field, „On the strength of shocked glasses,“ *Proc. R. Soc. Lond. A* 455, pp. 1275-1282, 1999.
- [20] T. Behner, C. E. J. Anderson, D. L. Orphal, V. Hohler, M. Moll and D. W. Templeton, „Penetration and Failure of Lead and Borosilicate Glass Against Rod Impact,“ *Int. J. Impact Engng.*, 35(6), pp. 447-456, 2008.
- [21] K. A. Dannemann, C. E. J. Anderson, S. Chocron and J. F. Spencer, „Damage Development in Confined Borosilicate and Soda-Lime Glasses,“ *Journal of the American Ceramic Society*, 95(2), pp. 721-729, February 2012.
- [22] S. Chocron, C. E. J. Anderson, K. A. Dannemann and A. E. Nicholls, „Pressure Effects on the Compressive Response of Confined Intact and Damaged Soda-Lime Glass,“ *Exp. MEch.*, 53(1), pp. 77-89, 2013.
- [23] J. C. LaSalvia, „Recent Progress o the Influence of Microstructure and Mechanical Properties on Ballistic Performance,“ *Ceramic Armor Materials by Design*, 134, pp. 557-570, 2001.
- [24] D. R. Curran, L. Seaman, T. Cooper and D. A. Shockey, „Micromechanical model for comminution and granular flow of brittle material under high strain rate application to penetration of ceramic targets,“ *Int. Journal of Impact Engineering*, vol.13(1), pp. 53-83, 1993.
- [25] C. E. J. Anderson and K. McCloud, „Simulations of a Gold Rod into Borosilicate Glass Using Experimentally Determined Constitutive Constants,“ *Proceedings of the 29th International Symposium on Ballistics*, 9-13 May 2016.
- [26] C. E. J. Anderson, T. Behner, T. J. Holmquist, M. Wickert, V. Hohler and D. W. Templeton, „Interface Defeat of Long Rods Impacting Borosilicate Glass,“ in *Proceedings of the 23rd International Symposium on Ballistics*, pp. 1049-1056, Tarragona, Spain, 2007.
- [27] G. Johnson and T. Holmquist, „Some Preliminary Constitutive Models for Glass Subjected to High-Velocity Impact,“ *Proceedings of the 32nd International Conference on Advanced Ceramics and Composites*, 2008.
- [28] S. Chocron, C. E. J. Anderson, K. A. Dannemann and A. E. Nicholls, „A Preliminary Mohr-Coulomb Model for CTH to Predict Long-Rod Penetration into Borosilicate Glass,“ *33rd Int. Conference on Adv. Ceramics and Composites*, Daytona Beach, FL, January 2009.
- [29] D. A. Shockey, D. Bergmannshoff, D. R. Curran and J. W. Simons, „Flow Behavior of Glass at the Tip of a Penetrator,“ *Ceramic Engineering and Science Proceedings*, 09 November 2009.

- [30] T. J. Holmquist and G. R. Johnson, „A Computational Constitutive Model for Glass Subjected to Large Strain, High Strain Rates, and High Pressures,” *J. Appl. Mech.*, *78*, 2011.
- [31] P. W. Bridgman and I. Simon, „Effects of very high pressures on glass,” *J. Appl. Phys.*, *24(4)*, pp. 405-413, 1953.
- [32] D. R. Uhlmann, „Densification of Alkali Silicate Glasses at High Pressure,” *J. Non-Cryst. Solids*, *13*, pp. 89-99, 1973.
- [33] T. Rouxel, H. Ji, T. Hammouda and A. Moreac, „Poisson's Ratio and the Densification of Glass Under High Pressure,” *Phys. Rev. Lett.*, *100*, p. 225501, 2008.
- [34] S. Sakka and J. D. Mackenzie, „High Pressure Effects on Glass,” *J. Non-Cryst. Solids*, *1*, pp. 107-142, 1969.
- [35] J. D. Mackenzie, „High-Pressure Effects on Oxide Glasses: I, Densification in Rigid State,” *J. Am. Ceram. Soc.*, *46(10)*, pp. 461-470, 1963.
- [36] P. W. Bridgman, „The Compression of 39 Substances to 100,000 kg/cm²,” *Proceedings of the American Academy of Arts and Sciences*, *76(3)*, pp. 55-87, 1948.
- [37] J. Cagnoux, „Shock-Wave Compression of a Borosilicate Glass up to 170 kbar,” *Shock Waves in Condensed Matter*, pp. 392-396, 1982.
- [38] N. Bourne, J. Millett, Z. Rosenberg and N. Murray, „On the Shock Induced Failure of Brittle Solids,” *J. Mech. Phys. Solids*, *46*, pp. 1887-1908, 1998.
- [39] C. S. Alexander, L. C. Chhabildas, W. D. Reinhart and D. W. Templeton, „Changes to the Shock Response of Fused Quartz Due to Glass Modification,” *Int. J. Impact Engng*, *35*, pp. 1376-1385, 2008.
- [40] G. Solvé and J. Cagnoux, „The behavior of Pyrex glas against a shaped-charge jet,” in *Shock Compression of Condensed Matter*, North-Holland, Amsterdam, S. C. Schmidt, J. N. Johnson and L. W. Davidson (eds), 1990, pp. 967-970.
- [41] L. A. Glenn, B. Moran and A. S. Kusubov, „Modeling Jet Penetration in Glass,” *Lawrence Livermore National Laboratory, CA., Technical Report No. UCRL-JC-103512*, 1990.
- [42] L. A. Glenn, „The fracture of a glass half-space by projectile impact,” *Journal of the Mechanics and Physics of Solids*, *24*, pp. 93-96, June 1976.
- [43] S. V. Rasorenov, G. I. Kanel, V. E. Fortov and M. M. Abasehov, „The fracture of glass under high pressure impulsive loading,” *High Press. Res.* *6*, pp. 225-232, 1991.
- [44] N. Brar, Z. Rosenberg and S. Bless, „Spall Strength and Failure Waves in Glass,” *J. Phys.*, *IV(1)*, pp. 639-644, 1991.
- [45] G. I. Kanel, A. A. Bogatch, S. V. Razorenov and Z. Chen, „Transformation of Shock Compression Pulses in Glass Due to the Failure Wave Phenomena,” *Journal of Applied Physics*, *92(9)*, p. 5045, November 2002.
- [46] T. Resseguier and F. Cottet, „Experimental and Numerical Study of Laser Induced Spallation in Glass,” *J. Appl. Phys.*, *77(8)*, pp. 3756-3761, 1995.
- [47] H. D. Espinosa and Y. Xu, „Micromechanics of Failure Waves in Glass: I, Experiments,” *J. Am. Ceram. Soc.*, *80(8)*, pp. 2061-2073, 1997.

- [48] Z. Rosenberg, D. Yaziv and S. Bless, „Spall Strength of Shock-Loaded Glass,” *J. de Appl. Phys.*, 58(8), pp. 3249-3251, 1985.
- [49] C. H. M. Simha and Y. M. Gupta, „Time-Dependent Inelastic Deformation of Shocked Soda-Lime Glass,” *J. Appl. Phys.*, 96, p. 1880, 2004.
- [50] S. Sundaram and R. J. Clifton, „Flow behavior of soda-lime glass at high pressures and high shear rates,” in *Shock compression of condensed matter, vol 429*, New York, AIP, 1998, pp. 517-520.
- [51] C. E. J. Anderson and T. J. Holmquist, „Application of a Computational Glass Model to Compute Propagation of Failure From Ballistic Impact of Borosilicate Glass Targets,” *Int. J. Impact Engng.*, 56, pp. 2-11, 2013.
- [52] P. W. Bridgman, *Studies in Large Plastic Flow and Fracture. Metallurgy and Metallurgical Engineering Series*, New York: McGraw Hill, 1952.
- [53] J. Handin, H. C. Heard and J. N. Magouirk, „Effects of the intermediate principal stress on the failure of limestone, dolomite, and glass at different temperatures and strain rates,” *Journal of Geophysical Research*, 72, pp. 611-640, 15 January 1967.
- [54] J. E. Gorfain, C. T. Key and C. S. Alexander, „Application of a Computational Glass Model to the Shock Response of Soda-Lime Glass,” *J. dynamic behavior mater.*, 2, pp. 283-305, 2016.
- [55] A. A. Griffith, „The phenomena of rupture and flow in solids,” *Phil. Trans. Roy. Soc. London*, 221, pp. 163-198, 1921.
- [56] A. A. Wereszczak, T. P. Kirkland, M. E. Ragan, K. T. J. Strong and H. Lin, „Size Scaling of Tensile Failure Stress in a Float Soda-Lime-Silicate Glass,” *Int. J. Appl. Glass Science*, 1(2), pp. 143-150, 2010.
- [57] X. Nie, W. Chen, A. Wereszczak and D. Templeton, „Effect of Loading Rate and Surface Conditions on the Flexural Strength of Borosilicate Glass,” *J. Am. Ceram. Soc.*, 92(6), pp. 1287-1295, 2009.
- [58] C. J. Anderson, C. Weiss and S. Chocron, *Impact Experiments into Borosilicate Glass at Three Scale Sizes*, San Antonio, TX: Southwest Research Institute, Technical Report No. 18.12544/018, 2009.
- [59] X. Sun, M. Khaleel and R. Davies, „Modeling of Stone-Impact Resistance of Monolithic Glass Ply using Continuum Damage Mechanics,” *Int. J. Damage Mech.*, 14, pp. 165-178, 2005.
- [60] T. J. Holmquist, G. R. Johnson, D. E. Grady, C. M. Lopatin and E. S. J. Hertel, „High Strain Rate Properties and Constitutive Modeling of Glass,” *Proc. 15th Int. Symp. Ballistics*, 1, pp. 237-244, 1995.
- [61] J. T. Chojnacki and W. W. Chen, „Mechanical Response of Borosilicate and Soda-Lime Glass under Dynamic Triaxial Compression,” *J. Dynamic Behavior Mater.*, 2, pp. 251-258, 2016.
- [62] S. Chocron, K. A. Dannemann, J. D. Walker, A. E. Nicholls and C. E. J. Anderson, „Static and Dynamic Confined Compression of Borosilicate Glass,” *Proceedings of DYMAT 9th International Conference MEchanical and Physical Behavior of Materials under Dynamic Loading*, pp. 67-72, 2009.
- [63] S. Chocron, C. E. J. Anderson, A. E. Nicholls and K. A. Dannemann, „Characterization of Confined Intact and Damaged Borosilicate Glass,” *J. Am. Ceram. Soc.*, 93, pp. 3390-3398, 2010.
- [64] X. Nie and W. Chen, „High-Rate Progressive Failure of Borosilicate Glass under Mechanical Confinement at High Temperatures,” *Experimental Mechanics* 53(1), January 2012.

- [65] „Matmatch,“ [Online]. Available: <https://matmatch.com/learn/material/borosilicate-glass>. [access on 25th September 2020].
- [66] K. W. Peter, „Densification and Flow Phenomena of Glass in Indentation Experiments,“ *J. Non-Cryst. Solids*, 5, pp. 130-115, 1970.
- [67] F. M. Ernsberger, „Mechanical Properties of Glasses,“ *J. Non-Cryst. Solids*, 25, pp. 293-321, 1977.
- [68] H. Horii and S. Nemat-Nasser, „Brittle Failure in Compression: Splitting, Faulting and Brittle-Ductile Transition,“ *Philos. Trans. R. Soc. London, Ser. A*, 319, pp. 337-374, 1986.
- [69] J. Lankford, C. E. J. Anderson, A. J. Nagy, J. D. Walker, A. E. Nicholls and R. A. Page, „Inelastic Response of Confined Aluminum Oxide Under Dynamic Loading Conditions,“ *J. Mater. Sci.*, 33(6), pp. 1619-1625, 1998.
- [70] J. Lankford, W. W. Prebedon, J. M. Staehler, G. Subhash, B. J. Pletka and C. E. Anderson, „The Role of Plasticity as a Limiting Factor in the Compressive Failure of High Strength Ceramics,“ *Mech. Mater.*, 29, pp. 205-218, 1998.
- [71] S. Chocron, C. E. J. Anderson and A. E. Nicholls, „Constitutive Model for Borosilicate Glass and Application to Long-Rod Penetration,“ *Proceedings of the 23th Int. Symp. Ballistics*, 2, pp. 1073-1081, 2007.
- [72] S. Chocron, K. A. Dannemann, J. D. Walker, A. E. Nicholls and C. E. J. Anderson, „Constitutive Model for Damaged Borosilicate Glass under Confinement,“ *J. Am. Cer. Soc.*, 90(8), pp. 2549-2555, 2007.
- [73] G. Mavko, T. Mukerji and J. Dvorkin, *The Rock Physics Handbook* (2nd ed.), Cambridge, U. K.: Cambridge University Press, 2009.
- [74] D. R. Curran, D. A. Shockey and J. Simons, „Mesomechanical Constitutive Relations for Glass and Ceramic Armor,“ *Ceramic Engineering and Science Proceedings*, 29(6), pp. 1-13, April 2009.
- [75] D. E. Grady and L. C. Chhabildas, „Shock-Wave Properties of Soda-Lime Glass,“ *Report SAND-96-2571C at the 14th US Army Symposium on Solid Mechanics*, Myrtle Beach, SC, October 1996.
- [76] S. J. Bless, N. S. Brar and Z. Rosenberg, „Strength of Soda Lime Glass under Shock Compression,“ in *Shock Waves in Condensed Matter*, Amsterdam, North Holland, 1988, pp. 309-312.
- [77] Z. Rosenberg, N. S. Brar and S. J. Bless, „Determination of the Strength of Shock Loaded Ceramics Using Double Impact Techniques,“ in *Shock Compression of Condensed Matter*, Amsterdam, Elsevier, 1990, pp. 385-388.
- [78] Z. Rosenberg, Y. Ashuach and E. Dekel, „More on the Behavior of Soda Lime Glass under Shock Loading,“ *Int. Journal of Impact Engineering*, 35, pp. 820-828, 2008.
- [79] C. S. Alexander, T. J. Vogler, W. D. Reinhart, D. E. Grady, M. E. Kipp and C. L. C., „Influence of shock wave measurement technique on the determination of Hugoniot states,“ in *Proceedings of symposium on Shock Compression of Condensed Matter*, p. 1229, Baltimore, 2005.
- [80] C. S. Alexander, „Dynamic Response of Soda-Lime Glass,“ *Tech. Rep. Sandia*, p. <https://www.osti.gov/biblio/1147908>, 2007.
- [81] G. I. Kanel, A. M. Molodets and A. N. Dremin, *Combust. Explos. Shock Waves* 13, p. 722, 1977.

- [82] N. K. Bourne and Z. Rosenberg, „The Dynamic Response of Soda-Lime Glass,“ in *Shock Compression of Condensed Matter*, New York, American Institute of Physics, Woodbury, 1995, pp. 567-572.
- [83] N. Bourne, Z. Rosenberg and J. Millett, „The plate impact response of three glasses,“ in *Structures under Shock and Impact IV*, Southampton, N. Jones; C.A. Brebbia; A.J. Watson, 1996.
- [84] D. P. Dandekar, „Index of Refraction and Mechanical Behavior of Soda Lime Glass under Shock and Release Wave Propagation,“ *J. App. Physics* 84 (12), p. 6614, 1998.
- [85] H. Senf, E. Strassburger and H. Rothenhausler, „Stress Wave Induced Damage and Fracture in Impacted Glasses,“ *Proc. EURO DYMAT 94, J. de Phys. IV, C8, 4*, pp. 741-746, 1994.
- [86] H. Senf, E. Strassburger and H. Rothenhausler, „Visualization of Fracture Nucleation During Impact in Glass,“ *Metallurgical and Materials Applications of Shock-Wave and High-Strain-Rate Phenomena*, pp. 163-170, 1995.
- [87] E. Strassburger and H. Senf, „Experimental Investigations of Wave and Fracture Phenomena in Impacted Ceramics and Glasses,“ *ARL-CR-214*, 1995.
- [88] E. Strassburger, P. Patel, J. W. McCauley and D. W. Templeton, „High-Speed Photographic Study of Wave and Fracture Propagation in Fused Silica,“ *Proc. 22nd Int. Symp. Ballistics*, 2, pp. 761-768, 2005.
- [89] E. Strassburger, P. Patel, J. W. McCauley and D. W. Templeton, „Wave Propagation and Impact Damage in Transparent Laminates,“ *Proc. 23rd Int. Symp. Ballistics*, 2, pp. 1381-1388, 2007.
- [90] E. Strassburger, M. Hunzinger, J. W. McCauley and P. Patel, „Experimental Methods for Characterization of Transparent Armor Materials,“ *Adv. Ceram. Armor*, 31(5), pp. 183-198, 2010.
- [91] S. J. Bless and T. Chen, „Impact damage in layered glass,“ *Int. J. of Fracture*, 162, pp. 151-158, March 2010.
- [92] E. Strassburger, S. Bauer and G. Popko, „Damage visualization and deformation measurement in glass laminates during projectile penetration,“ *Defence Technology* 10, 2, pp. 226-238, June 2014.
- [93] S. J. Bless, N. S. Brar and Z. Rosenberg, „Failure of ceramic and glass rods under dynamic compression,“ in *Shock Compression of Condensed Matter*, Amsterdam, 939-942, 1989, pp. 939-942.
- [94] N. H. Murray, N. K. Bourne, J. E. Field and Z. Rosenberg, „Symmetrical Taylor impact of glass bars,“ in *Shock Compression of Condensed Matter*, New York, American Institute of Physics, 1997, pp. 533-536.
- [95] D. D. Radford, G. R. Willmott and J. E. Field, „The effect of structure on failure front velocities in glass rods,“ in *Shock Compression of Condensed Matter*, Melville, American Institute of Physics, 2003, pp. 755-758.
- [96] S. M. Walley, "An Introduction to the Properties of Silica Glass in Ballistic Applications," *Strain* 23, pp. 470-500, 21 December 2014.
- [97] G. I. Kanel, S. V. Rasorenov and V. E. Fortov, „The failure waves and spallations in homogeneous brittle materials,“ *Shock Compression of Condensed Matter*, pp. 451-454, 1991.
- [98] N. S. Brar, S. J. Bless and Z. Rosenberg, „Impact-Induced Failure Waves in Glass Bars and Plates,“ *J. Appl. Phys.*, 59(26), pp. 3396-3398, 1991.
- [99] G. F. Raiser, „Plate Impact Response of Ceramics and Glasses,“ *Journal of Applied Physics*, 75, p. 3862, 1994.

- [100] D. L. Orphal, J. C. E. Anderson, T. Behner and D. W. Templeton, „Failure and penetration response of borosilicate glass during multiple short-rod impact,” *Int. J. Impact Engng* 36, pp. 1173-1181, 2009.
- [101] P. I. Zubkov, G. N. Kulipanov, L. A. Luk'yanchikov, L. A. Merzhievskii, K. A. Ten, V. M. Titov, B. P. Tolochko, M. G. Fedotov, M. R. Sharafutdinov and M. A. Sheromov, „Observation of Compression and Failure Waves in PMMA by Means of Synchrotron Radiation,” *Combustion, Explosion and Shock Waves*, Vol. 39, No. 2, pp. 240-242, 2003.
- [102] N. Bourne, Z. Rosenberg, Y. Mebar, T. Obara and J. Field, „A High-Speed Photographic Study of Fracture Wave Propagation in Glasses,” *Journal de Physique IV Colloque*, 04(C8), pp. C8-635-C8-640, 1994.
- [103] D. P. Dandekar and P. A. Beaulieu, „Failure wave under shock wave compression in soda-lime glass,” in *Metallurgical and Materials Applications of Shock-Wave and High-Strain-Rate Phenomena*, New York, Elsevier, 1995, pp. 211-218.
- [104] N. K. Bourne and J. C. F. Millett, „Shock-Induced Interfacial Failure in Glass Laminates,” *Proc. R. Soc. Lond. A*, 456, pp. 2673-2688, 2000.
- [105] N. K. Bourne, J. C. F. Millett and Z. Rosenberg, „The Shock Wave Response of a Filled Glass,” *Proc. R. Soc. Lond. A*, 452, pp. 1945-1951, 1996.
- [106] N. K. Bourne, Z. Rosenberg and J. E. Field, „High-Speed Photography of Compressive Failure Waves in Glasses,” *J. Appl. Phys.*, 78, pp. 3736-3739, 1995.
- [107] S. Chocron, D. D. Barnette, T. J. Holmquist, C. E. J. Anderson, R. P. Bigger and T. Z. Moore, „Damage Threshold of Borosilicate Glass under Plate Impact,” *J. Dynamic Behavior Mater.*, 2, pp. 167-180, 2016.
- [108] W. W. Chen, M. C. Hudspeth, B. Claus, N. D. Parab, J. T. Black, K. Fezzaa and S. N. Luo, „In situ damage assessment using synchrotron X-rays in materials loaded by a Hopkinson bar,” *Phil. Trans. R. Soc. A* 372, p. 20130191, 2014.
- [109] S. Luo, B. J. Jensen, D. E. Hooks, K. Fezzaa, K. J. Ramos, J. D. Yeager, K. Kwitkowski and T. Shimada, „Gas gun shock experiments with single-pulse X-ray phase contrast imaging and diffraction at the Advanced Photon Source,” *Rev. Sci. Instrum.* 83, p. 073903, 2012.
- [110] M. Hudspeth et. al., „High speed synchrotron X-ray phase contrast imaging of dynamic material response to split Hopkinson bar loading,” *Rev. Sci. Instrum.* 84, pp. 25102-25107, 2013.
- [111] D. D. Radford, W. G. Proud and J. E. Field, „The deviatoric response of three dense glasses under shock loading conditions,” *Shock Compression of Condensed Matter*, pp. 807-810, 2001.
- [112] C. S. Alexander, L. C. Chhabildas and D. W. Templeton, „The Hugoniot elastic limit of soda-lime glass,” *Shock Compression of Condensed Matter*, CP955, pp. 733-738, 2007.
- [113] C. Kettenbeil, PhD Thesis - Dynamic Strength of Silica Glasses at High Pressures and Strain Rates, California Institute of Technology, 2019.
- [114] T. J. Vogler, C. S. Alexander, T. F. Thornhill and W. D. Reinhart, „Pressure-shear experiments on granular materials,” Technical Report, Sandia National Laboratories, United States, 2011.
- [115] R. J. Clifton, M. Mello and N. S. Brar, „Effect of shear on failure waves in soda lime glass,” in *Shock compression of condensed matter*, vol 429, New York, AIP, 1998, pp. 521-524.
- [116] X. Nie, W. W. Chen, X. Sun and D. W. Templeton, „Dynamic Failure of Borosilicate Glass under Compression/Shear Loading Experiments,” *J. Am. Ceram. Soc.*, 90(8), pp. 2556-2562, 2007.

- [117] X. Nie, W. W. Chen and D. W. Templeton, „Dynamic Ring-on-Ring Equibiaxial Flexural Strength of Borosilicate Glass,” *Int. J. Appl. Ceram. Technol.*, 7(5), pp. 616-624, 2010.
- [118] H. Luo and W. Chen, „Dynamic Compressive Responses of Intact and Damaged AD995 Alumina,” *Int. J. Appl. Ceram. Technol.*, 1(3), pp. 254-260, 2004.
- [119] X. Nie and W. Chen, „Temperature and Confinement Pressure Effects on Dynamic Response of Damaged Borosilicate Glass,” *American Ceramic Society, 35th Int. Conf. on Advanced Ceramics and Composites*, 2011.
- [120] M. E. Grady and D. E. Kipp, „Dynamic rock fragmentation,” in *Fracture mechanics of rock*, London, Academic Press, 1987, pp. 429-475.
- [121] D. E. Grady and M. E. Kipp, „The growth of unstable thermoplastic shear with application to steady-wave shock compression,” *J Mech Phys Solids*, 35, pp. 95-119, 1987.
- [122] D. E. Grady and M. E. Kipp, „Continuum modelling of explosive fracture in oil shale,” *International Journal of Rock Mechanics and Mining Sciences & Geomechanics Abstracts*, 17(3), pp. 147-157, 1980.
- [123] C. S. Desai and H. J. Siriwardane, *Constitutive Laws for Engineering Materials with Emphasis on Geologic Materials*, Englewood Cliffs, New Jersey: Prentice-Hall, Inc., 1984.
- [124] P. A. Forquin, A. Arias and R. Zaera, „An Experimental Method of Measuring the Confined Compression Strength of High-Performance Concretes to Analyse Their Ballistic Behaviour,” *Journal de Physique IV*, 134, pp. 629-634, August 2006.
- [125] K. A. Dannemann, A. E. Nicholls, S. Chocron, J. D. Walker and C. E. J. Anderson, „Compression Testing and Response of SiC-N Ceramics: Intact, Damaged and Powder,” in *American Ceramic Society 29th International Conference on Advanced Ceramics and Composites*, Cocoa Beach, FL, 2005.
- [126] K. A. Dannemann, A. E. Nicholls, C. E. J. Anderson, S. Chocron and J. D. Walker, „Response and Characterization of Confined Borosilicate Glass: Intact and Damaged,” in *Advances in Ceramic Armor II: Ceramic Engineering and Science Proceedings*, Hoboken, NJ, Wiley, 2006, pp. 119-130.
- [127] K. A. Dannemann, S. Chocron, A. E. Nicholls and C. E. J. Anderson, „Compressive Damage Development in Confined Borosilicate Glass,” *Materials Science and Engineering A*, 478(1), pp. 340-350, 2008.
- [128] D. C. Drucker and W. Prager, „Soil Mechanics and Plastic Analysis or Limit Design,” *Q. Appl. Math.*, 10(2), pp. 157-175, 1952.
- [129] S. Timoshenko and J. N. Goodier, *Theory of Elasticity*, 1st ed., New York: McGraw-Hill, 1951.
- [130] A. A. Wereszczak, K. E. Johanns, T. P. Kirkland, C. E. Anderson, T. Behner, P. Patel and D. Templeton, „Strength and Contact Damage Responses in a Soda-Lime-Silicate and a Borosilicate Glass,” *Paper FP-05, 25th Army Science Conference, Orlando*, 27-30 November 2006.
- [131] D. A. Shockey, D. Bergmannshoff, D. R. Curran and J. W. Simons, „Physics of Glass Failure During Rod Penetration,” *Ceramic Engineering and Science Proceedings*, Vol. 29(6), pp. 23-32, 08 December 2008.
- [132] S. Chocron and C. E. J. Anderson, „Numerical Simulations of the Penetration of Glass Using Two Pressure-Dependent Constitutive Models,” in *Predictive Modeling of Dynamic Processes: A Tribute to Klaus Thoma*, Edited by S. Hiermaier, NY, Springer, 2009, pp. 167-187.
- [133] D. A. Shockey, J. W. Simons and D. R. Curran, „The Damage Mechanism Route to Better Armor Materials,” *Int. J. Appl. Ceram. Technol.*, 7(5), pp. 566-573, 2010.

- [134] T. J. Holmquist and G. R. Johnson, „Response of silicon carbide to high velocity impact,“ *J. Appl. Phys.*, *91*, pp. 5858-5866, 2002.
- [135] G. R. Johnson and T. Holmquist, „Response of Boron Carbide Subjected to Large Strains, High Strain Rates, and High Pressures,“ *Journal of Applied Physics*, *85(12)*, pp. 8060-8073, 1999.
- [136] A. M. Rajendran, „Modeling the Impact Behavior of AD85 Ceramic under Multiaxial Loading,“ *Int. J. Impact Eng.* *15(6)*, pp. 749-768, 1994.
- [137] S. Satapathy and S. Bless, „Cavity Expansion Resistance of Brittle Materials Obeying a Two-Curve Pressure-Shear Behavior,“ *J. Appl. Phys.*, *88(7)*, pp. 4004-4012, 2000.
- [138] C. H. Simha, S. J. Bless and A. Bedford, „Computational Modeling of the Penetration Response of a High-Purity Ceramic,“ *Int. J. Impact Eng.*, *27(1)*, pp. 65-86, 2002.
- [139] C. E. J. Anderson, D. L. Orphal, T. Behner and D. W. Templeton, „Failure and Penetration Response of Borosilicate Glass During Short-rod Impact,“ *Int. J. Impact Engng.*, *36(6)*, pp. 789-798, 2009.
- [140] C. E. J. Anderson, R. P. Bigger and C. E. Weiss, „Crack and Damage Velocities in Ballistic Experiments,“ *Int J of Applied Glass Science*, *5(4)*, pp. 374-383, 6 October 2014.
- [141] T. J. Holmquist, G. R. Johnson and C. A. Gerlach, „An improved computational constitutive model for glass,“ *Phil. Trans. R. Soc. A.*, *375*, p. 20160182, 2017.
- [142] T. J. Holmquist and A. A. Wereszczak, „The Internal Tensile Strength of a Borosilicate Glass Determined from Laser Shock Experiments and Computational Analysis,“ *Int. Journal of Applied Glass Science*, *5(4)*, pp. 345-352, December 2014.
- [143] S. J. Hiermaier, *Structures Under Crash and Impact*, Freiburg: Springer Verlag, ISBN 978-0-387-73863-5, 2008.
- [144] P. Ludwik, *Elemente der technologischen Mechanik*, Berlin: Springer, 1909.
- [145] T. C. Doyle and J. L. Ericksen, „Nonlinear Elasticity,“ *Advances in Applied Mechanics*, *4*, pp. 53-115, 1956.
- [146] B. R. Seth, „Generalized Strain Measure with Application to Physical Problems,“ in *Reiner M., Abir D. (eds) Second Order Effects in Elasticity, Plasticity and Fluid Dynamics*, Oxford, Pergamon Press, 1964.
- [147] H. R., „Constitutive Inequalities for Isotropic Elastic Solids Under Finite Strain,“ *Proceedings of the Royal Society of London*, *A314*, pp. 457-472, 1970.
- [148] Z. P. Bažant and L. Cedolin, *Stability of Structures*, New York and Oxford: Oxford University Press, 1991.
- [149] B. P. Haigh, „Elastic Limit of a Ductile Metal,“ *Engineering*, *109*, pp. 158-160, 1920.
- [150] H. M. Westergaard, „On the Resistance of Ductile Materials to Combined Stresses in Two or Three Directions Perpendicular to one Another,“ *Journal Franklin Institute*, *189*, pp. 627-640, 1920.
- [151] R. v. Mises, „Mechanik der festen Körper im plastisch deformablen Zustand,“ *Nachr. Königl. Ges. Wiss. Göttingen, Math.-phys. Kl.*, pp. 582-592, 1913.
- [152] H. Tresca, „Mémoires sur l'écoulement des corps solides soumis à des fortes pressions,“ *C. R. Acad. Sci. Paris*, *59*, pp. 754-758, 1864.

- [153] G. R. Johnson and W. H. Cook, „A Constitutive Model and Data for Metals Subjected to Large Strains, High Strain Rates and High Temperatures,“ in *Proceedings to the Seventh International Symposium on Ballistics*, Den Haag, 1983.
- [154] D. Gross and T. Seelig, *Fracture Mechanics*, 3rd ed., Springer, 2018.
- [155] D. Broek, *Elementary Engineering Fracture Mechanics*, Kluwer Academic Publications, 1986.
- [156] D. R. Curran, L. Seaman and D. A. Shockey, „Dynamic Failure of Solids,“ *Physics Reports*, 147, pp. 253-388, 1987.
- [157] S. Knell, A numerical modeling approach for the transient response of solids at the mesoscale, PhD Thesis, 2011.
- [158] N. Durr, Mesoscale modeling of dynamic fracture and shock compression in quartzite and sandstone, PhD Thesis, 2017.
- [159] D. Krajcinovic, „Damage Mechanics,“ *Mechanics of Materials*, 8, pp. 117-197, 1989.
- [160] J. Lemaitre, *A Course on Damage Mechanics*, Berlin: Springer, 1992.
- [161] O. Allix and F. Hild, *Continuum Damage Mechanics of Materials and Structures*, Amsterdam: Elsevier, 2002.
- [162] L. Kachanov, „Time of the Rupture Process Under Creep Conditions,“ *Izv. Akad. Nauk SSSR*, 8, pp. 26-31, 1958.
- [163] Y. N. Rabatnov, „On the Equation of State for Creep,“ in *Koiter, W. T. (ed.) Progress in Applied Mechanics, Prager Anniversary Volume*, New York, MacMillan, 1963, pp. 307-315.
- [164] J. Lemaitre, „Evaluation of Dissipation and Damage in Metal Submitted to Dynamic Loading,“ in *Proceedings of the First International Conference on the Mechanical Behaviour of Materials*, Kyoto, Japan, 1971.
- [165] M. A. Meyers, *Dynamic Behavior of Materials*, New York, USA: Wiley, 1994.
- [166] H. A. Bethe, „On the Theory of Shock Waves for an Arbitrary Equation of State,“ in *Johnson J., Cheret R. (eds.) Classic Papers in Shock Compression Science*, New York, Springer, 1942.
- [167] S. Thunborg, G. E. Ingram and R. A. Graham, „Compressed Gas Gun for Controlled Planar Impacts Over a Wide Velocity Range,“ *Review of Scientific Instruments*, 35(1), pp. 11-14, 1964.
- [168] L. M. Barker and C. D. Lundergan, „Dynamic Response of Aluminum,“ *Journal of Applied Physics*, 35(4), pp. 1203-1212, 1964.
- [169] L. C. Chhabildas and J. R. Asay, „Risetime measurements of shock transitions in aluminum, copper, and steel,“ *J. Appl. Phys.* 50(4), pp. 2749-2756, 1979.
- [170] R. G. McQueen and S. P. Marsh, „Equation of State for Nineteen Metallic Elements from Shock-Wave Measurements to Two Megabars,“ *Journal of Applied Physics*, 31(7), pp. 1253-1269, 1960.
- [171] A. H. Jones, W. M. Isbell and C. J. Maiden, „Measurement of the Very-High-Pressure Properties of Materials using a Light-Gas Gun,“ *Journal of Applied Physics*, 37(9), pp. 3493-3499, 1966.
- [172] W. D. Crozier and W. Hume, „High-Velocity, Light-Gas Gun,“ *Journal of Applied Physics*, 28(8), pp. 892-894, 1957.

- [173] G. R. Fowles, G. E. Duvall, J. Asay, P. Bellamy, F. Feistmann, D. Grady, T. Michaels and R. Mitchell, „Gas Gun for Impact Studies,“ *Review of Scientific Instruments*, 41(7), pp. 984-996, 1970.
- [174] I. Rohr, H. Nahme and K. Thoma, „Material characterization and constitutive modelling of ductile high strength steel for a wide range of strain rates,“ *Int. J. Imp. Engineering*, 31, pp. 401-433, 2005.
- [175] H. Nahme and M. J. Worswick, „Dynamic properties and spall plane formation of brass,“ in *Proc. Eurodymat*, pp. 707-712, Oxford, UK, 1994.
- [176] J. M. Walsh and M. H. Rice, „Dynamic Compression of Liquids from Measurements on Strong Shock Waves,“ *J. Chem. Phys.*, 26, p. p. 815, 1957.
- [177] M. H. Rice, R. G. McQueen and J. M. Walsh, „Compression of Solids by Strong Shock Waves,“ *Solid State Phys.*, 6, pp. 1-63, 1958.
- [178] J. R. Asay and M. Shahinpoor, *High-Pressure Shock Compression of Solids*, 1993.
- [179] R. Menikoff, „Empirical Equations of State for Solids,“ in *Horie Y. (ed.) Shock Wave Science and Technology Reference Library, Vol. 2, Solids I*, Berlin, Heidelberg, Springer, 2007.
- [180] J. H. Tillotson, „Metallic Equations of State for Hypervelocity Impact,“ General Atomic Division of General Dynamics Report GA-3216, San Diego, CA, 1962.
- [181] W. Herrmann, „Constitutive Equation for the Dynamic Compaction of Ductile Porous Materials,“ *Journal of Applied Physics*, 40, pp. 2490-2499, 1969.
- [182] E. Grüneisen, „Theorie des festen Zustandes einatomiger Elemente,“ *Analen der Physik*, 39, pp. 257-306, 1912.
- [183] E. Grüneisen, „Zustand des festen Körpers,“ in *Greiger H., Scheel K. (eds.) Handbuch der Physik, Vol. 10*, Berlin, Springer, 1926, pp. 1-59.
- [184] J. C. Slater, *Introduction to Chemical Physics*, New York: McGraw-Hill, 1939.
- [185] C. E. J. Anderson, „An overview of the theory of hydrocodes,“ *Int. J. Impact Engng*, Vol. 5, pp. 33-59, 1987.
- [186] M. L. Wilkins, „Fundamental Methods in Hydrodynamics,“ in *Adler B., et al. (eds.) Methods in Computational Physics, Vol. 3: 211*, New York, Academic Press, 1964.
- [187] W. F. Noh, „Fundamental Methods in Hydrodynamics,“ in *Adler B. et al. (eds.) Methods in Computational Physics, Vol 3: 117*, New York, Academic Press, 1964.
- [188] D. J. Benson, „Computational Methods in Lagrangian and Eulerian Hydrocodes,“ *Computer Methods in Applied Mechanics and Engineering*, 99, pp. 235-394, 1992.
- [189] K. J. Bathe, *Finite Element Procedures*, Englewood Cliffs: Prentice Hall, 1996.
- [190] T. J. R. Hughes, *Finite Element Method - Linear Static and Dynamic Finite Element Analysis*, Englewood Cliffs: Prentice-Hall, 1987.
- [191] O. C. Zienkiewicz, R. L. Taylor and J. Z. Zhu, *The Finite Element Method: Its Basis and Fundamentals*, Amsterdam: Butterworth-Heinemann, 2005.
- [192] F. B. Hildebrand, *Advanced Calculus for Applications*, Englewood Cliffs: Prentice-Hall, 1962.

- [193] R. Courant, K. O. Friedrichs and H. Lewy, „Über die partiellen Differenzgleichungen der mathematischen Physik,“ *Mathematische Annalen*, 100, pp. 32-74, 1928.
- [194] R. Courant, K. O. Friedrichs and H. Lewy, „On Partial Difference Equations of Mathematical Physics,“ *IBM Journal of Research Developments*, 11, pp. 215-234, 1967.
- [195] AUTODYN, „Interactive Non-Linear Dynamic Analysis Software Theory Manual,“ Century Dynamics, 1998.
- [196] M. Grujicic, W. C. Bell, P. S. Glomski, B. Pandurangan, et al., „Multi-Length Scale Modeling of High-Pressure-Induced Phase Transformations in Soda-Lime Glass,“ *Journal of Materials Engineering and Performance*, 20(7), pp. 1144-1156, 2010.
- [197] M. Grujicic, W. C. Bell, B. Pandurangan, B. A. Cheeseman, et al., „The effect of high-pressure densification on ballistic-penetration resistance of a soda-lime glass,“ *Proc Inst Mech Eng, Vol 225(4)*, pp. 298-315, 2011.
- [198] E. Holmström, J. Samela and K. Nordlund, „Atomistic simulations of fracture in silica glass through hypervelocity impact,“ *Europhysics Letters Association*, 96(1), September 2011.
- [199] W. Hu, Y. Wang, J. Yu, C.-F. Yen and F. Bobaru, „Impact damage on a thin glass plate with a thin polycarbonate backing,“ *Int. J. of Impact Engng*, 62, pp. 152-165, 2013.
- [200] L. V. Woodcock, C. A. Angell and P. Cheeseman, „Molecular dynamics studies of the vitreous state: Simple ionic systems and silica,“ *J. Chem. Phys.*, 65, pp. 1565-1577, 1976.
- [201] R. G. D. Valle and E. Venuti, „High-pressure densification of silica glass: a molecular-dynamics simulation,“ *Phys. Rev. B*, 54(6), pp. 3809-3816, 1996.
- [202] K. Trachenko and M. T. Dove, „Densification of silica glass under pressure,“ *J. Phys. Condens. Matter*, 14, pp. 7449-7459, 2002.
- [203] Y. Liang, C. R. Miranda and S. Scandolo, „Mechanical strength and coordinate defects in compressed silica glass: Molecular dynamics simulations,“ *Phys. Rev. B*, 75, p. 024205, 2007.
- [204] R. G. Barsoum, „Phase Transformations in Glass Associated with Hyper-Velocity Impact and Implications in Constitutive Modeling,“ *Proceedings of the 29th International Symposium on Ballistics*, 9-13 May 2016.
- [205] I. Nurhuda, „Simulation of crack propagation in glass panels using finite element analysis,“ *Australian Journal of Structural Engineering*, 12, pp. 225-236, 2012.
- [206] J. Pelfrene, S. Dam, R. Sevenois, F. Gilabert and W. Van Paepegem, „Fracture Simulation of Structural Glass by Element Deletion in Explicit FEM,“ in *Proceedings of the Conference on Architectural and Structural Applications of Glass - Challenging Glass 5*, Ghent University, Belgium, 2016.
- [207] G. T. Camacho and M. Ortiz, „Computational modeling of impact damage in brittle materials,“ *Int. J. Solids Struct.*, 33(20-22), pp. 2899-2938, 1996.
- [208] D. Ngo and A. C. Scordelis, „Finite element analysis of reinforced concrete beams,“ *Journal of the American Concrete Institute*, 64, pp. 152-163, 1967.
- [209] Y. R. Rashid, „Analysis of reinforced concrete pressure vessels,“ *Nuclear Engineering and Design*, 7, pp. 334-344, 1968.

- [210] M. Grujicic, B. Pandurangan, W. C. Bell, N. Coutris, B. A. Cheeseman, C. Fountzoulas and P. Patel, „An Improved Mechanical Material Model for Ballistic Soda-Lime Glass,” *J. Mater. Eng. Perform.*, **18**(8), pp. 1012-1028, 2009.
- [211] C. Denoual and F. Hild, „Dynamic fragmentation of brittle solids: a multi-scale model,” *Eur. J. Mech. Solids A*, **21**, pp. 105-120, 2002.
- [212] M. Yazdchi, S. Valliappan and W. Zhang, „A continuum model for dynamic damage evolution of anisotropic brittle materials,” *Int. J. Numer. Meth. Eng.*, **39**, pp. 1555-1583, 1996.
- [213] G. R. Johnson and T. J. Holmquist, „An Improved Computational Constitutive Model for Brittle Materials,” *High Pressure Sci. Technol.*, pp. 981-984, 1994.
- [214] D. E. Grady, „Impact Breach and Fragmentation of Glass Plate,” *Int. J. Impact Engng*, **38**(6), pp. 446-450, June 2011.
- [215] M. Grujicic, B. Pandurangan and N. Coutris, „A Computational Investigation of the Multi-Hit Ballistic-Protection Performance of Laminated Transparent-armor Systems,” *Journal of Materials Engineering and Performance*, **21**(6), pp. 837-848, June 2012.
- [216] R. C. Becker, „A Glass Model Capturing High-Rate Fracture Observations,” *Tech. Rep. ARLTR-6086*, August 2012.
- [217] A. Brady and B. Schuster, „A Computational Study of the ARL Glass Model and its Predictions of Ballistic Penetration and Fracture Conoid Development,” *Proceedings of the 28th International Symposium on Ballistics*, 22-26 September 2014.
- [218] G. R. Johnson and T. J. Holmquist, „A computational constitutive model for brittle materials subjected to large strains, high strain rates, and high pressures,” in Meyers M. A., Murr L. E., Staudhammer K. P. (eds.), *Shock Waves and High-Strain Rate Phenomena in Materials*, New York, Marcel Dekker, 1992, pp. 1075-1081.
- [219] W.-F. Chen and D. J. Han, *Plasticity for Structural Engineers*, J. Ross Publishing, 2007.
- [220] G. R. Johnson, R. A. Stryk, T. J. Holmquist and S. R. Beissel, „Numerical algorithms in a Lagrangian hydrocode,” Report No. WL-TR-1997-7039, 1997.
- [221] W. D. Reinhart, L. C. Chhabildas and T. J. Vogler, „Investigating Phase Transitions and Strength in Single-Crystal Sapphire Using Shock-Reshock Loading Techniques,” *Int. Journal of Impact Engineering*, **33**, pp. 655-669, 2006.
- [222] G. R. Johnson and W. H. Cook, „Fracture Characteristics of Three Metals Subjected to Various Strains, Strain Rates, Temperatures and Pressures,” *Engineering Fracture Mechanics*, Vol. 21, No. 1, pp. 31-48, 1985.
- [223] L. M. Barker and R. E. Hollenbach, „Laser interferometer for measuring high velocities of any reflecting surface,” *Journal of Applied Physics* **43**, pp. 4669-4675, 1972.
- [224] L. M. Barker and K. W. Schuler, „Correction to the velocity-per-fringe relationship for the VISAR interferometer,” *Journal of Applied Physics* **45**, pp. 3692-3693, 1974.
- [225] W. F. Hemsing, „Velocity sensing interferometer (VISAR) modification,” *Review of Scientific Instruments* **50**, pp. 73-78, 1979.
- [226] L. M. Barker, „The accuracy of VISAR instrumentation,” in *AIP Conference Proceedings 429*, 1997.

- [227] O. T. Strand, L. V. Berzins, D. R. Goosman, W. W. Kuhlow, P. D. Sargis and T. L. Whitworth, „Velocimetry using heterodyne techniques,“ in *Proceedings of the Society of Photo-Optical Instrumentation Engineers (SPIE), 26th International Congress on High Speed Photography and Photonics*, 2005.
- [228] O. T. Strand, D. R. Goosman, C. Martinez, T. L. Whitworth and W. W. Kuhlow, „Compact system for high-speed velocimetry using heterodyne techniques,“ *Review of Scientific Instruments* 77, 083108, 2006.
- [229] A. Saettler, G. Popko, S. Nau and R. Heiser, „Investigation of the projectile movement inside a gun tube with a photonic doppler velocimeter (PDV),“ in *Proceedings of the 27th international symposium on ballistics*, Freiburg, Germany, 2013.
- [230] M. Eckerle and G. Popko, „Aufbau und Charakterisierung eines "Photonic Doppler Velocimeters",“ Internal Report E 05/11, Efringen-Kirchen, Germany, 2011.
- [231] J. A. Zukas, *High velocity impact dynamics*, New York: John Wiley & Sons, 1990.
- [232] M. Swain and J. Hagan, „Indentation plasticity and the ensuing fracture of glass,“ *Journal of Applied Physics* 9, p. 2207, 1976.
- [233] Y. Horie, *Shock Wave Science and Technology Reference Library, Volume 2*, Springer, 2007.
- [234] D. E. Grady, "The spall strength of condensed matter," *J. Mech. Phys. Solids*, vol. 36, pp. 353-384, 1988.
- [235] J. A. Seibert and J. M. Boone, „X-ray imaging physics for nuclear medicine technologists, part 2: x-ray interactions and image formation,“ *J Nucl Med Technol*, 33, pp. 3-18, 2005.
- [236] J. Hsieh, *Computed tomography: Principles, design, artifacts, and recent advances*, Bellingham, Wash., Hoboken, N.J.: SPIE Press; John Wiley & Sons, 2009.
- [237] R. Schulze, U. Heil, D. Gross, D. D. Bruellmann, E. Dranischnikow, U. Schwanecke and E. Schoemer, „Artefacts in CBCT: a review,“ *Dentomaxillofacial Radiology, Jg. 40, Nr. 5*, pp. 265-273, 2011.
- [238] T. M. Buzug, *Computed Tomography - From Photon Statistics to Modern Cone-Beam CT*, Berlin: Springer, 2008.
- [239] L. W. Goldman, „Principles of CT and CT technology,“ *J Nucl Med Technol*, 35(3), pp. 115-28; quiz 129-30, 2007.
- [240] L. W. Goldman, „Principles of CT: Radiation Dose and Image Quality,“ *J. Nucl. Med. Technol.*, vol.35, no.4, pp. 213-225, 2007.
- [241] Z. F., „Phase contrast, a new method for the microscopic observation of transparent objects,“ *Physica* 9, pp. 686-698, 1942.
- [242] T. Gureyev and S. Wilkins, „On X-ray phase imaging with a point source,“ *J. Opt. Soc. Am. A* 15, pp. 579-585, 1998.
- [243] M. Stampanoni, A. Groso, A. Isenegger, G. Mikuljan, Q. Chen, A. Bertrand, S. Henein, R. Betemps, U. Frommherz, P. Bohler, D. Meister, M. Lange and R. Abela, „Trends in synchrotron-based tomographic imaging: the SLS experience,“ *Developments in X-Ray Tomography V, Proceedings of the Society of Photo-Optical Instrumentation Engineers (Spie)*, 6318, pp. U199-U212, 2006.
- [244] M. Böge, „First operation of the Swiss Light Source,“ *Proc. EPAC 2002*, pp. 39-43, 2002.

- [245] A. Groso, R. Abela and M. Stampanoni, „Implementation of a fast method for high resolution phase contrast tomography,“ *Optics Express*, 14, pp. 8103-8110, 2006.
- [246] D. Paganin, S. C. Mayo, T. E. Gureyev, P. R. Miller and S. W. Wilkins, „Simultaneous phase and amplitude extraction from a single defocused image of a homogeneous object,“ *Journal of Microscopy*, 206, pp. 33-40, 2002.
- [247] S. A. McDonald, F. Marone, C. Hintermüller, G. Mikuljan, C. David, F. Pfeiffer and M. Stampanoni, „Advanced phase-contrast imaging using a grating interferometer,“ *J. Synchrotron Rad.*, 16, pp. 562-572, 2009.
- [248] F. Marone and M. Stampanoni, „Regridding reconstruction algorithm for real time tomographic imaging,“ *J. Synchrotron Rad.*, 19, pp. 1029-1037, 2012.
- [249] F. Marone, A. Studer, H. Billich, L. Sala and M. Stampanoni, „Towards on-the-fly data post-processing for real-time tomographic imaging at TOMCAT,“ *Advanced Structural and Chemical Imaging*, 3, p. 1, 2017.
- [250] „www.psi.ch,“ [Online]. Available: <https://www.psi.ch/de/about/geschichte-des-psi>. [access on 16th November 2020].
- [251] A. Sheppard, „Australian National University - Department of applied mathematics,“ Australian National University, 15. January 2019. [Online]. Available: <https://physics.anu.edu.au/appmaths/capabilities/mango.php>. [access on 30th June 2020].
- [252] A. Sheppard, R. Sok and H. Averdunk, „Techniques for image enhancement and segmentation of tomographic images of porous materials,“ *Physica A: Statistical mechanics and its applications*, 339, pp. 145-151, 2004.
- [253] C. Duff-Tytler, „Fujitsu,“ Fujitsu Australia Limited, 31. July 2013. [Online]. Available: <https://www.fujitsu.com/au/about/resources/news/press-releases/2013/20130731-01.html>. [access on 29th June 2020].
- [254] K. R. Mecke, „Additivity, Convexity, and Beyond: Applications of Minkowski Functionals in Statistical Physics,“ *Lecture Notes in Physics*, 554, pp. 111-184, 1 November 2008.
- [255] R. T. Armstrong, J. E. McClure, V. Robins, Z. Liu, C. H. Arns, S. Schlüter and S. Berg, „Porous Media Characterization Using Minkowski Functionals: Theories, Applications and Future Directions,“ *Transport in Porous Media*, 130, pp. 305-335, 2019.
- [256] E. AG, „Strain Gauge Amplifier - User Manual,“ Switzerland, Niederrohrdorf.
- [257] A. K. Srivastava and P. C. Gope, *Strength of Materials*, Prentice-Hall Of India Pvt. Limited, 2007.
- [258] W. Toqueboeuf, B. Mortaigne and C. Cottenot, „Dynamic Behaviour of Polycarbonate/Polyurethane Multilayer for Transparent Armor,“ *J. Phys IV Colloque*, 7(C3), pp. 499-504, 1997.
- [259] G. Design, „Granta Design sample materials data provided by ANSYS Workbench version 19.1,“ 2018.
- [260] M. Richards, R. Clegg and S. Howlett, „Ballistic Performance Assessment of Glass Laminates Through Experimental and Numerical Investigation,“ in *18th International Symposium and Exhibition on Ballistics*, San Antonio, Texas, USA, 1999.
- [261] T. G. Talladay and D. W. Templeton, „A computational comparison of high strain rate strength and failure models for glass,“ in *Proceedings of the 27th Int Symp on Ballistics*, Freiburg, Germany, 2013.

- [262] E. A. Ferriter, I. A. McCulloh and W. deRosset, „Techniques used to estimate limit velocity in ballistics testing with small sample size,“ in *Proceedings of the 13th Annual U.S. Army research Laboratory/U.S. Military Academy Technical Symposium, 72-95*, NY, 2005.
- [263] J. W. Forbes, *Shock Wave Compression of Condensed Matter*, Berlin, Heidelberg: Springer-Verlag, 2012.
- [264] D. A. Matuska, „HULL Users Manual,“ *AFATL-TR-84-59*, June 1984.

9 Appendix

9.1 Transformation equation for the shock wave velocity

The Rankine-Hugoniot equations are usually derived in the laboratory frame of reference, also referred to as the Eulerian coordinate system. Especially for the evaluation of PPI test data, it is, however, more convenient to do the analysis in Lagrangian coordinates. Here, the coordinate system is tied to material instead of spatial points.

This section was already pre-published by the author in [A1]. Equations are derived, which can be used to transform the shock wave equations from one coordinate system to the other. More detailed information can be found in [263](p. 329 et seq).

The starting point is the conservation of mass in a rectangular cuboid of area A , initial length $\Delta h = \Delta x = x_0$ and initial density ρ_0 at time t . After a time interval Δt , the cuboid gets compressed lengthwise while keeping its cross-sectional area A . In the Lagrangian frame of reference, this compression has no influence on the density and length, since the coordinate system is deforming together with the mass points. Since the total mass has to be the same in both coordinate systems, this gives equation

$$A \cdot \rho_0 \cdot \Delta h = A \cdot \rho(t + \Delta t) \cdot \Delta x(t + \Delta t) \quad 9.1$$

which can be transcribed to

$$\frac{\partial x}{\partial h} = \frac{\rho_0}{\rho} \quad 9.2$$

A relationship for steady shock waves can be obtained using the total time derivative of $x(h, t)$:

$$dx = \left(\frac{\partial x}{\partial t} \right)_h dt + \left(\frac{\partial x}{\partial h} \right)_t dh \quad 9.3$$

Respectively:

$$\frac{dx}{dt} = \left(\frac{\partial x}{\partial t} \right)_h + \left(\frac{\partial x}{\partial h} \right)_t \frac{dh}{dt} \quad 9.4$$

In this equation, $\frac{dx}{dt} = \tilde{U}_s$ denotes the shock wave velocity in the Eulerian frame of reference, while $\frac{dh}{dt} = U_s$ and $\left(\frac{\partial x}{\partial h} \right)_t = u_p$ denote the shock wave velocity and particle velocity in the Lagrangian frame of reference.

Combining equation 9.2 and equation 9.4 gives an equation that can be used to transform the shock wave velocity from one coordinate system to the other:

$$\tilde{U}_{s,i+1} = u_{p,i} + \frac{\rho_0}{\rho_i} U_{s,i+1} \quad 9.5$$

Here, the states in front of the shock wave are denoted by the index i and the states behind the shock wave by the index $(i + 1)$.

9.2 Material models used in Autodyn

Table 9.1: Improved SLG model of the present work.

Equation of State	Polynomial
Reference Density	2.53 g/cm ³
Bulk Modulus $K1$	42.479 GPa
Parameter $K2$	-24.649 GPa
Parameter $K3$	51.782 GPa
Expansion Parameter $T1$	42.479 GPa
Hugoniot Elastic Limit	5 GPa
P_{HEL}	2.59470 GPa
σ_{HEL}	3.60796 GPa
Erosion	Geometric Strain
Erosion Strain	1.0
Type of Geometric Strain	Instantaneous

Strength	Johnson-Holmquist
Shear Modulus	30.4 GPa
Model Type	Continuous (JH2)
Intact Strength Constant A	0.94525
Intact Strength Exponent N	0.52471
Strain Rate Constant C	0.003
B ($D = 0.25$)	0.71438
M ($D = 0.25$)	0.47539
B ($D = 0.5$)	0.70185
M ($D = 0.5$)	0.58138
B ($D = 1.0$)	0.71543
M ($D = 1.0$)	0.80122
Max. Fracture Strength Ratio	0.582
Failure	Johnson Holmquist
Hydrostatic Tensile Limit	-35 MPa
Model Type	Continuous (JH2)
Damage Constant, $D1$	0.4
Damage Constant, $D2$	0.4
Bulking Constant, Beta	1.0
Damage Type	Gradual (JH2)
Tensile Failure	Hydro (Pmin)

Table 9.2: Floatglass by Holmquist et al. [60], modifications by Richards et al. [260] are added in red.

Equation of State	Polynomial
Reference Density	2.53 g/cm ³
Bulk Modulus $K1$	45.4 GPa
Parameter $K2$	-138 GPa
Parameter $K3$	290 GPa
Parameter $B0$	0
Parameter $B1$	0
Parameter $T1$	45.4 GPa
Parameter $T2$	0
Reference Temperature	295.15 K
Specific Heat	0
Thermal Conductivity	0
Erosion	Geometric Strain
Erosion Strain	1.0
Type of Geometric Strain	Instantaneous

Strength	Johnson-Holmquist
Shear Modulus	30.4 GPa
Model Type	Continuous (JH2)
Hugoniot Elastic Limit	5.95 GPa
Intact Strength Constant A	0.93
Intact Strength Exponent N	0.77
Strain Rate Constant C	0.003
Fractured Strength Constant B	0.2 (0.35)
Fractured Strength Exponent M	1.0 (0.4)
Max. Fracture Strength Ratio	0.5
Failure	Johnson Holmquist
Hydrostatic Tensile Limit	-150 MPa (-35 MPa)
Model Type	Continuous (JH2)
Damage Constant, $D1$	0.043 (0.053)
Damage Constant, $D2$	0.85
Bulking Constant, Beta	1.0
Damage Type	Gradual (JH2)
Tensile Failure	Hydro (Pmin)

Table 9.3: Steel 4340 by Johnson et al. [222].

Equation of State	Linear
Reference Density	7.83 g/cm ³
Bulk Modulus	159 GPa
Reference Temperature	300 K
Specific Heat	477 J/kgK
Thermal Conductivity	0
Strength	
Johnson Cook	
Shear Modulus	77 GPa
Yield Stress	792 MPa
Hardening Constant	510 MPa
Hardening Exponent	0.26
Strain Rate Constant	0.014
Thermal Softening Exp.	1.03
Melting Temperature	1793 K
Ref. Strain Rate	1 /s
Strain Rate Correction	1st Order
Failure	
Johnson Cook	
D1	0.05
D2	3.44
D3	-2.12
D4	0.002
D5	0.61
Erosion	
Geometric Strain	
Erosion Strain	1.5

Table 9.4: Copper adopted from Autodyn® database [264].

Equation of State	Linear
Reference Density	0.95 g/cm ³
Bulk Modulus	1.7 GPa
Reference Temperature	300 K
Strength	
Piecewise JC	
Shear Modulus	46.4 GPa
Yield Stress	120 MPa
Eff. Pl. Strain 1	0.3
Eff. Pl. Strain 2	1.0e+20
Yield Stress 1	450 MPa
Yield Stress 2	450 MPa
Erosion	
Geometric Strain	
Erosion Strain	1.5

Table 9.5: Polyurethane adopted from Autodyn® database [258] and modified.

Equation of State	Linear
Reference Density	0.95 g/cm ³
Bulk Modulus	1.7 GPa
Reference Temperature	300 K
Strength	Piecewise JC
Shear Modulus	102 MPa
Yield Stress	0.2 MPa
Eff. Pl. Strain 1	0.02
Eff. Pl. Strain 2	0.04
Eff. Pl. Strain 3	0.1
Eff. Pl. Strain 4	0.2
Eff. Pl. Strain 5	0.5
Eff. Pl. Strain 6	0.8
Eff. Pl. Strain 7	0.9
Eff. Pl. Strain 8	1.2
Yield Stress 1	0.9 MPa
Yield Stress 2	2.0 MPa
Yield Stress 3	4.0 MPa
Yield Stress 4	5.0 MPa
Yield Stress 5	10 MPa
Yield Stress 6	22 MPa
Yield Stress 7	30 MPa
Yield Stress 8	60 MPa
Failure	Principal Stress
Tensile Failure Stress	34.5 MPa
Erosion	Geometric Strain
Erosion Strain	4.0

Table 9.6: Tungsten carbide projectile core.

Equation of State	Rigid
Reference Density	14.34 g/cm ³

9.3 Additional Lagrange diagrams

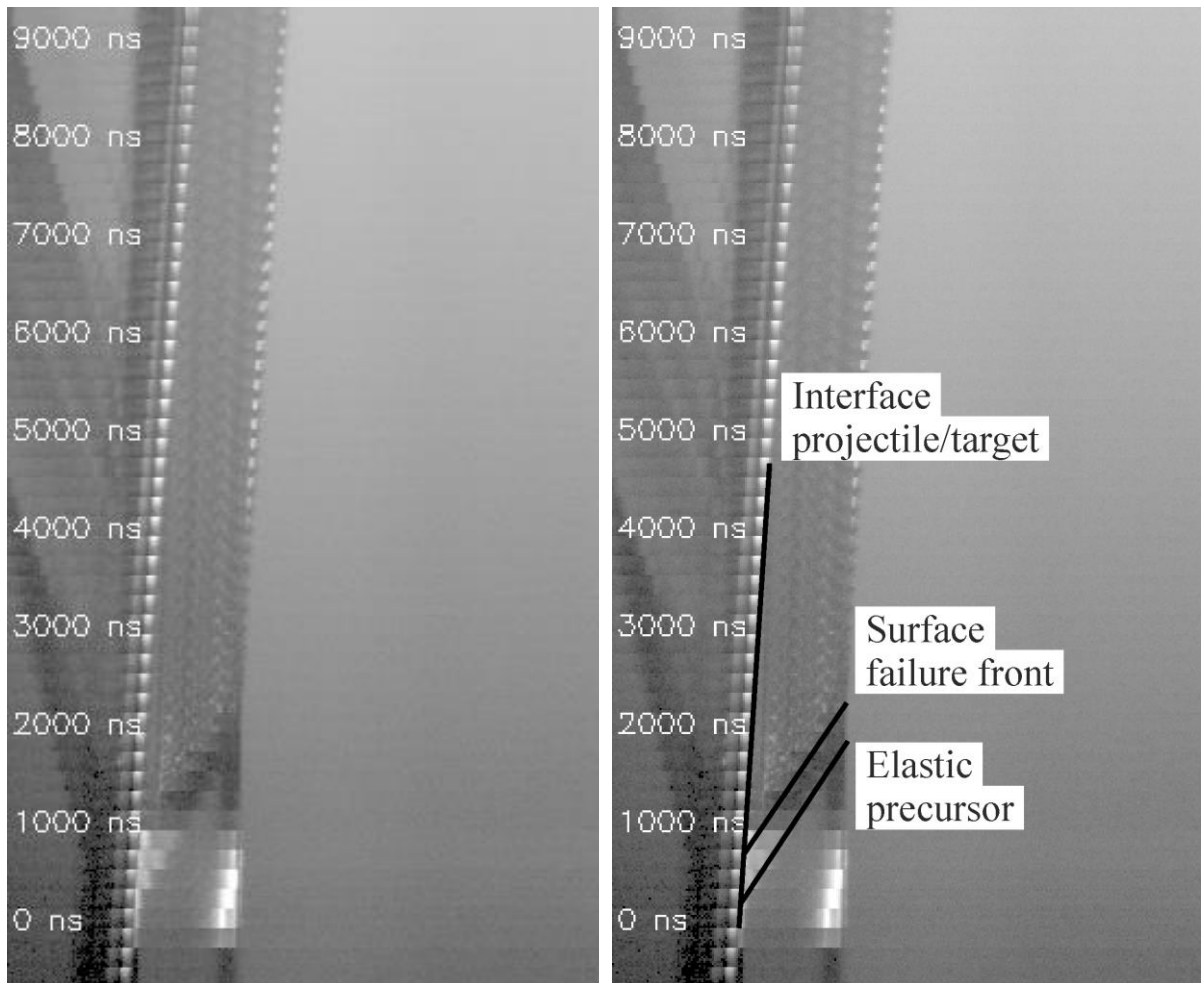


Figure 9.1: Streak analysis for test no. 4146: 2 mm al vs. 7.85 mm SLG, $v_p = 493$ m/s [A1].

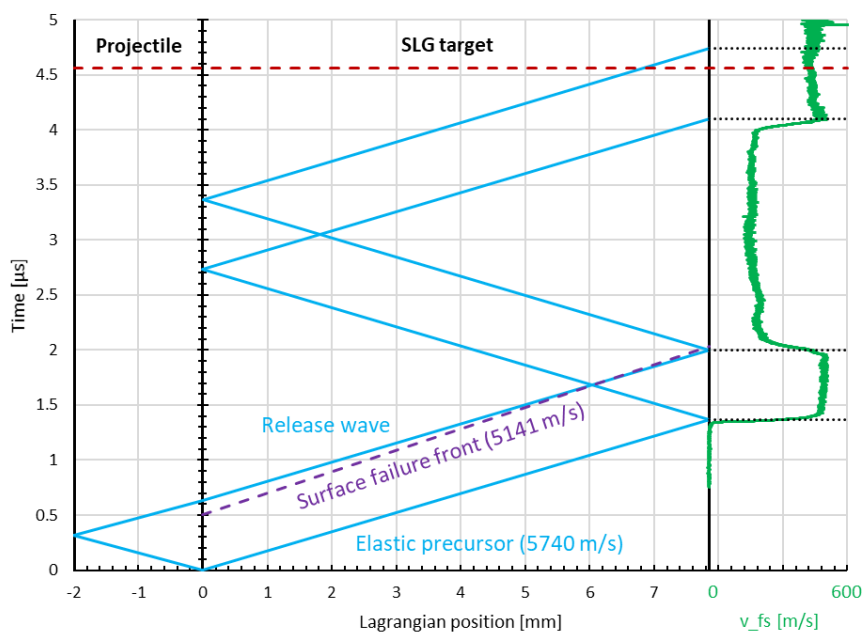


Figure 9.2: Lagrangian diagram for test no. 4146: 2 mm al vs. 7.85 mm SLG, $v_p = 493$ m/s [A1].

9.4 Loading path analysis diagrams for each PPI test

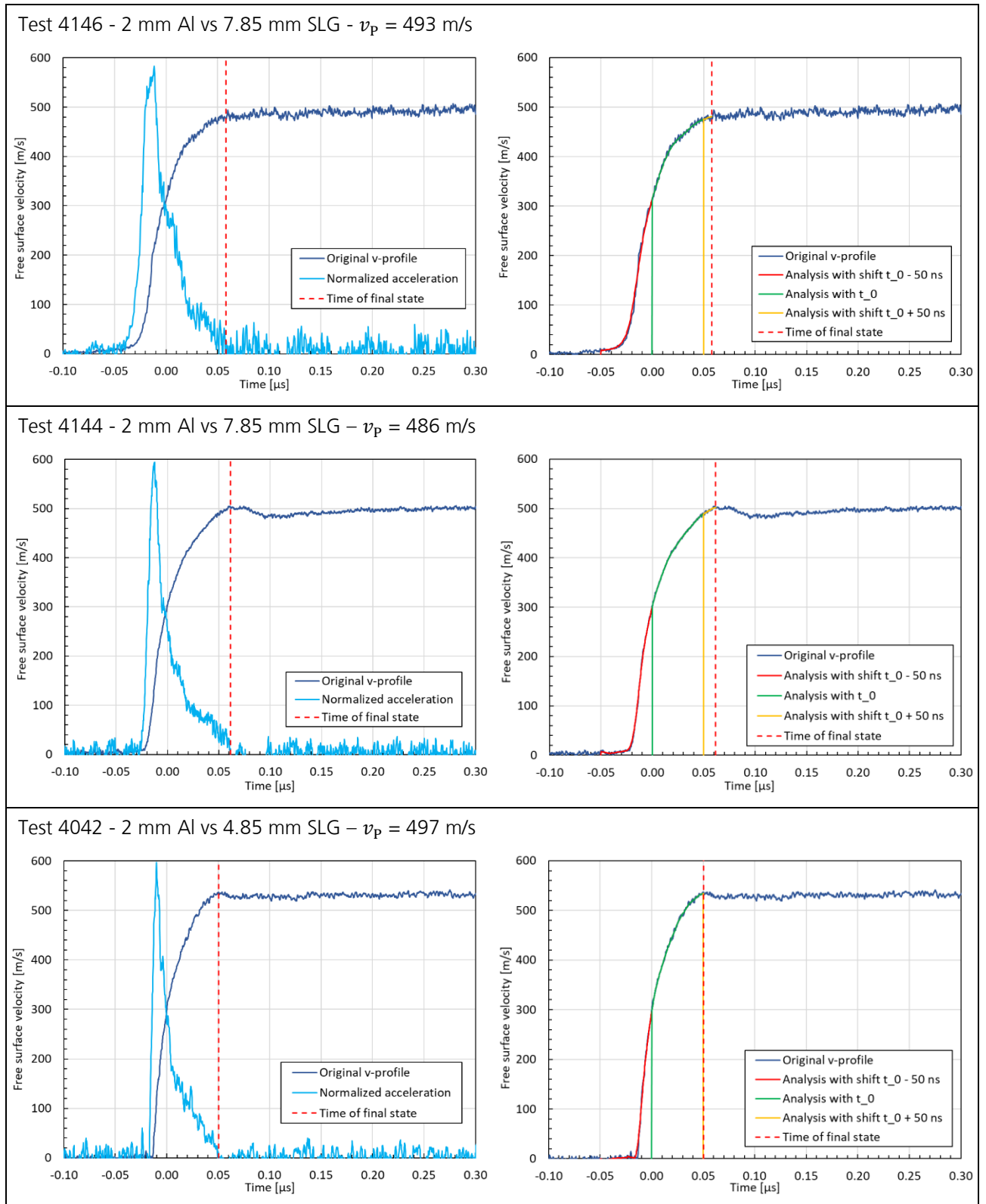


Figure 9.3: Analysis diagrams of the PPI tests; left side: determination of final state with normalized acceleration signal; right side: smoothed input data with different t_0 offsets for the incremental analysis.

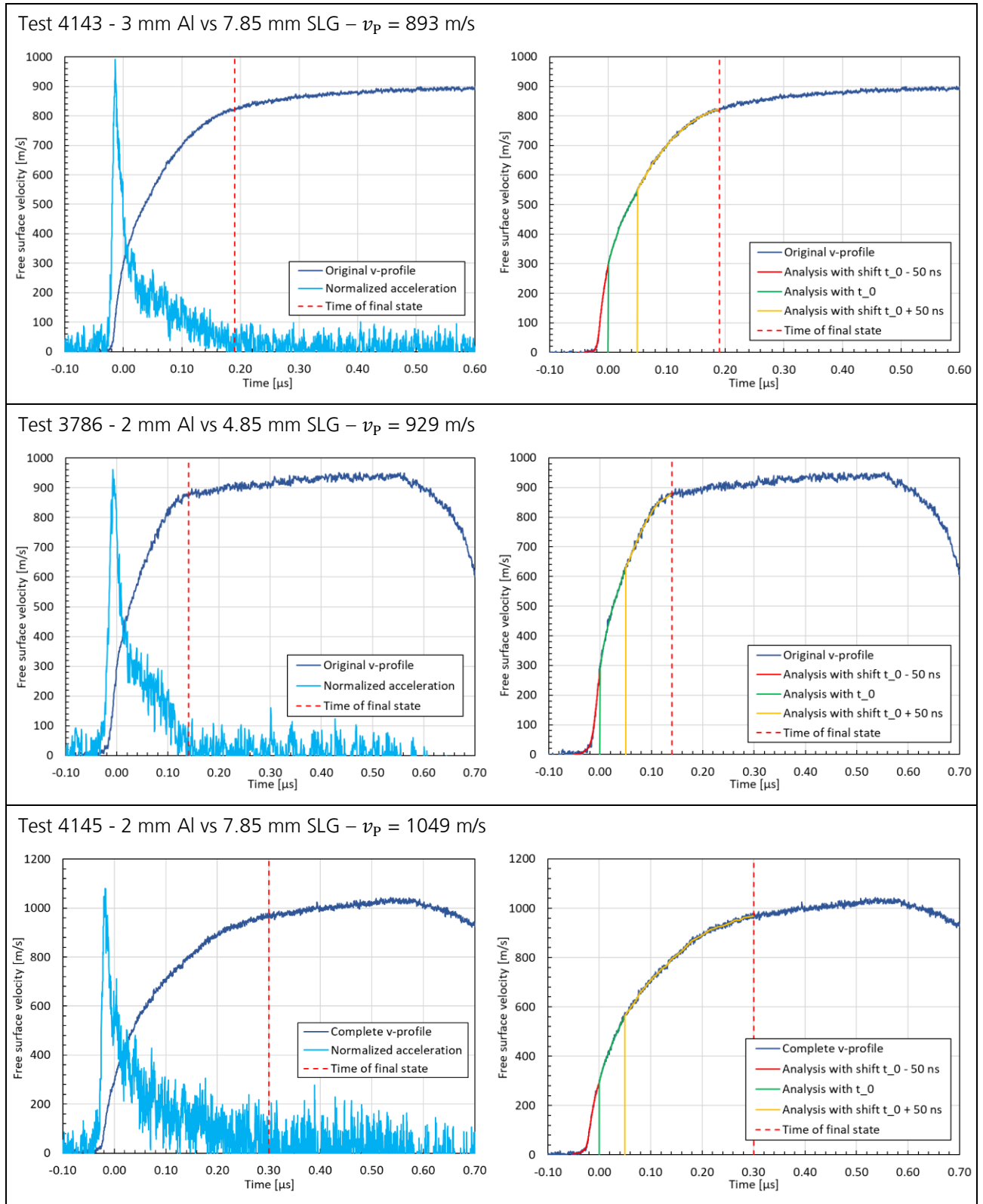


Figure 9.4: Analysis diagrams of the PPI tests; left side: determination of final state with normalized acceleration signal; right side: smoothed input data with different t_0 offsets for the incremental analysis.

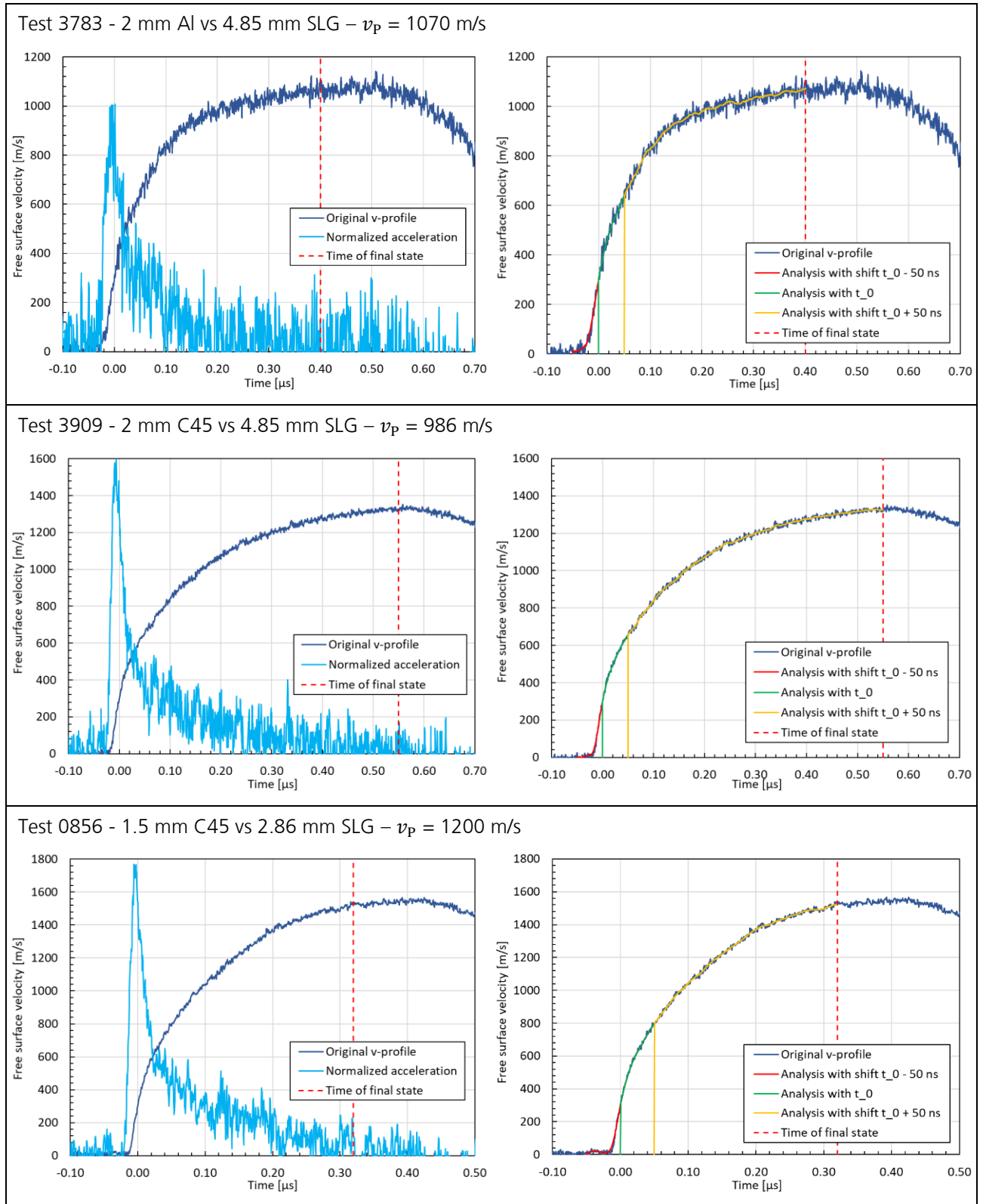


Figure 9.5: Analysis diagrams of the PPI tests; left side: determination of final state with normalized acceleration signal; right side: smoothed input data with different t_0 offsets for the incremental analysis.

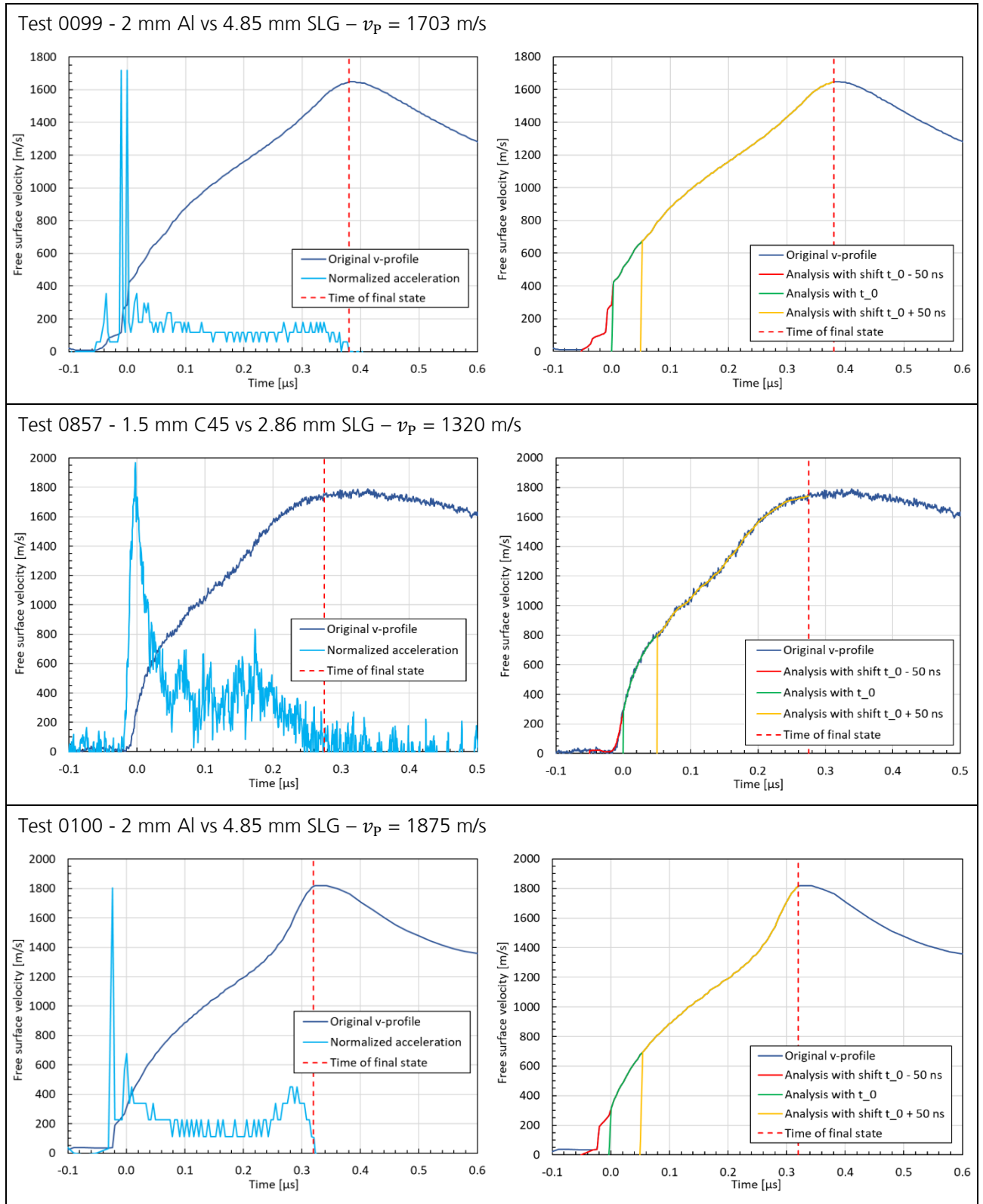


Figure 9.6: Analysis diagrams of the PPI tests; left side: determination of final state with normalized acceleration signal; right side: smoothed input data with different t_0 offsets for the incremental analysis.

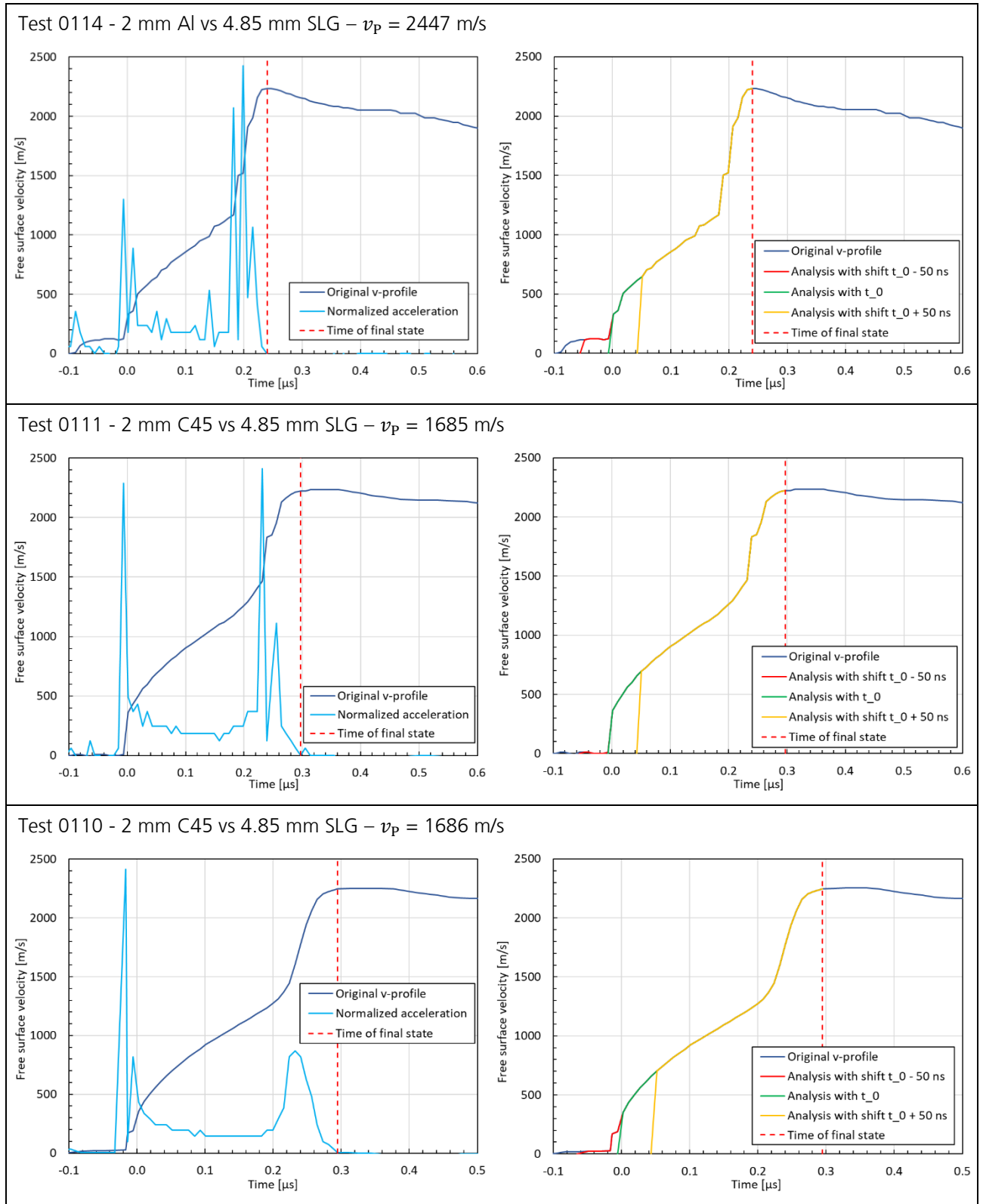


Figure 9.7: Analysis diagrams of the PPI tests; left side: determination of final state with normalized acceleration signal; right side: smoothed input data with different t_0 offsets for the incremental analysis.

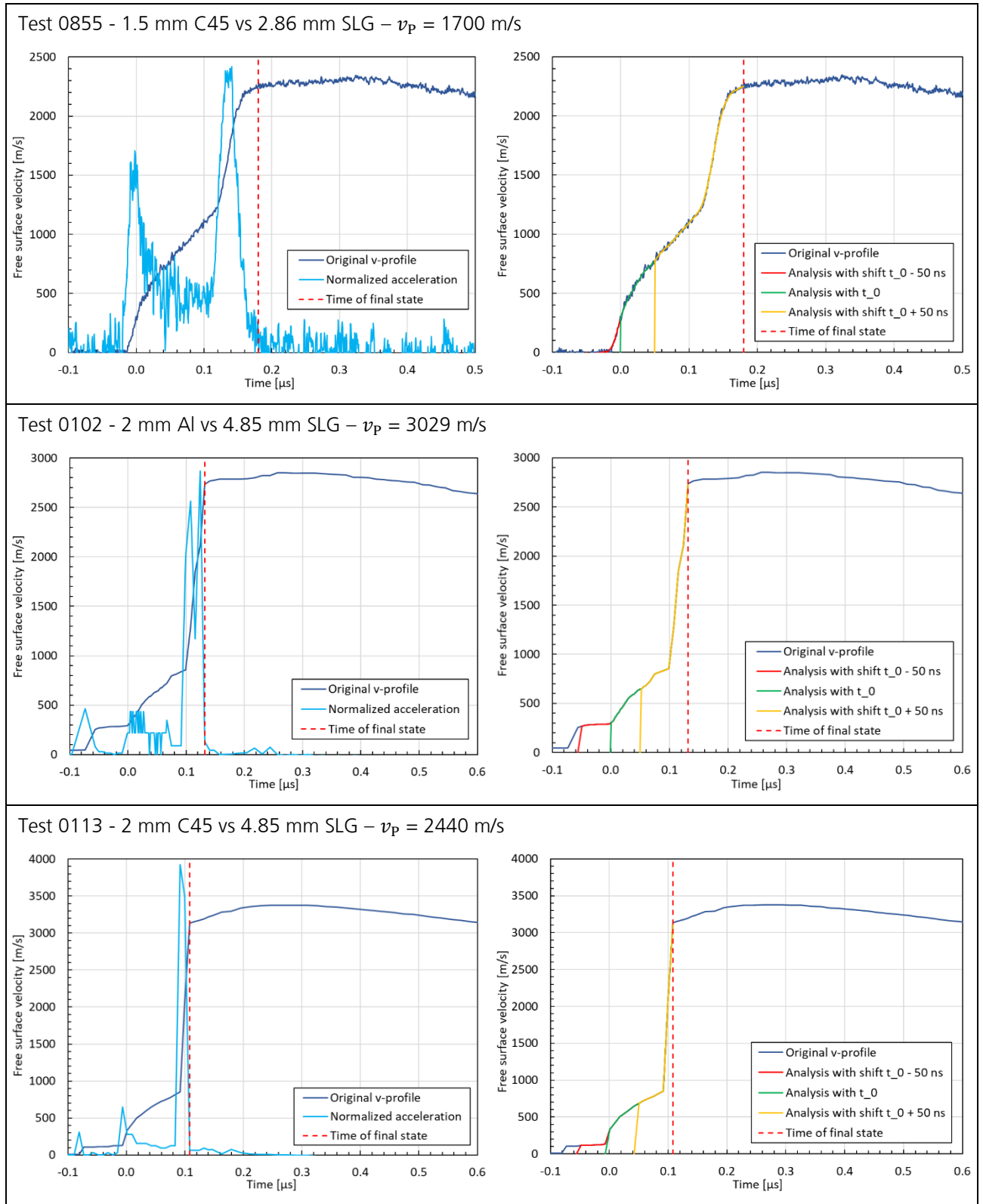


Figure 9.8: Analysis diagrams of the PPI tests; left side: determination of final state with normalized acceleration signal; right side: smoothed input data with different t_0 offsets for the incremental analysis.

9.5 Incremental analysis of literature data

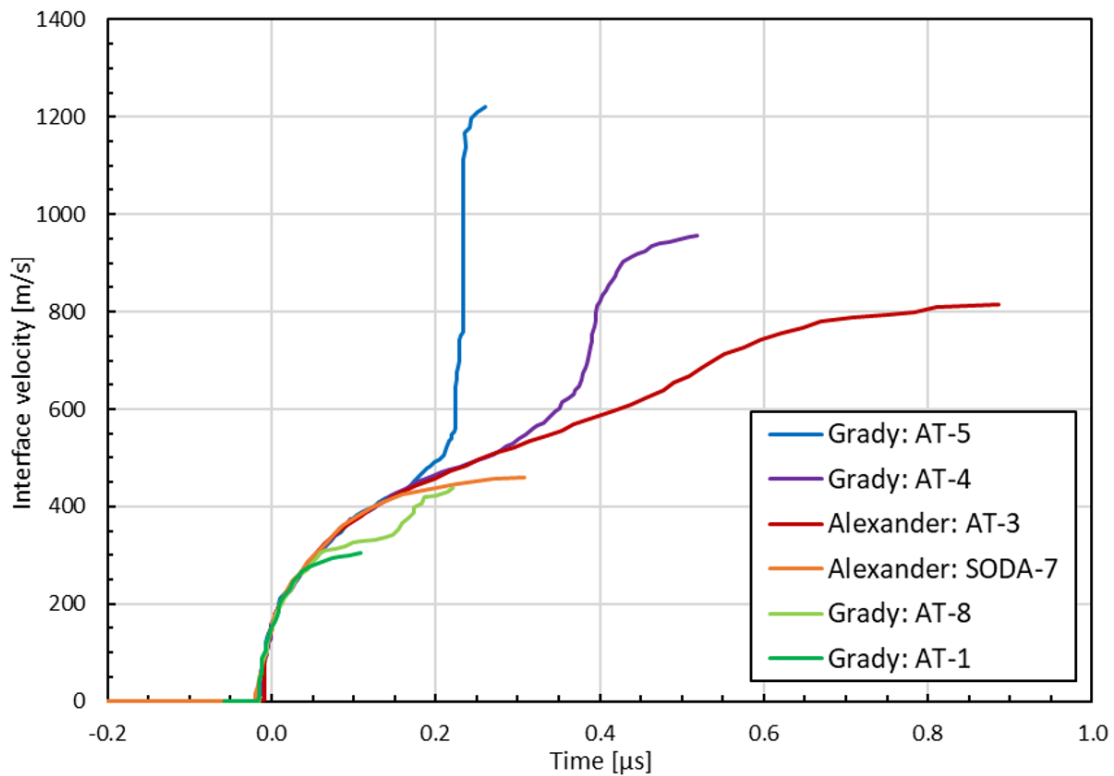


Figure 9.9: Velocity profiles from other publications: To facilitate comparison, a selection of different experimental curves were taken and analyzed with the incremental analysis method. From Grady et al. [75] four measurements were chosen (AT-1, AT-4, AT-5 and AT-8). From Alexander et al. [39] the curves SODA-7 and AT-3 were reanalyzed. The displayed velocity curves are digitized from the original graphs and shifted along the x-axis in such a way that they reach an interface velocity of 150 m/s at t_0 (Figure was pre-published by the author in [A1]).

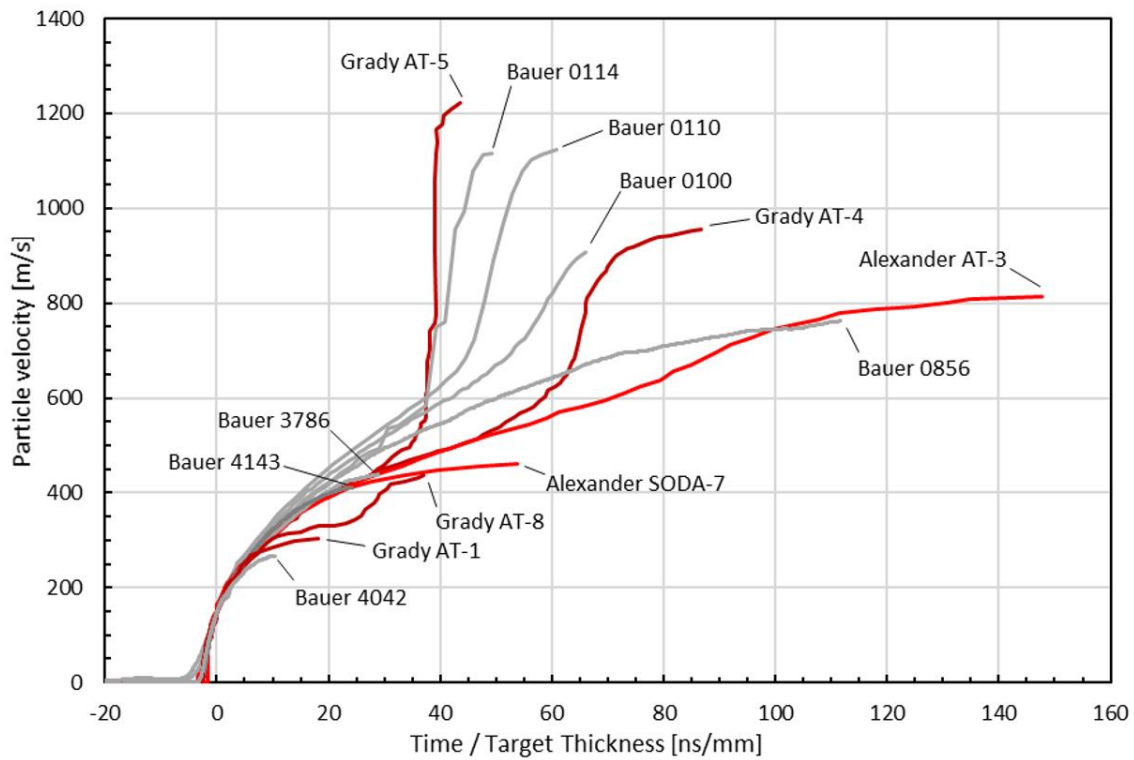


Figure 9.10: Comparison of loading profiles taken from literature and a selection of the tests from the present work. The time axis was divided by the target thickness in order to make the velocity profiles directly comparable. The particle velocity of the literature data was approximated by the interface velocity (Figure 9.9). Although some differences are visible in the velocity profiles, the Hugoniot states resulting from the incremental analysis are in good agreement (Figure 4.41) (Figure was pre-published by the author in [A1]).

9.6 Influence of the CAC separation parameters

In this section, the results of several CAC parameter studies are presented. The CAC separation process is conducted using slight variations of the parameter sets presented in Table 5.3 and Table 5.4. The influence of the resulting $V_{f,c}(z)$ and $\bar{V}_{f,c}$ is evaluated to get an estimation of the systematical error $s^*(\bar{V}_{f,c})$.

Table 9.7 lists two sets of CAC parameters for specimen no. 21202 (ref. Figure 5.27, pre-damaged at $v_p = 72$ m/s). Set 1 are the thresholds determined in a preliminary iteration. The resulting segmentation is illustrated in Figure 9.11 on the left side. The picture shows the center y -slices of the top, middle and bottom analysis volumes. All voxels identified as "crack" are colored red while "glass" voxels are colored white. The corresponding total volume fraction of the cracks $V_{f,c}(z)$ is illustrated as a solid blue line in the diagram on the right. The dashed blue line indicates the corresponding mean value of $\bar{V}_{f,c} = 0.528$ %.

In comparison, the result of the final parameter set (set 2, Table 9.7) is shown in the middle image of Figure 9.11. More cracks are apparent resulting in a much better agreement with the cracks visible in the tomogram (ref. Figure 5.27). $V_{f,c}(z)$ of set 2 is shown as a thick black line in the diagram at the right side. At all z positions, set 2 yields a higher volume fraction than set 1, especially near the bottom of the specimen. Consequently, the mean value of $\bar{V}_{f,c} = 0.854$ % (black dashed line) is also larger.

With set 2, several residual ring artifacts located near the rotation axis are misidentified as "crack". In order to exclude these voxels, a thin cylindrical mask is added at the center and another analysis is conducted. The results of this analysis are plotted as red lines in the diagram of Figure 9.11. Adding the mask has only a marginal influence on the resulting $V_{f,c}(z)$ (red line vs. black line). This also applies to the resulting mean value of $\bar{V}_{f,c} = 0.853$ %. The difference is negligible as the masked volume is much smaller than the total volume.

Although more crack voxels are correctly identified as "crack" using set 2, a fraction of the cracks is still missing in the separated images. However, this set is taken as the final parameter set, since further loosening of the "crack" thresholds would result in a significant increase of artifacts being mistakenly identified as "cracks".

Based on the observed influence of the parameter sets on $\bar{V}_{f,c}$, it is inferred that the systematical error $s^*(\bar{V}_{f,c})$ is much larger than the statistical error of $s(\bar{V}_{f,c}) = 0.004$ %. A value of $s^*(\bar{V}_{f,c}) = 0.2$ % is estimated for specimen 21202.

Table 9.7: CAC parameter sets of specimen 21202 ($v_p = 72$ m/s); set 1 was determined in a preliminary iteration, set 2 is the final set; ITH = Intensity threshold, GTH = Gradient threshold, TITH = Tight intensity threshold, TGTH = Tight gradient threshold.

CAC separation parameters	Top		Mid		Bot	
	Set 1	Set 2	Set 1	Set 2	Set 1	Set 2
"crack" ITH	31800	32400	31800	32600	31800	32800
"glass" ITH	32400	32800	32400	33000	32400	33100
"not crack" GTH	1500	1100	2000	1100	1500	1300
"not glass" GTH	900	950	1400	950	900	1000
"maybe crack" TITH	32100	32600	32100	32800	31800	32950
"maybe glass" TITH	32400	32800	32400	33000	32400	33100
"maybe not crack" TGTH	1500	1100	2000	1100	1500	1300
"maybe not glass" TGTH	1500	1100	2000	1100	1500	1300

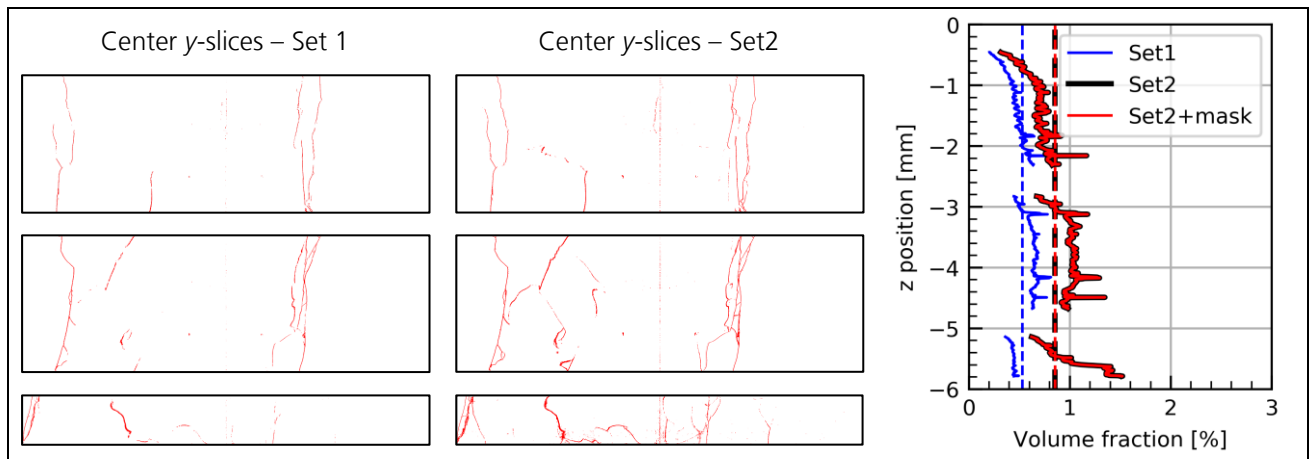


Figure 9.11: Influence of the CAC parameters on the separation result of specimen 21202: center y-slices of a preliminary iteration (set 1, left image) and the final parameter set (set 2, middle image); voxels identified as "crack" are colored red while "glass" voxels are colored white; the corresponding total volume fraction of the cracks is illustrated in the diagram on the right.

The parameter variation for specimen 21194 (ref. Figure 5.28, pre-damaged at $v_p = 144$ m/s) is carried out similar to those of specimen 21202. Table 9.8 lists the thresholds of a preliminary iteration (set 1) and the final segmentation parameters (set 2). The corresponding results are illustrated in Figure 9.12. The image on the left side shows the center y-slices of set 1 ("crack" voxels = red, "glass" voxels = white). The result of set 2 is illustrated in the middle image. With set 1, many cracks visible in the tomogram (ref. Figure 5.28) are missing. With set 2, more cracks are correctly identified. However, the amount of artifact voxels misidentified as "crack" also increases. To remove some of these voxels, another analysis is carried out using set 2 in combination with an additional "isolated clusters 64" filter and a mask. The filter identifies all clusters of "crack" voxels consisting of less than 64 voxels and relabels them as "glass". The cylindrical mask (colored black in the middle image of Figure 9.12) excludes a region with several residual ring artifacts from the analysis. The resulting $V_{f,c}(z)$ is illustrated in the diagram on the right side of Figure 9.12.

With set 2 (black line), $V_{f,c}(z)$ is generally higher than with set 1 (blue line). Especially in the top analysis volume, around $z \approx -1$ mm, set 2 results in a higher local maximum. This maximum gets reduced by the additional “isolated clusters 64” filter and the mask (red line). However, the differences between the results of all three analyses are only marginal yielding mean values of $\bar{V}_{f,c} = 0.35$ % for set 1, $\bar{V}_{f,c} = 0.48$ % for set 2 and $\bar{V}_{f,c} = 0.45$ % for set 2 in combination with the “isolated clusters 64” filter and the mask.

As more cracks are misidentified in specimen 21194 than in specimen 21202, the systematical error is estimated to be larger. A value of $s^*(\bar{V}_{f,c}) = 0.4$ % is estimated, which equals almost the mean value of $\bar{V}_{f,c} = 0.45$ %. Since the result is associated with large uncertainty, it is not suited for a classification of the degree of damage. An additional reason to exclude specimen 21194 from the further analysis is the result of the micro-CT analysis (section 5.3.3.6). The damage observed in this specimen clearly differs from specimens damaged at similar velocities. Therefore, it is not representative for the intermediate velocity range.

Table 9.8: CAC parameter sets of specimen 21194 ($v_p = 144$ m/s); set 1 was determined in a preliminary iteration, set 2 is the final set; ITH = Intensity threshold, GTH = Gradient threshold, TITH = Tight intensity threshold, TGTH = Tight gradient threshold.

CAC separation parameters	Top		Mid		Bot	
	Set 1	Set 2	Set 1	Set 2	Set 1	Set 2
“crack” ITH	32800	33000	32900	33000	32600	33000
“glass” ITH	33000	33200	33300	33400	33200	33200
“not crack” GTH	1300	1000	1600	1100	1900	900
“not glass” GTH	850	800	1100	850	1500	800
“maybe crack” TITH	32900	33100	33100	33200	32900	33100
“maybe glass” TITH	33000	33200	33300	33400	33200	33200
“maybe not crack” TGTH	1300	1000	1600	1100	1900	900
“maybe not glass” TGTH	1300	1000	1600	1100	1900	800

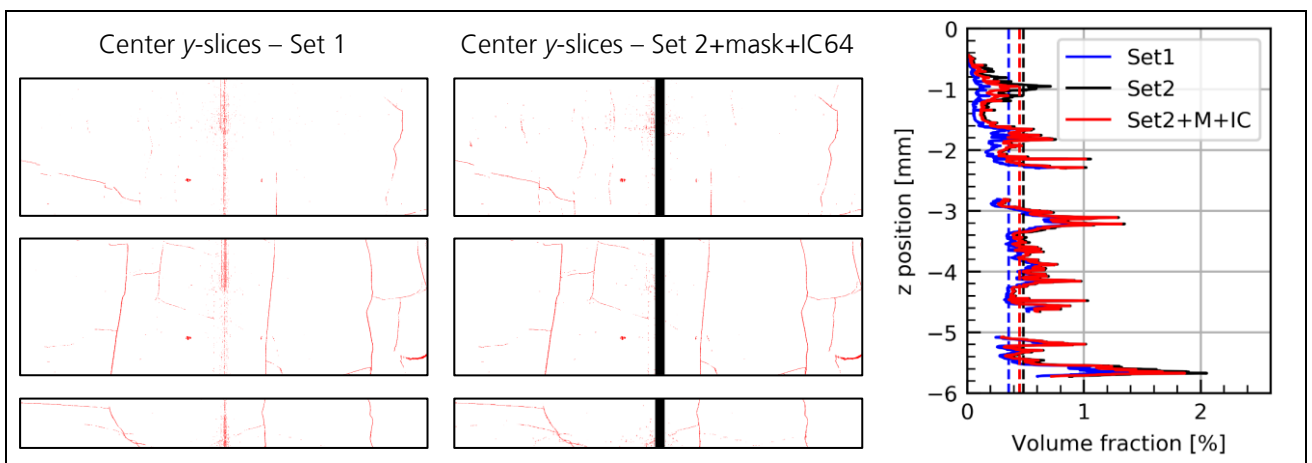


Figure 9.12: Influence of the CAC parameters on the separation result of specimen 21194: center y-slices of a preliminary iteration (set 1, left image) and the final parameter set (middle image, set 2 with a cylindrical mask and an “isolated clusters 64” filter); voxels identified as “crack” are colored red, “glass” voxels are colored white and masked voxels are colored black; the corresponding total volume fraction of the cracks is illustrated in the diagram on the right.

Table 9.9 lists two sets of CAC parameters for specimen no. 21201 (ref. Figure 5.29, pre-damaged at $v_p = 266$ m/s). The results of the segmentation process are illustrated in Figure 9.13. Similar to the observations of the previous specimens, many cracks are missing with the preliminary iteration set 1 (image on the left). The corresponding $V_{f,c}(z)$ is illustrated as blue line in the diagram on the right side. The final parameters of set 2, in combination with the “isolated clusters 64” filter and the mask, result in a better segmentation (middle image). The corresponding $V_{f,c}(z)$ is shown as a red line in the diagram. Without the “isolated clusters 64” filter and the mask, the result differs only slightly (black line in the diagram).

The resulting mean values are $\bar{V}_{f,c} = 1.06\%$ for set 1, $\bar{V}_{f,c} = 2.07\%$ for set 2 and $\bar{V}_{f,c} = 1.95\%$ for set 2 in combination with the “isolated clusters 64” filter and the mask.

Based on the observed influence of the parameter sets on $\bar{V}_{f,c}$, it is inferred that the systematical error $s^*(\bar{V}_{f,c})$ is much larger than the statistical error of $s(\bar{V}_{f,c}) = 0.03\%$. A value of $s^*(\bar{V}_{f,c}) = 0.6\%$ is estimated for specimen 21201 (similar to the error of specimen 21200).

Table 9.9: CAC parameter sets of specimen 21201 ($v_p = 266$ m/s); set 1 was determined in a preliminary iteration, set 2 is the final set; ITH = Intensity threshold, GTH = Gradient threshold, TITH = Tight intensity threshold, TGTH = Tight gradient threshold.

CAC separation parameters	Top		Mid		Bot	
	Set 1	Set 2	Set 1	Set 2	Set 1	Set 2
“crack” ITH	33000	33200	32800	33200	32600	32900
“glass” ITH	33200	33350	33300	33500	32900	33100
“not crack” GTH	1500	900	2100	1000	2100	800
“not glass” GTH	850	800	1800	850	1100	700
“maybe crack” TITH	33100	33300	33000	33350	32700	33000
“maybe glass” TITH	33200	33350	33300	33500	32900	33100
“maybe not crack” TGTH	1500	900	2100	1000	2100	800
“maybe not glass” TGTH	1500	900	2100	1000	2100	800

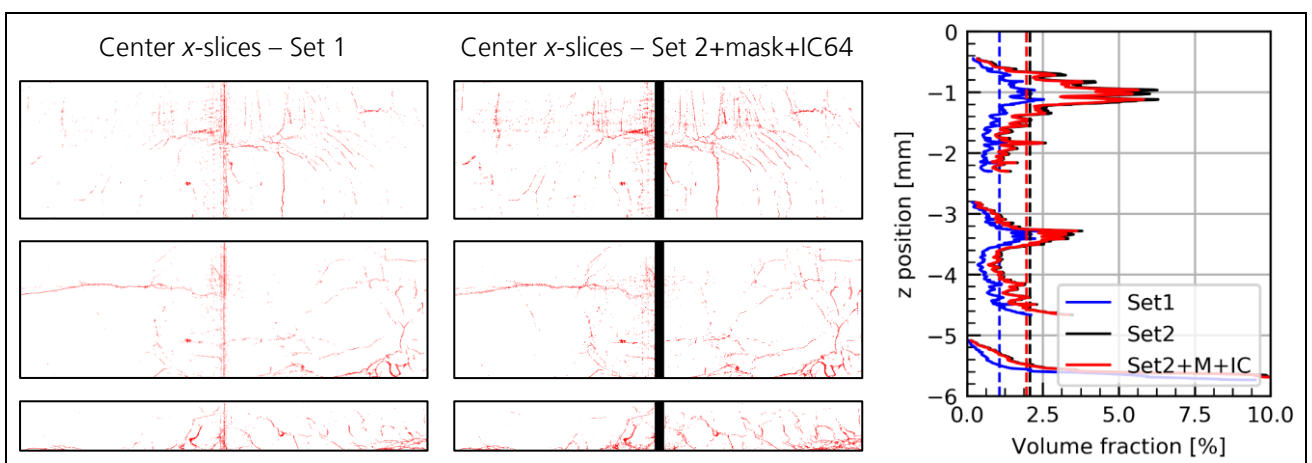


Figure 9.13: Influence of the CAC parameters on the separation result of specimen 21201: center x-slices of a preliminary iteration (set 1, left image) and the final parameter set (middle image, set 2 with a cylindrical mask and an “isolated clusters 64” filter); voxels identified as “crack” are colored red, “glass” voxels are colored white and masked voxels are colored black; the corresponding total volume fraction of the cracks is illustrated in the diagram on the right.

For specimen no. 21200 (ref. Figure 5.30, pre-damaged at $v_p = 407$ m/s), the results of three parameter variations are investigated. The variations are applied to the top analysis volume only, as its separation is the most challenging. The thresholds of the “mid” and “bot” analysis volumes are kept constant at their final values (Table 5.4).

Table 9.10 lists the three sets of CAC parameters. Set 1 and set 2 are determined in preliminary iterations and set 3 comprises the final segmentation thresholds. The resulting segmentations and the original tomogram are illustrated in Figure 9.14. The figure illustrates the center y- and z-slices of the “top” analysis volume. Comparing the black cracks of the tomogram with the red “crack” voxels of the segmented images reveals that many cracks are missing with set 1. More cracks are identified successfully with set 2 and set 3. The corresponding $V_{f,c}(z)$ is illustrated in the diagram on the right side of Figure 9.14. The result of set 1 is illustrated by a purple line, set 2 by a blue line and set 3 by a black line. In addition, a red line indicates the result of set 3 in combination with the “isolated clusters 64” filter. As the difference between the black and the red line is only marginal, the influence of the “isolated clusters 64” filter is negligible.

However, the different parameter sets yield significantly different curves. Especially near the position of the distinct horizontal crack plane at $z \approx -1$ mm, the local maximum increases from 5 % (set 1) to more than 11 % (set 3). The resulting mean values of the top analysis volume are $\bar{V}_{f,c}(\text{top}) = 1.1$ % for set 1, $\bar{V}_{f,c}(\text{top}) = 1.8$ % for set 2 and $\bar{V}_{f,c}(\text{top}) = 2.4$ % for set 3.

Based on the observed influence of the parameter sets on $\bar{V}_{f,c}$, it is inferred that the systematical error $s^*(\bar{V}_{f,c})$ is much larger than the statistical error of $s(\bar{V}_{f,c}) = 0.05$ %. A value of $s^*(\bar{V}_{f,c}) = 0.6$ % is estimated for specimen 21200 (similar to the error of specimen 21201).

Table 9.10: CAC parameter sets of “top” analysis volume of specimen 21200 ($v_p = 407$ m/s); set 1 and set 2 were determined in preliminary iterations, set 3 is the final set; ITH = Intensity threshold, GTH = Gradient threshold, TITH = Tight intensity threshold, TGTH = Tight gradient threshold.

CAC separation parameters of “top” analysis volume	Set 1	Set 2	Set 3
“crack” ITH	32800	33000	33000
“glass” ITH	33200	33250	33400
“not crack” GTH	1050	800	800
“not glass” GTH	800	750	650
“maybe crack” TITH	33000	33150	33200
“maybe glass” TITH	33200	33250	33400
“maybe not crack” TGTH	1050	800	800
“maybe not glass” TGTH	1050	800	800

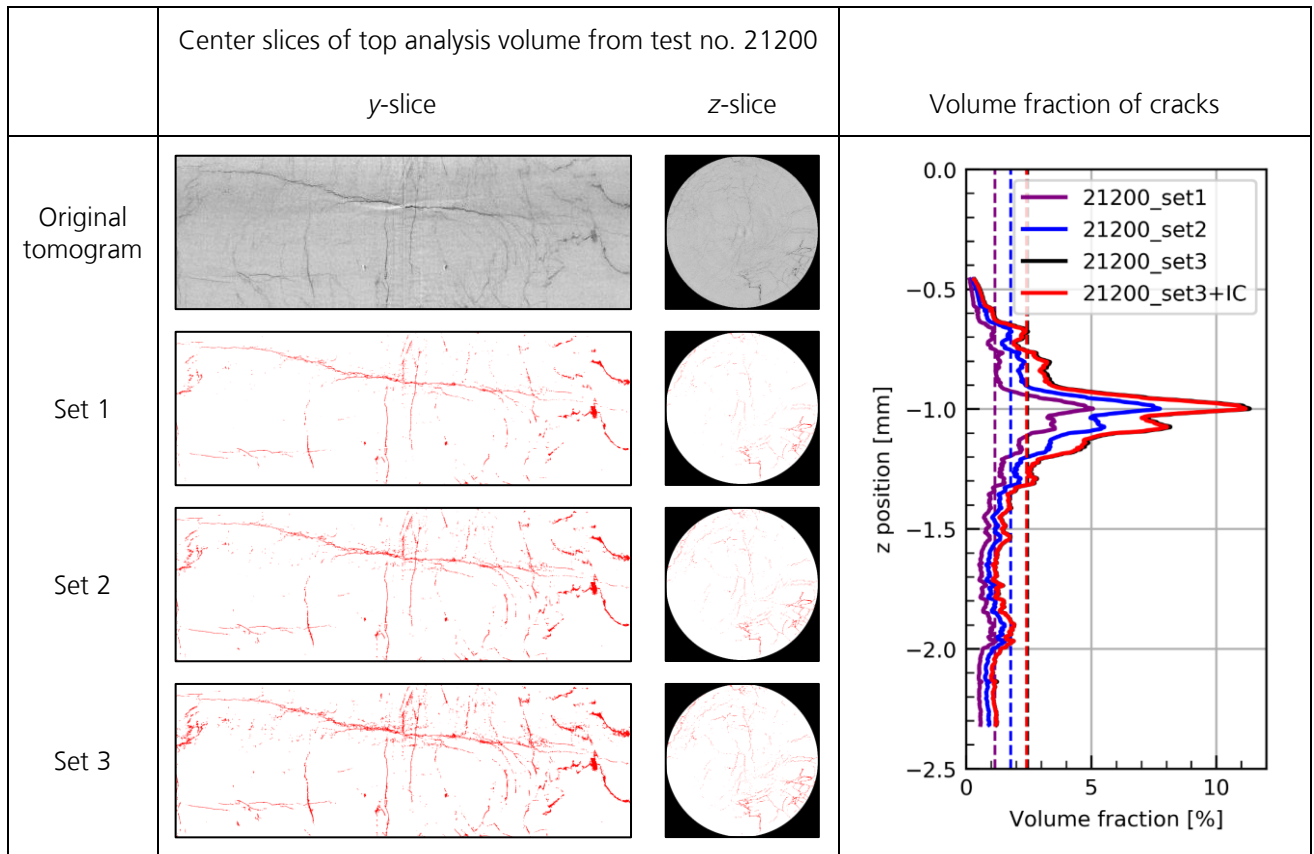


Figure 9.14: Influence of the CAC parameters on the separation result of specimen 21201: center y- and z-slices of the top analysis volume. The slices in the first row illustrate the original gray scale tomogram; the subsequent rows show the segmentation results of the different parameter sets (voxels identified as “crack” are colored red, “glass” voxels are colored white); the corresponding total volume fraction of the cracks is illustrated in the diagram on the right.

For specimen 20979+P (ref. Figure 5.31, pre-damaged at $v_p = 69$ m/s and subjected to a quasi-static load in a confined pressure test), no parameter variation is outlined. However, as the statistical error of this specimen, $s(\bar{V}_{f,c}) = 0.04\%$, is almost similar to those of specimen 21200, the systematical error is adopted. Therefore, an error of $s^*(\bar{V}_{f,c}) = 0.6\%$ is estimated, similar to specimens 21200 and 21201.

9.7 Compilation of all X-ray CT results of pre-damaged SLG cylinders

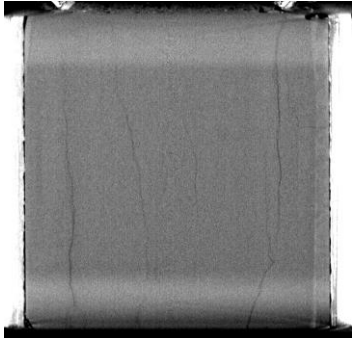
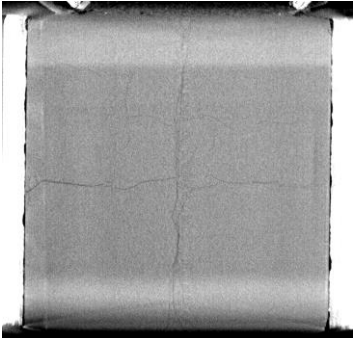
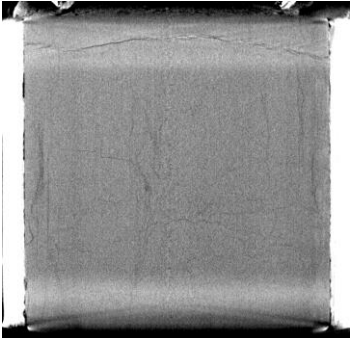
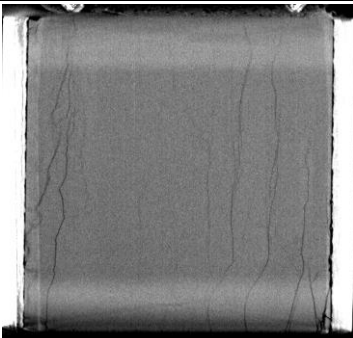
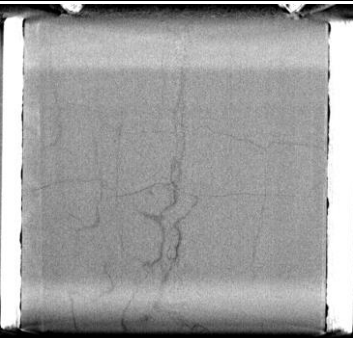
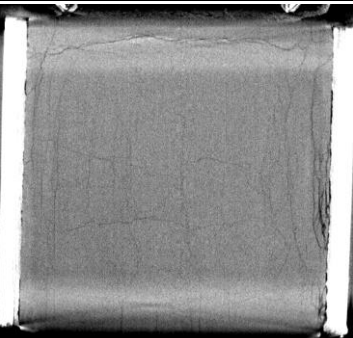
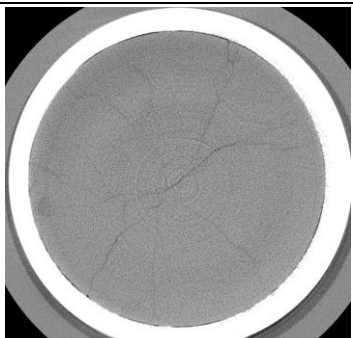
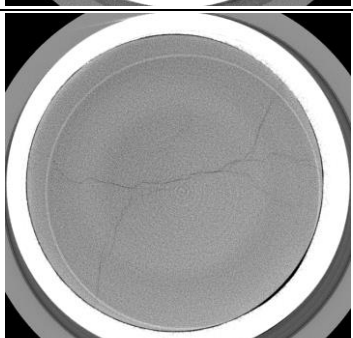
20981 – 70 m/s – high strength	20982 – 73 m/s – high strength	20983 – 186 m/s – intermediate
		
		
		
		
		
		

Figure 9.15: Slices of X-ray tomograms of pre-damaged SLG cylinders from tests no. 20981, 20982 and 20983; images from top to bottom: center x-slice & y-slice, z-slices from different positions (top, middle & bottom third of specimen).

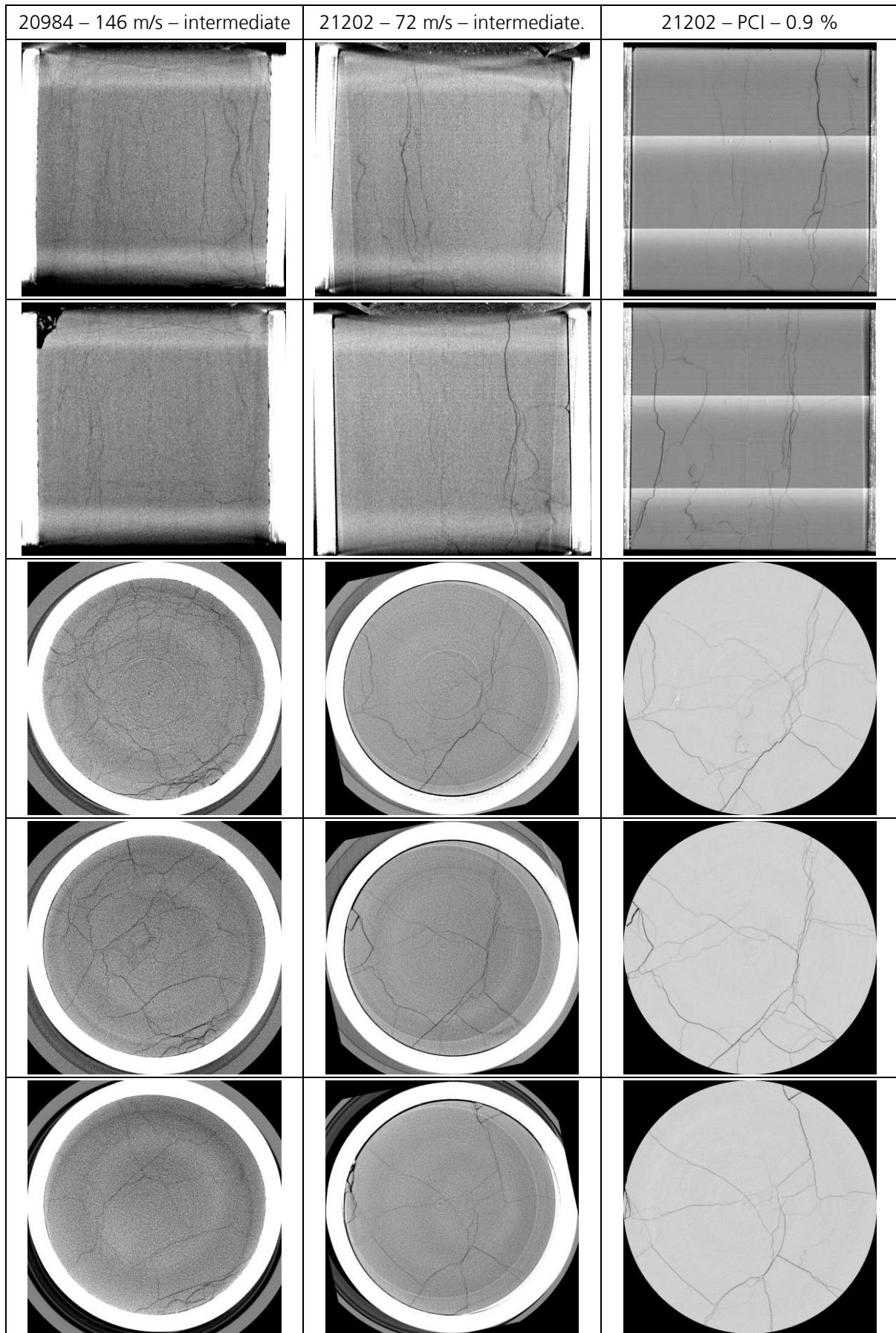


Figure 9.16: Slices of X-ray tomograms of pre-damaged SLG cylinders from tests no. 20984 and 21202; images from top to bottom: center x-slice & y-slice, z-slices from different positions (top, middle & bottom third of specimen); the PCI x- & y-slices of 21202 are rotated by 78° around the z-axis.

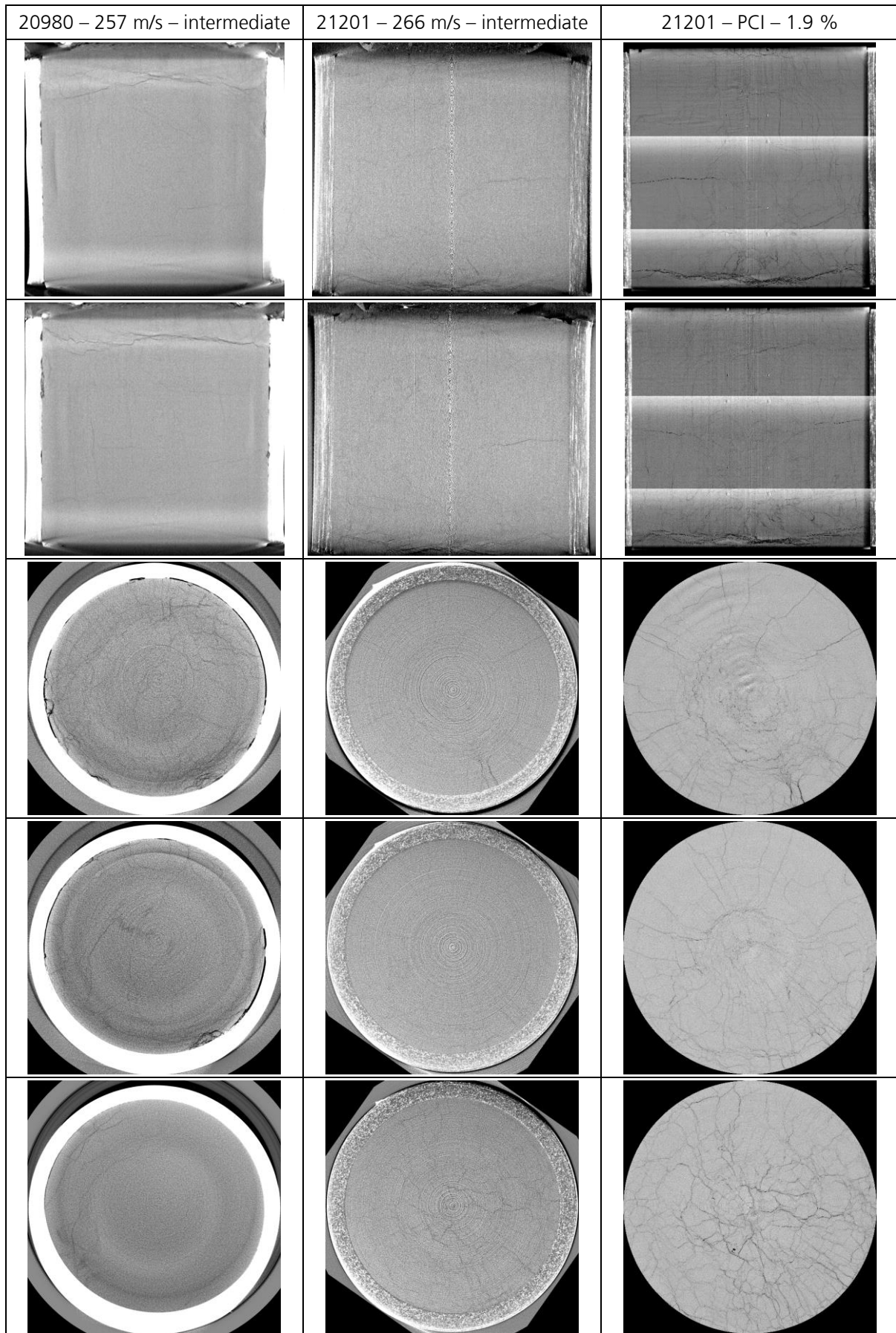


Figure 9.17: Slices of X-ray tomograms of pre-damaged SLG cylinders from tests no. 20980 and 21201; images from top to bottom: center x-slice & y-slice, z-slices from different positions (top, middle & bottom third of specimen); the PCI x- & y-slices of 21201 are rotated by 215° around the z-axis.

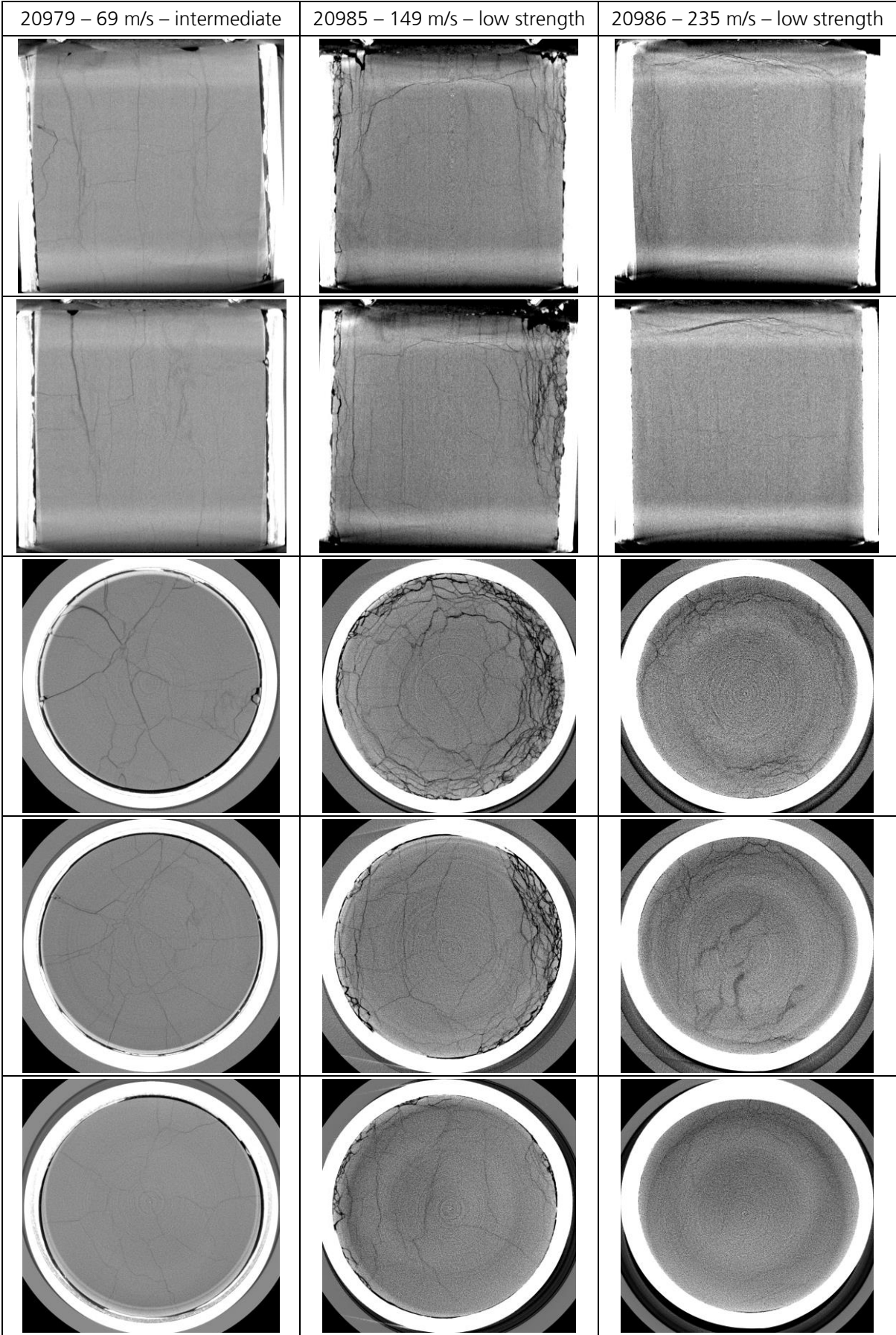


Figure 9.18: Slices of X-ray tomograms of pre-damaged SLG cylinders from tests no. 20979, 20985 and 20986; images from top to bottom: center x-slice & y-slice, z-slices from different positions (top, middle & bottom third of specimen).

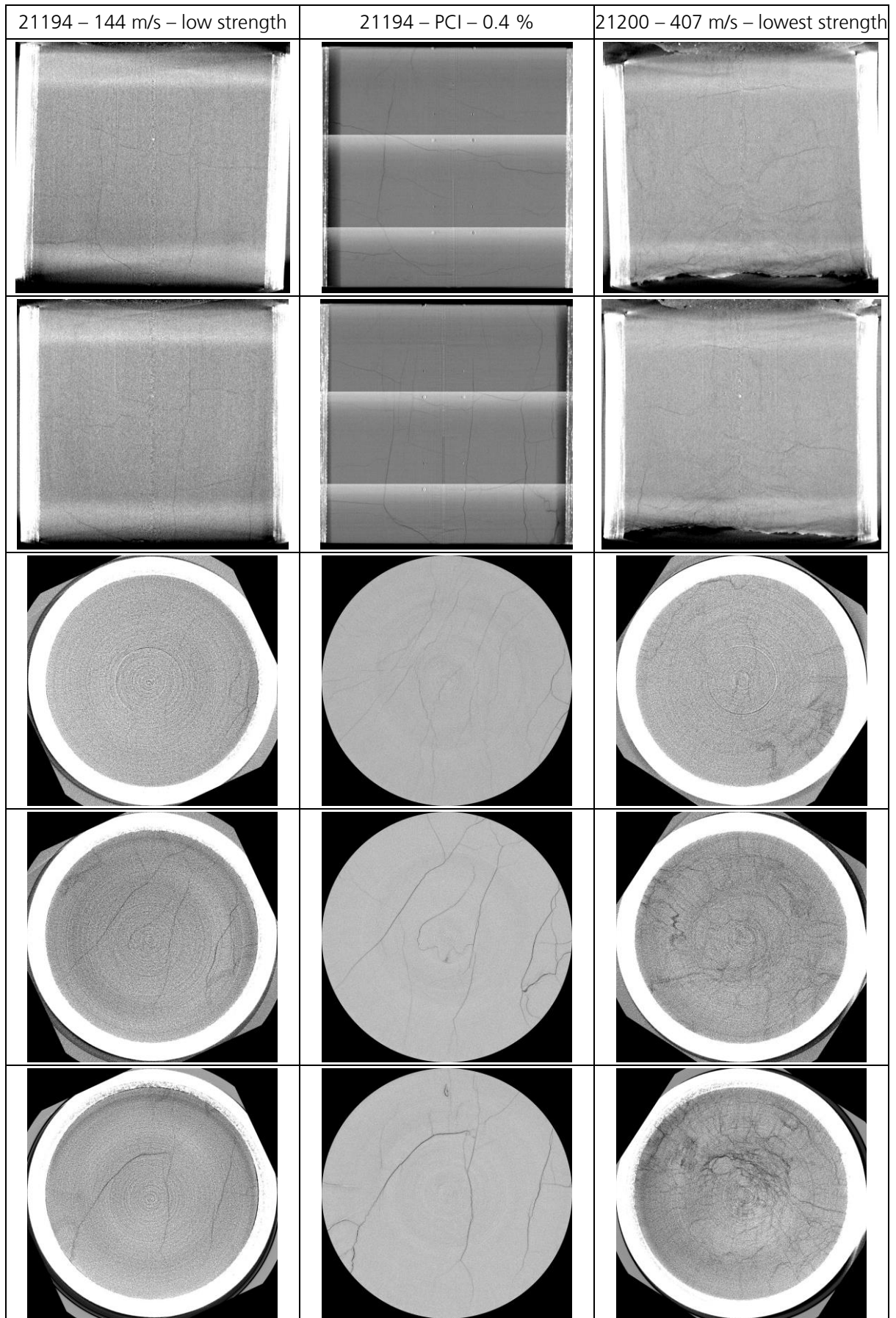


Figure 9.19: Slices of X-ray tomograms of pre-damaged SLG cylinders from tests no. 21194 and 21200; images from top to bottom: center x-slice & y-slice, z-slices from different positions (top, middle & bottom third of specimen); the PCI x- & y-slices of 21194 are rotated by 335° around the z-axis.



Figure 9.20: Slices of X-ray tomograms of pre-damaged SLG cylinders from tests no. 21200 and 20979+P; images from top to bottom: center x-slice & y-slice, z-slices from different positions (top, middle & bottom third of specimen); the PCI x- & y-slices of 21200 (20979+P) are rotated by 123° (139°) around the z-axis.

10 Notation and abbreviations

Continuum mechanical description

I	Identity matrix
δ_{ij}	Kronecker delta
$\mathbf{e}_1, \mathbf{e}_2, \mathbf{e}_3$	Standard unit vectors of a Cartesian coordinate system
t	Time
M	Material point
${}^0\mathbf{x}$	Position vector in reference configuration
${}^t\mathbf{x}$	Position vector in current configuration
\mathbf{u}	Displacement vector
\mathbf{v}	Velocity vector
\mathbf{F}	Material deformation gradient
$d^0\mathbf{x}$	Infinitesimal line element in reference configuration
$d^t\mathbf{x}$	Infinitesimal line element in current configuration
\mathbf{E}	Green-Lagrange strain tensor
E_{ijkl}	Components of the fourth order elasticity tensor
λ_L, μ_L	Lamé constants
$\boldsymbol{\varepsilon}$	Strain tensor
$\varepsilon_{\text{engin}}$	Uniaxial engineering strain
$\varepsilon_{\text{true}}$	Uniaxial true strain
l	Length
$\boldsymbol{\sigma}$	Cauchy stress tensor
\mathbf{t}	Stress vector
\mathbf{n}	Surface normal vector
$\sigma_I, \sigma_{II}, \sigma_{III}$	Principal stresses or eigenvalues of the Cauchy stress tensor
I_1, I_2, I_3	Invariants of the Cauchy stress tensor
\mathbf{P}	Spherical stress tensor
P	Hydrostatic pressure
\mathbf{S}	Deviatoric stress tensor
S_I, S_{II}, S_{III}	Eigenvalues of the deviatoric stress tensor
J_1, J_2, J_3	Invariants of the deviatoric stress tensor
$\boldsymbol{\rho}$	Deviatoric stress vector

Haigh-Westergaard coordinates

ξ	Distance between the deviatoric plane and the origin of the stress space
ρ	Length of the deviatoric stress vector
θ	Lode angle

Plasticity description

$R_{p0.2}$	Stress threshold corresponding to 0.2 % plastic strain
Y	Yield stress
$F(\boldsymbol{\sigma})$	Yield function
$G(\boldsymbol{\sigma})$	Plastic potential
$K(g)$	Hardening function
g	Hardening parameter
$\varepsilon_{\text{eff}}^p$	Effective plastic strain
$\boldsymbol{\sigma}_B$	Back stress tensor
T	Hydrostatic tensile limit
κ	Yield stress under pure shear loading
α, β	Drucker-Prager material constants
$\phi, C, \alpha_{\pm}, \beta_{\pm}, R_{mc}$	Mohr-Coulomb material constants
$d\varepsilon^p$	Plastic strain increment
$d\lambda$	Scalar factor of the normality condition

Failure description

D	Damage parameter
S	Total area of a cross section
S_D	Area of internal voids
ε_p^f	Equivalent plastic strain to failure
$\Delta\varepsilon_p$	Incremental plastic strain

PPI analysis

v_p	Impact velocity
v_{fs}	Free surface velocity
d_T	Thickness of the target
$(P_0, \rho_0, V_0, e_0, u_{p,0})$	State variables of the initial state
$(P_H, \rho_H, V_H, e_H, u_{p,H})$	State variables of the Hugoniot state
σ_x	Longitudinal stress
σ_y, σ_z	Transversal stresses
σ_{eq}	Equivalent stress (von Mises)
τ	Shear stress
h	Lagrange position
A	Cross sectional area
dt	Time increment
c_0, S	Material parameters of a linear U_s - $u_{p,H}$ relation
μ	Volumetric compression
η	$1 - \frac{\rho_0}{\rho_H}$

Notations of selective analysis:

u_p	Particle velocity
$u_{p,el}$	Particle velocity behind the elastic precursor
$u_{p,final}$	Particle velocity of the final state
U_s	Shock velocity
t_{el}	Arrival time of the elastic precursor
t_{pl}	Arrival time of the plastic shock wave
Δt_{el-pl}	Time difference between the arrival of precursor and shock wave
σ_{final}	Longitudinal stress of the final state
ε_{final}	Longitudinal strain of the final state
μ_{final}	Volumetric compression of the final state

Notations of incremental analysis:

t_0	Arrival time of the elastic precursor
i	Index of the loading step
$\tilde{U}_{s,i+1}$	Eulerian Shock velocity of step i
$U_{s,i+1}$	Lagrangian Shock velocity of step i
Δt_{i+1}	Time difference between the arrival of precursor and shock wave $U_{s,i+1}$
σ_{i+1}	Longitudinal stress after step i
ε_{i+1}	Longitudinal strain after step i
μ_{i+1}	Engineering volumetric compression after step i
$\mu_{\text{true},i+1}$	True volumetric compression after step i

Material constitutive description

ρ	Density
V	Mass-specific volume
e	Mass-specific internal energy
e_{tot}	Mass-specific total energy
S	Mass-specific entropy
T	Temperature
E	Elastic modulus or Young's modulus
G	Shear modulus
K	Bulk modulus
M	Longitudinal modulus
ν	Poisson's ratio
c_p	Longitudinal wave speed
c_s	Shear wave speed
$\Gamma(V)$	Mie-Grüneisen parameter
3α	Volumetric thermal expansion
K_T	Isothermal bulk modulus
c_V	Specific heat capacity at constant volume
K_1, K_2, K_3, B_0, B_1	Material parameters of a polynomial EOS
\tilde{K}_1	Expansive bulk modulus

Additional notations for the JH2 model description

ΔP	Bulking pressure increment
U	Elastic internal distortional energy
β	Material parameter representing the fraction of converted energy
D_1, D_2	Material parameters for the calculation of ε_p^f
HEL	Longitudinal stress at the Hugoniot elastic limit
P_{HEL}	Hydrostatic pressure at the Hugoniot elastic limit
μ_{HEL}	Volumetric compression at the Hugoniot elastic limit
σ_{HEL}	Equivalent stress at the Hugoniot elastic limit
$\sigma_{D=0}(\dot{\varepsilon}^*, P)$	Intact yield function
$\sigma_{D=1}(\dot{\varepsilon}^*, P)$	Failed yield function
$\sigma_{yield}(\dot{\varepsilon}^*, P, D)$	General yield function
A, N	Material parameters defining the intact yield function
B, M, σ_{max}	Material parameters defining the failed yield function
C	Material parameter of the strain rate effect
$\dot{\varepsilon}^*$	Normalized equivalent strain rate

Notations of CT analysis

\min_{float}	Lower gray scale threshold of image conversion
\max_{float}	Upper gray scale threshold of image conversion
$V_{f,c}$	Total volume fraction of cracks
$\bar{V}_{f,c}$	Mean total volume fraction of cracks
$s(\bar{V}_{f,c})$	Statistical error of $\bar{V}_{f,c}$
$s^*(\bar{V}_{f,c})$	Systematical error of $\bar{V}_{f,c}$
$N_{crack}(z)$	Amount of "crack" voxels at position z
$N_{glass}(z)$	Amount of "glass" voxels at position z
i	Horizontal slice index
N	Total number of horizontal slices

Notations of PDV measurement

σ_t	Accuracy of the time measurement
σ_v	Accuracy of the velocity measurement
λ_0	Wave length of the laser

Notations of confined compression tests

U_d	Bridge output voltage of the strain gauges
k	Gauge factor
f_{amp}	Amplification factor
U_s	Bridge power supply
r_{inner}	Inner radius of the confinement
r_{outer}	Outer radius of the confinement
E_{conf}	Young's modulus of the confinement
$\varepsilon_{\text{hoop}}$	Hoop strain of the confinement
F_{axi}	Axial force of the tungsten carbide stamp
σ_{stamp}	Axial stress in tungsten carbide stamp
Δl_{stamp}	Axial displacement of the tungsten carbide stamps
Δl_{test}	Axial displacement between striped markers
r_{stamp}	Radius of the tungsten carbide stamps
A_{stamp}	Pressure surface of the stamps
σ_{axi}	Axial stress in the specimen
σ_{rad}	Radial stress in the specimen
ε_{axi}	Axial strain in the specimen
$\varepsilon_{\text{axi,max}}$	Axial failure strain in unconfined compression test
$\sigma_{\text{axi,max}}$	Axial failure stress in unconfined compression test
$r_{0,\text{spec}}$	Initial radius of the specimen
Δr_{spec}	Radial displacement of the specimen
Δl_{spec}	Axial displacement in the specimen
$V_{0,\text{spec}}$	Initial volume of the specimen
V_{spec}	Actual volume of the specimen
L	Actual length of the specimen
$l_{0,\text{spec}}$	Initial length of the specimen

$l_{0,\text{ref}}$	Initial distance between the markers in the reference setup
$l_{0,\text{test}}$	Initial distance between the markers in the test setup
Δl_{ref}	Measured axial displacement of the markers in the reference setup
Δl_{test}	Measured axial displacement of the markers in the test setup
$\Delta l_{\text{align,ref}}$	Initial displacement of the reference setup due to gaps/misalignments
$\Delta l_{\text{align,test}}$	Initial displacement of the test setup due to gaps/misalignments
Δl_{ref}^*	Displacement caused by elastic deformation of the stamps in the reference setup
Δl_{test}^*	Displacement caused by elastic deformation of the stamps in the test setup
$F_{\text{TH,low}}$	Lower force threshold for the extrapolation of $\Delta l_{\text{align,ref}}$ and $\Delta l_{\text{align,test}}$
$F_{\text{TH,high}}$	Upper force threshold for the extrapolation of $\Delta l_{\text{align,ref}}$ and $\Delta l_{\text{align,test}}$
m	Proportionality factor between σ_{rad} and $\varepsilon_{\text{hoop}}$
a_0, a_1, a_2	Fit coefficients determined by simulations

Notations of impact simulations

x	Horizontal distance to the impact surface
y	Vertical distance to the rotation axis
V_i	Volume of element i in the impact simulation
D_i	Damage of element i in the impact simulation
\bar{D}	Mean damage of the specimen in the impact simulation
v_R	Residual velocity of the projectile
v_{BL}	Ballistic limit velocity
α	Jonas-Lambert fit parameter

Abbreviations

Al	Aluminum (6061 T6511 or EN AW 2007 T4)
ANU	Australian National University
ARL	Army Research Laboratory
C45	Commercial C45 steel
CAC	Converging active contours
CFL	Courant-Friedrichs-Lewy
CT	Computed tomography
DICOM	Digital imaging and communications in medicine
EMI	Ernst-Mach-Institut
EOS	Equation of state
EZRT	Entwicklungszentrum Röntgentechnik
FDM	Finite difference method
FEM	Finite element method
FFT	Fast Fourier transform
FVM	Finite volume method
GTH	Gradient threshold
HEL	Hugoniot elastic limit
ITH	Intensity threshold
JH1 model	Johnson-Holmquist-1 model
JH2 model	Johnson-Holmquist-2 model
Mango	Medial axis and network generation
MFM	Mesh-free methods
MTS machine	Mechanical testing servo-hydraulic machine
NATO	North Atlantic Treaty Organization
NCI	National computational infrastructure
NetCDF	Network common data format
PC	Polycarbonate
PCI	Phase-contrast imaging
PDV	Photonic Doppler velocimetry
PMMA	Polymethylmethacrylate
PNG	portable network graphics

PPI	Planar plate impact
PSI	Paul Scherrer Institut
PSPI	Pressure-shear plate impact
PU	Polyurethane
RVE	Representative volume element
SD	Standard deviation
SHPB	Split Hopkinson pressure bar
SLG	Soda-lime glass
SLS	Swiss Light Source
TC	Tungsten carbide
TGTH	Tight gradient threshold
TIFF	Tagged image file format
TITH	Tight intensity threshold
TOMCAT	Tomographic microscopy and coherent radiology experiments
VISAR	Velocity interferometer system for any reflector

11 Acknowledgments

This research work has been carried out in the course of my activity as a scientific researcher at the Fraunhofer Institute for High-Speed Dynamics, Ernst-Mach-Institut, EMI, in Freiburg and Kandern, Germany.

First of all, I would like to express my sincere gratitude to my doctoral supervisor Professor Stefan Hiermaier, without whom I would not have been able to accomplish this research. His enthusiasm for the topic and his support and appreciation of my work pushed me to successfully complete this extensive thesis. Furthermore, his confidence and patience gave me the opportunity to research the topic very comprehensively.

Further, I would like to thank the second examiner Professor Gebbeken and the external examiner Professor Nik Petrinic. It is a great honor that they took the time and effort to evaluate my work.

I would particularly like to thank my supervisor Elmar Straßburger. I am extremely grateful for his guidance and feedback at all times. His expertise and overall insights in this field of research greatly helped me to shape the direction of this thesis. I am also grateful that he gave me enough space and kept me free of many obligations during the critical final phase of writing up the thesis.

Further, I would like to express my gratitude and appreciation for Dr. Frank Bagusat and Dr. Martin Sauer for their advice and very dedicated feedback on my work. The numerous discussions on the PPI topic have helped me a lot to interpret the results. They also helped in an essential matter by conducting the PPI tests on the single-stage accelerators, together with Siegfried Pfändler, Michael Maurer and Werner Stein. I am also thankful to Gregor Popko for supporting the setup of the PDV measurements.

Many thanks also to Dirk Heidenreich for his vigorous support of the setup and the conduction of the PPI tests on the two-stage accelerator. He also helped in designing the demountable confinements. Furthermore I would like to express my gratitude to Thomas Wünsch, Peter Herud and Enrico Pauly for the conduction of the pre-damaging tests and the dedicated preparation and processing of the glass samples.

I would also like to acknowledge Ralph Langkemper, Dr. Victoria Heusinger and Dr. Stefan Moser for conducting the CT scans and for their constructive advice and feedback. Special thanks to Ines Butz for the support of the CT analysis and for establishing contact with the researchers of the ANU, improving the results in an essential matter. A big thanks to Robert Middleton and Dr. Anna Herring for granting me access to the computational facilities and software of the ANU and for supporting me with the data processing. I also want to thank Dr. Margie Olbinado and Dr. Federica Marone for conducting the PCI scans at the PSI.

I am very thankful to Philipp Hahn for his dedicated and extremely helpful support of the compression tests at the MTS machine. I also want to thank Thomas Greuter and Christian Brenneis for their support during the pre-tests.

Acknowledgments

Furthermore, I would like to thank all current and former colleagues at the Fraunhofer EMI for their steady helpfulness and the very pleasant working atmosphere. Special thanks to Dr. Nathanaël Durr for the numerous constructive discussions and his in-depth feedback on the theoretical basics. I also want to thank Dr. Norbert Heider, Dr. Hartwig Nahme, Bernd Dutschke, Vincent Denefeld and Dr. Jörn van Keuk, for their advice and the numerous and fruitful discussions.

I would also like to acknowledge my current head of department Axel Sättler and the former department managers Dr. Manfred Salk and Dr. Marek Dolak, who have always supported me in my work.

Last but not least, I would like to thank my family from the bottom of my heart for their consistent support throughout my whole life. I am especially grateful to my parents for giving me moral and financial support in every stage of my life and to my girlfriend Julia for backing me up during the stressful periods of this work.